University of Southampton

Faculty of Engineering, Science & Mathematics

School of Ocean & Earth Sciences

Hydrothermal alteration of upper oceanic crust formed at fast spreading rates

By

Christopher E Smith-Duque

Vols. I and II

Thesis for the degree of Doctor of Philosophy

May 2009

University of Southampton

Abstract

FACULTY OF ENGINEERING, SCIENCE & MATHEMATICS
SCHOOL OF OCEAN AND EARTH SCIENCES

Doctor of Philosophy

HYDROTHERMAL ALTERATION OF UPPER OCEANIC CRUST FORMED AT FAST SPREADING RATES

by Christopher E Smith-Duque

Hydrothermal circulation plays a fundamental role in the chemical transfer from deep in the Earth's interior to the ocean crust, the oceans and the atmosphere. It is also on of the principal mechanisms for heat transfer from the mantle to the oceans, atmosphere and ultimately, outer space. This process fundamentally influences the composition of the ocean crust during formation and aging as it spreads away from the ridge axis. However, despite much research into hydrothermal alteration of oceanic crust questions still remain including: the thermal and chemical evolution of hydrothermal fluids, the geometry of hydrothermal fluid flow, and the factors that control the nature and extent of hydrothermal alteration of oceanic crust.

In this study, whole rock and secondary mineral characteristics of drilled-in situ ocean crust are used to (i) Characterise hydrothermal alteration for a range of drilled, in-situ fast spread ocean crust sites (ii) assess the factors that control hydrothermal alteration within fast spread ocean crust and (iii) assess the evolution and architecture of hydrothermal fluid.

Deep Sea Drilling Project, Ocean Drilling Program, and Integrated Ocean Drilling Program Sites 504, 896, 843, 1179, 1149, 1224, 1243 and 1256 represent some the most significant penetrations into the upper portion of intermediate and fast spread crust to date. Analyses of whole rock chemical changes, Sr, O. C and S isotope systematics, petrographic observations and analysis of secondary minerals indicate that all sites underwent variable degrees of cold seawater dominated hydrothermal alteration. All these sites represent variations in the composition of the upper crust, basement topography, sedimentation rates, spreading rates, capping rocks, and age. Comparisons between these factors and style and intensity of alteration for each site indicate that spreading rate and age exherts the strongest influence on hydrothermal activity.

Sites 1256 and 504 are the only sites in which both low temperature and high temperature alteration are recovered, both sites now have complete chemical and isotopic records which trace the evolution of hydrothermal fluid through the crust. Chemical and isotopic analyses of anhydrite within the ocean crust and consideration of the sulfur budget at these sites imply that the majority of hydrothermal fluid is heated to moderate temperatures (~250^{o}C) and returns to the oceans as warm diffuse fluids at unaccounted for venting sites.

Contents

Volume I

Volume II

List of tables

List of Figures

Graduate School of the National Oceanography Centre, Southampton

PhD. Dissertation by

Christopher E Smith-Duque

Declaration

The work presented in this thesis is my own, and was done wholly whilst in candidature for a research degree at this university. Where I have consulted or quoted from the published work of others, the source is always clearly attributed. I have acknowledged all main sources of help, and where parts of this work have been published, or have been submitted for publication, this has been clearly stated; in such cases co-authors have contributed in an advisory capacity only

Signed:

Date:

Graduate School of the National Oceanography Centre, Southampton

This PhD. Dissertation by

Christopher E Smith-Duque

Has been produced under the supervision of the following persons

Supervisors

Prof. Damon A.H. teagle

Prof. Martin Palmer

Chair of Advisory Panel

Prof. Steve Roberts

Acknowledgements

Time for some unrelenting over-the-top melodrama, the kind of which would put an academy award acceptance speech to shame!. No experience in my life has compared to the experience this PhD has given me and arguably I have lived more in the last 4 years than I have ever done at any other point in my life. If someone told me as a child that I would be participating in cutting edge science, travelling to some of the most exciting parts of the world, and writing an enormous 'book' about it all I would have treated them in the same light as your average 'clairvoyant' and told them to get lost!. In terms of my PhD, and the experiences I have had, Damon Teagle has, with out a doubt, been the most influential. For my participation on IODP Exp 309 to the Guatemala basin, arguably one of the most exciting periods of my life, I have Damon to thank. In addition, Damon has actively encouraged and supported me during conferences and he has been very supportive in promoting my work and involvement within IODP to other geoscientists. Where advice and direction was needed Damon was always able, often at short notice, to point me in the right direction in terms of my project. In addition, Damon's reading and editing have been instrumental in the production of this thesis. Damon is solely responsible for turning me into a Scientist and he has enabled me to experience every aspect of the scientific process.

Through my experiences during this PhD, I have been fortunate enough to have people that have given me relentless support and encouragement no matter how cranky or anti-social I was feeling!. The list is long, and would read like film credits if I were to mention everyone. However, a few key people stand out:

Matthew Cooper, Andy Milton, and Darryl Greene have been of tremendous support all of whom run around like a "*blue ass fly*" to run an efficient and reliable geochemistry lab. Thanks must also go to Matthew and Andy for the time they took to turn me into a chemist and the training on the myriad of techniques I used to analyse my samples. For NOC'S gossip, I could always turn to Bob and John, who made for me far too many thin sections. Thanks goes to Mike Balshaw for analysing many of my carbonate samples, and for taking the time to explain the inner workings of a Europa Geo 20-20 Mass Spce!. Thanks must also go to Jeff alt (University of Michigan), for Oxygen analysis a the University of Michigan, Mike Odling (University of Edinburgh), for XRF analyses, Neil Banerjee (University of Wstern Ontario) for great coffee and

whole rock oxygen analyses. Special thanks goes to Tina Hayes, who guided me through the labs in the beginning of my PhD, I will remember for cheery disposition and her ability to make anyone smile. In addition Tim Brewer, who ran many of my samples by XRF, and taught me petrology as an undergraduate at the Universtiy of Leicester, will also be remembered.

On many occasions, Rosalind Coggon, a former student of Damon, has been the friendly face that would answer all my questions, no matter how ridiculous. In addition, Roz took the time to demonstrate many of the sample preparation techniques that were essential for analysis of my samples.

The Shipboard Scientific Party of IODP EXP 309 will not be an easy bunch of people to forget!. Their combined knowledge and experience is second to none and every one was more than happy to help and advise me during the cruise. I am especially grateful to Christine Laverne, an excellent petrologist and artist, who helped me hone my own petrographic skills, and has inspired new directions in my own art work. Christine, Laura and I did our best to avoid cabin fever by describing the 5000 veins recovered during Exp 309, in various languages an guises, and in doing so coined '*no vein no pain*'.

In addition to Damon Teagle's editing, Martin Palmer has, at exceptionally short notice, read and made many helpful suggestions in my thesis, whilst at the same time given me positive feedback.

In the last four years, I have made many great friends in Southampton, who I have shared some amazing experiences with, being with friends or on some silly climbing miss-adventure have proven to be the ultimate escape. These people have helped my maintain a healthy level of insanity, which, I think is essential to the completion of any PhD. During my PhD I also give thanks to Marc, with whom I shared a great year of van trips, tea rooms, 'cyder', climbing, and other worthy distractions from this thesis.

The final acknowledgement unquestionably goes to my Mum and Dad. Without their immeasurable support, completion of this PhD would not have been possible. Everything from carting my stuff around, financial support, putting up with me when I come home, and (most importantly) moral support, means I am forever in their debt and serves as a constant reminder of how lucky I am to have such a loving and caring family.

‘No *Vein...*

No *Gain!’*

Chapter 1

Introduction

1. Introduction

1.1. Rationale

The formation of the oceanic crust is the result of decompression melting of the upper mantle due to the divergence of the oceanic lithosphere on mantle convection cells. The heat driving mantle convection and the heat from the cooling of new oceanic crust is essentially the driving force behind hydrothermal circulation. Cold seawater that enters the crust, heats up, and reacts with the oceanic crust before returning to the oceans as a naturally buoyant, hot, hydrothermal fluid.

The hydrothermal alteration of the oceanic crust at the ridge axis and the ridge flanks has a profound impact on the chemistry of the ocean crust, the oceans, the atmosphere, and, indirectly the continental crust and mantle through subduction of altered crust. The heat and nutrients carried by hydrothermal fluids provides energy to a unique range of biological communities. In addition, hydrothermal systems are responsible for the formation of significant base-metal ore deposits, hence active systems provide important analogues for ancient volcanic-hosted massive sulfide deposits. However, the factors that influence the geometry and extent of hydrothermal systems, such as fluid and heat fluxes, the evolving chemical compositions of fluids as they circulate through the systems and, the architecture of the flow system remain poorly understood. Seismic velocity profiles of ocean crust and mid ocean ridges, sampling of ophiolites, and recovery of in-situ samples of modern ocean crust have contributed to the current understanding of how the ocean crust forms and its structure. In terms of stratigraphy, ocean crust formed at fast spreading rates is relatively simple; consisting of seafloor sediment, extrusive lavas, sheeted dykes, gabbroic bodies and residual mantle rocks in near-idealised layering. Ocean crust formed at fast spreading rates, therefore, offers the best chance of characterising hydrothermal alteration. Because oceanic crust formed at fast spreading rates covers 30% of the Earth's surface, it is one of the most important tectonic regimes on Earth.

The aims of this thesis are; 1) characterise alteration of ocean crust formed at fast spreading rates, 2) to quantify and assess the variability of hydrothermal alteration in fast spread crust, and 3) to elucidate which factors (such as crustal age, sediment cover sedimentation rate, lava morphology, cap-rocks or basement

topography) most strongly influence the style and intensity of hydrothermal exchange with the oceans.
This will be accomplished through the characterization of cores and regional information from various sites drilled into the ocean crust formed at fast spreading rates including Site 1256, the first recovery of a complete section of intact upper oceanic crust down to gabbros.

1.2. Structure and formation of ocean crust

The diverging plates of the oceanic lithosphere create weakness and space which can accommodate new intrusions and eruptions on the seafloor. Our current understanding of the processes which form oceanic crust, and the nature of its composition, structure, and alteration, are based on a combination of remote geophysical surveys, in-situ sampling of modern oceanic crust by drilling, and sampling of ophiolites, (e.g. Runcorn, 1959; Vine and Matthews, 1963; Gass, 1968; Lister, 1972; Mottl and Wheat, 1994; Alt, et al., 1996). Dredging, submersible dives and shallow drilling in tectonic windows have also contributed to our current knowledge of crustal formation. There are, however, problems when dealing with rocks recovered from tectonic windows and ophiolites: 1) Ophiolites such as the Troodos ophiolite are thought to have formed in a supra-subduction zone setting (Miyashiro, 1973; Jenner et al., 1987), which differs from the setting of mid-ocean ridges in major ocean basins, 2) Post obduction processes, such as regional metamorphism, and deformation often obscures the original, in-situ alteration and igneous features and 3), The relationships seen within tectonic windows, between the different lithologies, their transitions, and their geological context are largely lost or very poorly understood because there is no complete section of oceanic crust from any one site. Rocks recovered from such sites, therefore, must be treated with caution when one draws any interpretation for modern ocean crust. The best way to address the problem is by deep drilling of a complete, in-situ section of modern oceanic crust. However, despite over 30 years of ocean drilling there are very few sites where depths greater than 50 m into crustal basement have been penetrated. This hampers study of ocean crust in three dimensions.

Based on geophysical surveys, the majority of ocean crust is approximately 6.5 ± 0.7 km thick (White et al., 1992) and it generally contains four seismically

distinct layers at most ocean crust sites. These consist of; 1) sediment, 2) a low velocity upper layer, 3) a high velocity lower layer, and 4) a deep very high velocity layer that makes up the upper mantle (>8 km/s^{-1}) (Runcorn, 1959). These seismic layers have been assigned a lithology according to the association with the Troodos succession in Cyprus (Gass 1968) and their similarity with other ophiolites including the Oman and the Papua New Guinea. The following assemblage is now adopted as typical ocean crust structure, in ascending order of depth (Figure 1.1); 1) pelagic sediments (present in most crust), 2) hydrothermal sediments (may or may not be present), 3) extrusive volcanic rocks, 4) sheeted dykes, 5) gabbros, which overlie gabbro norites and basal mafic cumulates, and 6) residual mantle rocks (Penrose Conference Participants, 1972). In truth, the structure of ocean crust is not ubiquitous, because the ocean crust is, exhibiting a wide range of tectonic settings, structures and lithologies.

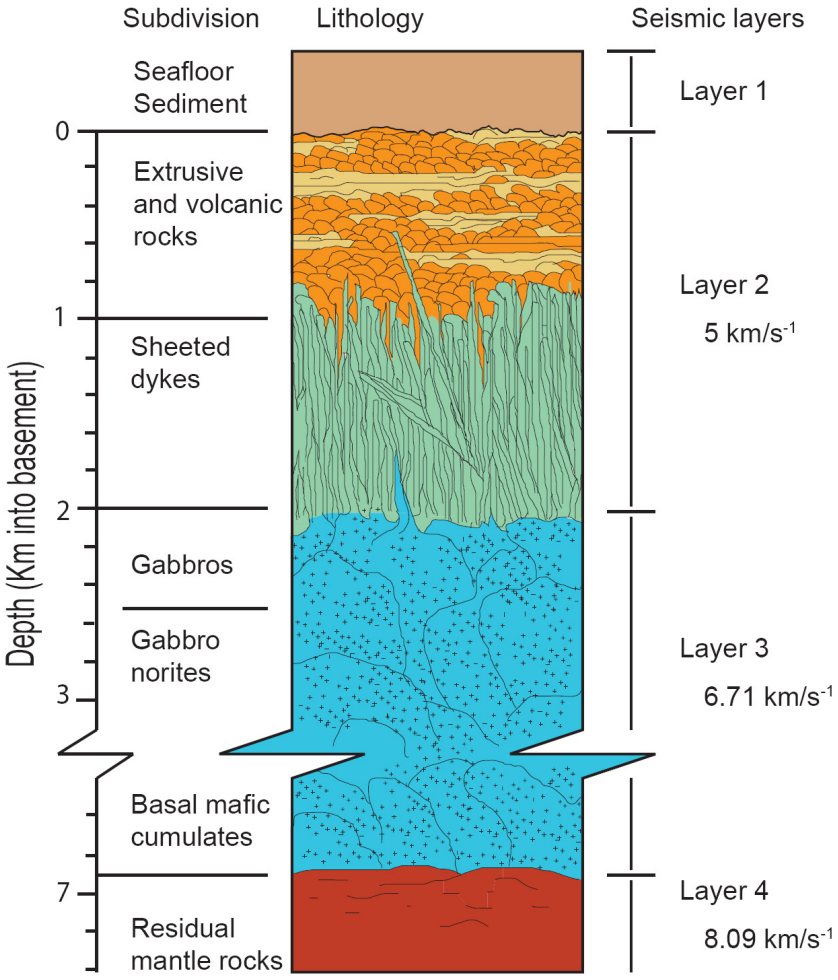

Figure 1.1. Idealized crustal section with associated geophysical boundaries after Penrose Conference Participants (1972).

1.3. Affects of spreading rate

Spreading rate is thought to have a large impact on crustal heterogeneity. Axial melt lenses at fast-spreading centres appear to be continuous on the time scales of observation with an approximately steady-state of magma intrusion and cooling (Sinton and Detrick., 1992). This leads to a higher occurrence of hydrothermal vents along the axis than on ridge flanks or abyssal plains, and a crust that more closely fits an idealized layered structure, with smooth basement topography and abundant sheet flows (Haymon et al., 1991; Macdonald, 1998; Karson, 2002; Carbotte & Scheirer, 2004;). Ocean crust formed at slower spreading rates (<40 mm/yr full rate) can have complex structures, with intermittent magmatism limiting supply at segment ends and resulting in thinner crust. This is thought to generate large throw faults that open tectonic windows and disrupt the crustal structure; leading to cooling of the crust at greater depths (Huang & Solomon., 1988; Mevel & Cannet., 1991; Baker, et al., 1996).

60 % of all ocean crust is formed at fast spreading rates and it forms approximately 30 % of the Earth's surface, hence understanding the nature of this type of ocean crust is of profound importance if we are to constrain the role of hydrothermal circulation within ocean crust. Despite this, most of our knowledge of oceanic crust comes from deep cores of slow or intermediate spreading oceanic crust, as this is where the Deep Sea Drilling Project (DSDP), Ocean Drilling Program (ODP) and Integrated Ocean Drilling Program (IODP) have been most successful at recovering samples (e.g., DSDP/ODP Hole 504B; Alt et al., 1993). Figure 1.2 illustrates the distribution of penetrations greater than 50 m sub-basement according to age and spreading rate.

Only two ODP and IODP Holes penetrate through the entire volcanic section of the upper crust and into the sheeted dyke complex. ODP Hole 504B, located on the southern flank of the Costa-Rica Rift is perhaps the best sampled and studied in-situ basement site to date, penetrating a 6.9 Ma section of ocean crust to the base of the sheeted dyke complex (Alt et al., 1993). ODP/IODP Hole 1256D represents a greater portion

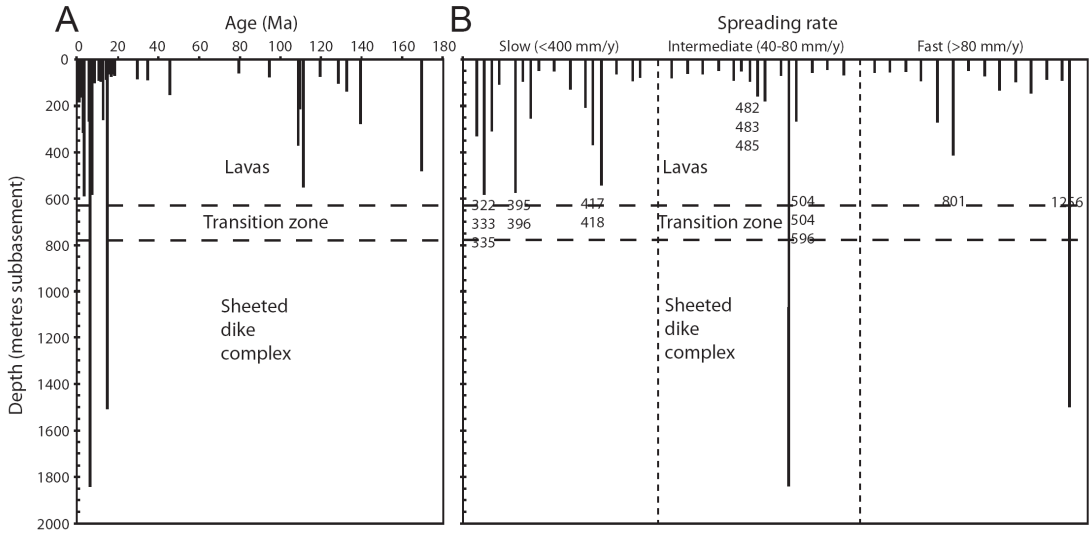

Figure 1.2 A) Basement age vs. depth of basement penetration for holes that penetrate >50m sub-basement, and B) depth of penetration in holes with basement with spreading rate divisions. (Modified from Wilson et al., 2003; Teagle et al., 2006)

of the ocean crust because it has recovered a complete lava and dyke section together with (for the first time) gabbro (Wilson et al., 2006, Teagle et al., 2006). Site 1256 formed at approximately 15 Ma at a superfast spreading rate (220 mm/yr), and, through geophysical surveys and observations of the recovered core, it represents perhaps the simplest structure that closely fits the idealised 'Penrose' crust structure (Penrose Conference Participants, 1972). In addition to Sites 504 and 1256, a number of other shorter penetrations of ocean crust formed at intermediate to fast spreading rates also provide valuable insights into the hydrothermal alteration of volcanic rocks in areas with differing ages, spreading rates, lithologies, and sedimentary burial. These Sites include 896, 843, 1224, 1243, 1149, and 1179 (Figure 1.6).

1.4. Hydrothermal alteration

The study of hydrothermal fluids began when Victorian scientists speculated that the ore deposits of Trondheim in Norway, Rio Tinto in Spain and the Rammelsberg deposit of Germany were formed by exhalation of hot hydrothermal fluids (e.g., Vogt, 1894, 1899). Similar deposits were found in the Troodos ophiolite, Cyprus, in the form of sulphide lenses with underlying stockworks within the host rock. Gass (1968) first implied that the Troodos ophiolite actually represents an obducted slice of ocean crust, therefore modern ocean crust may be undergoing hydrothermal activity in a similar fashion to these deposits.

Sedimentary geochemistry led to the first proposal of hydrothermal circulation by Boström et al, (1969). They suggested that it provided a mechanism for input of Fe and Mn into the oceans and the presence of sediments at the active mid-ocean ridge system with low Al/Al + Fe + Mn ratios. In addition, lavas with slowly cooled interiors were observed to have depletions in Mn, Fe, and Co, compared to fresh glass at the pillow margins, which was similarly interpreted to be the result of element leaching by percolating fluids in cooling fractures within the pillow basalts (Corliss, 1971).

Detection of active hydrothermal venting was carried out by measuring temperature and turbidity above mid-ocean ridges, using a series of thermistors in tow. The sharp temperature anomalies above the Galapagos vent site were hypothesised by Williams et al, (1974) to be the result of plumes of hot water rising buoyantly from a hydrothermal vent. Other lines of evidence for the presence of hydrothermal venting was obtained by experimentation. Before the direct observation of hydrothermal venting, reactions between basalt and seawater were performed. Natural to artificial seawater with variable temperatures, pressures, water-rock ratios, and durations was reacted with basalts with grain sizes that vary from glassy to coarse grained. A detailed review of these experiments is given by Mottl (1983). The most successful experiments by Mottl and Holland, (1978) and Mottl et al., (1979) were able to predict the chemistry of the seafloor hydrothermal vent sites and the chemical changes exhibited by basalts during alteration to greenschist-facies assemblages. Confirmation of deep sea hydrothermal venting at mid-ocean ridge sites occurred in 1979 with a diving expedition using the deep sea submersible '*Alvin*', in which deep

sea hydrothermal fluids venting from chimneys on top of sulphide lenses at mid ocean ridges were observed (Corliss et al., 1979). Future expeditions revealed that such deep sea vents were commonplace along mid-ocean ridges across the world (Edmond, 1980; Macdonald et al., 1980; Detrick and Honnorez, 1986; Rona et al., 1986; Craig et al., 1987; Campbell et al., 1988; Murton and Klinkhammer, 1994; German et al., 1995).

1.4.1. Geometry of hydrothermal systems

Recent understanding of hydrothermal systems in ocean crust comes from numerical modelling and analysis of samples recovered at various deep sea drill sites, diving expeditions, and ophiolites (e.g., Gass, 1968; Chapman and Spooner, 1977; Corliss et al., 1979; Alt et al., 1996). The heating of cold seawater that percolates through the upper ocean crust causes interactions with the host rock, leading to changes in the chemistry of the seawater (which evolves to become a hydrothermal fluid) and alteration of the host rock. The cooling of the oceanic lithosphere and the mid-ocean ridge magma chamber releases heat, which is transferred to the hydrothermal fluids. Hot (~350-450^{o}C) buoyant hydrothermal fluids will rise and vent to into the oceans, thus completing the hydrothermal convection cell. This process enables transfer of heat form the mantle and basement rocks to the oceans. The heat facilitates reactions between the wall rock and fluid, allowing chemical transfer to take place.

Site 504 was the first recovery of a complete volcanic section from true oceanic crust (except ophiolites) and it penetrated over 1km of the underlying sheeted dyke complex. Thus, it has become the reference section for the petrology, geochemistry, hydrothermal alteration, and magmatic and physical properties of the ocean crust (e.g. Becker et al., 1989; Alt et al., 1996). Site 504 penetrated 274.5 m of sediment, 571.5 m of volcanic rocks, 209 m transition zone rocks and 1050 m of sheeted dyke complex. The volcanic rocks are dominated by low temperature alteration, with celadonite, saponite, iron-oxyhydroxides, zeolite and carbonate secondary minerals formed by oxidizing seawater circulating through the upper crust. The extent of oxidation decreases downhole as a result of restricted fluid flow (Alt et al., 1996) towards the lithological transition zone, which is dominated by disseminated metal sulphide mineralization. Alteration of the upper dykes includes; 1)

early chlorite, actinolite, albite-oligoclase, and titanite, followed by 2) quartz, epidote, and sulphides, then 3) anhydrite, and finally 4) zeolite and local calcite. Inferences of temperatures within the upper dykes range from 350-380^{o}C (Alt et al., 1996). In addition to the alteration observed in the upper sheeted dykes, alteration of the lower sheeted dykes includes loss of Al, Mg, Ca, Cu and S, and the formation of hornblende and calcic secondary plagioclase in alteration halos and patches at temperatures of ~300-400^{o}C. Alt et al, (1996) report heterogenous alteration within the sheeted dykes and that the geometry of fracturing exerts a strong control over the intensity of alteration at Site 504 (Alt et al., (1996). Observations from Site 504, ophiolites, and other penetrations of in-situ basement rocks led to the definition of three zones that make up a hydrothermal system. These are, the recharge zone, the reaction zone and finally the discharge zone (Alt et al., 1995), which are outlined in Figure 1.3.

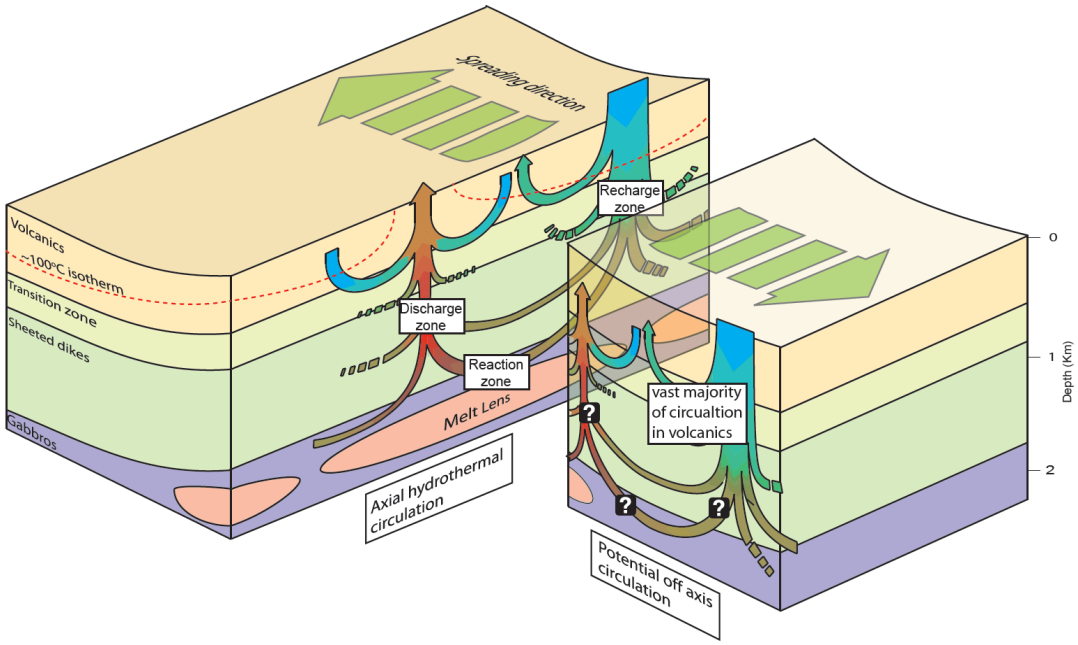

Figure 1.3. Stylised model of a hydrothermal system outlining possible directions of fluid flow and their evolution within oceanic basement. The Recharge zone outlines the area of regional recharge at which seawater percolates into the ocean crust, slowly heating up (~0 to ~150^{o}C) whilst interacting with the ocean crust. The Reaction zone is the hypothetical area on or near a large heat source e.g. the mid-ocean ridge magma chamber where the fluid intensively reacts with the host rock to form hot (~400^{o}C), black smoker-type hydrothermal fluids. After reaction, the hot buoyant fluid rises and cools slightly to (~350^{o}C) and discharges at vent sites. Based on Alt et al. (1995). Potential off axis hydrothermal fluid flow is also included.

Recharge zones may be defined as areas in which cold seawater enters the ocean crust and causes variable alteration of volcanic glass and primary igneous minerals and precipitation of low temperature phases, such as clay minerals, iron-oxyhydroxides, carbonates and zeolites. It is thought that most seawater circulates within the upper volcanics and that only a minority of seawater actually penetrates into higher temperature regimes due to lower porosity deeper in the crust and restrictions created from secondary mineral precipitates (Alt, 1995). For this reason, the 'recharge' zone can be split into open (cold, <40^{o}C, seawater dominated) and restricted (warmer 100^{o} to 200^{o}C slightly more evolved) systems. Unlike 'open' circulation, iron-oxyhydroxides and celadonite are no longer present in restricted systems, which implies reducing conditions (Alt 1989a; Alt, 1995; Teagle et al., 1996; Alt, 1998). Active alteration within the 'recharge' zone may persist for 10's of millions of years during a passive off axis circulation (Parsons and Sclater, 1977) within the upper 200-300m of crust (Fisher et al., 1990). At Site 504 both ridge flank processes and axial hydrothermal processes overlap (Alt, 1995). Observations of higher temperature assemblages, for example chlorite, actinolite, prehnite (greenschist facies) occur at depth, under more restricted fluid flow regimes (Alt, 1995). In addition, the increased abundance of anhydrite (at temperatures above ~120^{o}C) and the increased albitization of plagioclase indicate increased temperature and greater interaction with basalt within this regime. Although the change from low temperature phases to greenschist phases has only been recorded in-situ in two Sites (Site 1256 and Site 504), observations of alteration in the upper oceanic crust are well documented (e.g. Andrews, 1977; Staudigel et al., 1981; Bohlke et al., 1981; Laverne and Vivier, 1983; Alt and Honnorez, 1984; Bohlke et al., 1984; Staudigel and Hart, 1985; Berndt and Seyfried, 1986; Alt et al., 1986a, 1992; Alt, 1993; Teagle et al., 1996).

The reaction zone is the theorised location at which cool hydrothermal fluids at depth evolve to become hot hydrothermal fluids by reacting near, or close to, a heat source, such as a magma chamber, before they return to the oceans as hot (~350-400^{o}C) black smoker type fluids at mid-ocean ridges. The mineral phases actinolite, prehnite, chlorite, secondary Ca-plagioclase are more abundant. In the lower sheeted dykes and gabbroic bodies at Sites 504 and 1256 respectively, secondary clinopyroxene, Mg-hornblende, and calcic plagioclase are prevalent with recorded temperatures in excess of 425^{o}C (Wilson Teagle Acton et al., 2006; Vanko and

Laverne, 1998). Despite much work (e.g. Constantinou, 1980; Richardson et al., 1987; Alt, 1994; Alt et al., 1995; Embley et al., 1998; Coggon, 2006; Vanko and Laverne, 1998), the nature and processes by which fluids acquire black smoker-like fluid compositions remains poorly understood. Vanko and Laverne, (1998) suggest that the reaction zone can be separated temporally as conditions evolve from initial fluid infiltration to steady state and finally waning hydrothermal activity. Because the majority of sampled black smoker fluids with seawater chlorinity have depleted Na concentrations, it is commonly assumed that this arises from albitization in the reaction zone prior to upwelling (Von Damm, 1995). Although albitization is observed in rocks at reaction zone temperatures (250^{o}C-400^{o}C) (Gillis and Thompson, 1993), experimental studies by Berndt and Seyfried, (1993) indicate that the conditions for the formation of black smoker type fluids deep in the crust can not be explained by the formation of albite and oligoclase in the reaction zone. Vanko and Laverne, (1998) report early widespread magmatic plagioclase (An_{40-90}) and clinopyroxene replaced by secondary plagioclase (An_{54-95}), hornblende and minor secondary clinopyroxene. They imply that these observations of calcic plagioclase at Site 504 and within the Oman Ophiolite satisfy the conditions for black smoker fluid formation determined by Berndt and Seyfried, (1993) and that hydrothermal anorthitization is common in modern ocean crust.

Hydrothermal upflow occurs where hot buoyant hydrothermal fluids, having acquired their black smoker compositions, return to the oceans through narrow conduits, ultimately forming hydrothermal vent systems where fluids may mix with cold seawater, i.e., the discharge zone shown in Figure 1.3.1. Such feeder zones were first found in ophiolites (Constantinou, 1980), and later observed within the ocean crust on fault scarps and drill cores (e.g., Embley et al., 1998). This is supported by the observation of epidote at the base of the sheeted dykes and gabbros at Site 504 and 1256 (e.g., Alt, 1995; Teagle et al., 2006). Formation of this mineral requires high volumes of water passing through to the rock (e.g., Richardson et al., 1987). Epidote at Sites 504 and 1256 is thought to be formed during focussed upflow (Alt, 1995; Teagle et al., 2006), although it can be found within the 'reaction zone', for example in ophiolites (Richardson et al, 1987). The geometry of ridge-flank hydrothermal circulation has been further studied by the distribution of microeathquakes at the East Pacific Rise, which are interpreted to be the result of hydrothermal cracking. These studies have shown that along axes, hydrothermal circulation is strongly aligned to the

ridge axes, with a clearly defined recharge zone above an axial discontinuity and a band that lies directly above the axial magma chamber (Tolstoy et al., 2008).

1.4.2. Modelling of hydrothermal fluid flow

The evolution of hydrothermal fluid through the ocean crust and alteration of the ocean crust requires significant heat to drive the system. Early models of heat flow were based on the principle that heat flow and bathymetry is highest at mid ocean ridges (MOR), because this is the surface expression of the rising limb of a convection cell (Holmes, 1931). An alternative model proposed the cooling of a ridged plate moving at constant velocity away from the ridge axis, which acts as a hot boundary. This model was shown to roughly agree with measured heat flow data gathered from various sites around the world (Langseth et al., 1966; Lister, 1972). Lister (1972) used measurements of low heatflow and the non-refractive scatter in flank areas to infer that hydrothermal circulation was the dominant mechanism for heat transfer.

Heat flow and bathymetry data shows an empirical relationship between heatflow and age, and depth with age, that is similar for all oceans (Sclater and Francheteau, 1970; Sclater et al., 1971). This is consistent with the simple model of thermal contraction that leads to isostatically compensated density increases (McKenzie and Sclater, 1971; Sclater et al., 1971; Davis and Lister, 1974). In addition, geophysical evidence implies that plate thickness increases with age (Parker and Oldenburg, 1973). Heat flow, however does not vary indefinitely with age, and as crust ages (~65-70 Myr) heatflow and bathymetry approaches a constant value (Richter, 1973; Richter and Parsons, 1975; Mckenzie and Weiss, 1975; Parsons and Sclater, 1977).

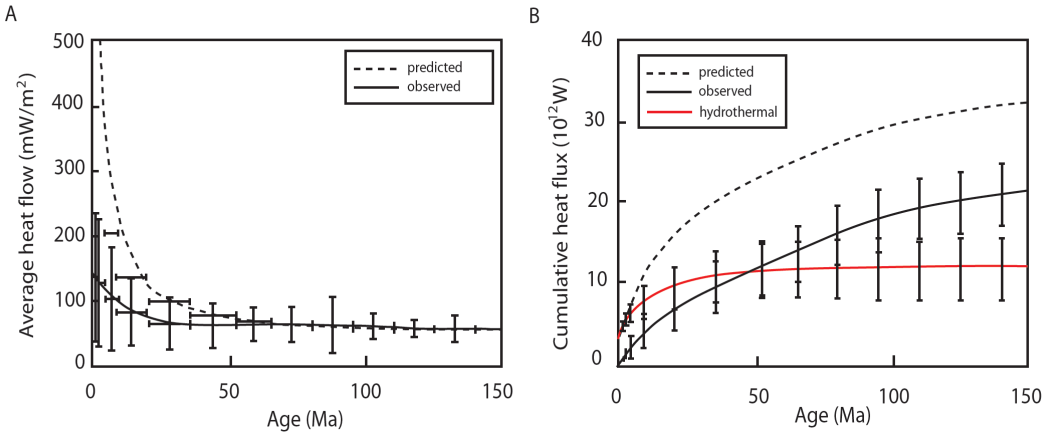

Figure 1.4. (a) Observed and predicted average conductive heat flow vs age, (b) cumulative heat flux vs. age partitioned into observed (conductive) and hydrothermal (predicted – observed). The predicted model is based on the lithospheric cooling model GDH1 (After Stein and Stein, 1994).

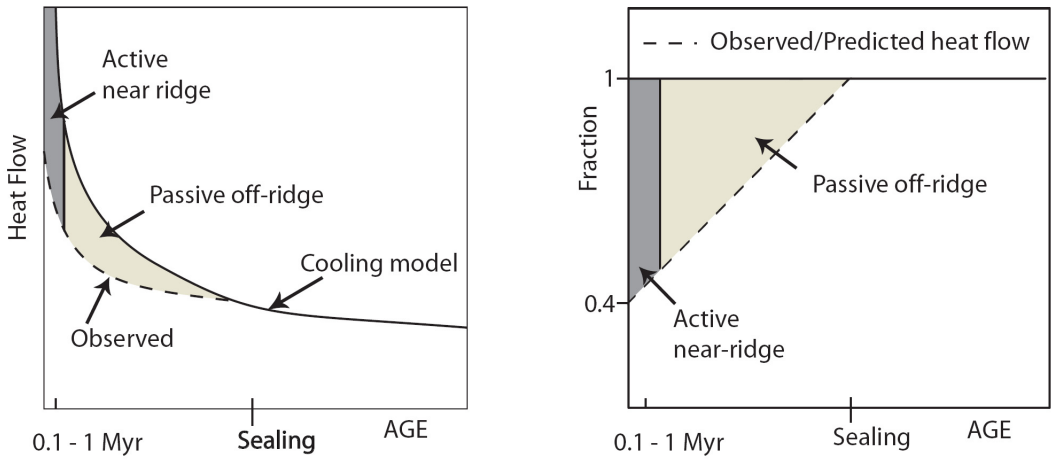

Figure 1.5. Heat flow discrepancy thought to be caused by hydrothermal activity presented as either a), directly from heat flow data or b), a fraction of the predicted heat flow that is observed. Ridge and off axis flow are divided within the discrepancy based on age. Sealing age marks the point at which the precipitation of secondary minerals by hydrothermal activity 'seals' interconnected pore space and fractures (From Stein et al., 1994).

Ultimately these relationships culminated in the lithospheric cooling model GDH1 (Global Depth and Heat flow), which is derived from the joint inversion of variation in seafloor depth and heat flow with age, as indicated in Figure 1.4 (Stein and Stein, 1994). When global heat flow data (Stein et al., 1994) is compared to the GDH1 model a large discrepancy occurs which can only be reconciled by cooling as a result of hydrothermal cooling (Stein and Stein, 1992; Stein et al., 1994) (Figure 1.4).

1.4.3. Ridge flank hydrothermal circulation.

The importance of ridge flank hydrothermal alteration is clearly illustrated by the heat flow models shown in Figure 1.4. In these models approximately 11±4 x 10^{12} W of the predicted global oceanic heat flux (32 x 10^{12} W) can be attributed to hydrothermal flux, of which only 3.2±0.3 x 10^{12} W occurs within 1 Myr of ocean crust formation at the ridge axis. Therefore, even at the most conservative of estimates, ~70% of all hydrothermal heat flux must occur by off axial low temperature alteration (Figure 1.5) (Stein et al., 1995). A more recent estimate of mid ocean ridge (MOR) hydrothermal heat flow of 1.8 ± 0.3 TW (Mottl., 2003) suggests that only 15 % of this heat flow is associated with active MOR systems. Modelling of fluid flow based on basement relief, distribution of sediment cover, conductive heat transfer through sediments and thermal and geochemical homogenisation of pore fluids at the sediment basement imply that passive, off axis hydrothermal circulation takes place and that it is induced by topographic variations (Fisher et al., 1990; 1994). The importance of ridge flank hydrothermal circulation is underlined by the oceanic budget of Mg. A review of heat and mass budget constraints and the composition of black smoker fluids in Mottl and Wheat, (1993) implies that 10-40% of riverine Mg can be taken up by high temperature alteration at the ridge axes (Mottl and Wheat, 1994). Most heat loss occurs on ridge flanks, where temperatures are lower and seawater flux is higher, therefore Mottl and Wheat (1994) suggest that heat loss on flanks, and therefore, upwelling must occur over a wide area (5-30% of seafloor up to 65 Ma) and that temperatures of ~20^{o}C would mean that a barely detectable loss of Mg <1-2% from the seawater would be enough to reconcile Mg mass balance in the oceans. Recent swath map, seismic, and seafloor heat flux data from a range of basement outcrops covering 14500 km^2 of the coccos plate indicate that a high proportion of heat is extracted by advection, requiring a fluid discharge rate of 4-80 x 10^3 litres per second of off axis flow within the area (Hutnak et al., 2008). Limits on the extent of ridge flank circulation are based on studies of heat flow anomalies, tied to sediment thickness, and seismic profiles at Site 504 and 896 (Davis et al., 2004) and extensive modelling based on basement relief, sediment cover, heat transfer, and pore fluid chemistry by Fisher et al, (1990), and Fisher et al, (1994). These studies suggest that significant circulation in ridge flanks only takes place in the upper 100-300 m of ocean crust. Recent insights into basement outcrops on ridge flanks indicate that

advective extraction and fluid flow may be facilitated by high permeability conduits (Fisher et al., 2003a 2003b; Wheat et al., 2004; Hutnak, 2008) and basement outcrops, such as seamounts, acting as areas of focussed fluid flow (Wheat and Mottl, 2000; Fisher et al., 2003).

Hydrothermal evolution of pore fluids and basement geochemistry of the Juan de Fuca Ridge have been extensively studied (Davis et al., 1992; Mottl and Wheat, 1994; Wheat and Mottl, 1994; Thompson et al., 1995; Davis et al., 1997; Wheat and Mottl, 2000). Studies of a transect of the eastern flank of the Juan de Fuca Ridge reveal that pore fluids deviate increasingly from seawater with increasing crustal age (Wheat and Mottl, 1994; Davies et al.,1997; Elderfield et al., 1999; Hunter et al., 1999; Fisher and Davis, 2000; Marescotti et al., 2000). The dependence of basement fluid composition on basement temperature, which in turn is linked to crustal age, sediment cover and depth of fluid circulation (Wheat and Mottl, 1994) has been outlined by recent analyses of carbonate veins along the eastern flank of the Juan de Fuca Ridge (Coggon et al., 2004). These studies indicate that the fluids from which the carbonate veins were precipitated had evolution trends that mirror the near-basement pore fluid compositions and that precipitation occurred for the entire duration of low temperature basement alteration. Elemental leaching from basement and sediment, and incorporation into secondary minerals has been traced by leeched Sr, Ca, Fe, and Mn from basalt and uptake of Mg, Sr, Ca, Fe, and Mn by carbonates, and the removal of Mg, Mn and Fe into clays (Coggon et al., 2004). These studies support the earlier interpretation that off-axis circulation persists for tens of millions of years after crustal formation (e.g., Mottl and Wheat, 1993; Stein et al., 1994; Elderfield and Schultz, 1996;).

1.4.4. Summary.

Despite the uncertainties and factors that might influence these interpretations including sedimentation rates, sample bias, local variations in heat flow and bathymetry and rock chemistry (Stein et al., 1995), off-axis fluid flow and diffuse venting appears to make up the vast majority of hydrothermal circulation within the ocean crust. In addition is plays a critical role in balancing heat flow, fluid fluxes and chemical fluxes. Observations of alteration within the oceanic crust show extensive

variability in the style and intensity of alteration. Global estimates of the heat, fluid and chemical fluxes on mid-ocean ridge axes and flanks (e.g. Palmer and Edmond, 1989; Bickle and Teagle, 1992; Elderfield and Schultz, 1996; Alt, 2003; Mottl, 2003; Mottl and Wheat, 1993; Staudigel, 2003; Teagle et al., 2003; Davis, 2004; Wheat et al., 2004; Stein and Fisher, 2003; Gillis et al., 2005; Hutnak et al., 2008) remain poorly understood due to the lack of regional high resolution data sets and sampling of in-situ basement. The factors that have been implicated to account for this include; variations in the structure of the oceanic crust, sedimentation rates, basement topography, lithology and the nature of mid ocean ridge magma chambers. Recent studies, however, suggest that spreading rate may have a significant role in the style and intensity of hydrothermal alteration. (e.g., Haymon et al., 1991; Karson, 2002; Alt et al., 1996; Teagle, 2003).

1.5 Aims and outline of this thesis

The aim of this thesis is to assess which factors affect the style and intensity of hydrothermal alteration of ocean crust formed at fast spreading rates by observations and analyses of a range of in-situ basement sites formed at fast to superfast spreading rates. The visible manifestation of hydrothermal processes at basement sites are the replacement of primary igneous phases and filling of fractures and vesicles with secondary minerals.

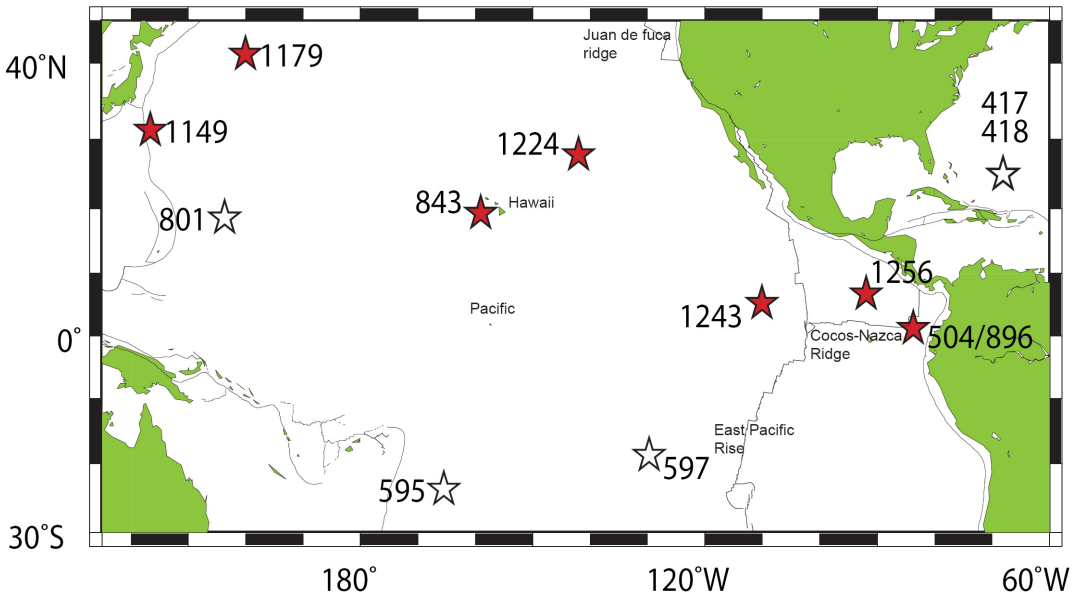

Figure 1.6. Locations of in-situ basement sections studied in this thesis (red) and Sites with potential for further analyses (clear) that formed at intermediate and fast spreading rates.

Chemical analyses of the secondary minerals, together with fresh and altered whole rock samples, are used to assess the chemical changes associated with alteration, the extent of fluid-rock interaction and the compositions of the fluids from which the secondary minerals precipitated. In addition, an assessment of the tectonic settings, the architecture, sedimentary history, and basement topography of each site will be made. Figure 1.6 shows the location for all basement sections that are covered in this study.

Chapter 2

The analytical techniques and methods used, including precision and accuracies are described in Chapter 2. Measurements of major elements, trace elements, rare-earth

elements (REE), $^{87}Sr/^{86}Sr$, $\delta^{18}O$, $\delta^{13}C$, and Fe^{2+}/Fe^{3+} were carried out on whole rock specimens, mineral separates, and glass samples. In addition, leaching experiments carried out on a selection of least altered whole rock samples and clay minerals are also reviewed here.

Chapter 3

The geology, petrography and chemistry of Site 1179 is described here. The first of the major sites to be studied, Site 1179 penetrates ~100m of ~129 Ma basement on the North West Pacific Ocean on the Pacific-Inzanagi ridge. This Site formed at a fast spreading rate, it has undergone relatively little sedimentation, and has a smooth basement topography. Petrographic descriptions and analyses of major elements, trace elements, REE, $^{87}Sr/^{86}Sr$, $\delta^{18}O$, $\delta^{13}C$, and Fe^{2+}/Fe^{3+} are used to characterise and quantify alteration at this Site. In addition, chemical changes were calculated from calculated precursor compositions following Gresens (1967) and Grant (1982). Precursor compositions were assessed in several different ways in order to determine chemical changes that reflect, as close as possible, changes from the primary igneous composition. In this chapter, links between Site 1179 basement and nearby Shatsky Rise plume are tested by assessing the variations on whole-rock $^{87}Sr/^{86}Sr$ and the influence alteration may have on what may be presumed to be the primary compositions of the basalt

Chapter 4

Site 1256 is described and discussed in a similar way to Site 1179. Site 1256 represents the most complete in-situ section of modern ocean crust recovered to date, with penetration encompassing the lavas, transition zone, sheeted dykes, and into the gabbros. With perhaps the highest resolution of samples, Site 1256 presents the best opportunity characterise hydrothermal alteration for a large section of upper ocean crust formed at superfast spreading rates. To this end whole rock samples, glass separates, and mineral separates are analysed for major elements, trace elements, rare-earth elements (REE), $^{87}Sr/^{86}Sr$, $\delta^{18}O$, $\delta^{13}C$, Pb-isotopic ratios, and Nd-isotopic ratios. Following the methods outlined in Chapter 3 (Site 1179), the chemical changes at Site 1256 are calculated. A range of glass samples and leached whole rocks constrain

primary mineralogy. The nature of low temperature fluid though the analysis of carbonate veins is also discussed. Anhydrite at Site 1256 and the nature of high temperature fluid evolution at Site 1256 is discussed in Chapter 8.

Chapter 5

In this Chapter the petrology and chemistry of Site 1149 is discussed in detail. At an age of 132 Ma with ~130 metres of penetration, Site 1149 is important because it represents relatively old ocean crust formed at fast spreading rates. Analyses of recovered samples include; major elements, trace elements, rare-earth elements (REE), $^{87}Sr/^{86}Sr$, $\delta^{18}O$, $\delta^{13}C$, from secondary minerals and whole rock samples. Characterisation of alteration at this site is achieved by petrographic observations, analysis of the chemical change from the primary igneous protolith, and studies of the fluid chemistry from analysis of carbonate.

Chapter 6

Here, brief summaries discuss the geology and petrography of DSDP/ODP Sites 504, 896, 1243, 1224, and 843. These sites penetrate oceanic basement in a wide rage of tectonic and geological settings at different ages. Thus, they are essential for a true global appraisal of hydrothermal activity of ocean crust formed at fast spreading rates. In order to improve resolution for a more complete assessment of alteration and chemical change, additional whole rock and carbonate data was collected for Sites 843, 1224, and 1243 during this study. These include major elements, trace elements, rare-earth elements (REE), $^{87}Sr/^{86}Sr$, $\delta^{18}O$, $\delta^{13}C$, which are used to quantify chemical change and to assess the nature of the low temperature fluid to which all secondary minerals at these sites precipitated. Site 504 penetrates the extrusive section and most of the dykes, and because it is currently the best documented sample of modern ocean crust, it is the reference section to which all other oceanic basement sites are compared.

Chapter 7

Chapter 7 forms the synthesis of the petrographic, geochemical, tectonic and geological features for all the Sites that this study covers. Sites 1179, 1256, 504, 896, 1224, 1243, and 843 are a comprehensive suite that span over 170 m.y. of crustal accretion at intermediate to fast spreading rates in the Pacific. The differing tectonic settings, sedimentary rates, basement topography, igneous stratigraphy, age, and spreading rates encountered at each Site are all factors that may act as a control on hydrothermal activity in oceanic crust. The influence of these parameters on hydrothermal activity in upper oceanic crust is discussed.

Chapter 8

Anhydrite at Site 1256 offers new insights into fluid evolution during mid-ocean ridge hydrothermal circulation. In this chapter, anhydrite from both Site 1256 and 504 (the only basement sites that are deep enough to recover in-situ anhydrite) is compared. Because anhydrite ($CaSO_4$) undergoes retrograde solubility and precipitates at temperatures greater than ~120^{o}C, the REE, $^{87}Sr/^{86}Sr$, $\delta^{18}O$, Sr/Ca and petrographic observations can be used to constrain fluid evolution at warm (100^{o}C) to hot (400^{o}C) temperatures; including, the geometry and timing of fluid flow and fluid/rock interactions. The distribution and abundance of anhydrite is also used to make inferences into the nature of sulfate during hydrothermal circulation.

Chapter 2

Sample preparation and analytical methods

2. Sample preparation and analytical methods

2.1 Introduction

This chapter describes the analytical techniques employed to characterise the hydrothermal alteration of ocean crust formed at fast spreading rates. The sample suite comprises volcanic and intrusive rocks, secondary mineral separates, and glass samples from scientific ocean drilling sites on fast spread ocean crust.

The combined dataset produced from these techniques includes: major element concentrations, trace element concentrations, rare earth element (REE) concentrations, Sr, $\delta^{18}O$ and $\delta^{13}C$ isotope ratios, C and S, H_2O concentrations, and Fe^{2+}/Fe^{3+} ratios. Analytical precision, accuracy and detection limits for all analyses are evaluated in here.

2.2 Sample selection and preparation.

The method of preparation used for each sample is described in this section. This section also highlights any potential uncertainty that is inherently associated with the procedures described for each sample suite. Samples include: Whole rock samples, whole rock leached residues and leachates, volcanic glass, and mineral separates (carbonates, clay minerals, clay mineral leaches, and anhydrite).

2.2.1 Whole Rock samples

Whole rock samples consist of core sections and fragments, all of which were chosen to best represent the variations in alteration and lithology that occurred at each site. Subsamples that represent all the geological features within each sample were prepared for polished thin sections for petrographic study. Samples for geochemical analyses with distinct zones of alteration were separated, where possible, into sub samples by sawing with thin diamond rock saw blades. To obtain a homogenous sample for geochemical analyses veins and heterogeneities were avoided. The samples were then

prepared by grinding rough edges on a coarse diamond grinder followed by grinding on a lap with a fine (100μm) corundum powder to remove saw
marks and weathering rinds. To remove remaining mud from sawing and corundum powder the samples were scrubbed, washed in tap water, and repeatedly ultra-sonicated using 18.2Ω milliQ water until the water remained clear after each ultrasonic step.

Samples were measured for specific gravity by recording the mass of the sample at in air at ~1atm followed by measuring an immersed sample on a submerged gondola shown in Figure 2.1.

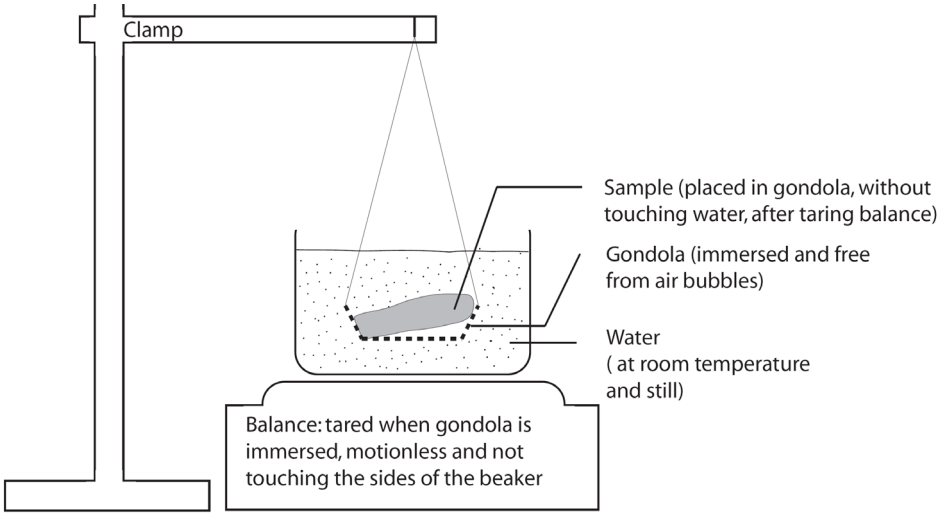

Figure 2.1. Set up for measuring displacement of rock samples.

Specific gravity was calculated using the following expression:

$$\rho_{sg} = \frac{x_{mass(air)}}{x_{mass(water)}}$$

All specific gravity measurements were calibrated by measurements of pure quartz and barite samples both of which have known specific gravities. Repetitions of the internal standard (quartz) measured at 2.65 with an error of 0.57% (n=32). After measurement of specific gravity, whole rock samples were dried overnight at 70^{o}C, crushed on a pure iron fly press to coarse mm-sized chips, and ground to fine powder in a pure Cr-steel tema. For crushing, samples were bagged and the bag was wrapped with a clean sheet of paper to avoid contact between the metal plates on the fly press and the sample. Any paper and plastic was removed from the sample after crushing and the fly press was cleaned after each use. Grinding continued until the powder was not gritty to

the touch. The pure Cr-steel tema was cleaned after each use and periodically 'flushed' by grinding pure acid washed low iron sand for ~2 minutes. All cleaning and crushing work was carried out in a clean sample preparation room using vacuum extractors to minimise cross-contamination from airborne whole rock powder. In addition, clean nitrile gloves were worn to handle samples. Dissolution of whole rock samples is described in Section 2.2.6.

2.2.2 Glass samples

Separates of fresh glass recovered from ODP/IODP Hole 1256D were run for their Sr-isotopic compositions and trace and REE concentrations in order to deduce the primary composition of basement at Site 1256. Samples were selected on the basis of least alteration and to give a representative distribution through the extrusive section of Site 1256 basement. Selected samples were highly vitreous with no signs of devitrification, discolouration from secondary minerals, oxidation and vesicles.

Glass samples were lightly crushed using a pure agate pestle and mortar into 1 mm sized chips, cleaned in an ultrasonic bath repeatedly until water was clear and dried. The glass chips were subsequently hand picked and further washed in an ultrasonic bath using 18.2Ω MilliQ water to ensure absolute purity. A subsample of glass chippings 10 mg, accurately weighed to 4 significant figures, was taken for standard HF dissolution (Section 2.2.6) and made up to a mother solution with a dilution factor of 350-450. This mother solution was then further subsampled for trace and REE measurements by ICP-MS (Section 2.3). Most samples were also analysed for Sr-isotopic composition by TIMS (Section 2.3).

2.2.3 Whole rock leachates

In order to ascertain the primary $^{87}Sr/^{86}Sr$ value and trace and REE composition for ODP/IODP Sites 1179, 1149, 843 and 1256 whole rock samples were selected for leaching experiments which are discussed in detail in section 2.5. All leachates underwent standard HF dissolution (Section 2.2.6) to be made into mother solutions.

The mother solutions are subsampled for analysis of $^{87}Sr/^{86}Sr$ by TIMS and trace and REE by ICP-MS.

2.2.4 Carbonate and anhydrite mineral separates

For this study basalt samples containing carbonate veins or patches were chosen for analysis. 25, 19 and 7 carbonate samples were hand picked from ODP Holes 1149D, 1179D and 843B respectively. Anhydrite from Sites 504B (9 samples) and 1256D (20 samples) were also sampled.

Carbonate and anhydrite vein separates were crushed in an agate mortar and pestle, sieved and hand picked. The separates of pure (99% pure by visual observation) carbonate were then leached in 3M HNO_3 for >24 hr and residue was centrifuged for 2 minutes to reduce contamination from other secondary minerals, particularly clays. The leachate was evaporated and re-dissolved in 2% HCl to form carbonate mother solutions. Anhydrite was dissolved by using 18.2Ω MilliQ water (heated to 70^{o}C and left overnight) and then centrifuged to remove non-dissolved particulates. The remaining solution is carefully removed from the centrifuge tube and accurately weighed into 12 mL HDPE vials. Mother solutions for carbonate and anhydrite were accurately made with more 18.2Ω MilliQ water and ~2 drops of conc. (sb) HNO_3 to keep the trace metals in solution. Final mother weight was ~10 mL. An aliquot of this mother solution was accurately subsampled and analysed for Trace and REE concentrations by ICP-MS following the procedure outlined in Section 2.2. Additional subsamples from the mother solution were analysed for Sr isotope measurement by TIMS (Section 2.2), major element concentrations by ICP-MS (Section 2.3). A subsample of pure carbonate powder was also sampled (~10-30 mg accurately weighed) for $\delta^{13}C$ and $\delta^{18}O$ measurement. Pure anhydrite powder was also subsampled for $\delta^{18}O$ measurement (Section 2.3).

2.2.5 Clay mineral separates and leachates

Basement rocks from ODP, IODP Hole 1256C, D and ODP Hole 1149B and D were sampled for secondary clay minerals. Pure clay samples were separated by hand picking from veins, alteration patches and breccia matrices. Clay separates are powdered using a pure agate pestle and mortar and then a 50 to 100 mg sub-sample

(accurately weighed) is transferred to a clean Teflon Salivex vial for leaching. Clay leaching is done to effectively further purify the sample so that we only measure the Sr isotope ratios, trace elements and REE bound into the crystal structure of the clay mineral. Interlayer cations may have been introduced at any time after the formation of the clay and therefore these will obscure data relating to the original clay.

1 mL of 1M NH_4Cl solution was added to the sample prior to agitation for 30 minutes on a laboratory agitator. The sample is left to stand overnight, then it is centrifuged to ensure solid material remains at the bottom of the Teflon vial. The leachate was removed and discarded, using clean disposable 3 mL pipettes, and then fresh 1mL 1N NH_4Cl is added to the solid sample in the same Teflon vial. 30 minutes of agitation followed by centrifugation was repeated. This process was repeated 4 times so overall there are 5 leaches including the first stage that was left overnight. Pipettes were cleaned by filling the pipette with ~10% HNO_3 prior to immersing the full pipette in a beaker of the same acid overnight. After acid cleaning pipettes were emptied of the cleaning acid and rinsed with 18.2Ω MilliQ water. The pipettes were filled and emptied with 18.2Ω MilliQ water 3 times before drying in a warm lab oven.

The residue is dried and reweighed before undergoing standard HF, HNO_3, HCl digestion identical to the procedure used for whole rock dissolution (section 2.2). A subsample of the mother solution is accurately weighed into clean Teflon Salivex vials, dried and dissolved in 2% HNO_3 (In/Re Spike). The sample is then transferred into weighed, clean, labelled scintillation vials and rinsed out the Teflon Salivex vial to ensure all the sample has been removed from the Salivex vial. Additional 2% HNO_3 (In/Re Spike) is added to the sample for a total dilution factor of ~1000 fold for analyses by ICP-MS (Section 2.3) and accurately weighed. Blanks and standards, as described in section 2.3, are also prepared for ICP-MS analyses. An aliquot of mother solution sufficient to contain 1μg Sr is taken for Sr isotope analyses (Section 2.3). Trace element, REE and Sr-isotopic ratio data for clay mineral analyses is presented in Appendix table D, 2.

2.2.6 Sample dissolution

All the following procedures were carried out in a Class 100 clean room and all preparation was carried out using appropriate clean suits, synthetic nitrile gloves and goggles. Teflon vials are cleaned by an initial rinse with 18.2Ω milliQ water and, if

necessary wiped using lint free clean room towels. The Teflon vials are then submerged for 24 hours in warm (90°C) commercial grade (ARISTAR) 6M HCl, rinsed using 18.2Ω milliQ water and submerged for 24 hours in warm (90°C) ARISTAR 8M HNO_3. The vials are rinsed with 18.2Ω milliQ water three times to ensure all trace of acid is removed and they are left to dry in an air-filtered drying rack at room temperature until ready for use. Scintillation vials, used to present a sample daughter to ICP-MS and ICP-AES, are cleaned by filling the vials with a weak ~2M HNO_3 acid solution. The vials are left to stand overnight after which the vials are emptied of acid and rinsed out 3 times with pure 18.2Ω milliQ water. The vials are left to dry naturally in a clean air filtered cupboard until ready for use. The same procedure is used to clean HDPE bottles and centrifuge tubes.

Typically ~50 mg of whole rock powder, accurately weighed to 4 significant figures, was subsampled for standard HF dissolution and made up to a mother solution (~20-30 mL) with a dilution factor of 350-450. Standard HF dissolution is carried out by dissolving the rock powder in a ~6 mL mixture (3 mL each) of concentrated sub-boiled, distilled (sb) HF and concentrated (sb) 16M HNO_3 overnight in Teflon Salivex vials. The samples are dried down and then dissolved in conc. ~3 mL (sb) HCl overnight. Finally the samples are again dried down, re-dissolved in ~3 mL (sb) 6M HCl and are left overnight at 130°C to ensure total dissolution.

The mother solution is made up by firstly washing out the dissolved sample from the Teflon Salivex vials in 6M (sb) HCl and 18.2Ω MilliQ water into clean, accurately weighed, labelled HDPE bottles. Approximately 1 mL of 6M (sb) HCl followed by ~2mL pure 18.2Ω milliQ water is added to the now empty Teflon Salivex vial to rinse out any remaining sample into the HDPE bottle. The solution is then diluted to an appropriate dilution factor (350-450) by accurately adding 18.2Ω MilliQ water. The mother solution can then be subsampled for Sr isotopic analysis, major and trace element analysis by ICP-AES and trace and REE by ICP-MS. Roughly 20 g of selected whole rock powder, where possible was subsampled for major and trace element analysis by XRF, carbon, and sulphur analyses.

For each batch of samples procedural blanks were prepared and analysed by ICP-MS and ICP-AES.

2.3 Analytical techniques

This section describes the analytical techniques and all preparation uniquely associated with each technique. Errors, precision, accuracy and uncertainty of each technique are discussed. Analytical techniques used in this study include X-ray Fluorescence spectrometry (XRF), Inductively Coupled Plasma Mass Spectrometry (ICP-MS), Thermal Ionisation Mass Spectrometry (TIMS), Inductively Coupled Plasma Adsorption Emission Spectrometry (ICP-AES), Stable isotope analysis (Geo 20-20 mass spectrometer), C and S analysis (LECO CS 225 CS-analyser), and ferric-ferrous ratio determination by titration.

2.3.1 X-Ray Fluorescence Spectrometry

Major and trace element oxide analyses were carried out at both the University of Leicester and Edinburgh University by X-ray fluorescence spectrometry (XRF). Samples for major element analyses were prepared by fusion using a lithium borate flux.

Rock powders were dried at 110^{o}C for over 1 hr and a precisely weighed aliquot (~1g) of sample was ignited at 950^{o}C to determine LOI (Loss On Ignition). Volatiles including H_2O, CO_2 and S within the rock are driven off. A slight mass gain caused by the oxidation of FeO to Fe_2O_3 (Ferrous to Ferric iron) may also occur during this process. LOI is determined by weighing the sample prior to ignition of samples at 950^{o}C for 1 to 1hr 30 minutes. This is followed by cooling in a desiccator and a second weighing after ignition. Nearly all LOI in whole rock analyses of basement sites in this study can be attributed to water since values for C and S are low for most samples. Therefore, we can assume that LOI approximates to H_2O.

For the major elements Si, Mn, Al, Fe, Ti, Mg, Ca, Na, K, and P fusion beads were prepared with a eutectic mixture of lithium metaborate ($LiBO_2$) and lithium14 tetraborate, $Li_2B_4O_7$ (Johnson – Matthey Spectroflux JM100B). Based in the mass of the unignited powder, a sample/flux ratio of 1:5 was used and the sample was fused (in a Pt 5 % Au crucible) at 1100^{o}C in a muffle furnace. The crucible was reweighed and any weight loss was made up with additional flux. The second stage fusion is carried

out over a Meker burner and the mixture is swirled to ensure homogeneity. The sample is then cast in a graphite mould and flattened to a thin disk using an aluminium plunger. The mould and plunger are maintained at 220^{o}C.

Concentrations of Ba, Co, Cr, Cu, Ga, Nb, Ni, Pb, Rb, Sc, Sr, V, Y, Zn and Zr were measured by XRF analysis of pressed powder pellets. Six grams of rock powder were mixed with four drops of 2% polyvinyl alcohol. The mixture was formed into a 38-mm disc on a tungsten carbide disc that was backed and surrounded by boric acid. The disc was then compressed in a hydraulic press at 0.6 tonnes/cm^2 and the resultant sample was then analysed.

The fused pellets and pressed disc samples were analysed on a Phillips PW2404 automatic X-Ray Spectrometer at the University of Leicester using a Rh-tube and the Compton scattering method (Harvey, 1989). The machine was calibrated for low compatible trace element concentrations. The background was positioned as near as possible to the peaks and long count times are used. The raw data is corrected for matrix effects by using theoretical alpha coefficients calculated on the major-elements using the Philips software. The coefficients were calculated to allow for the following discrepancies: 1), The amount of extra flux replacing volatile components in the sample, so analytical totals are 100% less LOI. 2), the intensities of long-wavelength trace-elements (La, Ce, Nd, Cu, Ni, Co, Cr, V, Ba, and Sc) were corrected for matrix effects using alpha coefficents based on major-element concentrations measured simultaneously on the samples. 3) The shorter trace element lines were corrected for matrix effects by using the count rate on the RhKα Compton scatter line as an internal standard (Reynolds, 1963). 4) Synthetic standards were used to correct for line overlap.

	Reference standard (% error)			Mean % error
	BHVO-1	G2	GSP-1	
Major elements (wt %)				
SiO_2	0.002	0.09	0.04	0.04
TiO_2	0.37	4.17	1.54	2.02
Al_2O_3	0.14	1.69	0.07	0.63
Fe_2O_3	7.46	5.93	5.13	6.17
MnO	1.19	0.001	0.001	0.4
MgO	0.28	1.33	1.04	0.88
CaO	0.18	1.02	0.48	0.56
Na_2O	0.44	0.49	0.71	0.55
K_2O	3.85	0.22	0.18	1.42
P_2O_5	1.1	0.001	3.57	1.56
LOI	n/d	n/d	n/d	n/a
Trace elements (ppm)				
Sc	8.81	14.29	3.23	8.77
V	0.95	0.001	3.77	1.57
Cr	0.35	3.45	7.69	3.83
Cu	n/d	18.18	9.09	13.64
Zn	0.76	1.16	0.96	0.96
Ga	4.76	0.005	0.005	1.59
Rb	n/d	1.18	2.36	1.77
Sr	3.47	2.3	0.43	2.07
Y	1.45	18.18	15.38	11.67
Zr	0.11	0.03	0.49	0.21
Nb	5.26	0.003	0.36	1.87
Ba	7.91	0.21	4.73	4.29
Pb	23.08	3.33	7.27	11.23
Th	n/d	1.21	0.94	1.08
U	n/d	3.38	5.51	4.45

Table 2.1. Percentage error of elemental concentrations based on repeated runs (n=3) of international standards BHVO-1, G2, and GSP-1. Percentages are % relative standard deviation.

Calibration of the mass-spectrometer was based on the standards from USGS and CRPG using values from Jochum et al, (1990) for Nb and Zr, and Govindaraju (1994) for all other elements. Typical analytical in this method a number of Geochemical Reference Materials are used to construct calibrations for individual elements and to evaluate precision and accuracy. For samples analysed at the University of Leicester, precision is estimated for each element from multiple analyses of USGS reference materials G-2 (granite), GSP-1 (granodiorite), and BHVO-1 (basalt), and these are shown in Table 2.1. A similar procedure was carried out at the University of Edinburgh and this is outlined in Table 2.2 (Fitton et al., 1998). Samples were run at two different institutions because of variable budgetary and machine time constraints.

	BCR-1			BIR-1			BHVO-1			W-2			DNC-1		
XRF:	Mean	1σ	n	Mean	1σ	n	Mean	1σ	n	Mean	1σ	n	Mean	1σ	n
Nb	13.3	0.1	3	0.6	0.2	3	20.1	0.1	3						
Zr	190.8	0.4	3	13.4	0.3	3	177.7	0.4	3						
Y	37.2	0.2	3	16.4	0.6	3	28.1	0.4	3						
Sr	333.7	0.4	3	110.6	0.4	3	403.0	0.9	3						
Rb	48.1	0.6	3	0.2	0.3	3	9.6	0.3	3						
Th	6.1	0.4	15				1.4	0.5	15	2.5	0.5	10	0.4	0.3	10
Pb	14.0	0.4	15				2.5	0.5	15	8.0	0.4	10	6.2	0.4	10
La	24.9	0.7	15	0.9	1.1	15	14.7	2.1	3						
Ce	53.7	1.3	15	1.0	1.8	15	39.2	0.6	3						
Nd	28.6	1.0	15	2.0	1.0	15	26.4	0.8	3						
Zn	126.3	0.5	3	69.6	0.2	3	105.1	0.6	3						
Cu	26.6	0.5	3	118.0	0.5	3	132.2	3.0	3						
Ni	14.2	0.2	3	152.8	1.0	3	114.3	1.2	3						
Co	37.7		1	52.9		1	43.3		1	48.9	1.1	6	57.0	0.8	6
Cr	28.0	1.0	3	375.0	2.0	3	287.7	0.5	3						
V	390.2	1.4	3	313.7	2.8	3	308.1	1.5	3						
Ba	682.3	6.1	3	17.3	2.0	3	133.6	3.1	3						
Sc	31.7	0.9	3	39.5	0.3	3	29.8	0.4	3						
Ga	21.9		1	16.0		1	21.3		1	18.5	0.4	6	14.7	0.4	6

NAA:	JB-1a	JB-1a	JB-1a	JB-1a			
Run no:	33.1.13	34.1.13	35.1.13	36.1.13	Average	1σ	JB-1a*
La (ppm)	37.40	37.20	37.10	36.30	36.98	0.47	38.10
Ce (ppm)	66.30	61.20	63.50	62.30	63.34	2.18	66.10
Nd (ppm)	25.30	23.10	25.50	25.40	24.81	1.18	25.50
Sm (ppm)	5.11	5.11	5.10	4.95	5.07	0.08	5.07
Eu (ppm)	1.55	1.51	1.48	1.49	1.51	0.03	1.47
Gd (ppm)	n/d	n/d	n/d	5.80	5.80	n/a	5.54
Tb (ppm)	0.66	0.59	0.79	0.77	0.70	0.09	0.69
Yb (ppm)	2.14	2.04	2.08	2.17	2.11	0.06	2.10
Lu (ppm)	0.27	0.22	0.27	0.35	0.28	0.05	0.32
Ta (ppm)	1.62	1.56	1.65	1.63	1.62	0.04	2.00
Th (ppm)	9.69	8.94	9.45	9.40	9.37	0.31	8.80
Hf (ppm)	3.65	3.50	3.62	3.61	3.60	0.07	3.48
U (ppm)	1.98	1.98	1.82	1.76	1.89	0.11	1.60

Table 2.2 Precision and accuracy of major and trace element analysis by XRF based on repeated runs of internationally recognised standards BCR-1, BIR-1, BHVO-1, and JB-1a. After Fitton et al., (1998). All values are in ppm Recommended standard values are taken from Govindaraju, (1994).

2.3.2 C and S analyses for whole rock samples

Measurements of CO_2 and Sulphur content were carried out on a LECO CS 225 CS-analyser at the University of Leicester. Samples are accurately weighed into crucibles containing accelerant chips of iron and tungsten prior to loading into a radio frequency induction furnace. Oxygen was initially purged, then allowed to stream for the duration of combustion. Combustion continued until all the accelerant chips were molten and carbon and sulphur was released as CO_2, CO and SO_2 gas respectively. The gasses pass through a dust filter that prevents silicates, which may cause infra-red wavelength overlap, from entering the infrared cells. Combustion gases were passed through a drying tube of Magnesium Perchlorate to the SO_2 infra red cell. Once determined, the

gases passed through a Platinised Silica Gel catalyst to convert any CO to CO_2, and any SO_2 was trapped out as SO_3.

CO_2 content was measured in the CO_2 infrared cell. The infrared cells have a Tungsten filament at the source that is heated to ~850^oC.The infrared beam is chopped to ~85 Hz and filtered to a monochromatic infrared wavelength that maches the energy of the CO_2 and SO_2 adsorption wavelengths respectively. Output is monitored at 4 Hz, converted to a digital signal and the areas of the peaks are integrated. These values are corrected for sample weight, blank value, and calibration factors to return a total C/S result. The lower limit of detection for C is 10 ppm, with a precision of ± 5 % and for S the lower limit is 10 ppm with a precision of ± 8 %.

2.3.3 Inductively Coupled Plasma Mass Spectrometry

All samples in this study has been measured for their trace and rare earth element (REE) concentrations (Rb, Sr, Y, Zr, Nb, Ba, La, Ce, Pr, Nd, Sm, Eu, Gd, Tb, Dy, Ho, Er, Tm, Yb, Lu, Cs, Hf, Ta Th, U,) by inductively coupled plasma mass spectrometry (ICP-MS) using a VG Plasmaquad PQ2+ and a Thermo Fisher X-Series mk II mass spectrometer located at the National Oceanography Centre (NOC), Southampton.

A subsample (accurately weighed) of mother solution was dried down in Teflon salivex vials, allowed to cool and then ~2 mL of 0.5M HNO_3 solution which is spiked with a known concentration of Indium and Rhenium was added to the sample for dissolution. The internal spike is used to correct the measurements for drift during a sample run, and it can be used as a reference to calibrate the mass spectrometers to the appropriate mass for each element that is being measured. The sample was then transferred to accurately wighed, clean scintillation vials and accurately made up to ~10 mL (~1000 to 2000 fold dilution) daughter solution using the same In-Re spiked acid. The spike acts as an internal standard during analysis. To retain an appropriate dilution, a number of samples including some clay mineral separates, anhydrites and carbonates, were only made up to ~1-3 mL and were presented to the ICP-MS manually during the analysis. For each batch of samples two blanks and at least four international rock standards where prepared. Standards include BHVO-1, JB-1a, JGB-1, BRR-1, BIR-1, and JB-3.

Optimum sensitivity and stability during the run was achieved by running a synthetic multi-element tuning solution containing Co, Y, In, La, Re, Bi and U and leaving the machine to stabilise for 30 minutes before each run. Samples, standards and blanks were run under peak-jumping mode for 4 x 30 seconds per sample. A three minute pause between each sample is made in which a wash consisting of an aqueous 2% HNO_3 solution is ran until background levels are achieved. For the low volume samples, the peak jumping mode was reduced to 5 x 20 seconds so all the low volume sample presented to the machine is analysed. For the low volume samples, the sampling tube was shortened and placed manually into the sample immediately after cleaning. Anomalous and suspicious results were re-run at the end of the procedure. Raw counts per second data was processed in a spreadsheet (2004-2007) or by the Thermo Fisher X-2 series ICP-MS software package (2007-2008) to apply a blank, interference, drift, and internal matrix corrections. In addition, calibration with external international rock standards is applied (Govindaraju, 1994).

.

Element	Solution ppt	Rock ppb	Element	Solution ppt	Rock ppb
85Rb	1.8	2.68	157Gd	0.7	1.13
86Sr	8.2	12.28	159Tb	0.2	0.29
89Y	8.6	12.89	163Dy	1.5	2.30
90Zr	16	251.1	165Ho	0.4	0.60
93Nb	3.1	4.73	166Er	1.5	2.22
115In	0.1	0.20	169Tm	0.3	0.41
133Cs	0.2	0.25	172Yb	1.9	2.85
135Ba	31	45.9	175Lu	0.3	0.51
139La	0.6	0.86	178Hf	4.8	7.25
140Ce	0.8	1.21	181Ta	4.8	7.13
141Pr	0.2	0.27	185Re	0.1	0.17
146Nd	1.1	1.70	208Pb	12	18.3
147Sm	0.1	0.17	232Th	0.5	0.80
153Eu	0.2	0.24	238U	0.2	0.26

Table 2.3. Detection limits for ICP-MS. Detection limits for solutions (ppt) is derived from the calibrated blank plus 3 x the standard deviation of the blank. Detection limits for the rock samples (ppb), are calculated from 3 times the standard deviation of the blank x 1500, the average dilution factor from solid samples. Calibration is sourced from six blank solutions. Blank solutions have a variation of ~30%

Detection limits of the ICP-MS technique for each element are given in Table 2.3. Typical detection limits are in the parts per trillion (ppt) range. The limit of determination for any given element at NOC is 3 times the detection limit. This is essentially the lowest concentration which has a quantifiable error. At these levels,

errors are considered too high to be acceptable; therefore there is a set quantification limit of 10 times the detection limit. Since ICP-MS has low detection limits and a high degrees of precision and accuracy for REE and some trace elements, its use is favoured above XRF analysis since REE and trace elements typically occur in low concentrations in basalts and secondary minerals.

Time	Li	Sc	Rb	Sr	Y	Zr	Nb	Cs	Ba	La
JB-3 Run 1	7.20	33.9	14.9	403	26.8	96.4	1.98	0.93	233	8.26
JB-3 Run 2	7.35	35.2	15.4	410	27.4	99.2	2.02	0.97	234	8.48
JB-3 Run 3	7.19	34.0	14.8	401	26.9	96.9	1.99	0.93	233	8.21
JB-3 Run 4	7.14	34.0	14.9	400	26.8	96.3	1.97	0.94	234	8.22
JB-3 Run 5	7.18	33.6	15.0	404	26.7	96.9	1.98	0.94	236	8.29
JB-3 Run 6	7.19	33.9	14.9	402	26.7	96.0	1.97	0.93	237	8.30
Average	7.21	34.10	14.96	403	26.87	96.95	1.98	0.94	234	8.29
ST DEV	0.07	0.57	0.21	3.5	0.27	1.14	0.02	0.01	1.87	0.10
%RSD	0.99	1.68	1.42	0.9	0.99	1.18	0.89	1.39	0.80	1.18

Time	Ce	Pr	Nd	Sm	Eu	Gd	Tb	Dy	Ho
JB-3 Run 1	20.8	3.25	15.7	4.21	1.31	4.60	0.73	4.52	0.93
JB-3 Run 2	21.1	3.32	15.9	4.27	1.34	4.67	0.75	4.57	0.94
JB-3 Run 3	20.7	3.22	15.6	4.24	1.31	4.60	0.73	4.50	0.92
JB-3 Run 4	20.8	3.25	15.6	4.21	1.31	4.60	0.73	4.48	0.93
JB-3 Run 5	21.1	3.26	15.7	4.23	1.31	4.63	0.73	4.53	0.93
JB-3 Run 6	21.1	3.26	15.6	4.26	1.32	4.64	0.74	4.52	0.93
Average	20.91	3.26	15.66	4.24	1.32	4.62	0.73	4.52	0.93
ST DEV	0.18	0.03	0.12	0.03	0.01	0.03	0.01	0.03	0.01
%RSD	0.87	0.97	0.74	0.60	0.94	0.62	0.86	0.67	0.62

Time	Er	Tm	Yb	Lu	Hf	Ta	Pb	Th	U
JB-3 Run 1	2.63	0.39	2.53	0.38	2.63	0.16	5.57	1.20	0.45
JB-3 Run 2	2.66	0.39	2.56	0.39	2.67	0.16	5.62	1.22	0.46
JB-3 Run 3	2.62	0.38	2.51	0.38	2.63	0.12	5.57	1.20	0.46
JB-3 Run 4	2.61	0.38	2.51	0.38	2.63	0.13	5.58	1.20	0.46
JB-3 Run 5	2.62	0.39	2.51	0.38	2.61	0.15	5.56	1.20	0.46
JB-3 Run 6	2.63	0.39	2.52	0.38	2.63	0.15	5.58	1.21	0.46
Average	2.63	0.39	2.52	0.38	2.64	0.14	5.58	1.21	0.46
ST DEV	0.02	0.00	0.02	0.00	0.02	0.02	0.02	0.01	0.00
%RSD	0.71	0.49	0.80	0.64	0.70	12.08	0.40	0.56	0.69

Table 2.4. Internal reproducibility example of the ThermoFisher X-Series MK-2 ICP-MS from measurement of an internationally recognised standard JB-3. at the National Oceanography Centre, Southampton. Concentrations are in ppm.

The precision and accuracy for each element is given in Appendix Tables E,1 and E,2 and an example is shown in Table 2.4. Variations in precision between different elements are directly related to abundance. Low abundance elements will yield a low number of counts on the detector; therefore values returned for these

elements will have greater uncertainty than that of a high abundance element. Internal error is based on repeated runs of rock standards BIR-1, BRR-1, JB-1a, JB-3, JB-2, and BHVO2. Internationally accepted reference values are sourced from Terashima et al, (1994) and Gladney et al, (1987a. 1987b)

2.3.4 Inductively Coupled Plasma Adsorption Emission Spectroscopy

Carbonate and anhydrite mineral separates were measured for major elements Ca, Mg, Sr, Fe and Mn. In addition, a number of whole rock samples were measured for major elements Ti, Al, Fe(total), Mn, Mg, Ca, Na, K, and P, and trace elements Sc, V, Cr, Co, Ni, Cu, Zn, Sr, Y, Zr, Ba, La, and Ce due to insufficient sample volume available for major and trace analysis by XRF. All elements in each batch were measured simultaneously by ICP-AES at the NOC, Southampton, using a Perkin Elmer 4300 DV ICPAES analyzer. Carbonates, anhydrites and whole rock samples were run as individual batches with synthetic standards prepared from ARISTAR ICP-MS primary standards.

A subsample of the primary standards were accurately diluted into clean HDPE vials to an appropriate range so as to incorporate all possible concentration variability within carbonate, anhydrite, and basement rocks. Elemental ratio precision is 0.2 % and the concentration errors are 0.5 %. Whole rock major and trace element precision is determined by an average of the percentage difference between the accepted major and trace element concentrations and measured concentrations of five internationally recognised standards. Accuracy was determined from a repeated run of the internal standard BAS 206 (Table 2.5. A and B). Detection limits for the Major and trace elements for whole rock samples are provided in Table 2.6. Table 2.7 shows detection limits for major element analyses of carbonates and anhydrites.

A	Na_2O	MgO	Al_2O_3	P_2O_5	K_2O	CaO	TiO_2	MnO	$Fe_2O_3(T)$
Accepted reference values									
JGb1	1.20	7.85	17.49	0.06	0.24	11.90	1.60	0.19	15.06
JB-3	2.73	5.19	17.20	0.29	0.78	9.79	1.44	0.18	11.82
JB-1A	2.73	7.83	14.45	0.26	1.40	9.31	1.28	0.15	9.05
BIR-1	1.75	9.68	15.35	0.05	0.03	13.24	0.96	0.17	11.26
BHVO2	2.22	7.23	13.50	0.27	0.52	11.40	2.73	0.17	12.34
ICP-AES measurements									
JGb1	1.18	8.04	18.11	0.04	0.22	11.87	1.62	0.19	16.05
JB-3	2.39	4.76	16.02	0.29	0.66	8.86	1.30	0.16	11.34
JB-1A	2.54	7.54	14.16	0.25	1.26	8.74	1.22	0.14	8.95
BIR-1	1.80	9.97	16.18	0.04	0.02	13.45	0.98	0.17	12.15
BHVO2	2.22	7.59	14.29	0.27	0.51	11.62	2.85	0.17	13.37
% Differece									
JGb1	1.36	-2.32	-3.41	28.40	7.80	0.25	-1.53	1.50	-6.19
JB-3	14.12	9.01	7.37	2.46	18.10	10.46	10.83	11.70	4.26
JB-1A	7.50	3.87	2.04	5.11	11.03	6.55	5.00	9.42	1.10
BIR-1	-2.55	-2.90	-5.12	3.27	19.56	-1.58	-1.63	-0.07	-7.33
BHVO2	-0.07	-4.73	-5.55	-1.42	2.66	-1.85	-4.28	0.51	-7.69
Average error	**4.07**	**0.59**	**-0.93**	**7.56**	**11.83**	**2.77**	**1.68**	**4.61**	**-3.17**
Reproducibility									
BAS 206	2.69	6.81	14.33	0.17	0.16	9.55	2.10	0.25	15.34
BAS 206	2.74	6.95	14.52	0.18	0.17	9.60	2.10	0.25	15.41
BAS 206	2.74	6.86	14.52	0.17	0.17	9.63	2.09	0.25	15.38
Average	2.72	6.87	14.46	0.17	0.17	9.59	2.10	0.25	15.38
SD	0.03	0.07	0.11	0.01	0.01	0.04	0.01	0.00	0.04
%RSD	**1.14**	**1.05**	**0.74**	**4.15**	**2.17**	**0.41**	**0.16**	**0.73**	**0.24**

B	Sc	V	Cr	Co	Ni	Cu	Zn	Sr	Ba	La	Ce
Accepted reference values											
JGb1	36.0	640.0	58.3	61.0	25.4	86.0	110.0	327.0	64.3	3.4	7.9
JB-3	33.8	378.0	59.0	35.0	37.0	196.0	103.0	395.0	245.0	8.4	21.3
JB-1A	29.0	203.0	392.0	38.1	140.0	56.7	85.0	443.0	504.0	37.7	66.9
BIR-1	43.0	319.0	391.0	52.0	166.0	119.0	72.0	109.0	7.7	0.6	1.9
BHVO2	32.0	317.0	280.0	45.0	119.0	127.0	103.0	394.0	131.0	15.2	37.6
ICP-AES measurements											
JGb1	32.1	661.1	54.3	60.5	24.1	84.0	122.0	319.7	59.0	3.4	5.4
JB-3	28.6	349.9	50.2	30.4	35.0	171.5	106.2	356.9	205.2	7.3	15.7
JB-1A	24.9	190.1	343.0	36.3	119.6	49.4	86.3	413.6	454.5	36.2	54.6
BIR-1	41.6	327.1	391.7	53.5	148.4	122.3	79.9	105.2	5.9	1.1	0.4
BHVO2	30.2	327.0	290.8	45.6	117.4	130.3	115.2	389.8	127.4	15.4	35.0
% Differece											
JGb1	10.5	-3.2	7.4	0.9	5.5	2.4	-9.8	2.3	9.1	1.1	47.2
JB-3	18.1	8.0	17.5	15.1	5.9	14.3	-3.0	10.7	19.4	14.7	45.4
JB-1A	16.0	6.8	14.3	5.0	17.0	14.8	-1.6	7.1	10.9	4.0	22.5
BIR-1	3.2	-2.5	-0.2	-2.8	11.9	-2.7	-9.9	3.7	29.5	-42.2	370.2
BHVO2	5.9	-3.1	-3.7	-1.3	1.4	-2.5	-10.6	1.2	2.8	-1.2	7.5
Average error	**10.7**	**1.2**	**7.1**	**3.4**	**8.3**	**5.3**	**-7.0**	**5.0**	**14.3**	**-4.7**	**98.6**
Reproducibility											
BAS 206	46.8	467.8	81.1	54.9	52.1	66.1	149.2	99.9	41.0	4.5	12.2
BAS 206	47.0	470.6	80.0	53.7	52.8	67.8	142.9	101.3	41.5	4.4	10.2
BAS 206	46.9	468.7	80.2	52.8	53.6	68.4	139.1	99.4	40.9	4.4	9.7
Average	46.9	469.0	80.4	53.8	52.8	67.4	143.7	100.2	41.1	4.4	10.7
SD	0.1	1.4	0.6	1.1	0.8	1.2	5.1	1.0	0.3	0.1	1.3
%RSD	**0.2**	**0.3**	**0.7**	**2.0**	**1.5**	**1.8**	**3.6**	**1.0**	**0.7**	**0.5**	**12.4**

Table 2.5 a) Precision and accuracy for ICP-AES major (wt %) and b) trace element measurements (ppm). The measurements from five international standards are compared to the recommended values taken from Govindaraju (1994). The accuracy is measured from repeats of BAS 206 internal standard.

Element	Solution ppb	Rock ppm	Element	Solution ppb	Rock ppm
Na	19.81	21.80	Cr	0.47	0.52
Mg	21.46	23.61	Co	1.59	1.75
Al	16.28	17.91	Ni	1.14	1.26
P	112.97	124.27	Cu	0.55	0.61
K	15.65	17.22	Zn	1.54	1.70
Ca	18.11	19.93	Sr	0.06	0.07
Ti	1.03	1.14	Y	0.06	0.07
Mn	0.94	1.03	Zr	0.77	0.84
Fe	5.97	6.57	Ba	0.14	0.16
Sc	0.03	0.03	La	0.18	0.20
V	3.79	4.17	Ce	2.26	2.48

Table 2.6. Detection limits for ICP-AES. Detection limits are calculated as the average of 12 blanks + three times the standard deviation of the blank for solutions. Sample (solid rock) is calculated from the average of the twelve blanks + 3 times the standard deviation of the blank times the average dilution factor (~1100).

		Mg ppm	Ca ppm	Sr ppm	Mn ppm	Fe ppm
Solution	ppb	0.35	13.14	0.05	0.11	0.22
Rock	ppm	0.12	4.38	0.02	0.04	0.07

Table 2.7.Detection limits for carbonate and anhydrite major elements Detection limits are calculated as the average of 12 blanks + three times the standard deviation of the blank for solutions. Sample (solid rock) is calculated from the average of the twelve blanks + 3 times the standard deviation of the blank times the average dilution factor (~1100).

2.3.4 Reproducibility between XRF, ICP-MS, and ICP-AES.

Trace elements Rb, Sr, Y, Zr, Nb, Ba, La, and Ce were measured by XRF and ICP-MS. Reproducibility for Sr, Y, Zr, Nb are below 14%. Given the lower detection limits for ICP-MS for Rb, Sr, Y, Zr, Nb, Ba, La and Ce, ICP-MS measurements were used for concentrations for these elements.

Concentrations in ppm	Method	Rb	Sr	Y	Zr	Nb	Ba	La	Ce
n value (BAS206)	ICP-MS	24	24	24	24	24	24	24	24
Average		1.64	89.59	51.30	127.15	3.93	37.31	3.90	12.47
standard deviation		0.24	7.25	3.47	8.95	0.44	3.42	0.42	0.99
% accuracy		**14.8**	**8.1**	**6.8**	**7.0**	**11.2**	**9.2**	**10.7**	**7.9**
n value (BAS206)	XRF	5	5	5	5	5	5	2	2
Average		2.35	101.36	50.04	126.94	4.40	46.66	5.17	17.33
standard deviation		0.95	0.91	0.44	0.60	0.22	3.55	1.65	1.03
% accuracy		**40.55**	**0.90**	**0.87**	**0.47**	**5.06**	**7.61**	**31.97**	**5.97**
% (ICP-MS vs. XRF)		**-43.0**	**-13.1**	**2.5**	**0.2**	**-11.9**	**-25.1**	**-32.5**	**-39.0**

Table 2.8. Comparison of XRF and ICP-MS trace element analyses including reproducibility (given as % difference).

Concentration in wt %	ICP-AES	Al_2O_3	Fe_2O_3	MgO	CaO	Na_2O	K_2O	TiO_2	MnO	P_2O_5
n value(BAS 206)	Count	3	3	3	3	3	3	3	3	3
Average		469.03	14.46	15.38	6.87	9.59	2.72	0.17	2.10	0.25
standard deviation		1.43	0.11	0.04	0.07	0.04	0.03	0.01	0.01	0.00
% accuracy		**0.30**	**0.76**	**0.23**	**1.03**	**0.42**	**1.06**	**3.46**	**0.28**	**0.00**
	ICP-AES	Sr	Ba	La	Ce	Cu	Ni	Cr	V	
n value (BAS 206)	Count	3	3	3	3	3	3	3	3	
Average		100.20	41.13	4.43	10.70	143.73	67.43	52.83	80.43	
standard deviation		0.98	0.32	0.06	1.32	5.10	1.19	0.75	0.59	
% accuracy		**0.98**	**0.78**	**1.30**	**12.36**	**3.55**	**1.77**	**1.42**	**0.73**	
	XRF	Al_2O_3	Fe_2O_3	MgO	CaO	Na_2O	K_2O	TiO_2	MnO	P_2O_5
	Count	4	2	2	2	2	2	2	2	2
Average		495.08	13.82	14.33	6.78	9.54	2.60	0.17	2.02	0.25
standard deviation		4.95	0.18	0.16	0.01	0.14	0.16	0.01	0.02	0.01
% accuracy		**1.00**	**1.28**	**1.14**	**0.10**	**1.48**	**5.98**	**4.21**	**1.23**	**3.09**
% Difference (XRF vs. ICP-AES)		**5.26**	**-4.64**	**-7.34**	**-1.45**	**-0.56**	**-4.74**	**0.79**	**-3.98**	**0.60**
	XRF	Sr	Ba	La	Ce	Cu	Ni	Cr	V	
n value (BAS206)	Count	5	5	5	5	5	5	2	2	
Average		2.35	101.36	50.04	126.94	4.40	46.66	5.17	17.33	
standard deviation		0.95	0.91	0.44	0.60	0.22	3.55	1.65	1.03	
% accuracy		**40.55**	**0.90**	**0.87**	**0.47**	**5.06**	**7.61**	**31.97**	**5.97**	
% Difference (XRF vs. ICP-AES)		**1.14**	**11.85**	**14.22**	**38.26**	**-13.14**	**-2.47**	**-10.25**	**3.46**	

Table 2.9. Comparison of XRF and ICP-AES trace element analyses including reproducibility (given as % difference)

Concentrations in ppm	ICP-MS	Sr	Ba	La	Ce
n value (BAS206)	Count	24	24	24	24
Average		89.59	37.31	3.90	12.47
standard deviation		7.25	3.42	0.42	0.99
% accuracy		**8.1**	**9.2**	**10.7**	**7.9**
	ICP-AES	Sr	Ba	La	Ce
n value (BAS 206)	Count	3	3	3	3
Average		100.20	41.13	4.43	10.70
standard deviation		0.98	0.32	0.06	1.32
% accuracy		**0.98**	**0.78**	**1.30**	**12.36**
% Difference (ICP-MS vs. ICP-AES)		**-11.85**	**-10.24**	**-13.66**	**14.21**
n=18	JGb1	JB-3	JB-1A	BIR-1	BHVO2
Method	R2	R2	R2	R2	R2
All	0.999	0.997	0.998	0.998	0.999
n=5	R2			R2	
Sr	0.989		Al	0.749	
Ba	0.997		Fe	0.949	
La	0.998		Mg	0.978	
Ce	0.990		Ca	0.982	
Zn	0.937		Na	0.962	
Cu	0.959		K	0.996	
Ni	0.989		Ti	0.989	
Cr	0.982		Mn	0.761	
V	0.990		P	0.998	

Table 2.10. Comparison of ICP-AES and ICP-MS trace element analyses, including standards JGb1, JB-3, JB-1A, BIR-1, and BHVO2. R^2 is given for the reproducibility of each element and for each standard.

Comparison between XRF and ICP-AES results (Table 2.9) indicates reproducibility better than 8 % on major elements. Trace elements are variable; Sr, Ni and V are better than 3.5 %, Ba, La, Cu, and Cr are between 10 and 14.2 %, and Ce is ~40 %. For trace elements, the ICP-AES is used because it has better sensitivity for such elements. Major elements measured by XRF are preferentially used over ICP-AES due to sensitivity. Reproducibility of known standards between ICP-MS (X-Series MK 2) and ICP-AES (Table 2.10) for major elements and trace elements is good for most elements (R^2 ranges from 0.93 to 0.99 n=5). Mn (R^2 = 0.76) and Al (R^2 =0.75) are poor, however good reproducibility between these elements for ICP-MS and ICP-AES in BAS-206 (Table 2.9) indicate that the major element concentrations run by ICP-AES are comparable and reliable.

2.3.5 Sr isotope measurement by Thermal Ionisation Mass Spectrometry (TIMS)

Ratios of Sr were determined at NOCS by TIMS on a seven collector VG Sector 54 mass spectrometer. Prior to separating Sr, measurements of Sr concentration were made by ICP-MS for all samples in order that we could subsample sufficient mother solution to contain ~ 1 μg of Sr.

Sr was isolated by standard ionic Sr Spec resin using 80 μL Sr-Spec columns. Resin sufficient to fill the stalk of the column is added followed by cleaning by passing through 1.5 mL 18.2Ω MilliQ H_2O, 1.5 mL (sb)3M HNO_3, and 1.5 mL Elga H_2O. The columns are conditioned with 1.5 mL (sb)3M HNO_3. The sample (~1 μg of Sr) in mother dried down and dissolved in 200 μL (sb)3M HNO_3) is loaded and washed in with 200 μL (sb)3M HNO_3. The columns are eluted with 2.5 mL 3M HNO_3 and the sample is collected by passing 1.5 mL Elga H_2O. The sample is dried down and loaded onto outgassed Ta filaments using a Ta activator solution.

For each sample the Ta filament is slowly warmed to 2.7A in a vacuum ($<1*10^{-7}$ mbar). The beam is then detected and raised to ~2V by successive focussing of the beam and small increases in the current. Once a stable beam is achieved 150 ratios are recorded in multidynamic mode. An average is automatically selected based on a maximum of 10% rejection. Samples with high Rb counts, high levels of fractionation, and 2σ greater than 25 are repeated. Each turret (20 samples) includes 2 standards (NIST SRM-987) which are used to monitor instrumental error. The average $^{87}Sr/^{86}Sr$

value for NIST SRM-987 measured in dynamic mode, using the stable isotope normalization of $^{86}Sr/^{88}Sr = 0.1194$ was 0.710260 ± 0.000021 (2sd) over a period from June, 2005 – August, 2008 (n = 48).

2.3.6 $\delta^{13}C$ and $\delta^{18}O$ Measurements for carbonate mineral separates

Stable isotope measurements of $\delta^{18}O$ and $\delta^{13}C$ within the carbonate samples were performed at the NOC, Southampton using Europa Scientific Geo 20-20 mass spectrometer. Accurately weighed pure carbonate powder samples were mixed with 100 % orthophosphoric acid and converted into CO_2 gas using the CAPS preparation system in which the following reaction takes place.

$$3CaCO_3 + 2H_3PO_4 \rightarrow Ca_3(PO_4)_2 + 3H_2O + 3CO_2$$

Orthophosphoric acid converts the carbonate sample into CO_2 for measurement. 12 measurements (6x standard reference and 6x sample) and an average is obtained for each sample. Drift is corrected by measuring the difference between the standard and reference in each run. The internal laboratory standard is 'Southampton Carrera Marble' SC1 is calibrated against international standard, NBS1A.

All values for $\delta^{18}O$ and $\delta^{13}C$ are measured against the Vienna Standard Mean Ocean Water (VSMOW) and Vienna PeeDee Belemnite (V-PDB) respectively and presented using the delta notation of Craig (1961) following Equation 2.4

Equation 2.4. expression used to report $\delta^{18}O$ samples relative to VSMOW.

$$\delta^{18}O‰ = 1000 \times \frac{\left[\left(^{18}O/^{16}O\right)_{sample} - \left(^{18}O/^{16}O\right)_{VSMOW}\right]}{\left(^{18}O/^{16}O\right)_{VSMOW}}$$

Repeated runs of blind standards over a period from 27/06/2007 and 12/07/2007 indicates an instrumental error of 0.6 % and 1.3 % for carbon and oxygen respectively (Table 2.11). Precision based on analyses of standard NBS SRC is 0.28/1 μL for Carbon and 0.54/1 μL for Oxygen.

Run date	Oxygen	Carbon	Run date	Oxygen	Carbon
27/06/2007	1.946	-2.188	11/07/2007	1.932	-2.195
	1.958	-2.199		1.942	-2.153
	1.968	-2.215		1.931	-2.202
28/06/2007	1.951	-2.202	12/07/2007	1.946	-2.216
	1.961	-2.202		1.963	-2.169
	1.976	-2.182		1.961	-2.213
05/07/2007	1.942	-2.201			
	1.948	-2.216	N	18.00	18.00
	1.953	-2.242	Average	1.95	-2.20
08/07/2007	1.968	-2.140	SD	0.01	0.03
	1.943	-2.265	REFERENCE	***1.950***	***-2.200***
	1.950	-2.222	Int. Precision	**0.64**	**-1.33**
	‰ VSMOW	‰ VPDB	Ext. accuracy	**-0.11**	**-0.06**

Table 2.11. Instrumental precision and accuracy of the Geo 20-20 mass spectrometer based on repeats of recent blind runs of the NBS SRC standard.

2.3.7 Stable isotope measurements of whole rock samples and anhydrites

Anhydrite mineral separates from ODP Site 504 and IODP Site 1256 and whole rock samples from ODP Sites 1256, 1179, and 1149 were measured for oxygen and sulfur stable isotopes. Oxygen isotope analyses were carried out at the University of Michigan by reacting pure, powdered mineral separates with BrF_5 in externally heated nickel reaction vessels to release the oxygen from anhydrite (Clayton and Mayeda, 1963). The resultant O_2 is converted to CO_2 following reaction with heated carbon rods and a platinum catalyst. Oxygen isotope ratios were measured using a Finnigan Delta-S mass spectrometer. Sample unknowns were measured with an NBS 28 quartz standard which returned a mean $\delta^{18}O$ value of 9.6‰ ± 0.21. This compares well to the accepted value of 9.68 ‰ (IAEA, 2007). In addition NBS 127 $BaSO_4$ standards were run with the anhydrite unknowns. Yields of O from anhydrite and barite are ~50 %. Measured $\delta^{18}O$ values are corrected to the accepted value of 9.34 ‰ for NBS 127 $BaSO_4$ and all isotopic compositions are reported using the δ notation, relative to VSMOW (Equation 2.4., Craig 1961)

In addition to analyses carried out at the University of Michigan, whole rock $\delta^{18}O$ from ODP Sites 1256, 1179, and 1149 were measured at the University of Western Ontario following the method of Clayton and Mayeda (1963), as modified by Borthwick and Harmon (1982) for use with ClF_3. Between 8-10 mg of sample was

accurately weighed out and placed under vacuum overnight at 150°C in order to remove absorbed water. The samples were then dried under vacuum for 2 hours at 300°C. Oxygen was liberated from the silicate mineral structure by reacting the dried samples with ClF_3 at 550°C in sealed Ni reaction vessels overnight. The released oxygen gas was then quantitatively converted to CO_2 over a red-hot carbon rod and yields were measured to evaluate whether the conversion had gone to completion. Oxygen isotopic ratios were then measured using a dual-inlet DeltaPlus XL mass spectrometer. The $\delta^{18}O$ values of ORX (internal laboratory standard quartz), NBS-30 (biotite) and NBS-28 (quartz) were +11.4 ± 0.2‰, +5.1 ± 0.1‰ and +9.7 ± 0.3‰, respectively, which compares well with their accepted $\delta^{18}O$ values of +11.5‰, +5.1‰ and +9.6‰. Reproducibility of the $\delta^{18}O$ values for standards and samples was generally better than ±0.2‰.

Sulphur isotope ratios for the whole rock samples and the anhydrites were measured at the U.S Geological Survey stable isotope laboratory in Denver. CO. The samples were liberated of SO_2 gas by combustion using an elemental analyzer. The SO_2 gas is transferred directly to a Micromass Optima mass spectrometer for analysis by continuous flow mode. Sulphur isotope values are reported using the standard delta notation relative to the Canyon Diabalo Troillite (CDT) where IAEA-S-1 = 0.30 ‰ and IAEA-S-2 = 22.67 ‰ vs.CDT (Coplen and Krouse, 1998). Analytical precision is better than ± 0.2 % SE for all samples measured.

2.3.8 Ferric/Ferrous ratio measurements

The Ferric/Ferrous ratio of 27 whole rock samples from Site 1179 were measured, following the procedure of Kolthoff and Sandall (1950) by titration using potassium permanganate and sodium oxalate. 0.5 g of powdered whole rock sample is accurately weighed into 60mL HDPE bottles ready for analysis. Before the titration can begin the postassium permanganate ($KMnO_4$) was standardized.

4 g of $KMnO_4$ crystals are accurately weighed into a dark Winchester bottle with 2 L of 18.2 Ω MilliQ water. The bottle shaken and stored in a dark cupboard for 1 week (Shaken regularly) to equilibrate. Contact with any light source is kept to a minimum during this period to prevent oxidation of $KMnO_4$. The solution is then passed through a glass wool filter to remove any insoluble residue.

Sodium oxalate crystals $(COONa)_2$ are accurately weighed (~0.1 g) into 250 mL conical flasks. 150 mL of 18.2 Ω MilliQ water is added to dissolve the sodium oxalate followed by 10 mL of concentrated H_2SO_4. This reaction forms $H_2C_2O_4$ and Na_2SO_4 (Equation 2.5).

Equation 2.5. Reaction of aqueous sodium oxalate with H_2SO_4.

$$(COONa)_2 + H_2SO_4 \rightarrow H_2C_2O_4 + Na_2SO_4$$

Repeated titrations of $KMnO_4$ with the prepared sodium oxalate solution is used to determine the iron equivalents of 1mL of $KMnO_4$ solution. A graduated burette, washed with 18.2 Ω MilliQ water and rinsed with $KMnO_4$ is filled with the prepared $KMnO_4$. The $KMnO_4$ solution is titrated with the sodium oxalate solution (in the conical flask) until the first permanent pink colour is observed. The titre reading is taken and the titration procedure is repeated until a consistent result is produced. The reaction. Between the sodium oxalate and $KMnO_4$ proceeds as for equation 2.6. Iron equivalents are calculated from equation 2.7. Table 2.12 shows the results of the standardisation. The $KMnO_4$ concentration used in this study was 0.0127 mol/L.

Equation 2.6. Reaction between sodium oxalate and potassium permanganate during titration.

$$2MnO_4^+ + 5H_2C_2O_4 + H^+ \rightarrow 2Mn^{2+} + 10CO_2 + 8H_2O$$

Equation 2.7. Calculation of the concentration of potassium permanganate (as equivalent to iron).

$$[MnO_4] \text{ mol/L} = 1000/\text{titre} \times (2/5 \times \text{mass } (COONa)_2/\text{M.W. } (COONa)_2)$$

Titration	Mass $(COONa)_2$	Titre $[MnO_4^-]$ (mL)	$[MnO_4^-]$ mol/l
1 (practice)	0.1024	25.0	0.0123
2 (practice)	0.1016	24.0	0.0126
3	0.1062	25.0	0.0127
4	0.1023	24.1	0.0127
5	0.1046	24.6	0.0127
6	0.1084	25.5	0.0127
		Average	**0.0127**

Table 2.12. Standardisation of $KMnO_4$ by titration with sodium oxalate. Two practice titrations followed by 4 titrations were undertaken. The average of the 4 working titrations was taken as the standard concentration.
Whole rock powders (in 60 mL HDPE bottles) were dissolved by adding 8 mL 1:1 H_2SO_4 and 5 mL concentrated HF. The bottle is capped, placed in a hot water bath and allowed to simmer for 20 minutes for total dissolution. Dissolution time was determined by dissolution experiments on a sample taken from the Troodos ophiolite (Teagle, 1993).

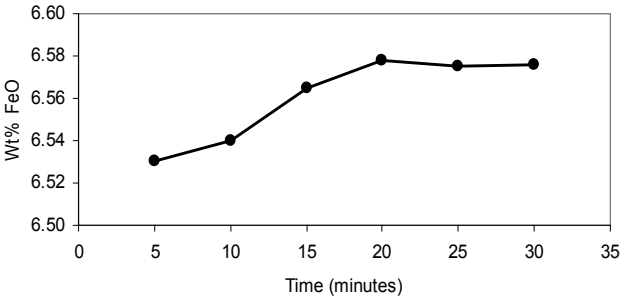

Figure 2.2. Plot of dissolution time period vs. FeO (wt%) indicating optimal dissolution time. After Teagle, (1993).

A plot from one sample of decomposition time vs. FeO (wt%) indicates that 20 minutes is optimal for decomposition of basalts (Figure 2.2). During simmering the titration solution is prepared by adding 10 mL 1:1 H_2SO_4 and 10 mL saturated boric acid solution to 300 mL of 18.2 Ω MilliQ water. Saturated boric acid is prepared by dissolving ~56 g of H_3BO_3 crystals in 1 litre of distilled water. During the last few minutes of sample dissolution a burette with an accuracy of 0.01 mL is filled with the standardised $KMnO_4$ solution (Shaken to maintain homogenous concentration). The dissolved sample solution is transferred and washed into a beaker which is then titrated immediately via the reaction pathway shown in Equation 2.8.

Equation 2.8. Reaction during titration of the dissolved sample and the potassium permanganate

$$KMnO_4 + 5Fe^{2+} + 8H^+ \rightarrow Mn^{2+} + 5Fe^{3+} + 4H_2O$$

Equation 2.9 and 2.10 Calculation of the ferrous and ferric iron content.

$$FeO\ (wt\%) = 100 \times (5 \times titre/1000 \times [MnO_4])/mass\ of\ solid\ sample$$

$$Fe_2O_3 \text{ (wt \%)} = \text{Wt\% FeO x } 1.1113$$

The titration is stopped with the first sign of a pale semi-permanent (fades in <1 minute) pink hue is observed within the solution. The ferric and ferrous content is then calculated from the titre following equations 2.9 and 2.10.

Analytical precision was determined by multiple repeats of samples. After initial 6 fold repetition of each sample this was reduced to 2 fold repletion as technique improved. Ferric/ferrous values were screened to obtain the most consistent repeats for each sample. Table 2.13 shows the ferric ferrous ratios and internal analytical precision for some examples. Internal errors are better than 1.2%.

	Sample volume (g)	Titre	Ferrous (wt%)	Ferric (wt%)
Sample		191 1179D, 20R1 60-67cm b		
25/09/2006	0.5070	3.25	4.0681	4.5209
25/09/2006	0.5052	3.25	4.0826	4.5370
		average	**4.0754**	**4.5289**
		SD	0.0102	0.0114
		Precision	0.2515	0.2515
Sample		191 1179D, 19R2 31-36 cm		
01/10/2006	0.5028	5.70	7.1944	7.9952
01/10/2006	0.5035	5.60	7.0584	7.8440
01/10/2006	0.5013	5.70	7.2160	8.0191
01/10/2006	0.5011	5.65	7.1555	7.9519
		average	**7.1561**	**7.9525**
		SD	0.0698	0.0775
		Precision	0.9749	0.9749
Sample		191 1179D ,20R1 60-67 cm		
09/11/2006	0.5136	3.15	3.8923	4.3255
09/11/2006	0.5066	3.05	3.8208	4.2460
09/11/2006	0.5080	3.05	3.8102	4.2343
		average	**3.8411**	**4.2686**
		SD	0.0446	0.0496
		Precision	1.1618	1.1618
Sample		191 1179D, 19R2 31-36 cm b		
09/11/2006	0.5075	5.85	7.3154	8.1296
09/11/2006	0.5046	5.80	7.2945	8.1064
09/11/2006	0.5042	5.85	7.3633	8.1828
09/11/2006	0.5003	5.95	7.5475	8.3875
		average	**7.3244**	**8.1396**
		SD	0.0352	0.0392
		Precision	0.4811	0.4811

Table 2.13. Precision of first 4 unknown samples with acceptable ratios.

2.5. Whole rock leaching experiments

2.5.1 Introduction

Basalt recovered from basement at a range of Sites including ODP/IODP Sites 1179, 1149, 843, and 1256 has been analysed for a range of parameters (Sr isotopic ratios, trace elements and REE) to characterise the chemical changes that occur within ocean crust during low temperature seawater-basalt exchange (See 'methods').

A comprehensive assessment of the chemical changes that occur within individual sites and subsequently, the levels of fluid rock interaction and true extent of alteration can only be achieved if the primary composition of the basement at the time of formation is known. Traditionally, this is achieved by analysing fresh basalt and glass samples, or by acid leaching of the least altered samples to remove secondary mineral assemblages. Acid leaching can only be used to determine the primary isotopic signatures, because acid attack will greatly affect major and trace element compositions (e.g., Mahoney, 1987 and Mahoney, et al, 1983). Average regional compositional estimates, e.g. 'Typical MORB' Sr-isotopic compositions 0.70240-0.70256 (Saunders et al., 1988) provide a useful comparison for estimating the influence of alteration against a common standard and they provide a benchmark for the range of compositions expected. Because individual sites demonstrate variable precursor compositions, the regional averages are not able to estimate site-specific primary compositions. Only by locating unaltered material, or removal of secondary mineral phases by leaching, can insights into primary compositional variation be made, and thus provide a baseline from which we can assess the true extent of alteration.

In this study leaching experiments are carried out on a range of basalts in order to determine the primary 'precursor' composition of the basalts across a range of sites formed at fast spreading rates. The procedures follow those of Mahoney (1987), and Mahoney et al., (1983). For ODP Samples 206-1256D-24R-1, 132-139 cm and 27R-2, 56-62 cm analysis of the multiple leaching steps were carried out to assess the effectiveness of the leaching method.

2.5.2 Method

In order to ascertain the primary $^{87}Sr/^{86}Sr$ value and trace and REE composition for ODP/IODP Sites 1256, 1149, 1179, 843 three whole rock samples from each Site were selected for leaching experiments. The least altered samples and one fresh and alteration halo pair were chosen because; a) least altered samples contain the least amount of secondary phases, therefore we are more likely to find the precursor compositions, and b) the sample pair will act as a direct comparison between leached 'fresh' basalt and leached 'altered' basalt. In three ODP/IODP Site 1256D samples, a number of leachate stages were retained and analysed for $^{87}Sr/^{86}Sr$ (if enough Sr is present) and REE. 300 mg of sample powder were leached by adding 10 mL 6M HCl into a Teflon beaker and agitated for 30 minutes in an ultrasonic bath. The leachate is then carefully removed and stored in a separate Teflon beaker. The residue is repeatedly attacked by this method until visible colouration of the leachate no longer occurs even after agitation.

The leached residue was then dried, accurately weighed, and then underwent standard HF dissolution (See chapter 2, methods) to be made into mother solutions. For ODP Samples 206-1256D-24R-1, 132-139 cm, 27R-2, 56-62 cm (background) and 27R-2, 56-62 cm (halo), the leachates were recovered after each stage. These were dried and were accurately dissolved into mother solutions in ~3M HCl. The volume of the leachates was not measured therefore; concentrations of trace elements and REE reflect the concentrations of the mother solution. All the mother solutions were subsampled for analysis of $^{87}Sr/^{86}Sr$ by TIMS and trace and REE by ICP-MS. Due to insufficient strontium in the later leachate stages, only stages 1, 3, 5, and 7 (if available) were subsampled for $^{87}Sr/^{86}Sr$ by TIMS.

Expedition, hole, core, interval (cm)	**206 1256 24R-1 132-139**	206 1256 24R-1 132-139	206 1256 24R-1 132-139	206 1256 24R-1 132-139	206 1256 24R-1 132-139	206 1256 24R-1 132-139	**206 1256 24R-1 132-139**
Depth (mbsf)	**420.82**	420.82	420.82	420.82	420.82	420.82	**420.82**
Lithological unit	**5**	5	5	5	5	5	**5**
Rock type	**Sheet flow**	Sheet flow	Sheet flow	Sheet flow	Sheet flow	Sheet flow	**sheet flow**
Notes	**bkd**	bkd	bkd	bkd	bkd	bkd	**bkd**
leech stage	**Untreated**	1	2	3	4	5	**Leached residue**
$^{87}Sr/^{86}Sr$ (m)	**0.702968**	0.704038	0.702864	0.702840	0.702872	0.702816	**0.702835**
2 SE	**11**	10	27	11	11	11	**11**
$^{87}Sr/^{86}Sr$ (t)	**0.702963**	0.704030	0.702861	0.702837	0.702869	0.702814	**0.702834**
Rb (ppb)(**ppm**)	**0.69**	1.288	0.502	0.138	0.134	0.088	**0.07**
Sr (ppb)(**ppm**)	**109.3**	120.7	131.2	45.4	38.3	30.1	**65.1**
Y (ppb)(**ppm**)	**54.2**	269.1	39.8	8.8	7.5	5.7	**20.4**
Zr (ppb)(**ppm**)	**114.9**	325.1	317.1	65.0	63.6	46.2	**31.8**
Nb (ppb)(**ppm**)	**3.81**	2.546	12.4	3.323	3.517	3.365	**0.53**
Cs (ppb)(**ppm**)	**0.009**	0.031	0.003	0.001	0.001	0.001	**0.000**
Ba (ppb)(**ppm**)	**14.12**	20.37	28.97	8.42	6.54	4.70	**8.00**
La (ppb)(**ppm**)	**3.55**	29.94	2.42	0.43	0.26	0.18	**0.37**
Ce (ppb)(**ppm**)	**10.58**	91.74	6.38	1.05	0.66	0.48	**1.26**
Pr (ppb)(**ppm**)	**1.85**	15.03	1.02	0.17	0.12	0.09	**0.27**
Nd (ppb)(**ppm**)	**11.56**	84.19	5.68	0.98	0.70	0.52	**2.02**
Sm (ppb)(**ppm**)	**3.96**	28.24	2.24	0.44	0.33	0.25	**1.12**
Eu (ppb)(**ppm**)	**1.41**	4.23	1.68	0.50	0.38	0.29	**0.78**
Gd (ppb)(**ppm**)	**6.15**	31.88	2.86	0.59	0.48	0.35	**1.66**
Tb (ppb)(**ppm**)	**1.13**	6.28	0.70	0.15	0.13	0.09	**0.40**
Dy (ppb)(**ppm**)	**7.43**	41.02	5.44	1.21	1.03	0.77	**3.03**
Ho (ppb)(**ppm**)	**1.75**	8.78	1.34	0.30	0.26	0.19	**0.71**
Er (ppb)(**ppm**)	**5.18**	23.76	4.23	0.95	0.83	0.62	**2.06**
Tm (ppb)(**ppm**)	**0.71**	3.19	0.69	0.15	0.14	0.10	**0.31**
Yb (ppb)(**ppm**)	**5.13**	20.59	5.12	1.15	1.09	0.81	**2.18**
Lu (ppb)(**ppm**)	**0.78**	3.01	0.81	0.18	0.17	0.13	**0.35**
Hf (ppb)(**ppm**)	**2.85**	8.42	8.24	1.82	1.70	1.18	**1.00**
Ta (ppb)(**ppm**)	**0.28**	0.32	0.82	0.15	0.14	0.14	**0.13**
Pb (ppb)(**ppm**)	**0.57**	3.15	0.81	0.27	0.41	0.16	**0.11**
Th (ppb)(**ppm**)	**0.262**	1.667	0.327	0.053	0.046	0.031	**0.032**
U (ppb)(**ppm**)	**0.081**	0.363	0.172	0.033	0.028	0.020	**0.019**

Table 2.14. Example Sr-isotopic, REE, and trace element data for leached samples at Sites 1256. Bold samples are leached and un-leached powder analyses. Complete table is located in Appendix Table E, 3.

2.5.3 Results

2.5.3.1 Sr Isotopes

Sr-isotopic results for all treated, untreated and leachates are listed in Appendix Table E.3 2.16. $^{87}Sr/^{86}Sr$ for untreated samples range from 0.702816 to 0.708754, whereas treated samples range from 0.702435 to 0.705686. Figure 2.3 shows the Sr isotopic ratio of treated and untreated samples compared to the expected range of Sr-isotopic compositions for fresh MORB, seawater and the range of measured whole rock $^{87}Sr/^{86}Sr$ at each site. Initial results show that all leached residues produce lower $^{87}Sr/^{86}Sr$ than the original un-leached whole rock. In the least altered samples, $^{87}Sr/^{86}Sr$ was reduced to values that closely resemble the average range for fresh MORB (0.70240-0.70256, Saunders et al., 1988). In addition Sr isotopic measurements of leached residues from ODP Site 843B in this study are comparable to leached samples measured by King et al, (1993). Two acid washed (6N HCl) samples from ODP Site 1179 (Mahoney, et al, 2005) compare well to the samples leached in this study (Figure 2.3). The leached residues that exhibit the greatest extent of alteration have elevated $^{87}Sr/^{86}Sr$ values when compared to other leached samples from the same site (Figure 2.3). In addition, these samples also exhibit the greatest reduction in radiogenic Sr.

Strontium isotopic measurements for leachates from samples ODP Leg 206-1256D-24R-1, 132-139 cm, 27R-2, 56-62 cm (background) and 27R-2, 56-62 cm (halo) are recorded in Table 2.5.1. The difficulty in obtaining precise Sr isotopic measurements in solutions that contain 0.1 μg Sr or less has led to incomplete leachate data for sample ODP 206-1256D-27R-2, 56-62 cm (halo). For each leachate, Sr isotopic compositions are plotted against leachate stage (Figure 2.4). For all samples there is a sharp decrease in $^{87}Sr/^{86}Sr$ followed by a levelling off at compositions close to primary MORB. In sample ODP Leg 206-1256D-24R-1, 132-139 cm the last two leachates analysed have $^{87}Sr/^{86}Sr$ values that are comparable to the Sr isotopic composition of the final leached residue. Slight variation in the Sr-isotopic composition of the leachates occurs in leach stage 3 (Figure 2.4) in samples ODP Leg 206-1256D 27R-2, 56-62 cm 'background' and 27R-2, 56-62 cm 'halo'. Leachates recovered from stages 5, 6, and 7 contain more radiogenic Sr than stage 3.

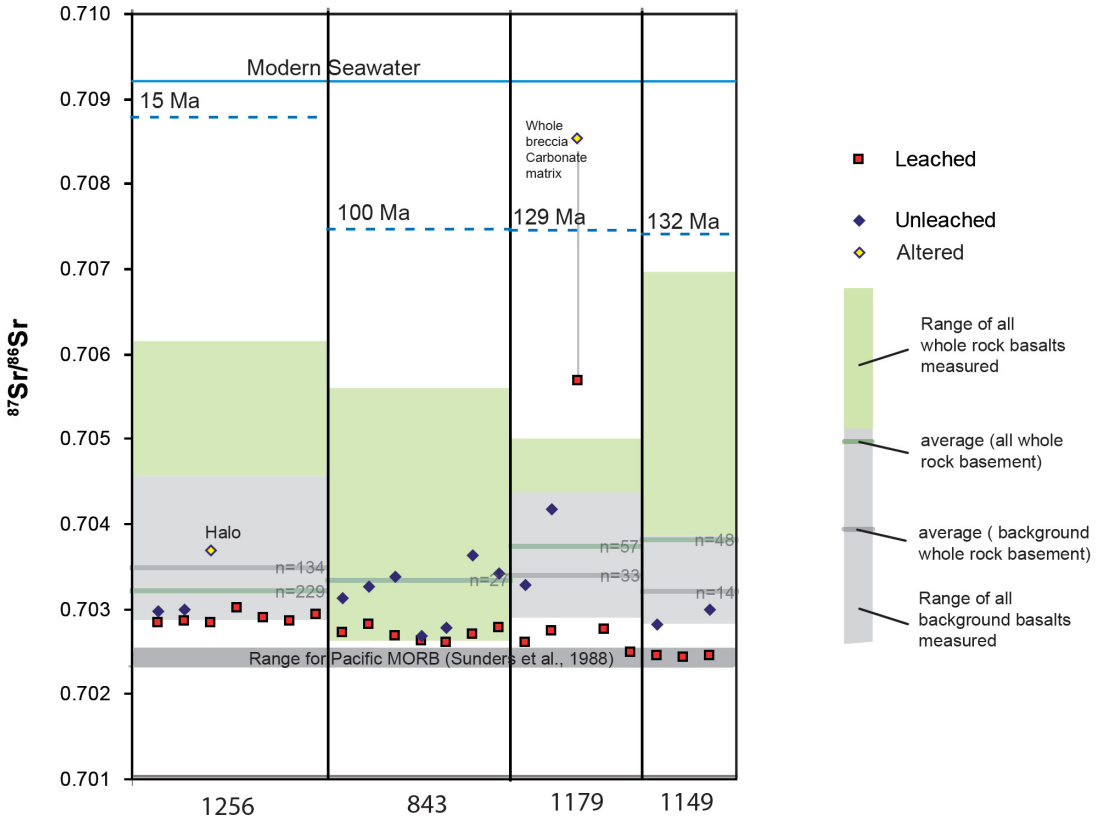

Figure 2.3. Sr isotopic composition of treated vs. untreated samples and range of measured basement samples for ODP/IODP Sites 1256, 843 (This study and King et al., 1993), 1179 and 1149. The Sr-isotopic composition of Pacific MORB (Saunders, et al., 1988), modern seawater and seawater (t) for each site is included (McArthur, et al., 2001). Acid washed samples are from (Mahoney. et al, 2005). Basement compositions are sourced from the following: Site 1256: this study, Harris and Cooper (unpub. Data) and Wilson et al., (2003), Site 843: This study, King et al., (1993), Site 1179: This study, Sano and Hayasaka, (2004), Site 1149: This study and Hauff, et al., (2003).

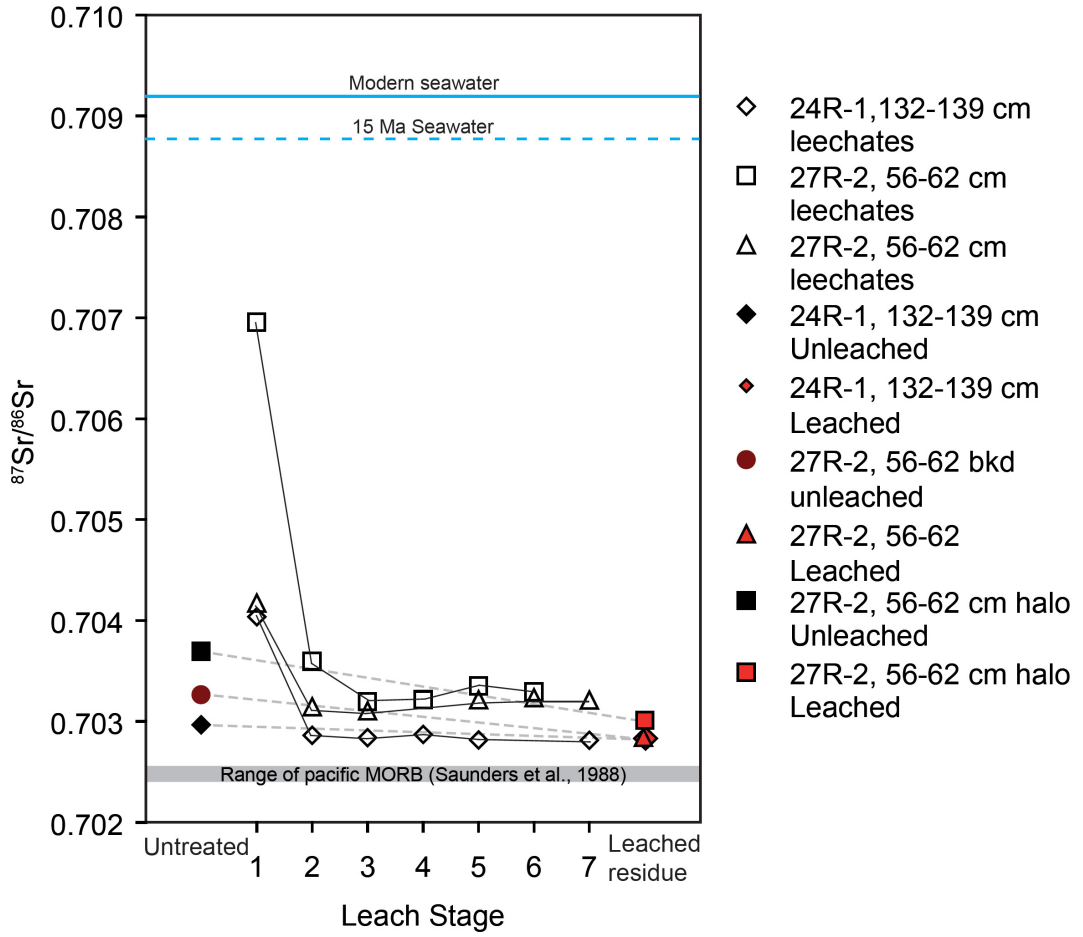

Figure 2.4. Strontium isotopic composition vs. leachate stage for ODP/IODP Site 1256 basalts. Untreated (black filled) and treated samples (red filled)are shown together with the Sr isotopic composition of seawater at 15 Ma (dashed) and present day (solid line) (McArthur, et al., 2001) and the range Pacific MORB (Saunders, et al., 1988).

2.5.3.2 Trace and REE

Trace and REE data for untreated whole rock samples, treated samples, and leachates are presented in Table 2.16. Initial plots of chondrite normalised REE for treated vs. untreated samples with average MORB are shown for each site in Figure 2.5. Site 843 also includes additional data from King et al, (1993). All treated samples have lower concentrations compared to average MORB, which exhibits a similar composition to the untreated samples.

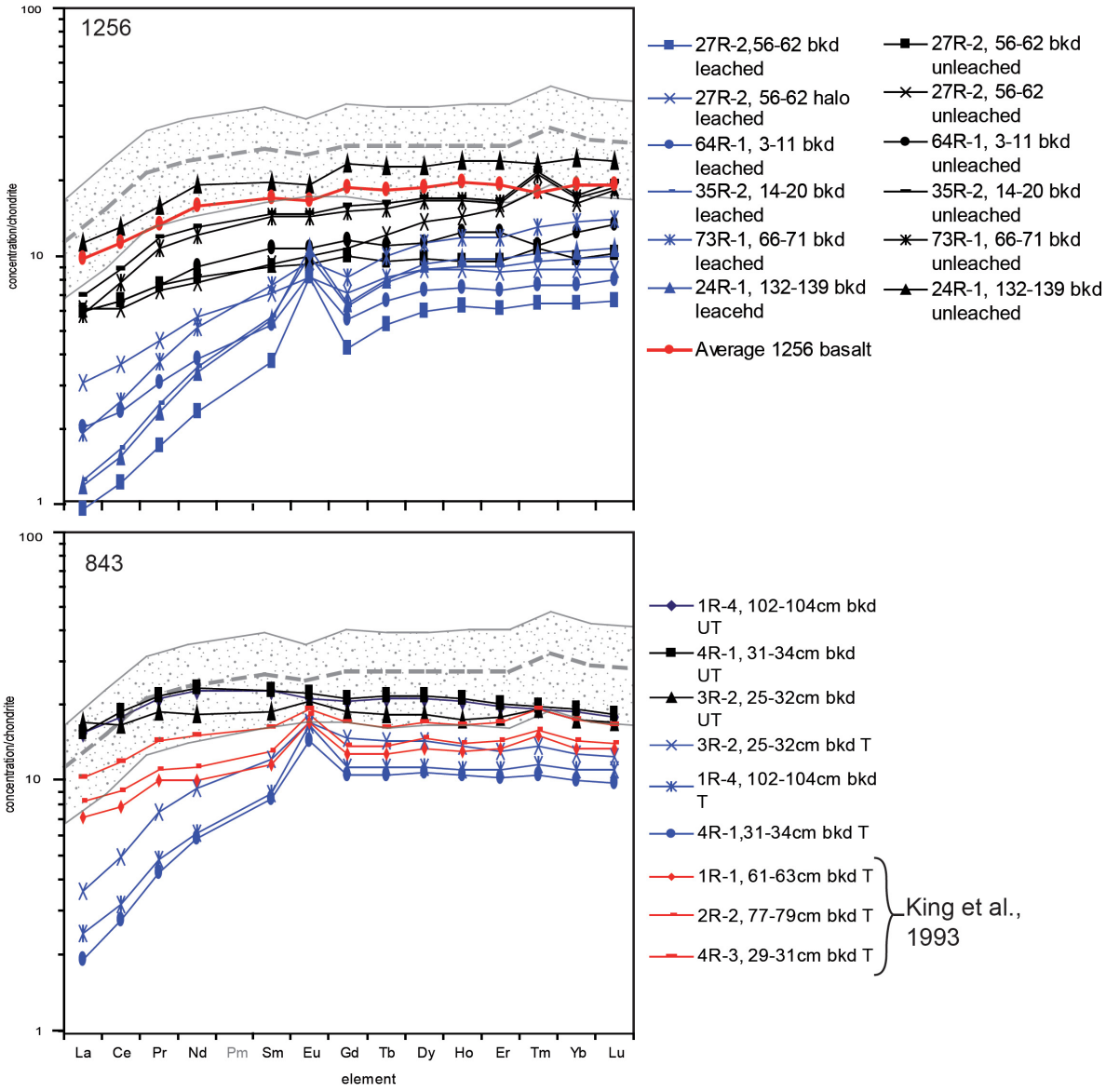

Figure 2.5. Chondrite normalised REE patterns for untreated (black) and leached (blue) whole rock samples at Sites 1256, 843, 1179 and 1149 Buff mott = Buff coloured mottled halo, Brn = brown, Bkd = background. T = treated, UT = untreated. Grey represents the data range of pacific MORB from Janney and Castillo, (1997). Pm is not measured.

In all samples across all sites the concentration of REE, especially LREE, is lower in the treated samples when compared directly with the untreated sample (Figure 2.5). In addition, all the leached samples exhibit positive europium anomalies compared to the flat, and commonly slightly negative anomalies seen in the untreated samples (Figure 2.5). REE in 'treated' samples; ODP Leg 206-1256D, 27R-2, 56-62 cm 'halo' and 20R-1, 100-105 cm 'brn bkd' have a similar chondrite normalised REE patterns to the

treated samples, however, small but significant differences include higher concentrations and a weaker Eu anomaly compared to the least altered treated samples.

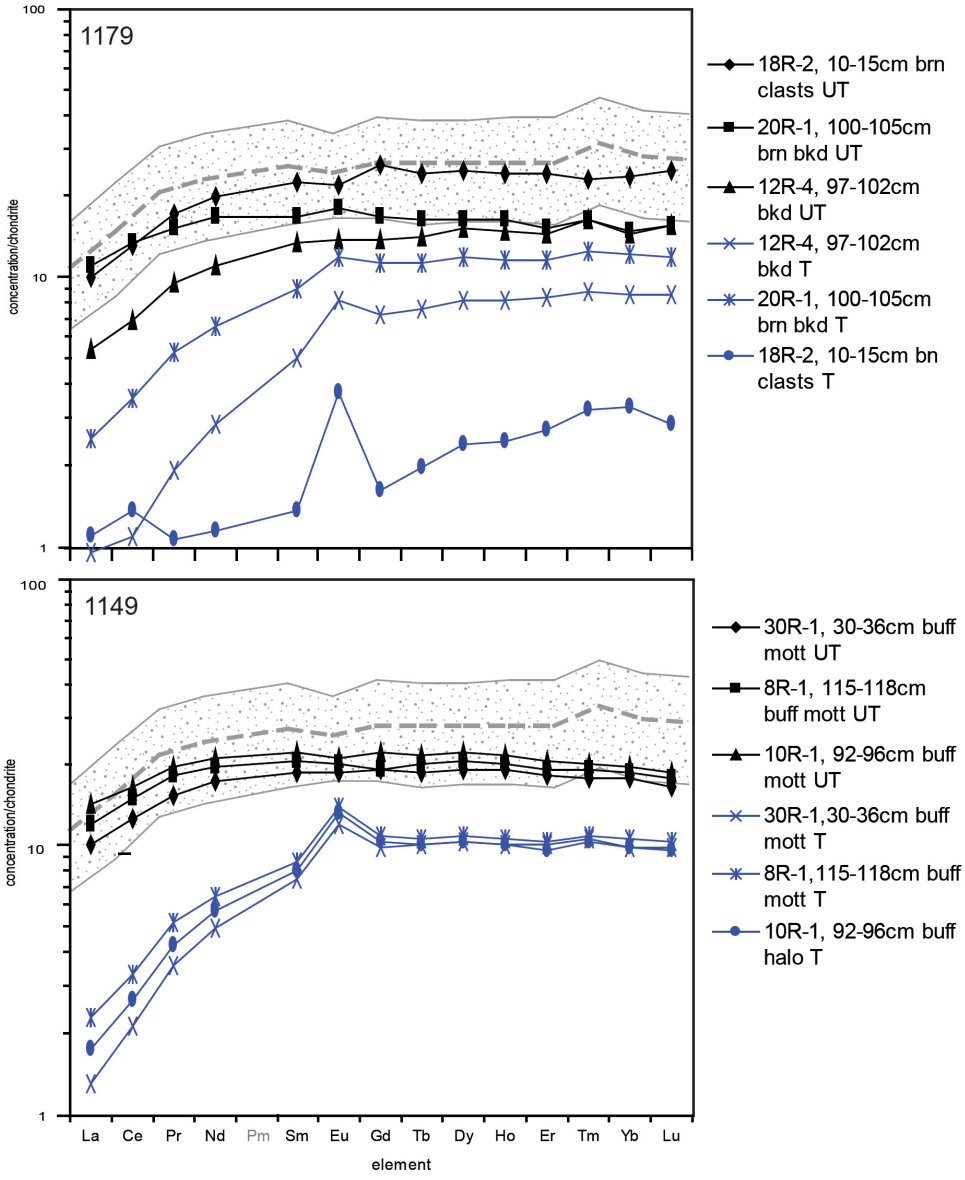

Figure 2.5. Continued.

Trace and REE data for each individual leachate are shown in Table 2.4 for samples 206-1256D-24R-1, 132-139 cm, 27R-2, 56-62 cm (background) and 27R-2, 56-62 cm (halo). All the samples studied record a steep followed by a gradual decline in trace element and REE concentration with each successive leach (Figure 2.6). REE concentrations of leachates 7 to 13 from all samples are variable although they exhibit

an overall decrease in concentration. The decrease in trace elements and REE in Figure 2.6 is observed in both labile and high field strength elements.

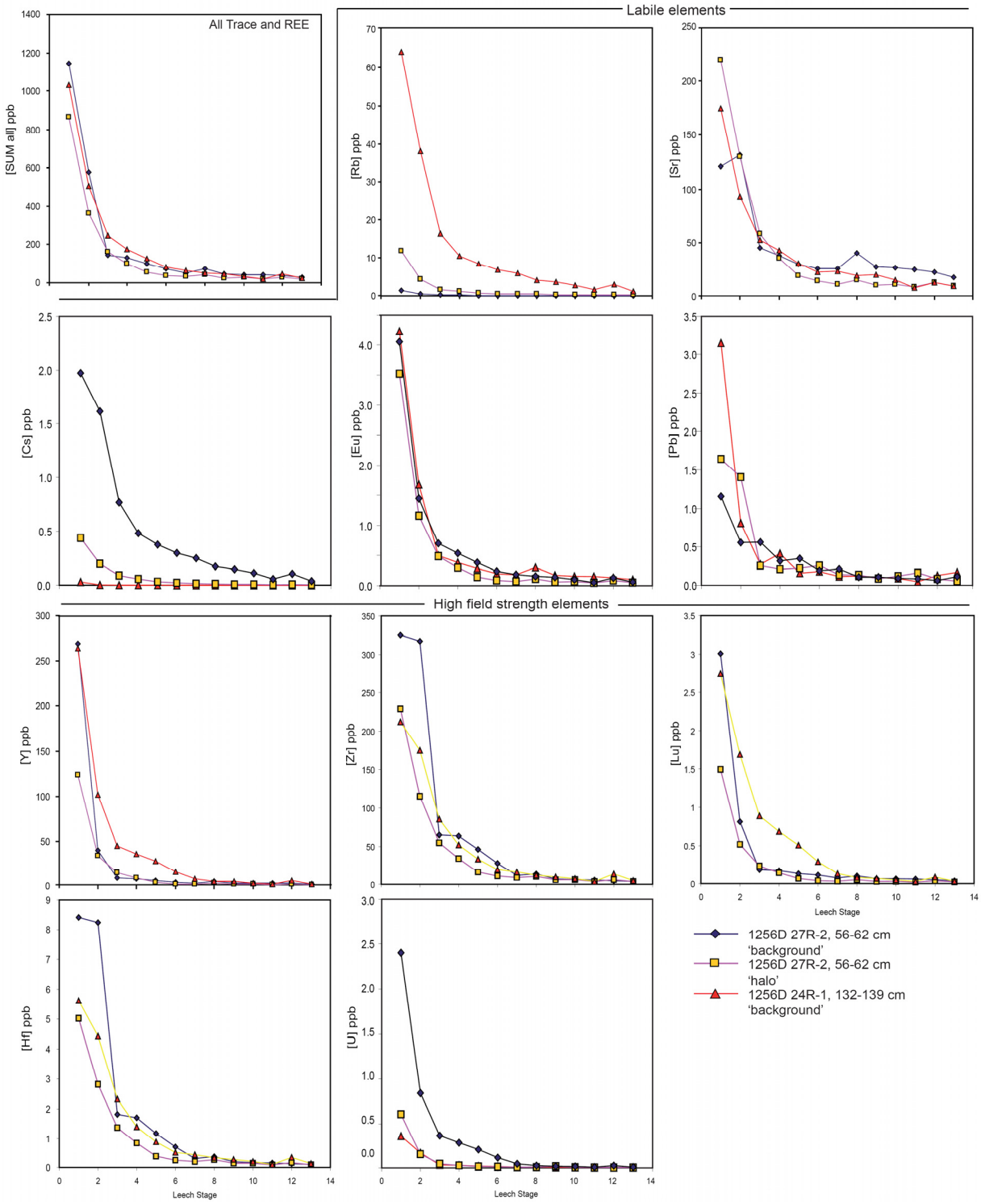

Figure 2.6. Examples of labile and high field strength trace and rare earth elements and sum of all Trace and REE vs. leach stage.

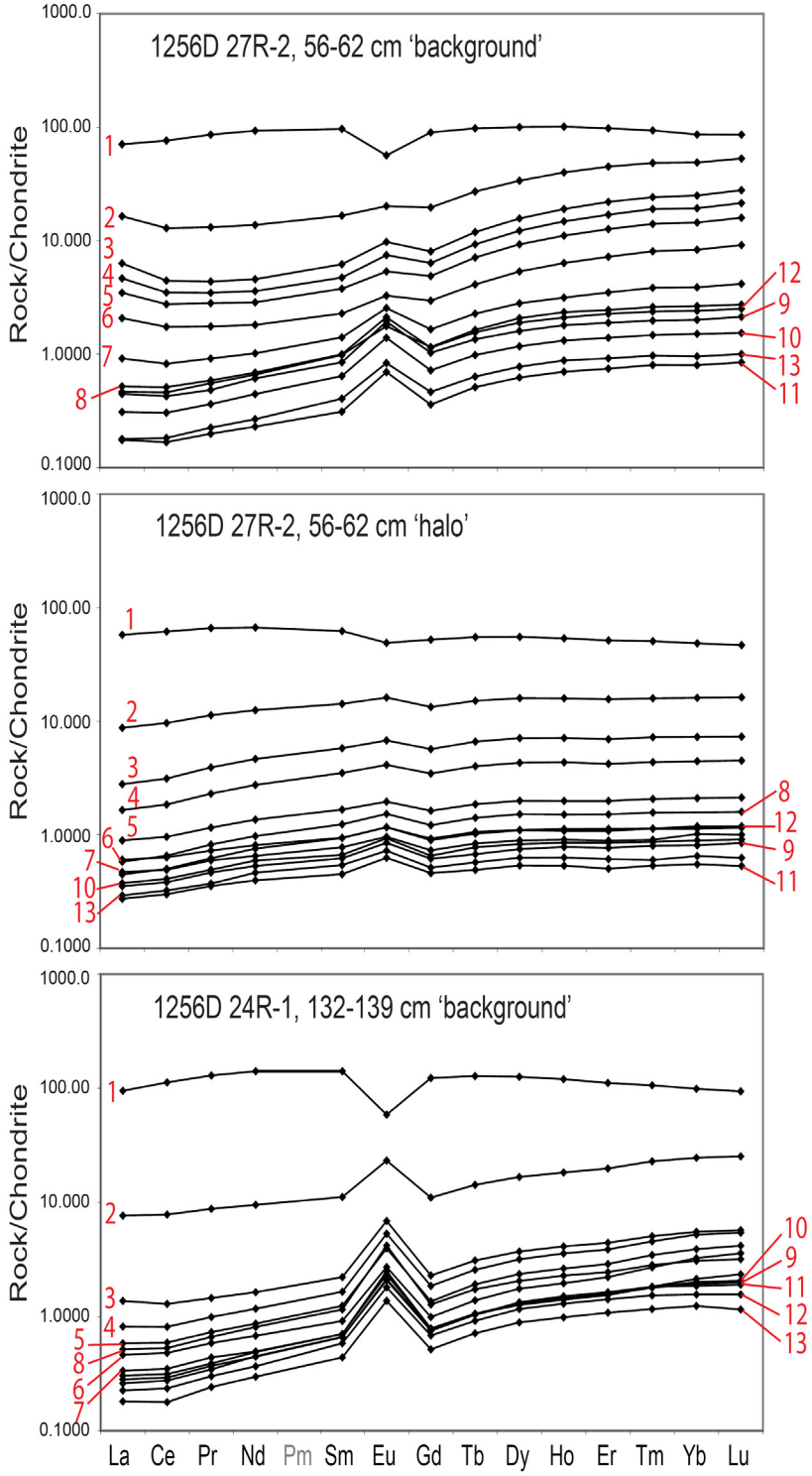

Figure 2.7. Chondrite normalised leachate REE patterns for Samples 1256D-27R-2, 56-62 cm 'background' and 'halo' and 1256D-24R-1, 132-139 cm 'background'. Numbers 1-13 indicate the leachate stage.

With the exception of Ce (0.67 ppb) Er (0.74 ppb) and Yb (0.80 ppb) in sample 1256D-27R-2, 56-62cm bkd, values for REE in leachates 7 to 13 are less than 0.5 ppb. Some REE concentrations are as low as 0.01 ppb. These concentrations are approaching the

detection limits (see 'methods') of the ICP-MS technique, which may account for the variability seen in the latter stages of the leaching process. Although all reasonable steps have been taken to ensure a clean experiment, contamination may affect the data because REE and trace elements are being recorded at such low concentrations.

Chondrite normalised REE patterns for the leachates recovered from each leach stage are shown in Figure 2.7. The successive decrease in the effect of leaching is reflected by the decrease in concentrations of REE, however, all samples show a relative change in the proportions of LREE to HREE and Eu. In all leach stages, LREE are relatively depleted compared to HREE, and from stages 1-7 this trend becomes more prominent. At stages 7 to 13 the trends remain very similar albeit at very low and variable concentrations (Figures 2.7). The chondrite normalised patterns for leachates 7 to 13 exhibit patterns that are variably elevated above preceding leachates. For example sample 1256D-27R-2, 56-62 cm 'background' leachate 12 has higher concentrations than 9, 10, and 11 (Figure 2.7). Sample 1256D-27R-2, 56-62 cm 'halo' shows the same trends, albeit not as distinct as the other samples, particularly sample 1256D-27R-2, 56-62 cm 'background'.

A plot of Eu anomaly vs. leachate stage and unleached/leached whole rock Eu is shown in Figure 2.8. Eu anomaly switches from neutral (Eu*/Eu of ~1) to positive within one leach stage followed by a variable increase and levelling off. Treated samples all have a higher Eu*/Eu compared to their untreated whole rock counterparts.

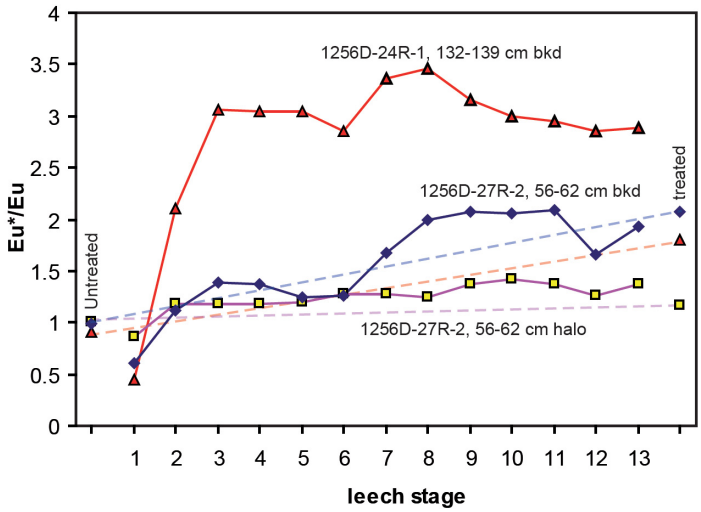

Figure 2.8. Eu*/Eu vs. Leach stage for ODP Leg 206-1256D-24R-1, 132-139 cm 'bkd', 27R-2, 56-62 cm 'bkd' and 27R-2, 56-62 cm 'halo'. Untreated whole rock and leached (treated) residues are included for comparison.

2.5.4 Discussion

2.5.4.1 Sr-isotopes

The variation in the Sr-isotopic composition of seawater through time has been recorded (McArthur, 2001). The Sr-isotopic composition of seawater at the time of formation at ODP/IODP Sites 1256, 1149, 1179, and 843B is significantly more radiogenic than the Sr-isotopic composition of Pacific MORB. This provides a useful scale that we can use to trace the origins of a particular mineral phase, to quantify the degree of alteration within a rock, or to determine if any seawater has exchanged with original Sr within primary mineral phases, for example Sr in plagioclase. The wide variation in the Sr-isotopic composition of untreated whole rock samples in oceanic basement (Figure 2.3) reflects variation in the intensity of alteration in oceanic crust. This, however, does not distinguish between high temperature, hydrothermal dominated alteration or low temperature seawater dominated alteration. It is well reported that seawater Sr will exchange more readily with primary igneous phases (e.g., plagioclase) at higher (~350^{o}C) temperatures (Teagle et al, 1998). In cold seawater dominated alteration, however, the variation in $^{87}Sr/^{86}Sr$ in basement rocks is primarily due to the presence of secondary minerals (saponite, celadonite, carbonate, iron-oxyhydroxides, and zeolites) with little or no isotopic exchange with the primary igneous phases. The replacement of mesostasis (interstitial glass) by saponite and other secondary phases may be one area where Sr-isotopic exchange could readily take place (e.g. Teagle et al, 1996, Teagle et al, 1998, and this study). Because all/most of the radiogenic Sr in the whole rock is present in secondary phases, then leaching of the secondary phases should remove the radiogenic seawater derived Sr and return the whole rock back to its precursor Sr-isotopic composition.

The reduction in radiogenic Sr in the leached residues (Figure 2.3) reflects the leaching of secondary minerals from the basaltic groundmass. The elevated $^{87}Sr/^{86}Sr$ in the altered and treated samples compared with the less altered and treated samples in each site suggests that; either not all the secondary minerals have been removed and that partial replacement of primary phases makes them more resilient to leaching, or that some radiogenic Sr has exchanged with Sr in the primary mineralogy.

The sharp decrease in radiogenic Sr in the leachates from Samples 206-1256D, 24R-1, 132-139 cm ‘bkd’, 27R-2, 56-60 cm ‘halo’, and 27R-2, 56-62 cm ‘bkd’ (Figure

2.4), suggest that the majority of secondary mineral phases are removed within the first 2-3 leaches. Because we expect cold seawater-derived secondary mineral phases to have near seawater $^{87}Sr/^{86}Sr$, a leach containing only secondary phases would have a similarly radiogenic composition. The actual $^{87}Sr/^{86}Sr$ values for the leachates indicate that a significant proportion of primary mineral phases are being dissolved. This is reflected in the later leaches where the amount of secondary mineral phases present in the groundmass is reduced and that a greater proportion of primary phases are present. Stages 5 and 7 have Sr-isotopic compositions that are comparable to MORB. Leachate 3 in samples 206-1256D, 27R-2, 56-60 cm 'halo', and 27R-2, 56-62 cm 'bkd' have an unexpectedly low $^{87}Sr/^{86}Sr$ (Figure 2.4) given that we would expect a steady decrease in secondary mineral content after each leach stage. Suspended particles of residue within the leachate may be responsible for the low $^{87}Sr/^{86}Sr$ because additional MORB Sr will be present in the leachate.

2.5.4.2 Trace and REE

Analysis of trace and REE in leachates indicate that the leaching method used in this study removed the vast majority of secondary phases in the rock and a small, but significant, proportion of the basaltic groundmass. Evidence for the removal of secondary phases from the basaltic sample is based on the following four points; 1) The depletion of REE, in particular LREE, reflects removal of mineral phases in which trace and REE are more easily partitioned into.

Figure 2.9 illustrates the partition coefficients for the major rock forming minerals in a basaltic melt. With the exception of plagioclase (LREE enriched) and phlogopite (Slight LREE enriched), the major constituents of basalt, clinopyroxene, and olivine do not partition into LREE and REE particularly well. LREE have the lowest compatibility of all the major basalt-forming minerals particularly clinopyroxene. The low REE concentrations and the chondrite normalised REE patterns of the residue (Figure 2.5) indicates that it is made up of primary phases, in particular clinopyroxene. 2) The presence of a positive Eu anomaly in the residue suggests that plagioclase is relatively resilient to repeated acid attack because Eu strongly partitions into the plagioclase crystal lattice. The strong partitioning occurs because Ca^{2+} and Eu^{2+} have a similar ionic radii and charge. However, contrary to the depleted LREE patterns seen in

Figure 2.7, which implies that plagioclase is being removed in preference to other primary phases, the strong Eu anomaly in the residues most likely reflects a strengthening plagioclase signal by preferential removal of secondary mineral phases over that of plagioclase. 3) Trace elements such as Rb, Y, Ba, like REE, are more readily able to substitute with large ions in the crystal lattices of secondary minerals; for example, saponite and celadonite. The depletion of Rb is consistent with the leaching experiments carried out by Mahoney, (1987) who suggests that plagioclase and clinopyroxene cannot accommodate Rb. Carbonates will harbour Sr since it can substitute for Ca^{2+}. 4) X-ray diffraction traces of treated samples in Mahoney et al., (1983) show strong peaks for well crystallised plagioclase and clinopyroxene and no carbonates, clay or zeolite peaks despite their occurrence in the untreated samples.

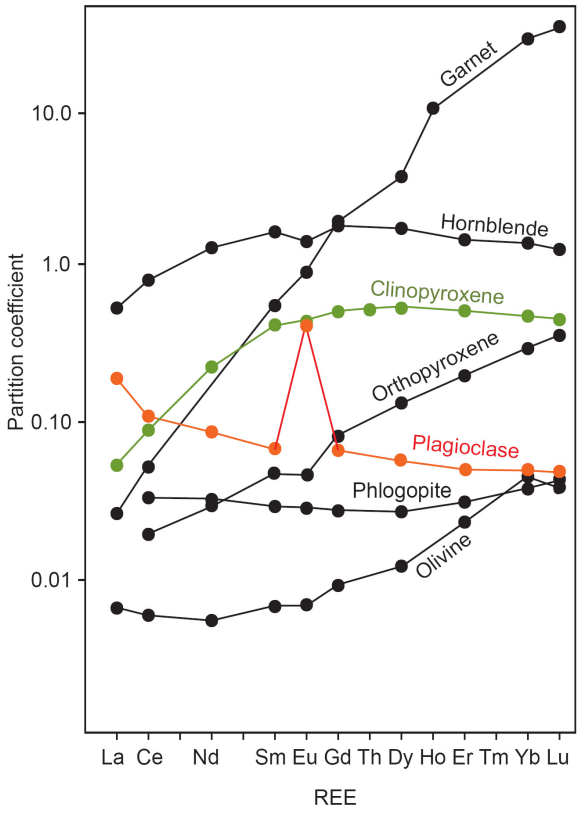

Figure 2.9. Partition coefficients vs. atomic number (REE) in common minerals in basaltic melts. Redrawn from Rollinson, (1993). Residues in this leaching experiment closely resemble clinopyroxene and plagioclase.

The leaching effects on the more altered sample (1256D-27R-2, 56-62 cm 'halo') are very similar to its fresh counterpart (1256D-27R-2, 56-62 cm 'background') and the other leached residues. However, differences include a weaker Eu anomaly in the residue and leachates, and a smaller difference between the LREE and HREE

concentrations in the leachates and residue. This supports the evidence from the Sr-isotopic compositions of the 'altered' residues that leaching of secondary mineral phases in this sample is incomplete.

The change in Eu and patterns of HREE and LREE in the leachates (Figure 2.7) suggest a very sharp increase in the proportion of plagioclase and clinopyroxene to secondary phases that are being leached, ultimately leading to leachates that are almost exclusively leaching plagioclase and clinopyroxene. Dissolution of primary groundmass is the most likely cause for the shift from negative Eu anomaly to positive Eu anomalies, because the proportion of plagioclase in the leachate increases. In addition, the increased depletion of LREE compared to HREE, and the low but relatively consistent levels of trace and REE in the last seven leachates in each sample, is consistent with the removal of secondary phases followed by near exclusive dissolution of primary mineral phases in the latter leach stages. This is reflected by the large drop in concentration of trace elements and overall REE and trace element concentration (Figure 2.6) within the first 3 leaches and the minor but variable changes in concentration in leaches 7-13.

2.5.4.3 Leaching model

Figure 2.10 demonstrates the process in which each successive leachate removes an ever smaller proportion of secondary mineral phases leading to an increase in the relative proportion of primary basalt, which is always leached. The result is a reduction in overall volume in the residue but it removes most of the secondary phases. The effect this would have on the proportion of MORB vs. seawater derived compositions is also shown in Figure 2.10, as estimated by the Sr-isotopic composition in the leachates and the residue. By combining the effects of leaching on Sr isotopic composition and Sr concentration the leaching mechanism can be demonstrated (Figure 2.11). The predicted leach path for the residue is shown including a cut-off point in which the concentration of Sr is too low for measuring

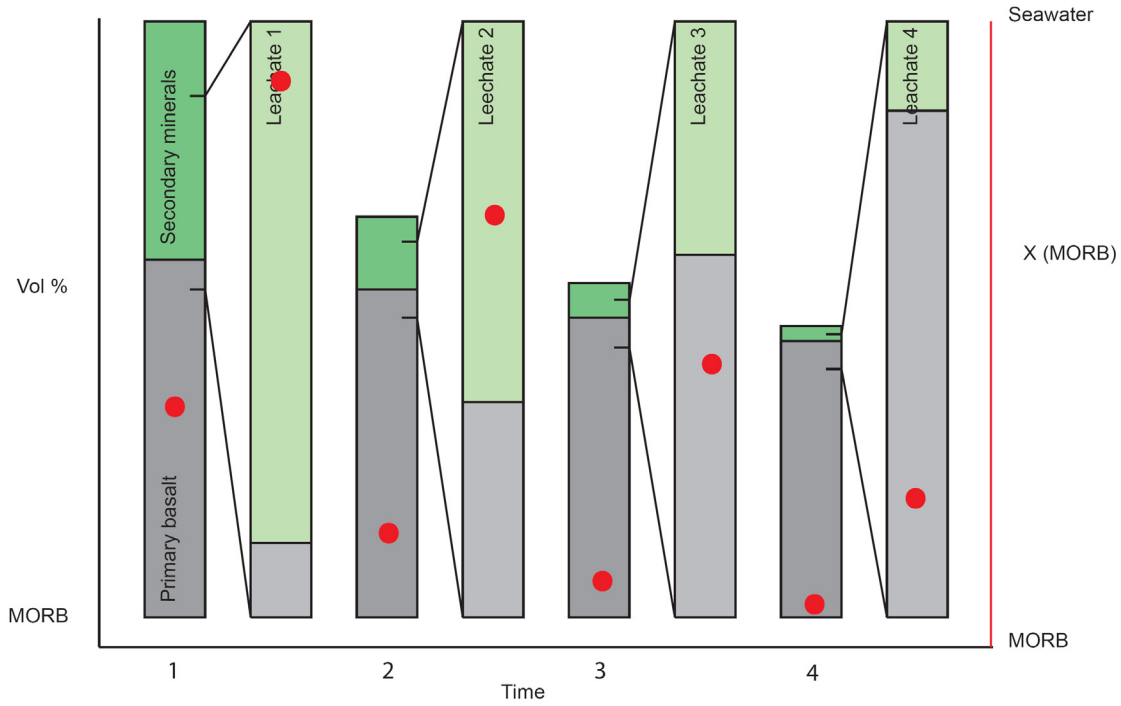

Figure 2.10. Illustration of the relative proportions of primary basalt/secondary minerals leached in each stage and their effect on the relative proportion of radiogenic Sr at each stage. During repetitive leaching a reduction in overall volume of remaining residue which is explained by the take up of secondary minerals and a percentage of basalt by the acid.

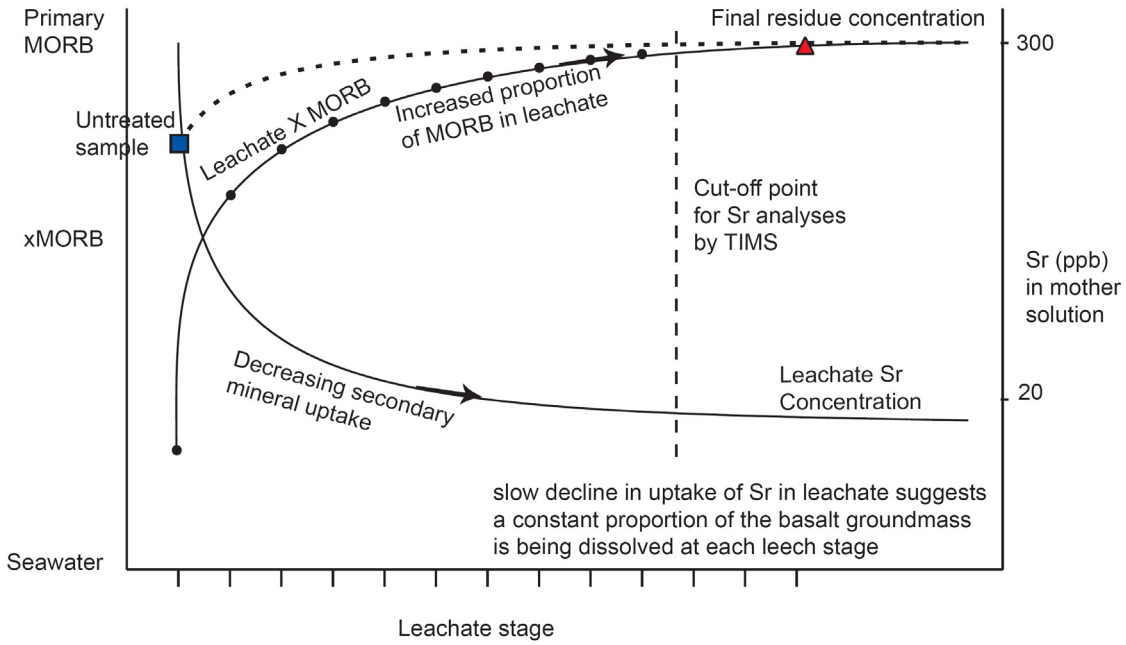

Figure 2.11. Model demonstrating the effects of aggressive multi-step leaching on basaltic rocks. Here we use Sr as an example becasue it serves as a useful guide to estimate the relative proportion of seawater dominated phases (low temperature secondary minerals).

accurate Sr isotopic compositions. To accurately define the curves shown in Figure 2.11 would require leaching of a larger volume of sample (~1g), or smaller volume of acid (if sample limited) combined with more frequent acid changes, for example, every 5 minutes rather than every 30 minutes.

2.5.4.4 Primary MORB Sr-isotopic composition

This study has shown that aggressive leaching of the least altered whole rock basaltic samples is able to remove the vast majority of low temperature, seawater-derived secondary mineral phases. Trace and REE patterns and concentrations for treated samples reflect the compositions of primary igneous phases, including plagioclase, which harbours primary Sr. Strontium isotopic compositions of the treated samples and the final measured leachates reflect primary Sr. Therefore in this study a selection of the treated samples is used to estimate the Sr-isotopic composition of primary MORB for each site (Table 2.17). Only the least altered 'treated' samples are used in which the majority of seawater-derived radiogenic Sr has been removed.

	1256D	1149D	1179D	843B
Selected age corrected Sr-isotopic compositions from least altered 'treated' samples	0.702834	0.702400	0.702486	0.702610
	0.702834	0.702416	0.702490	0.702620
	0.702849	0.702418	0.702521	0.702650
	0.702859			0.702659
	0.702901			0.702696
	0.702928			0.702700
				0.702790
std dev	0.000038	0.000010	0.000019	0.000037
Average	0.702868	0.702411	0.702499	0.702656

Table 2.17. Average 'fresh' MORB $^{87}Sr/^{76}Sr$ for ODP/IODP Sites 1256, 1149, 1179 and 843. Age corrected Sr-isotopic compositions for 'treated' samples from each site were chosen based on samples that contain the least alteration and lowest proportion of radiogenic Sr. Given the relatively low standard deviations (10 to 38 $x10^{-5}$) the range of Sr-isotopic compositions in the leeched residues probably reflect primary variability.

2.5.5 Conclusions

- Acid Leaching successfully removed most/all secondary minerals from the basalt revealing, in all but the most altered sample, Sr-isotopic compositions close to primary igneous values. Chondrite normalised REE patterns suggest that the residue is composed of primary phases, which is supported by XRD analyses by Mahoney et al., (1983) of similar experiments.
- Multiple leaching steps reveal a rapid leaching phase, which is dominated by the dissolution of secondary mineral phases, followed by slow leaching phase in which the relative proportion of primary igneous phases being leached is greater than the secondary mineral phases and the concentrations are more varied, as indicated by the Sr-isotopic composition and chondrite normalised REE patterns of the leachates.
- Only the most fresh basalts should be leached because more pervasively altered samples, such as 1256D-27R-2, 56-62 cm 'halo' will contain more secondary minerals, requiring a prohibitively large number of leach steps.
- 7 leaches are required to remove the bulk of secondary minerals from a basalt sample because basaltic-like compositions in the leachate, as shown by the observation that the $^{87}Sr/^{86}Sr$ in the last measurable leachate for each sample closely matches the Sr-isotopic composition of the final residue.
- Strontium isotopic compositions for primary MORB at ODP/IODP Sites 1256, 1149, 1179, and 843 have been determined by selection of the least altered treated samples.

Chapter 3

Site 1179

3. Site 1179

3.1. Abstract

ODP Hole 1179D (41°04.8'N, 159°57.8'E) is situated in the north east Pacific and penetrates ~100 m into 129 Ma basement that formed at the fast spreading east-northeast trending Pacific-Izanagi ridge. This site has relatively smooth basement topography, and endured only slow (<1 m/m.y.) rates of sedimentation until the Miocene. Mineral, chemical and isotopic evidence is presented for hydrothermal alteration at this site.

The basement rocks of Hole 1179D comprise 79% massive flows, 16% pillow lavas, 4% breccia and 1% inter-pillow sediments. They are slightly to strongly (5-80%) altered to saponite, calcite, celadonite, and iron-oxyhydroxides. Strong alteration predominantly occurs within the pillow lavas and breccias, with intensity increasing with depth. The lower portion of the hole is more strongly oxidized with increased abundance of iron-oxyhydroxides and less common celadonite.

Variable changes in whole rock chemistry include large increases in $Fe_2O_3{}^T$, K_2O, CO_2, H_2O, Rb, Cs, Ba, Ta Th, and U together with decreases in SiO_2, MnO, MgO, Ni. Most initial (128 Ma) $^{87}Sr/^{86}Sr$ ratios (0.7024 to 0.7048) are significantly higher than reported values for Mesozoic Pacific MORB (0.7024-0.7028) and leachates (0.70249-0.70252). This may be due in part to contamination from the near by Shatsky Rise plume, but it also indicates that the rocks have undergone significant (~13 %) Sr-isotopic exchange with seawater. Carbonate vein $\delta^{18}O$ and $\delta^{13}C$ values range from 26 to 31 ‰ ± 0.1% $_{(VSMOW)}$ and -0.1 to 2.4 ‰ ± 0.1 ‰ $_{(VPDB)}$ respectively, the latter are typical of veins formed from seawater. Temperature estimates based on oxygen isotopic measurements of carbonate veins range from 12 to 40 °C. Some carbonate $^{87}Sr/^{86}Sr$ ratios from Hole 1179D are significantly more radiogenic than 129 Ma seawater, requiring prolonged periods (40 to 100 M.y.) of seawater alteration of the ocean crust, this example clearly illustrates the inherent problems associated with using $^{87}Sr/^{86}Sr$ ratios of basement carbonates to assess the timing of secondary mineral precipitation and dating oceanic basement. In addition, comparisons between formation temperatures, $\delta^{13}C$, and Sr-isotopic ratios carbonates from other basement sites suggest that sedimentary burial rates appear to exert an influence on the nature of alteration in upper oceanic crust.

3.2. Introduction

Site 1179 (41°04.8′ N, 159°57.8′ E) is located in the northwest Pacific plate approximately 1600 km west of Japan on 129 Ma (Mid-Hauterivian) crust, as indicated by northeast trending M-series magnetic lineations that young toward the northwest (Nakanishi et al., 1999). Site 1179 lies approximately 240 km northwest of the Shatsky Rise (Figure 3.2.1). Palaeomagnetic data indicate that the Pacific plate has drifted northward ~30° since the Cretaceous, which suggests that the crust at Site 1179 likely formed ~10° north of the equator (Sager and Pringle, 1988; Larson, et al., 1992).

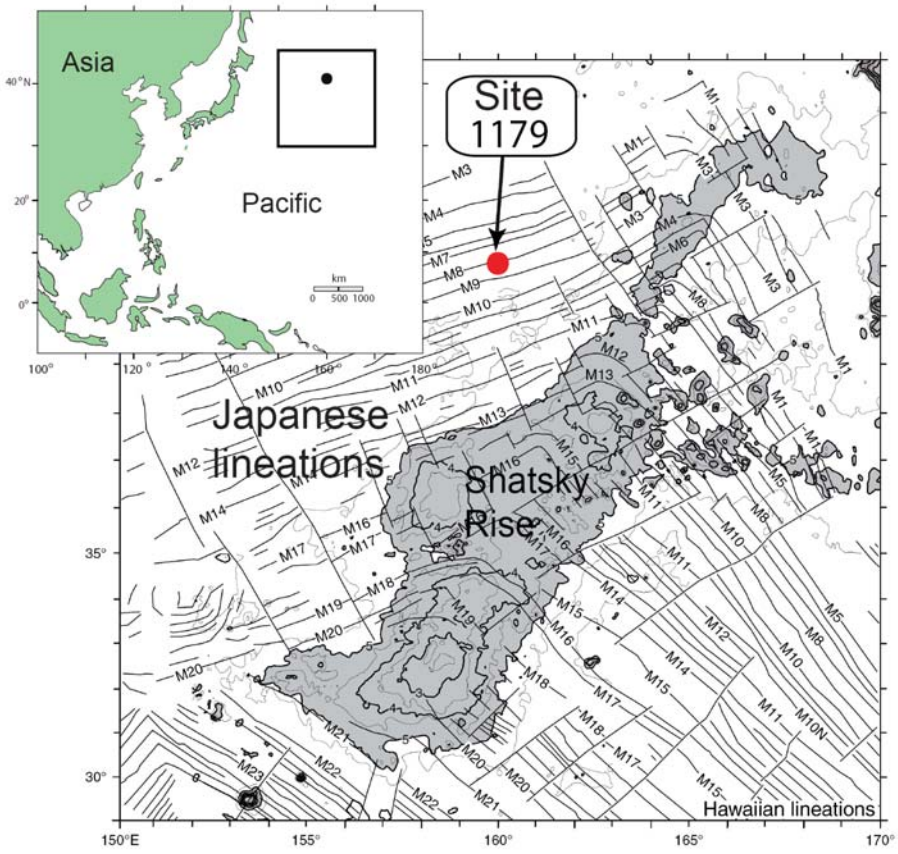

Figure 3.2. Location of Site 1179 (Kanazawa et al., 2001)

The Japanese and Hawaiian magnetic lineations intersect about an axis where the trend shifts from west-north west to north-east. The intersection implies that the spreading ridges that formed the lithosphere converged at a triple junction which formed the north west corner of the Pacific plate (Larson and Chase, 1972; Sager et al., 1988). The oceanic plateau, Shatsky Rise formed at the triple junction of the Pacific, Izanagi, and Farallon plates between 150 and 130 Ma (Nakanishi et al., 1999; Sager et

al., 1988, 1999). The timing of Shatsky Rise is similar to that of the Ontong Java plateau which corresponds to a period of super plume activity (Larson, 1991). Seismic profiles of Site 1179 with apparent reflector displacements suggest that Site 1179 may be located within a graben ~1 Km across (Kanazawa et al., 2001). Figure 3.2 illustrates the correlation between the stratigraphy based on direct observation of the core and the seismic profile of Site 1179. The strong reflector in Figure 3.2 marks the boundary between sediment and basement rock, although the actual contact was not recovered.

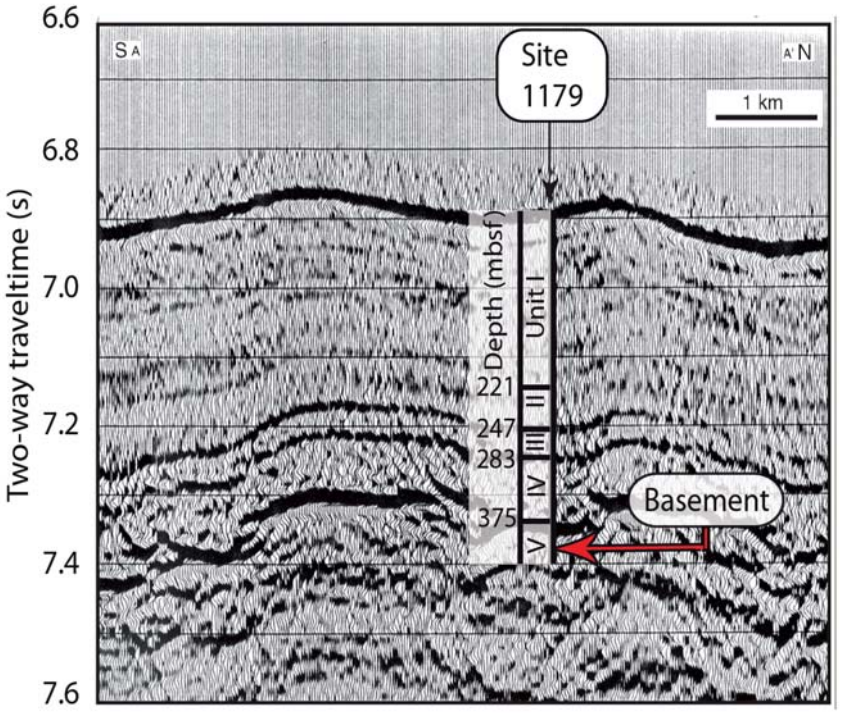

Figure 3.2. Seismic profile of Site 1179 with the correlated stratigraphy of Hole 1179D shown. The thick reflector at ~7.3 seconds marks the oceanic basement. Scaling of the lithostratigraphic column was carried out using the velocity-depth relationship of Carlson et al. (1986) to calculate the two-way traveltime of unit boundaries derived from core observations (Kanazawa et al., 2001).

Hole 1179D penetrates a 375 m-thick sedimentary section followed by 100 m of upper oceanic crust to a total depth of 475 mbsf. However, logging in ODP Hole 1179D was restricted to a depth of 260 mbsf because a bridge in the hole precluded the transit of wireline geophysical tools, therefore core-log integration of basement to determine the true distribution of rock types was not possible.

The sedimentary section consists of four units. The uppermost Unit 1 comprises 221.5 m of clay and radiolarian-bearing diatom ooze of late Miocene to Pleistocene age with common ash beds. Unit 2 comprises 24.5 m of clay-rich diatom-bearing

radiolarian ooze of late Miocene age which overlies a 37.5 m of barren brown pelagic clay (Unit 3). The sediments of Unit 4 were not recovered, with only chert nodules and porcellanite fragments obtained from this 93.7 m-thick unit. The evolution of sediment thickness though time is illustrated in Figure 3.3. A lack of sediment recovered in Unit 4 means we can only assume a constant sedimentation rate of ~1.3 m/Myr for the deposition of Unit 4. The gap in the record extends to the early Miocene (~18 Ma) in which the base of Unit 3 records a low sedimentation rate of ~1.3 m/Myr. The very low levels of sedimentation persisted until the Mid-Miocene (~14 Ma), when there is a dramatic increase in sedimentation rate (~19 to 30 m/Myr). Sediment recovery is 78.5% with 100% recovery of the clay and oozes and only 6.75% recovery of Unit 4.

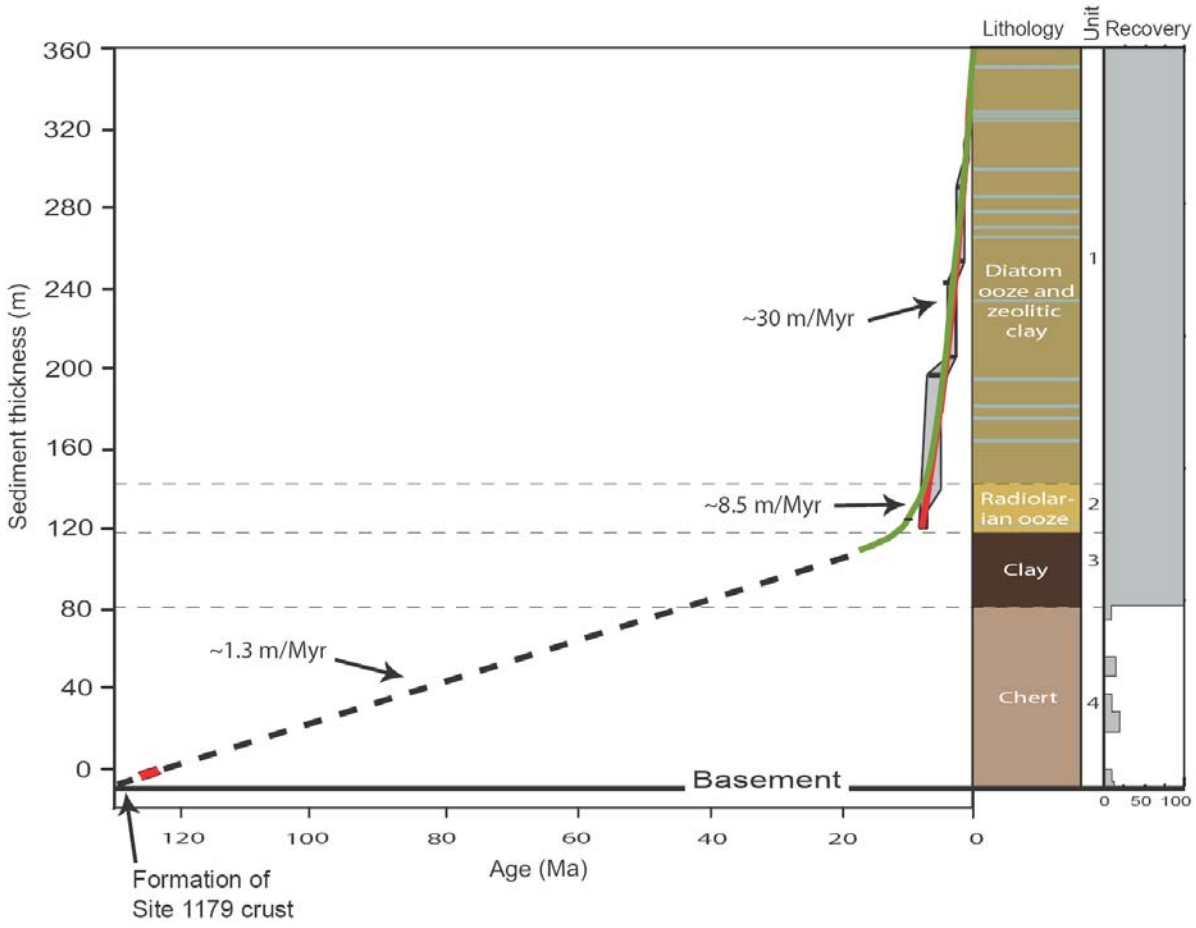

Figure 3.3. Plot of sediment cover vs. time at Site 1179. Sedimentation rates are derived from a combination of palaeomagnetic (Green line) and biostratigraphic (Red line) data. The grey field indicates error margin in biostratigraphy. A lack of palaeomagnetic and biostratigraphic data resulting from low core recovery. No fossil evidence for time period 123 Ma to 18 Ma leaves a gap in the record. This is filled in by the dashed line by extrapolation from the earliest record and the start of the palaeomagnetic data. (Modified from Kanazawa et al., 2001)

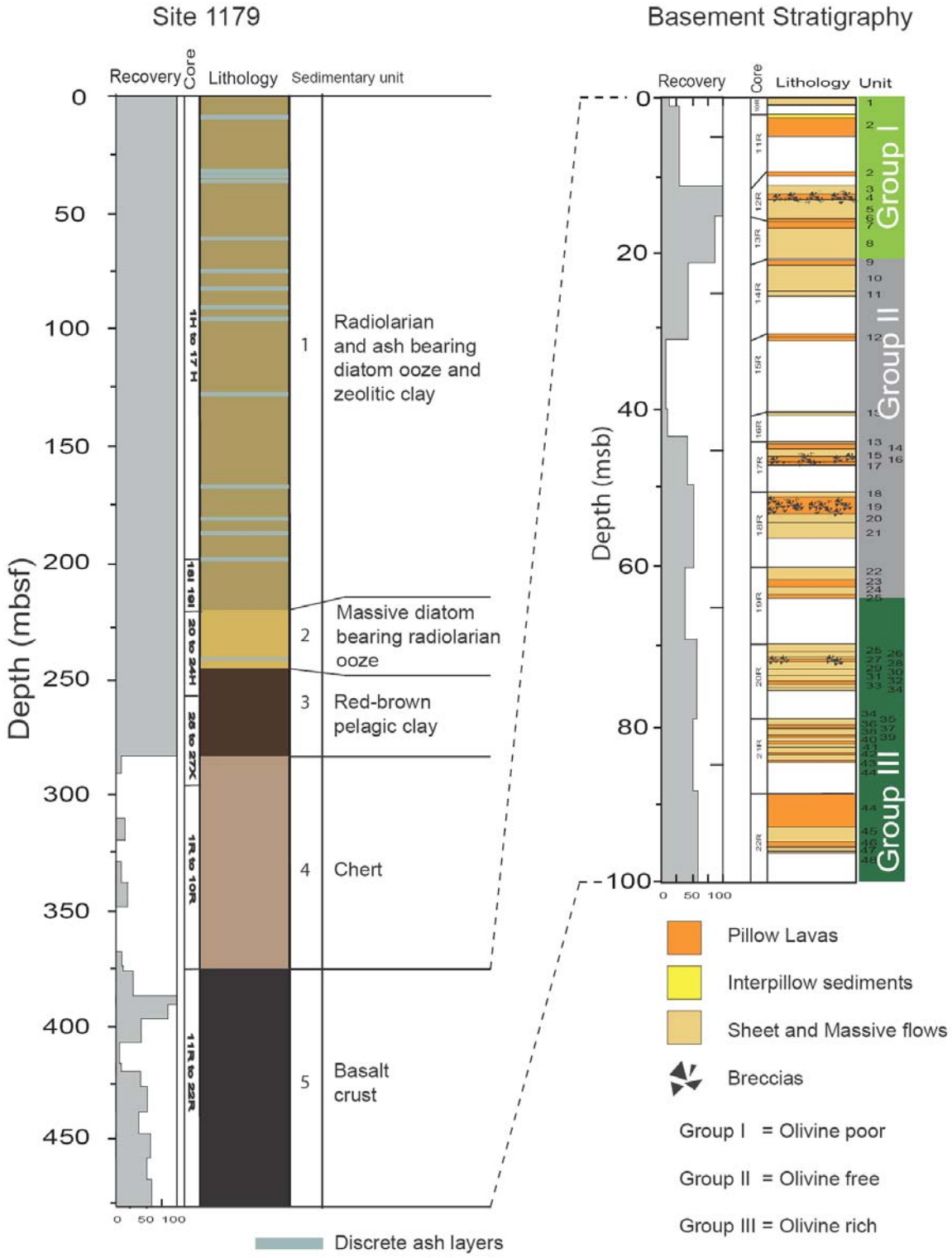

Figure 3.4. Summary lithostratigraphic column for Site 1179, including core recovery, lithology and lithostratigraphic unit columns. ODP Holes 1179A (0-10 mbsf), 1179B (0-55 mbsf) and 1179C (0-292 mbsf) make up the sedimentary succession. The stratigraphy from a depth of 282 to 475 mbsf was interpreted from Hole 1179D recovered material. (Kanazawa et al., 2001).

Basement rocks recovered from Hole 1179D consist of cryptocrystalline to medium grained basalts of which 79% are massive flows, 16% pillow lavas, and 4% breccia. A further 1% of the recovered core consists of interpillow sediments. Recovery averages 43.5 % with low recovery in intervals 0-10 msb (<27 %) and 30-43 msb (<10 %). The basement section is divided into 48 igneous units based on lithological differences, flow and/or cooling margins (Figure. 3.4). The most distinct petrological change is the presence or absence of olivine. Group I basalts (Units 1-8, 0-21 msb) are olivine poor. Group II (Units 9-24, 21-64 msb) are olivine free and aphyric and Group III (Units 25-48, 64-100 msb) are olivine rich with olivine present as phenocrysts and within the groundmass. Groups I and II basalts are fine grained with subophitic texture whereas Group III basalts tend to be ophitic of medium grain size in the thicker lava flows (Kanazawa et al., 2001).

Shipboard XRF analysis and petrographic analysis indicate that these basalts are primitive tholeiitic MORB with the lavas of Group II being the most fractionated, which is closely followed by those of Group II. Group III basalts are chemically distinguished from the other groups by high concentrations of MgO, Cr, Ni, and Sr, which is consistent with the presence of olivine and Cr-spinel (Kanazawa et al., 2001). The difference in olivine content and the secondary mineral assemblages between Groups II and III causes a distinct colour change. The upper 24 units are green due to secondary mineral precipitation of saponite and celadonite. The lower 24 units are brown due to the alteration of olivine to iddingsite and the increased abundance of iron-oxyhydroxides.

3.3. Basement Alteration

Secondary alteration phenomena for a representative suite of basalts have been described from hand specimen and thin sections from ODP Hole 1179D (See A. 1, Appendix). The extent and characteristics of alteration in ODP Hole 1179D ascertained include: 1) mineralogy, its extent, distribution and type 2) alteration halos, their relationships and their distribution 3) veins and breccia characteristics. These observations of basement alteration provide constraints for interpreting the geochemical analyses, because ultimately chemical variations must relate to the mineralogy and therefore the style and intensity of alteration. This provides a means to quantify and

characterise basement alteration at Site 1179. Various styles of alteration and their spatial and temporal characteristics have been identified by the nature of alteration halos, their relationship with veins and vesicles and the filling sequences within veins and their subsequent temporal relationships. Secondary mineral assemblages can be divided into four main types:

1. Saponite rich halos and patches. Increased abundance of saponite is present causing the occurrence of pale green to yellow/green halos. Saponite may have a minor abundance of iron-oxyhydroxides.
2. Saponite + iron-oxyhydroxides. Saponite commonly forms in conjunction with iron-oxyhydroxides. Varying levels of $Fe(O,OH)_x$ dictate the colour under thin section. Observations indicate green-brown to brown-red halos around fractures and vesicles filled with saponite + $Fe(O,OH)_x$.
3. Celadonite. Its presence is not ubiquitous, but it is commonly associated with saponite + $Fe(O,OH)_x$. It occurs in veins, within halos and fills vesicles. In halos, celadonite is nearly always patchy and it is commonly overprinted by Fe-oxyhydroxides. In areas where no overprinting has occurred, celadonite forms dark grey/green alteration halos
4. Complex halos. Contain multiple phases of green, brown and red halos caused by overprinting of celadonite by iron oxyhydroxides and later saponite. Additional later iron oxyhydroxides and/or celadonite may overprint the previous sequence.

The distribution of alteration styles is shown in Figure 3.5. All basement rocks recovered from ODP Hole 1179D are altered. Alteration intensity remains slight for the majority of rocks. However, rare moderate and high levels of alteration are present. The distribution of alteration styles remains fairly constant at 0-70 msb. Past 70 msb to the base of Hole 1179D brown alteration halos dominate. High volumes of brown halos coincide with low abundances of dark grey/green halos. Figures 3.6 shows typical secondary minerals observed in ODP Hole 1179D and Figure 3.7 show the typical effects of alteration on basement rock within the igneous groups and typical vein relationships throughout ODP Hole 1179D. Secondary mineral distribution in ODP Hole 1179D is shown on Figure 3.3.4, which utilizes compilation of shipboard and shorebased data from thin section, hand specimen and XRD. Distribution of secondary minerals throughout ODP Hole 1179D indicate that uniform massive flows contain a

higher abundance of Fe-oxyhydroxides, whereas pillow flows are more associated with saponite and carbonates.

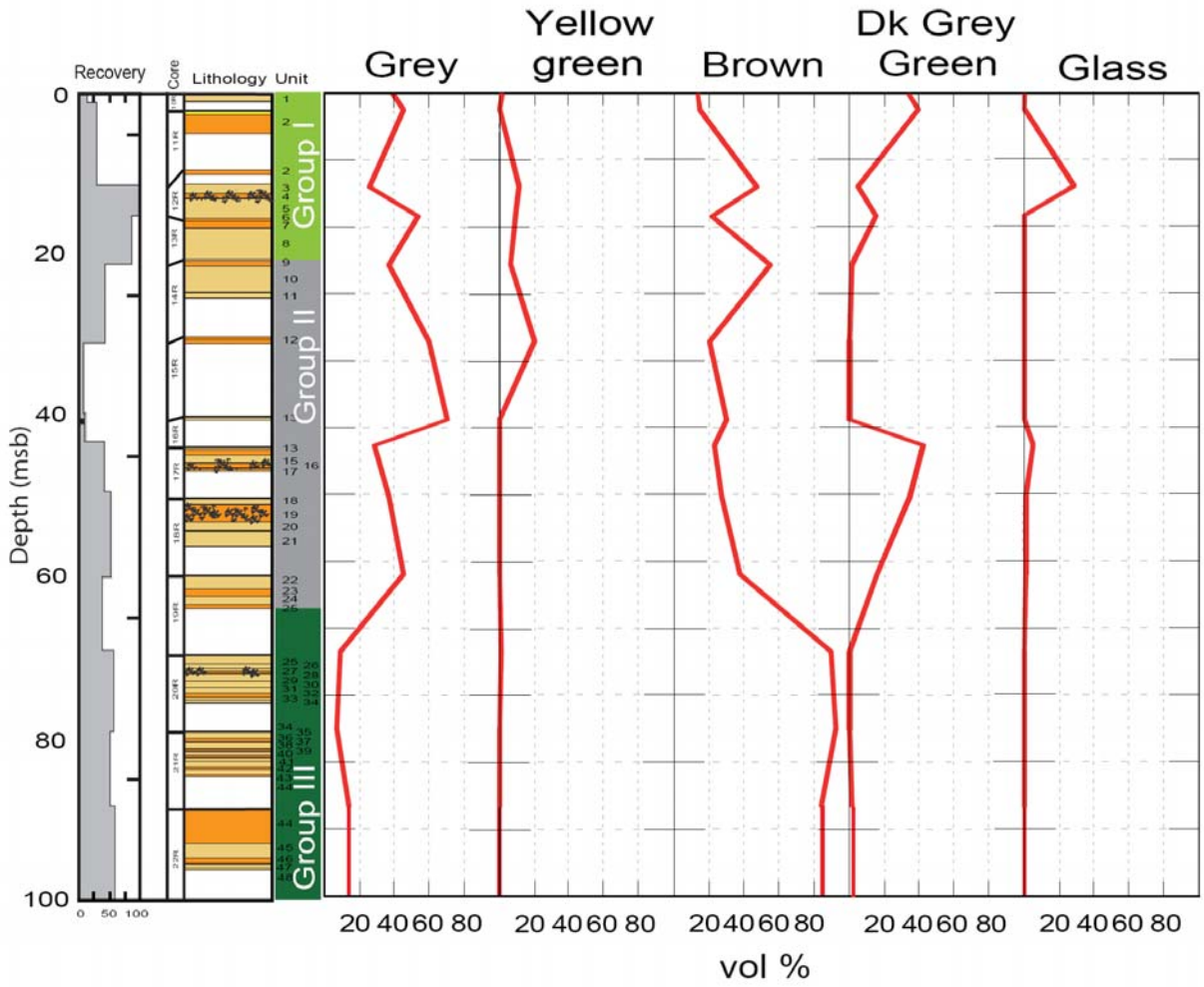

Figure 3.5. Distribution of alteration styles with depth in Hole 1179D. Styles of ateration are grouped depending on the observed secondary mineral. Grey (Saponite background), Yellow green (Saponite + Fe-oxyhydroxides), Brown (Fe-oxyhydroxides ± saponite), Dk Grey/green (Celadonite). Igneous stratigraphy is shown. Igneous groups are subdivided based on olivine presence. Group I basalts (Green) are olivine poor, group II basalts (Grey) are olivine free and group III basalts (Dark Green) are olivine rich. Percentages are based on direct observation of samples by eye. Results are calibrated to account for recovery.

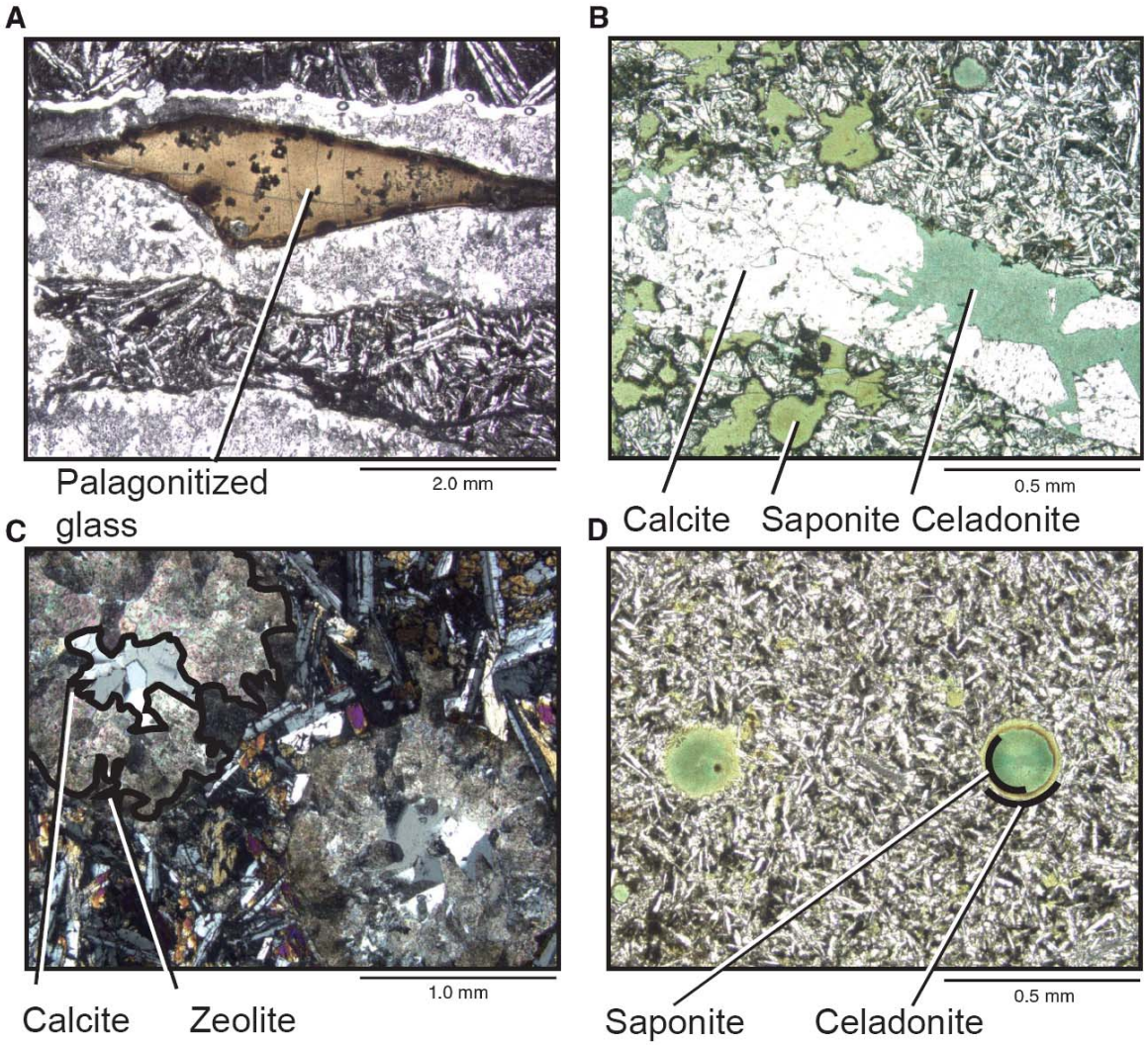

Figure 3.6. Photomicrographs showing secondary minerals in basalts from Hole 1179D. A. Palagonitized glass in hyaloclastite in plane-polarized light (Sample 191-1179D-20R-3, 139–142 cm) B. Vein with calcite and celadonite in matrix with smectite in plane-polarized light (Sample 191-1179D-12R-4, 83–86 cm). C. Vesicles with calcite and zeolite in cross-polarized light (Sample 191-1179D-22R-5, 135–137 cm) D. Vesicles with smectite and celadonite in plane-polarized light (Sample 191-1179D-12R-2, 13–15 cm). (Kanazawa et al., 2001).

3.3.1 Secondary minerals and halos

Saponite is the most abundant secondary mineral in Hole 1179D and it is present throughout the core in all basement rocks including massive flows and pillow basalts. Saponite in ocean crust is a trioctahedral Mg-rich smectite with relatively low Fe, Al and K unless saponite is intermixed with celadonite (e.g., Alt and Honnorez, 1984; Gillis and Robinson, 1990; Teagle et al., 1996; Alt and Teagle, 2003; Tabli and Honnorez, 2003).

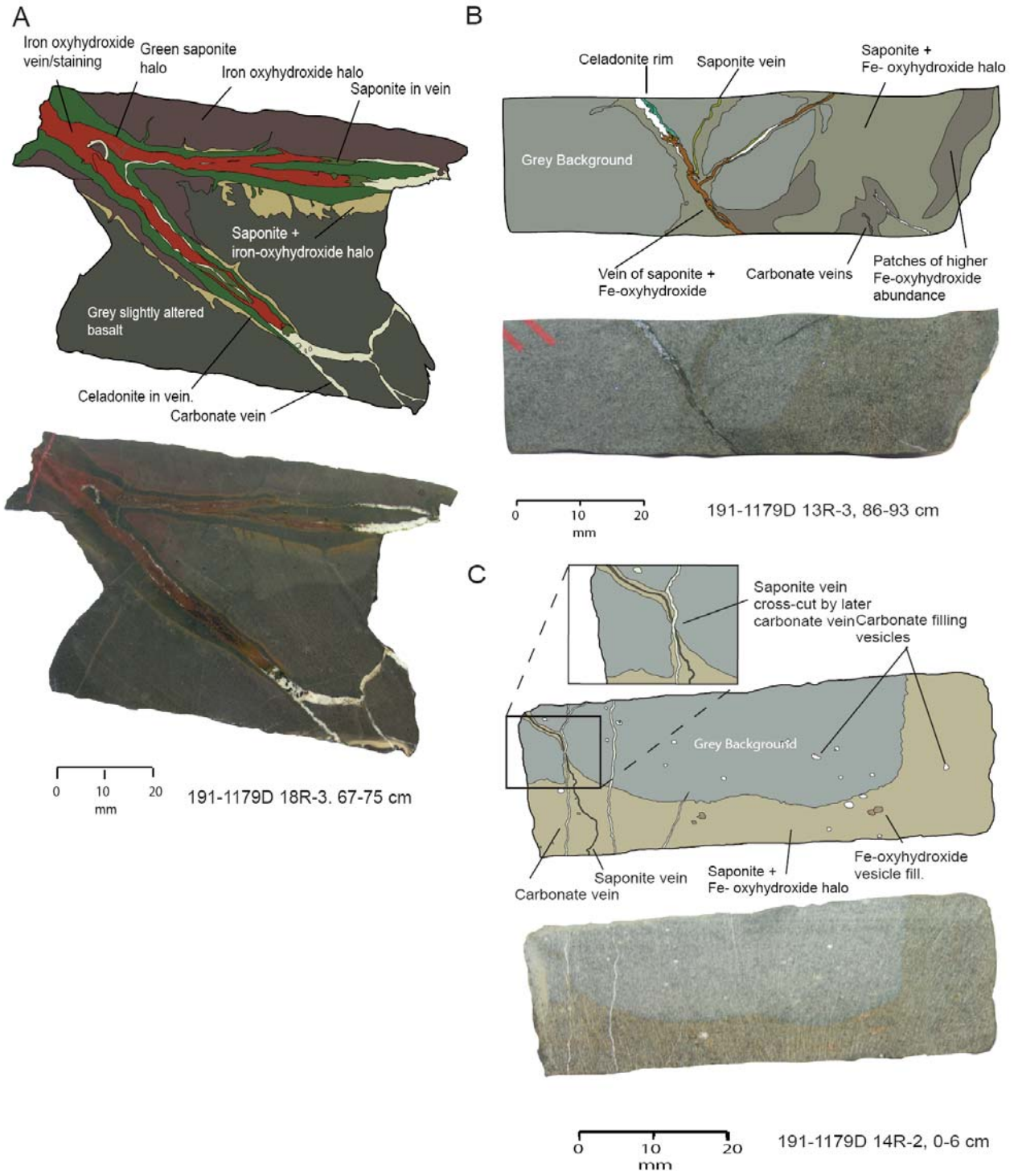

Figure 3.7. Typical alteration styles in Hole 1179D. A.) Sample 191-1179D-18R-3, 67-75 cm (53.7 msb) with high degree of oxidation overprinting earlier saponite and celadonite, which is only present in discrete areas within veins. B.) Sample 191-1179D-13R-3, 86-93 cm (19.3 msb)with veins of mixed composition and a halo of saponite and iron oxyhydroxide. This sample typifies alteration for the upper two thirds of Hole 1179D. Saponite + Fe-oxyhydroxides form the bulk of the alteration. Rare celadonite occurs on vein margins. C.) Sample 191-1179D-14R-2, 0-6 cm (22.9 msb) with calcite vein cross-cutting a saponite vein.

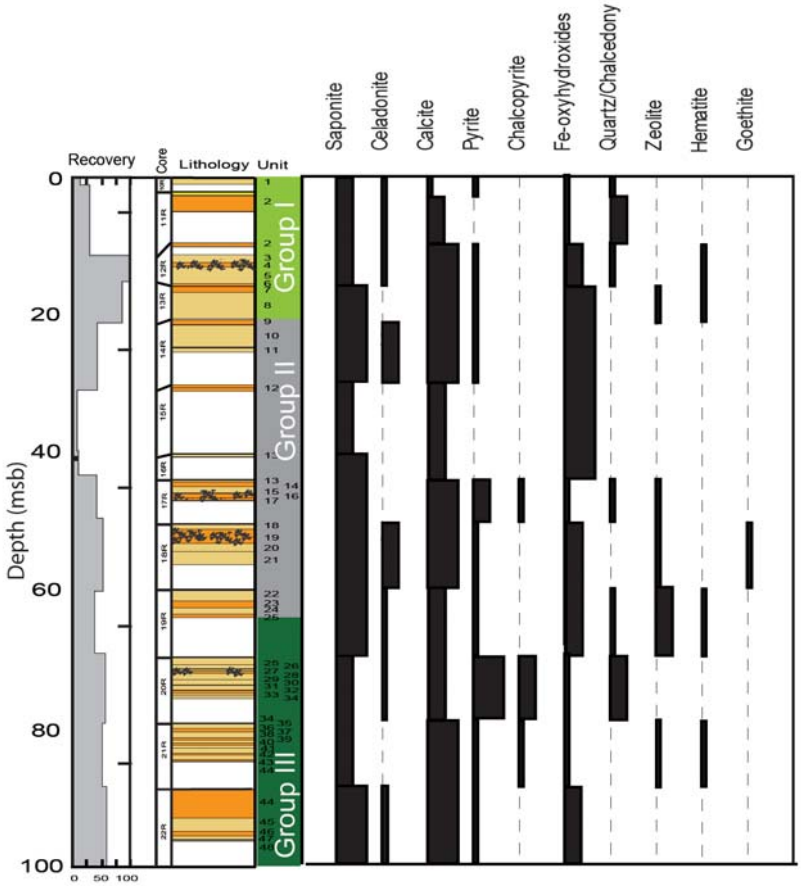

Figure 3.8. Plot of minerals vs. depth profile for ODP Hole 1179D basalts. Plot is based on macro, micro and shipboard X-ray diffraction analysis. The abundance of each mineral, relative to observations of the mineral within the core is indicated by thick/thin blocks. Thin blocks = occurs in only a few samples in core, medium sized blocks = present in some, but not all samples within the core, thick blocks = present in most/all samples within the core (Kanazawa et al., 2001).

Saponite fills vugs, vesicles and interstices and replaces glass, plagioclase $(Na,Ca)(Si,Al)_4O_8$ and olivine $((Mg,Fe)_2SiO_4)$ which can supply the necessary Mg, Ca, Na, Al, and Si to form saponite $(½Ca, Na)_{0.33}(Mg, Fe^{+2})_3(Si,Al)_4O_{10}(OH)_2 \cdot 4H_2O$. Other secondary phases may be associated with saponite including celadonite, calcite, iron-oxyhydroxides $(Fe(O,OH)_x)$, and rarely zeolite. Saponite is commonly observed in various hues of brown to green although some may be strongly stained red by iron-oxyhydroxides. Olivine is nearly always replaced by iddingsite (saponite + $Fe(O,OH)_x$). Shipboard XRD analysis of mineral separates from veins and whole rock (Kanazawa et al., 2001) and petrographic observations indicates that chlorite is not present.

Celadonite (typical formula: $K(Mg,Fe^{2+})(Fe^{3+},Al)[Si_4O_{10}](OH)_2$) is distinguished by colour in thin section and hand specimen. It is bright green with a blue

hue and it is characteristic in rocks with a high K content. Mg, Fe, Al and Si can all be supplied by the groundmass whereas K is sourced from seawater. Celadonite replaces mesostasis to form dark grey to green halos in hand specimens. Celadonite occurs on the margins of veins, fills vesicles and vugs, and is commonly present in discrete patches or rims in and around saponite and iron-oxyhydroxide halos. Celadonite in the groundmass is patchy and associated with replacement of mesostasis and phenocrysts. Sample 191-1179D-18R-1, 19-35 cm contains two celadonite veins with saponite margins. In addition, there is a celadonite halo. Localized zones in which oxidation and reduction have taken place is clearly evident from the presence of celadonite and iron-oxyhydroxides in the same sample (e.g. samples 191-1179D-18R-1, 19-35 cm, 19R-2, 105-110 cm, 20R-3, 13-18 cm, and 21R-3, 65-71 cm). Vesicles are commonly filled with celadonite and collomorphic $Fe(O,OH)_x$ / hematite.

Iron-oxyhydroxide commonly occurs throughout Site 1179 and it is distinguished by deep red to brown red opaque secondary minerals replacing mesostasis, clinopyroxene, olivine and occasionally plagioclase. Iron-oxyhydroxide typically forms red/red brown halos that are usually associated with iron-oxyhydroxide bearing veins (e.g. Sample 191-1179D-18R-3, 67-75 cm Figure 3.7). Alt and Teagle, (2003) demonstrated that iron-oxyhydroxide alteration occurs by diffusion perpendicular to fractures and the oxidizing conditions propagate inwards from the outer edge of the halo. Iron oxyhydroxide typically overprints celadonite and it is a common constituent in complex halos (Figure 3.7).

Carbonates ($CaCO_3$) typically occur as veins and vesicle fills throughout Site 1179, and it can be distinguished by its low to moderate relief and very high birefringence (4^{th} order interference colours). Carbonate can be formed from seawater, although replacement of feldspar during alteration could provide additional Ca. Rarely carbonate is present in groundmass replacing mesostasis.

3.3.2 Veins

Veins filled with secondary minerals are common throughout ODP Hole 1179D. The abundance of veins averages18 veins per metre of core, although this is similar to ODP Hole 1224 (18 veins per metre), which is located east of Honolulu (27°53.363´N, 141°58.758´W)(Paul, et al., 2006), it is relatively low compared to other basement sites

e.g. ODP Hole 1256D (27 veins per metre) (Teagle et al., 2006), ODP Hole 801C (24 veins per metre) and ODP Hole 504B (31 veins per metre) (Alt et al., 1996).

The volume percentage of vein minerals exhibits a general increase with depth. However, vein intensities are higher in two zones, one at ~20 to 30 msb and a second at 40-60 msb with 12 vol% and 25 vol% respectively (Figure 3.9). Veins are made up of saponite, iron-oxyhydroxides, calcium carbonate, saponite + iron oxyhydroxides, saponite + carbonate, celadonite, and saponite with varying amounts of celadonite and small amounts of zeolite. Vein widths typically vary from 0.1 to 2 mm, however, there are a number of very large, spectacular 8-17 mm carbonate and saponite ± celadonite veins (e.g. Samples 191-1179D 14R-2, 0-6 cm; 18R-3, 17-23 cm; 19R-3, 70-75 cm).

Saponite veins are abundant throughout ODP Hole 1179D. Saponite veins range in thickness from 0.1 mm to very large 10 mm thick veins, although most veins greater than 0.3 mm contain other mineral phases. Veins entirely composed of saponite largely cut across celadonite, and iron-oxyhydroxide veins although saponite veins which cut veins and halos composed of iron oxyhydroxides tend to incorporate some iron oxyhydroxides with these veins. Rarely, saponite veins are cross cut by iron oxyhydroxide, carbonate, and/or celadonite veins. Saponite textures vary from spherulitic/vermicular to fibrous. Saponite appears brown green or reddish in thin section depending on the presence of Fe-oxyhydroxides. Saponite veins commonly have saponite + Fe-oxyhydroxide halos that range in thickness from 0.1 mm to several cm. Such halos also occur on veins containing Fe-oxyhydroxides and veins which are composed of more than one mineral.

Iron-oxyhydroxide veins are common throughout ODP Hole 1179D (Figure. 3.9). Veins range in thickness from 0.1 to 10 mm thick although iron-oxyhydroxide tends to be only a minor phase in larger veins. Typical vein thicknesses where iron-oxyhydroxide forms the major component range from 0.1 to 0.5 mm. Iron oxyhydroxide veins cross cut celadonite veins and halos, however, saponite and carbonate in turn cross cut iron-oxyhydroxide veins. Some samples (e.g. Sample 191-1179D-18R-4, 24-28 cm) show saponite veins which have been stained by iron oxyhydroxide as they pass through iron rich halos (Figure. 3.9).

Carbonate veins are abundant throughout most of Hole 1179D and commonly form the major constituent in multi-mineralic veins. Carbonate has been identified as calcite by XRD and this calcite may exhibit prismatic, blocky or fibrous habits. (Kanazawa et al., 2001). Calcite veins range from 0.1 mm to 1mm with rare 10 mm

thick veins. Calcite can occur alone, in the middle of saponite and/or celadonite veins, on the exterior of saponite and/or celadonite veins or intergrown with saponite, celadonite or Fe-oxyhydroxides. Calcite veins appear to post-date saponite veins, with carbonate veins cutting across saponite veins.

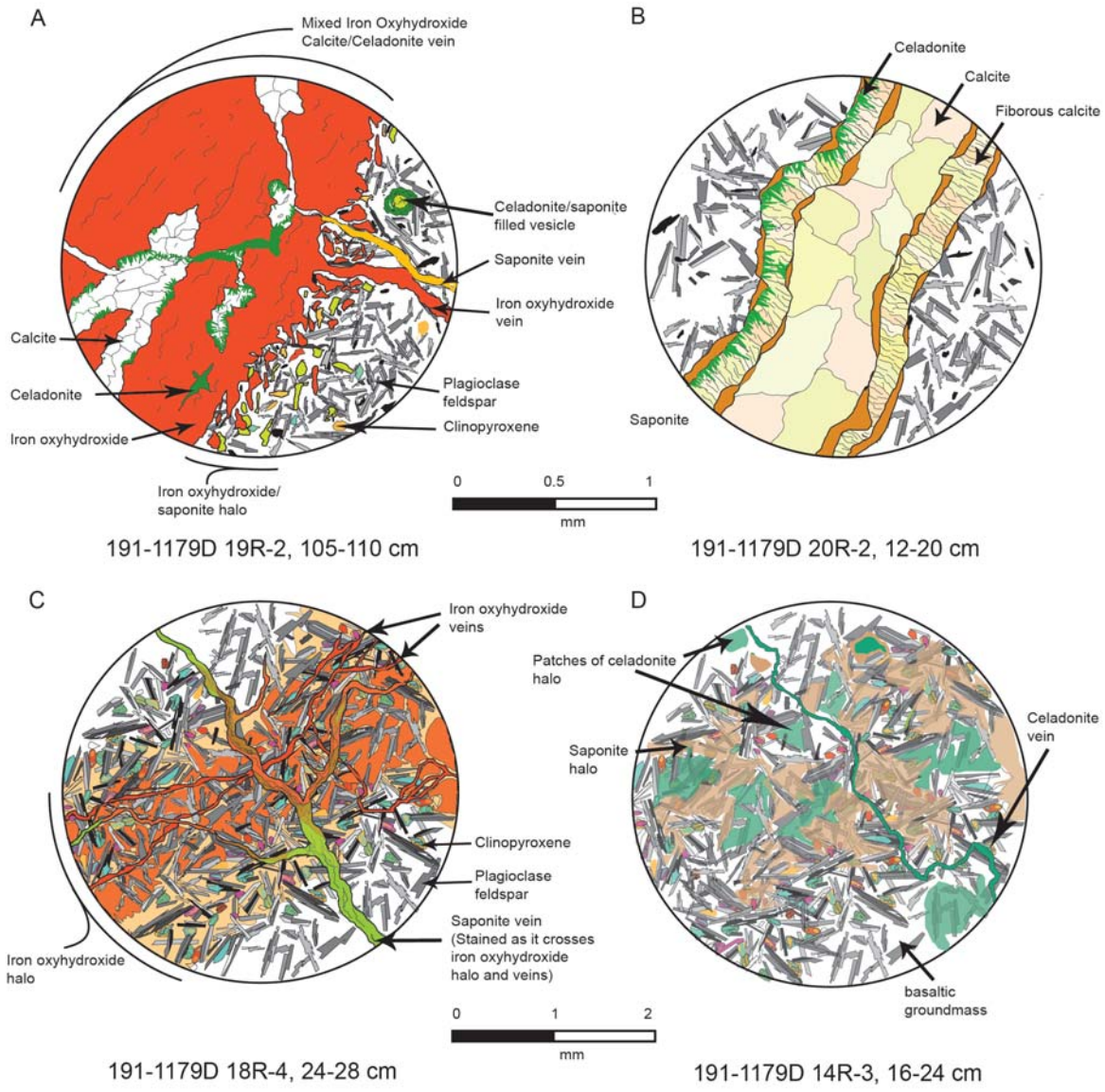

Figure 3.9. Vein relationships in ODP Hole 1179D. A) Sample 191-1179D 19R-2, 105-110 cm. Iron oxyhydroxide vein with subsidiary calcite, saponite and celadonite. B) Sample 191-1179D 20R-2, 12-20 cm. Calcite vein that has re-opened. Saponite and celadonite are present is minor phases, although celadonite is only present on one side. C) Sample 191-1179D 18R-4, 24-28 cm. Iron oxyhydroxide veins and associated halo, cross cut by saponite vein. The saponite vein is stained by the iron-oxyhydroxide as it passes over the iron-oxyhydroxide halo and vein. D) Sample 191-1179D 14R-3, 16-24 cm. Celadonite vein, and remnants of celadonite halo which is partially overprinted by saponite.

Celadonite veins are less common than carbonate, iron oxyhydroxide or saponite veins, however, they occur throughout the core. Typically celadonite is a constituent in multiminerallic veins, but, rare thin 0.1 mm veins are entirely composed of celadonite. Celadonite is typically fibrous or vermicular and generally forms on the vein margins although rarely, celadonite is present in the centre of the vein. Veins of celadonite are nearly always cross-cut by all other secondary mineral phases. The low abundance of celadonite might be attributed by the overprinting from later secondary mineral phases (Figure. 3.9D). Celadonite halos occur round celadonite-bearing veins and are commonly cross-cut by later Fe-oxyhydroxides and saponite veins and halos. Zeolite is a minor phase in some carbonate veins and rarely occurs, partly filling vesicles. Zeolites nearly always post-date other secondary phases.

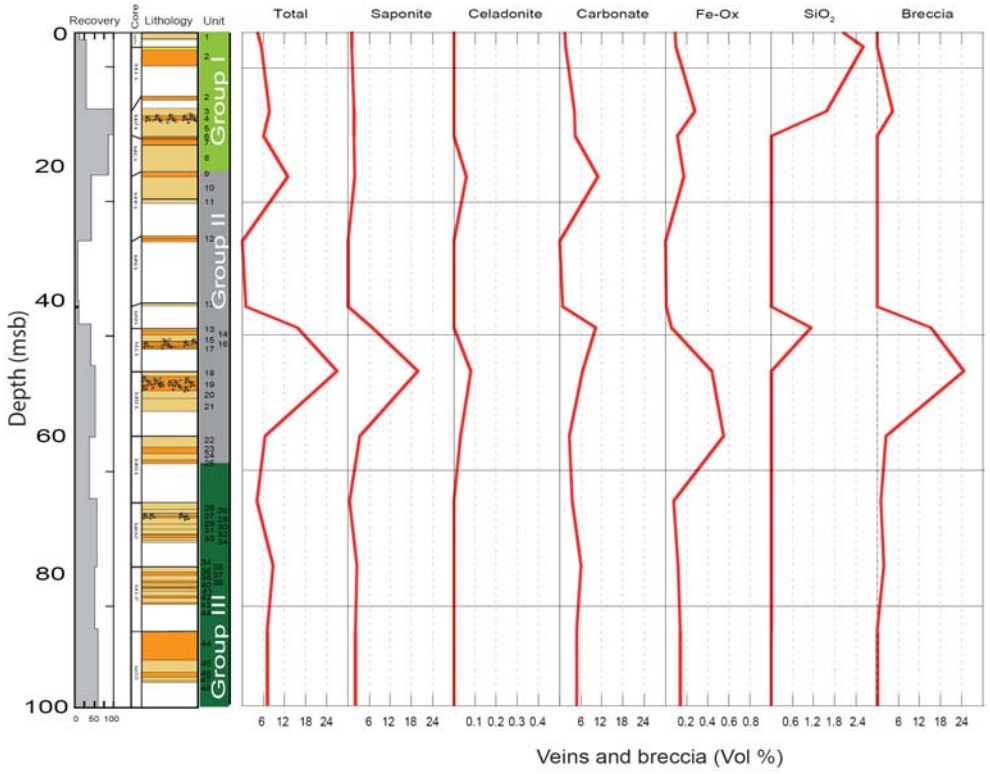

Figure 3.10. Distribution of veins and breccia in Hole 1179D in terms of volume %. Total % records the total volume of minerals in veins only. All data is normalized to account for core recovery.

The vast majority of veins are composed of more than one secondary mineral. Veins containing both saponite and calcite contain saponite in the centre with calcite along the margins and calcite located in the centre of veins with saponite/celadonite on the edges and at the vein tips. In Sample 191-1179D-20R-2, 12-20 cm a vein with a blocky carbonate centre is lined, discontinuously with saponite (Figure. 3.9B). This, in turn, is lined by fibrous calcite followed by an outer layer of saponite with one side

containing discontinuous, fibrous celadonite. Several phases of reopening and infill has probably taken place here.

3.3.3 Breccia

Hyaloclastite and fragmentation breccias are not common in the cores recovered from ODP Hole 1179D, consisting of only 3.3 % of the total recovered core in discrete intervals. The majority of breccia recovered was at the middle portion (43 to 50 msb) within Group III basalts (Figure 3.10). However, breccia tends to be of the most intensely altered samples (for example Figure 3.11). Due to the low to moderate rate of core recovery (Figure 3.4) it is highly likely that a large proportion of breccia remains unaccounted for, because less competent rocks are less likely to be recovered during drilling. A lack of wireline logging measurements unfortunately precludes the application of electrofacies to estimate the true lithological composition of Site 1179.

Hyaloclastite is primarily composed small angular glass fragments formed by quenching and fragmentation of basalt lava upon contact with cold seawater during eruption. The hyaloclastites in Hole 1179D are composed of calcite, saponite and numerous fragments of glass that are altered to saponite and/or iron-oxyhydroxides. Hyaloclastite breccia cement is made up of calcite and comminuted glass fragments (Figure 3.11 A). Clasts are ~90% glass, which are highly altered to saponite with increasing Fe-oxyhydroxide content towards the edges (based on colour changes). In addition, saponite and celadonite are locally present at these edges. A few basaltic clasts are present in the hyaloclastite breccias, these are all highly altered to saponite + Fe-oxyhydroxides. The matrix is primarily composed of blocky calcite, with some quartz.

Basaltic clastic or fragmentation breccias (Figure. 3.11 B) are predominantly composed of basalt clasts with a matrix of blocky calcite and saponite. Minor secondary sulfides including pyrite and chalcopyrite are present in greater abundances in breccias than the rest of the recovered core. Clasts are variably altered, some containing brown, saponite + Fe-oxyhydroxide halos with fresh cores. Clasts in basaltic breccia are rounded to subangular (e.g. Sample 191-1179D 18R-1, 52-58 cm Figure 3.11 C).

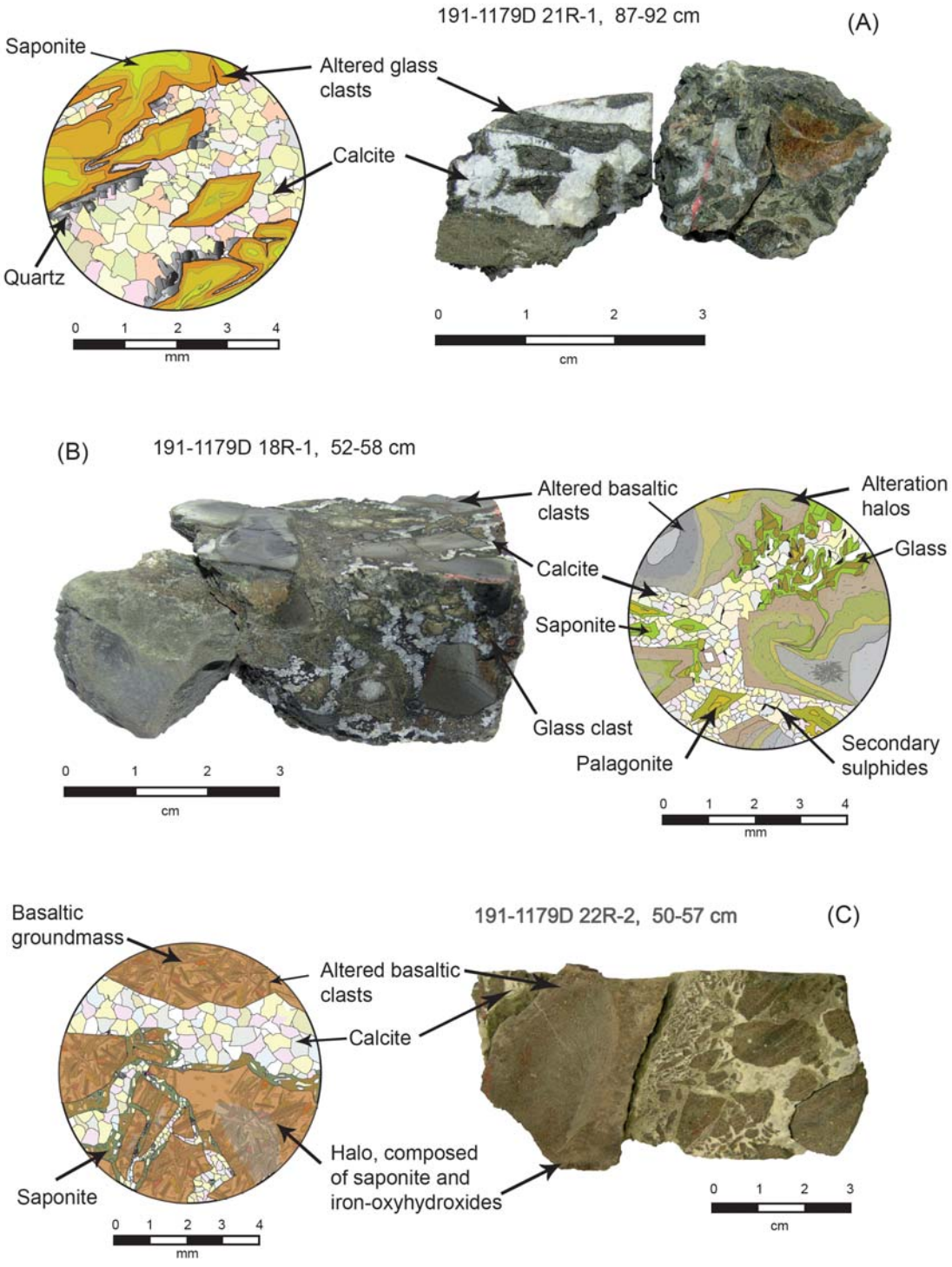

Figure 3.11. Examples of breccia types found in ODP Hole 1179D. (A) Sample 191-1179D 21R-1, 87-92 cm is a hyaloclastite breccia, primarily composed of altered glass fragments with a matrix dominated by calcite and minor quartz. (B) Sample 191-1179D 18R-1, 52-58 cm is a pillow breccia. Basaltic clasts with glassy rims and glass clasts are supported by a matrix of saponite and calcite. (C) Sample 191-1179D 22R-2, 50-57 cm represents a basalt clastic breccia. Calcite forms the matrix and clasts are basaltic.

The basaltic clasts often exhibit partially to completely altered glassy margins, some of which have concentric banding and alteration patterns suggesting that the clasts are from a pillow lava. The matrix is composed calcite and lesser amounts of saponite with minor secondary sulfides.

The occurrence of breccia at 5-10, 45-50 and 70–75 msb coincides with an overall increase in the abundance of quartz and sulfides when compared to the rest of the recovered core (Figure. 3.8). More breccia is likely to be present in basement at Site 1179 than was recovered due to the crumbly nature of the breccias because recovery remains biased towards fresher, more competent rock.

3.3.4 Summary

Secondary minerals at Site 1179 record the style and intensity of alteration. Alteration is slight and it is formed from high levels of low temperature, oxidizing seawater. Direct comparisons between the intensity of alteration, the vein abundance, and number of veins is illustrated by the distribution of veins, halos and breccias with depth.

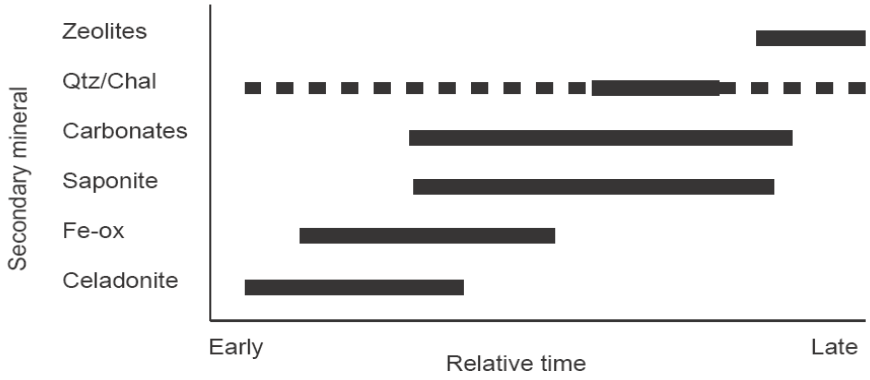

Figure 3.12. Relative timing of secondary mineral paragenisis for Site 1179 basement based on petrographic observations. (Fe-ox = Iron-oxyhydroxides; Qtz/Chal = Quartz and Chalcedony) Dashed line indicates uncertainty with the timing of quartz and chalcedony.

Site 1179 breccia recovery is almost certainly not representative due to preferential recovery of more competent rocks, therefore we have to regard the breccia and pillow lava percentage estimates as a minimum. The petrographic observations of alteration at Hole 1179D provide insights into the timing of secondary mineral formation. The relative paragenisis for secondary minerals for Site 1179 basement is given in Figure 3.12. The sequence of alteration follows a very similar trend to that of

other ODP holes observed in ocean crust e.g. Hole 801C (Alt and Teagle, 2003), Hole 896A (Teagle et al, 1996) and 504B (Alt et al, 1996), although there is a great degree of overlap in the sequence and any combination of alteration phases may be present in a particular sample. Celadonite appears to be the first phase, forming halos that propagate outwards from celadonite filled veins. Partial to total overprinting of celadonite by iron-oxyhydroxides make up the second alteration assemblage. celadonite filled veins and vesicles may partially fill with iron-oxyhydroxides. A transitional stage from iron-oxyhydroxides is observed in terms of mixtures of saponite and iron-oxyhydroxides with varying degrees of Fe content. Saponite, pervasive throughout all rocks of ODP Hole 1179D, overprints iron oxyhydroxide and celadonite, may have been aided by later reducing conditions, however, observation of secondary sulfides, which form under reducing conditions, is minimal. Lastly, late-stage calcite ± zeolite fill veins and to a lesser extent coarse grained portions of groundmass and vesicles.

3.4. Basement Geochemistry

An understanding of the magmatic processes at Site 1179 is required before we can estimate chemical changes associated with hydrothermal alteration. An analysis of the chemical nature of Site 1179 is derived from a suite of eighty-five samples from Hole 1179D that are analyzed for major and trace elements. Twenty-one of analyses were performed aboard ship (Kanazawa et al., 2001) (Table 3.1). The timing and location of Site 1179 formation coincides with the eruption of a large oceanic plateau, Shatsky Rise which formed during mid Cretaceous super-plume activity at the triple junction of the Pacific, Izanagi, and Farallon plates (Nakanishi et al., 1999; Sager et al., 1988, 1999). Although we would expect the 129 M.yr-old Site 1179 basement to exhibit typical MORB signatures, the proximity of Site 1179 to Shatksy Rise may have influenced the composition of the Site 1179 lavas.

Representative analyses (all Samples from each group)

	GP 1	SD	GP 2	SD	GP 3	SD	ALL 'Grey'	SD
Major elements (wt%)								
SiO_2	49.64	*0.95*	49.71	*1.36*	46.97	*2.54*	48.26	*1.39*
TiO_2	1.30	*0.08*	1.68	*0.24*	1.49	*0.18*	1.47	*0.24*
Al_2O_3	14.67	*0.63*	14.66	*0.99*	15.85	*1.06*	14.72	*0.89*
Fe_2O_3	10.99	*1.76*	11.28	*1.96*	10.73	*1.17*	10.36	*1.57*
MnO	0.17	*0.03*	0.18	*0.04*	0.22	*0.05*	0.19	*0.05*
MgO	7.15	*0.58*	6.74	*0.93*	6.27	*0.91*	6.81	*0.78*
CaO	10.68	*1.05*	9.98	*1.87*	11.78	*2.14*	11.95	*1.00*
Na_2O	2.82	*0.37*	3.06	*0.39*	2.94	*0.32*	2.75	*0.40*
K_2O	0.72	*0.26*	0.71	*0.56*	0.44	*0.24*	0.50	*0.25*
P_2O_5	0.11	*0.01*	0.15	*0.04*	0.17	*0.04*	0.14	*0.03*
C	0.07	*0.07*	0.05	*0.05*	0.34	*0.63*	0.09	*0.07*
S	0.01	*0.02*	0.01	*0.01*	0.03	*0.04*	0.02	*0.04*
LOI	1.44	*0.48*	1.48	*1.00*	2.85	*2.61*	2.52	*0.87*
Total	99.68	*0.37*	99.63	*0.49*	99.71	*0.40*	99.67	*0.54*
$Fe^{3+}/Fe^{(Total)}$	0.53	*0.09*	0.44	*0.14*	0.67	*0.11*	0.49	*0.09*
Mg#	56.4	*5.8*	54.2	*6.5*	53.5	*5.0*	56.8	*5.8*
Trace elements (ppm)								
Co	50	*5.18*	49	*4.37*	50	*5.48*	50	*4.04*
Cr	274	*48.44*	187	*81.08*	370	*49.87*	265	*89.46*
Cu	62	*24.44*	60	*33.26*	64	*28.51*	73	*31.90*
Ga	17	*0.81*	19	*1.48*	18	*1.54*	18	*1.25*
Ni	75	*12.34*	71	*15.82*	124	*33.92*	92	*34.90*
Sc	47	*3.63*	49	*4.52*	42	*2.90*	46	*4.00*
V	363	*21.53*	388	*51.73*	327	*40.65*	363	*42.16*
Zn	90	*6.67*	102	*22.62*	94	*12.04*	94	*12.45*
Rb (ICP)	12	*6.16*	11	*9.02*	6	*3.68*	10	*6.26*
Sr (XRF)	93	*10.54*	104	*24.87*	162	*28.02*	111	*33.34*
Y (XRF)	29	*2.71*	39	*8.10*	31	*3.21*	33	*6.24*
Zr (XRF)	75	*7.84*	100	*16.49*	104	*16.06*	86	*19.10*
Nb (ICP)	2.45	*0.51*	3.04	*1.03*	4.03	*1.23*	2.94	*1.02*
Cs	0.31	*0.23*	0.19	*0.16*	0.21	*0.22*	0.25	*0.21*
Ba	14.31	*7.38*	16.48	*10.31*	22.07	*13.13*	18.96	*12.40*
La	2.23	*0.51*	3.12	*0.79*	3.57	*0.84*	2.98	*1.04*
Ce	6.59	*0.94*	9.76	*1.75*	10.51	*1.80*	8.49	*2.40*
Pr	1.18	*0.11*	1.71	*0.27*	1.73	*0.27*	1.36	*0.33*
Nd	7.19	*0.63*	10.25	*1.51*	9.98	*1.27*	8.75	*1.85*
Sm	2.72	*0.28*	3.94	*0.63*	3.53	*0.62*	3.32	*0.81*
Eu	1.02	*0.07*	1.40	*0.18*	1.23	*0.14*	1.13	*0.22*
Gd	3.75	*0.40*	5.12	*0.91*	4.29	*0.38*	4.19	*0.77*
Tb	0.72	*0.04*	1.03	*0.17*	0.79	*0.07*	0.81	*0.16*
Dy	4.99	*0.39*	6.76	*1.02*	5.18	*0.70*	5.52	*1.03*
Ho	1.09	*0.06*	1.52	*0.24*	1.14	*0.09*	1.20	*0.24*
Er	3.08	*0.18*	4.12	*0.70*	3.05	*0.36*	3.29	*0.64*
Tm	0.44	*0.02*	0.61	*0.09*	0.45	*0.03*	0.48	*0.09*
Yb	3.30	*0.51*	4.39	*0.83*	3.36	*0.58*	3.83	*0.86*
Lu	0.46	*0.03*	0.62	*0.10*	0.46	*0.03*	0.50	*0.09*
Hf	1.80	*0.27*	2.46	*0.50*	2.29	*0.33*	2.00	*0.46*
Ta	0.08	*0.12*	0.15	*0.31*	0.04	*0.01*	0.07	*0.12*
Pb	0.34	*0.34*	0.40	*0.23*	0.41	*0.14*	0.41	*0.34*
Th	0.37	*0.93*	0.23	*0.08*	0.22	*0.09*	0.19	*0.10*
U	0.12	*0.06*	0.25	*0.28*	0.10	*0.03*	0.15	*0.08*

Table 3.1. Representative whole rock major, trace and rare earth element concentrations for samples recovered from ODP Hole 1179D. Major element oxides were measured by XRF as were trace elements Co, Cr, Cu, Ga, Ni, Sc, V, Zn, Sr, Y and Zr. All other elements are measured by ICP-MS. Mg# is the ratio of magnesium to iron expressed in wt% form: $Mg^{2+}/(Mg^{2+}+ Fe^{2+})$. Analyses use data from this study and Kanazawa, Sager, Escutia, et al., (2001).

3.4.1 Classification of Site 1179 basalts.

Major, trace and REE data may be used to classify the basement at Site 1179. A range of different basalt types is compared against Site 1179D basement. In addition a series of discrimination diagrams are discussed to define the origins of Site 1179.

Many of the major elements commonly used to classify igneous rocks are mobile during fluid rock interaction. Therefore because Site 1179 basement is altered, they may not be suitable for classifying precursor compositions, and thus igneous trends are drawn with caution. Concentrations of whole rock major element oxides of all basement rocks at Site 1179 are similar to MORB (Table 3.2). High K_2O at Site 1179 most likely reflects incorporation of secondary minerals (e.g. celadonite) by low temperature hydrothermal alteration.

	All least alt 1179D	SD	N-MORB	SD	OJP	SD	Shatsky Rise	SD
SiO_2	48.3	1.1	49.9	0.9	49.7	1.3	47.9	4.8
TiO_2	1.5	0.2	1.5	0.5	1.0	0.3	2.1	0.8
Al_2O_3	11.0	0.9	15.9	1.8	14.6	0.7	16.7	2.4
FeO	9.9	1.5	10.4	1.9	10.4	1	10.0	3.2
MnO	0.18	0.1	0.17	0.01	0.18	0.03	0.21	0.3
MgO	6.6	0.8	7.6	1.2	7.9	1.3	2.2	2.9
CaO	11.3	1.0	11.6	0.8	11.8	1.9	8.2	2.8
Na_2O	2.9	0.3	2.6	0.2	2.0	0.3	3.1	0.6
K_2O	0.65	0.3	0.17	0.1	0.36	1.1	2.43	0.9
P_2O_5	0.14	0.02	0.08	0.02	0.09	0.04	1.96	2.1
Mg#	57		56		57		26	

Table 3.2. Average major element concentrations for a selection of basalt types. N-MORB from McKenzie and O'Nions (1991), Ontong Java Plateau data from Fitton and Godard (2004), Shatsky Rise data from Tatsumi et al., (1998).

A standard AFM plot (Figure 3.13) of Site 1179 basalts suggests that Site 1179 basement is high-Fe tholeiite basalt however the slightly elevated Fe is more likely to be an effect of alteration. Determination of the ferric/ferrous iron ratio (Outlined in Chapter 2 'methods') allows a direct assessment of the ferric Fe content. A plot of $Fe^{3+}/Fe^{(Total)}$ vs. LOI (Figure 3.14) shows that Fe at Site 1179 is moderately to greatly oxidized and that oxidation increases with LOI. In addition $Fe^{3+}/Fe^{(Total)}$ vs. LOI trends back towards the expected primary composition for MORB ($Fe^{3+}/Fe^{(Total)}$ = 0.12, LOI =

0.2 wt %). These results coincide with the observation of iron-oxyhydroxide veins and halos in the whole rock. These observations imply that Site 1179 $Fe^{3+}/Fe^{(Total)}$ are influenced by low temperature hydrothermal alteration (e.g. Teagle et al., 1996), which precludes the use of Fe concentration analyses to assess primary magmatic conditions at Site 1179.

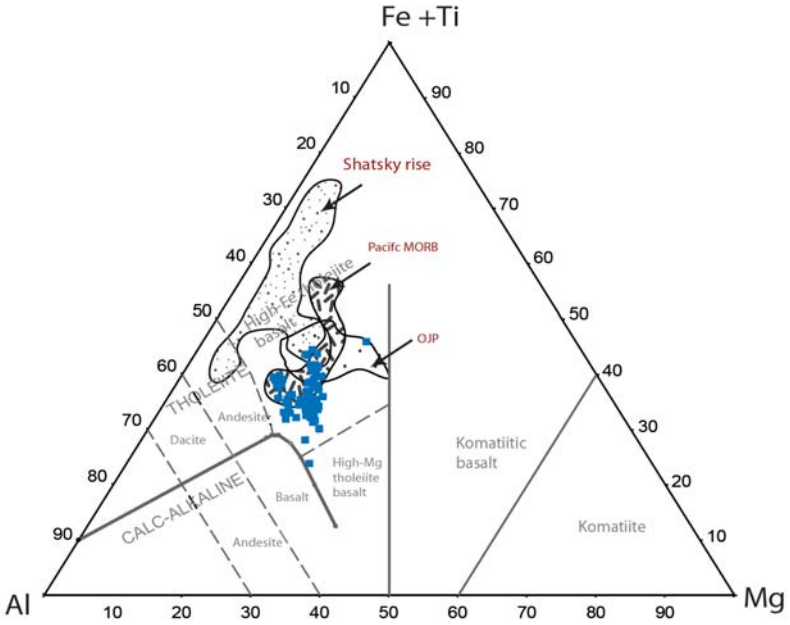

Figure 3.13. Ternary AFM diagram suggests Site 1179 basement (Blue squares) is high Fe-tholeiites. Its use however is limited since Al, Fe, and Mg are mobile during alteration. Shatsky Rise, Tatsumi et al, (1998); Ontong Java Plateau, Fitton and Godard (2004) and Pacific MORB is from Janney and Castillo, (1997).

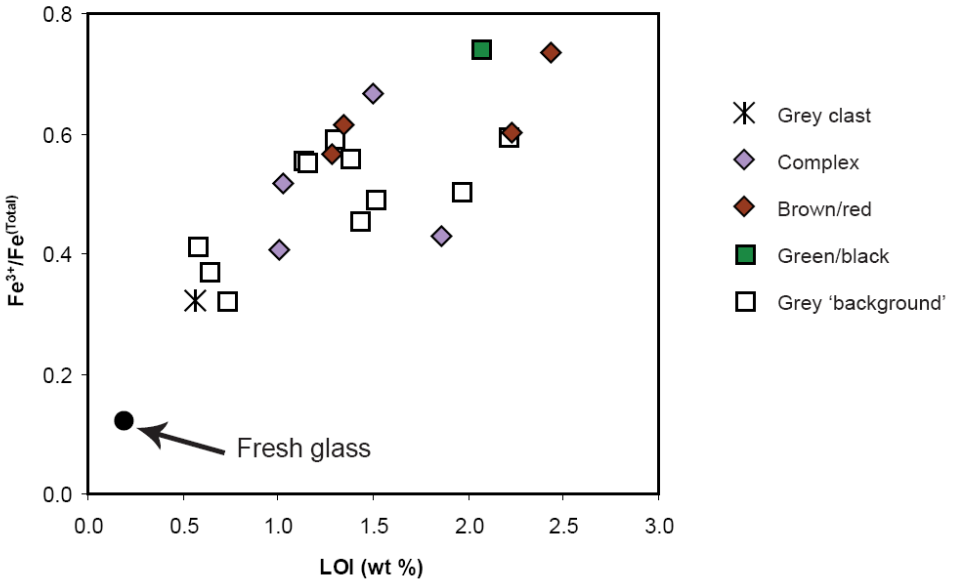

Figure 3.14. LOI vs. $Fe^{3+}/Fe^{(Total)}$ for Site 1179 whole rock samples. Alteration styles are highlighted. The composition of fresh glass is sourced from Puchett and Emmermann, (1983), Alt et al, (1989), and Danyushevsky, (2001).

Fractionation trends of Fe_2O_3 vs. SiO_2, SiO_2 vs. Mg number and Mg number vs. Sr (Figure 3.15 a and g) plot within the MORB field which suggests that Site 1179 basalts are typical MORB, because compositions, although scattered, plot within the fields for MORB and EPR.

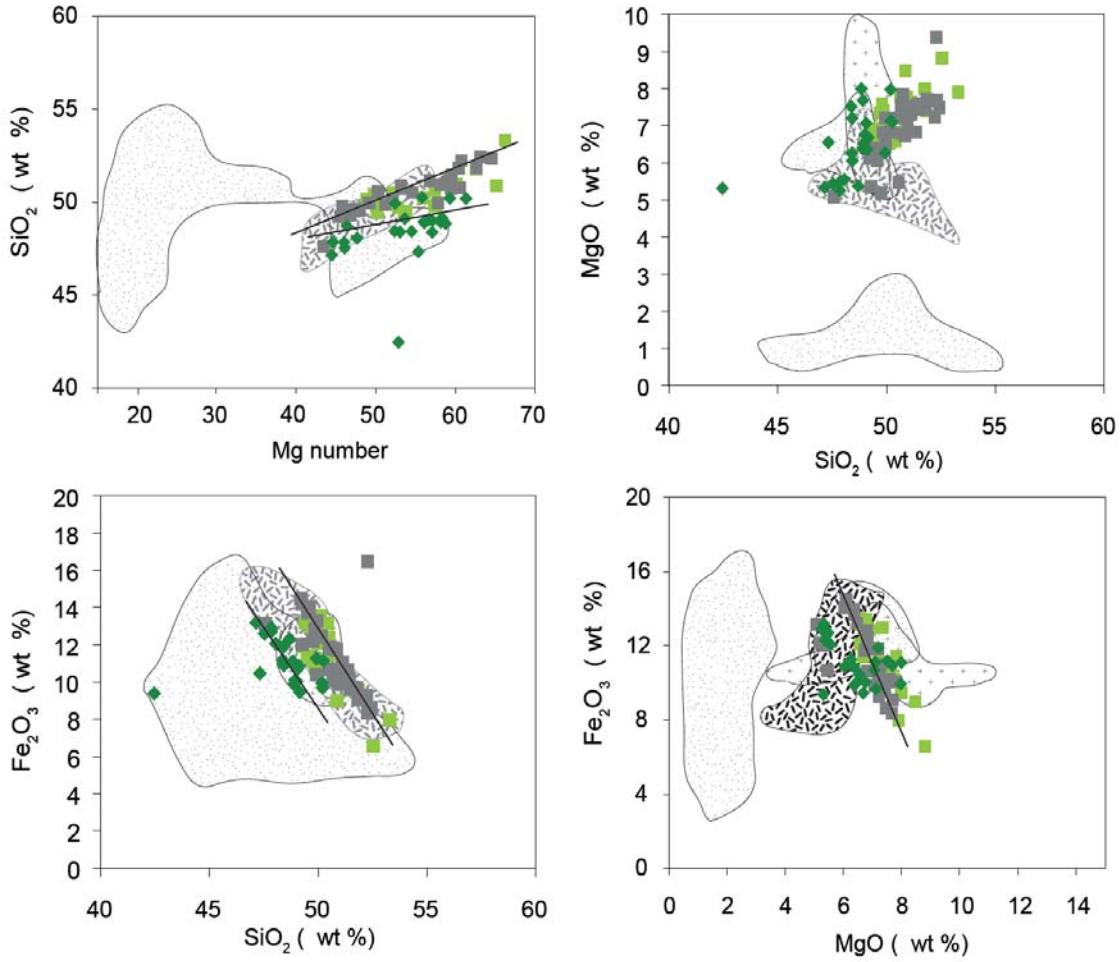

Figure 3.15. Selected major element plots vs. SiO_2, Mg number and MgO. Pale green squares, Group I; Grey squares, Group II; Dark green diamonds, Group III. Where possible Pacific MORB (heavy stippling), Janney and Castillo, (1997); Ontong Java Plateau (crosses), Fitton and Godard, (2004) and Shatsky Rise (light stippling), Tatsumi et al., (1998) fields are shown for comparison including trend lines.

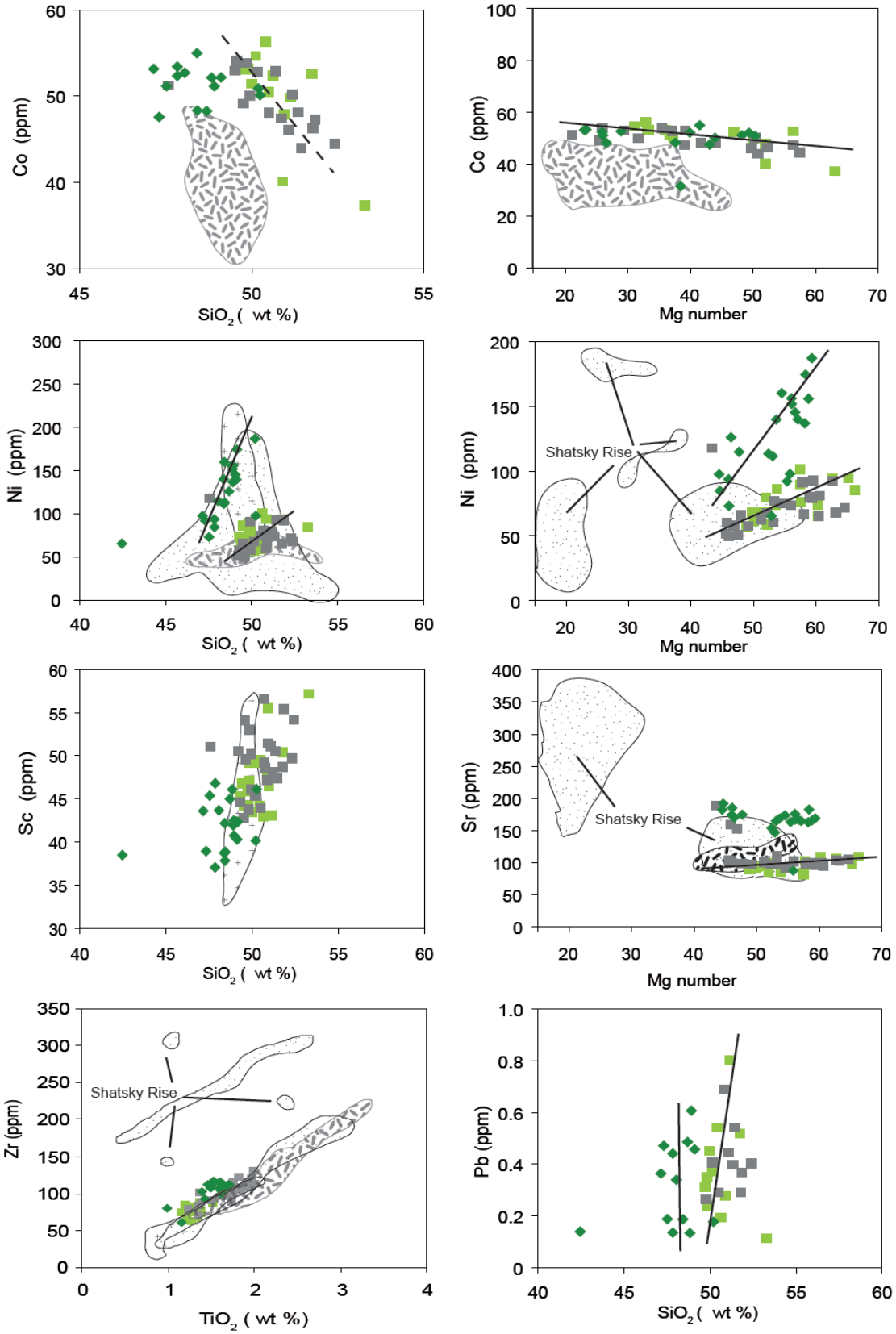

Figure 3.16. Selected trace element plots vs. SiO_2, Mg number and MgO and TiO_2 vs. Zr. Pale green squares, Group I; Grey squares, Group II; Dark green diamonds, Group III. Where possible Pacific MORB (heavy stippling), Janney and Castillo, (1997); Ontong Java Plateau (crosses), Fitton and Godard, (2004) and Shatsky Rise (light stippling), Tatsumi et al., (1998) fields are shown for comparison including trend lines.

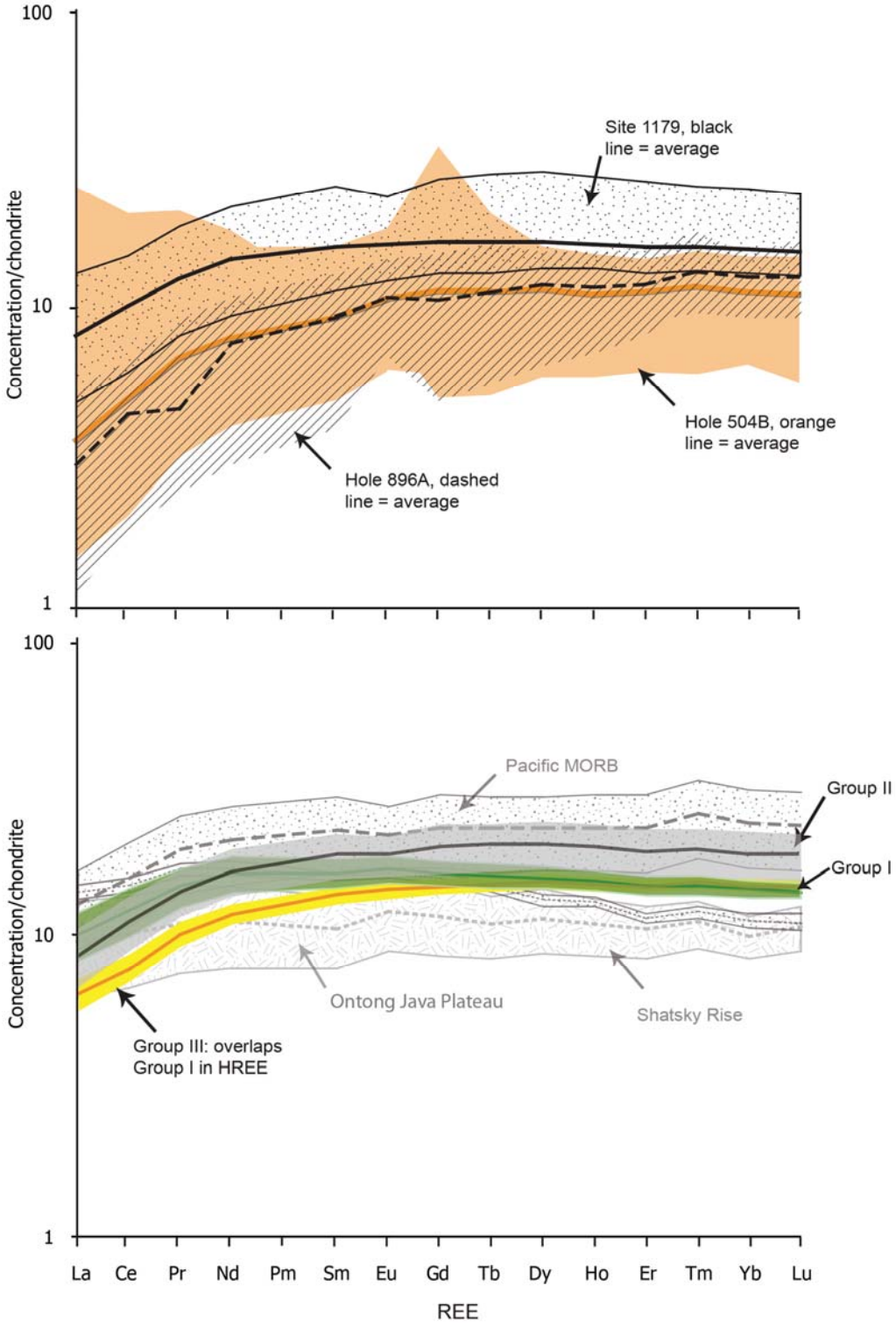

Figure 3.17. a) Range of chondrite-normalized rare earth element concentrations for Site 1179 Basalts. REE patterns for the trace element depleted basement Sites 504* and 896 (Teagle et al., 1996) are also shown. b) Average chondrite normalized REE patterns for igneous groups at Site 1179 in comparison to Shatsky Rise and Pacific MORB. Fields for Shatsky Rise and Pacific MORB indicate the standard deviation about the average. Chondrite-normalization factors from Taylor & Gorton (1977).* Hole 504B data is a compilation of Legs 69, 70 (Cann et al., 1983); 83 (Anderson et al., 1985), 111 (Becker, Sakai et al., 1989), and 140 (Erzinger et al., 1995). Pm is not analyzed.

Alteration will likely cause some of the scatter in geochemical plots. MORB-normalized major and trace element data from Site 1179 and various other sites (Figure 3.17) are very similar to EPR basalts and do not show a large degree of variation from the MORB normalization values. Elevated concentrations in elements K, Rb and Sr are likely to be caused by alteration.

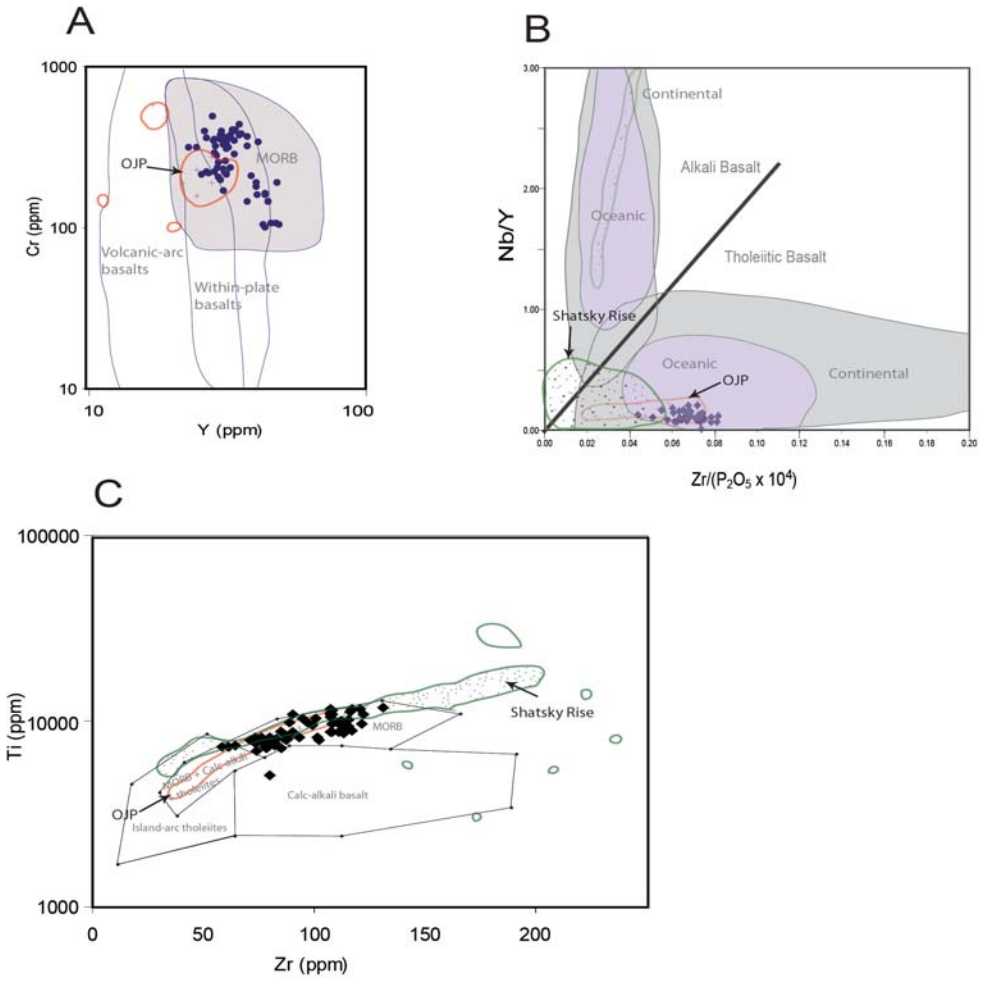

Figure 3.18. Classification of igneous rocks at Site 1179. (A) Y (ppm) vs. Cr (ppm). (after Pearce, 1982). (B) Plot of $Zr/(P_2O_5 \times 10^4)$ vs. Nb/Y places Site 1179 within the oceanic tholeiite field (after Floyd and Winchester, 1975). (C) Plot of Zr vs. Ti. Site 1179 basalt plot within the expected range for basalts (field after Pearce and Cann, 1973 data from Pearce, 1982). Shatsky Rise data from Tatsumi et al, (1998); Ontong Java Plateau data from Mahoney et al, (1993).

Concentrations of Ti, Cr, Y, Nb and Zr for Site 1179D and where possible, Shatsky Rise and the Ontong Java Plateau are plotted on a selection of discrimination diagrams which use large pools of data from rock in various tectonic settings to create fields (Figure 3.18). All plots for Site 1179 are within tholeiitic basalt fields indicating a strong likelihood that rocks from Site 1179 are MORB.

3.4.2 Igneous trends

Basement at Site 1179 is subdivided into three igneous groups based on olivine content (Kanazawa et al., 2001) and this subdivision is also apparent in whole rock geochemical data.

		wt %				ppm				
		TiO_2	MnO	MgO	K_2O	Cr	Cu	Ni	Sr	Y
Group I	Max	1.4	0.24	8.7	0.94	359	71	101	108	34
	Min	1.2	0.10	6.5	0.17	219	34	67	68	25
	Average	**1.3**	**0.14**	**7.5**	**0.58**	**294**	**51**	**82**	**93**	**29**
	Stdev	0.1	0.04	0.7	0.22	54	14	11	12	3
	n	11	11	11	11	8	8	10	12	12
		Low	Low	High	Mod	Mod	Mod	Mod	Mod	Mod
Group II	Max	1.9	0.23	7.4	0.92	209	93	78	103	46
	Min	1.5	0.15	5.4	0.33	158	26	49	87	38
	Average	**1.8**	**0.20**	**6.7**	**0.59**	**175**	**57**	**63**	**98**	**42**
	Stdev	0.1	0.02	0.7	0.25	23	21	11	5	3
	n	9	9	9	9	5	7	7	8	8
		High	Mod	Mod	Mod	Low	Mod	Low	Mod	High
Group III	Max	1.7	0.36	7.0	0.45	393	84	187	181	32
	Min	1.1	0.21	6.1	0.06	347	61	97	71	25
	Average	**1.5**	**0.25**	**6.7**	**0.21**	**365**	**70**	**142**	**134**	**29**
	Stdev	0.2	0.06	0.4	0.15	24	12	45	51	3
	n	5	5	5	5	3	3	4	5	5
		Mod	High	Mod	Low	High	High	High	High	Mod
						ppm				
		Zr	Nb	La	Ce	Nd	Dy	Er	Pb	Th
Group I	Max	88	3.3	2.8	6.9	7.9	5.2	3.3	0.41	2.70
	Min	67	1.4	1.5	4.9	5.6	4.4	2.9	0.09	0.11
	Average	**78**	**2.4**	**2.0**	**6.2**	**7.1**	**4.8**	**3.1**	**0.22**	**0.43**
	Stdev	6	0.6	0.4	0.7	0.7	0.3	0.1	0.09	0.85
	n	10	12	10	10	10	10	10	8	9
		Low	Low	Low	Low	Low	Low	Low	Low	High
Group II	Max	116	4.0	4.4	11.5	11.7	7.7	4.4	0.66	0.47
	Min	107	2.0	2.3	8.4	9.7	6.8	4.1	0.19	0.17
	Average	**107**	**3.0**	**3.0**	**9.7**	**10.6**	**7.1**	**4.3**	**0.33**	**0.23**
	Stdev	4	0.5	0.7	1.1	0.7	0.3	0.1	0.17	0.11
	n	5	8	8	8	8	8	7	6	7
		High	Mod	Mod	Mod	High	High	High	Mod	Mod
Group III	Max	112	6.0	4.7	11.7	10.0	5.7	2.8	0.80	0.27
	Min	99	1.7	1.5	5.2	6.1	4.4	2.5	0.24	0.06
	Average	**107**	**3.5**	**3.3**	**9.7**	**8.8**	**5.1**	**2.7**	**0.50**	**0.15**
	Stdev	7	1.7	1.3	3.1	1.8	0.6	0.2	0.28	0.11
	n	3	5	4	4	4	4	3	3	3
		High	High	Mod	Mod	Mod	Mod	Low	High	Low

Table 3.3. Summary of chemical variation between igneous groups at Site 1179 based on selection of least altered samples from each group. Elements which display the greatest variation in concentration are shown. A relative ranking for concentration is given for each element in each group (High, Moderate, Low). Max: largest value in group, Min: Lowest value in group, Average: mean average of all samples within group, stdev: standard deviation from the average.

Primary igneous variation within the groups is minimal, the characteristic features and chemical changes are discussed for each group. Petrographic evidence indicates that Group I basalts actually extend into Core 191-1179, 14R-1 and do not terminate at the boundary between Cores 191-1179, 13R-3 and 191-1179, 14R-1 as identified by (Kanazawa et al., 2001).

Figure 3.19 demonstrates the presence of olivine, iron content and a selection of major elements vs. TiO_2 of the samples which are used for this reclassification. Given that Group I and Group II were distinguishable from their low olivine and olivine free content respectively (Kanazawa et al., 2001), the samples highlighted in Figure 3.19 should be re-classified as Group I since there is olivine present in ODP 1179-191-14R-1. With respect to MnO, Fe_2O_3, Al_2O_3, and P_2O_5 vs. TiO_2, these samples share similar chemistry to the rest of Group I basalts (Figure 3.19). A stand alone Group III sample in Figure 3.19 exhibits similar chemistry to Group I samples. This may indicate variations in primary chemistry within Group III basalts, however more work is required to isolate the igneous origins of this sample, The sample is not marginal within Group III and it contains olivine, therefore its original classification remains.

Table 3.3 gives the ranges and average concentrations for elements that chemically define each igneous group from a selection of the least altered samples within each group. Selection of least altered samples is based on low LOI, K_2O, C, S and similarities with TiO_2 (Discussed in 'chemical changes'). The major element oxides variation between the igneous groups (Figure 3.20) and depth are largely indistinguishable with the exception of TiO_2 and MgO. TiO_2 concentrations are lower in Group I than Groups II and III. Kanazawa et al., (2001) document the presence of Ti –augites, however, this is based on petrographic observation only and would require microprobe analysis to confirm. It is most likely that Ti-magnetite is from primary magma.

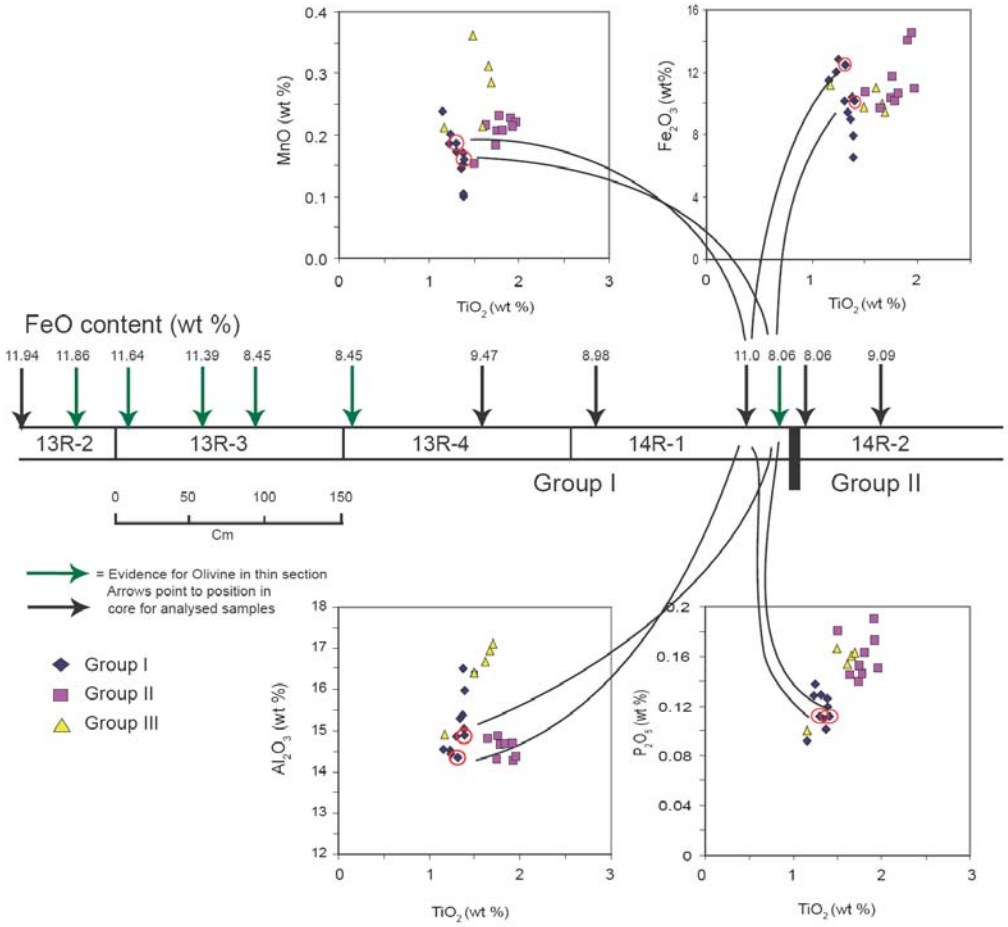

Figure. 3.19. Reclassification of Igneous Groups I and II based on the presence of olivine, FeO concentration and some example plots of major element oxides vs. TiO_2. Samples highlighted in red circles, which were classified as Group II by Kanazawa, Sager, Escutia, et al, (2001) chemically trend with Group I.

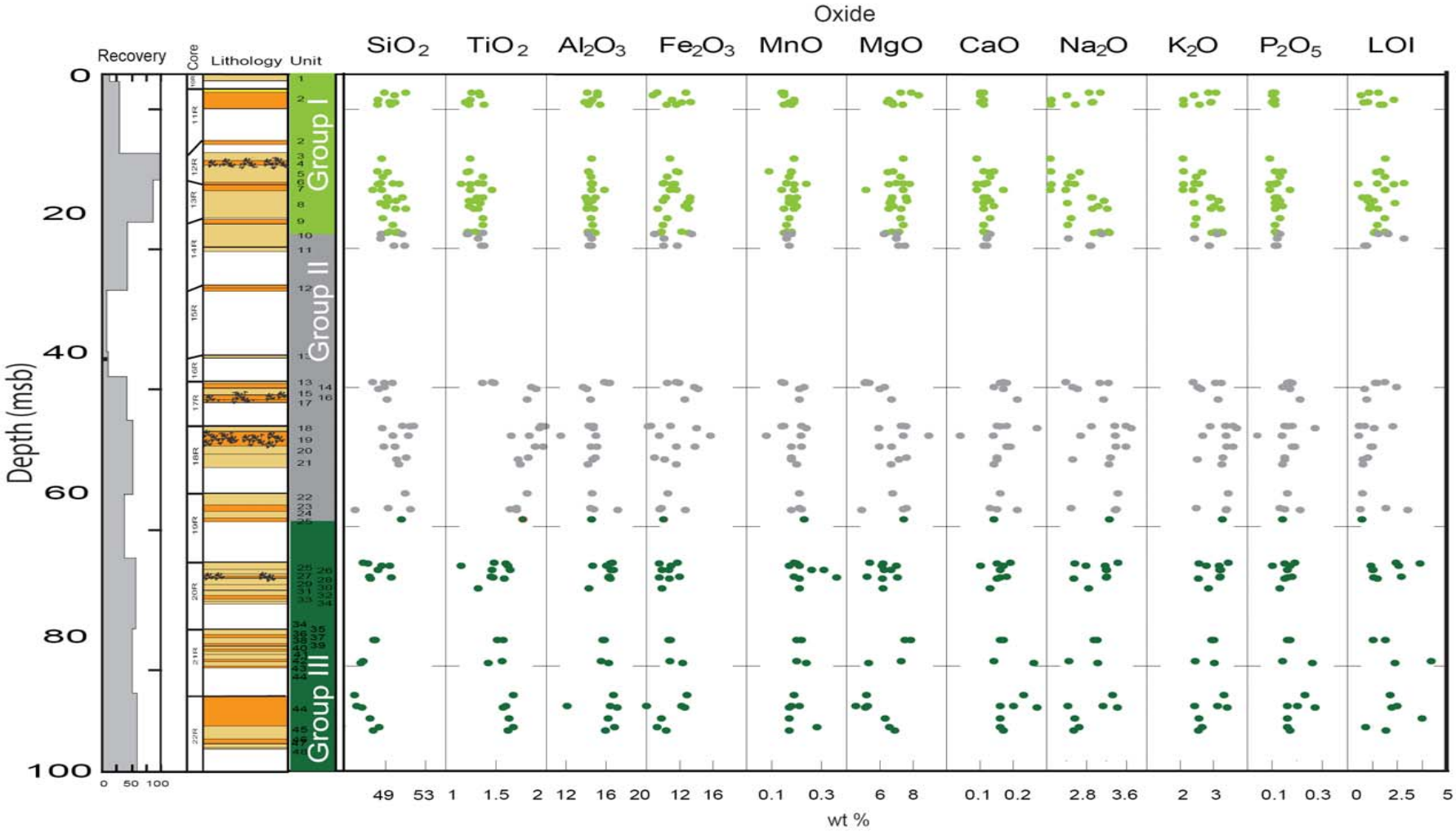

Figure 3.20. Major element oxides vs. depth for Site 1179 basalts. Varying x-axis scales are used so variation within each element is clearly apparent.

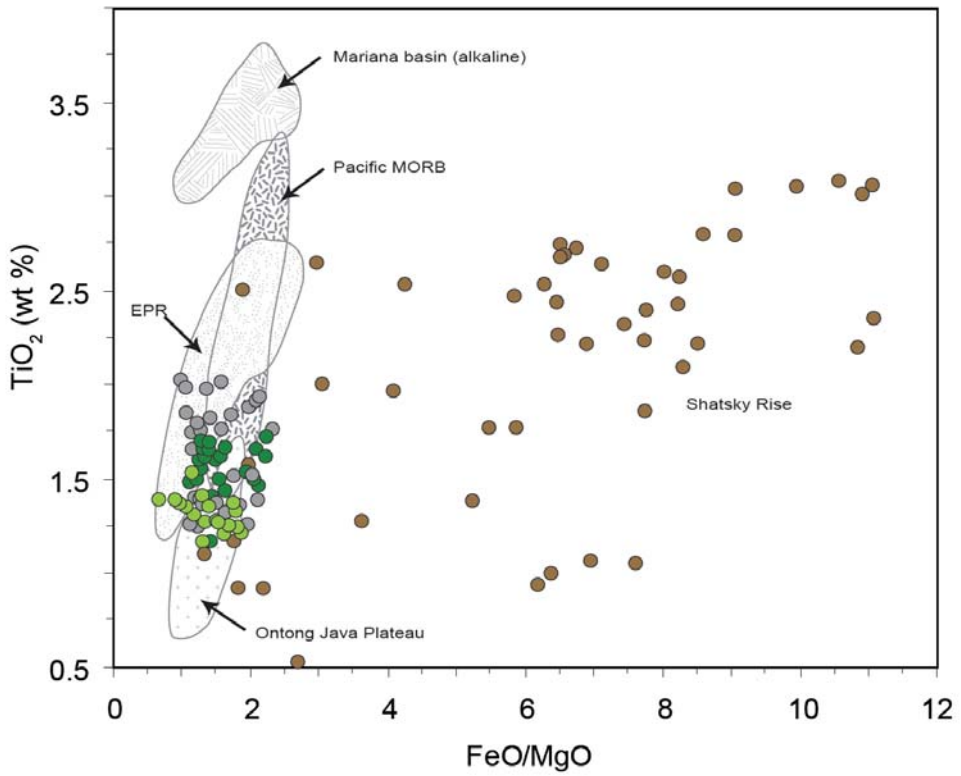

Figure 3.21. FeO/MgO vs. TiO2 plot for basalts from Site 1179D. Group I basalts (light green), Group II basalts (Grey) and Group III basalts (Dark green) are shown. Reference data sources from Pacific Ocean are Mariana Basin, Floyd and Castillo (1991); Ontong Java Plateau, and East Pacific Rise, Mahoney et al (1993); Shatsky Rise (Light brown), Tatsumi et al, (1998).

The concentration MgO is slightly higher in Group I basalts than in Groups II and III. The presence of olivine in Groups I and III and Ti in oxides in Group II is borne out in a TiO_2 vs. FeO*/MgO (Figure 3.21). Although there is overlap between FeO*/MgO, Group III basalts have higher TiO_2 than Group I. Trace and REE element concentrations are more distinctive with Cr, Cu, Ni, Sr, Y, Zr, Nb, La, Ce, Nd, Dy, Er, Pb, and Th concentrations indicating the greatest variability across the igneous groups. Cr concentrations reflect the presence of Cr – Spinel in Group III (Kanazawa et al., 2001) which contrasts with Group II (low Cr and no spinel). Group I basalts have relatively low concentrations of Zr, Nb, La, Ce, Nd, Dy, Er, Pb and Th compared to Groups II and III. Group II has relatively high concentrations of Y, Zr, Nd, Dy, and Er and Group III exhibits high concentrations in Cr, Cu, Ni, Sr, Zr, Nb, and Pb. Strontium concentrations are markedly elevated in Group III. This may be a manifestation of increased alteration intensity causing a greater incorporation of seawater Sr into the basalts, elevated CaO (average: 11.86 wt %) in Group III compared to Group 1 (average: 10.6 wt %) and Group II (average: 10.2 wt %).

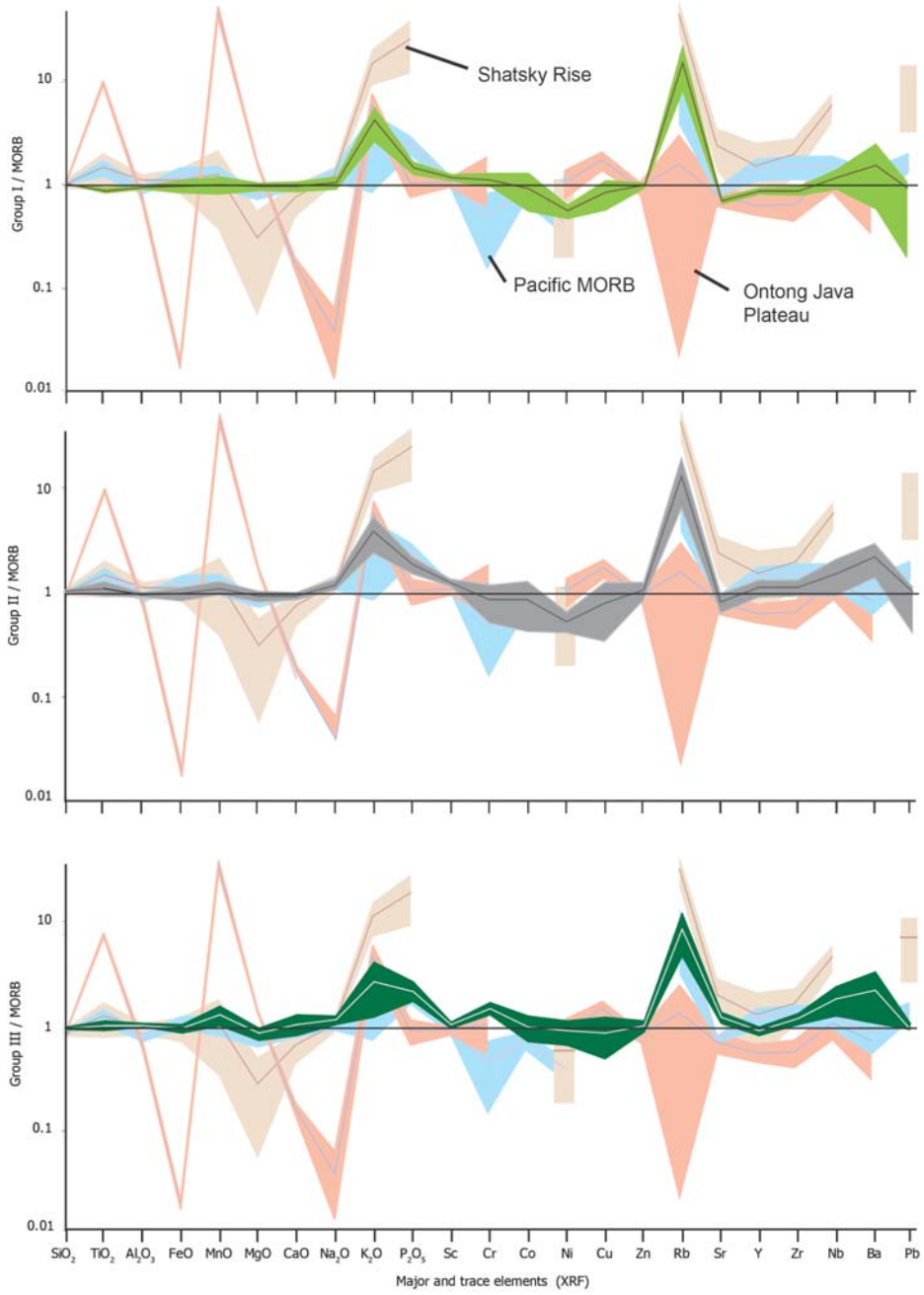

Figure 3.22. MORB-normalized major and trace element diagrams for all samples in Group I, II and II basalts from Hole 1179D. For comparison Pacific MORB (blue), Janney and Castillo, (1997); Ontong Java Plateau (Orange), Fitton and Godard, (2004) and Shatsky Rise (brown), Tatsumi et al., (1998) fields are shown. MORB normalization for major and REE elements taken from Sun and McDonough (1989) and trace elements from Pearce (1983) and Pearce (1982).

Figure 3.22 displays MORB normalized (Sun and McDonough, 1989; Pearce, 1982, 1983) average major and trace element compositions for all samples in each igneous group, compared to Pacific MORB, and the lavas from the Ontong Java Plateau and Shatsky Rise. Overall Site 1179 groups do not deviate greatly from MORB, although all groups have elevated K_2O, Rb, Ba and Pb compared to MORB.

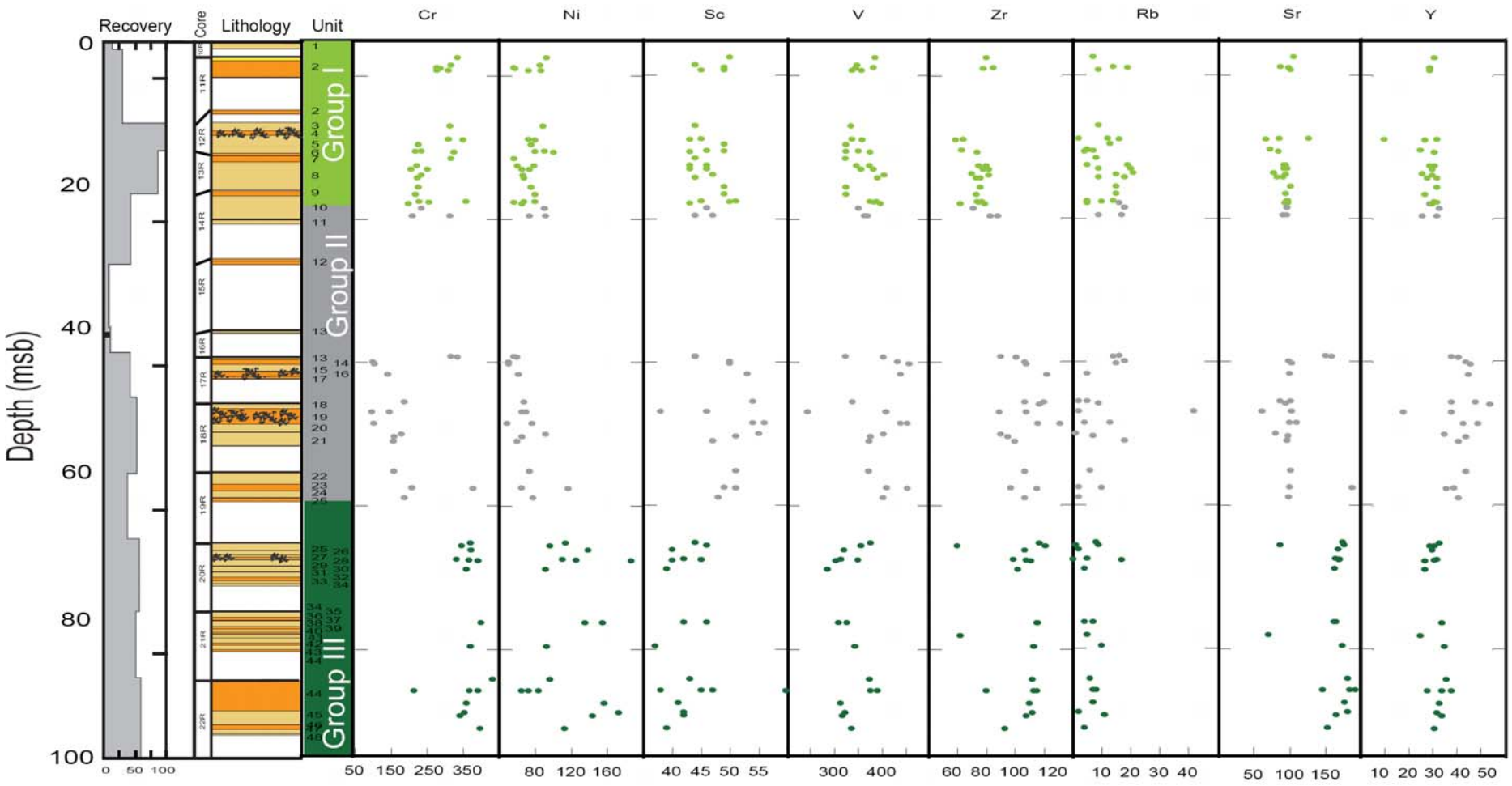

Figure 3.23. Selected trace and REE concentrations vs. depth for Site 1179 basalts. Igneous groups are indicated as; green = Group I, grey = Group II, dark green = Group III. Core recovery and lithology is also shown (Concentrations are in ppm).

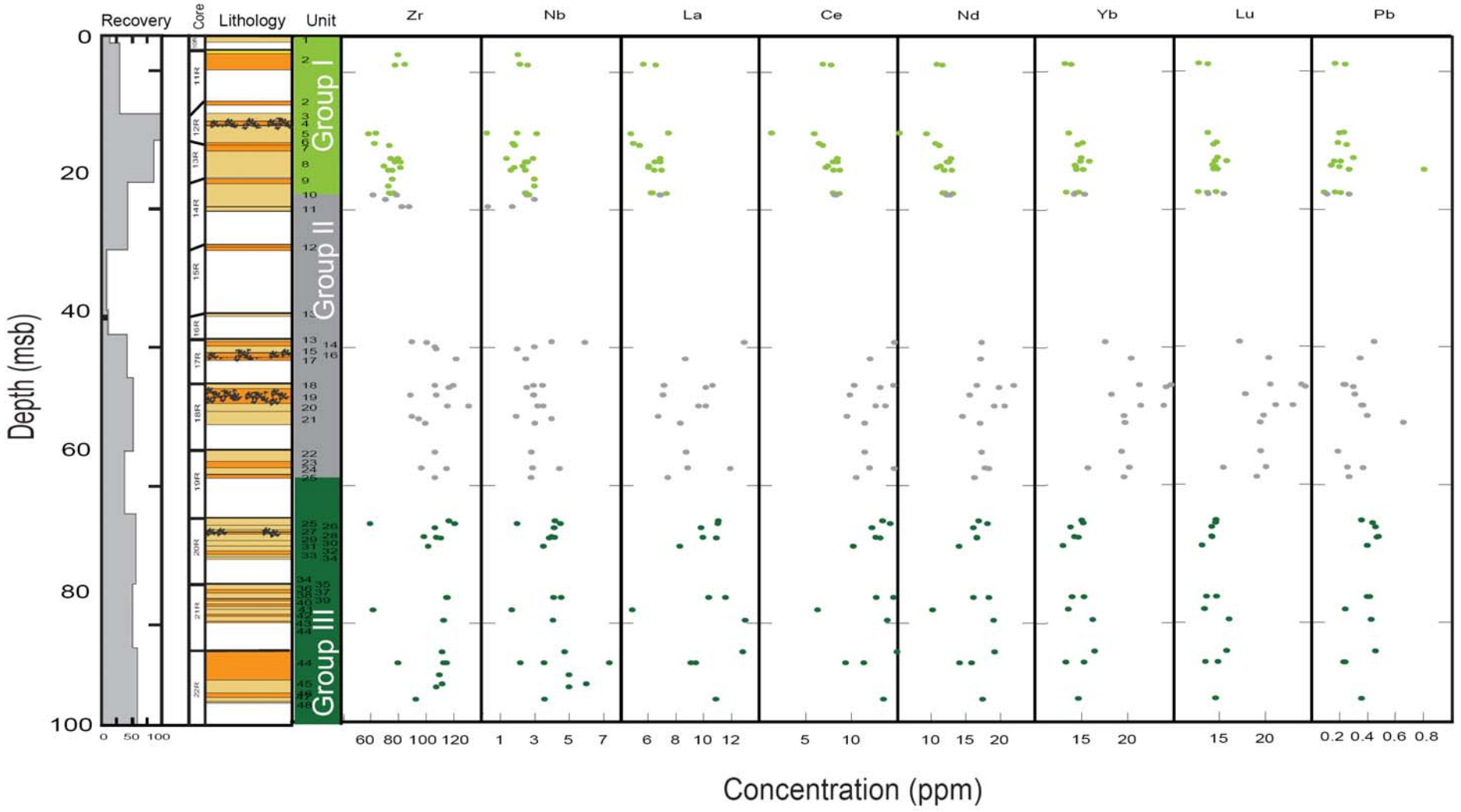

Figure 3.23. Continued ...

Elevated K_2O and Rb reflect the incorporation of secondary minerals (celadonite and saponite) by seawater interaction with basalt. Overall Site 1179 basement REE does not vary greatly with depth, Figure 3.23 shows selected REE concentrations vs. depth. Distinct petrological changes between groups are indicated by trend lines. Group I is distinguished by low Zr, Sr, Nb, La, Ce and Lu where as Group II is characterised by high concentrations of Sc, V, Y, Yb and Lu and low Cr. Group III contains high concentrations of Cr, Sr, Nb, La and Ce and low concentrations of Sc, Y, Yb and Lu.

Overall Site 1179 basement chondrite normalized REE patterns are homogenous with a slight depletion of light REE (Figure 3.17. The average REE patterns for each group are similar to average Pacific-MORB (Figure 3.17 but have slightly higher REE concentrations compared to other drilled basement sites in the Pacific basement (Figure 3.17. Group I basalts have the greatest depletion of light REE (La – Nd). Group II basalts have a similar pattern to Group I rocks albeit less LREE depleted (Figure 3.17. Group II chondrite normalised REE pattern is the most similar to Pacific MORB. Group III basalts are the least depleted in LREE, La, Ce and Pr, but have lower HREE with a pattern that resembles MORB.

Plots of major and trace elements vs. SiO_2, MgO and Mg-number (Figure 3.15 and 3.16) indicate fractionation. Fe, Mg, Sc, Co, Ni and Pb vs Silica (Figures 3.15 and 3.16) plots exhibit variable trends within the igneous groups at site 1179. Si vs Fe (Figure 3.15) Indicates that as Si concentrations are reduced, Fe concentrations increase. This may be an alteration affect because an increase in the relative proportion of iron will reduce the proportions of the other major elements. MgO vs SiO_2 shows an overall trend of increasing Mg with Si. Sc and Ni (Group III especially) show increased concentrations with silica. No fractionation trend can be detected for Group III Co vs. SiO_2 although, like Ni they are relatively high in concentration due to the presence of olivine. Pb concentrations vary, but they appear largely independent of silica, with Group II showing a very slight trend towards increasing silica content.

Silica vs. Mg number (Figure 3.15) display a good trend suggesting fractionation in all groups. It also compares well with Pacific MORB. Co vs Mg number (Figure 3.16) has a slight negative trend with Mg number. Fe_2O_3 vs. MgO (Figure 3.15) also shows a negative trend in all groups, indicating fractionation. Ni vs. Mg number shows a positive trend for all igneous groups. Because olivine commonly contains Ni, we expect Group III basalts to contain the highest concentrations of Ni.

The weak trend between Sr and Mg number (Figure 3.16) in Groups I and II is most likely the result of mobility of Sr during low temperature hydrothermal alteration.

3.4.3 Shatsky Rise.

By directly comparing Site 1179 chemical data to data available for Shatsky Rise, interactions between the Site 1179 and Shatsky rise should be indicated by chemical similarities between the two sites. Major element oxides for Site 1179 basement remain chemically distinct to that of Shatsky, follow MORB trends (Table 3.2). The chondrite normalized REE patterns exhibited in Figure 3.17b illustrates that Shatsky Rise data is distinct from Site 1179 with elevated trace elements and depletion of HREE. Fractionation trends (Figures 3.15 and 3.16) also indicate no association with Shatsky Rise.
Group III REE patterns hint at perhaps a slight Shatsky plume influence, because this group follows a similar trend of relatively low depletion of LREE followed by depletion of HREE.

Site 1179D basalts appear to show no plume characteristics of the type exhibited by Shatsky Rise or the Ontong Java Plateau. Microprobe analysis of phenocrysts, combined with leaching experiments to remove alteration effects will be required for a more detailed study of the igneous petrogenesis of Site 1179 basalts. However, the chemistry thus far suggests Site 1179 is chemically distinct from Shatsky Rise. The variation in chemistry within the groups most likely relates to fractionation and seawater interaction with Site 1179 basement.

3.4.4 Whole rock chemical changes

Full assessment of the nature and extent of hydrothermal alteration, necessitates calculation of chemical change caused by hydrothermal alteration. This may be achieved by comparing the compositions of altered rocks to a fresh ‘protolith’. If available, fresh glass from the margins of a pillow lava can be used as a guide to assess precursor compositions. However, the lack of phenocrysts in glass precludes their use as an absolute measure for precursor compositions and, where alteration is pervasive,

fresh glass is frequently not available. An average of a selection of least altered rocks may be chosen to represent fresh basement, however, if the rocks are fractionated the primary chemistry for each sample will differ from one another, meaning sourcing a suitable protolith becomes very difficult. Site 1179 presents a challenge for assessing the chemical changes associated with hydrothermal alteration because basement is pervasively altered, there is evidence of fractionation (See chapters 4 and 5 respectively), and there are no fresh glass samples.

For comparisons between the fresh and altered state of basement rocks at Site 1179, immobile elements are extensively used to determine protolith compositions (e.g. Teagle and Alt, 2004; Coggon, 2006). A range of techniques developed for this purpose (Gresens, 1967; Grant, 1982; Maclean, 1990; Maclean and Barret, 1993) are applied to Site 1179 to determine their effectiveness and ultimately to calculate chemical change for Site 1179.

3.4.4.1 Selection of protoliths

Figure 3.24 is a summary which outlines the process by which the precursor composition is found and the chemical changes are calculated. All whole rock samples were measured for chemical change according to a calculated precursor composition based on Ti, which is assumed immobile/incompatible. Calculation of the precursor composition using a Ti-monitor is done using least altered samples, which are selected based on a variety of factors outlined in Figure 3.24.

In addition to change calculated from a precursor, figure 3.24 summarises the process to which chemical change in all altered Site 1179 samples are calculated from their least altered host sample or a least altered sample that is in close proximity to the altered sample. Samples with no direct host are paired with samples that share similar concentrations of Ti, Y and Zr (All of which are assumed to be immobile and incompatible).

Whilst two different methods for determining sample by sample precursor compositions are used, chemical change is calculated using the same method. The following section explains this method using an example from the Site 1179 dataset.

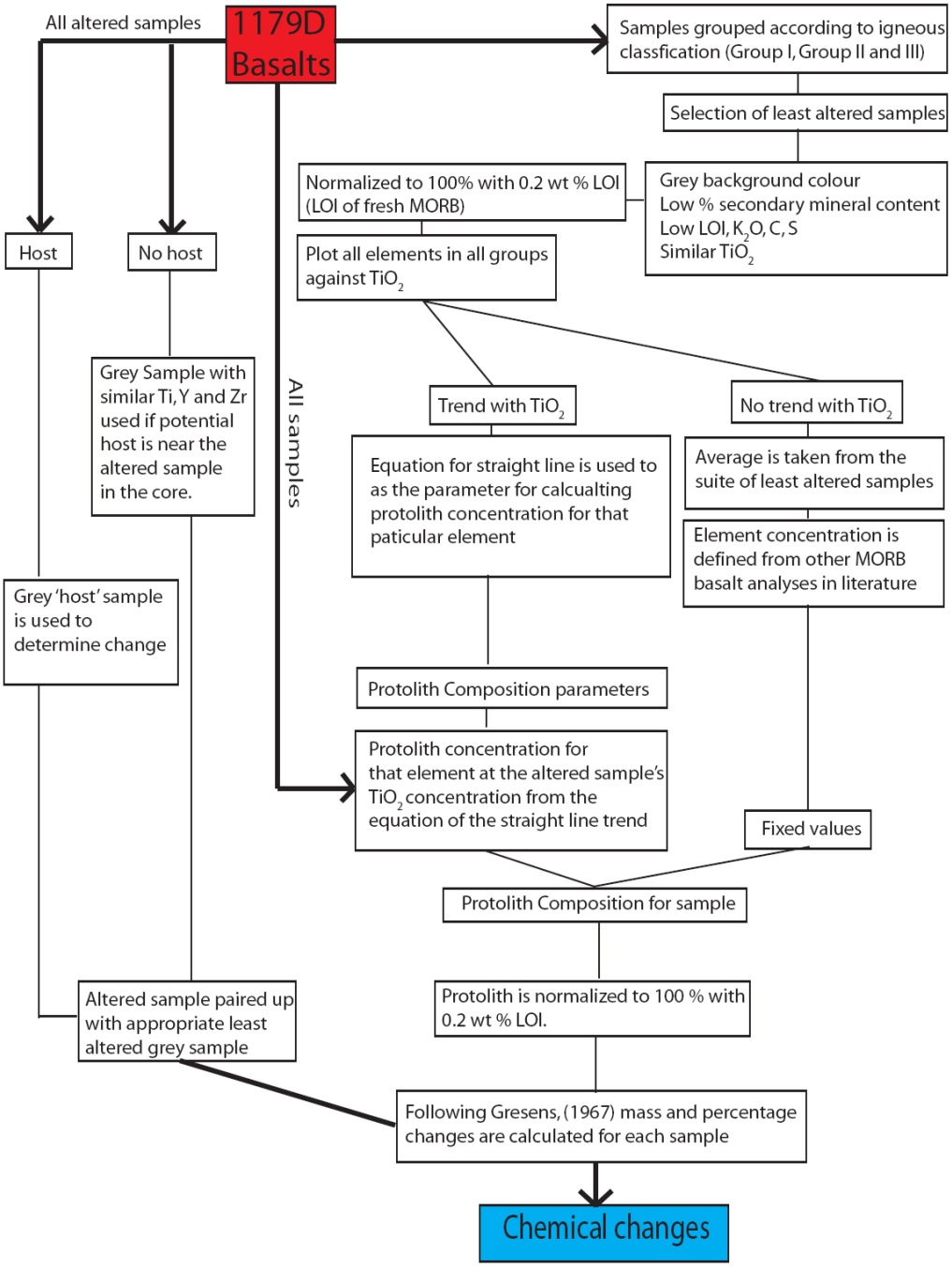

Figure 3.24. Summary flow diagram indicating the process by which the chemical changes for Site 1179 are calculated.

3.4.4.2 Calculating chemical changes from host samples

All altered samples from Site 1179 are measured against an appropriate sample pair to assess chemical changes, be it from a grey host rock sampled from the same specimen or by selection of an appropriate grey rock. For the sample pair, the net gains and losses

of each element are calculated on a sample by sample basis following Gresens (1967). Gresens (1967) argues that any chemical change from a parent rock to an altered rock should take into account volume change. Therefore, any change for a chemical component (ΔX) can be calculated as follows:

$$\Delta X = (D^A/D^P)X^A(V^A/V^P)-X^P$$

Where D and V are density and volume, 'P' and 'A' are the parent and altered rock subsamples for the chemical component 'X'. The volume ratio (V^A/V^P or FV) is worked out assuming there has been no change in mass during hydrothermal alteration (See *3.4.4.3*, assumptions). Before ΔX can be deduced the volume ratio for each element in each sample pair. The volume ratio needs to be calculated from the following expression:

$$FV = (X^P/X^A)(D^P/D^A)$$

Figure 3.25 shows two examples from Hole 1179D where the FV has been calculated for each element based on analyses of halos compared to the least altered 'background' rock in the sample pair. FV values ~1 suggest little or no change in concentration of any given element as a result of alteration, such elements are deemed immobile. In addition, groups of elements with similar FV indicate that change has occurred solely as a result of volume change and may also be immobile. For each sample, an approximate FV is calculated from the average of the immobile elements to represent the volume ratio of the altered and parent rocks. With the FV (V^A/V^P) value chosen, ΔX is calculated for each element for each sample and the percentage gains and losses for each element are calculated for each sample pair. The sensitivity of this method of calculating chemical change is governed by the range of FV values chosen. Selection of an appropriate 'host' sample for samples which have no 'fresh' counterpart is carried out based on proximity to the altered sample in the core, colour and similarities in incompatible elements, for example Ti, Zr, Y, and Nb.

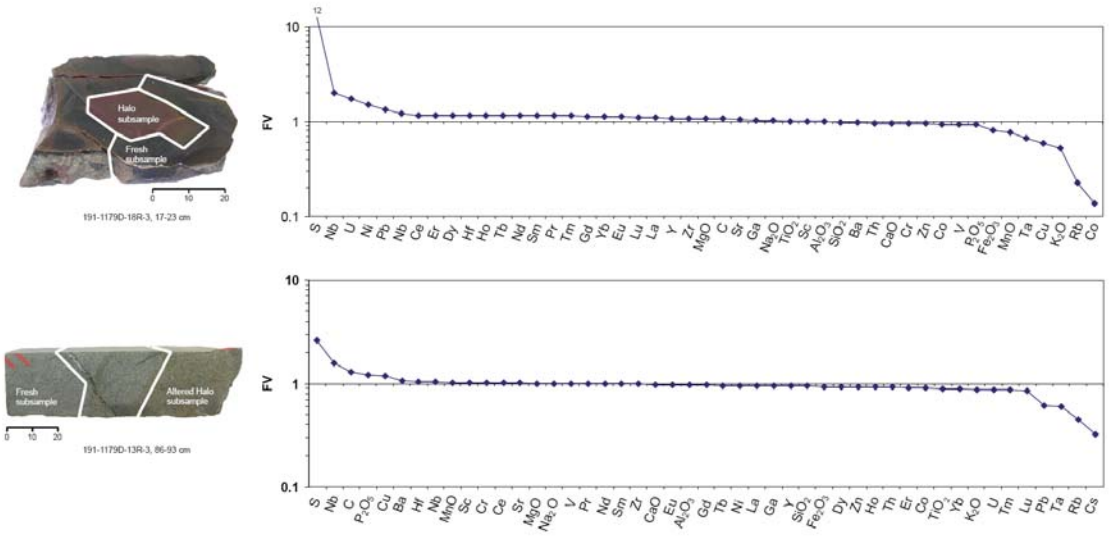

Figure 3.25. Examples of sample pairs from Site 1179 in which major trace and REE have been analyzed for both the altered and least altered hosts. Values for FV, determined by Gresen's analysis of halos vs. least altered background indicate immobile elements. Elements which are similar in FV (FV~1) are deemed immobile and can only change in concentration by a change in volume.

These elements are used because they are the most consistently immobile when FV was calculated for the samples compared to hosts. Gresen's equations are then applied in order to calculate ΔX and % change in concentration. Both analysis by host and 'selected host' are combined to form a suite of results derived from 'paired' samples.

3.4.4.3 Calculating chemical changes from a protolith.

Because all samples at Site 1179 are altered, it is necessary to calculate appropriate protoliths for all the samples at Site 1179. An appropriate protolith for each sample at Site 1179D is calculated based upon the use of immobile element concentrations from a suite of least altered samples for each igneous Group. The assumptions that are made in this calculation and their validity are outlined below:

1. Incompatible element Ti is immobile, therefore we can use it as a monitor of fractionation to estimate the protolith (Coggon, 2006)

If an element is to be used as a monitor for chemical change then Immobile and incompatible elements should not be affected by alteration. Figure 3.26 plots TiO_2 for all fresh vs. altered whole rock sample pairs (where the altered subsample is

immediately adjacent or to the 'fresh' host) for Site 1179. Despite the possibility that the least altered samples may not represent totally fresh rocks, they are useful for comparison with the more altered subsample. Comparisons indicate good reproducibility of TiO_2 despite alteration ($R^2 = 0.94$) indicating that it is relatively immobile during alteration

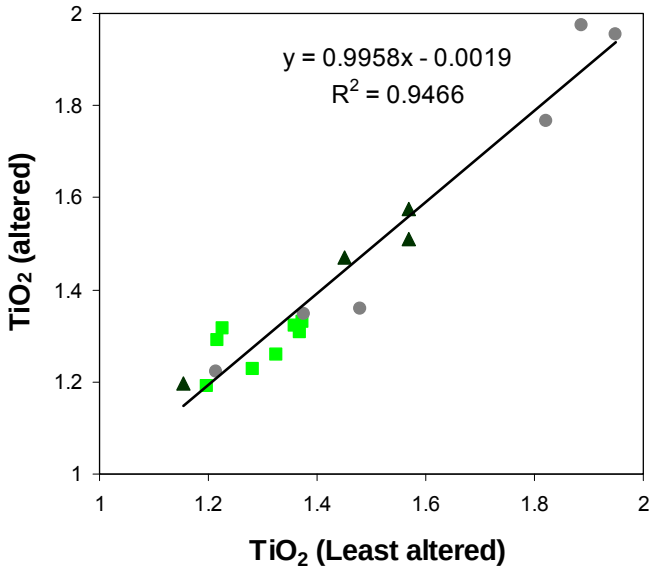

Figure 3.26. Comparison of TiO_2 (wt %) between least altered and altered sample pairs at Site 1179. Samples that have undergone significant volume change, and altered samples with no pair within the same core are excluded.

2. No change in mass as a result of alteration, therefore the concentration of Ti is unaffected by alteration.

This is possibly the least certain assumption and in reality it is included to simplify the assessment of chemical change. A plot of LOI vs. specific gravity for Site 1179 whole rock samples exhibits very little correlation between density and LOI. Only a very slight trend towards decreasing density due to the addition of water is present, however the uncertainty is too great to use the correlation to predict density changes. Two possible end member mechanisms to decrease density are to 1) decrease mass without changing volume, for example, replacement of more dense primary igneous phases with less dense secondary phases or 2) increase the volume without changing the mass, for example opening of cracks during cooling of the oceanic basement. Decreases in density at Site 1179 are likely to be the result of the incorporation of veins and/or the extensive replacement of primary mineral phases by secondary phases.

Because whole rock samples were selected to minimise veins, amygdales and vesicles, only breccias at Site 1179 are likely to have experienced significant volume

change. Loss of mass and an increase in density at Site 1179 causes an average increase in concentration of immobile elements of ~2% given that the average LOI for Site 1179 whole rocks (1.72) corresponds to a predicted specific gravity of 2.76 compared to 2.82 for an LOI of 0 wt%. The percentage change is small when compared to the 'magmatic' error associated with estimates of the precursor compositions, the analytical error and the errors associated with the standard deviations for each population of chemical changes.

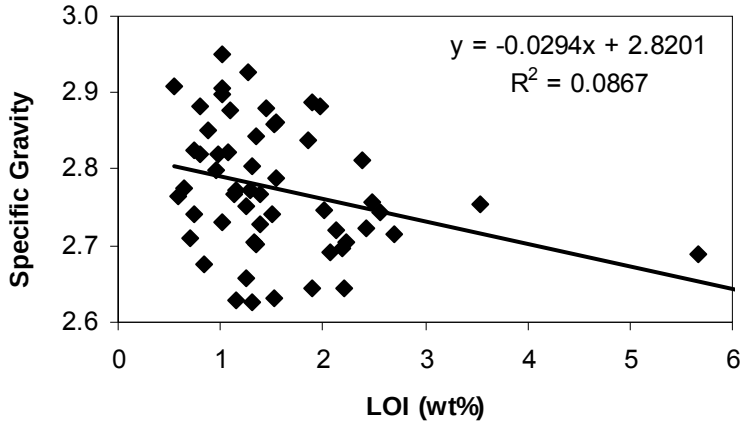

Figure 3.27. Specific gravity vs. LOI for Site 1179 whole rock basalts.

3. The suite of rocks from which the protolith is calculated are the least altered rocks.

This assumption forms the basis for selecting appropriate samples from which we can determine precursor compositions. A selection of least altered samples is made for each igneous group according to colour, percentage of secondary minerals, low LOI, K_2O, C, S and similarities in TiO_2. Each of these filters helps to reduce the effect of alteration when calculating the precursor. Grey coloured basalts suggest that most of the primary igneous textures remain, extensive alteration usually alters the colour of a rock in hand specimen (e.g., brown halos). Secondary mineralogy is largely detected by petrographic analysis and the volume percentage of each secondary mineral phase may be ascertained by point counting for each sample, the least altered samples should contain low volumes of secondary minerals. LOI, as mentioned earlier in this report indicates the volume of volatile phases lost during XRF analysis, which, unless large amounts of CO_3 are present, is predominantly made up of water incorporated due to hydration of primary minerals during alteration. All fresh MORB LOI is ~0.2 wt% (Danyushevsky, 2001; Dixon et al., 1989; Alt et al., 1989) therefore samples with low LOI are selected. In addition to elevated LOI, high K_2O, C, and S suggest alteration,

because K is present in clay minerals, high C is indicative of carbonates, and secondary sulfides lead to increases in S concentration. Based on the filters outlined above, it is assumed that the least altered samples for Site 1179 have been selected appropriately.

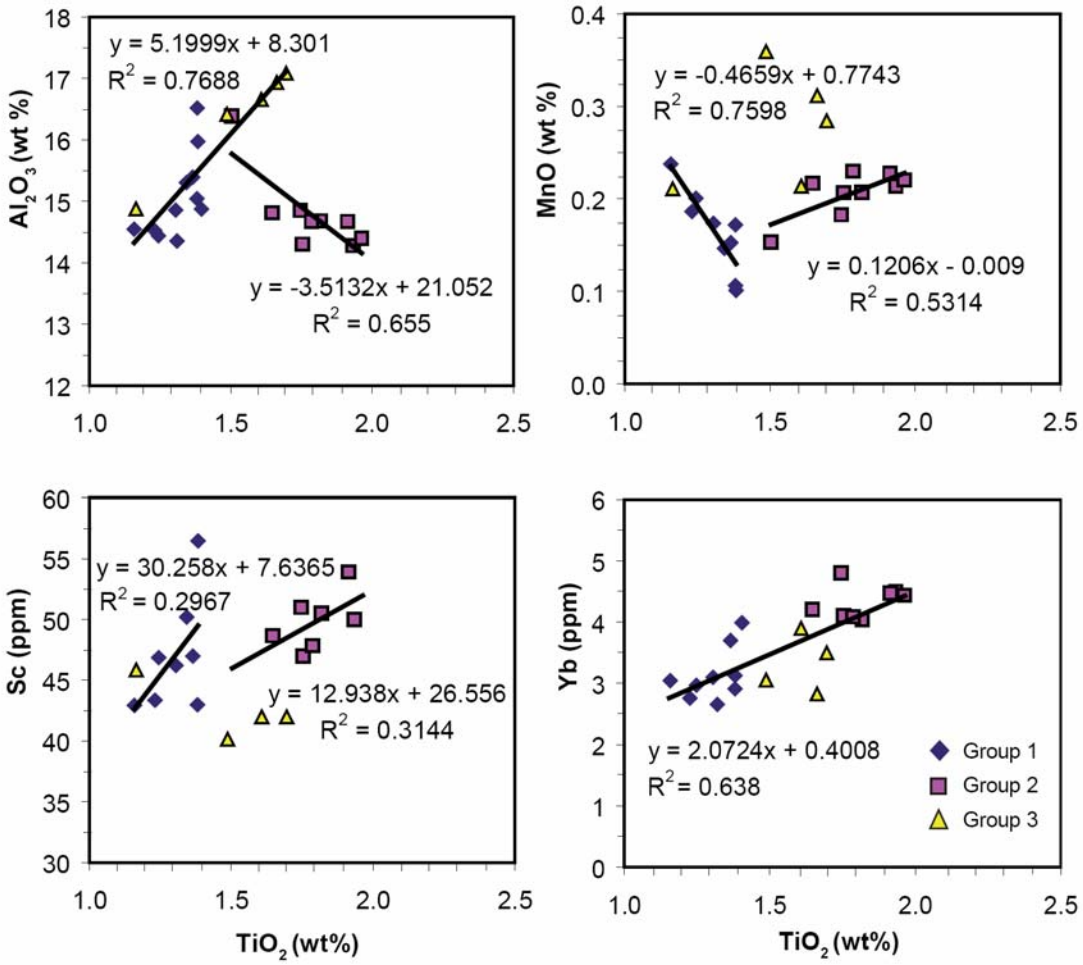

Figure 3.28. Examples of plots vs. TiO_2 for elements from the least altered samples in each group. Trends within individual groups and trends across all groups may be present. The equations for these trend lines are used to calculate protolith concentrations where x is the TiO_2 value of the altered sample.

All the least altered samples are normalized to 100 % total assuming 0.2 wt% LOI. This is done to remove (as much as possible) the effect of additional water in the rock. Since TiO_2 is assumed to be the most immobile element, plots of elements against TiO_2 should (if the effect of alteration is minimal) indicate fractionation trends either within groups or between groups. Figure 3.28 shows a few examples of elements vs. TiO_2 and their trends (if any).

Where a trend is seen, the equation of the straight line can be used to calculate the protolith composition for any sample within the appropriate igneous group (See Appendix C,1)

For example given the straight line equation for MnO in a sample from Group I that has a TiO_2 value of e.g., 1.28 wt% the precursor MnO value would be:

$$= -0.4659 \times 1.28 + 0.7743$$

$$= 0.18 \text{ (wt \%)}$$

Where no trend is seen for a particular element, a precursor composition is selected from an average concentration of the least altered samples. For several elements, where alteration may have still severely affected their concentration, despite careful selection of altered samples, a value from an appropriate MORB is chosen from the literature. Table 3.4 summarises these values and their source. Calculating each element either from an average, from the trend line and selecting the appropriate concentrations from the literature gives a protolith composition (normalized to 100% at 0.2 wt% LOI) from which one can calculate the chemical changes in that sample.

Element	Concentration	Unit	Reference
K_2O	0.17	wt %	Makenzie and O'Nions, (1991)
LOI	0.2	wt %	Alt, et al, (1989); Danyushevsky, (2001); Dixon et al, (1988)
S	0.1	wt %	Alt, et al, (1989)
CO_2	150	ppm	Dixon, et al, (1988)
Sr	100	ppm	Pearce, (1983)
Ba	6.9	ppm	Hofmann and White, (1983)
Rb	0.61	ppm	Hofmann and White, (1983)
U	0.1	ppm	Sun and Mcdonough, (1989)
Th	0.12	ppm	Sun and Mcdonough, (1989)

Table 3.4. List of protolith element concentrations derived from sources other than Site 1179 samples.

Because TiO_2 is assumed to be immobile, only TiO_2 is used for 'FV' or volume factor when carrying out Gresen's analysis. In addition, the variation in density for each sample is sufficiently small that it can be ignored, therefore $(D^P/D^A) = 1$. The sensitivity of comparing altered samples vs. immobile element defined protolith or host rocks is dependent on the variation between the immobile elements of the altered rock and host/protolith (immobility). Values of change that are within the range of immobility are considered too small to represent real chemical change. Figure 3.29 shows an example of immobility range for one sample based on the variability of Ti, Y, Zr, and Nb. Sensitivity is calculated for each sample and averaged to obtain a sensitivity range

for Site 1179. In Figure 3.29 a number of REE appear to be more immobile than that of Ti, Y, Zr, or Nb. Future study may be required, in which chemical change calculations using a variety of immobile elements are compared. Such a study may reduce the levels of uncertainty associated with this type of calculation.

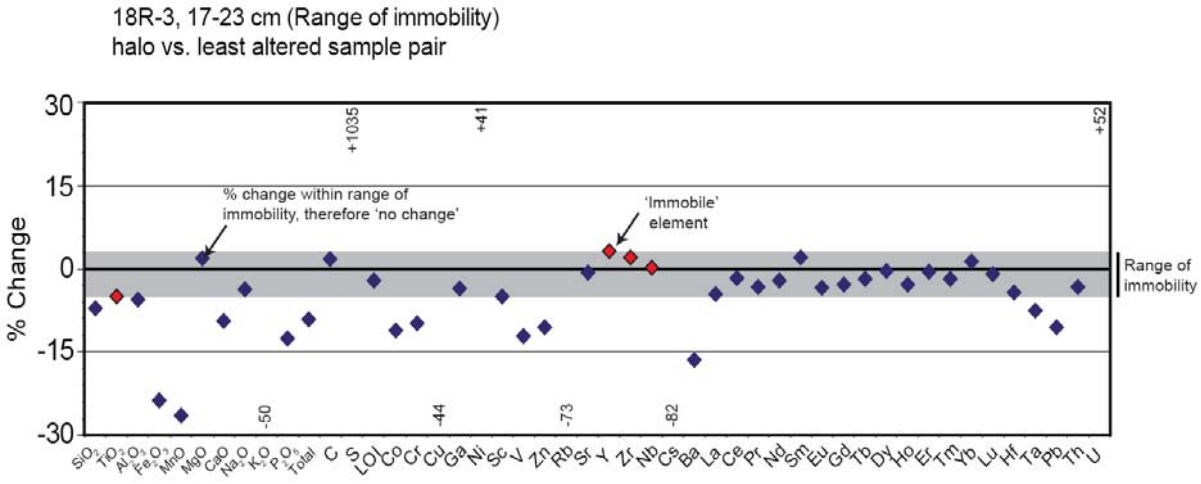

Figure 3.29. Range of immobility for sample 191-1179D-18R-3, 17-23 cm based on variations Ti, Y, Zr, Nb between halo and least altered 'host' rock. Points which fall within this range (grey field) represent no change.

Multi element plots for major trace and REE show the average mass and percentage chemical changes associated with each igneous group, alteration style, and lithology. The chemical change associated with igneous groups, alteration styles and lithologies shown include both methods of calculating chemical change (least altered sample pair and sample by sample protolith methods). The chemical changes deduced for each alteration style are ultimately used to estimate chemical change for Site 1179.

3.4.4.3 Errors associated with chemical change

All calculations for chemical change are subject to analytical, and assumption errors. These include 1) Analytical errors, that are the result of detection limits and reproducibility of results during analysis (See Chapter 2, Methods), 2) the error associated with the range of fresh sample mobile element concentrations that trend with TiO_2 or the standard deviation of the average precursor value for each element (Discussed in section 3.4.4.1), 3) the standard deviation resulting from the range of

chemical between each sample for any given population, 4) Dilution or concentration of elements as a result of unaccounted for mass change. Such error will cause errors in the magmatic trend calculations and the calculation of chemical change outlined in section 3.4.4.2.

For each sample, propagated errors associated with precursor compositions and chemical change is calculated (shown as error bars in each plot). Analytical errors are shown in Chapter 2 (Methods) and errors associated with the primary magmatic variation of elements in the least altered samples, and the standard deviations are shown in appendix C, 1)i. Errors associated with mass changes are assumed to be ~5%.

3.4.4.4 Results: Igneous groups

Figure 3.28 A and B shows the calculated absolute and percentage chemical change for all elements sorted by igneous groups at Site 1179 that have been calculated from least altered sample pairs. Figure 3.31 A and B Shows the calculated absolute and percentage chemical change for all elements sorted by igneous groups at Site 1179 that have been measured against calculated precursor compositions. Almost every element measured in Figure 3.30 has errors that greatly exceed the calculated change. In addition, the change measured for most elements falls within the range of immobility (~10 %) predicted from the range of change observed in Ti, Y, and Zr (Figure 3.29). Elements with change discernable above error and the immobility range include a decrease in MgO and S in Group III rocks and an increase in C in Group II rocks. Despite the propagated errors and high variability within each group, other notable changes include increased Fe, K, Rb, Cs and Pb across all groups and increased C and U in Groups II and III, and increased LOI in Groups I and III. Chemical change in Site 1179 igneous groups, as measured from sample by sample protoliths, in Figure 3.31 A and B exhibits similarly large errors associated with the range of changes between each sample, the error in the straight line trends with TiO_2 and the range of the least altered samples. Error exceeds the value for chemical change in almost every group, however large overall increases in K_2O, C, LOI, Rb, Cs and Ba, and decreases in MnO, CaO and S are indicated. Even if errors are ignored, most chemical change is within the range of immobility ~10% of Ti, Y, Zr and Nb. Chemical change in the altered samples within each igneous group appears to be greater than the change observed in the least altered

samples. These changes include greater incorporation of Fe_2O_3, K_2O, C, Rb, and a greater reduction of MnO, MgO, CaO, S, Cu, in the altered samples compared to the background rocks at Site 1179.

Chemical change within the sample vs. pair plot (Figure 3.30) is lower than the chemical change calculated from the sample by sample protolith (Figure 3.31). When compared to least altered pairs, all groups exhibit increases in Fe_2O_2, K_2O, Rb, Nb, Cs, Ba, Pb and decreased S. Within the igneous groups, Group III exhibits the greatest chemical change with the greatest increase in K_2O, C, LOI, Sr, REE and decreases in SiO_2, MgO, MnO, and S. With the exception of Fe_2O_3, K_2O, LOI, Rb, Cs, Ta and Pb, Group I rocks exhibit the least chemical change, most elements, particularly REE exhibit no change (below sensitivity).

All rocks show chemical change, whilst altered rocks show the greatest degree of change with greater increases in Fe, K, C, LOI, Rb and decreases in MgO, S, and Ni than the least altered samples. The most extreme changes include MnO (-534 %, Group III), K_2O (+ 237 to 519 %), C (+ 126 to 1167 %), LOI (+647 to 1226 %), Rb (+ 755 to 2318 %), and Ba (+185 Group III). These changes occur predominantly within the 'altered' sample set, however, change between each group is variable with no one group demonstrating significant change above the others. In agreement with petrographic observations of secondary minerals within all Site 1179 rocks, the difference in change between rocks calculated from a protolith compared to those derived from the host rock strongly implies that all rocks, including the 'least altered' samples are altered and that the changes measured from sample pairs can only be regarded as minimum values. High error reflects the great variability of alteration styles and intensities present within each group, indicating that igneous group is not exerting a great influence on alteration.

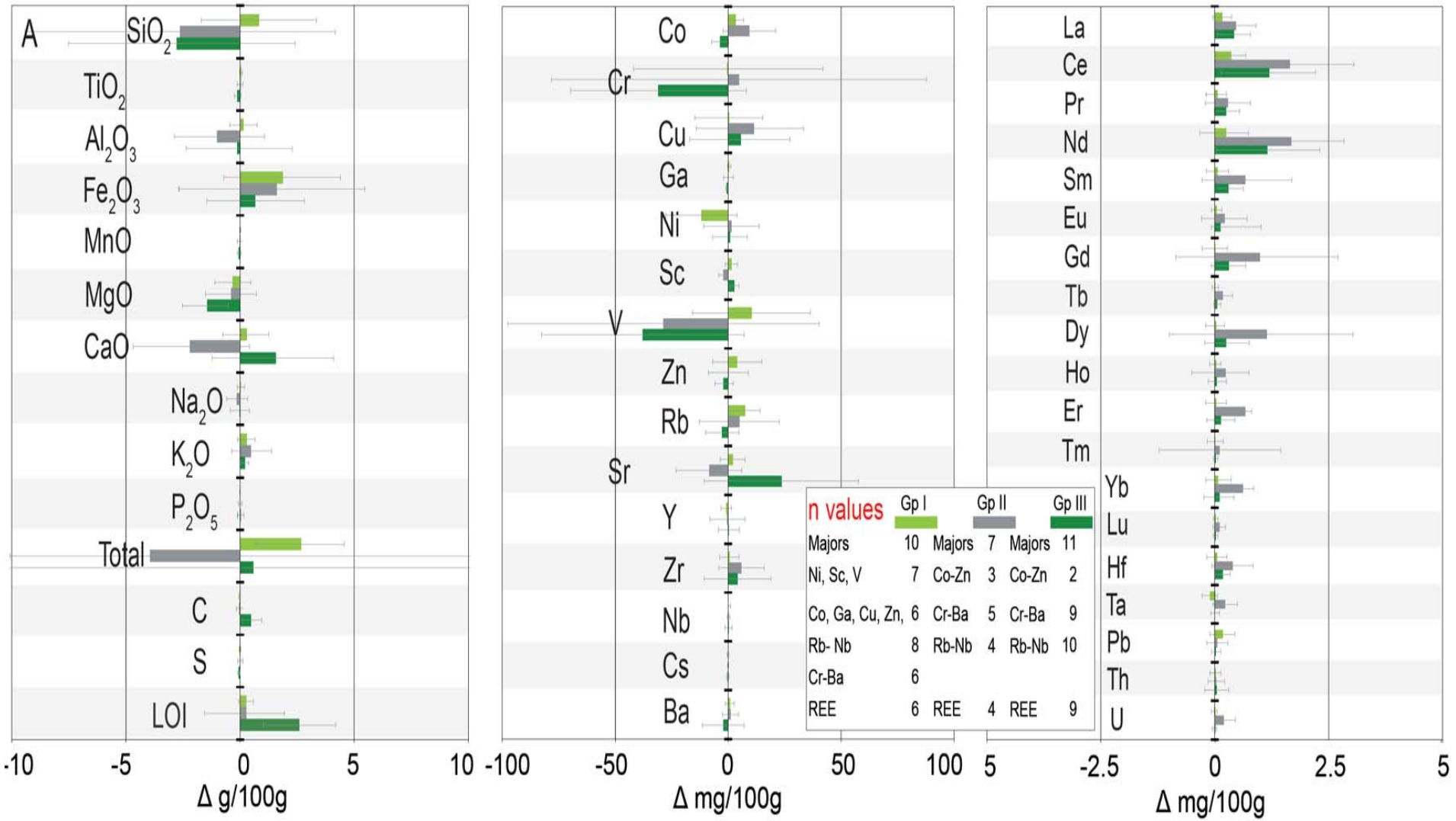

Figure 3.30 Chemical change (A) and % chemical change (B) for each igneous group at Site 1179D calculated from the least altered 'host' or sample pair. Bars indicate the propagated error including standard deviation of the range of changes within each igneous group.

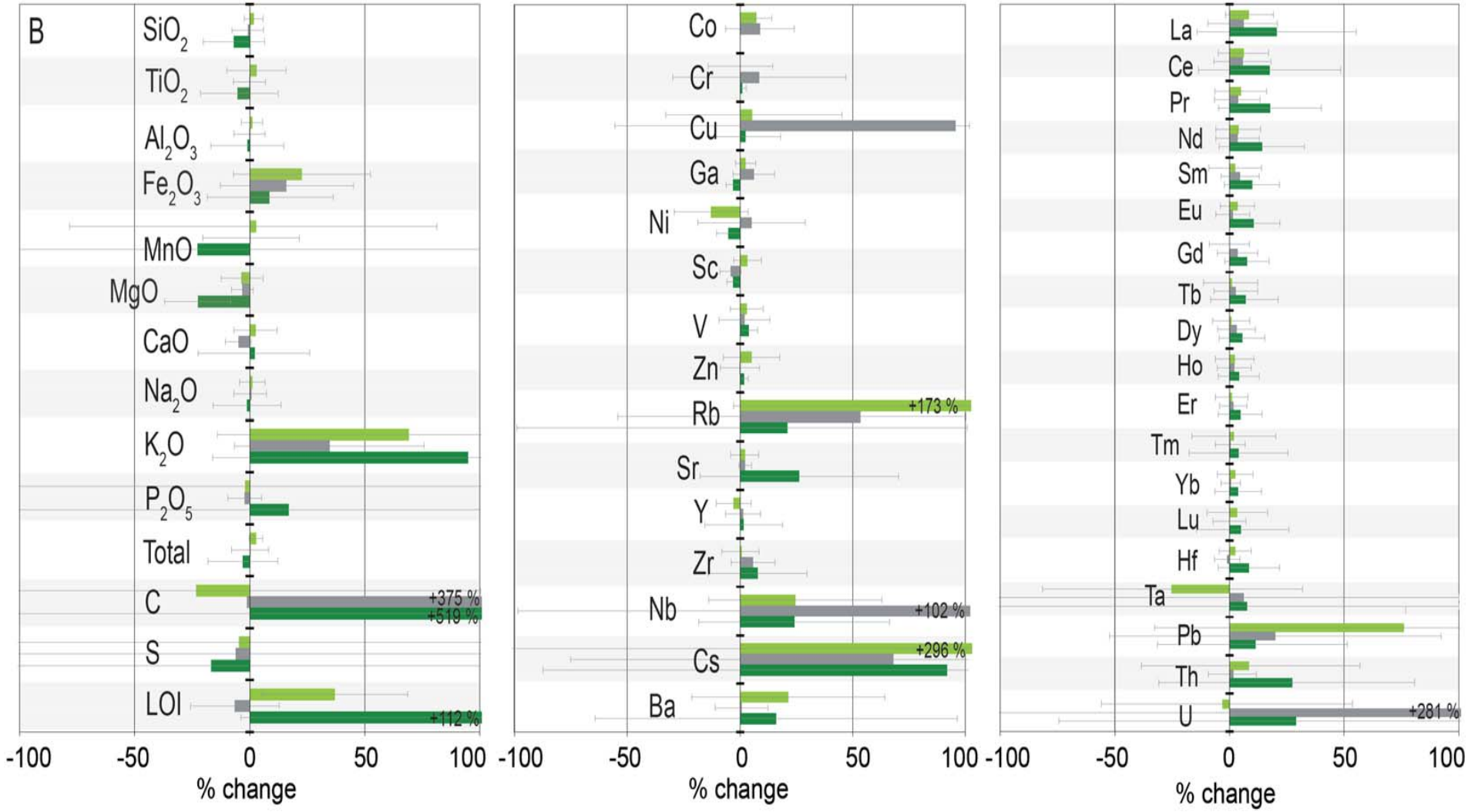
B
SiO2
TiO2
Al2O3
Fe2O3
MnO
MgO
CaO
Na2O
K2O
P2O5
Total
C
S
LOI
+375 %
+519 %
+112 %
-100
-50
0
50
100
% change
Co
Cr
Cu
Ga
Ni
Sc
V
Zn
Rb
Sr
Y
Zr
Nb
Cs
Ba
+173 %
+102 %
+296 %
La
Ce
Pr
Nd
Sm
Eu
Gd
Tb
Dy
Ho
Er
Tm
Yb
Lu
Hf
Ta
Pb
Th
U
+281 %

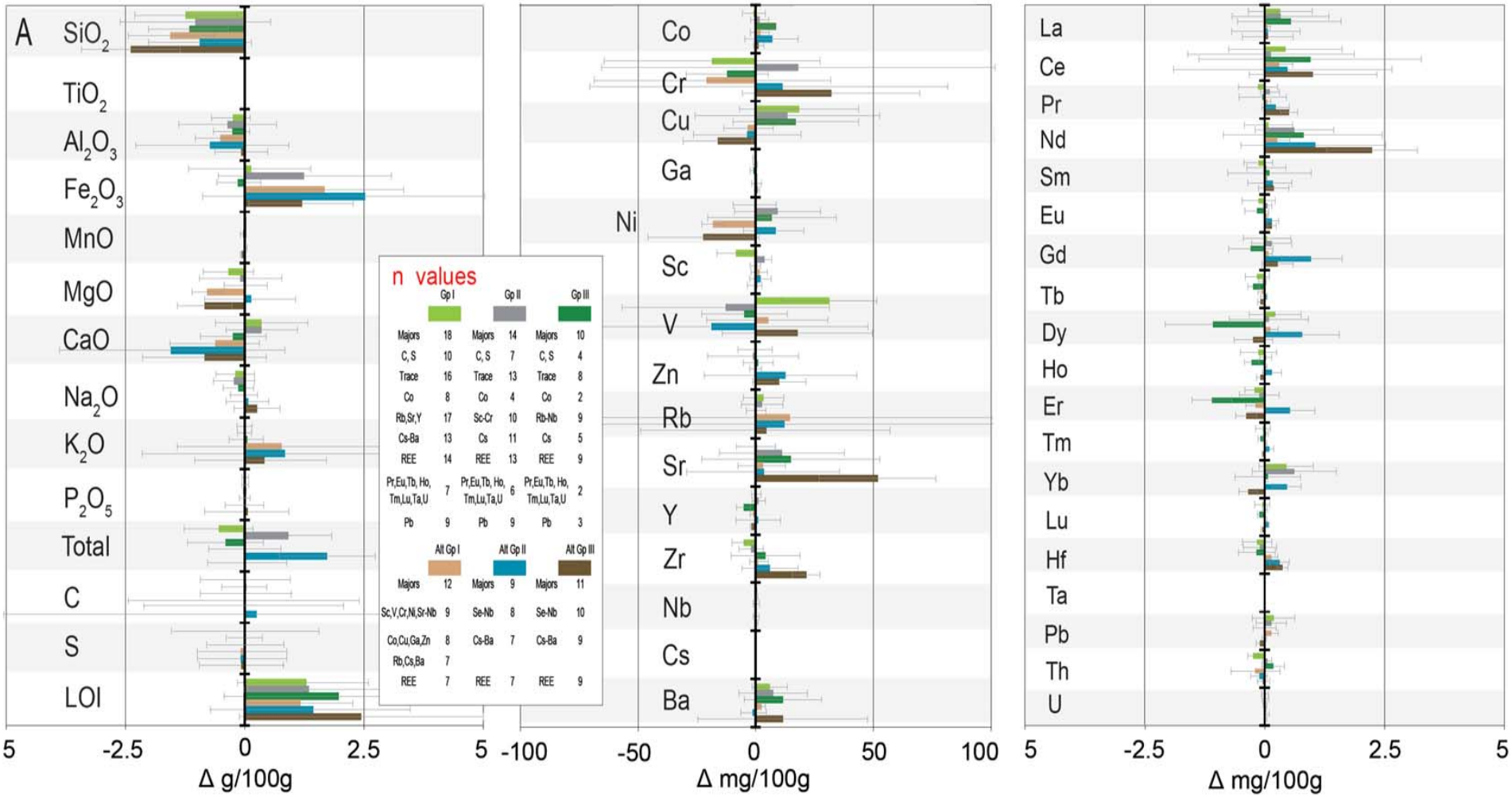

Figure 3.31 Chemical change (A) and % chemical change (B) for each igneous group at Site 1179D calculated from a calculated sample by sample protolith. Fresh and altered rocks are shown separately to highlight chemical change within the least altered rocks at Site 1179. Bars indicate propagated error including standard deviation of the range of changes within each igneous group.

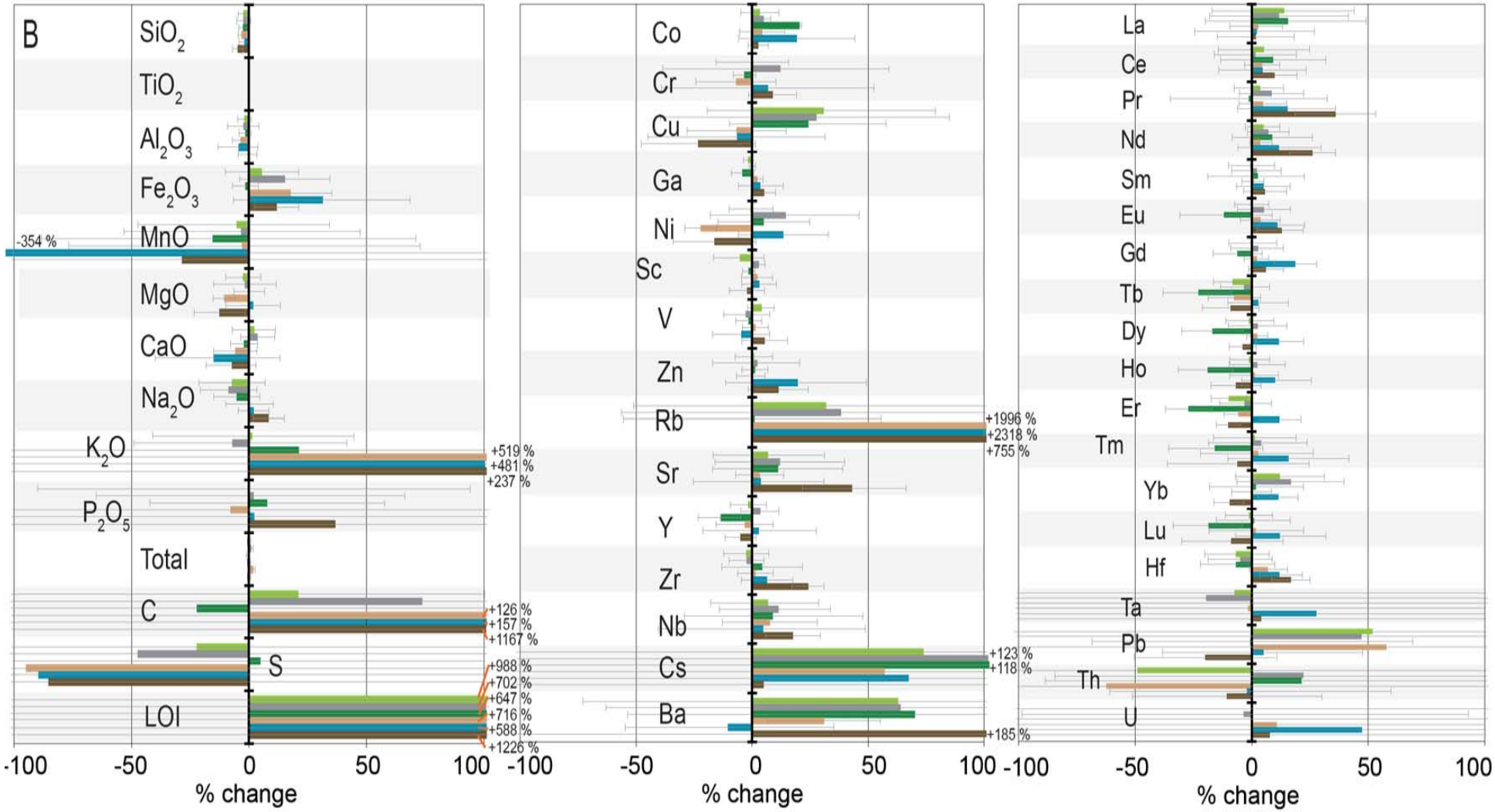
B
SiO2
TiO2
Al2O3
Fe2O3
MnO
MgO
CaO
Na2O
K2O
P2O5
Total
C
S
LOI
-354 %
+519 %
+481 %
+237 %
+126 %
+157 %
+1167 %
+988 %
+702 %
+647 %
+716 %
+588 %
+1226 %
-100
-50
0
50
100
% change
Co
Cr
Cu
Ga
Ni
Sc
V
Zn
Rb
Sr
Y
Zr
Nb
Cs
Ba
+1996 %
+2318 %
+755 %
+123 %
+118 %
+185 %
La
Ce
Pr
Nd
Sm
Eu
Gd
Tb
Dy
Ho
Er
Tm
Yb
Lu
Hf
Ta
Pb
Th
U

3.4.4.5 *Alteration styles*

The chemical changes of the various alteration styles at Site 1179 are recorded in Figure 3.32 and 3.33 with the results from both protolith calculations and host rocks, respectively. Chemical changes as a result of veins and chemical changes in breccias are also included in Figure 3.33. Chemical changes as a result of vein mineral precipitates are calculated from a weighted average (according to volume % of core recovered for each mineral) of the compositions from mineral separates. Analysis of carbonate veins (see later section) from site 1179D are used in conjunction with analyses of other vein minerals from a range of basement sites (Table 3.5). A lack of data for other secondary minerals at Site 1179 necessitates the use of data from other sites, despite the potential for regional variations in mineral compositions. Table D.4 in Appendix shows the mineral compositions used.

Mineral	Site source	Reference
Saponite	504	Bach et al, (1996), Noack et al (1996)
	896	Laverne et al, (1996), Teagle et al, (1996)
	1224	Paul et al, (2006)
	843	Waggoner (1993), Alt (1993)
	1256	This study
Celadonite	504	Bach et al, (1996), Noack et al (1996)
	896	Laverne et al, (1996), Teagle et al, (1996)
	843	Alt (1993)
	1256	This Study
Iron-ox	504	Noack (1993)
	843	Alt (1993)
Carbonate	504	Noack (1993)
	896	Teagle et al, (1996)
	843	Alt (1993)
	1179	This study

Table 3.5 Sources for secondary mineral data from other ODP sites and this study. Secondary mineral compositions were calculated as an average of all available compositions from basement within the Pacific Ocean.

Chemical changes within breccias in Figure 3.33 are based on the entire breccia, including matrix. Calculation of whole breccia is based on a weighted average of change associated within the clasts, including an estimate of any clast material in the matrix, and the composition of secondary minerals within the matrix. Calculation of the secondary mineral composition within the matrix shares the same data outlined in Table 3.5 and it is weighted according to the proportions of each mineral present within the matrix. Because measurement of clasts and matrix was carried out for Sample 1179D, 18R-1, 52-57 cm, calculating a matrix composition for this sample was not necessary.

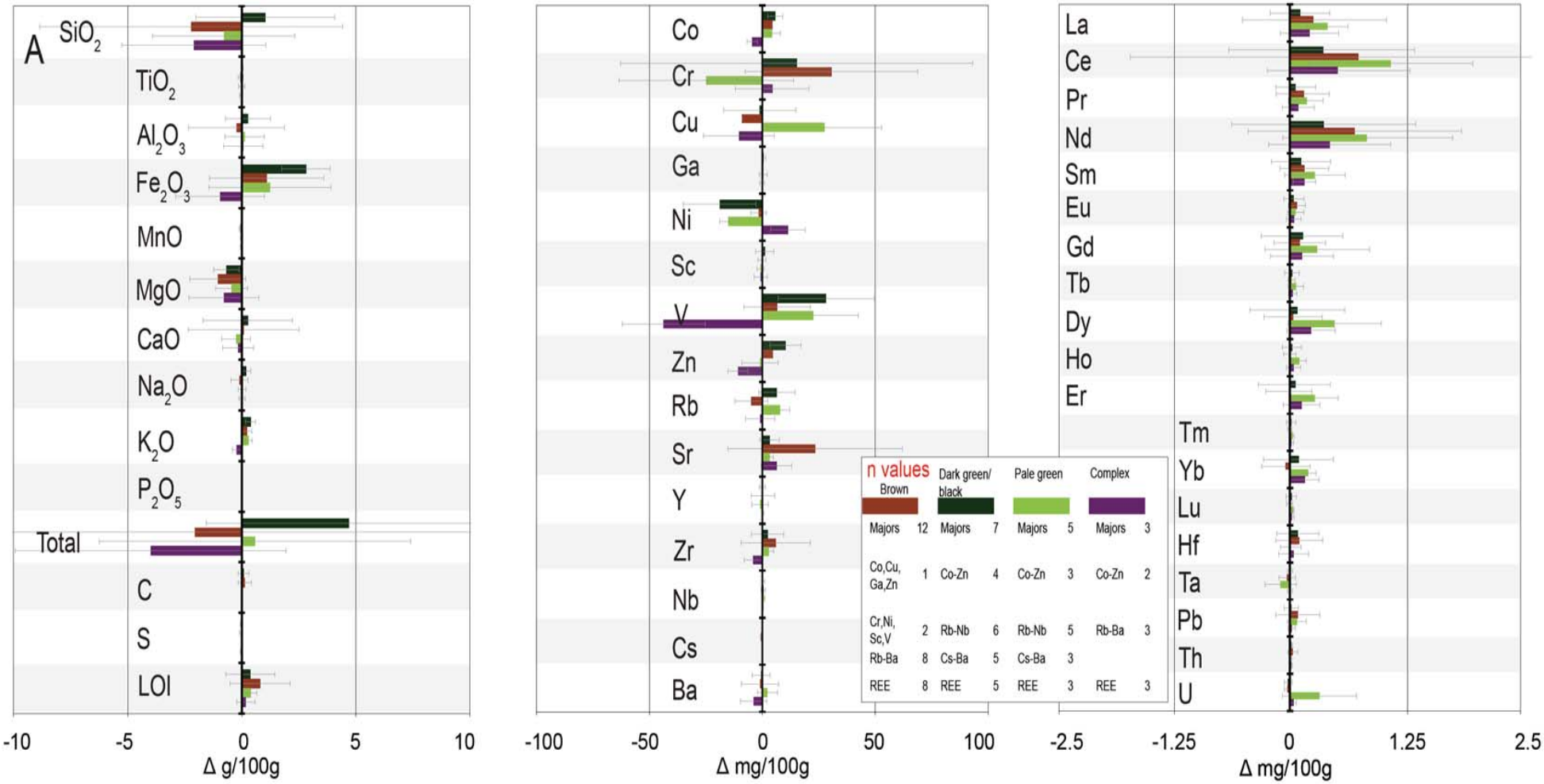

Figure 3.32. Mass (A) and percentage (B) chemical changes associated with alteration styles at Site 1179. Changes are calculated based on least altered sample pair (grey). Bars indicate propagated error including the standard deviation of the range of changes within each alteration style.

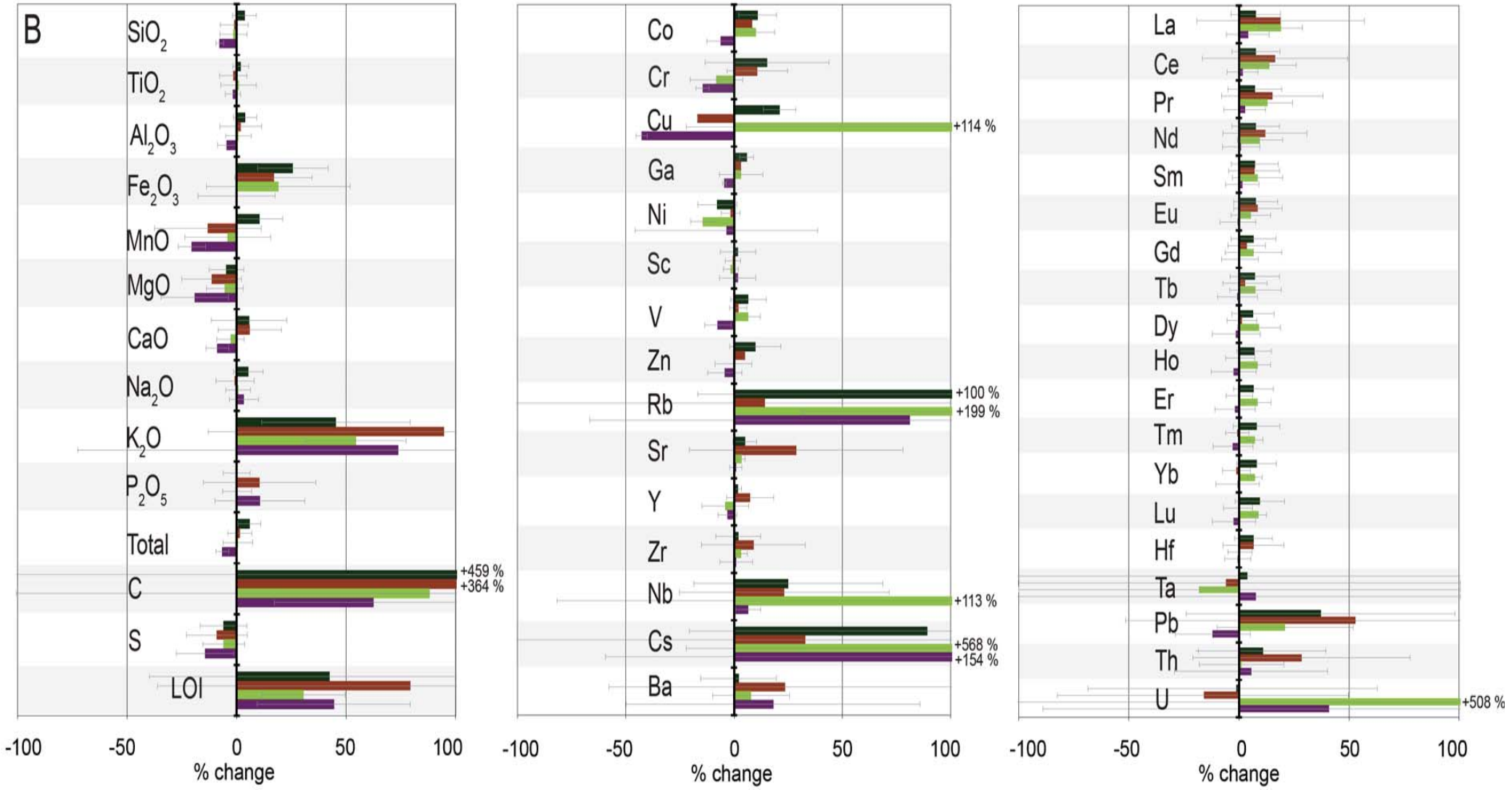
B
SiO2
TiO2
Al2O3
Fe2O3
MnO
MgO
CaO
Na2O
K2O
P2O5
Total
C
S
LOI
+459 %
+364 %
-100
-50
0
50
100
% change
Co
Cr
Cu
Ga
Ni
Sc
V
Zn
Rb
Sr
Y
Zr
Nb
Cs
Ba
+114 %
+100 %
+199 %
+113 %
+568 %
+154 %
La
Ce
Pr
Nd
Sm
Eu
Gd
Tb
Dy
Ho
Er
Tm
Yb
Lu
Hf
Ta
Pb
Th
U
+508 %

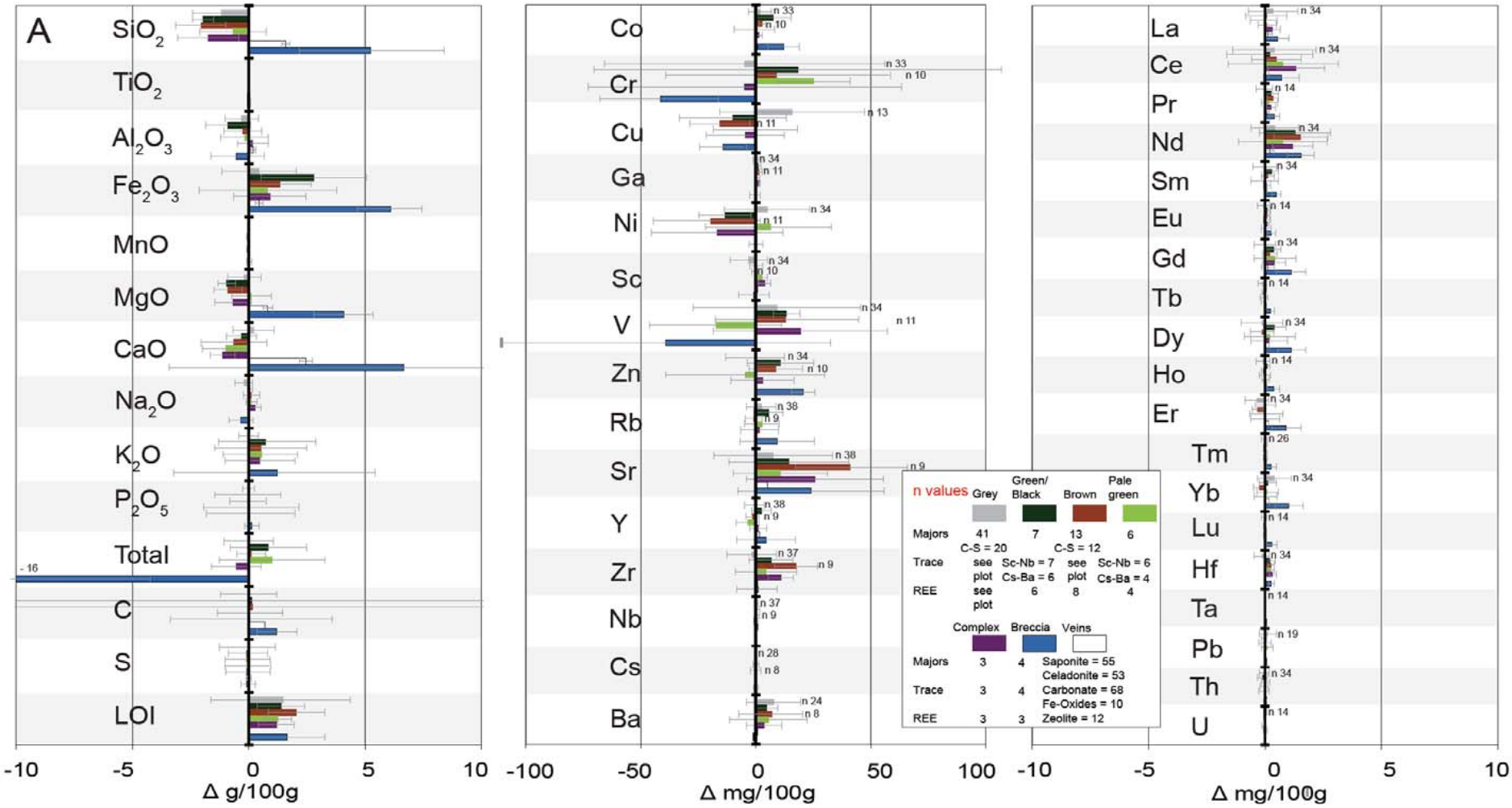

Figure 3.33. Mass (A) and percentage (B) chemical changes associated with alteration styles at Site 1179. Changes are calculated based on calculated sample by sample protoliths. Changes as a result of veins and brecciation, are based on a weighting of the calculated/analyzed matrix composition and clasts. Veins are based on observed abundances for each vein mineral. Bars indicate propagated error including the standard deviation of the range of changes within each alteration style.

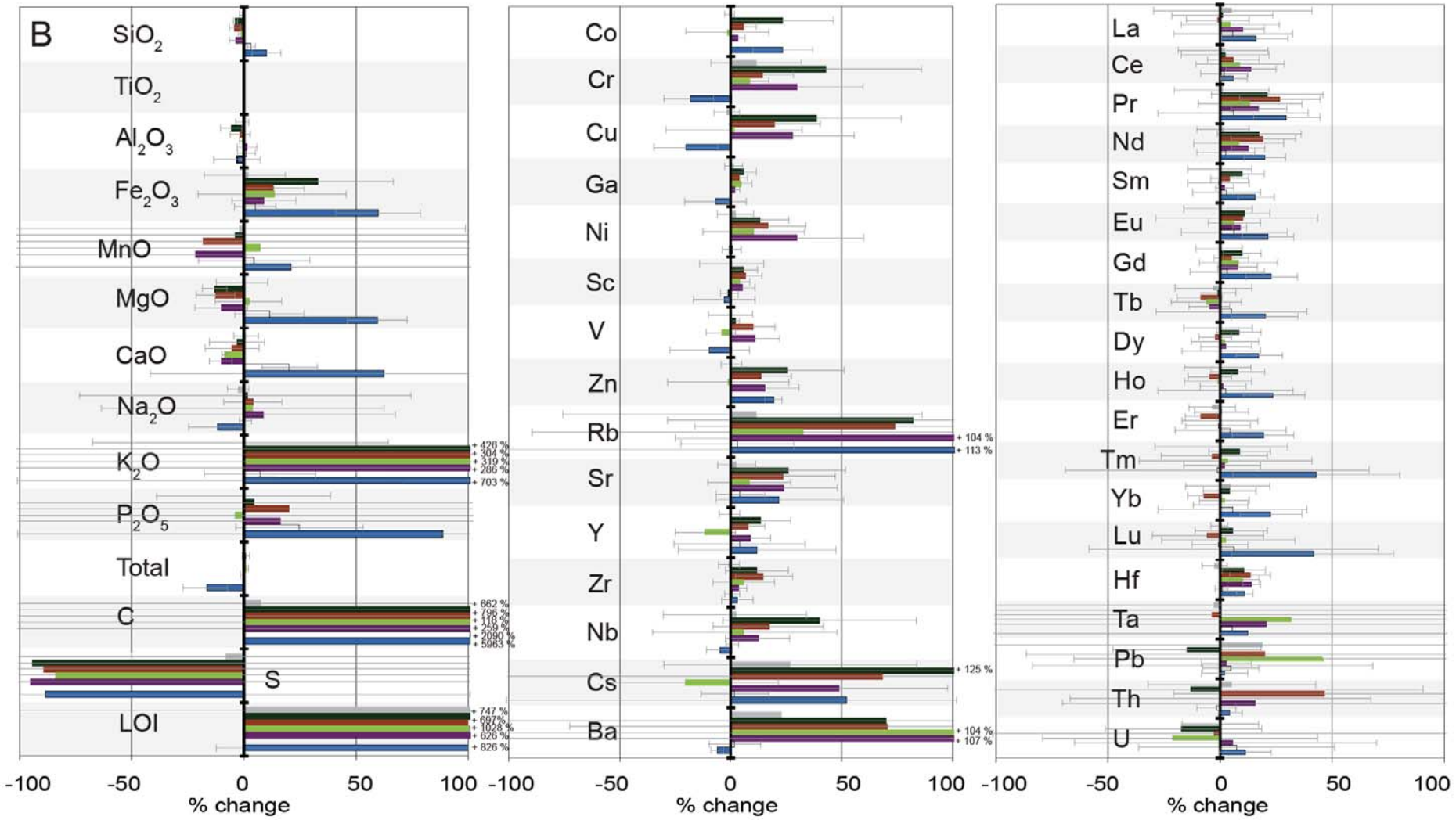
B
SiO2
TiO2
Al2O3
Fe2O3
MnO
MgO
CaO
Na2O
K2O
P2O5
Total
C
S
LOI
+ 426 %
+ 304 %
+ 319 %
+ 286 %
+ 703 %
+ 662 %
+ 747 %
+ 697 %
+ 1028 %
+ 626 %
+ 826 %
-100
-50
0
50
100
% change
Co
Cr
Cu
Ga
Ni
Sc
V
Zn
Rb
Sr
Y
Zr
Nb
Cs
Ba
+ 104 %
+ 113 %
+ 125 %
+ 104 %
+ 107 %
La
Ce
Pr
Nd
Sm
Eu
Gd
Tb
Dy
Ho
Er
Tm
Yb
Lu
Hf
Ta
Pb
Th
U

Overall the results in Figure 3.32 and 3.33 mirror those displayed in Figure 3.31 because chemical changes as measured from the calculated protoliths are greater than those measured from host rocks. This reaffirms the problems associated with calculating chemical change from least altered rocks alone, therefore it is more appropriate to compare all rocks from calculated protolith compositions.

Overall, all alteration styles exhibit increases in $Fe_2O_3^T$, K_2O, C, LOI, Ni, Rb, Cs, Ba, Pr, Ta, and, with the exception of veins and breccia, decreases in SiO_2, MnO, MgO, S, and U. Within halos and background, Iron, K_2O, C and LOI reflect the secondary mineralogy of Site 1179, which supports the presence of celadonite, and iron-oxyhydroxide. Although carbonate and saponite is present in the groundmass, the chemical changes in Table 3.6 actually show a small reduction in CaO and MgO. This may be due to the replacement of primary phases such as plagioclase and olivine. Veins and breccia demonstrate increases in CaO and MgO, which are consistent with abundant saponite and carbonate within veins and matrixes. Very large increases in C (+ 118 to >5000 %) reflect carbonate in veins, matrix and groundmass. Rb and Cs concentrations undergo massive increases across all groups and alteration styles except veins. This can be attributed to their low field strength (ionic potential = valence/ionic radius: <2) hence their mobility during hydrothermal alteration (Jenner, 1996). All Group I alkali metals appear to undergo some change, implying that they are readily substituted. K, Sr, Rb, and Cs readily substitute into crystal lattices of minerals by cation substitution and are enriched by hydrothermal processes (Staudigel and Hart, 1985; Teagle et al., 1996).

Table 3.6 summarises the chemical changes associated with each alteration style. Brown rocks exhibit the largest increases in P_2O_5 (+ 20 %), Pr (+ 27 %) and Th (+ 47 %) and large increases in Fe_2O_3, K_2O, LOI and C. Dark green/ dark grey rocks underwent the largest increase in Fe_2O_3 (+ 30 %), K_2O (> 400 %), Cr (+ 13 %), Co, (+ 20 %), Sr (+ 14 %) and Cs (+ 125 %). Dark green halos also exhibit some relatively large reductions in Al_2O_3 (- 6 %), and MgO (- 13 %). In both these halo types, the additional K and Fe reflect incorporation of celadonite and iron-oxyhydroxides. Dark green halos, in which celadonite is observed in greater abundance, have the greatest increase in K. Green rocks do not exhibit great increases in abundance, and there is effectively no change in Fe, reflecting the lack of iron oxyhydroxides that make up this alteration style. Complex halos represent overprinting, therefore we would expect the chemical changes to reflect all other alteration styles. Changes include decreased SiO_2,

MnO, MgO, S and increased Fe_2O_3, K_2O, P_2O_5, C, LOI, all trace elements, Ta, Th and U. Within grey background rocks, change is minimal. The relative lack of secondary minerals within grey rocks is consistent with the low levels of chemical change

	Grey bkd	Brown	Dk gy/gn	Green	Complex	breccia
SiO_2	(-)	(-)	(-)	(-)	(-)	+
TiO_2						
Al_2O_3						
$Fe_2O_3^T$		+	+	+	(+)	+
MnO		-			-	+
MgO		-	-		-	++
CaO					-	++
Na_2O						-
K_2O		+++	+++	+++	+++	+++
P_2O_5		+			+	++
C		+++	+++	+++	+++	++++
S		- -	- -	- -	--	- -
LOI	+++	++++	+++	+++	+++	+++
Co			+			+
Cr	+		+			-
Cu		-	-			-
Ga						
Ni		-	-		-	
Sc						
V						-
Zn			+			+
Rb	+	-	++	+	+	+++
Sr		+	+		+	+
Y				-		+
Zr		+			+	
Nb			+		+	
Cs	+		+++	-		++
Ba	+	+++	++	+++	++	
La					+	+
Ce					+	
Pr		+	+	+	+	+
Nd		+	+		+	+
Sm						+
Eu		+	+			+
Gd						+
Tb						+
Dy						+
Ho						+
Er						+
Tm						+
Yb						+
Lu						+
Hf		+	+	+	+	+
Ta				+	+	+
Pb	+	+	-	+		
Th		+	-		+	
U			-	-		+

Table 3.6. Summary table of the chemical changes associated with each alteration type, Including veins and whole breccia samples. (+,-) < 10% increase (applied to Fe and Si only) +,- = >10% change, ++, - - = > 50 % change, +++ = > 100 % change, ++++ = > 1000 % change.

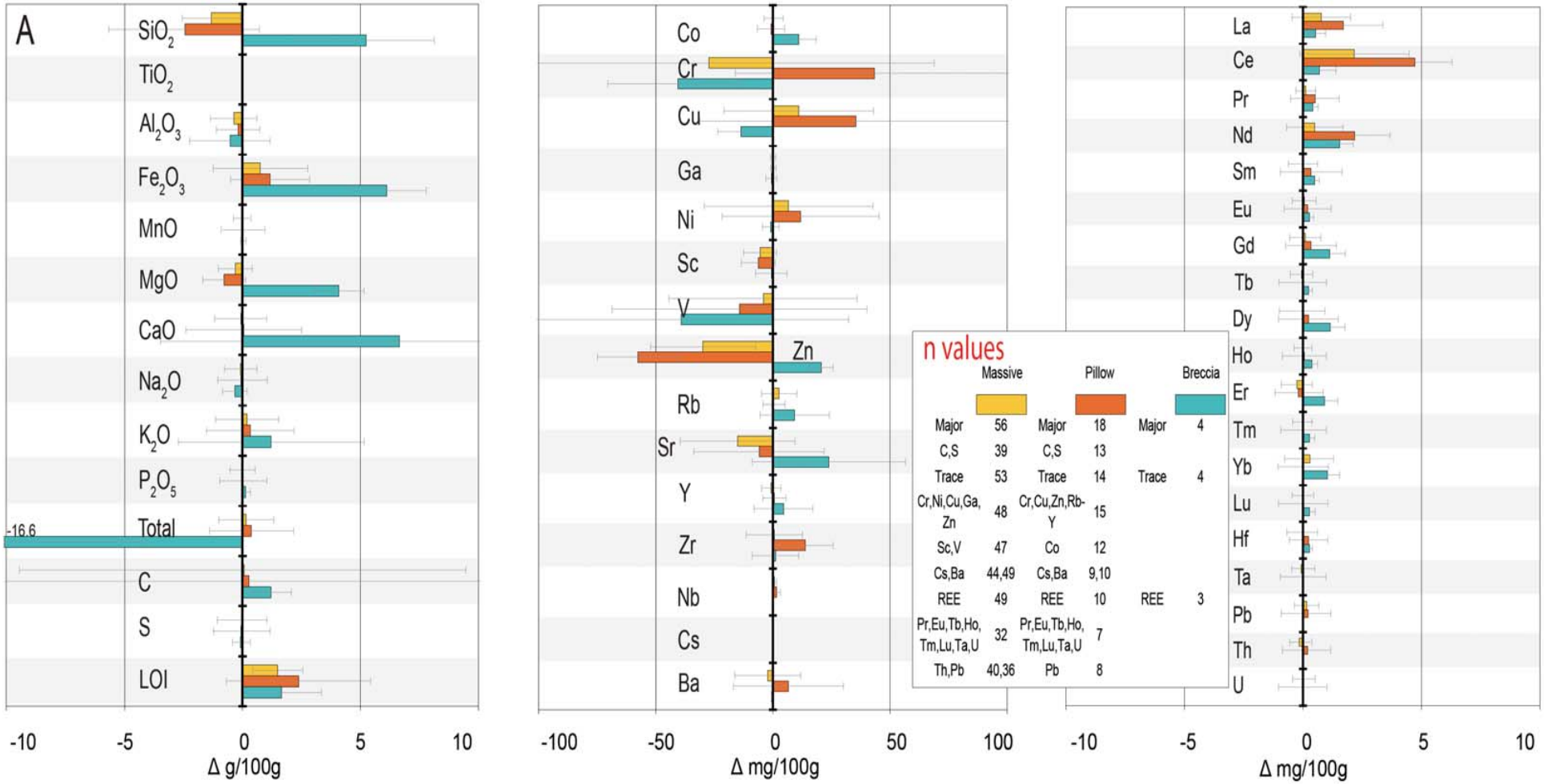

Figure 3.34. Absolute (A) and percentage (B) chemical changes from calculated sample by sample protoliths at Site 1179 sorted by lithology. A= absolute chemical change (g/100g and mg/100g) and B= % change. Bars indicate the propagated error including standard deviation of the range of changes within each lithology.

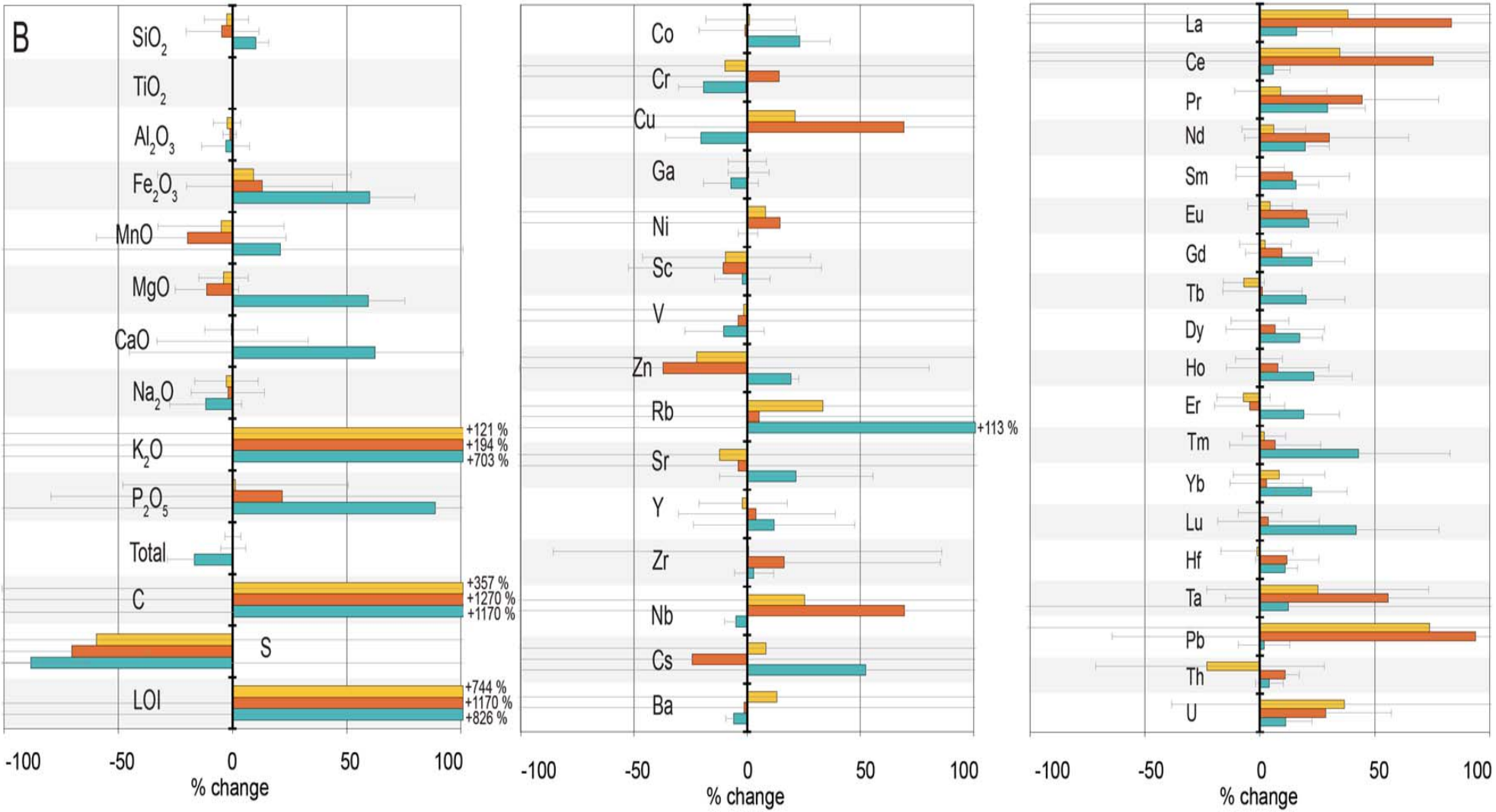
B
SiO2
TiO2
Al2O3
Fe2O3
MnO
MgO
CaO
Na2O
K2O
P2O5
Total
C
S
LOI
+121 %
+194 %
+703 %
+357 %
+1270 %
+1170 %
+744 %
+1170 %
+826 %
-100
-50
0
50
100
% change
Co
Cr
Cu
Ga
Ni
Sc
V
Zn
Rb
Sr
Y
Zr
Nb
Cs
Ba
+113 %
La
Ce
Pr
Nd
Sm
Eu
Gd
Tb
Dy
Ho
Er
Tm
Yb
Lu
Hf
Ta
Pb
Th
U

The greatest chemical changes are observed in the breccias. The replacement of groundmass by breccia matrices and alteration within clasts has resulted in large changes across the majority of elements, most notably SiO_2 (+ 10 %), Fe_2O_3 (+ 60 %), MgO (+60 %) CaO (+ 60 %), K_2O (+ >700 %), C (+ >5000 %), LOI (+ >800 %), and Rb (+ 100%). High CaO and C reflect the large amounts of observed carbonates. Additional Fe and K is likely to be sourced from iron-oxyhydroxides, celadonite and saponite respectively. High LOI and low Si reflect the increased water-rock interaction that has formed the breccias and the loss of primary phases during replacement by secondary minerals.

3.4.4.6 *Chemical change associated with lithology*

The chemical change associated with lithology is shown in Figure 3.34. Classification of each sample, based on work by Kanazawa et al., (2001), allows an assessment of potential chemical change associated with lithological variation to be made. Following the method outlined earlier, breccias are calculated as whole rocks.

	Massive flows	Pillow lavas	Whole breccia		Massive flows	Pillow lavas	Whole breccia
SiO_2	(-)	(-)	+	Y			+
TiO_2				Zr		+	
Al_2O_3				Nb	+	++	
$Fe_2O_3{}^T$		+	+	Cs		-	++
MnO		-	+	Ba	+		
MgO		-	++	La	+	++	+
CaO			++	Ce	+	++	
Na_2O			-	Pr		+	+
K_2O	+++	+++	+++	Nd		+	+
P_2O_5		+	++	Sm		+	+
C	+++	++++	++++	Eu		+	+
S	--	- -	- -	Gd			+
LOI	+++	++++	+++	Tb			+
				Dy			+
Co			+	Ho			+
Cr		+	-	Er			+
Cu	+	++	-	Tm			+
Ga				Yb			+
Ni				Lu			+
Sc		-		Hf		+	+
V			-	Ta	+	++	+
Zn	-		+	Pb	++	++	
Rb	+		+++	Th	++	+++	
Sr	-		+	U	+	+	+

Table 3.7. Summary table of the chemical changes associated with lithology at Site 1179. (+) = less than 10 % change (applies to SiO_2), + = >10 % change, ++ = >50 % change, +++ = >100 % change, ++++ = >1000 % change (vice versa for negative values).

When compared to pillow lavas and massive flows breccias almost always exhibit the greatest chemical changes. Pillow lavas exhibit the next greatest level of change followed by massive flows (see summary Table 3.7). Chill margins, interpillow sediments, and abundant fractures that are present in within the pillow lavas probably contribute to higher water/rock ratios, In addition, the increased space available to hydrothermal fluids allows for precipitation of secondary minerals. In contrast massive flows have relatively few chill margins and fractures, making them relatively impermeable and less susceptible to alteration. Given that the majority of Site 1179 is made up of massive units (See stratigraphy), alteration at Site 1179 is slight. However, because recovery may be biased towards more competent massive flows, and that breccias and pillows appear to be much more altered, alteration observed from recovered cores must represent a minimum value.

3.4.4.7 Summary

The chemical changes as a result of alteration broadly reflect the observed style and intensity of alteration at Site 1179. Measurement of chemical change both by calculating a protolith for each sample and by using a least altered host sample has shown that even the 'least altered' grey rocks have undergone alteration, which means chemical changes must be calculated from the protolith. Variation between the alteration styles is not easy to detect because there is significant overlap of different alteration styles. In addition, the variable intensity of alteration within each style further contributes to the high range of values for change observed within each style, igneous group and lithology. General trends include greater changes within breccias and pillow lavas, which is consistent with petrographic observations, and greater Fe and K in iron-oxyhydroxide (brown) and celadonite (dark green) rich halos respectively. Complex halos represent varying proportions of two or more alteration styles. This has imparted relatively high levels of change within the host rock at Site 1179.

Veins and breccia demonstrate very high levels of chemical change at Site 1179, therefore calculation of a whole Hole 1179 chemical change must include breccia and veins together with all the alteration styles observed at Site 1179. Figure 3.35 is a plot of chemical change for Site 1179. Figures are calculated from a weighted average of all alteration styles observed at Site 1179, including veins and breccias. Weightings are based on the proportion of core that is covered with a particular alteration style, and the proportion of veins and breccias within the recovered core.

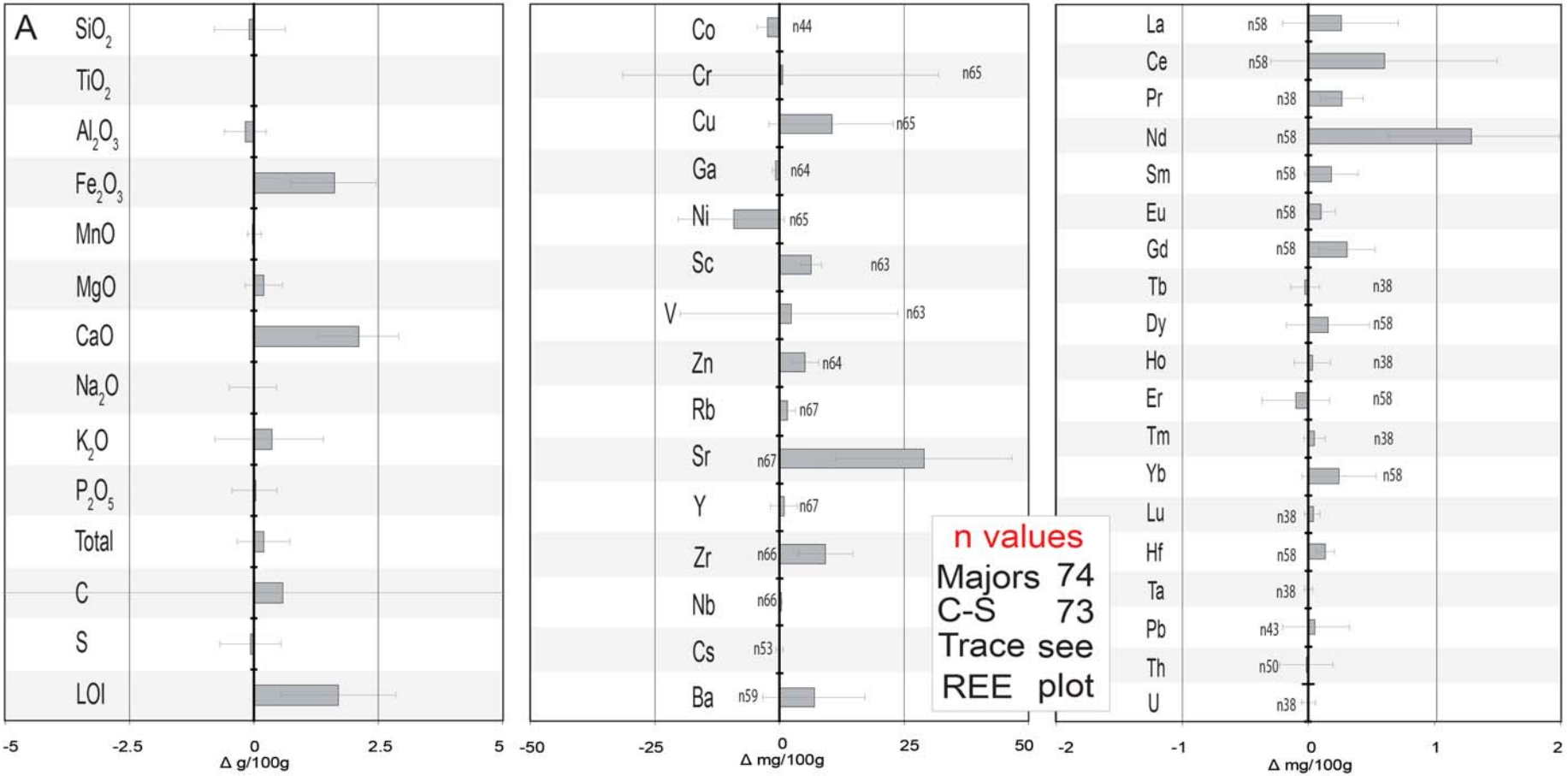

Figure 3.35. Chemical changes from calculated sample by sample protoliths at Site 1179. A= absolute chemical change (g/100g and mg/100g) and B= % change. Bars indicate the propagated error which includes the standard deviations of the range of changes observed within Site 1179 basement. Weighted averages are based on volume percentages of veins, breccias, grey background, dark green halos, green halos, brown halos and complex halos.

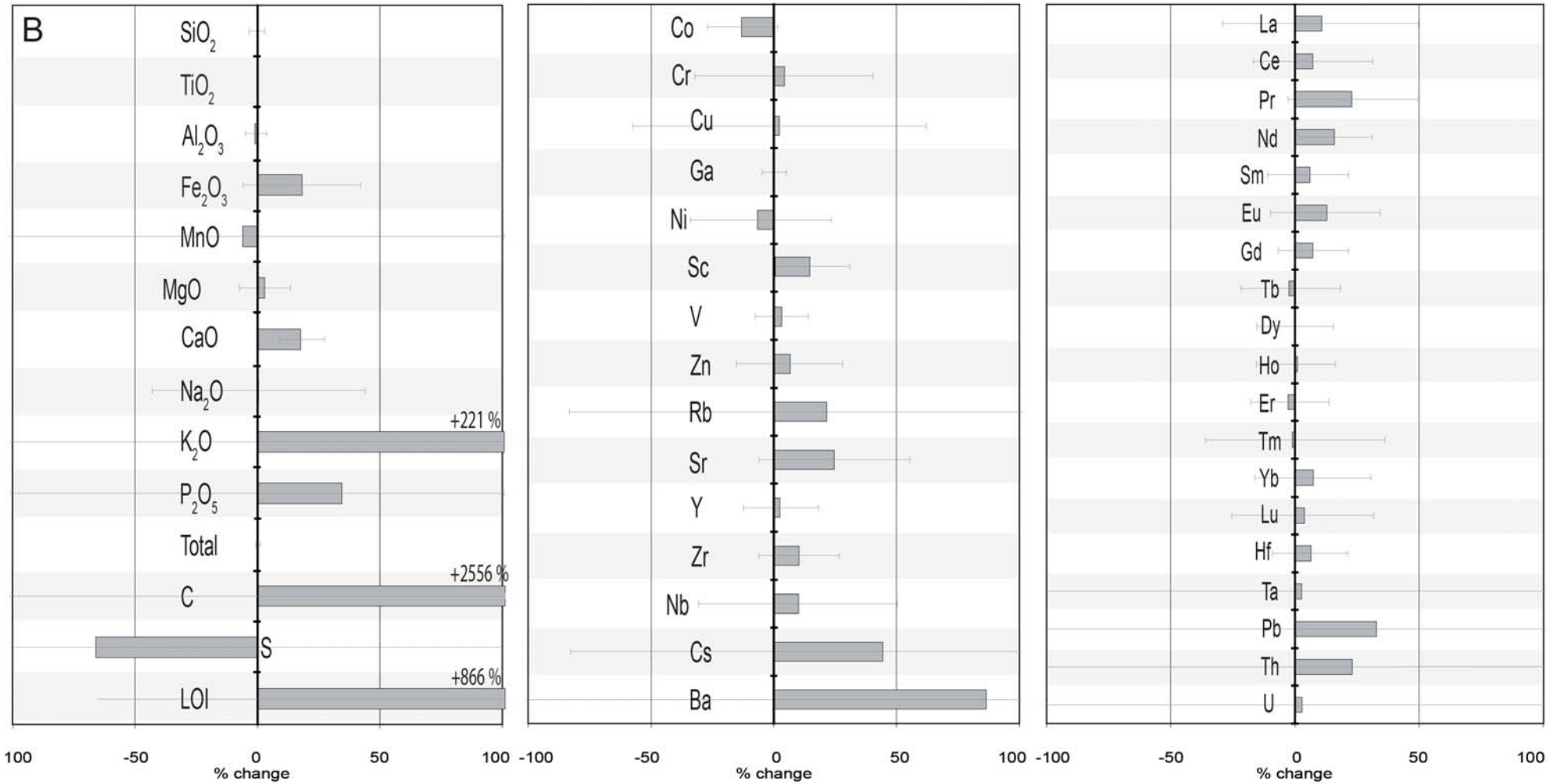
B
SiO2
TiO2
Al2O3
Fe2O3
MnO
MgO
CaO
Na2O
K2O
P2O5
Total
C
S
LOI
+221 %
+2556 %
+866 %
100
-50
0
50
100
% change
Co
Cr
Cu
Ga
Ni
Sc
V
Zn
Rb
Sr
Y
Zr
Nb
Cs
Ba
-100
-50
0
50
100
% change
La
Ce
Pr
Nd
Sm
Eu
Gd
Tb
Dy
Ho
Er
Tm
Yb
Lu
Hf
Ta
Pb
Th
U
-100
-50
0
50
100
% change

Element	Change %	Element	Change %	Element	Change %	Element	Change %
SiO_2		Sc		Ba	++	Yb	
TiO_2		V		La	+	Lu	
Al_2O_3		Cr	+	Cr		Hf	
Fe_2O_3	+	Co		Pr	+	Ta	
MnO		Ni		Nd	+	Pb	+
MgO		Cu	-	Sm		Th	++
CaO	+	Zn		Eu	+	U	+
Na_2O		Rb	+	Gd			
K_2O	+++	Sr	+	Tb			
P_2O_5	+	Y		Dy			
C	++++	Zr	+	Ho			
S	--	Nb	+	Ef			
LOI	+++	Cs	+	Tm			

Table 3.8. Summary of chemical change at Site 1179.+ = >10 % change, ++ = >50 % change, +++ = >100 % change, ++++ = >1000 % change (vice versa for negative values).

Chemical change at Site 1179 is low, with most elements exhibiting less than 25% change. Many elements demonstrate change of less than 10%, which is below the sensitivity (based on immobile elements discussed earlier) range, and therefore can be regarded as no change. High error, associated with the range of chemical changes within each sample, analytical error and errors in the selection of appropriate protoliths overwhelm the apparent changes for many elements in Figure 3.35. However, with the exception of V, Ni, Cr, Cu, Cs,Ta, Pb, Th, and U, error associated with selection of protolith compositions are relatively small compared to error associated with averaging large ranges of chemical change. Although change in all elements are shown in Table 3.8, one remains cautious of making any interpretations based on the changes associated with V, Ni, Cr, Cu, Cs, Ta, Pb, Th, and U because of the uncertain protolith compositions. Increases in Fe_2O_3, CaO, K_2O, C and LOI reflect the incorporation of iron-oxyhydroxides, carbonates, and celadonite.

The competence of the massive flows potentially makes them easier to recover during drilling, therefore it is likely that sampling is biased towards these rocks and that pillow lavas and breccias may be vastly underestimated. Chemical and petrographic evidence imply that pillow lavas and breccias at Site 1179 have undergone the most chemical change, therefore, until a comprehensive survey of lithostratigraphy is carried out for Site any estimate for chemical change at Site 1179 must represent a minimum value.

3.5. Whole Rock Isotopic Results

In this study 38 whole rock samples were measured for $^{87}Sr/^{86}Sr$ ratios and 25 for $\delta^{18}O$ (Table 3.9). A further 19 samples were measured for $^{87}Sr/^{86}Sr$ by Sano and Hayasaka, (2004). Whole rock samples have subsequently been age corrected to an initial value of 129 Ma, making the assumption that alteration occurred early in the history of the ocean crust, and they are plotted against depth in Figure 3.36. $^{87}Sr/^{86}Sr$ results range from 0.7023 to 0.7048 and are slightly to moderately elevated above the average value for Pacific MORB (0.7024-0.70256) (Saunders, et al., 1988). Variation with depth is slight, with only a small increase to more radiogenic $^{87}Sr/^{86}Sr$ ratios with depth. Strontium isotopic variation within different styles of alteration is slight with the most elevated $^{87}Sr/^{86}Sr$ ratios located in brown oxidation halos and grey basalt. In sample pairs where grey 'fresh' basalt is juxtaposed against a zone of more intense alteration the Sr isotopic ratio is elevated in the altered zone, reflecting increased seawater interaction during alteration.

The highest $^{87}Sr/^{86}Sr$ value measured was from a breccia sample (191-1179D 22R-2, 50-57 cm) with a value of 0.70483. This value indicates as much as ~ 45 % of the strontium is sourced from seawater. A low value of 0.702337 observed in a sample of slightly altered brown-grey basalt (191-1179D-11R-2, 37-43 cm) may reflect the primary $^{87}Sr/^{86}Sr$ for Site 1179 basalts, however, this value falls below the expected range for MORB basalts. In addition this sample has high Rb (35.4 ppm) which implies that considerable Rb enrichment took place after formation, enrichment of Rb may preclude accurate age correction. Following leaching experiments discussed in Chapter Two of this thesis, primary $^{87}Sr/^{86}Sr$ values range from 0.70252 to 0.70348. Two samples, including one acid washed sample, have values of 0.70250 (191-1179D-14R-1, 116-123 cm) and 0.70249 (191-1179D-13R3, 26-29 cm, acid washed) respectively. These values fall within the range expected for fresh MORB (Figure 3.34). Most samples at Site 1179 are elevated above the expected range for MORB. One possibility is that a component of Shatsky Rise mantle is present leading to elevated $^{87}Sr/^{86}Sr$ in Site 1179 basalts, as has been suggested by Sano and Hayasaka (2003). Figure 3.37 indicates most basalt samples plot over the Shatsky Rise field, however, these samples are not leached or acid washed therefore these samples alone can not be used deduce the primary Sr-isotopic composition of basement at Site 1179. Figure 3.37 also includes two acid washed whole rock basalts from Hole 1179.

Core	Set	Interval	Depth (mbsf)	Depth (msb)	Rock type	Gp	Unit	Alteration Style	[Sr] ppm	[Rb] ppm	$^{87}Sr/^{86}Sr$ (measured)	± 2SE	$^{87}Sr/^{86}Sr$ (initial)	$\delta^{18}O$ (VSMOW)
10	R-1	56-61	375.6	0.6	MF	I	1	Gy	154	22.2	0.703272	7	0.702376	8.8
10	R-1	56-61	375.6	0.6	MF	I	1	Gn Hlo			0.703392	8		9.5
10	R-1	82-89	375.8	0.8	MF	I	1	Gn Hlo						10.4
10	R-1	82-89	375.8	0.8	MF	I	1	Gy						9.9
11	R-1	44-50	377.4	2.4	MF	I	1	Gy						8.6
11	R-1	44-50	377.4	2.4	MF	I	1	Gy						8.5
11	R-1	86-88	378.0	3.0	Pillow	I	2	Gy	96	2.0	0.703300	12	0.703217*	
11	R-2	9-13	378.3	3.3	Pillow	I	2	Gy	96	20.0	0.703832	10	0.702744*	
11	R-2	37-43	378.6	3.6	Pillow	I	2	Gy	121	35.4	0.704165	11	0.702338	
11	R-2	84-86	379.3	4.3	Pillow	I	2	Gy	102	9.0	0.703379	11	0.702927*	
12	R-1	36-39	387.1	12.1	Pillow	I	2	Gy	100	9.1	0.703401	10	0.702921*	
12	R-2	61-69	388.0	13.0	Pillow	I	3	Gy						9.6
12	R-2	69-71	388.9	13.9	IS	I	3	Gy	86	12.0	0.703748	8	0.703008*	
12	R-2	143-149	389.7	14.7	Breccia	I	5	Gy	101	13.0	0.703586	11	0.702908*	
13	R-1	15-18	390.6	15.6	Pillow	I	7	Gy	125	5.0	0.703264	11	0.703054*	
12	R-3	89-92	390.6	15.6	MF	I	6	Gy	86	7.2	0.703719	12	0.703278*	
12	R-4	97-102	391.8	16.8	MF	I	6	Gy	85	3.5	0.703290	11	0.702922	
13	R-1	116-120	392.1	17.1	MF	I	8	Gy	101	7.8	0.703569	9	0.703162	
13	R-2	74-82	392.6	17.6	MF	I	8	Bn/dk Gy	110	21.6	0.703951	18	0.702727	7.9
13	R-2	74-82	392.6	17.6	MF	I	8	Gy	95	8.5	0.703290	9	0.703290	7.7
13	R-3	68-74	393.7	18.7	MF	I	8	Gy	68	19.6	0.704328	8	0.702539	
13	R-3	86-93	393.9	18.9	MF	I	8	Gy	156	16.1	0.704339	25	0.702821	
13	R-3	86-93	394.3	19.3	MF	I	8	Bn ph	131	30.4	0.704042	9	0.703397	8.8
13	R-4	83-85	395.6	20.6	MF	I	8	Gy	102	15.0	0.703643	9	0.702863*	8.6
14	R-1	18-20	396.6	21.6	MF	II	10	Gy	95	15.0	0.703467	10	0.702630*	
14	R-1	116-123	397.6	22.6	MF	II	10	Gy	122	18.6	0.703857	9	0.702503	8.4
14	R-1	116-123	397.6	22.6	MF	II	10	Bn/dk Gn	151	8.9	0.703452	9	0.703085	8.4
14	R-1	134-142	397.7	22.7	MF	II	10	Bn hlo	155	36.0	0.704087	9	0.702594	9.0
14	R-1	134-142	397.7	22.7	MF	II	10	Gy	153	16.5	0.704044	9	0.703408	8.5
14	R-2	0-6	397.9	22.9	MF	II	10	Bn/dk Gy	98	16.0	0.703134	10	0.702404	
14	R-2	0-6	397.9	22.9	MF	II	10	Gy	94	5.2	0.703422	10	0.702788	
14	R-2	16-24	399.2	24.2	MF	II	10	Gy						8.1
14	R-2	16-24	399.2	24.2	MF	II	10	Bn						8.6
14	R-2	63-65	398.5	23.5	MF	II	10	Gy	97	18.0	0.704035	8	0.703051*	
17	R-1	40-42	419.2	44.2	Pillow	II	14	Gy	150	16.0	0.703632	11	0.703066*	9.0
17	R-1	40-46	419.3	44.3	Pillow	II	14	Bn/dk Gy	233	25.0	0.703431	10	0.702971	9.2
17	R-1	111-113	419.9	44.9	MF	II	15	Gy	99	18.0	0.703804	10	0.702840*	
17	R-2	11.-13	420.2	45.2	MF	II	15	Gy	103	15.0	0.703692	8	0.702920*	
18	R-1	19-35	423.0	48.0	MF	II	19	Gy						8.0
18	R-1	19-35	423.0	48.0	MF	II	19	Bn						8.9
18	R-1	52-58	425.8	50.8	b reccia	II	19	Bn bgd	57	7.4	0.703989	8	0.703168	
18	R-2	10.-15	426.9	51.9	b reccia	II	19	Gy	141	2.9	0.704965	13	0.704835	7.8
18	R-2	10.-15	426.9	51.9	b reccia	II	19	matrix	79	61.2	0.708754	9	0.703930	19.7
18	R-3	17-23	428.5	53.5	MF	II	20	Gy						9.4
18	R-3	17-23	428.5	53.5	MF	II	20	Gy/gn/bn	110	3.8	0.703505	13	0.703279	9.4
18	R-4	87-90	430.3	55.3	MF	II	21	Gy	98	7.0	0.703229	8	0.702856*	
18	R-4	124-129	431.0	56.0	MF	II	21	Gy	53	10.3	0.703830	10	0.702607	
18	R-3	102-108	438.9	63.9	MF	II	24	Gy	77	1.0	0.703192	8	0.703108	
19	R-3	102-108	438.9	63.9	MF	II	24	Bn	58	1.8	0.704127	9	0.703936	
20	R-1	60-67	445.2	70.2	Pillow	III	25	Bn bgd	112	6.9	0.703450	7	0.703062	
20	R-1	100-105	445.6	70.6	Pillow	III	25	Bn bgd	120	9.9	0.703639	11	0.703122	8.7
20	R-1	100-105	445.6	70.6	Pillow	III	25	Gy	176	0.8	0.704170	8	0.703491	10.1
20	R-2	12.-20	446.2	71.2	MF	III	26	Gy						8.3
20	R-2	12.-20	446.2	71.2	MF	III	26	Bn hlo	237	4.5	0.703948	8	0.703906	8.4
20	R-3	13.-18	447.3	72.3	MF	III	29	Gy	96	11.6	0.703876	9	0.703119	
20	R-3	64-67	447.5	72.5	MF	III	29	Gy	164	5.0	0.702955	8	0.702790*	
20	R-3	128-132	448.9	73.9	MF	III	30	Gy/Bn mot	92	3.1	0.703581	10	0.703372	
21	R-2	61-69	456.3	81.3	Pillow	III	37							8.0
21	R-2	61-69	456.3	81.3	Pillow	III	37	Gy/bn ph	238	12.9	0.703425	9	0.703087	9.0
21	R-4	33-38	459.6	84.6	MF	III	41	Bn mott	117	8.3	0.703404	8	0.702962	
22	R-1	42-48	464.2	89.2	Pillow	III	44	Bn mott	108	4.1	0.703268	10	0.703031	
22	R-2	50-57	465.8	90.8	MF	III	45	Gy/Bn Hlo	233	14.0	0.704180	8	0.703807	15.2
22	R-2	50-57	465.8	90.8	Pillow	III	44	Bn mott	296	11.3	0.703236	8	0.703026	8.7
22	R-3	34-40	466.8	91.8	Pillow	III	44	Bn mott	119	5.4	0.703370	8	0.703086	
22	R-4	72-75	468.8	93.8	MF	III	45	Gy	181	2.0	0.702885	11	0.702813*	
22	R-4	120-123	469.3	94.3	Pillow	III	46	Gy	165	11.0	0.703411	9	0.703058*	
22	R-5	64-71	470.4	95.4	MF	III	47	Bn hlo	254	7.7	0.703495	8	0.703307	9.2
22	R-5	64-71	470.4	95.4	MF	III	47	Gy	243	4.4	0.703151	8	0.703006	8.8
22	R-5	128-134	471.1	96.1	MF	III	47	Bn/Gy+CO3	129	7.6	0.703386	10	0.703019	
Acid washed samples (Mahoney et al., 2005)														
13	R-3	26-29	393.1	18.1	MF	I	8	Gy	94	11.5	0.703140	18	0.702490	
22	R-5	80.83	470.6	95.6	MF	III	47	Gy	118	2.1	0.702860	18	0.702760[1]	
Leached Samples														
12	R-4	97-102	391.8	16.8	MF	I	6	Leached	56	0.7	0.702598	11	0.702521	
18	R-2	10-15	426.9	51.9	Breccia	II	19	Leached	51	39.0	0.705786	10	0.700997	
20	R-1	100-105	445.6	70.6	Pillow	III	25	Leached	71	2.9	0.702744	14	0.702486	

Table 3.9. (previous page) Measured and initial strontium isotopic ratios for whole rock basalts in ODP Hole 1179D. Initial Sr-isotopic ratios are calculated assuming early alteration at Site 1179 i.e. ~129 Ma. Data with * suffix refers to analyses carried out by Sano and Hayasaka, (2004). Whole rock $\delta^{18}O_{(VSMOW)}$ are also included. Acid washed samples analyzed by Mahoney (2005). Leached samples following aggressive multi-step acid leeching method by Mahoney, (1987) and Mahoney et al., (1983). Gy (Grey background), Bn (Brown), Gn (Green), ph (Patch), hlo (Halo), dk (Dark), bgd (Background), mot (mottled). MF= massive flow, IS = interpillow sediment.

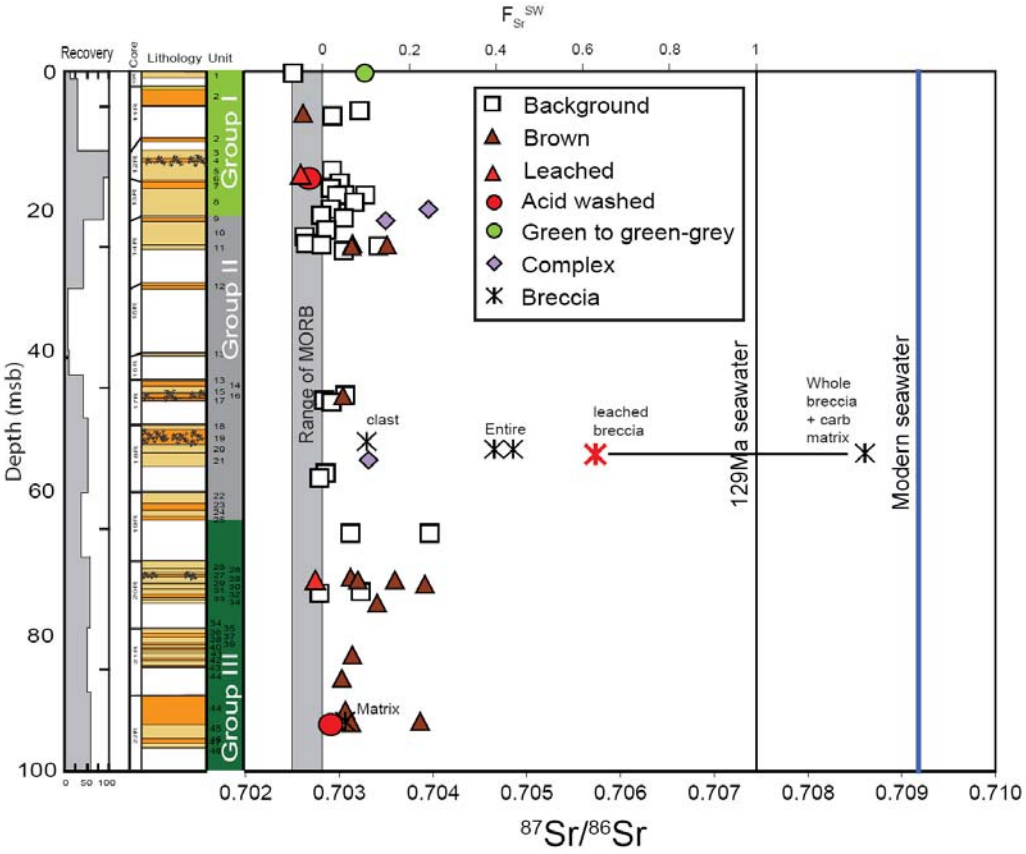

Figure 3.36. Initial $^{87}Sr/^{86}Sr$ of whole rocks vs. depth in Hole 1179D. Alteration styles are shown. (2003), red circles indicate samples that have been acid washed before analysis (Mahoney et al., 2005). Range for fresh MORB (0.70240-0.70256) is given (Saunders, et al., 1988). The Sr-isotopic composition of modern seawater and seawater at 129 Ma is derived from McArthur et al, (2001). F_{sr}^{SW} indicates the seawater Sr component within the basalts based on Bach and Humphris, (1999) where 1 = 100% seawater Sr and 0 = no seawater Sr.

The effect of acid washing has been to remove ferromanganese phases and any organic material that may effect the strontium isotopic measurement (Mahoney et al., 2005). These samples have much lower $^{87}Sr/^{86}Sr$ ratios than the unwashed samples and they plot firmly in the EPR/Mesozoic MORB fields. In addition, leached basalts from Site 1179 (0.70249 – 0.70252 ± 19) in this study (see Chapter 2) indicate primary $^{87}Sr/^{86}Sr$ within the range for MORB which suggests that hydrothermal alteration precipitating

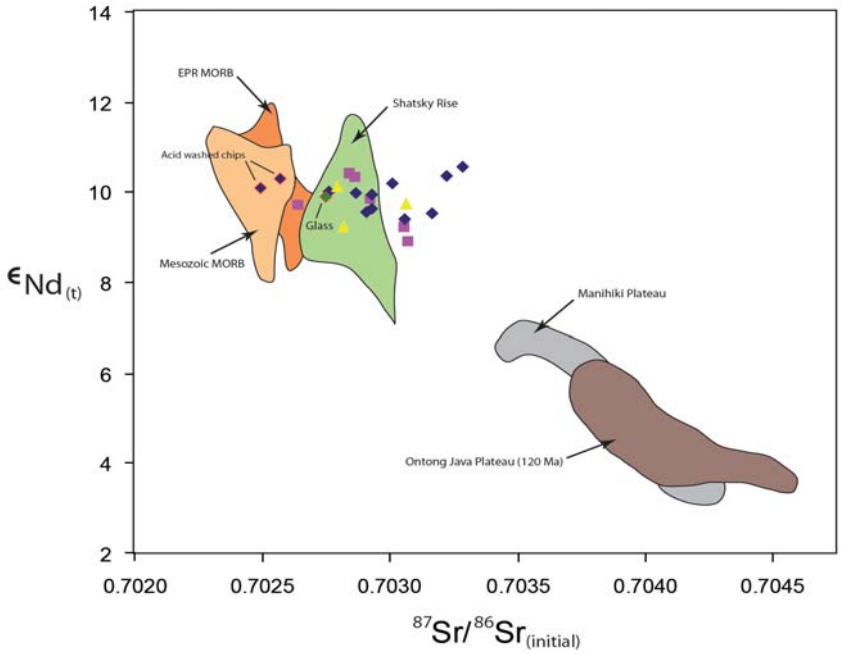

Figure 3.37. Strontium isotopic ratio vs. $^{\epsilon}Nd_{(t)}$ of whole rock samples from Site 1179. Blue diamonds (Group I), Squares (Group II), triangles (Group III) (after Sano and Hayasaka, 2003). Blue diamonds with red margins are acid washed (Mahoney et al., 2005). Data sources for MORB and basalts from oceanic plateaus of OJP and Manihiki sourced from Tejada et al, (1996); Tejada et al. (2002), and Mahoney and Spencer, (1991) for Ontong Java; Mahoney and Spencer (1991) for Manihiki; Janey and Castillo, (1997) for Mesozoic MORB; and Castillo et al., (2000) for EPR MORBs.

secondary minerals is the main mechanism for altering the strontium isotopic ratios at Site 1179. Figure 3.36 indicates an estimate of seawater Sr component (F_{Sr}^{SW}) based on Bach and Humphris (1999) expression:

$$F_{Sr}^{SW} = \left({}^{87}Sr/{}^{86}Sr_{WR} - {}^{87}Sr/{}^{86}Sr_{protolith}\right)/\left({}^{87}Sr/{}^{86}Sr_{SW} - {}^{87}Sr/{}^{86}Sr_{protolith}\right)$$

In the case of Site 1179, the protolith is the average of all leached samples (0.702499 ± 18) and seawater is set at 129 Ma seawater (0.70745) after McArthur (2001). Figure 3.38 is a histogram of F_{Sr}^{SW} for all Site 1179 whole rocks and each alteration style. The weighted value for Site 1179 is 0.13 (13% seawater) based on weighted average $^{87}Sr/^{86}Sr$ for each alteration style and the proportion of recovered core that exhibits each style of alteration. Grey background predictably incorporates the least seawater (0.05, 5% seawater). Dark green (0.075, 7.5% seawater) is the next least altered. Brown

incorporates ~10% seawater Sr and complex halos and breccias are highly variable and these range from 2% seawater to 30% seawater and 7% to 47% seawater respectively. Complex halos and breccias are highly variable, and given the variation in alteration style and intensity the degree of substitution between seawater and basaltic Sr is also likely to vary.

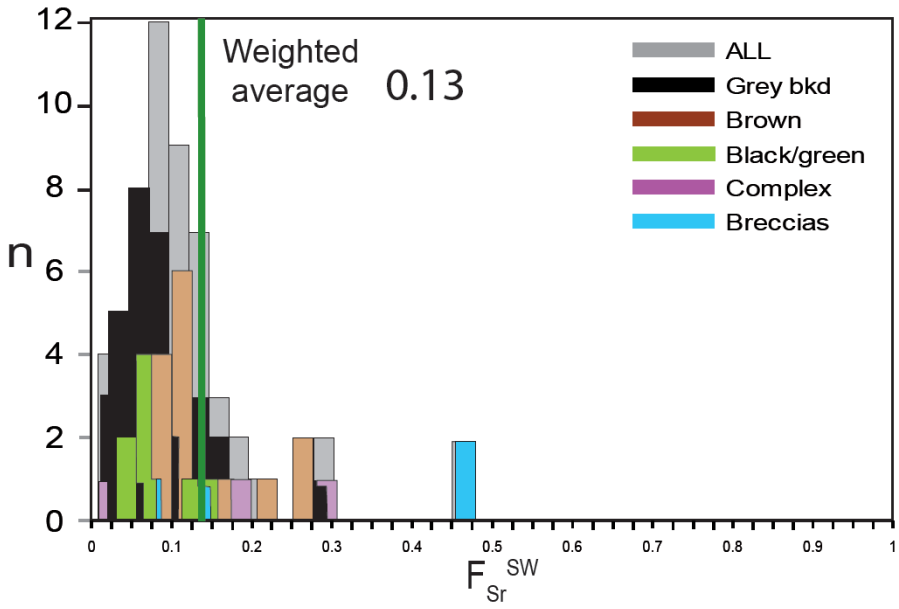

Figure 3.38. F_{Sr}^{SW} for Site 1179 basalts based on Bach and Humphris (1999) calculation for seawater Sr component. Each alteration style is included together with all samples and an average weighted value for Site 1179. Histogram bins = 0.025. One breccia exhibits an F_{Sr}^{SW} of 1.25, above seawater at 129 Ma.

Variations in the $\delta^{18}O$ of oxygen of volcanic basement rocks within the ocean crust are the result of either oxygen isotopic exchange between the hydrothermal fluid and primary minerals, or the dissolution and reprecipitation of secondary minerals. O-isotopic exchange depends on fractionation during precipitation of each secondary mineral present and temperature therefore the whole rock O-isotopic composition of Site 1179 basement can be used to assess the style and intensity of alteration and the conditions to which alteration took place. Recent work indicates that fresh MORB ranges from, 5.37 to 5.91 $‰_{(VSMOW)}$ (Garcia et al., 2008; Cooper et al., 2004; Eiler et al., 2000). Elevated $\delta^{18}O$ in as a result of low temperature alteration of extrusive lava sequences has been observed in a number of locations, including the McQaurie island ophiolite (Coggon, 2006), Site 504 (Alt et al., 1986), and the Troodos ophiolite (Spooner et al., 1974). At these sites values range from 5.8 to 13 $‰_{(VSMOW)}$ (Coggon, 2006; Alt et al., 1986; Cocker et al., 1982; Spooner et al., 1974) many of which are well

above the fresh MORB $\delta^{18}O_{(VSMOW)}$ discussed earlier. Taylor (1974) recognised that oxygen isotopic fractionation during the precipitation of clay and carbonate minerals increases the $\delta^{18}O$ of rock. The abundance of carbonate and clay minerals within rocks recovered from the upper oceanic crust at Site 1179 should, therefore, be translated into elevated $\delta^{18}O$.

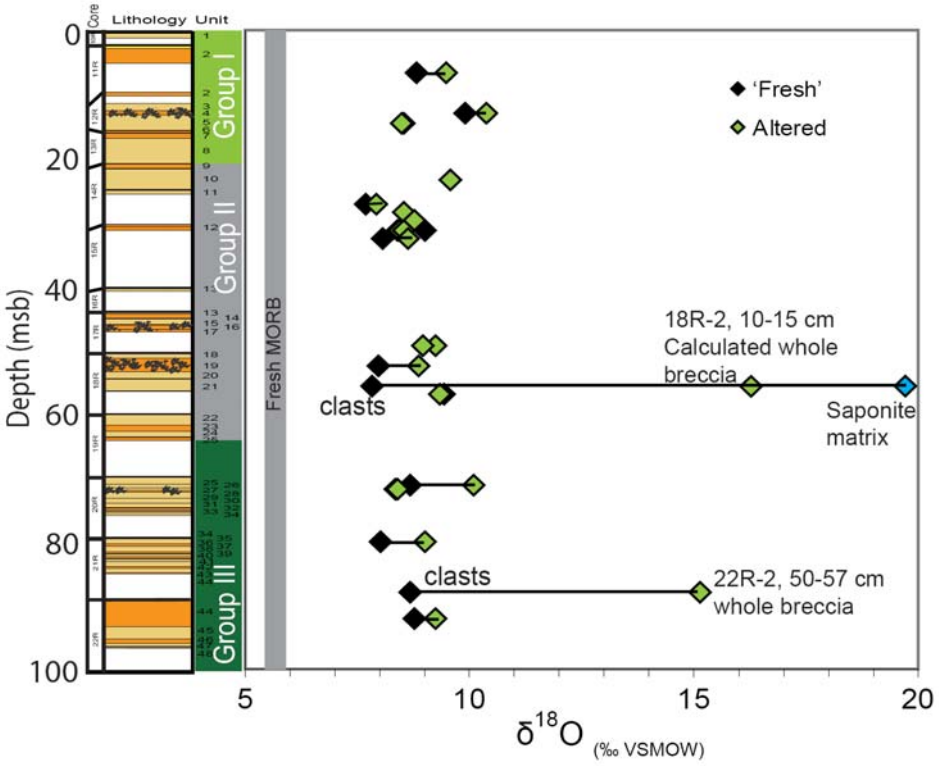

Figure 3.39. $\delta^{18}O$ vs. depth for Site 1179 whole rock samples. Fresh and altered sample pairs are indicated with tie lines. Samples 191-1179D-18R-2, 10-15 cm and 22R-2, 50-57 cm highlight the difference between matrix, whole breccias and clasts. Whole breccia for Sample 191-1179D, 18R-2, 10-15 cm was calculated by mass balance on observation of 70% matrix and 30% clasts. Fresh MORB range from Garcia et al, (2008), Cooper et al, (2004), and Eiler et al, (2000).

Whole rock $\delta^{18}O$ at Site 1179 ranges from 7.7 to 19.7 $‰_{(VSMOW)}$ with an average value of 9.3 ‰ (n=35). Only two Samples (191-1179D-18R-2, 10-15 cm and 22R-2, 50-57, cm) have values above 11 ‰. both of which are breccias composed of basaltic clasts with a matrix of carbonate. On a plot of $\delta^{18}O$ vs. depth for Site 1179 altered whole rock samples (Figure 3.39) exhibit elevated $\delta^{18}O$ relative to their least altered counterparts and they are elevated compared to the expected value for fresh MORB (5.8-6.0 ‰, Cocker et al., 1982). Because carbonate $\delta^{18}O$ is elevated (20-30 $‰_{(VSMOW)}$) compared to seawater (0 $‰_{(VSMOW)}$) and there are abundant secondary minerals present in Site 1179 whole rock samples, elevated $\delta^{18}O$ is expected. No trend with depth is observed. All whole rock samples at Site 1179 are enriched compared to fresh basalt (Figure 3.39)

due to the replacement of mesostasis, olivine, plagioclase and clinopyroxene with saponite, iron-oxyhydroxides, calcite and zeolite. Elevated $\delta^{18}O$ in background samples (Figure 3.37) indicate that all rocks at Site 1179 are altered. As a result of their high carbonate content, both breccia matrix samples measured in Figure 3.39 have strongly enriched ^{18}O

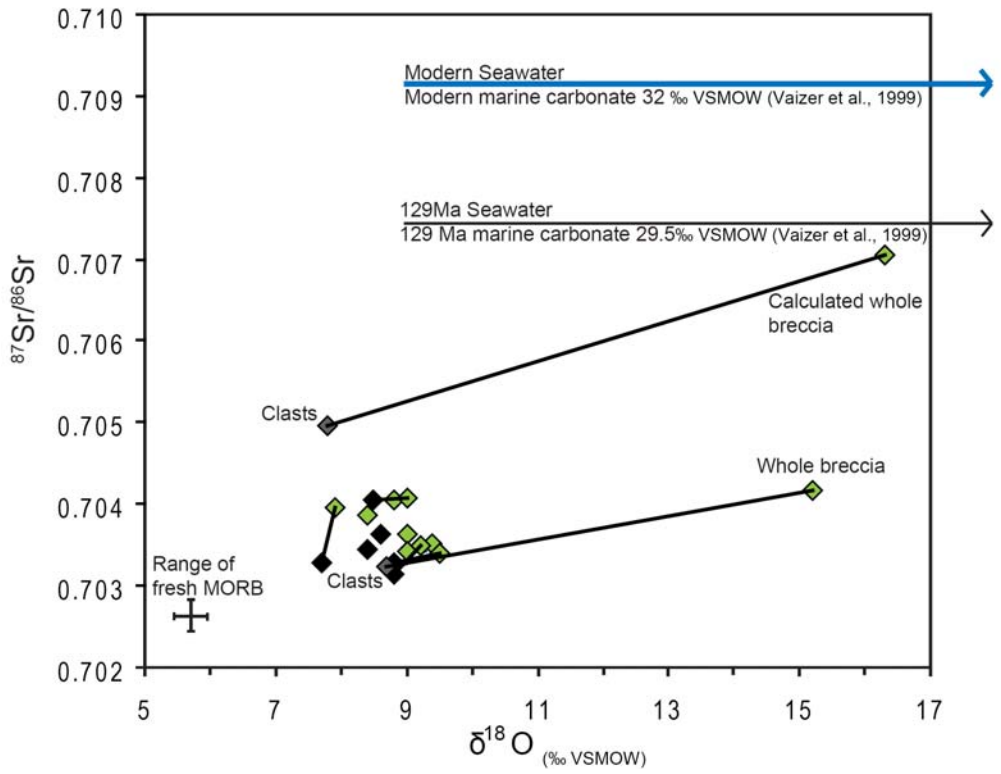

Figure 3.40. $\delta^{18}O$ vs. $^{87}Sr/^{86}Sr$ for Site 1179 whole rock samples. Sample pairs are drawn with tie lines. Green = altered, Black/Grey = least altered and clasts respectively. The range of fresh MORB is based on Garcia et al, (2008), Cooper et al, (2004), and Eiler et al, (2000) for carbonates, and Saunders et al, (1988) for $^{87}Sr/^{86}Sr$. Seawater $\delta^{18}O$ and $^{87}Sr/^{86}Sr$ are from Vazier et al, (1999) and McArthur et al, (2001) respectively.

Figure 3.40 shows whole rock $\delta^{18}O$ vs. $^{87}Sr/^{86}Sr$ for Site 1179 whole rock samples. In all sample pairs the Sr-isotopic ratio increases with $\delta^{18}O$ moving away from the range of $\delta^{18}O$ and $^{87}Sr/^{86}Sr$ associated with pristine MORB as shown in Figure 3.40. Breccias indicate the most dramatic changes. The concomitant increase in $^{87}Sr/^{86}Sr$ with $\delta^{18}O$ further highlights the affect of alteration at Site 1179 basement.

3.6. Carbonate mineral separates

Calcite veins were sampled throughout ODP Hole 1179D and analysed for O, C, and Sr isotopic compositions and trace element concentrations. Comparisons of carbonate isotopic data from basement penetrations provide insights into the timing and controls of hydrothermal alteration in shallow, low temperature regimes. This study indicates that estimates made with regards to the timing of alteration are greatly influenced by the nature and extent of interaction with the basement, which in turn appears to be influenced by the extent of sedimentation.

Variation in the calculated temperatures, strontium isotopic data and petrographic relationships from carbonate veins are indicative of continued hydrothermal activity at Site 1179. In addition insights into the uptake of CO_2 into the ocean crust are made through Site 1179 carbonates.

3.6.1 Results

Table 3.10 shows the carbonate isotopic data for Site 1179. Isotopic data for ODP Hole 1179D are compared with $\delta^{18}O$, $\delta^{13}C$ and $^{87}Sr/^{86}Sr$ analyses from other basement sites (Figure 3.41). $\delta^{13}C$ ranges from -0.11 to 2.4 ‰ ± 0.1 (VPDB) with an average $\delta^{13}C$ of 1.9 and there is a general trend towards higher values with depth Site 1179. These are typical values for precipitation of carbonate from seawater (Teagle et al., 1996) and they are broadly similar to $\delta^{13}C$ of carbonates in other basaltic sites (Figure 3.41).

		1179D	1179D	1179D	1179D	1179D	1179D	1179D	1179D	1179D	1179D
Expedition, hole, core, section, interval (cm)		11 01W 44-50	11 02W 37-43	12 R2 81-88	12 03W 56-63	13 02W 74-82	13 04W 5./16	14 01W 134-142	14 R2 0-6	14 R3 59-64	14 R3 59-64
Depth	(mbsf)	378	379	389	390	393	394	398	398	402	402
Depth	(msb)	2	3	14	15	17	19	22	23	27	27
Unit		2	2	4	6	8	8	10	10	11	11
Host rock		Pillow	Pillow	Massive Flow	Massive Flow	Massive Flow	Massive Flow	Massive Flow	Massive Flow	Massive Flow	Massive Flow
$^{87}Sr/^{86}Sr$	(measured)	0.707259	0.707483		0.707485	0.707476	0.707439	0.707421		0.707501	0.707473
Error	2σ	10	9		9	8	9	9		19	9
$^{87}Sr/^{86}Sr$	(initial)	0.707256	0.707483		0.707483	0.707473	0.707414	0.707106			
$\delta^{13}C$	(SMOW)	2.0	2.0	2.1	1.9	2.1	2.0		2.2	2.0	2.3
$\delta^{18}O$	(SMOW)	28.4	31.3	31.1	31.3	30.9	30.0		30.6	28.7	29.9
	$T^{O}C$	25	12	13	12	14	18		15	24	18
Sr/Ca	(mmol/mol)	0.03	0.17		0.16	0.14	0.09	0.14		0.13	0.13
Mg	(ppm)	480	5793		5762	4945	4050	15004		3731	4443
Mn	(ppm)	2894	137		71	1017	1973	2551		2596	1171
Fe	(ppm)	341	306		262	141	827	11023		253	151
Rb	(ppm)	0.02	0.02		0.04	0.14	0.51	6.66			
Sr	(ppm)	37	272		103	230	107	112		112	112
Y	(ppm)	41.0	3.3		1.6	2.6	22.4	10.7			
Zr	(ppm)	0.06	0.53		0.13	0.64	0.52	0.94			
Nb	(ppb)	4.84	3.40		-0.50	10.8	2115	1.47			
Cs	(ppb)	0.63	0.32		0.48	0.84	527	79			
Ba	(ppm)	0.21	0.60		0.18	0.39	11.64	1.55			
La	(ppm)	5.38	0.60		0.41	0.30	0.87	1.73			
Ce	(ppm)	4.96	0.07		0.23	0.17	0.73	1.61			
Pr	(ppm)	4.56	0.31		0.30	0.19	0.89	2.06			
Nd	(ppm)	5.18	0.31		0.28	0.20	1.01	2.27			
Sm	(ppm)	5.46	0.26		0.24	0.20	1.11	2.34			
Eu	(ppm)	4.72	0.23		0.20	0.16	0.92	1.62			
Gd	(ppm)	7.30	0.36		0.25	0.24	1.59	2.56			
Tb	(ppm)	8.09	0.37		0.25	0.26	1.60	2.78			
Dy	(ppm)	8.78	0.48		0.26	0.30	1.57	2.91			
Ho	(ppm)	9.47	0.61		0.32	0.35	1.67	3.02			
Er	(ppm)	9.08	0.78		0.31	0.37	1.58	3.05			
Tm	(ppm)	7.52	0.98		0.35	0.40	1.53	3.17			
Yb	(ppm)	5.34	1.08		0.38	0.39	1.37	3.03			
Lu	(ppm)	4.47	1.38		0.39	0.49	1.60	3.21			
Hf	(ppb)	11.3	2.3		1.5	1.0	1505.7	21.5			
Ta	(ppb)	140	48		5	436	168	42			
Pb	(ppb)	59	31		20	39	296	337			
Th	(ppb)	0.0	0.7		2.0	2.0	141.1	13.5			
U	(ppb)	2	33		8	27	207	31			

Table 3.10. Analyses of Strontium, Carbon, and Oxygen isotopic compositions and Major element, Trace element and REE concentrations for ODP Hole 1179D vein carbonate mineral separates. Calculated temperatures assume equilibrium with seawater where $\delta^{18}O = 0$ (Craig, 1967). Initial Sr values are shown based on 129 Ma seawater.

		1179D	1179D	1179D	1179D	1179D	1179D	1179D	1179D	1179D	1179D
Expedition, hole, core, section, interval (cm)		18 01W 52-58	18 04W 124-129	19 02W 68-72	20 R2 12.-20	21 03W 65-71	21 04W 33-38	22 R1 42-48	22 01W 95-101	22 02W 50-57	22 03W 34-40
Depth	(mbsf)	426	431	436	446	459	460	464.2	465	466	466
Depth	(msb)	50	56	60	71	83	84	89	90	90	91
Unit		19	21	23	26	39	41	44	44	45	44
Host rock		Breccia	Massive Flow	Pillow	Massive Flow	Pillow	Massive Flow	Pillow	Pillow	Massive Flow	Pillow
$^{87}Sr/^{86}Sr$	(measured)	0.707137	0.707477	0.707515		0.707933	0.707527	0.707467	0.707491	0.707481	0.707480
Error	2σ	17	10	9		16	10		8	13	9
$^{87}Sr/^{86}Sr$	(initial)	0.707135	0.707469	0.707513		0.707780	0.707526		0.707478	0.707480	0.707479
$\delta^{13}C$	(SMOW)	2.4		2.4	1.1	1.6	2.2	1.9	2.3	2.2	2.3
$\delta^{18}O$	(SMOW)	26.5		30.7	30.4	28.3	30.1	25.6	30.6	30.0	30.2
	$T^{O}C$	34		15	16	26	17	40	15	18	17
Sr/Ca	(mmol/mol)	0.04	0.17	0.17		0.12	0.17		0.17	0.16	0.16
Mg	(ppm)	543	5095	6489		4914	6277		6375	5891	6049
Mn	(ppm)	3724	1111	227		1508	308		39	987	137
Fe	(ppm)	403	618	16984		559	196		216	139	555
Rb	(ppm)	0.02	0.25	0.12		3.26	0.05		0.67	0.03	0.01
Sr	(ppm)	56	162	266		113	223		146	140	138
Y	(ppm)	9.3	3.5	12.0		9.3	5.6		18.5	0.0	4.4
Zr	(ppm)	0.22	0.40	0.33		0.22	0.37		0.57	0.00	0.13
Nb	(ppb)	1.62	8.18	2.17		1.62	3.24		2.73		-0.63
Cs	(ppb)	0.60	2.69	0.96		0.60	0.74		2.04		0.53
Ba	(ppm)	0.49	0.47	1.99		0.49	0.98		13.25	0.00	0.12
La	(ppm)	2.78	0.48	1.88		15.93	1.52		5.50	4.88	1.60
Ce	(ppm)	3.64	0.17	1.87		11.88	0.14		1.09	0.86	0.39
Pr	(ppm)	3.45	0.33	2.52		13.96	0.97		3.36	2.41	0.92
Nd	(ppm)	3.67	0.37	2.82		12.89	0.97		3.15	2.20	0.87
Sm	(ppm)	3.18	0.36	3.09		10.28	0.78		2.40	1.48	0.60
Eu	(ppm)	2.70	0.29	2.98		9.86	0.69		2.21	1.15	0.52
Gd	(ppm)	3.20	0.47	3.29		10.42	0.91		2.53	1.50	0.67
Tb	(ppm)	2.99	0.57	3.26		9.73	0.82		2.49	1.48	0.65
Dy	(ppm)	2.67	0.61	3.32		9.51	0.91		2.66	1.48	0.66
Ho	(ppm)	2.59	0.79	3.40		9.74	1.10		3.10	1.75	0.79
Er	(ppm)	2.34	0.93	3.41		9.95	1.22		3.34	1.97	0.87
Tm	(ppm)	2.19	1.06	3.44		10.13	1.33		3.51	2.08	0.94
Yb	(ppm)	1.84	1.22	3.37		9.96	1.37		3.50	2.26	1.03
Lu	(ppm)	1.68	1.43	3.49		10.34	1.52		3.93	2.37	1.10
Hf	(ppb)	2.5	3.7	6.2		2.5	2.5		6.0		1.0
Ta	(ppb)	126	3	4		126	14		3		18
Pb	(ppb)	26	335	45		26	54		29		13
Th	(ppb)	2.0	7.8	1.7		2.0	1.8		0.6		0.4
U	(ppb)	17	23	37		17	29		27		10

Table 3.10 Continued ...

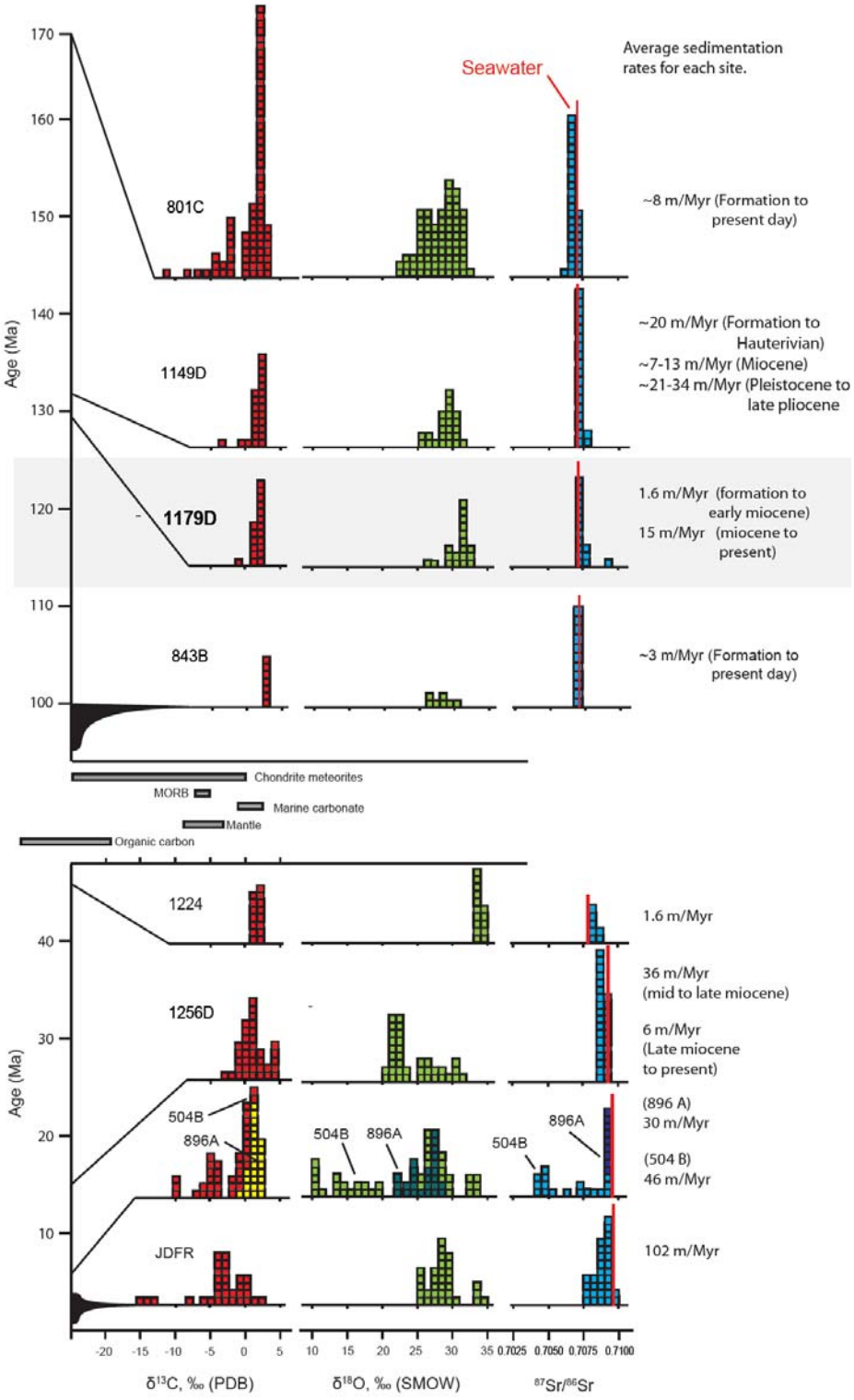

Figure 3.41. Isotopic frequency and variation at various sites in Pacific Ocean crust. $\delta^{13}C$, $\delta^{18}O$ and $^{87}Sr/^{86}Sr$ is shown together with age of ocean crust formation and the seawater strontium isotopic composition at the time of formation. Sedimentary rates are included. JDFR after Coggon et al., (2004); DSDP and ODP Hole 504B (Teagle pers comm, 2007); 896 data from Teagle, et al., (1996); ODP Hole 1256D, (Coggon, et al 2006); Site 1224, (Paul et al., 2006); ODP Hole 801C, (Alt, 2003). Sites 843 and 1149 carbonate data are from this study.

$\delta^{13}C$ for MORB is negative (0 to -2.5), and $\delta^{13}C$ of marine carbonate from sediment ranges from -6 to +6 (Land, 1980) and seawater $\delta^{13}C$ ranges from -0.8 to +2.2 (Kroopnick, 1985) therefore the range for carbonate veins at Site 1179 (-0.11 to 2,4 ‰) imply that $\delta^{13}C$ underwent little of no fractionation during precipitation of carbonate from HCO_3^- in seawater. The $\delta^{13}C$ of seawater at 129 Ma is ~1.5 ‰ (Veizer et al., 1999). Most samples at Site 1179 have $\delta^{13}C$ values above ancient seawater ~2 ‰, which suggests that a large majority of the carbonates must have formed after formation of Site 1179 basement. Sites in which samples of carbonate were recovered from deep penetrations, for example ODP Holes 801C, 504B and 896A exhibit $\delta^{13}C$ values that closely resemble MORB compositions (0 to -2.5) and mantle compositions (~2 to -4) (Figure 3.40). Recovery of basalt from deep penetrations has allowed sampling of carbonate that has precipitated from a potentially more evolved, warmer fluid that has undergone greater interaction with basement rocks, therefore carbonates from deep in the crust are likely to have a large component of MORB carbon (Alt et al., 1996). Sites with low sedimentation rates, or extended periods of low sedimentation (i.e. 1224, 843, 1179, and 1149) have relatively high $\delta^{13}C$ that closely resembles marine carbonate. This suggests that low sedimentation facilitated access of cold seawater into basement, and that the carbonates precipitated from seawater. Carbonate $\delta^{18}O$ values range from 25.5 to 31.3 ‰ ± 0.1 (VSMOW). Trends of $\delta^{18}O$ with depth are not discernable.

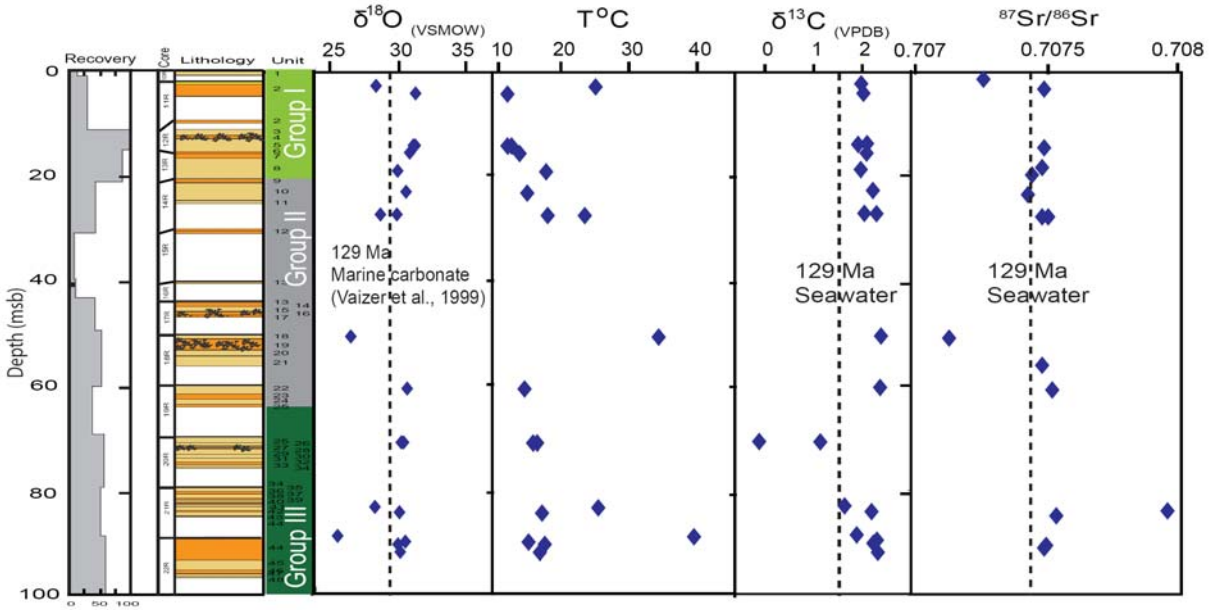

Figure 3.42. Isotopic variation of carbonates from ODP Hole 1179D with depth. Estimates of seawater composition at 129 Ma are based on plots of LMC for the last 500 Ma (Phanerozoic) by Veizer et al., (1999). Seawater Sr-isotopic composition after McArthur, (2001).

Temperatures of formation were estimated from $\delta^{18}O$ analysis following Friedman and O'Neil, (1977).

$$1000 \ln \alpha_w^c = 2.78(10^6 T^{-2}) - 2.89$$

The following assumptions are made with the temperature estimates: 1) Exchange reactions must reach equilibrium, 2) Isotopic composition has not changed after equilibrium is achieved, and thus represents the final composition, and 3) that 129 Ma Seawater $\delta_w = 0$ ‰. $\delta^{18}O$ data from LMC shells (Brachiopods, belemnites, oysters, foraminifera) for the last 500 Ma (Veizer et al., 1999) were used to obtain an δ_w for 129 Ma seawater. Calculated temperatures that range from 12 to 39°C (Appendix D, 3) suggest that low temperature seawater dominated alteration is responsible for carbonate precipitation. The irregular temperature profile vs. depth (Figure 3.42) may be related to channelled fluid flow.

3.6.2 Strontium isotopes

Measured strontium isotopic compositions for Site 1179 carbonates range from 0.707137 to 0.707938. The majority of these values are above the strontium isotopic composition of 129 Ma seawater (~0.70745, McArthur et al., 2001) at the time of Site 1179 basement formation. There is no trend with depth (Figure 3.42).
The high $^{87}Sr/^{86}Sr$ at Site 1179 carbonates suggest that seawater interaction with basalts is low when compared to some other basement sites for example., Holes 896A (Teagle, et al., 1996), 1256D (Coggon, et al 2006) and 504B (Teagle pers comm, 2007). Figure 3.41 plots the measured carbonate $^{87}Sr/^{86}Sr$ with the seawater strontium isotopic curve through time. Assuming no interaction with basalts, the majority of carbonates must have precipitated at least ~40 Myr after the formation of Site 1179. One sample 191-1179D 21R-3, 65-71 cm has a strontium isotopic composition of 0.707933 therefore must have formed at least 100 Myr after basement formation. Four calcite vein samples have $^{87}Sr/^{86}Sr$ values that are lower than seawater at 129 Ma. Three of these values may be attributed to formation at times when the strontium isotopic value of seawater was lower than at 129 Ma, between 124 and 85 Ma (Figure 3.43). However sample 191-1179D 18R-1, 52-58 cm has a $^{87}Sr/^{86}Sr$ ratio of 0.707137, well below the lowest

$^{87}Sr/^{86}Sr$ ratio of seawater after formation of Site 1179. This sample requires that the formation fluid interacted with basalt before precipitation of that sample.

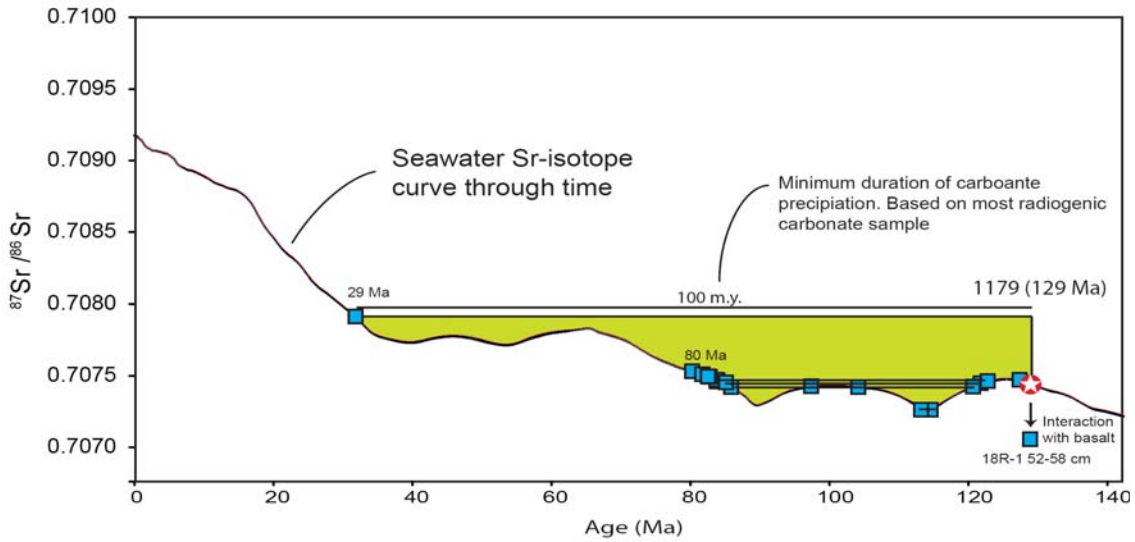

Figure 3.43. Seawater Sr isotopic composition with time. Carbonate $^{87}Sr/^{86}Sr$ (blue squares) are plotted to intersect the seawater Sr curve. Lines joining samples are where the same sample may cross the curve at several points. The later plots indicate that episodic carbonate precipitation has occurred for at least 100 Ma. Curve derived from McArthur et al, 2001.

Although direct precipitation of calcite from seawater is possible, from the variability of the strontium isotopic ratios and previous work on the precipitation of carbonate (Teagle et al., 1996; Coggon et al., 2004) it is likely that a component of basaltic Sr is present in an unknown proportion of the samples. Therefore, the use of the seawater Sr isotopic curve in carbonates as a dating method in oceanic basement (Staudigel et al., 1981; Staudigel and Hart, 1985) is precluded.

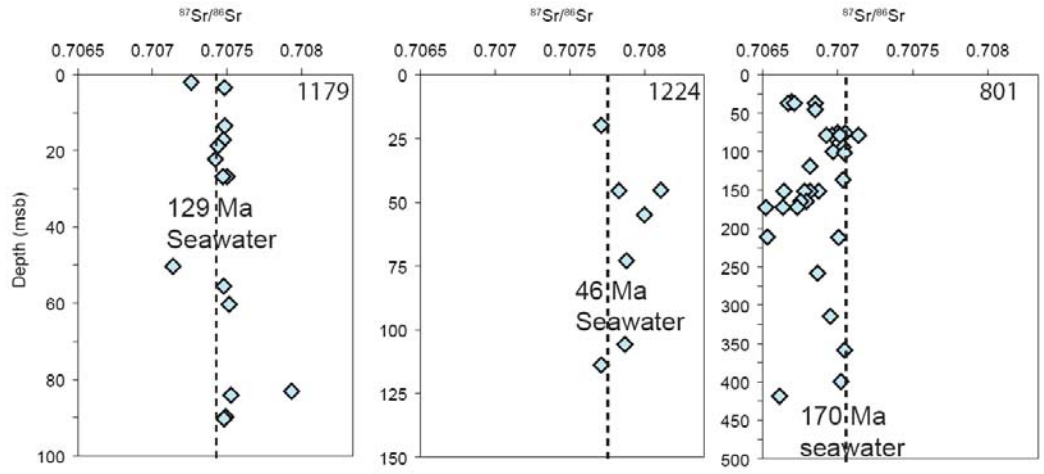

Figure 3.44. Sr-isotopic profiles of carbonates at Site 1179, 1224 and 801 together with seawater at the time of formation. 801 carbonates sourced from Alt, (2003)

Carbonate $^{87}Sr/^{86}Sr$ at the most well characterized basement sites tend to have values lower than that of seawater at the time of basement formation suggesting the inclusion of significant basaltic strontium. At sites where the strontium isotopic composition of some carbonates is greater than contemporaneous seawater (e.g. Holes 801C, 1224 and 1179D, Figure 3.44), the sedimentation rate is low (Figure 3.41). This suggests that sediment cover has an influence on the amount of interaction between seawater and basalt. In areas with high sedimentation rates (e.g. Juan de Fuca Ridge, 504B, 896A or 1256D, Figure 3.41) seawater and rocks are heated (due to insulation from the sedimentary layer) resulting in greater exchange between the fluids and basement.

3.6.3 Major element analysis

Concentrations of Sr, Mg, Fe, Mn and Ca were measured by ICP-AES (Table 3.11). Elemental analysis of Site 1179 carbonates have a distinct calcite signature. Sr concentrations range from 37 ppm to 266 ppm and Mg concentrations range from ~480 ppm to ~14000 ppm. Work by Coggon et al., (2004) in which both calcite and aragonite were sampled indicate a clear distinction between the Fe and Mn concentrations of each mineral type. Aragonite has very low Fe and Mn concentrations, whereas calcite has higher concentrations.

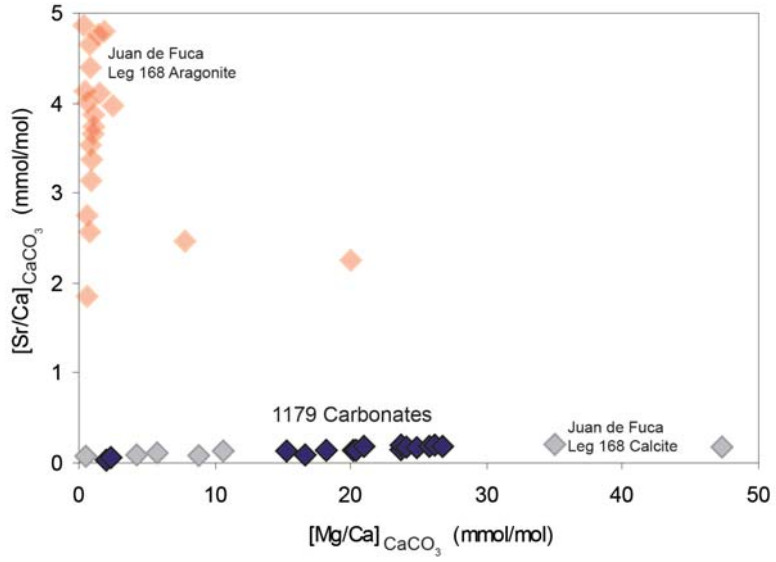

Figure 3.45. [Mg/Ca] and [Sr/Ca] concentrations in carbonate samples recovered from Site 1179. Error is less than the width of the data points. Data from the eastern flank of the Juan de Fuca Ridge (Coggon, 2004) is shown for comparison between aragonite and calcite.

Similar results occur with Sr and Mg concentrations at Site 1179 (Figure 3.45). Carbonate Fe and Mn also point to calcite compositions with average concentrations of 1950 ppm and 1250 ppm, respectively.

3.6.4 Constraints on fluid evolution

Relationships between calculated temperature, Mg, Ca, Mn and $^{87}Sr/^{86}Sr$ are used to describe the evolving composition of low temperature hydrothermal fluid and determine the conditions in which carbonate at Site 1179 formed. Evidence for fluid/basalt mixing and its effect on fluid chemistry is discussed.

The amount of exchange from magnesium in basalt for calcium in seawater is directly related to temperature (Coggon et al., 2004), and the Mg/Ca temperature dependence is well calibrated for calcite. A plot of temperature vs. Mg/Ca for Site 1179 calcite samples in Figure 3.46 illustrates this trend it suggests that the fluids are either mixtures of seawater or basalt.

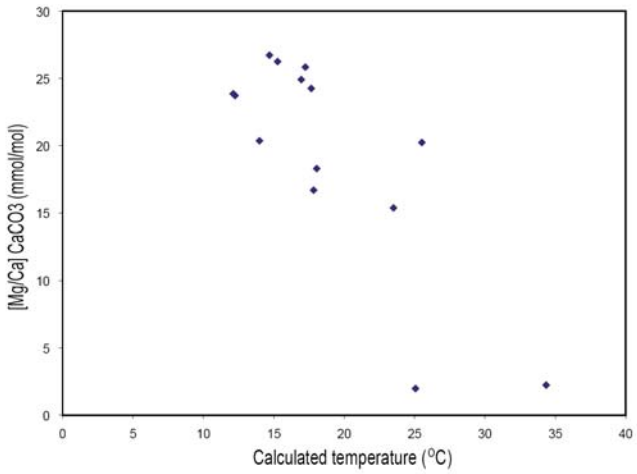

Figure 3.46 Plot of $[Mg/Ca]_{(CaCO3)}$ vs. calculated temperature from $\delta^{18}O$ measurement. Increased temperature results in increased exchange of Mg and Ca between seawater and basalt. Calcite formed at higher temperature formed from fluid that has lost Mg to basalt.

The evolution of Mn in hydrothermal fluids is represented in Figure 3.47. Site 1179 carbonates exhibit increasing $[Mn/Ca]_{CaCO3}$ with temperature. Possible causes for the increase in Mn concentration include mixing of upwelling, more evolved fluids (unlikely given the very low temperatures of formation) or the extra Mn came from interaction with basalts (e.g., Teagle et al., 1996, Coggon et al., 2004). Given the

temperature dependence of Mg/Ca, Sr/Ca and strontium isotopic evidence it is the most likely explanation for the relationship seen in Figure 3.48. The evolution of fluid from which carbonate precipitated from shows no sign of diverging pathways, which suggests the carbonates formed from the same evolving fluid, including the very young (~29 Ma) sample 1179D-21R-3, 65-71 cm.

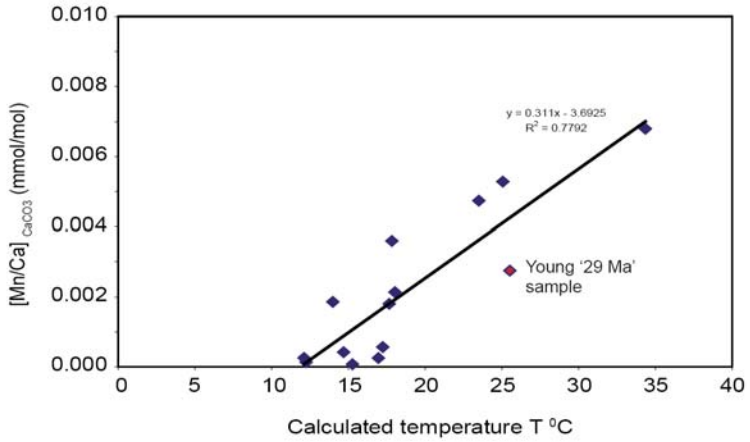

Figure 3.47. $[Mn/Ca]_{(CaCO3)}$ vs. calculated temperature from $\delta^{18}O$ analysis for carbonate vein seperates in Hole 1179D.

Following Coggon et al, (2004), calculation of the fluid Mg/Ca and Sr/Ca ratios to which carbonate precipitated from is carried out using the following partition coefficients:

$$K_D^{Sr-Ca} = \frac{[Sr/Ca]_{CaCO_3}}{[Sr/Ca]_{fluid}} \qquad \text{and} \qquad K_D^{Mg-Ca} = \frac{[Mg/Ca]_{CaCO_3}}{[Mg/Ca]_{fluid}}$$

K_D is determined experimentally by compositional analysis of $CaCO_3$ synthetically grown from a known solution or by comparing natural carbonates with known formation fluid compositions (e.g., Hartley & Mucci, 1996; Carpenter & Lohmann, 1992; Oomori et al., 1987). The partitioning of Mg^{2+} ions into calcite is highly dependent on temperature (Oomori et al., 1987), but also on precipitation rate, solution composition and concentrations of other trace elements (Hartey and Mucci, 1996; Rimstidt et al., 1998). A theoretical temperature dependent K_{cc}^{Mg-Ca} has been developed (Rimstidt et al., 1998) and the recent review of calcite partition coefficients by Coggon et al., (2004) and Coggon (2006) suggest that the K_{cc}^{Mg-Ca} developed by Rimstidt et al., (1998) is the most appropriate, where:

$$LogK_{cc}^{Mg-Ca} = 4.436 - \frac{1348}{T} - 0.005339T$$

(where T is in Kelvin)

The Sr content of calcite is partially controlled by the concentration of Mg (Mucci and Morse, 1983; Hart et al., 1994) and Sr should also be affected by temperature. Hence, following the review of partition coefficients by Coggon et al, (2004), the equation determined by Rimstidt et al. (1998) is deemed the most appropriate expression.

$$LogK_{cc}^{Sr-Ca} = -1.874 + \frac{179.2}{T} + 0.0006248T$$

Typical chemical exchange between seawater and basalt include; the leaching of basaltic Sr and Ca to the fluid, and the loss of Mg from the fluid to clay minerals and chlorite in the basalts. At higher temperatures, the level of interaction increases and more Sr and Ca will be removed from basalts. Therefore, calcite precipitated from a fluid which has undergone interaction with basalt will have lower $[Mg/Ca]_{fluid}$ and $[Sr/Ca]_{fluid}$ ratios than seawater. High temperatures in carbonates correlate with low Mg/Ca and Sr/Ca values for fluids (Figure 3.48 a and b respectively) although in calcites Sr/Ca is much less sensitive to changes in temperature.

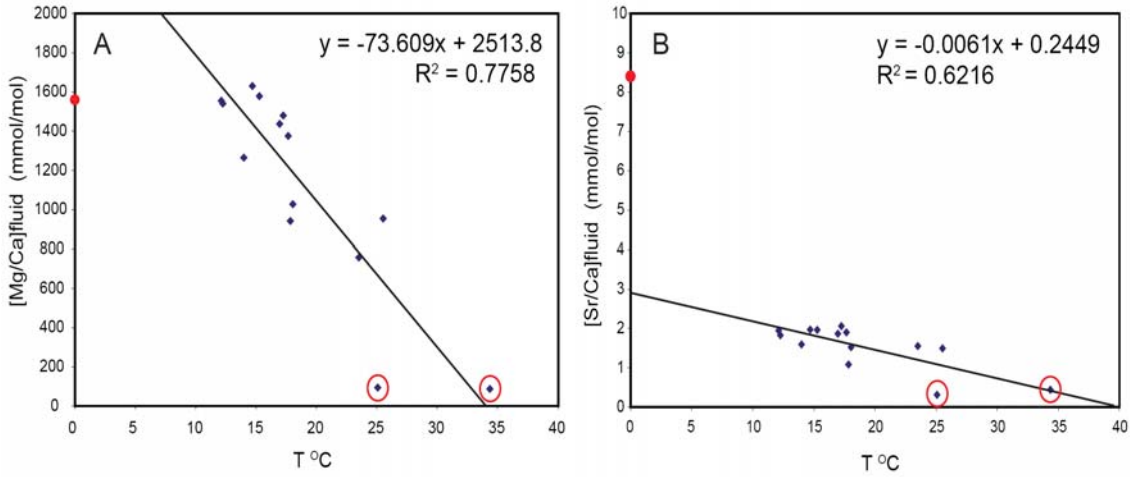

Figure 3.48. The dependence of $[Mg/Ca]_{fluid}$ (A)and $[Sr/Ca]_{fluid}$ (B) on calculated temperature based on $\delta^{18}O$ measurements in Hole 1179D carbonates. Red point indicates 129 Ma seawater values for [Mg/Ca] (based on Mg and Ca concentration time curves from marine evaporates in Horita et al., 2002) and [Sr/Ca] (from Sr/Ca time curves derived from cretaceous rudist bivalves and belemnites in Steuber and Veizer., 2002). Red circled samples 191-1179D, 11R-1, 44-50 cm and 18R-1, 52-58 cm indicate samples with the highest basaltic component.

The calculated $[Sr/Ca]_{Fluid}$ ratios decrease with increasing temperature (Figure 3.48 b). The fluid evolution exhibited by carbonates recovered from the Juan de Fuca ridge transect obtained by Coggon et al., (2004) are similar to those obtained in this study of Site 1179. The samples highlighted by red circles in Figure 3.48 (191-1179D-11R-1, 44-50 cm, 18R-1 52-58 cm) have the lowest Mg/Ca, Sr/Ca and $^{87}Sr/^{86}Sr$ ratios and they are relatively high in temperature. This suggests that increased temperature causes increased leaching of Ca from basalts. A significant uptake of Sr into fluids from basalts should result in higher Sr/Ca ratios in the carbonates together with low $^{87}Sr/^{86}Sr$ however such a trend is not observed when Sr-isotopic composition is compared against Sr/Ca figure 3.47 Figure 3.50 illustrates the relationship between age, formation temperature and the Sr isotopic ratio of the carbonate samples. A slight trend between $^{87}Sr/^{86}Sr$ and temperature is evident but a relationship with age is not clear, although the 'younger' samples (i.e. with high $^{87}Sr/^{86}Sr$) tend to have been formed at lower temperatures. Samples 191-1179D-21R-3, 65-71 cm (Blue circle in Figure. 3.50), 191-1179D-11R-1, 44-50 cm (Red circle in Figure 3.51) and 191-1179D-18R-1, 52-58 cm (Green circle in Figure 3.50) do not follow the same trend of the other carbonates. The outlier Sample 191-1179D-21R-3, 65-71 cm ('29' Ma sample), implies that this carbonate precipitated from a different fluid, possibly perhaps from renewed fluid flow. Samples 191-1179D-11R-1, 44-50 cm 18R-1, 52-58 cm exhibit low strontium isotopic ratios and relatively high temperatures compared with the other 1179D carbonates. These samples may represent a slightly more evolved localised fluid with a high proportion of basaltic Sr.

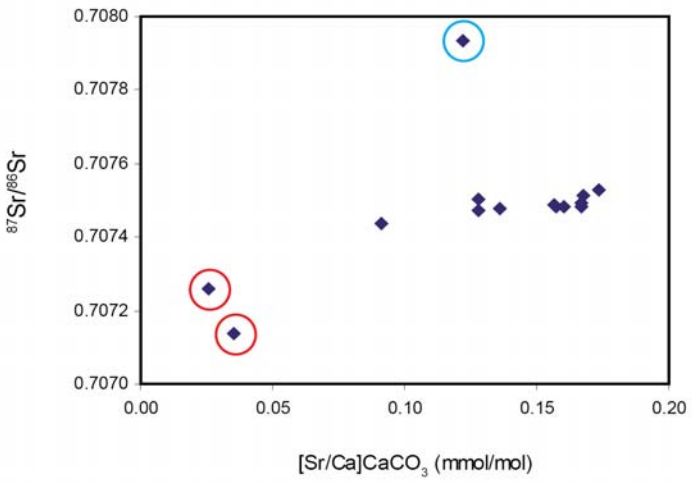

Figure 3.49. Sr/Ca vs $^{87}Sr/^{86}Sr$ for carbonate veins at Site 1179D. Red circled samples 191-1179D, 11R-1, 44-50 cm and 18R-1, 52-58 cm. Blue circled sample is the '29' ma sample 191-1179D, 21R-3, 65-71 cm.

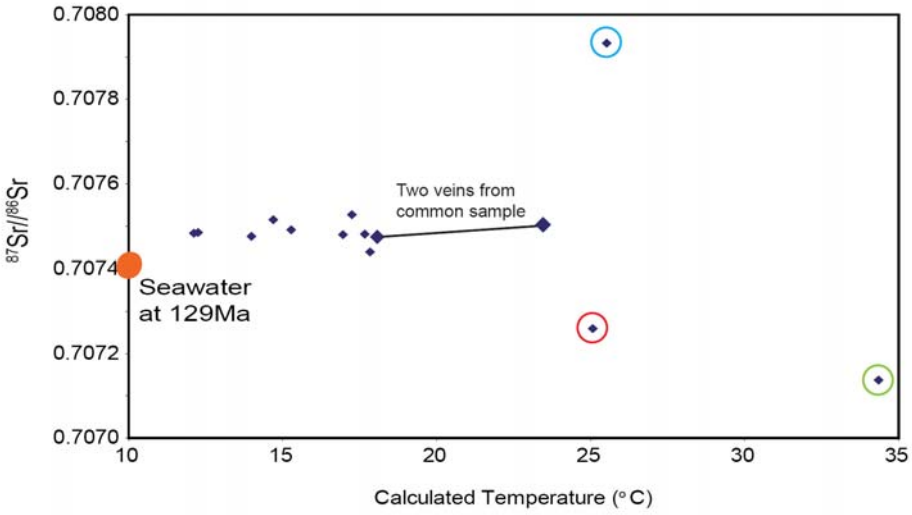

Figure 3.50. Carbonate $^{87}Sr/^{86}Sr$ vs. calculated temperature. Red circle indicates the Sr isotopic composition of seawater at 129 Ma (McArthur et al., 2001). Tie line indicates samples that share a common host (191-1179D, 14R-3, 59-64). Outlier Samples 91-1179D-21R-3, 65-71 cm (Blue circle), 191-1179D-11R-1, 44-50 cm (Red circle) and 191-1179D-18R-1, 52-58 cm (Green circle) represent carbonates from a different hydrothermal fluid, possibly at different times.

Two veins recovered from sample 191-1179D-14R-3, 59-64 exhibit different Sr-isotopic ratios and calculated temperatures. One has have high $^{87}Sr/^{86}Sr$ and temperature and the other with a lower $^{87}Sr/^{86}Sr$ and temperature respectively (Figure 3.50). This implies that two separate precipitation events took place within this sample. No cross cutting relationship was observed, so their relative timing remains unknown. It is not known if any of the carbonates formed within the relatively late period (Miocene) of rapid sedimentation. Given the $^{87}Sr/^{86}Sr$ values, it is more likely that carbonates formed during the slow sedimentation period, because slow sedimentation has persisted over the majority of the time since Site 1179 formation.

3.6.5 Carbon uptake in the oceanic crust

The abundances and distribution of secondary carbonates in the 100 m section of upper oceanic crust at Site 1179 have been measured to determine the carbon content of oceanic crust. Whole rock C contents were measured on a CS-analyser and estimates for the bulk CO_2 of Site 1179 were made by averaging each alteration type and weighted according to the proportion of that alteration type. The CO_2 content of veins and breccia at Site 1179 were added to whole-rock CO_2 to determine bulk CO_2 at Site

1179. Figure 3.51 shows the downhole variation of carbonate in veins/breccia, carbonate veins per metre and whole rock CO_2 content.

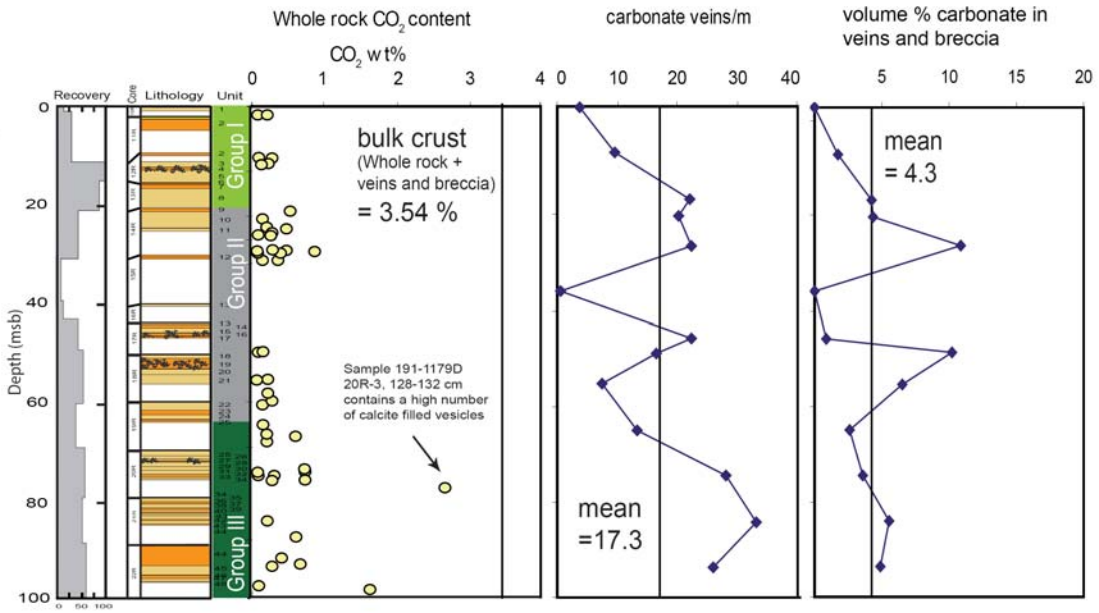

Figure 3.51. Downhole variation in carbon content for Site 1179. Carbonate veins per metre and the volume % plot are normalized to 100% core recovery. Cores 191-1179D-20R, 21R and 22R veins per metre are calculated from core photos since vein logs for these cores were completed by grouping veins into vein nets.

Variation of bulk rock CO_2 is minimal throughout ODP Hole 1179D. However, the abundance of carbonate veins increases with depth to around 33 veins per metre at 85 mbsf. The greatest abundance of carbonate occurs between 25 and 45-50 mbsf (Figure 3.41) which coincides with the recovery of breccias and high alteration at this depth. Although the highest number of veins occurs at the bottom of the core, the actual volume of carbonate in veins and breccia remains relatively low.

	Site	504	896	843	417/418	801	1179
		6.9	6.9	100	120	170	129
	Age	Ma	Ma	Ma	Ma	Ma	Ma
veins per metre	upper	2.6	8.2	18.5	-	21.4	17.34
	lower	0.4			-	20.2	
carbonate in veins and breccia	upper	0.07	0.45	4.9		3.01	1.76
	lower	0.03				3.08	
Bulk Crustal CO_2 Wt %	upper	0.21	0.51	2.4	4.9	4.05	2.05
	lower	0.14			0.8	3.05	

Table 3.11. Carbonate content for various Sites which penetrate ocean crust. 504, 896, 843, 417/418 and 801data from Alt and Teagle, (1999).

The difference between the normalized veins per metre plot and volume % carbonate at ~420 mbsf (Core 191-1179, 16-R) demonstrates the effects low recovery has on volume

calculations. This core has only 5.8% recovery, yet 4 carbonate veins are recovered in 18 cm of core, this translates to 22 veins per metre. The veins recovered are, however, very thin ~0.1 to 0.2 mm. Therefore, the total volume, even when extrapolated to account for recovery is negligible. Cores of low recovery must therefore, be used with caution. The calculated total CO_2 content of Site 1179 is 3.5%. The distribution and volume of carbonates at other sites is summarised in Table 3.11 (Alt and Teagle., 1999). In general older sites have higher amounts of carbonate (both within the basalt and in veins and breccia) than younger basement sites. This is consistent with continued precipitation of carbonate as the crust ages. Infill from reopened cracks fissures and pre-existing porspace increase carbonate content through time. Indeed, zones which are highly brecciated with either present or previously high porosity usually contain the highest proportions of carbonate, for example, 35-40 mbsf at Site 843 (Alt, 1993), parts of Hole 504B and the brecciated zone at 420 mbsf in Site 1179.

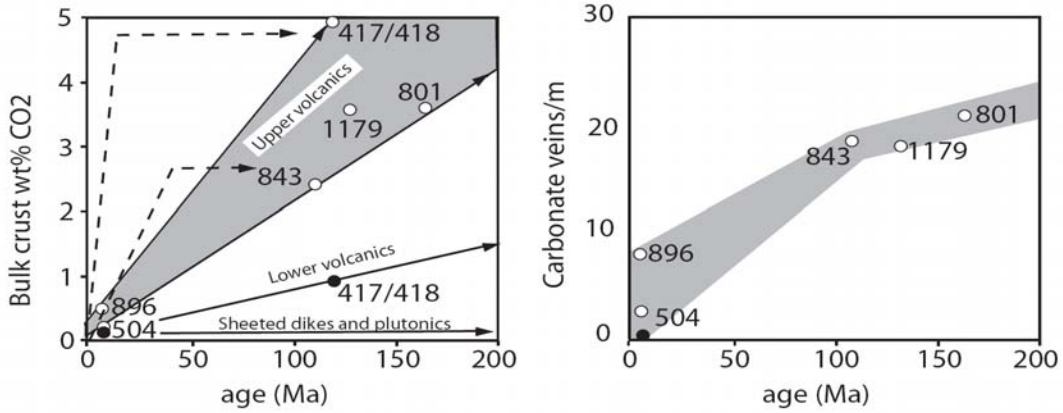

Figure 3.52.Carbonate data for bulk upper crustal sections vs. age from Alt and Teagle, (1999) with new data from Site 1179. (A) Indicates greater CO_2 contents with increasing age and (B) indicates the continued formation of carbonate veins well after 6 Ma. Sheeted dykes and plutonics have little or no CO_2 increase with time. Lower volcanics indicate a slight increase in CO_2 with time. Site 1179 has a similar concentration of CO_2 when compared to similarly aged counterparts. Open circles = upper crust, solid circles = lower crustal section. The dashed lines indicate possible pathways for uppermost crust assuming formation of all carbonate in the crust within 15 and 40 Ma (Alt and Teagle, 1999).

The relationship between carbonate content and age as compiled by Alt and Teagle, (1999), including Site 1179 is summarized in Figure 3.52. Older oceanic crust sites have higher CO_2 contents with the greatest incorporation of carbonate taking place in the upper volcanic section of the crust. Site 1179 has comparable bulk CO_2 to its similarly aged counterparts and carbonate veins per metre remain similar. As demonstrated in Table 3.11 and Figure 3.51, ODP Hole 896A has more than double the

amount of carbon in its basement than ODP Hole 504B. This is likely because Sites 896 and 504 were located on different parts of a ridge flank convection cell in which Site 504 was subject to horizontal flow and Site 896 was in an upflow zone on a basement high resulting in focused fluid flow and greater fluid fluxes (Alt and Teagle., 1999). Despite the drawbacks in using the seawater strontium isotopic curve as a tool for dating carbonates, Site 1179 carbonates exhibit values that indicate precipitation at least 40 Myr after formation of Site 1179. And one sample 191-1179D 35R-3, 65-71 cm must have formed at least 100 Myr later. Any incorporation of basaltic Sr into the formation fluid would mean the carbonates are even younger than what their measured $^{87}Sr/^{86}Sr$ values indicate. Interestingly, Sample 191-1179D 35R-3, 65-71 cm is not in an area of especially high alteration or brecciation, suggesting that late stage carbonate precipitation may have occurred even in areas of less focussed fluid flow.

Petrographic, mineralogic and geochemical evidence of multiple stages of carbonate precipitation at Site 1179 and other basement sites (Alt and Honnorez, 1984; Alt, 1993; Teagle et al., 1996) suggest renewed circulation takes place due to renewed fracture permeability created by tectonic activity. If such renewed circulation takes place and uptake of carbon is continuous throughout ocean crust over extended periods of time then we would expect older crust to have higher carbonate abundance. Table 3.11 indicates increased carbon content with age, although variation of carbon content of crusts at a similar age almost certainly reflect local heterogeneities. For example at Sites 504 and 896 (Alt and Teagle., 1999).

One possible major effect on carbonate precipitation is the depositional history of sediment. Younger sites with high sedimentation rates appear to have carbonates that are formed soon after site formation, (e.g. Sites 504, 6.9 Ma; 896, 6.9 Ma; 1256,15 Ma; and the JDFR, <3 Ma; Alt and Teagle, 1999) and they appear to be more heavily influenced by basalt interaction. Sites with slower rates of sedimentation appear to have more late-stage carbonates that are influenced by seawater interaction. A high sedimentary rate may have the effect of sealing the crust from seawater, thereby reducing carbonate precipitation and insulating fluids giving rise to higher temperatures and increased basaltic interaction (Teagle, et al., 1996). It is hard to be certain without sites from a variety of ages and sedimentary rates. Thus far data from old basement sites only comes from areas with low sedimentation rates and sampling of young sites has only taken place in areas of rapid deposition.

3.7. Discussion

3.7.1 Alteration in ODP Hole 1179D

Petrographic observation of secondary minerals of basalts from Hole 1179D is an indicator of the relative timing of alteration assemblages. The conditions at which saponite, iron-oxyhydroxides, celadonite and calcite precipitate change with time depends on levels of fluid flow, seawater chemical variations, structure fluid composition and temperature.

The order of secondary mineral paragenisis varies from that described in Section 3.2, saponite formation may precede iron-oxyhydroxide formation. Oxyhydroxides can clearly be seen to stain earlier saponite in many samples. Multiple bands with alternating saponite and oxyhydroxides reflect changes in the chemistry of basement fluid particularly with regard to K and Fe contents and redox potential (Kanazawa et al., 2001). Other examples include coexisting saponite + carbonates and celadonite + carbonates within veins. An increase in abundance of celadonite from 415 mbsf to 440 mbsf is indicative of relatively high fluid flow, perhaps during open seawater circulation. In places where celadonite has not been overprinted by iron-oxyhydroxides, fluid flow may have become more restricted, possibly due to a reduction in permeability. Increased iron-oxyhydroxide formation associated with elevated H_2O, Sr, Cu, Al and the slight losses in Mg and Ca at depths greater than 440 mbsf suggests decreasing cold seawater circulation with depth. This is contradictory to the increasing amount of $Fe(O,OH)_x$ with depth, which should point towards increased cold seawater circulation. Zones with locally high permeability may be controlling fluid circulation which may explain conflicting evidence. One important observation is that Hole 1179D exhibits a distinct lack of secondary sulfides. S^{2-} deficiency within the percolating seawater and/or a redox potential that was too high for reducing SO_4^{2-}, yet not high enough for more than partial oxidation of Fe^{2+}, may account for the lack of secondary sulfides (Kanazawa et al., 2001). It is unknown whether changes in seawater chemistry or local variations in fluid flow over time had the greater effect, but it is clear that changes in basement fluid chemistry had an impact on the sequence that secondary minerals form.

Observations from a number of young ocean crust sites suggest that all secondary mineral phases may form within 3 million years, although alteration may

continue for 100 million years. Comparisons between holes drilled of varying ages support this because mineralogy is similar at many sites (e.g. Teagle et al, 1996. Andrews, 1977., Böhlke et al., 1981., Alt and Teagle., 2003). Table 3.12 outlines the timing of secondary mineral paragenisis based on observations at young sites. Analysis of Sites younger than 3 Ma indicate that, at 3 Myr since crustal formation, alteration is incomplete, for example, at ODP Hole 648B which is less than 10 ka old, the only secondary mineral observed is celadonite. This suggests that celadonite formation in ocean crust occurs within the first 10 kyr of formation, although it may continue forming throughout the life of the ocean crust (Adamson and Richards, 1990).

Reference	Secondary Minerals observed	Age of sample	Site(s)
Adamson and Richards, 1990	Celadonite	<10 Ka	648
Humphris et al., 1980	Celadonite + Fe-oxyhydroxides	<1 Ma	424
Laverne and Vivier, 1983	Celadonite + Fe-ox + saponite	>2 Ma	506-510
E.g.,Andrews., 1977	Complete assemblage including carbonates and zeolites	3.2 Ma	332-335

Table 3.12. Constraints on secondary mineral paragenisis based on observations of very young crust.

Evidence for the potentially long duration for late stage hydrothermal alteration comes from strontium isotopic comparisons between the seawater strontium isotope curve and carbonates in an effort to constrain the timing of carbonate precipitation. The incorporation of basaltic Sr into seawater during seafloor alteration precludes the use of the Sr isotopic curve to date carbonate precipitation (Teagle et al., 1996). However, even assuming that the strontium isotopic ratio of the carbonates represents the fluid from which they precipitated, and that no subsequent exchange has taken place, then the majority of carbonates must have formed over a time period of at least 46 Ma after formation of Site 1179 ocean crust. One carbonate sample (191-1179D-21R-3, 65-71 cm), with a very high strontium isotopic ratio of 0.70778 suggests that it has precipitated as much as 100 Myr after basement formation at 129 Ma. Temperatures of the hydrothermal regime at Site 1179 have only been derived from $\delta^{18}O$ analysis of carbonates. Thus temperatures of formation of other secondary minerals can only be inferred from analysis of secondary minerals from other sites. Pure vein mineral separates from other vein minerals; including, saponite, iron-oxyhydroxide, and celadonite, will need to be selected and analyzed for $\delta^{18}O$ to constrain temperature regimes for these secondary minerals. Celadonites may form at temperatures up to 40^{o}C based on work on other in-situ celadonite samples by Seyfried et al., (1978) and Böhlke et al., (1984), whereas saponites can form at temperatures ranging from 15^{o}C to 170^{o}C

(e.g. Teagle et al., 1996). Calculated temperatures from carbonate veins range from 12 to 39^{o}C, which is typical of low temperature seafloor weathering. Although saponite was separated, some carbonate samples were picked from veins which contained simultaneous growth of saponite. This suggests that saponite also formed at low temperatures. Low temperatures may be explained by the lack of sediment cover allowing cold seawater to infiltrate more freely into the basement.

3.7.2 Chemical changes

Chemical changes as a result of hydrothermal alteration at Site 1179 measured from a calculated protolith and a host, indicate chemical changes associated with the secondary mineralogy at Site 1179. Increases in $Fe_2O_3^T$, K_2O, C, LOI, Rb, Cs, Ba, Ta, Th, U and decreases in SiO_2, MnO, MgO, Ni, Pr, Tb and Er are present throughout all alteration styles. Elements with low ionic field strength readily undergo cation substitution into crystal lattices, which may explain the very large chemical changes associated with Rb, Cs, Ba, Sr, Pr, Tb and to a lesser extent Th. Breccias have undergone the highest degree of chemical change. This includes increases in $Fe_2O_3^T$, K_2O, LOI, Zn, Zr, Cs, Ta and decreases in SiO_2, Cr, Ni, Pr, Tb and Er. Breccias are highly permeable rocks which are likely to be subject to higher fluid flow and, therefore fluid-rock interaction.

Distinction of the chemical changes for each alteration style is hampered by significant overlap created by sample selection, in which unavoidable portions of the sample contained more than one alteration style. In addition, significant overprinting from perhaps multiple stages of fluid flow will further obscure chemical changes that are distinctive to that style of alteration. Additional error comes from averaging for each sample set and the choice of protolith, because we assume TiO_2 is the most reliable immobile element and we also assume that no volume change has taken place.

3.7.3 Isotopic relationships

Whole rock $^{87}Sr/^{86}Sr$ at Site 1179 record the interaction of seawater with basalt as a result of hydrothermal alteration. Previous studies of seawater interaction with basalt have shown that altered basalts are enriched in ^{87}Sr by exchange with seawater (e.g.,

Alt and Teagle, 2003, Teagle, et al., 1996). Whole rock $^{87}Sr/^{86}Sr$ in Hole 1179D is elevated above MORB $^{87}Sr/^{86}Sr$ yet, not surprisingly, it remains well below contemporaneous seawater values. The increased $^{87}Sr/^{86}Sr$ with depth is a clear indicator of increased interaction with seawater; this is underlined by the overall increase in alteration with depth (Higher LOI and the increase in alteration halos). A suggestion by Sano and Hayasaka (2001) that the elevated $^{87}Sr/^{86}Sr$ may be related to interaction from the eruption of Shatsky Rise seems unlikely given that the evidence points to seafloor weathering. In addition, strontium isotopic values for acid washed samples from Mahoney et al, (2005) and leached whole rock samples in this study plot much closer to MORB values than the unwashed samples analysed by Sano and Hayasaka (2001).

The whole rock oxygen isotopic profile for Site 1179 basement are variably enriched compared to expected fresh glass compositions for upper oceanic crust. These enrichments are directly related to the incorporation of clay minerals, iron-oxyhydroxides and carbonates into the whole rock during low temperature seawater alteration. As shown in Figure 3.39, altered samples within sample pairs are further enriched in ^{18}O than their least altered 'fresh' hosts. No variability with depth or alteration style is present, however a small sample size and low depth of penetration into basement preclude a detailed study into the variations of whole rock $\delta^{18}O$ at Site 1179.

3.7.4 Carbonates

Isotopic results from Site 1179D carbonates are used as an indicator of fluid flow and may be indicative of the intensity of hydrothermal alteration. A relationship between seawater/basalt interaction, temperature and age is explored through carbonates. However, one must acknowledge the large assumptions made in assigning ages to strontium isotopic results.

The temperature dependence of the extent of hydrothermal alteration is indicated by strong trends between the strontium isotopic ratios of carbonate and temperature. Plots of carbonate $^{87}Sr/^{86}Sr$ vs. temperature show a slight negative trend, becasue fluids will exchange with basaltic Sr (Figure 3.50). This suggests that even small increases in temperature in Hole 1179D will increase alteration intensity. The

Mg/Ca and Sr/Ca fluid compositions derived from carbonates vs. temperature plots show that high temperatures in carbonates correlate with low Mg/Ca and Sr/Ca values. This is strong evidence for seawater basalt interaction

To explore the possibility that a relationship between $^{87}Sr/^{86}Sr$, temperature and age exists at Site 1179, an age hierarchy was devised for each carbonate sample using the seawater strontium isotopic curve as a guide (Figure 3.43). Although nearly all evidence points towards fluid interaction with basalt, the age hierarchy was devised assuming that all carbonates have been formed from fluids that have been subjected to the same amount of interaction with basalt. Therefore, the differences in observed $^{87}Sr/^{86}Sr$ reflect the change in seawater Sr isotopic composition with time.
The relationship indicates a weak trend, suggesting that older samples have low $^{87}Sr/^{86}Sr$ which correlates with the higher temperatures. One possible cause of this relationship is that

Older carbonates continued exchanging strontium after formation. Older carbonate specimens are expected to have lower $^{87}Sr/^{86}Sr$ values due to lower $^{87}Sr/^{86}Sr$ in phanerozoic seawater. Fluctuations in seawater $^{87}Sr/^{86}Sr$ ~40 Myr after the formation of Site 1179D basalts means caution must be taken in drawing temporal relationships between $^{87}Sr/^{86}Sr$ of carbonates and seawater $^{87}Sr/^{86}Sr$ over time. In modern ocean crust, where the $^{87}Sr/^{86}Sr$ of seawater has been steadily increasing at for the last 30 Ma, would predict stronger temperature vs. $^{87}Sr/^{86}Sr$ trends for modern oceanic crust, because any basalt interaction with high $^{87}Sr/^{86}Sr$ seawater should result in sharper increases in $^{87}Sr/^{86}Sr$. Calculated temperature from $\delta^{18}O$ analysis and $^{87}Sr/^{86}Sr$ were obtained from different sites with different ages and spreading rates (Figure 3.53).

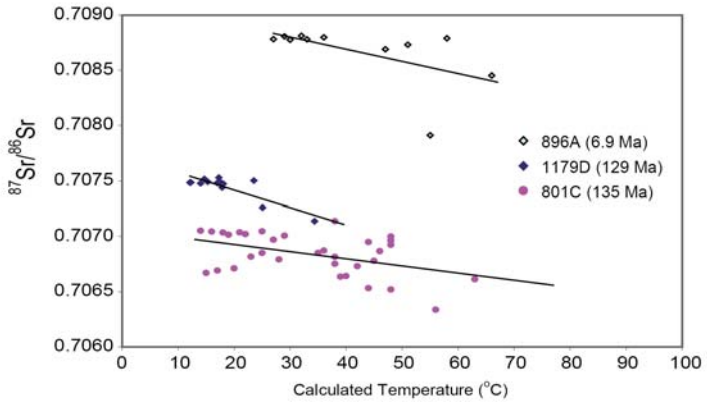

Figure 3.53 Calculated temperature vs. $^{87}Sr/^{86}Sr$ for ODP Holes 896A (Teagle et al 1996, 1179D and 801C (Alt and Teagle, 2003). Trend lines indicate the fluid evolution as increased temperatures result in more Sr-isotopic exchange.

These holes exhibits similar trends to Site 1179D indicating that similar processes are occurring despite the variation in spreading rate, sedimentation rate and age. A comparison between rates of sedimentation at different sites in ocean crust and their $^{87}Sr/^{86}Sr$ show that in areas with low sedimentation rates the $^{87}Sr/^{86}Sr$ of carbonates reflect the $^{87}Sr/^{86}Sr$ of seawater at the time of ocean crust formation, whereas sites that have experienced high sedimentation exhibit strontium isotopic values that are lower than seawater. This suggests that sediment cover may be allowing fluids to exchange with basaltic Sr, perhaps by warming up the fluids whilst sealing off the majority of cold seawater from the basement. Areas of ocean crust which have seen very little or no sedimentation, may have $^{87}Sr/^{86}Sr$ which have had very little to no contamination from basalts and therefore may represent the seawater values at the time of formation. Carbonates from more sites at differing ages, spreading rates and sedimentation rates are required to elucidate which processes have the greatest impact on carbonate precipitation.

Based on observations of secondary minerals of recovered core, ODP Hole 1179D contains 0.39 % carbonate. The percentage of CO_2 present at Site 1179 is 3.55 wt % with on average 17 veins per metre carbonate. The relationship between age and carbonate content at Site 1179 supports the evidence from other basement sites and high $^{87}Sr/^{86}Sr$ of some carbonate samples that incorporation of carbonate in the crust continues long after its formation. The variable CO_2 contents at various ODP and DSDP sites suggest factors such as hydrothermal upwelling, permeability and porosity and structure (Alt and Teagle., 1999) contribute to reduced rates for carbonate precipitation at older sites. The permeability of ocean crust which is intrinsically linked to structure may in turn be governed by spreading rates.

3.8. Conclusions

Hole 1179D penetrated 100 m into the upper volcanic section of ocean crust which has been slightly to moderately altered by seafloor weathering. Secondary mineral assemblages, whole rock geochemistry, and isotopic analysis of whole rock samples and secondary carbonates have helped to characterize the style and intensity of hydrothermal alteration at Site 1179D. Variations in TiO_2, Al_2O_3, Ni, Cr, Cu, Sr, V, Zn and Y reflect the igneous variation between olivine poor, olivine free and olivine rich basalts. Increases in $Fe_2O_3{}^T$, K_2O, C, LOI, Rb, Cs, Ba, Ta, Th, U and decreases in SiO_2, MnO, MgO, Ni, Pr, Tb and Er are present throughout all alteration styles.

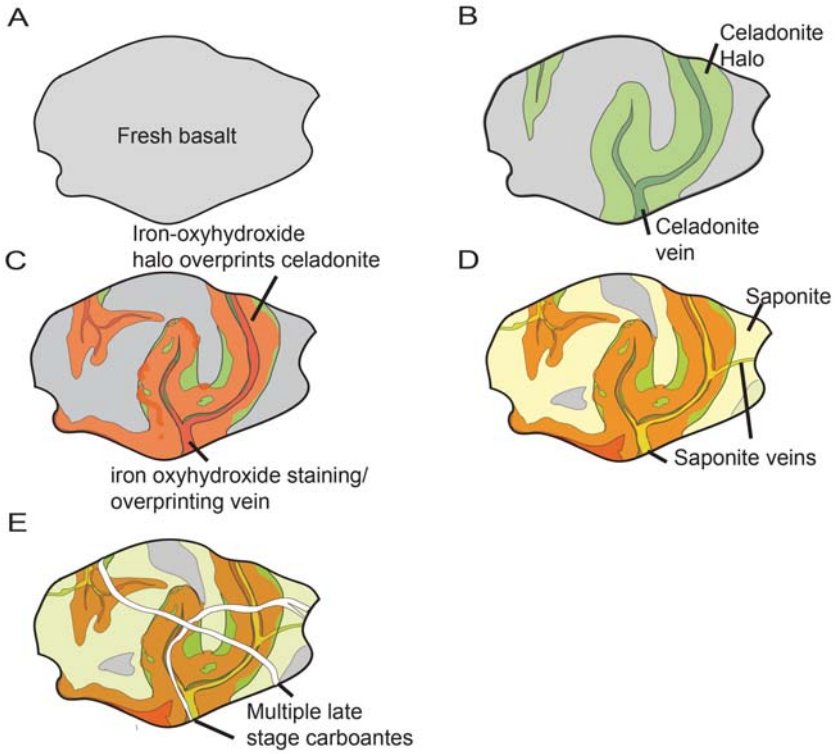

Figure 3.55. Generalized sequence of secondary mineral paragenisis during alteration of Site 1179 basalts. (A) Fresh basalt. (B) Low temperature celadonite veins and halos form from initial seafloor weathering. (C) Circulation of cold seawater resulting in oxidation and iron-oxyhydroxide rich alteration halos and veins, saponite may be present at this point but oxidation overprints any early saponite. (D) Saponite reflects reducing conditions forming veins, halos and the majority of background alteration. (E) Late stage carbonate veins fill fractures and re-opened veins.

Complex halos encompass the trends of many or the alteration styles superimposed on each other. Gains in nearly all elements are observed, especially S, Ni, Nb, Pb and U. In addition, variable losses include MnO, Cu, Rb and Th. Distinctions in the chemical changes associated with hydrothermal alteration at Site 1179 are hampered by

overprinting of different mineral phases and the difficulty in sampling only one alteration phase.

Despite significant overlap, the following sequence of secondary minerals occurs: celadonite formation which is followed by saponite + iron-oxyhydroxides and then pervasive saponite alteration. Later multiple stages of calcite ± zeolite cross-cut the previous stages (Figure 3.54). This sequence is similar to the alteration sequence found at Hole 801C (Alt and Teagle, 2003). Variations to this sequence are common, and they are primarily related to variations in fluid flow dictating the conditions at which minerals can form. The other highly likely cause is changes in the chemistry of seawater entering the ocean crust which has resulted in oxidation throughout the section and a lack of secondary sulfides. Multiple halos are thought to represent periodic changes in basement fluids the most notable chemical change is the increase in S and Pb. Significant overlap between alteration assemblages and lack of data from sample pairs makes the summary of chemical changes within each assemblage unreliable. Indications from carbonate veins suggest that later fluids from renewed fluid flow were present which may indicate upwelling of hydrothermal fluids.

$^{87}Sr/^{86}Sr$ values of carbonate precipitates and whole rocks and their relationship with intensity of hydrothermal alteration, depth and temperature all suggest that whole rock Sr isotopic compositions are the result of seafloor weathering with cold seawater interacting with basalts. In addition, leaching experiments carried out on Site 1179 basalt samples (Chapter 2) imply that the primary Sr-isotopic composition is reflects that of MORB. This is contrary to Sano and Myrashiro, (2001), who suggest that elevated $^{87}Sr/^{86}Sr$ in basalts are the result of interaction with Shatsky Rise.
Isotopic evidence from carbonates reveals an alteration history that spans at least 46 Myr since formation of Site 1179 because $^{87}Sr/^{86}Sr$ in most carbonate mineral separates is higher than 129 Ma seawater. The relationship between age and carbonate content at Site 1179 supports the evidence from other basement sites, and high $^{87}Sr/^{86}Sr$ of some carbonate samples that incorporation of carbonate in the crust continues long after its formation. The variable CO_2 contents at various ODP and DSDP sites suggest factors, such as hydrothermal upwelling, permeability and porosity, and structure may all influence carbonate uptake in the ocean crust (Alt and Teagle., 1999). More sampling of carbonates of different sites is required to elucidate which of these effects has the greatest impact on carbonate precipitation.

Chapter 4

Site 1256

4.1. Site 1256.

Site 1256 (6°44.2′N, 91°56.1′W) is located in the Guatemala Basin on the Cocos plate on the eastern flank of the East Pacific Rise (EPR). The site straddles the magnetic anomaly 5Bn-5Br which places the site at ~15 Ma. Site 1256 now currently lies ~1150 km east of the present spreading centre (crest of the EPR) and ~ 530 km north of the Cocos ridge (Figure 4.1). Site 1256 formed on a 400km long ridge segment, ~100 km north of the ridge triple junction between the Cocos, Pacific and Nazca plates (Wilson et al, 2003). Magnetic anomaly identifications in the central part of the Cocos plate and the corresponding part of the Pacific plate indicates that this site formed during a period of superfast spreading (220 mm/yr full rate) and has since moved eastward to its current location (Wilson, 1996).

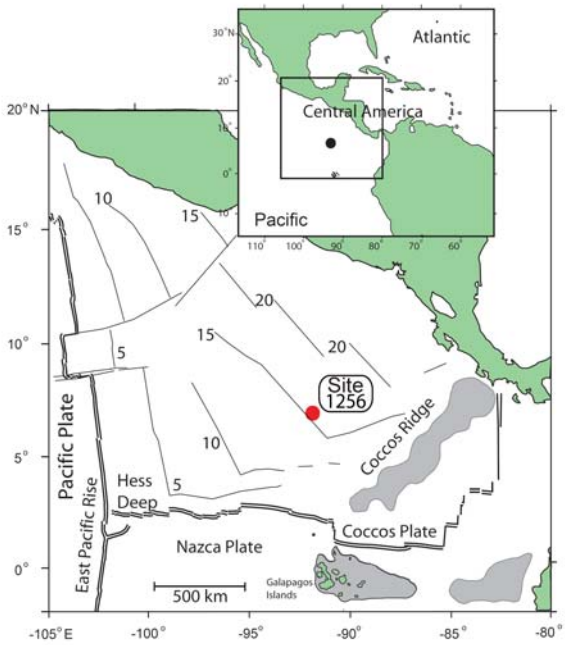

Figure 4.1. Location of Site 1256 (Modified from Wilson et al., 2003).

Regional topography at Site 1256 includes a series of seamounts around ~500 m high which rise above the sediment (15-20 km NE of Site 1256) and in the south a pronounced basement topography is evident with a relief of ~100 m in the form of subparralel ridges and narrow troughs. Seismic profiling during the site survey estimated the sediment pile to be ~250 m thick. The same profiling of the basement

indicates that the velocity of upper layer 2 is between 4.5-5 km/s, and that the Layer 2-3 transition lies between ~1200 and 1500 m subbasement with a total crustal thickness of ~5-5.5 km. Layer 2-3 (Figure 4.2).

Site 1256 was drilled to: 1) test the prediction, from the correlation of spreading rate with decreasing depth to the axial melt lens (Figure 4.2) (Carbotte, et al 1997; Purdy et al, 1992), that gabbros (representing the crystal melt lens) will be encountered between 900 and 1300 msb (metres sub-basement) (Wilson et al., 2003), 2) To determine if the gabbros are cumulate rocks from which the dykes and lavas are sourced, or if the gabbros are coarse grained equivalents of the extrusives frozen at the base of the sheeted dykes, 3) determine whether crustal accretion occurs at deeper levels by intrusion of multiple narrow sills (MacLeod and Yoauancq, 2000; Kelemen et al., 1997), or by the 'gabbro glacier model' which theorises that as ocean crust spreads away from the ridge axes, accumulated crystal residues in melt lenses subside to form the lower ocean crust (Henstock et al., 1993; Phipps et al., 1993; Quick et al., 1993), and 4) determine the cooling rates of magma chambers.

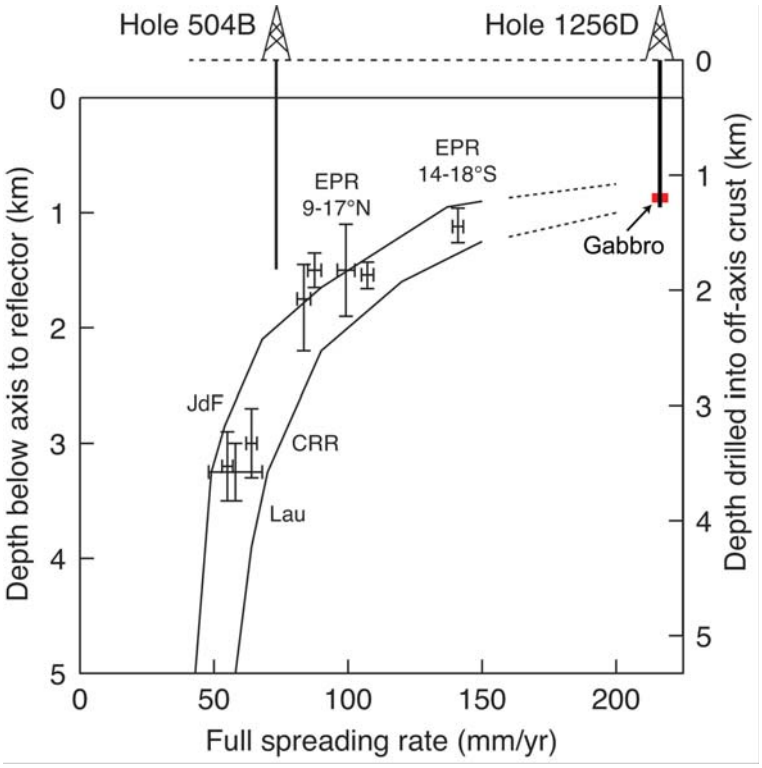

Figure 4.2. Depth to axial low-velocity zone plotted against spreading rate. Depth vs. spreading-rate predictions from two models of Phipps Morgan and Chen (1993) are shown, extrapolated subjectively to 200 mm/y (dashed lines). Penetration in Holes 504B and 1256D are shown by solid vertical lines, including the point at which gabbros were penetrated at Site 1256 (red box). Following core descriptions, a thickness of ~300 m of off axis lavas is shown for Hole 1256D and assumed for Hole 504B. EPR =

East Pacific Rise, JdF = Juan de Fuca Ridge, Lau = Valu Fa Ridge in Lau Basin, CRR = Costa Rica Rift Figure is modified from Wilson, et al, (2006).

In 2002 ODP Leg 206 Initiated Hole 1256D and drilled through 250 m of sediment and 502 m into basement. IDOP Expedition 309 returned to Hole 1256D in July-August 2005 and extended the hole to 1255 mbsf through the lithological transition zone and into the intrusives. IODP Expedition 312 further deepened the hole to 1507.1 mbsf and, for the first time, at 1407 mbsf, recovered gabbros from an intact section of ocean crust at Site 1256. Site 1256 possibly represents the most comprehensive example of upper ocean crust to date because it is one of only two sites to recover the lithological transition between the extrusive pillow and lava flows and intrusives, and the only site to recover gabbros (Wilson et al., 2006; Teagle et al., 2006). Hole 1256D and 504B are also the only penetrations of the ocean crust where the mineralogical transition zone between cold seawater derived alteration to hot hydrothermal alteration has been recovered (Teagle et al., 2006). Site 1256 provides us with the opportunity to characterize hydrothermal alteration for a complete section of oceanic crust, therefore allowing us to investigate the evolution of hydrothermal fluid composition from seawater to black smoker type fluid, chemical fluxes and heat fluxes at fast spreading rates, and their impact on oceanic crust as a whole. To this end, this study presents chemical and petrographic analysis of whole rock basement samples and secondary minerals at Site 1256. The style and intensity of alteration at Site 1256 is compared directly to that of Hole 504B the only other deep penetration of ocean crust.

4.1.2. Sedimentary stratigraphy

The sedimentary succession has been subdivided into two lithological units and subunits based on their clastic and biogenic components, visual core analysis, colour reflectance and physical properties (Figure 4.3) (Wilson et al., 2003).

Unit I is clay rich with minor carbonate-rich intervals and extends from 0-2.37 mbsf in Hole 1256A, 0-40.6 mbsf in Hole 1256B. Subunit IA comprises dark brown to yellow brown silty clays of Pleistocene age. The age is based on dating of the calcareous nannofossils that form the bulk of the biogenic component in this subunit. Subunit IB (Pliocene to late Miocene) is composed of clay rich nannofossil ooze, sandy silty clay, and a sandy silty nannofossil ooze (Wilson, et al., 2003). Unit II has no

subunit divisions and comprises late Miocene to middle Miocene calcareous nannofossil ooze with varying quantities clay and distinct microfossil groups (Wilson et al., 2003). Sedimentation rates are calculated based on biostratigraphic age constraints and the magnetostratigraphic record of the sedimentary sequence obtained during ODP Leg 206 (Figure 4.4). Sedimentation rates vary from ~6 to 36 m/m.y., with initial very rapid sedimentation (36.4 m/m.y) during the first ~ 4 Ma followed by relatively moderate fluctuating levels of sedimentation (6.3 – 13.6 m/m.y) for the remaining ~11 Ma of Site 1256 lifetime (Figure 4.4). The high sedimentation rates can be attributed to the Site's palaeolatitude, which placed it near the equator in an area of high productivity (Farrell et al., 1995). Later, slower sedimentation rates, which occurred later during the mid Miocene to present day, can be correlated with a sharp downturn in carbonate content from ~11.2 to 7.5 Ma that is often referred to as the carbonate crash (Farrell et al., 1995; Lyle et al., 1995).

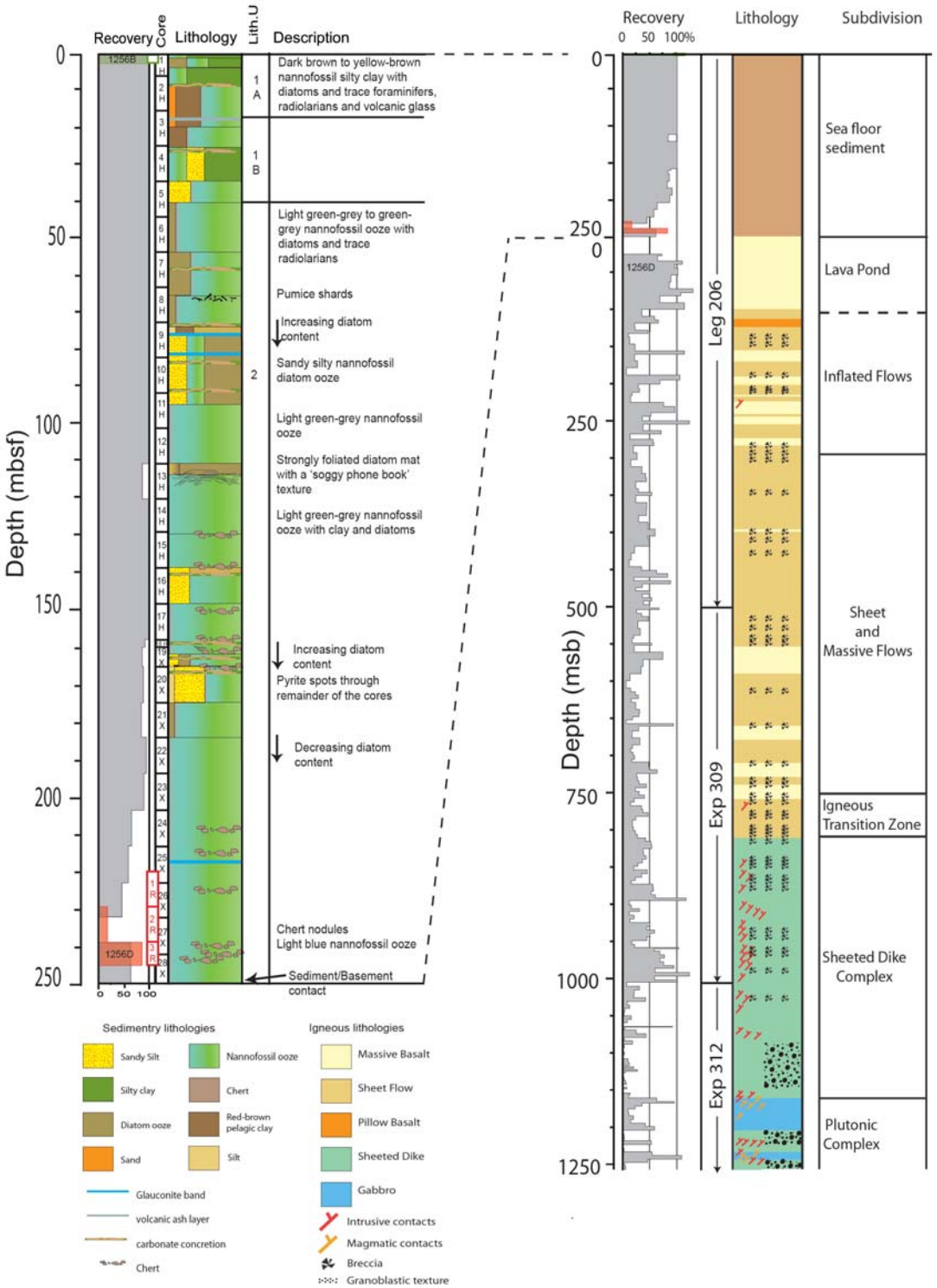

Figure 4.3. Site 1256 stratigraphy including core recovery, lithology and lithostratigraphic units. Modified from Wilson et al, (2003) and Teagle et al, (2006).

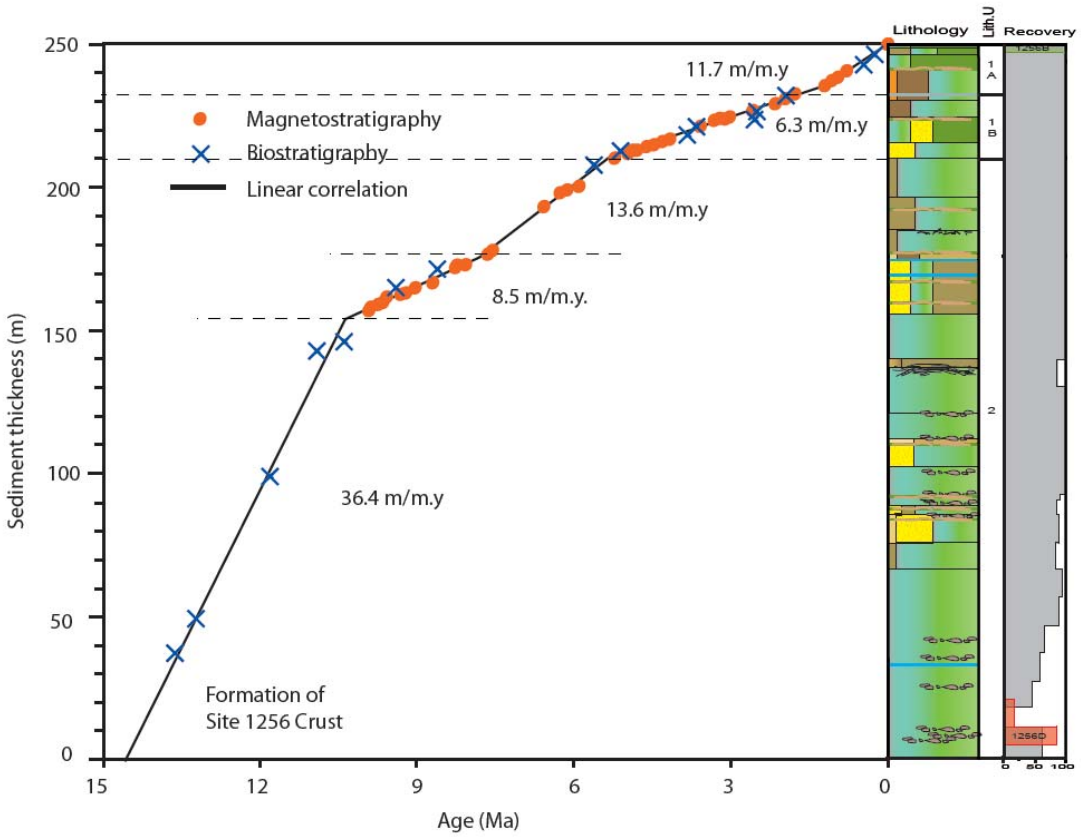

Figure 4.4. Sediment cover vs. time at Site 1256. Sedimentation rates are deduced from a combination of palaeomagnetic (red spots) and biostratigraphic (blue crosses) data. For reference the sedimentary stratigraphy is included. (Modified from Wilson et al., 2003).

4.1.3. Basement stratigraphy

Basement stratigraphy at Site 1256 is summarized in Figure 4.3. Recovery includes samples from all the lithologies within the upper oceanic crust, including off axis lava flows, sheeted and massive flows, massive lavas, sheeted dykes and gabbros.

The upper crust at Site 1256 comprises a 100m thick lava sequence dominated by a 75 m thick single flow. Such a thick flow requires basement relief at least as thick as this flow. The degree of basement relief normally only develops when the crust is between 5 and 10 km away from the axis (Macdonald et al., 1996). Immediately below the thick lava flow are sheet and massive flows (<3 m thick) with subvertical elongate flow top fractures filled with quenched glass and hyaloclastite (Wilson et al., 2003). These features are indicative of flow lobe inflation (Wilson et al., 2003), requiring eruption into a sub-horizontal surface off axis (Umino et al., 2000). The total thickness of off

axis lavas is estimated to be 284 m (Teagle et al., 2006). Below these lavas, a further 720 m of sheet and massive flows that erupted from the ridge axis make up the extrusive section down to 754 msb. Between 754 and 811 msb is the lithological transition zone from extrusive lavas to sheeted dykes. This is marked by mineralized (Disseminatred sulfides, chlorite, anhydrite, and quartz) breccia zones and the start of sub-vertical intrusive contacts that increase down-hole (Teagle et al., 2006). 811 msb marks the start of a ~350 m-thick, sheeted dike complex that is dominated by massive basalts. These basalts commonly have doleritic textures and may be cross-cut by subvertical dikes that have highly brecciated and mineralized chill margins. Between 1098 to 1157 msb, the basalts in the lower sheeted dyke complex are partly to completely recrystallized to granoblastic textures. This metamorphism is the result of gabbroic intrusions which first appear at 1407 mbsf (Koepke et al., 2008; Coggon et al., 2008). At this contact, two plutonic bodies (the upper being 52 m thick and the lower being 24 m thick) separated by a 24 m thick screen of granoblastic dykes was recovered. The upper gabbro is composed of gabbros, oxide gabbros, quartz-rich diorites and small trondjhemite dikelets. The lower gabbro consists of gabbro, oxide gabbro and subordinate orthopyroxene-bearing gabbro and trondjhemite. Both gabbros contain stoped dyke clasts that are partially resorbed. Hole 1256C consists of 18 igneous units whereas 1256D has been classified into 95 igneous units. Units were defined based on individual sheet flows, mineralogical similarity in sequences of small flows, chilled margins, breccia, dyke cooling margins, phenocryst/textural changes and mineralogical variations.

4.1.4. Bulk geochemistry

In addition to the samples analysed in this study, the bulk geochemistry of Site 1256 was determined by whole rock ICP-AES analyses of 16 basalt samples in Hole 1256C and 112 samples from Hole 1256D during preliminary studies of shipboard data (Teagle et al., 2006). Here a brief summary of the results and interpretations of Teagle et al, (2006) and Wilson et al, (2003) is made.

Reports by Neo et al, (2009), Teagle et al, (2006), and Wilson et al, (2003), indicate that the extrusive portion of Site 1256 has a composition typical of MORB.

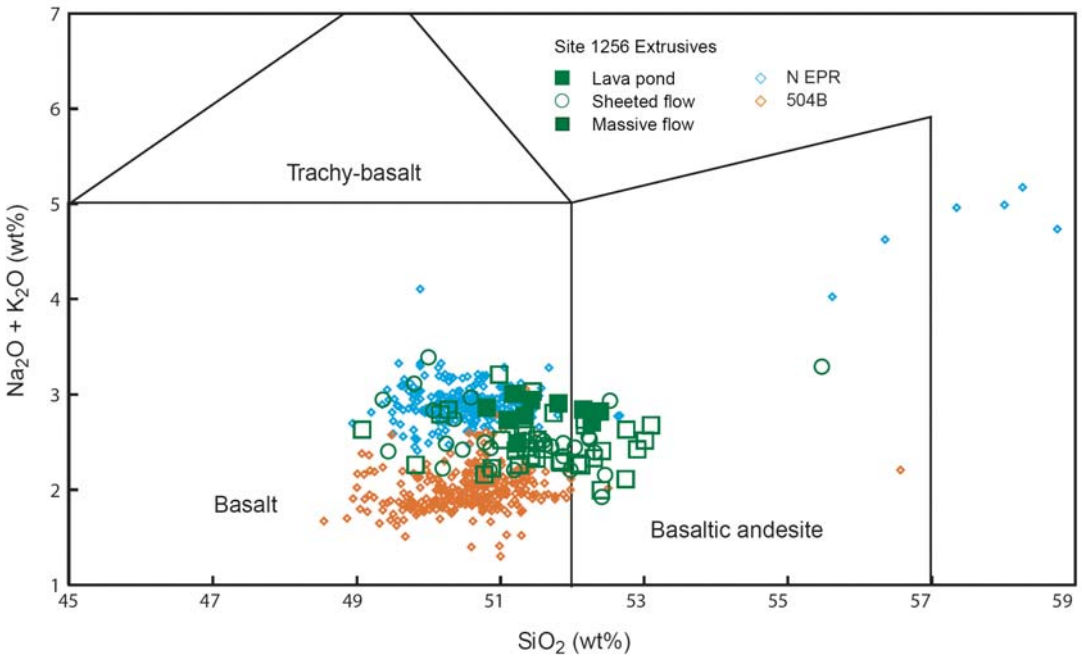

Figure 4.5. Total alkalis ($Na_2O + K_2O$) vs. silica for Site 1256 extrusives, rocks from the East Pacific Rise (EPR) (5°–10°N; Langmuir**,** www**.**petdb.org**,** 2001), and Site 504 rocks (Natland et al., 1983; Emmermann, 1985; Tual et al., 1985). N EPR = northern EPR, 504B = Hole 504B. Northern EPR data from C.H. Langmuir (unpubl. data, www.petdb.org**,** 1999). Site 504 data from Autio et al. (1983), Natland et al. (1983), Emmermann (1985), and Tual et al. (1985). (Modified from Teagle et al., 2006).

The compositional range of Site 1256 extrusive rocks, as compiled from samples analysed in this study, Neo et al, (2009), Teagle et al, (2006), and Wilson et al, (2003) are: 47–54 wt% SiO_2, 9.7–17.0 wt% FeO, 5.6–8.6 wt% MgO, 4.3–12.8 wt% CaO, 1.7–5.1 wt% Na_2O, 50–366 ppm Cr, 52–188 ppm Sr, 34–169 ppm Zr, and 3–106 ppm Ba. Mg# ranges 45–65 with an average value of 55. These values correspond to typical values for MORB (Su and Langmuir, 2003). In addition, the majority of samples from Site 1256 extrusives range from basalt to basaltic andesite on a Silica vs. Total Alkali diagram (Figure 4.5, after Teagle et al., 2006). Examples of the primary igneous trends at Site 1256 are shown on plots of Zr/Y vs Ti/Y and V/Y (Figure 4.6, Teagle et al., 2006). Both plots indicate that Site 1256 is less depleted in incompatible elements than comparable MORB rocks (North EPR and Site 504). Fractionation in Site 1256 may be caused by partial melting or a depleted mantle source. In addition to fractionation, considerable scatter in Site 1256 Ti/Y vs. Zr/Y and V/Y vs. Zr/Y compared to N EPR and Hole 504B (Figure 4.6), are thought to be caused by variation in the melt supply and stability of the magma chamber or off axis magmatism (Teagle et al., 2006). Geochemical evidence for off axis magmatism come from high concentrations of

incompatible elements (e.g. Zr, TiO_2, Y and V) and the greatest depletion of compatible elements (e.g. Cr and Ni) within the lava pond compared to other igneous groups at Site 1256 (Wilson et al., 2003).

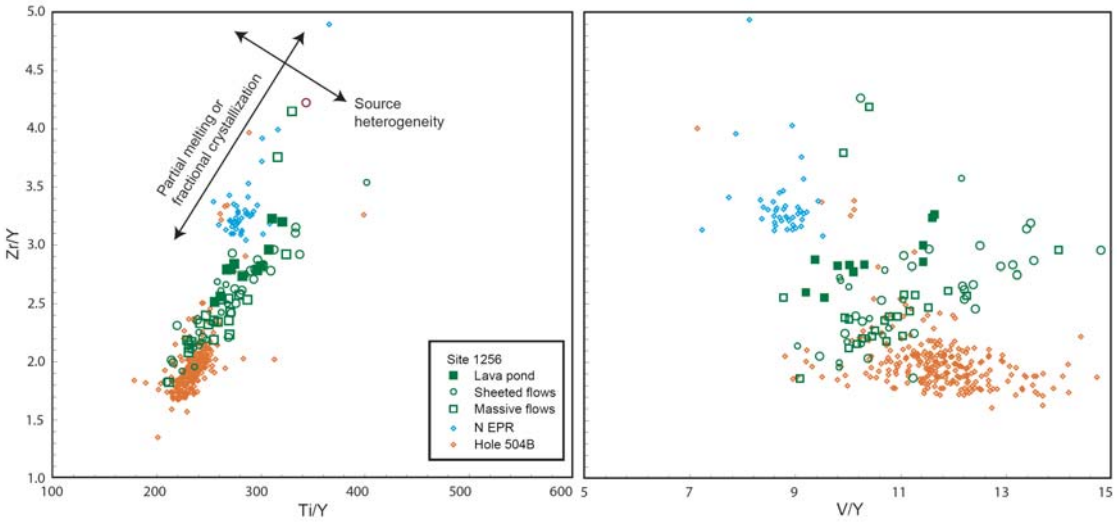

Figure 4.6. Incompatible trace element ratios, Zr/Y vs. Ti/Y and V/Y, plotted for Hole 1256D extrusive rocks and rocks from the northern East Pacific Rise (EPR; 5°–10°N) and the Costa Rica Rift (Site 504). Arrows show expected variation of ratios during either partial melting or fractional crystallization and variability explicable by source heterogeneity N EPR = northern EPR, 504B = Hole 504B near the Costa Rica Rift. Northern EPR data from C.H. Langmuir (unpubl. data, www.petdb.org, 1999). Site 504 data from Autio et al. (1983), Natland et al. (1983), Emmermann (1985), and Tual et al. (1985). (Modified from Teagle et al., 2006).

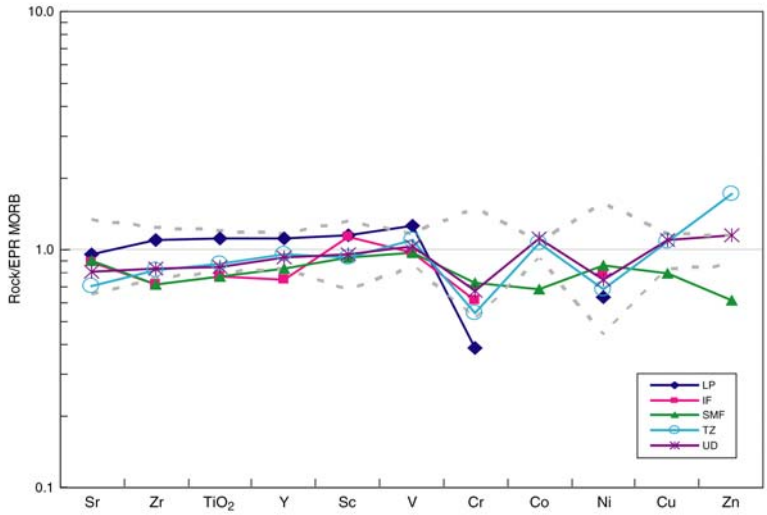

Figure 4.7. East Pacific Rise (EPR) mid-ocean ridge basalt (MORB)–normalized multi-element plot for averages of different lithological subdivisions from Hole 1256D (Leg 206 and Expedition 309). LP = lava pond, IF = inflated flow, SMF = sheet and massive flows, TZ = transition zone, UD = dikes. Values of Y, Sr, Zr, and TiO_2 are taken from Su and Langmuir (2003). Other elements are compiled from PetDB (online at petdb.org/index.jsp) with MgO >6.0 wt dashed lines represent range of MORB (After Teagle et al., 2006).

4.2. Basement Alteration

ODP/IODP Site 1256 is the only Site to penetrate and recover a complete in-situ section of the upper oceanic crust and it is only the second site to penetrate the sheeted dykes of ocean crust. It is also only the second in-situ basement Site after ODP Site 504 in which a transition from low temperature alteration to high temperature greenschist alteration is observed. Hence characterisation of the alteration at Site 1256 is critical to understanding how cold seawater evolves to hydrothermal fluids and the impact of seawater circulation on ocean crust formed at fast spreading rates. Here, the effects of cold seawater dominated alteration and deep high temperature alteration have been described for basement recovered at Site 1256. An assessment is made of the nature and extent of secondary mineralogy, which include the nature and distribution of alteration halos, veins, breccias, and contacts.

The alteration styles and intensity at Site 1256 vary with depth. Most rocks are slight (<10% secondary minerals) to moderately altered (~20-30% secondary minerals), however alteration intensity may vary from slight to extreme (>90% secondary minerals). Alteration effects include replacement of groundmass minerals, phenocrysts, and the filling of vesicles, interstices and fractures by secondary minerals. These can manifest themselves as veins, halos, breccias, and patches. Two alteration zones are defined at Site 1256. 1) low temperature seawater alteration with saponite, celadonite and iron-oxyhydroxides dominating secondary mineral assemblages, and 2) hydrothermal alteration, the transition of which is marked by the identification of chlorite-smectite in thin section at ~731 msb (in Core 309-1256D-112R), the occurrence of a mineralized volcanic breccia (in Core 309-1256D-122R) that defines the base of alteration transition, and finally the first appearance of actinolite in veins and the change from chlorite-smectite to chlorite dominated secondary mineralogy at ~777 msb (Core 309-1256D-122R) (Teagle et al, 2006). Figure 4.8 charts the occurrence of secondary minerals at Site 1256 vs. depth (Teagle et al, 2006). Due to the variation in alteration conditions, it becomes convenient to describe Site 1256 alteration in terms of ‘low temperature’ and ‘high temperature’.

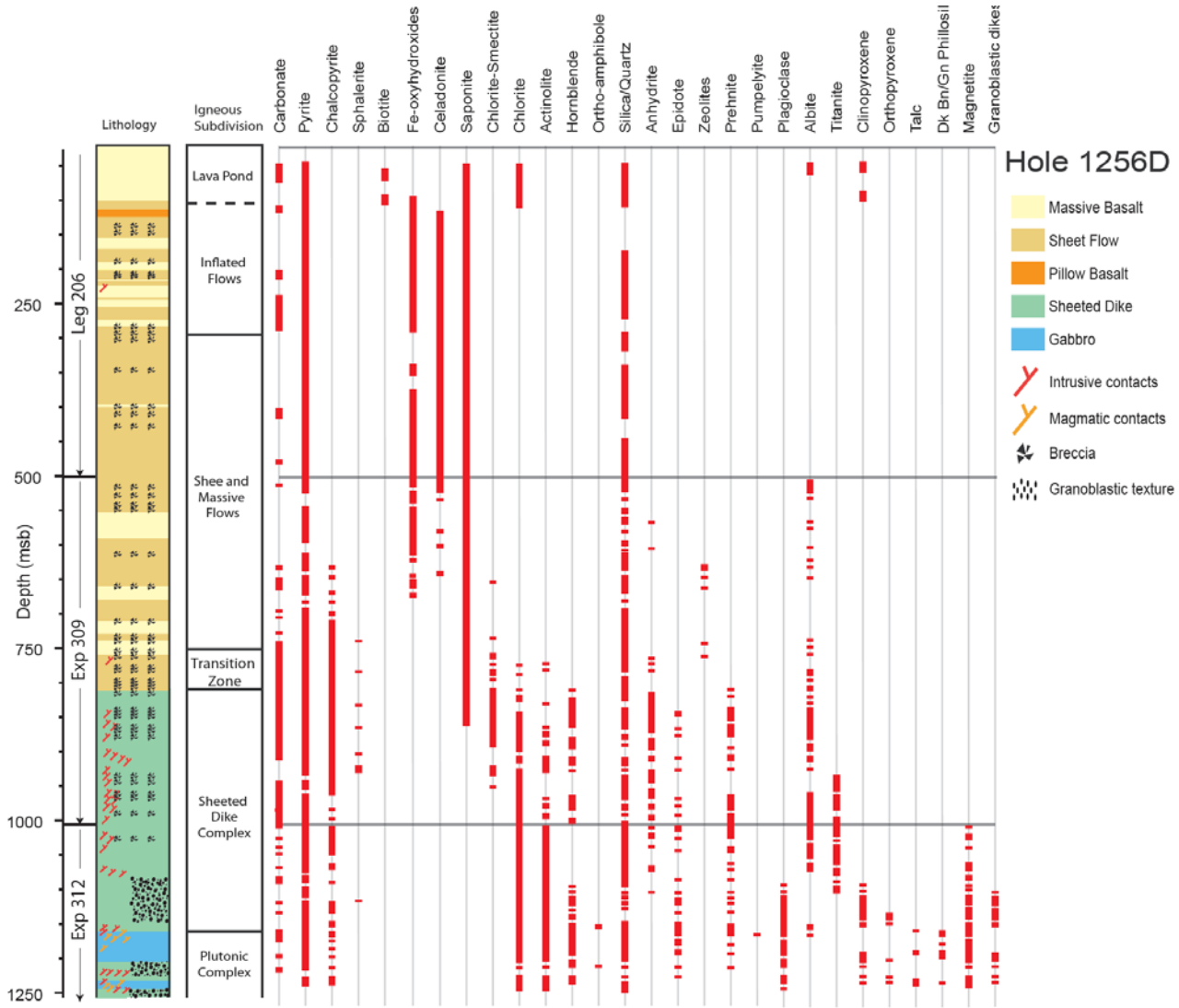

Figure 4.8, Distribution of secondary minerals vs. depth at ODP/IODP Site 1256. Leg 206 data from Wilson et al, (2003). Exp 309 and 312 data sourced from Teagle et al, (2006)

4.2.1 Low temperature alteration

Low temperature seawater-dominated alteration occurs at ODP/IODP Holes C and D to a depth of 777 msb. Alteration within the pillow lavas, sheeted flows, massive flows, and inflated flows ranges from slight to extreme. Secondary minerals include saponite, celadonite, iron-oxyhydroxide, calcite and aragonite, and secondary sulphides. Minor zeolite, rare anhydrite and, for the first time in ocean crust, a rare Ti-rich hydrogarnet (Laverne, 2005) occurs as a minor phase at Site 1256. Alteration characteristics include replacement of the groundmass and olivine phenocrysts to form pseudomorphs,

replacement of interstitial mesostasis, and the filling of vesicles and interstices. Veins and breccia matrices are filled with saponite, pyrite, silica, celadonite, calcium-carbonate and iron-oxyhydroxides, many of which are multi-minerallic. Associated halos commonly flank veins, of which most are black to dark green and more rarely brown. Where brown and back halos are superimposed, mixed halos may occur. A small but significant number of dark patches occur throughout Site 1256. These can be identified as zones of moderate to intense alteration with no apparent associated vein connecting the secondary mineral. They typically mirror the alteration seen within vein related halos, except alteration can be more intense.

4.2.1.1 Secondary minerals

Saponite at ODP/IODP Site 1256 is pale olive-brown to olive green, non- to slightly pleochroic in plane polarized light and exhibits first order interference colours in crossed polarized light. This is unlike chlorite, which is green and weakly pleochroic, and displays anomalous blue to tan interference colours. Saponite replaces plagioclase and clinopyroxene groundmass, pseudomorphically replaces olivine phenocrysts (Figure 4.9) and it fills vesicles, interstices, and veins (Figure 4.10A and C). Saponite is abundant throughout the extrusives, but becomes less common with depth in the dykes with the deepest reported occurrence of saponite at 858.9 msb (Figure 4.8).

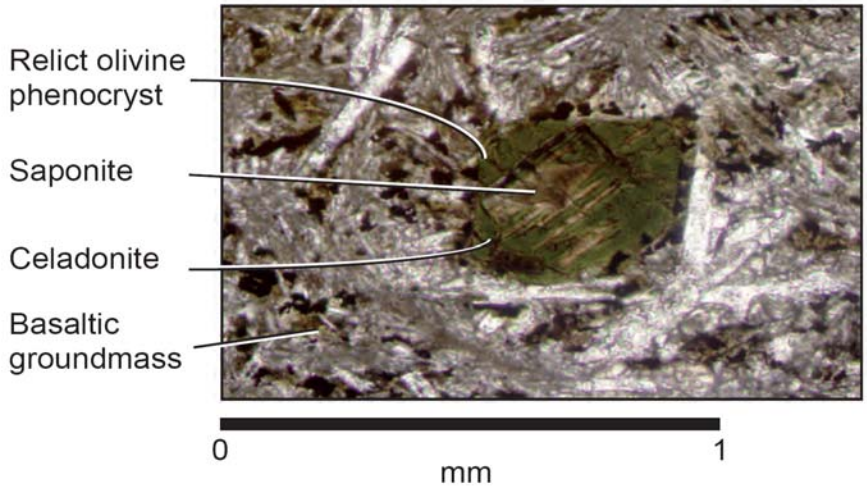

Figure 4.9. Olivine pseudomorphically replaced by celadonite (dark green) which is in turn replaced by saponite (brown) in Sample 206-1256C-8R-3, 136-140 cm (Wilson et al.,2003).

Celadonite, bright green to blue in plane-polarised light and in hand specimen, typically replaces interstices and fills vesicles and veins. Celadonite is less abundant than saponite and it is commonly intergrown with iron-oxyhydroxide and overprinted by saponite (Figure 4.10B), which can make identification difficult. It is therefore plausible that we may underestimate the presence of celadonite at ODP/IODP Site 1256. Celadonite occurs in the upper two thirds of the extrusives to a depth of 644.1 msb (Figure 4.8).

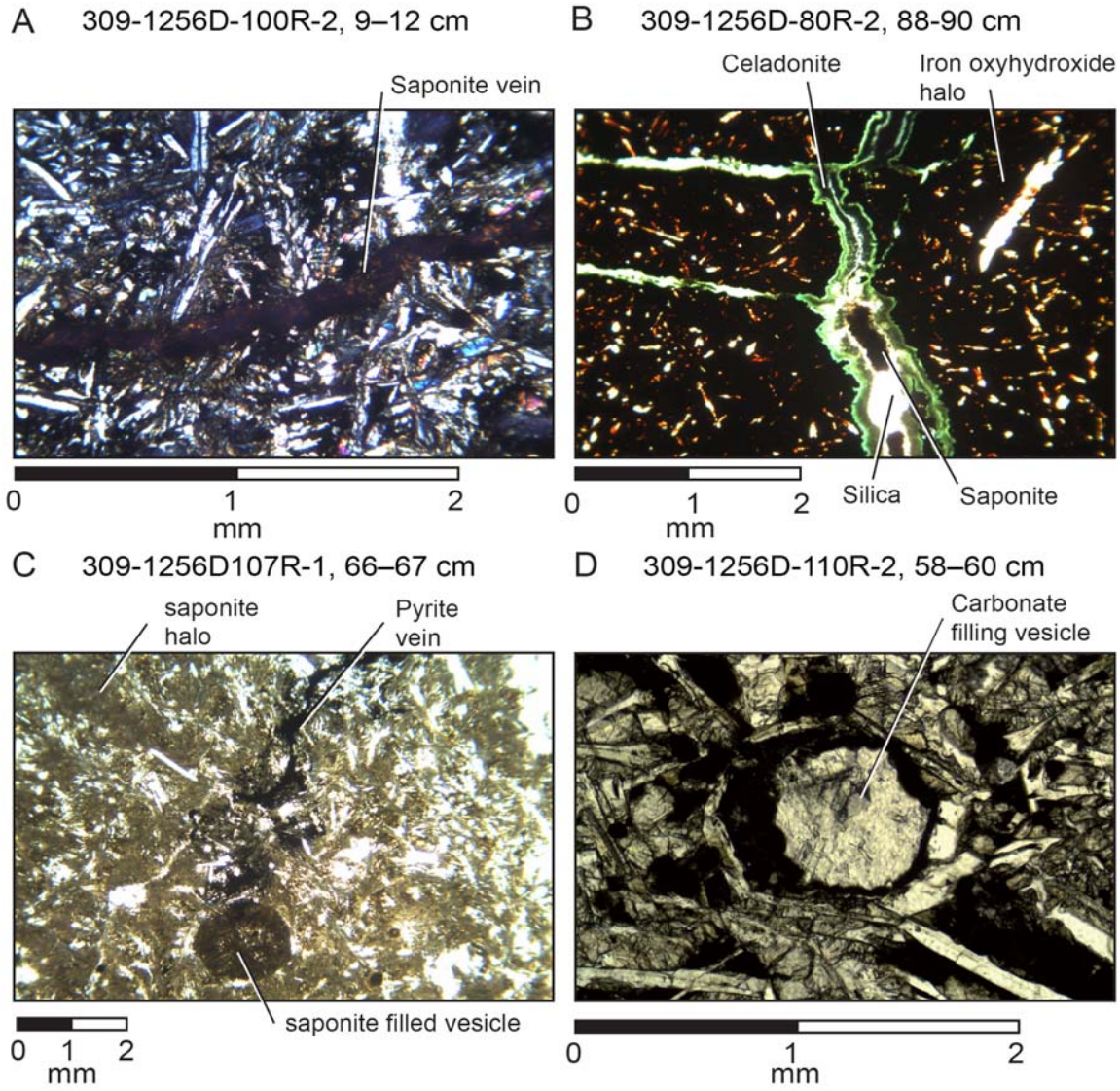

Figure 4.10. Examples of commonly occurring low-temperature secondary minerals at ODP/IODP Site 1256. A) Saponite filling vein B) Celadonite, saponite and silica filling vein surrounded by an iron oxyhydroxide halo, C) Pyrite vein with narrow pyrite rich halo and saponite halo. D) Carbonate filling vesicle Photomicrograph A = cross polarised light. Photomicrograph B, C and D = plane polarised light. Image D sourced from Teagle et al., (2006).

Iron-oxyhydroxides occur as dark brown to red brown patches that typically overprint the primary groundmass, fill vesicles, interstices, and veins. Iron-oxyhydroxides tends to occur in conjunction with celadonite (Figure 4.10B) and its occurrence with depth resembles that of celadonite. No Iron-oxyhydroxide is reported below 676 msb.

Carbonate and zeolite tend to form as late stage mineral phases that fill veins and vesicles and they rarely replace groundmass. Carbonate occurs as low relief anhedral crystals with first order interference (Figure 4.10D) and it is present throughout Site 1256. Zeolite (identified as, low relief fibrous crystals with very low interference colours) is only observed in discrete intervals within the lower portion of the volcanic section.

Secondary sulphides pyrite and chalcopyrite are identified in reflected light. Chalcopyrite ($CuFeS_2$) is yellow and tarnishes slightly more than pyrite (FeS_2), therefore commonly it will appear duller. Pyrite occurs throughout Site 1256, whereas chalcopyrite only occurs in the lower portion of the dykes and the extrusives. Sulphides overprint the groundmass and form disseminated anhedral to subhedral crystals in and around saponite, silicate veins and in altered groundmass (Figure 4.10C).

Anhydrite ($CaSO_4$) in the low-temperature zone is reported in several locations (Figure 4.8) as part of multi-minerallic veins or breccia matrixes within the lavas (Figure 4.11A). It may be distinguished by low to moderate relief and perfect cleavage at {010}, and good cleavage at {100} and {001}. High birefringence with third order colours also makes anhydrite distinctive. In the lower half of the sheet and massive flows, secondary albite partially replaces feldspar within the groundmass and some phenocrysts, for example in Sample 309-1256D-76R-2, 0-4 cm (Figure 4.11B). Albite ($NaAlSi_3O_8$) can be distinguished from other feldspars due to its low extinction angle $\sim<10^{o}$. Unusual Ti-rich hydrogarnets were identified in Sections 206-1256D-59R-2 to 74R-2 (411.7-499.3 msb) (Laverne, 2006) and 309-1256D-75R-1 to 99R-2 (502-669.1 msb). The hydrogarnets are very pale brown and they only occur in celadonite-filled vesicles and miarolitic voids or replacing olivine micro-crystals (Figure 4.11D). The host rock, (where no celadonite is present) is garnet free. Laverne (2006) reports a composition of 33-36 wt% SiO_2, 23-25 wt% TiO_2, 22-24 wt% CaO, and 9-13 wt% FeO^t, which tentatively identifies the mineral as Hydroschorlomite, a Ca-, Ti-, and Fe-rich andraditic garnet (Laverne, 2006; Laverne et al, 2006). In Sample 206-1256C-10R-1, 104-107 cm, biotite mica is reported, replacing an interstitial area within basalt (Figure 4.11C).

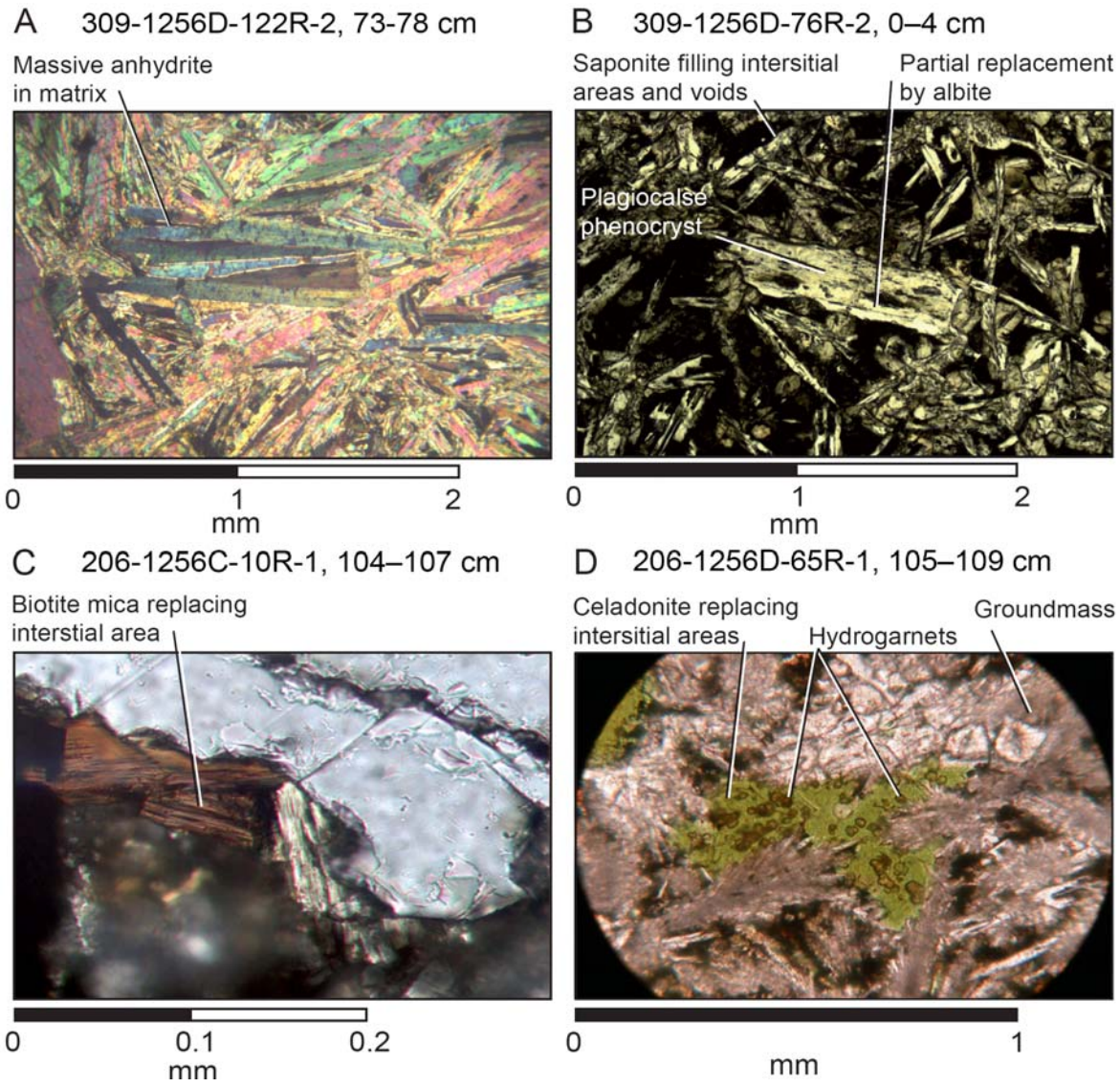

Figure 4.11. Examples of less abundant low-temperature secondary minerals at ODP/IODP Site 1256. A) Anhydrite matrix B) Partial replacement of a plagioclase phenocryst with albite. C) Discrete biotite mica replacing interstitial areas D) Rare Ti-rich hydrogarnets within celadonite replacing interstitial areas. Photomicrograph A = cross polarised light. Photomicrographs B, C, and D = plane polarised light. Image C from Wilson., (2003). Image B sourced from Teagle., (2006). Image D from Laverne, 2006.

4.2.1.2 Veins

Vein minerals related to low temperature alteration at Site 1256 include saponite, celadonite, iron oxyhydroxides, chalcedony and minor pyrite. This assemblage is present throughout most of the extrusive pillow lavas and sheet and massive flows and it is similar to assemblages from other shallow penetrations of ocean crust formed at intermediate to fast spreading rates (This study and e.g., Plank., 2000; Kanazawa et al., 2001; Wilkens et al., 1993; Orcutt et al., 2003; Morberly, 2003; Alt et al., 1996; Teagle et al., 1996; Alt et al., 1996; Stephen et al., 2003). Celadonite and iron-oxyhydroxides are not present below 644 msb and 676 msb respectively. Figure 4.12, and 4.13 demonstrate the distribution and abundance of veins at Site 1256.

Site 1256 has an average vein density of ~27 veins per metre that occupy ~1% by volume of core. The abundance and volume of veins is low compared to Sites 504 (31 vn/m) and 1149 (34 vn/m, 2.3 vol%), comparable to Site, 801 (24 vn/m), and high compared to Sites 1179 (18 vn/m) and 1224 (18 vn/m). At Site 1256, breccia matrixes and vein nets make up a further 1.37 % bringing the total volume of vein and breccia minerals to 2.37%. Veins/breccia matrices formed within the low temperature alteration regime make up ~2.3% of the total volume crust with an average vein density of ~21 veins per-metre. Saponite makes up the majority of veins that occur at low temperature at Site 1256 (78 % of vein minerals) and they range in thickness from <0.1 mm (sinous, hairline) to large 15 mm veins. They occur from the top of the basement to a depth of 850 msb and saponite is typically the major constituent in veins containing pyrite, quartz and chalcedony (Figure 4.14B). More rarely, saponite forms an accessory phase in calcite, anhydrite, and laumontite veins in which saponite is overprinted (Figure 4.2.8A). Celadonite occurs as a significant vein forming mineral (8% of veins) phase that is present down to a depth of 644.1 msb although it is not present in the inflated flows. Most celadonite is present as a minor phase with iron-oxyhydroxide which, in many veins, is overprinted by saponite (Sample 309-1256D-91R-1, 67-69 cm, Figure 4.15A). Most celadonite veins are ~0.2 mm thick although they range from <0.1 mm to 3mm. Iron-oxyhydroxides are a major vein forming mineral at Site 1256, being present in 11.3 % of veins. Veins range from 0.1 mm to very large 15 mm veins, for example 309-1256D-85R-2, 65-95 cm (Figure 4.14D). Iron oxyhydroxide veins typically occur in conjunction with celadonite, and within brown or black halos. They are not observed below ~676 msb (Figures 4.12 and 4.13). Iron-oxyhydroxide may also occur together

with carbonate, quartz and chalcedony. A minor but significant proportion of veins consist of quartz and chalcedony (8% of veins). They occur throughout the extrusives (Figures 4.12 and 4.13) with no real change in volume. Veins containing silica range from 0.1 to 10 mm thick. Silica veins form after saponite and iron-oxyhydroxide, commonly forming in the cores of veins or discrete by overprinting previous mineralogy. Anhydrite and carbonate commonly overprint silica in veins.

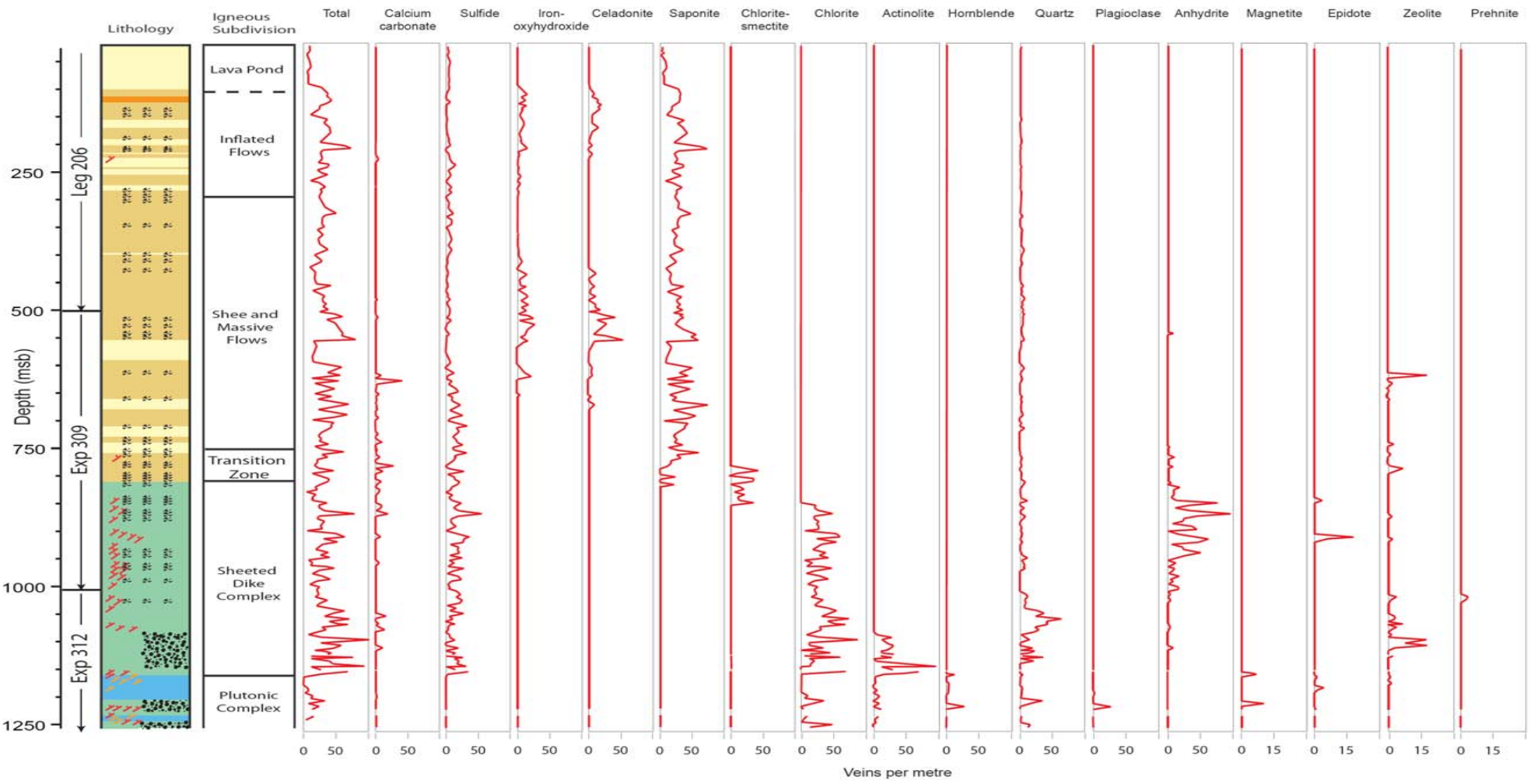

Figure 4.12. Distribution of secondary mineral veins with depth in Hole 1256D. Numbers of veins are normalized to account for core recovery. Leg 206 data from Wilson et al., (2003). Exp 309 and 312 data sourced from Teagle et al., (2006).

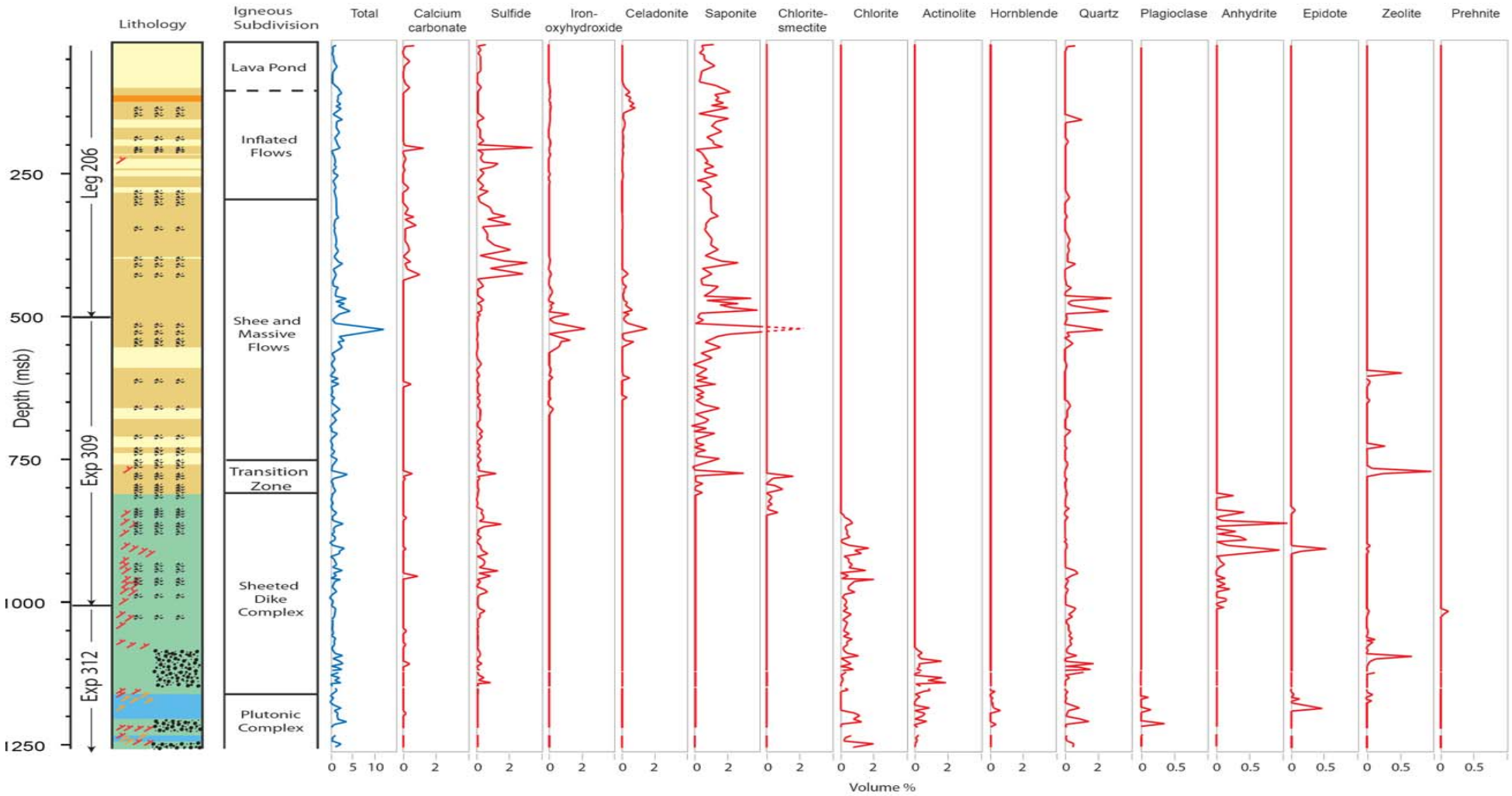

Figure 4.13. Abundance of secondary mineral veins with depth in Hole 1256D. Volumes are normalized to account for core recovery. Leg 206 data from Wilson et al., (2003). Exp 309 and 312 data sourced from Teagle et al., (2006).

Carbonate in veins (Figure 4.15C) occurs as a minor (0.4 % of veins), late stage phase that cross-cuts previous phases, including celadonite, iron-oxyhydroxide and saponite. Carbonate veins are most frequent at depths deeper than ~500 msb (Figure 4.12), yet the volume is comparatively high at shallow depths (Figure 4.13). Despite more numerous veins containing carbonate, carbonate forms a much smaller proportion of the vein material at depth. Anhydrite in the lower portion typically makes up a major constituent of the vein, for example 309-1256D-118R-1, 42-46 cm (Figure 4.15A). In terms of overprinting, two groups of anhydrite are observed; 1) anhydrite in veins overprints all secondary phases, including silicates, and 2) anhydrite which is cross-cut by quartz (e.g. Sample 309-1256D-118R-1, 11-13 cm).

Other minor phases present in low temperature veins include late-stage zeolite and sulphides (Figure 4.15B), including pyrite and chalcopyrite which increase in abundance in the lower half of the extrusives (Figures 4.13 and 4.14).

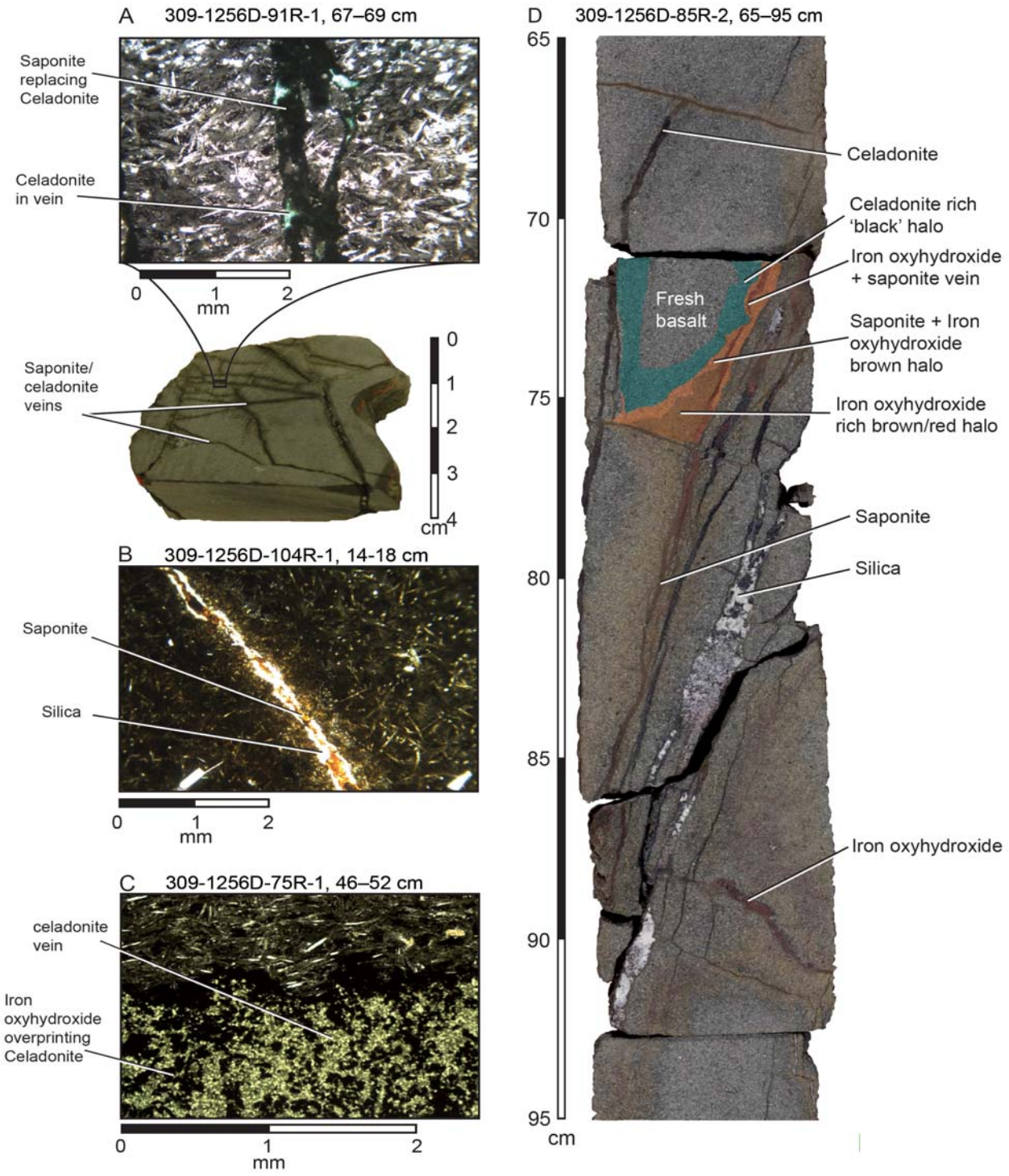

Figure 4.14. Low temperature vein mineral and some halo types present at ODP/IODP Site 1256. A) Saponite replacing an earlier celadonite vein in sample 309-1256D-91R-1, 67-69 cm. B) Saponite and Silica vein flanked by a mixed 'black' and brown halo in sample 309-1256D, 94R-1, 14-18 cm. C) Celadonite vein partially overprinted by iron-oxyhydroxides in 309-1256D-75R-1, 46-52 cm. D) Core interval exhibiting typical low temperature alteration at ODP/IODP Site 1256. C and D modified from Teagle et al., (2006).

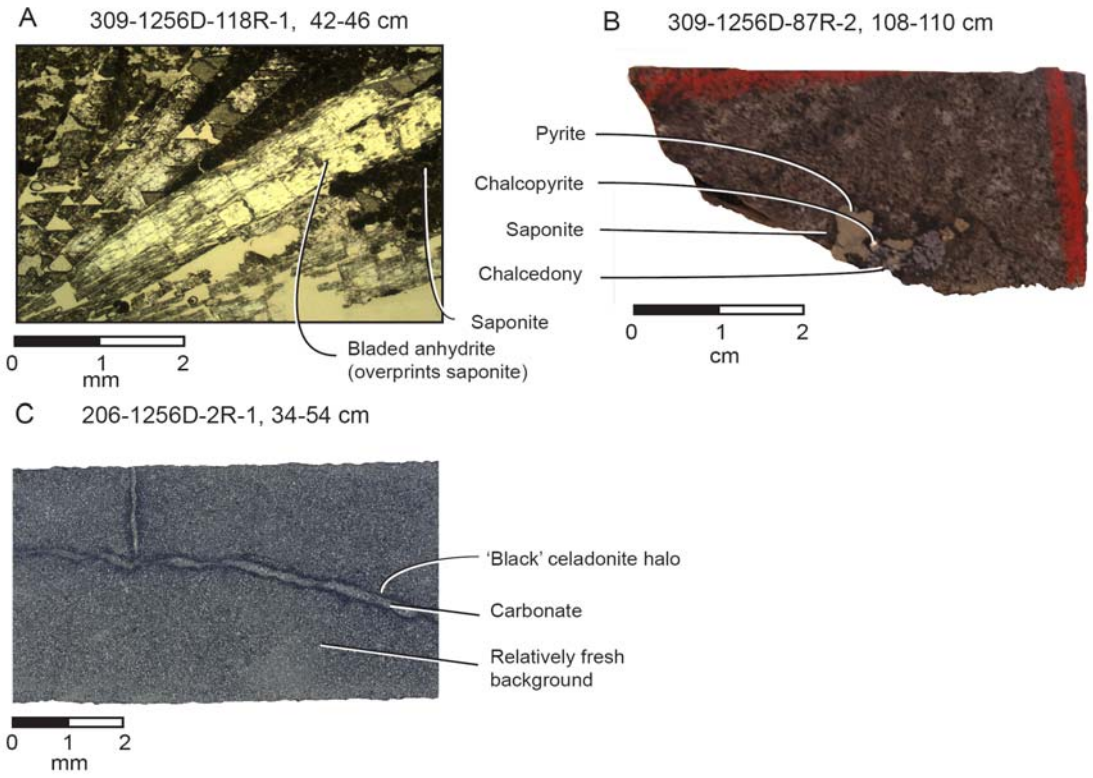

Figure 4.15. Minor low temperature vein forming minerals at ODP/IODP Site 1256. A) Anhydrite overprinting saponite in a vein in sample 309-1256D-118R-1, 42-46 cm (plane polarised light) after Teagle et al., (2006). B) Patchy pyrite, chalcopyrite, chalcedony and saponite vein in moderately altered patchy basalt, sample 309-1256D-87R-2, 108-110 cm. C) Carbonate vein with 'black' halo in Sample 206-1256D-2R-1, 34-54 cm (IODP Janus database http://iodp.tamu.edu/janusweb/imaging).

4.2.1.3 Halos

Low temperature alteration halos at Site 1256 are largely governed by zones of fracturing and surfaces which are exposed to circulating fluids. Halos typically flank veins, brecciated zones, and cooling fractures in a similar fashion to alteration halos observed at other basement sites (this study and e.g., Plank., et al, 2000; Kanazawa., et al, 2001; Wilkens et al., 1993; Orcutt et al., 2003; Morberly, 2003; Alt et al., 1996; Teagle et al, 1996; Alt et al, 1996; Stephen et al., 2003). Initial studies into the nature of halos at Site 1256 by Wilson et al., (2003) and Teagle et al., (2006) identified black, brown, light green, light grey, dark green halos, pyrite rich halos and mixed halos and recorded their distribution in the extrusive section of Site 1256 (Figure 4.16). Mixed halos are the result of overprinting, which can vary from sample to sample. These halos are by far the most common, making up ~1% of the total volume of core.

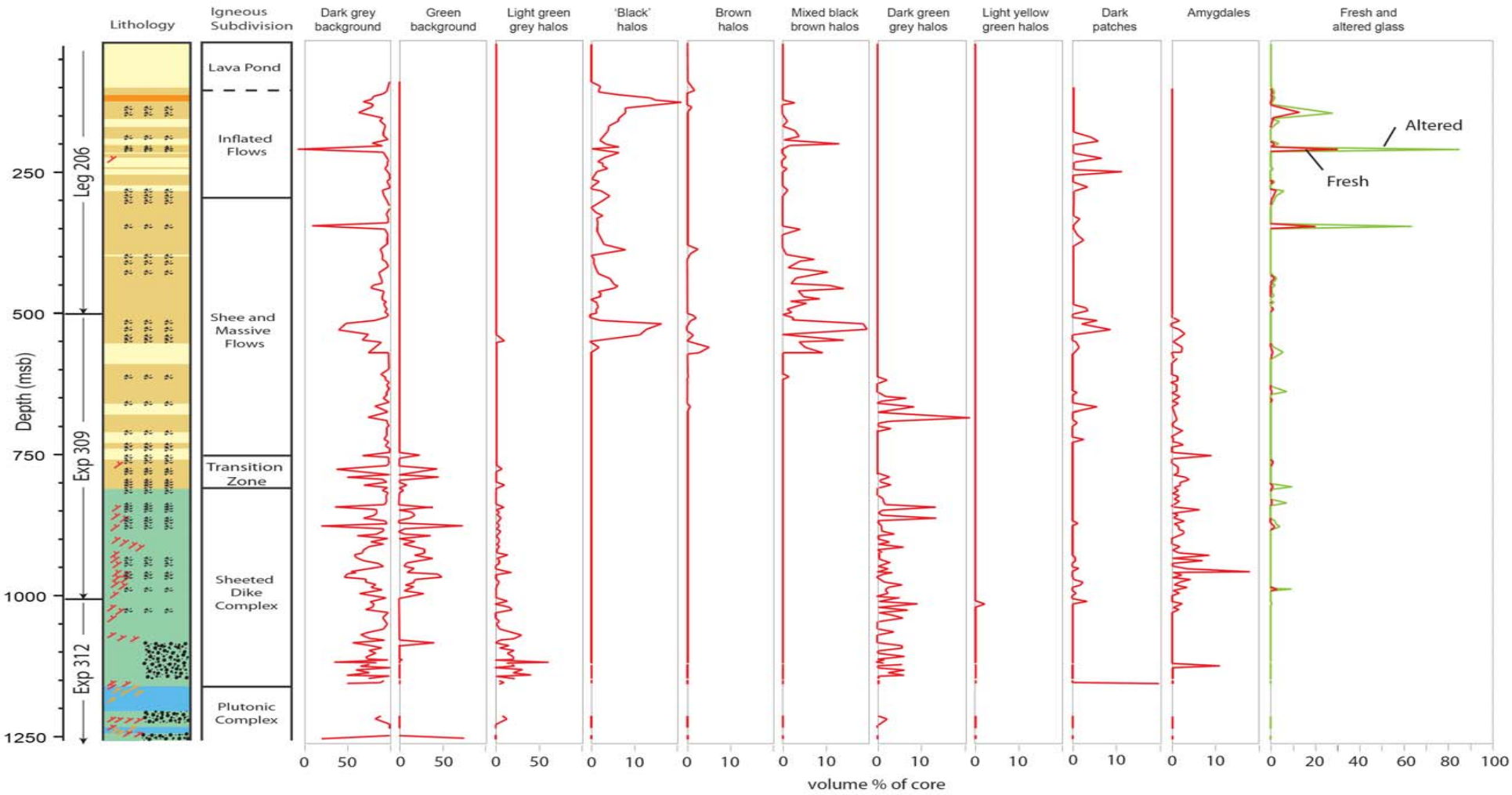

Figure 4.16. Abundance of alteration styles, amygdales and glass vs. depth in Hole 1256D. Volumes are normalized to account for core recovery. Leg 206 data from Wilson et al., (2003). Exp 309 and 312 data sourced from Teagle et al., (2006).

Brown and black halos make up 0.1% and 0.45% of the core and they occur throughout the Lavas to a depth of 754-820 mbsf (Figure 4.17D) (Teagle, et al., 2006).

Black halos is a blanket term used to define dark green, dark grey, and black halos at Site 1256, that are all characterised by the presence of celadonite together with saponite which replaces olivine and interstitial material and fills pore spaces (Figure 4.17C). Saponite typically overprints celadonite within these halos and is usually more abundant than celadonite. Minor later iron-oxyhydroxide can stain celadonite and saponite (Figure 4.17B). Halos range in width from 0.1 to 20 mm wide. Brown halos are associated with iron-oxyhydroxides and they occur adjacent to veins containing iron-oxyhydroxides, celadonite, saponite and silica minerals. The brown-orange-brown colouration is due to staining of the primary mineralogy and the filling of voids, vesicles, and replacement of olivine by iron oxyhydroxides. Brown halos are much narrower than either black or mixed halos, ranging in thickness from 0.1-5 mm.

Low temperature mixed halos are the result of brown halos overprinting black celadonite-rich halos. Mixed halos coincide with the occurrence of black and brown halos (Figure 4.16), with the deepest mixed halo occurs at 667 msb (Sample 309-1256D-101R-1, 133-134 cm). These halos vary greatly in width and extent of overprinting, ranging from 0.3 mm to 50 mm thick which may or may not exhibit banding or zoning within the halo. Zoning, for example in Section 309-1256D-85R-2, 65-95 cm reflects the variation in the intensity of iron-oxyhydroxide, saponite and celadonite emplacement.

Pyrite rich halos occur at 643 msb through to 807 msb. Dark green to dark grey halos in this case may either contain disseminated sulfides or a 0.3-6 mm pyrite front (Figure 4.17A). The halos may contain chlorite/smectite, thus they may represent slightly higher temperature alteration than the celadonite, saponite, iron-oxyhydroxide assemblage that is typical of low temperature seawater alteration. These halos are rare, making only 0.06% of the recovered core.

The predominant halos below 553.3 mbsf are dark to light green and dark to light grey halos (Teagle et al., (2006). These halos are characterised by the presence of saponite and the absence of celadonite and iron-oxyhydroxides. These halos can be distinguished from the ‘dark green’ halos observed within the celadonitic ‘black halo’ group by the lack of any blue hue. These green-grey halos are most common in Sections 309-1256D-91R-1 to 128R-1 (Figure 4.18C) and they range from 0.1 to 12

mm in width. Saponite partially replaces plagioclase, clinopyroxene, olivine phenocrysts and amygdales, and it fills vesicles.

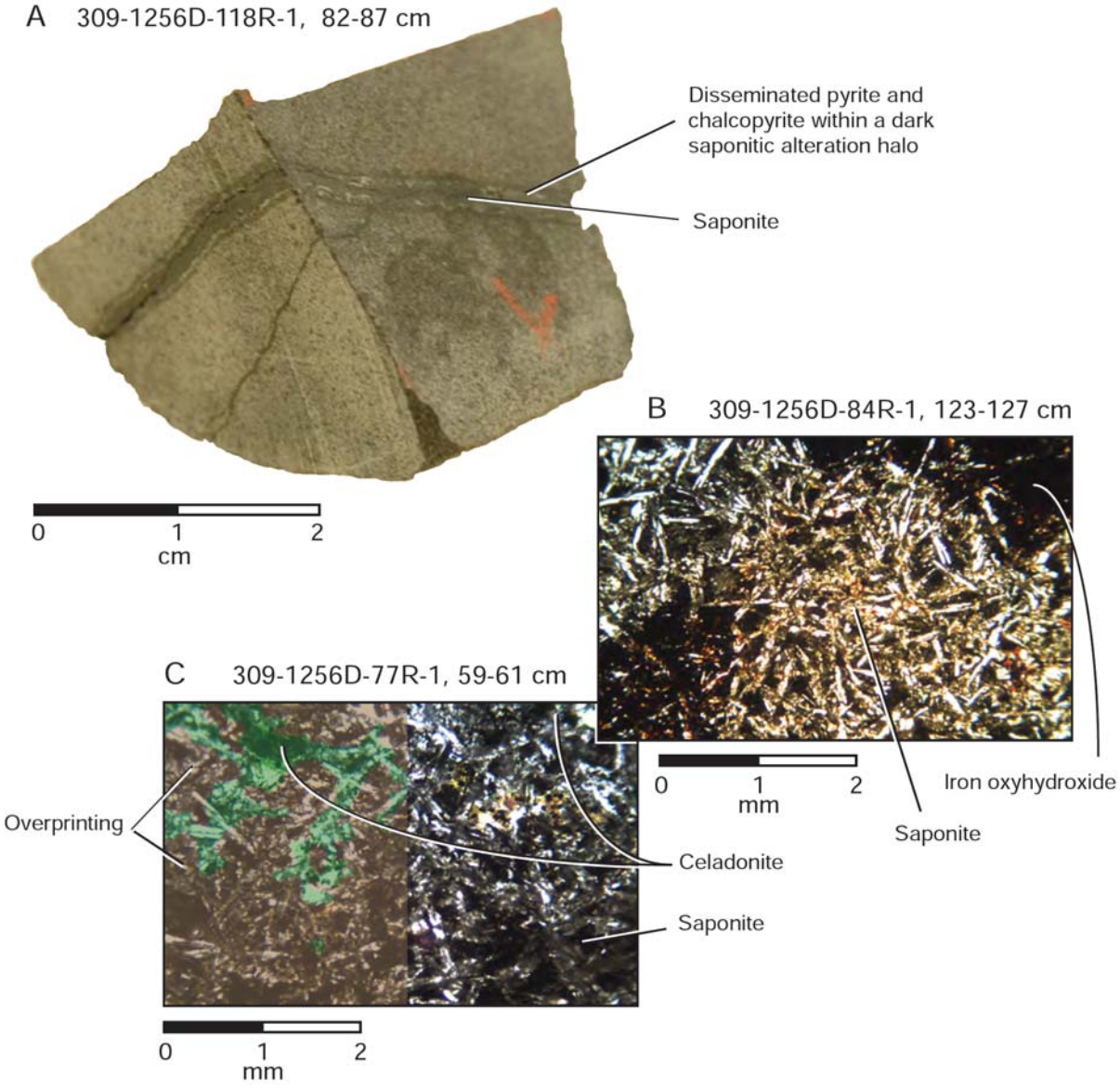

Figure 4.17. A) Pyrite rich dark grey saponite halo in Sample 309-1256D-118R-1, 82-97 cm. B) Example of iron oxyhydroxide overprinting a saponite halo in Sample 309-1256D-84R-1, 123-127 cm. C) 'Black' celadonite halo overprinted by a saponite halo in Sample 309-1256D-77R-1, 59-61 cm. Photomicrographs were taken in plane polarised light.

4.2.1.4 Breccias

Low-temperature breccias at Site 1256 comprise in-situ fragments of basalt or glass held together by a saponite and/or celadonite matrix (‘basaltic breccias’) or hyaloclastite, which is made up altered glass fragments in a matrix that largely, consists of saponite. Low temperature breccias make up ~0.5 % by volume of the recovered extrusives.

Basaltic breccias span a transition from vein nets, incipient brecciation to brecciation and they are composed of moderately to highly altered, angular in-situ basaltic clasts and minor glass fragments with a matrix of saponite and celadonite. Minor iron-oxyhydroxide, carbonate and silicates may be present. Sample 1256D 108R-2, 11-28 cm (676 msb) is a good example of a basalt breccia (Figure 4.18C). Clasts range in size from 1 mm to 80 mm. The basaltic clasts can have green dark grey or black alteration halos and the glass clasts are completely altered to saponite.

Hyaloclastite is present in small amounts throughout Site 1256 extrusives. They consist of angular to rounded, fresh to highly altered glassy clasts ranging in size from 2 mm to 50 mm in a matrix composed of saponite, numerous <1 mm completely replaced altered glass, and other minor phases. The smaller clasts show the greatest degree of alteration (>80 % secondary mineral replacement).

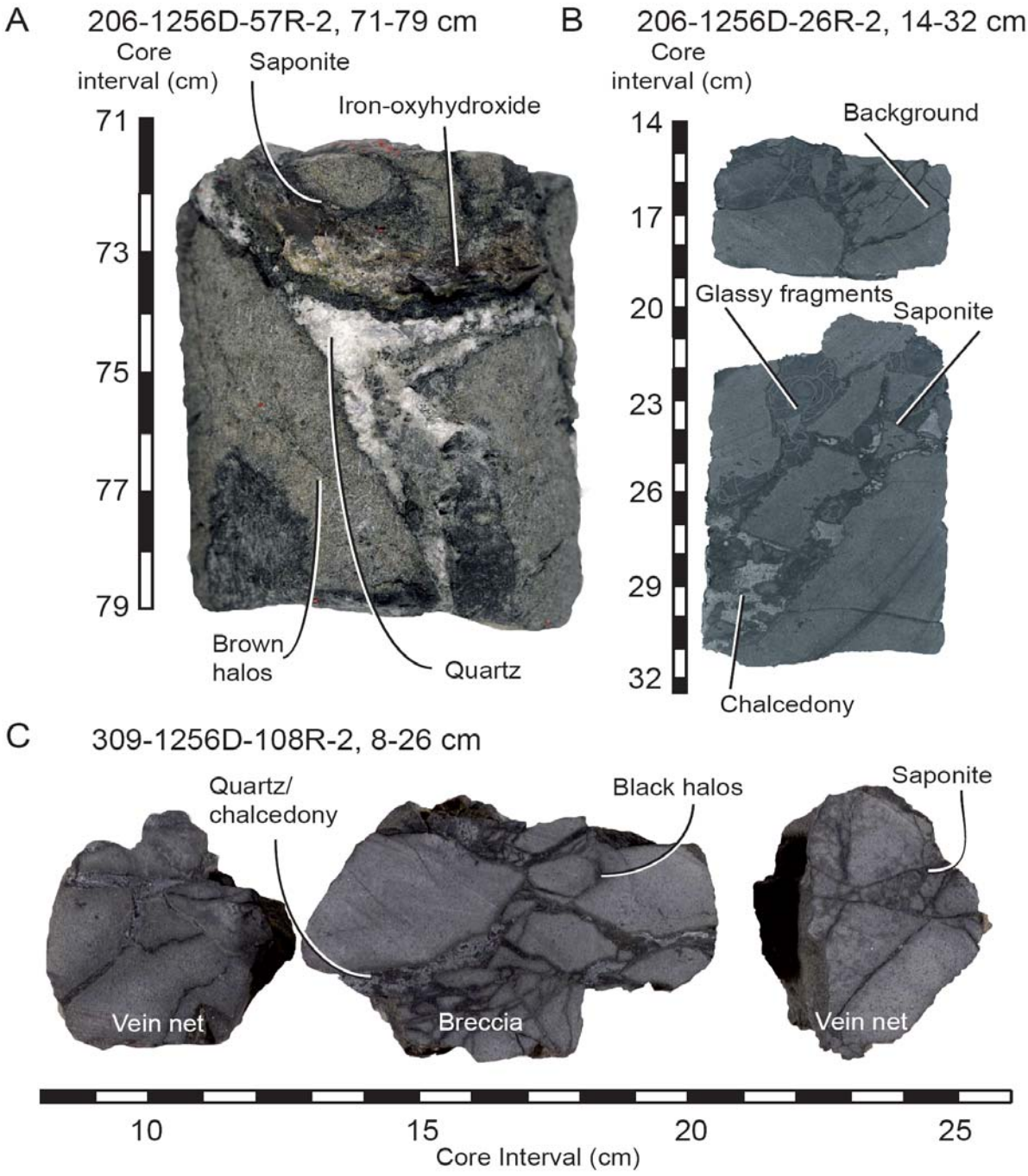

Figure 4.18. Examples of low temperature basaltic breccias. A) Example of basaltic breccia with saponite, iron-oxyhydroxide and quartz. B) basaltic breccia with relatively fresh clasts and a matrix of glassy fragments, saponite and chalcendony. C) Example stages of brecciation, including vein nets, and incipient breccia. A and B= Wilson et al., (2003). Teagle et al., (2006) for (C).

Alteration is most intense on the edges of the angular clasts, whereas elsewhere replacement is incomplete. Some clasts, that were originally angular, have alteration rims on the clasts that have ultimately led to rounded kernels with zones relating to alteration intensity (Figure 4.19A). Figure 4.19D illustrates how glass fragments can

become zoned and rounded. In some larger clasts, rare fresh glass may be preserved for example a large clast in Sample 206-1256D-51R-2, 14-16 cm (Figure 4.19B) is comprised almost entirely of fresh glass.

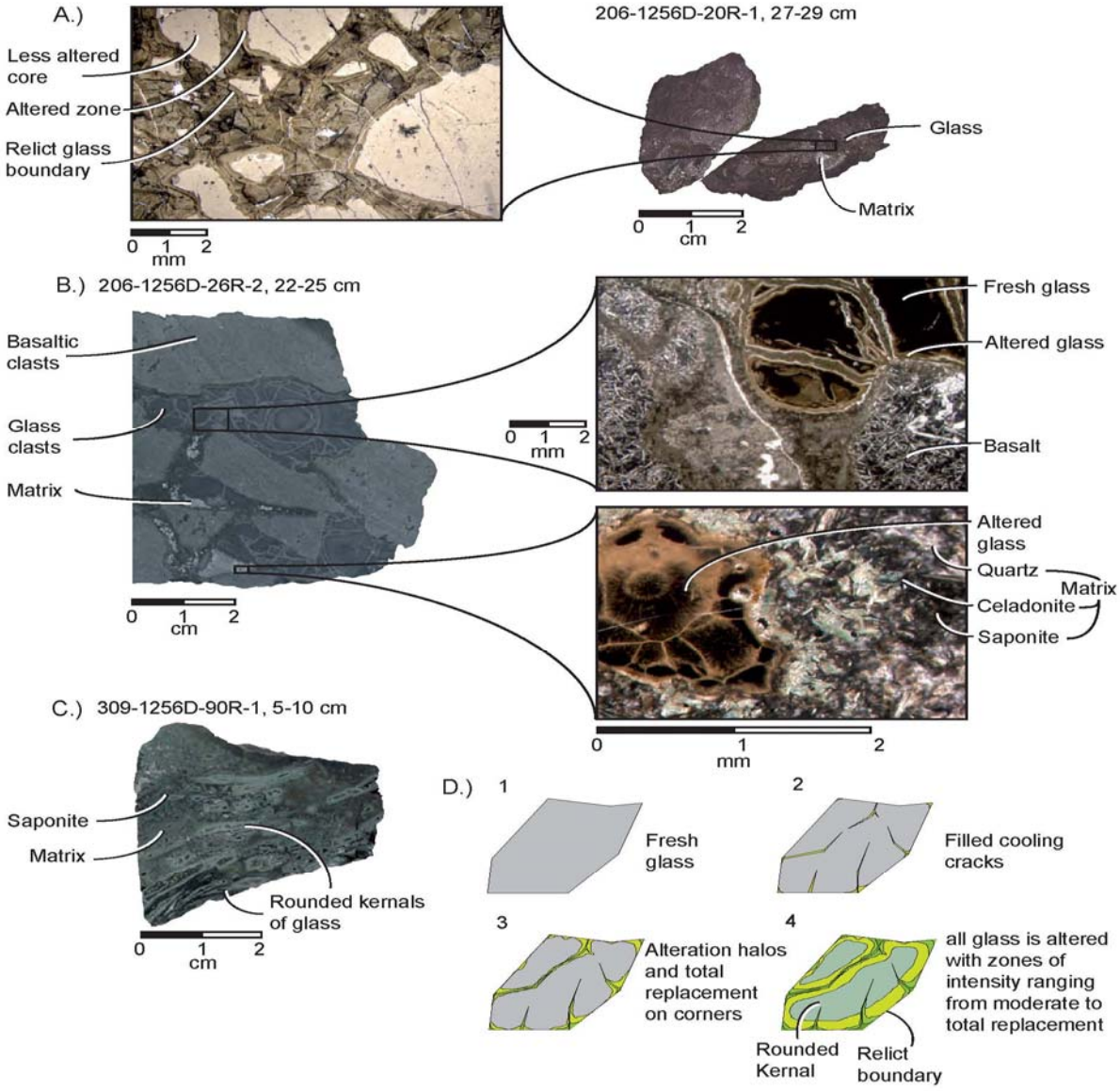

Figure 4.19. Hyaloclastite breccias. A) Glass breccia with moderate alteration and zoned glass clasts, B) Mixed basaltic/hyaloclastite breccia where basalt clasts are surrounded by moderately fresh glass fingers that have since brecciated, and in some cases altered. C) Hyaloclastite breccia with near total alteration of glass fragments. Elongate glass kernels have a preferred orientation and they are all altered to saponite, D) Step by step alteration sequence for glass fragments observed at ODP/IODP Site 1256. Photomicrographs are sourced from Wilson et al., (2003).

This sample (206-1256D-51R-2, 14-16 cm) contains numerous cooling fractures filled with saponite, which may represent incipient brecciation within the clast. Most glass clasts contain cooling fractures that are filled with saponite, chalcedony and/or pyrite (Figure 4.19B). The matrix is composed largely of saponite, however a number of minor phases can be present. For example, in Sample 309-1256D-90R-1, 5-10 cm (Figure 4.19C) the matrix is composed of 60 % saponite, 15 % quartz, 10 % pyrite, 10 % late-stage calcite and 5 % anhydrite (Teagle et al., 2006). Other intervals, such as 206-1256D-57R-1, 0-12 cm, and 62-78 cm are cemented by saponite, chalcedony, red jasper, large (mm sized) pyrite, and anhydrite (Wilson et al., 2003).

4.2.1.5 Intensely altered section

A 41 cm long intensively altered portion of core at 398.06 msb was recovered from Hole 1256D (Figure 4.20) Core 206-1256D-57R is 80-90% altered to celadonite and iron-oxyhydroxide, which, in hand specimen imparts a variable blue-green to brick red colouration (Figure 4.20B). The upper contact between the altered material and less altered dark grey basalt (Interval 206-1256D-57R-2, 116-120 cm) is sharp (Figure 4.20A).

In this highly altered zone, olivine is replaced by celadonite and iron-oxyhydroxide and clinopyroxene is replaced with a colourless smectite ± iron-oxyhydroxide (Figure 4.20C). Plagioclase is partially replaced by albite and a colourless phyllosilicate similar to that which replaces olivine. Rarely replacement is complete, leaving behind plagioclase pseudomorphs. Veinlets (<0.01 mm thick) of iron-oxyhydroxide and celadonite are numerous throughout the intensely altered section (Figure 4.20D). Vugs and patches are present within the 'red brick' portion of the altered basalt (Figures 4.2.13B and C). These range in size from 0.5 to 3mm and they are filled with the colourless phyllosilicate ± celadonite ± iron-oxyhydroxides. Larger vugs have rims of iron-oxyhydroxide followed by celadonite and a core of quartz and/or carbonate (Figure 4.20 c).

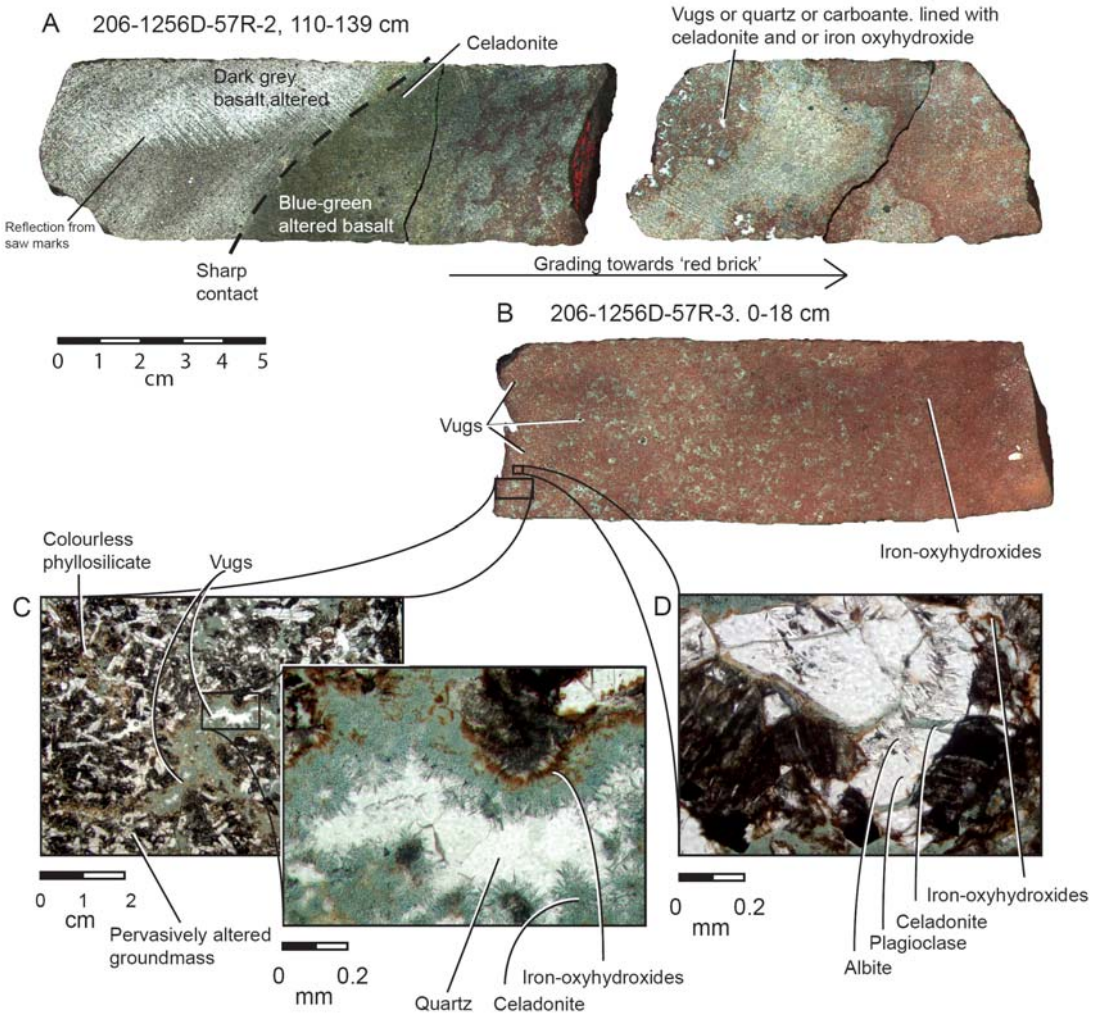

Figure 4.20. Intense low temperature alteration in Core 206-1256D-57R. A) Sharp transition from dark grey slightly altered basalt to strongly altered, celadonite rich alteration which grades to an iron-oxyhydroxide rich 'red brick' layer. B) Continuation of red brick, C) photomicrograph of vugs and intensely altered groundmass. Inset shows vug composed of iron-oxyhydroxides, celadonite and quartz (plane polarised light). D) Photomicrograph with primary plagioclase replaced by albite with veinlets of iron-oxyhydroxide and celadonite (Plane polarised light). Photomicrograph D is from Wilson et al, (2003). Core photos sourced from the ODP/IODP Online core images database.

4.2.1.6 *Summary*

Low temperature alteration at ODP/IODP Site 1256 is pervasive and ranges from slight to intense. Five secondary minerals assemblages are identified in the upper portion of Site 1256. These include 1) Celadonite ± saponite, which comprises dark celadonitic halos and patches surrounding celadonite veins, 2) Saponite ± iron oxyhydroxides that

form veins, fill vesicles and partially replace the groundmass to form green to brown halos and patches. 3) Iron-oxyhydroxide ± saponite, and sulphides form red/brown halos and patches, around saponite/iron-oxyhydroxide veins. These minerals also fill vesicles. 4) Quartz/Chalcendony/amorphous silica ± iron-oxyhydroxides form late stage veins and rarely fill vesicles and interstices. 5) Late stage carbonate, zeolite and anhydrite forming veins, filling previous veins filling vesicles and rarely present in alteration patches. The variation in alteration intensity throughout the extrusive section of Site 1256 suggests that, rather than a monotonous decrease in seawater interaction, that alteration intensity is controlled by primary basement variation, including the morphology of the lavas, distribution of fracturing, subtle changes in the composition and texture of the lavas (Teagle et al., 2006).

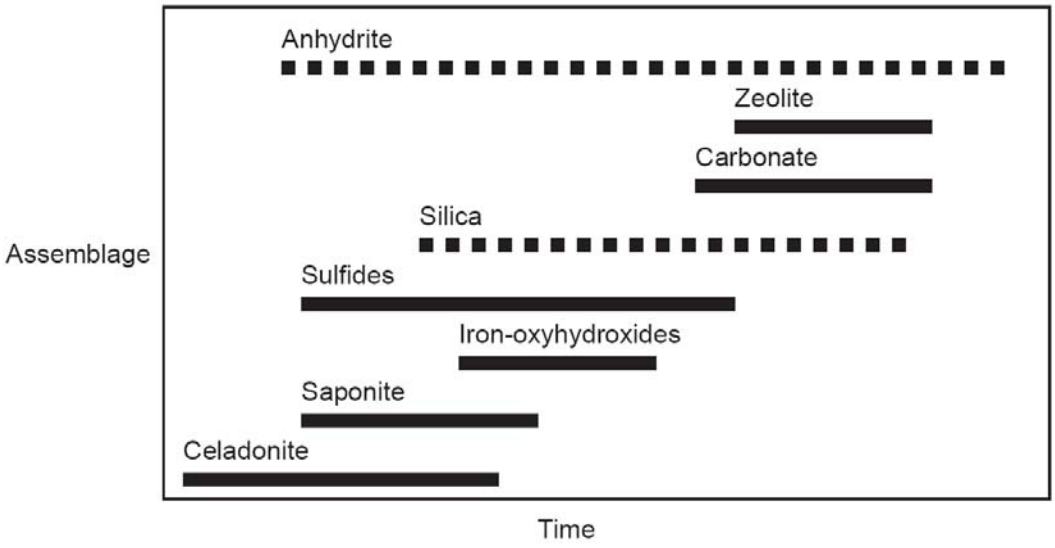

Figure 4.21. Timing of low temperature secondary mineral paragenisis at Site 1256.

An increase in temperature and, as a consequence, evolution in fluid composition is reflected in the partial replacement of primary plagioclase with albite and saponite below 375 msb (Figure 4.8). The presence of hydroschorlomite (Ti, Ca, Fe rich hydrogarnet) at depths of 411 to 669 mbsf further suggests that primary titanomagnetite was altered within this region of slightly warmer, more evolved fluids (Teagle et al., 2006). Fluid evolution is more apparent towards the base of the extrusive rocks with the decreased abundance of iron-oxyhydroxide and celadonite (Figure 4.8). Because anhydrite undergoes retrograde solubility at temperatures below ~100^{o}C, the presence of anhydrite, reflects an increase in temperature towards the lithological transition zone.

Petrographic observations including cross-cutting relationships, overprinting and vein geometry made by Wilson et al, (2003); Teagle et al., (2006), and this study provide insights into the timing of secondary mineral petrogenesis at ODP/IODP Site 1256. Figure 4.21 indicates the timing of secondary mineral paragenesis and Figure 4.22 illustrates the temporal relationships between each assemblage and the variation with depth.

Celadonite appears to be the earliest mineral phase becasue it is overprinted by all other phases. Celadonite initially fills fissures and voids and partially replaces the groundmass and fills vesicles within the confines of mm to cm sized halos that flank the celadonite veins. It has been suggested that the black halos form under anoxic conditions within 1-2 M.y. of lava emplacement (Böhlke et al, 1980; Honnorez, 1981; Laverne, 1993; Alt, 2004). Emplacement of saponite and iron-oxyhydroxides occurs after celadonite under oxidizing conditions, and commonly these phases overprint or replace celadonite. This overprinting is responsible for the variably mixed halos within ODP/IODP Site 1256 lavas. From ~600 to 731 mbsf, black and brown halos are absent and the initial alteration phase appears to be saponite, together with pyrite. These low temperature phases represent a slightly more evolved fluid in which limited wall rock interaction took place. Silicates appear to have formed after saponite followed by late stage carbonate and anhydrite. One anhydrite sample in the extrusives is overprinted by saponite, which suggests that there was a separate, earlier fluid that may be more evolved. Overall alteration within the extrusives remains at low temperature with slight elevation in temperature and wall rock interaction with depth.

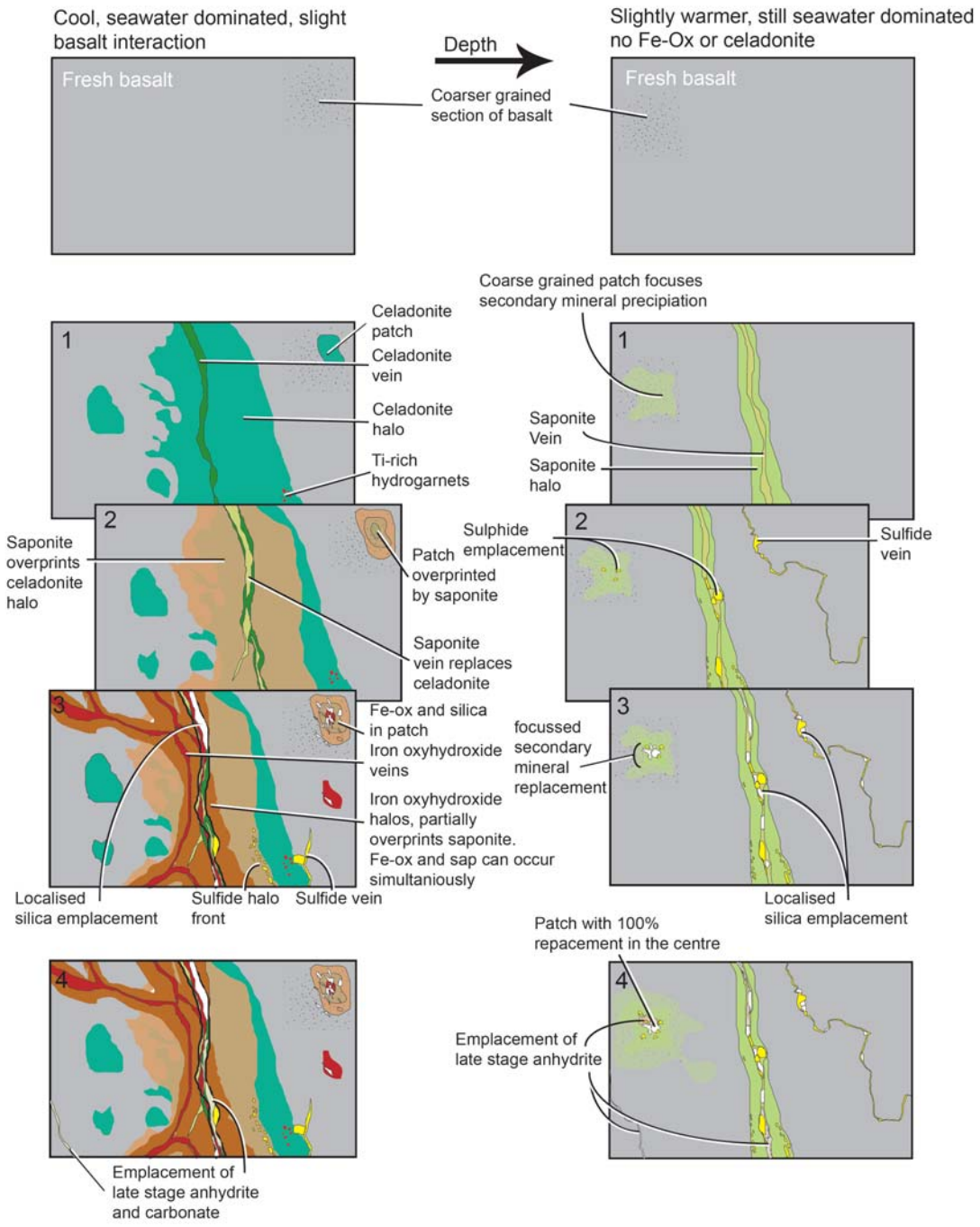

Figure 4.22. Summary of low temperature alteration at ODP/IODP Site 1256. Including common alteration styles and relative timing of secondary mineral paragenisis. Two regimes are suggested, The more shallow low <100°C assemblage consists of celadonite, saponite, iron-oxyhydroxides, carbonates and accessory quartz and chalcedony, carbonate ± zeolite, and rare anhydrite. The deeper, slightly elevated ~100 to ~150°C assemblage consists of saponite, pyrite ± chalcopyrite, minor silica, and anhydrite ± zeolite.

4.2.2 High temperature alteration

High temperature hydrothermal alteration is reported at ODP/IODP Site 1256 from a depth of 777 msb to the base of ODP/IODP Hole 1256D (~1250 msb). The start of high temperature hydrothermal alteration is marked by the first presence of actinolite, prehnite, titanite, and epidote at 777, 782, 801, and 845 msb, respectively (Figure 4.23). A high temperature hyaloclastite and a mineralised volcanic breccia in Sections 309-1256D-123R and 122R respectively, marks the beginning of hydrothermal alteration and the end of the transition from saponite to chlorite. The distribution of secondary minerals at Site 1256 (Figure 4.8) outline the change from low temperature dominated alteration to hydrothermal alteration. High temperature hydrothermal alteration at ODP/IODP Site 1256 varies from slight to intense with replacement of the primary igneous groundmass forming alteration patches, breccias, veins, and alteration halos. Detailed description and discussion of high temperature alteration at Site 1256 can be found in Teagle et al, (2006). Because this study will discuss only low temperature, seawater dominated alteration across a range of < 200 m sub-basement Sites, this section only provides a brief summary of the work by Teagle et al, (2006).

4.2.2.1 *Lowermost lavas and sheeted dykes*

From depths of 767.7 msb to 1060 msb chlorite is the most common secondary mineral in the sheeted dykes (Figure 4.8). Colourless to green, with pale green to colourless pleochroism in thin section, it pseudomorphically replaces plagioclase and more rarely clinopyroxene, fills vesicles, and veins (Teagle et al, 2006). Associated minerals include albite, which partially to completely replace plagioclase and forms in alteration halos and patches. Pyrite and rare chalcopyrite may form in alteration halos and patches and fills numerous multiminerallic veins and breccia matrixes respectively (Figure 4.23).

Actinolite occurs from 777 msb, and it is a major phase at depths greater than 1060 msb (Figure 4.8). Actinolite + chlorite ± secondary magnetite and titanite replaces clinopyroxene in the groundmass and phenocrysts (Figure 4.23). Below ~1098 msb, wispy brown pleochroic crystals of hornblende ± actinolite replace clinopyroxene and can from veins with associated halos. Quartz is abundant throughout ODP/IODP Site

1256, especially at ~1000 to 1150 msb and it is common in multiminerallic veins, alteration patches, and discretely replacing plagioclase.

Primary titanomagnetite at intervals 1005 to 1064 msb is partially replaced by titanite to varying intensities, depending in crystal size with larger crystals being the worst affected (Teagle et al., 2006). Late stage minerals that commonly occur in veins, or filling minor voids and halos/patches include prehnite, carbonates, anhydrite, and laumontite. Prehnite occurs at roughly the same depth as actinolite 782 msb and it can be identified as anhedral crystals with moderate relief and brilliant mid second order interference colours (Figure 4.23).

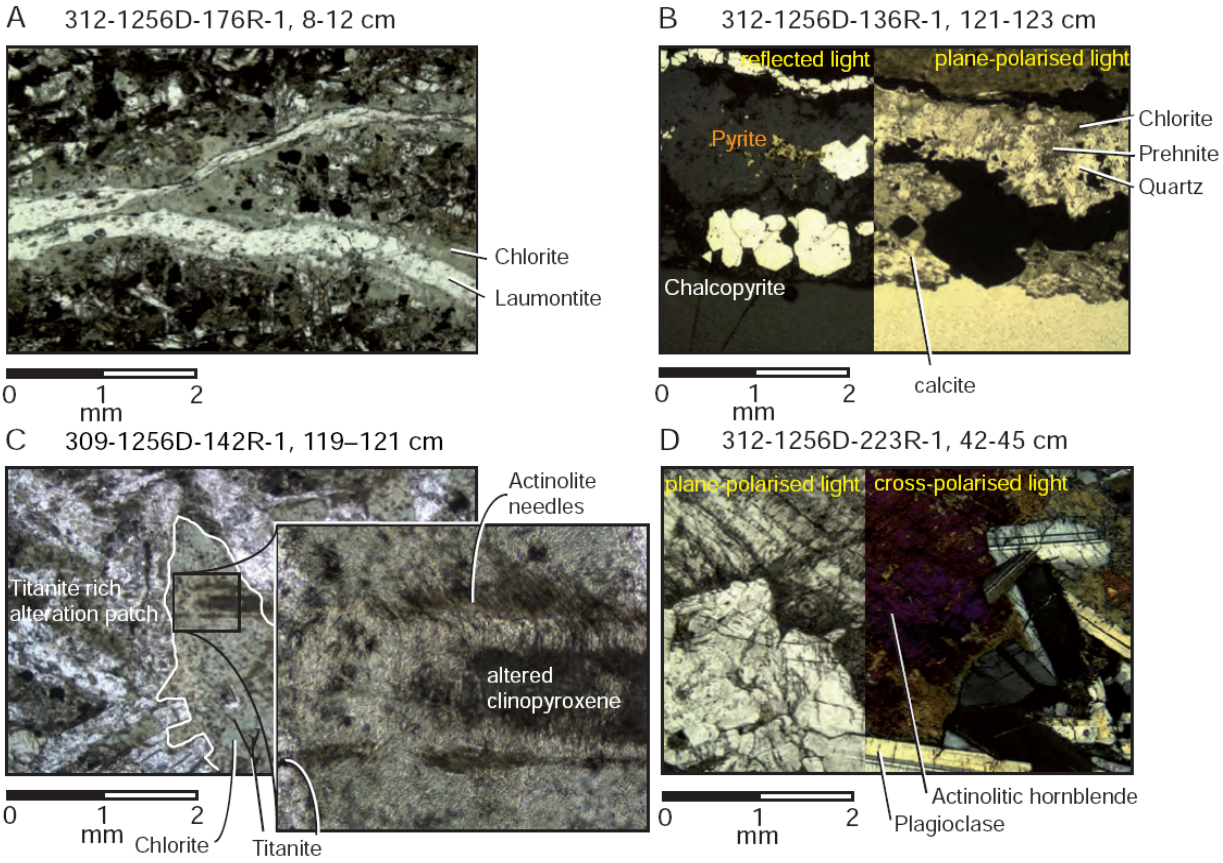

Figure 4.23. Examples of high temperature secondary minerals encountered within dykes. A) Laumontite and chlorite vein with a narrow chlorite halo (plane polarised light), B) complex vein of quartz, prehnite and chlorite with a lining of chalcopyrite and unevenly distributed pyrite in the centre. A later calcite fill is shown on the bottom edge of the vein, C) An example of a titanite rich chlorite alteration patch and clinopyroxene replaced by actinolite needles growing from the centre of the pyroxene (plane polarised light), and D) Example of actinolitic hornblende replacing plagioclase. An example from the gabbros is shown since hornblende from the sheeted dykes cannot be clearly shown in a figure. Photomicrographs are taken from Teagle et al., (2006).

Carbonates remain discrete, replacing interstitial areas and partially filling veins and vesicles. Anhydrite predominantly occurs in veins and rare breccia matrixes in the upper portion of the sheeted dykes. The increased abundance of anhydrite coincides with the presence of actinolite, chlorite, prehnite, and hornblende (Figure 4.23). This suggests that the increased temperature of the fluid (>120^{o}C) allowed greater precipitation of anhydrite.

Veins formed at high temperature within the lowermost lavas and sheeted dykes are abundant, with an average of ~35 veins per metre. The abundance of veins at ODP/IODP Site 1256 increases from ~1075 to 1161 msb (Figure 4.2.5) however this may reflect the decrease in core recovery within this interval (Teagle et al., 2006). Veins are typically between 0.1, hairline width to 1.5 mm wide and are commonly flanked by narrow 1-5 mm wide alteration halos. Chlorite ± quartz, pyrite, actinolite, anhydrite, laumontite, rare calcite in veins (Figure 4.24) are ubiquitous from depths of 845.4 to 1040 msb. At depths of 753.2 to 845.4 msb chlorite occurred alongside chlorite/smectite in veins (Figures 4.12 and 4.13). Below 1040 msb, actinolite is the most abundant mineral in veins that may contain (e.g. Figure 4.24) quartz, pyrite, titanite, and accessory phases prehnite, laumontite, secondary magnetite, anhydrite and rare epidote. Sample 309-1256D-149R-1, 73-76 cm is a unique example of an epidote rich vein within the sheeted dykes (Figure 4.24).

Halos associated with chlorite veins include dark grey, dark green, light gray, light green and mixed halos (Figure 4.24). Replacement varies from 10% and 100% (average 50%) and halos compare~0.4 vol% of core. Chlorite is the dominant secondary mineral in the upper sheeted dykes pseudomorphically replacing plagioclase, interstices and filling vesicles. In addition, titanite, actinolite, albite, and pyrite form minor phases within these halos. In the lower sheeted dykes (Figure 4.24) alteration in the halos is dominated by actinolite ± albite, pyrite, and minor quartz, chalcopyrite, and prehnite.

Alteration patches with up to 100% recrystallisiation are reported within the sheeted dykes to a depth of ~1030 msb. These patches range in intensity from moderate to total and they are composed of quartz, pyrite, chlorite, actinolite, anhydrite and zeolite from the centre to the rim, and they are surrounded by a less altered patch typically containing chlorite, quartz, pyrite, anhydrite ± prehnite, (e.g. Figure 4.25). Below 1030 msb patches are dominated by actinolite rather than chlorite, with actinolite replacing clinopyroxene.

Hydrothermal breccia at Site 1256 (Interval 309-1256D-122R-2) (Figure 4.26) is composed of basaltic clasts with a cement of chlorite-smectite, quartz and pyrite. The basaltic clasts are moderately to intensively altered with green chlorite/smectite-rich halos and rare pyrite. Hyaloclastites (Sections 309-1256D-123R-1 and 136R-1) are composed of glass clasts with a matrix of chlorite-smectite, quartz, anhydrite, and disseminated pyrite (Figure 4.26). A mineralised volcanic breccia is present in Sections 309-1256D-122R-1, 122R-2, and 135R-1 (Figure 4.26). These breccias are composed of glass and basaltic clasts with a cement of saponite, anhydrite, pyrite and chalcedony. The basaltic clasts contain moderate to intense halos in which clinopyroxene is replaced by chlorite-smectite and plagioclase is replaced by albite (Teagle et al., 2006).

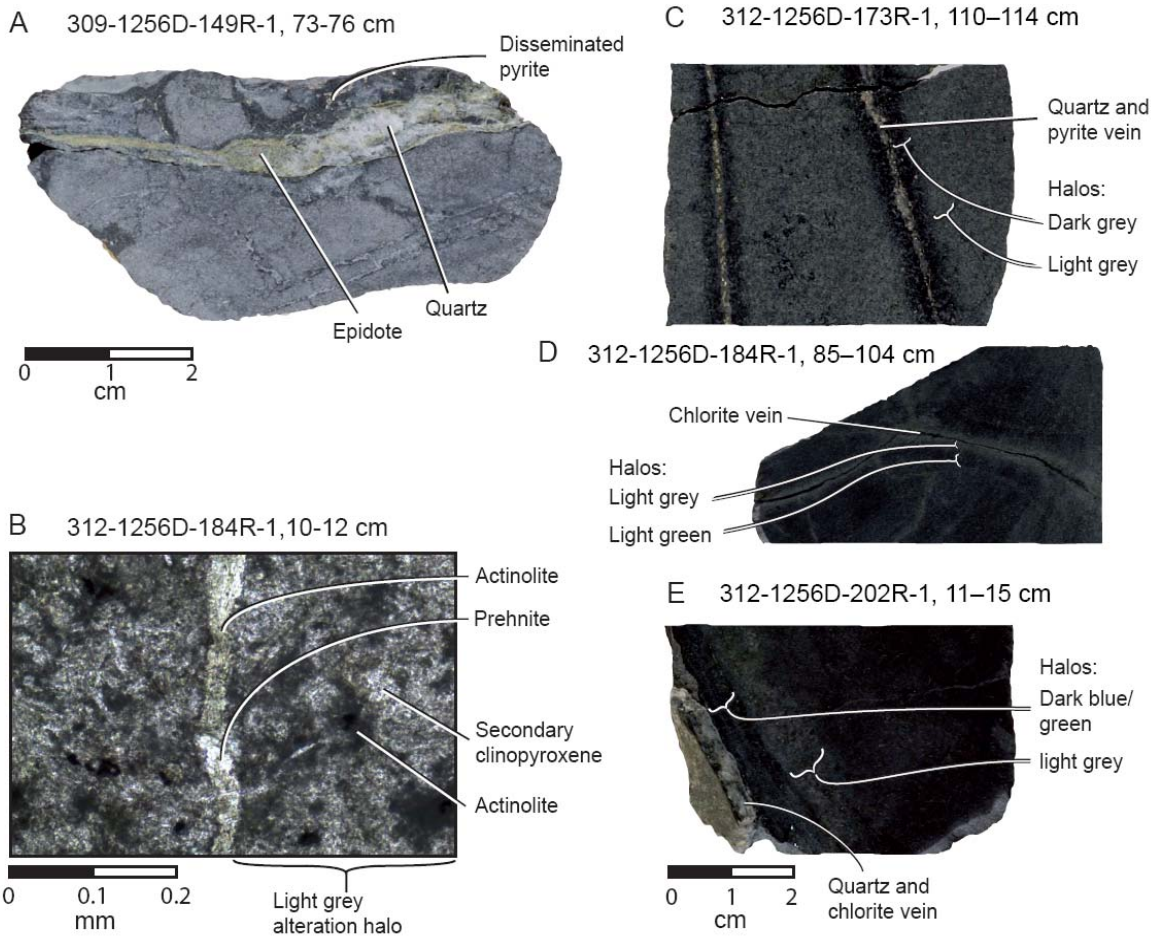

Figure 4.24. Examples of high temperature veins and alteration halos. A) Rare thick epidote and quartz vein and disseminated pyrite B) Actinolite and prehnite vein with secondary clinopyroxene and actinolite forming a light grey alteration halo (plane polarised light), C) Quartz and pyrite vein flanked by mixed dark grey and light grey halos, D) Chlorite vein with mixed light grey and light green halos, E) Quartz and chlorite vein flanked by dark blue and light grey halo. Photos and micrographs after Teagle et al., (2006).

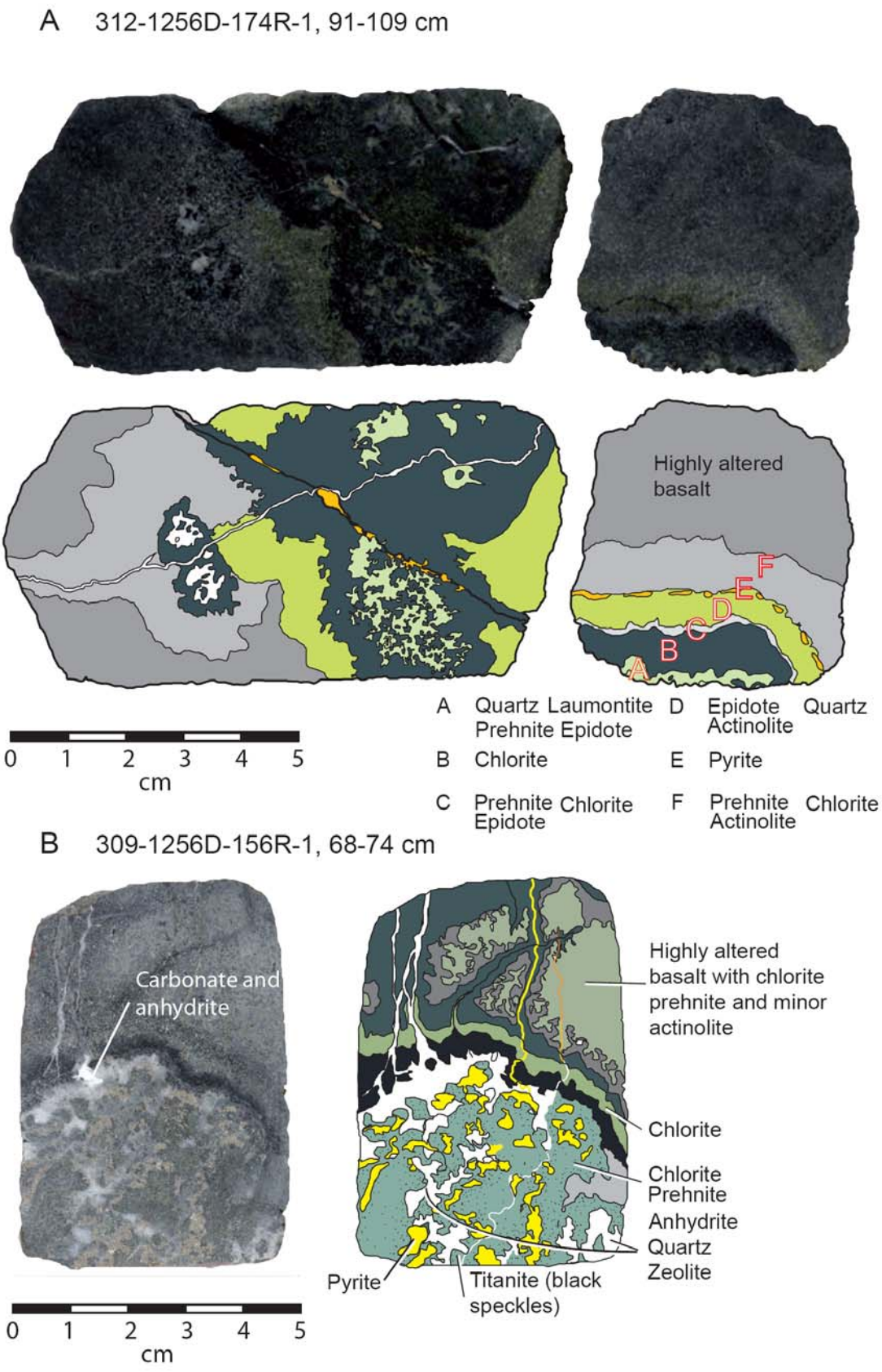

Figure 4.25. Spectacular examples of high temperature alteration patches. Photos sourced from Teagle et al, (2006)

4.2.2.3 Granoblastic dykes

The alteration of rocks encountered at 1348 to 1406.6 mbsf is profoundly different to the overlying dykes. Large portions (bands, veins or patches) have been partially and rarely, totally recrystallised to aggregates of subrounded equant crystals of secondary clinopyroxene, orthopyroxene, actinolitic hornblende, plagioclase, and minor magnetite and ilmenite (Figure 4.27).

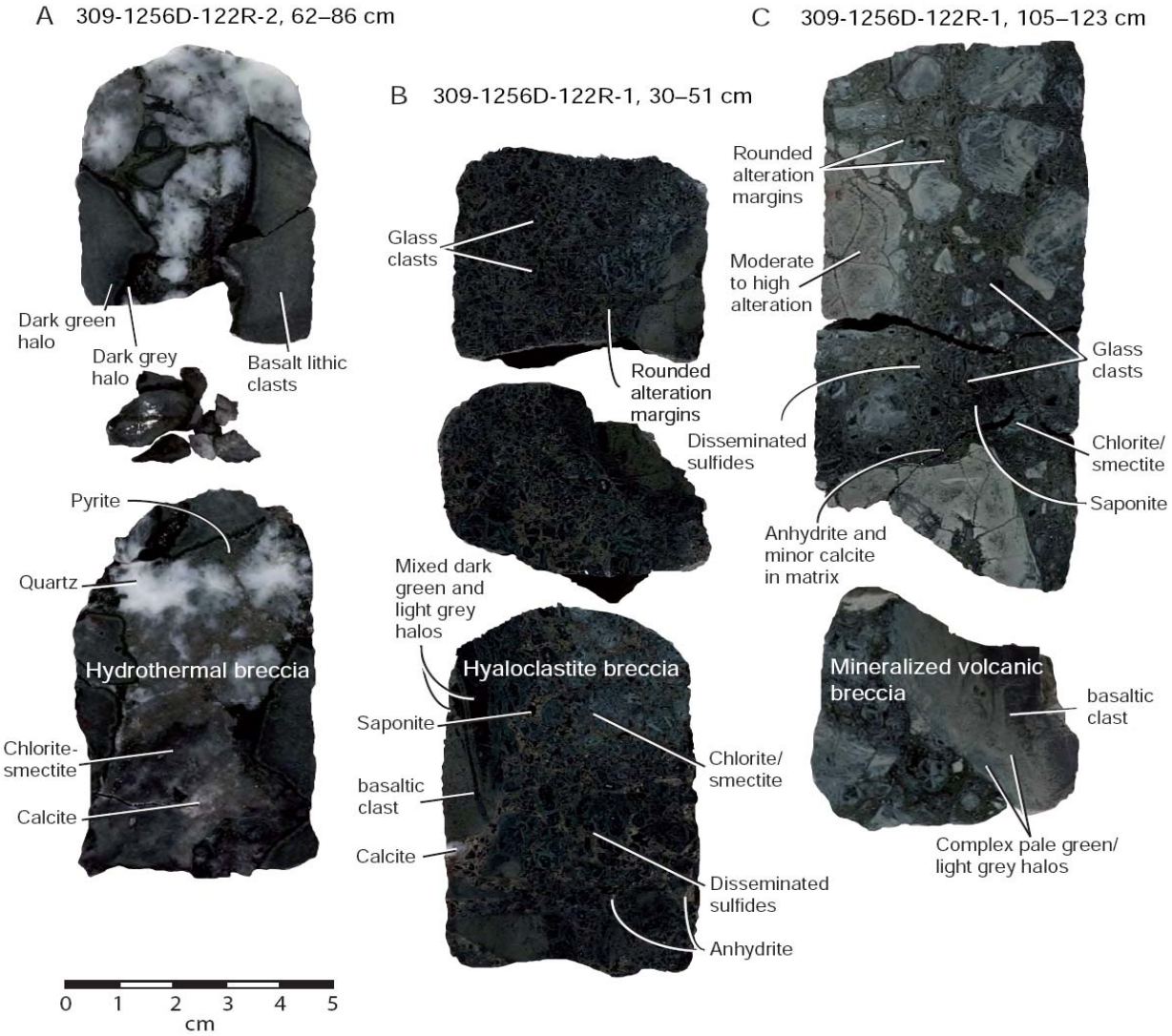

Figure 4.26. Examples of high temperature breccias at ODP/IODP Site 1256. A) Hydrothermal breccia with altered basalt lithic clasts in a pyrite, quartz, chlorite/smectite, and minor saponite, and carbonate matrix. B) Hyaloclastite breccia with rounded altered glass fragments and occasional basaltic clasts in a cement of chlorite/smectite, disseminated pyrite, saponite, and minor anhydrite and calcite. C) Mineralized volcanic breccia with moderate to highly altered basalt and glass clasts in a matrix of chlorite/smectite, disseminated sulfides, and minor anhydrite and calcite. Core photos are sourced from Teagle et al., (2006).

The most intense development of the granoblastic texture is from 1120 to 1147 msb, some ~10 metres above where the dykes overlie the gabbros, which are only partially to strongly recrystallized. Titanomagnetite in the lower dykes and the granoblastic dykes (1064.5-1156.6 msb) is recrystallized to magnetite ± ilmentite ± accessory titanite and possibly hematite and it commonly occurs within actinolite and secondary clinopyroxene.

Scant evidence is present for the timing of alteration within the granoblastic dykes, however rare cross cutting veins tentatively suggest that the granular clinopyroxene-orthopyroxene-magnetite-plagioclase assemblage formed earlier than the hornblende-actinolitic hornblende-plagioclase-quartz veins and the groundmass alteration. An earlier phase of background alteration may have occurred because rare secondary granoblastic clinopyroxenes have magnetite intrusions similar to those within the actinolite that replaces clinopyroxene in the upper dykes (Teagle et al., 2006).

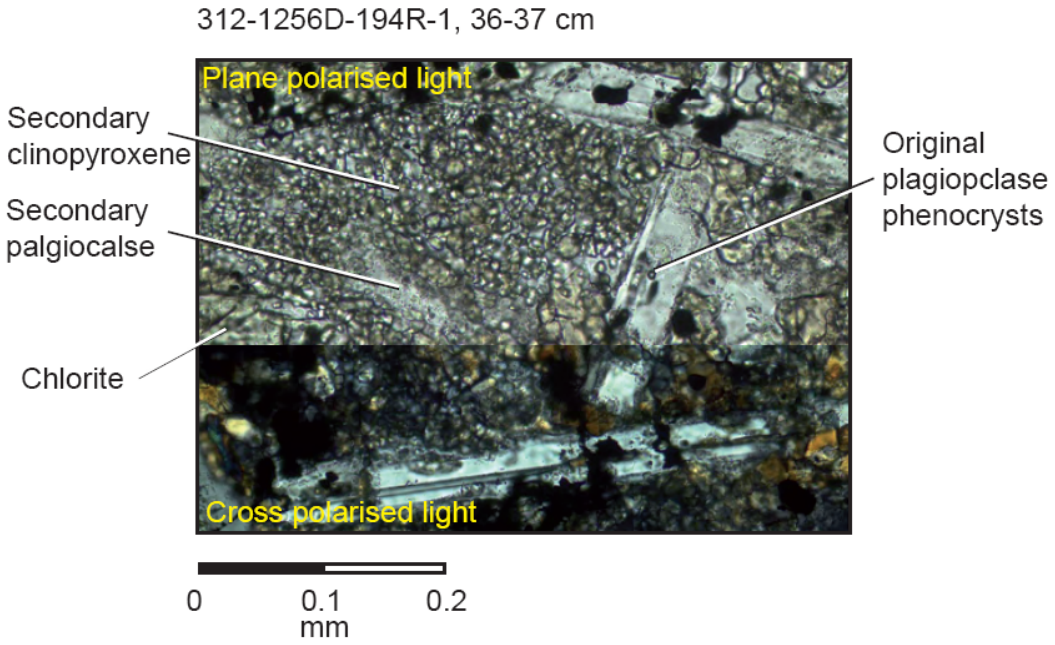

Figure 4.27. Example of near total recrystallisation of the primary igneous groundmass forming an granoblastic texture. (Teagle et al., 2006).

4.2.2.3 Plutonic section

Interval 312-1256D-213R-1, 52 cm to 234R-1, 33 cm (1406.62-1507.1 mbsf) comprises gabbroic rocks, leucocratic oxide diorites and trondhjemites, and dyke

screens. Depending on grain size, the rocks are all moderately to completely altered, with pegmatitc sections exhibiting the most intense alteration. Figure 4.28 shows the main rock types and alteration characteristics of the plutonic section at Site 1256. In gabbros clinopyroxene is replaced by actinolitic hornblende, and actinolite is observed intergrown with secondary pyrite, trace chalcopyrite, and rare pyrrhotite.

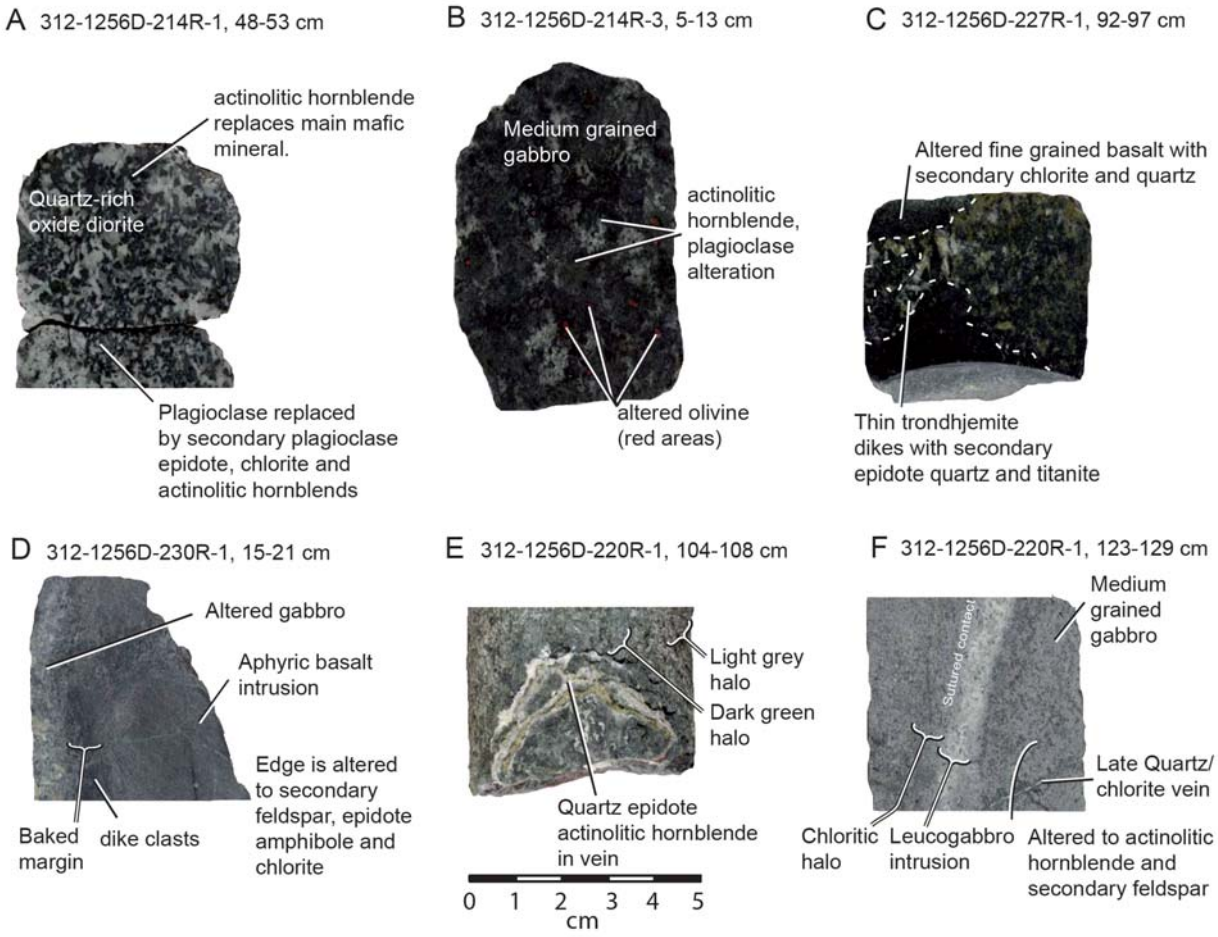

Figure 4.28. Examples of plutonic rocks at ODP/IODP Site 1256 and their alteration. A) Quartz-rich oxide diorite B) Medium grained gabbro with altered olivine clasts C) Altered fine grained basalt with thin trondhjemite dykes D) Gabbro with aphyric basalt intrusion E) Quartz, epidote, and actinolitic hornblende vein in gabbro F) Leucogabbro intruding into a medium grained gabbro. Photos modified from Teagle et al., (2006).

Alteration of the dyke screen and basaltic rocks below 1244 msb is dominated by actinolite ± chlorite, hornblende, secondary plagioclase, epidote, magnetite, pyrite, and quartz. Dark grey, grey-green, and green background reflects the variation in the replacement of clinopyroxene with actinolitic hornblende, amphibole, minor chlorite and rare ortho-amphibole (Figure 4.28). Localised cm-scale ‘clots’ of pyrrhotite + chalcopyrite and magnetite, and disseminated pyrrhotite are present in Sections 312-

1256D-223R-3 and 231R-4 to the base of 1256 respectively and in Sample 312-1256D-217R-1, 64-69 cm (Figure 4.29). Pumpellyite, previously only recorded in the lower sheeted dykes at Site 504, (Alt et al., 1993) was tentatively identified replacing plagioclase.

Olivine in Section 1256D-223R-2 and 214-R is partially to completely replaced by undetermined phyllosilicates, talc, and magnetite with outer rims of pale blue green amphibole and minor chlorite (Figure 4.28). Gabbro directly below the granoblastic dykes exhibits high to total alteration. Primary clinopyroxene is replaced by actinolitic hornblende (Figure 4.29) and plagioclase is altered to secondary feldspar, zeolite and clots (5-10 mm) of epidote. The top of gabbro 2 (Section 309-1256D-230R-1, 15 cm) is altered in a similar style to gabbro 1, although the contact between the gabbro and dyke screen is not recovered here. Throughout the plutonic section, igneous titanomagnetite and is partly to highly replaced by titanite and primary igneous sulfide is recrystallised to globules of pyrite ± chalcopyrite, and local pyrrhotite. Rare millerite (NiS) inclusions occur within plagioclase phenocrysts and in actinolitic hornblende psudomorphs (Teagle et al., 2006).

Veins in gabbros are sparse (~10 vn/m) compared to the sheeted dykes (~35 vn/m). Teagle et al., (2006) report diffuse 1-2 mm wide actinolitic hornblende halos with no ‘vein’ as such, that are cross cut by discrete 0.5-1mm actinolitic hornblende veins with alteration halos. In more intense alteration zones these veins are cross cut by epidote, quartz, and prehnite veins, which are, in-turn, cross cut by numerous chlorite and even later quartz-chlorite veins with narrow 2-5 mm halos.

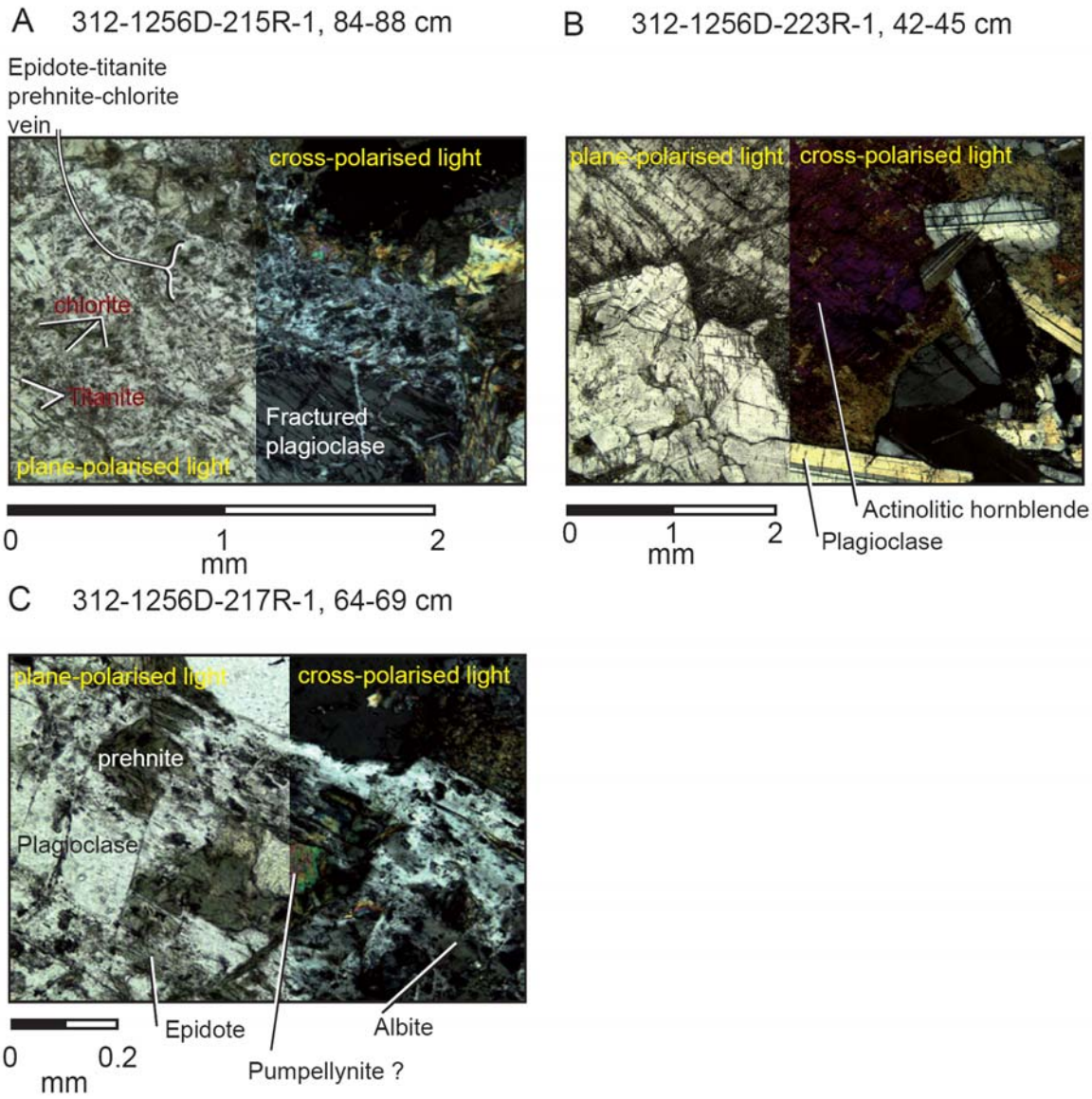

Figure 4.29. Some examples of high temperature alteration within gabbroic rocks at ODP/IODP Site 1256. A).Vein of epidote, titanite, prehnite, and chlorite and gabbro altered to titanite and minor chlorite B) Primary plagioclase partially altered to actinolitic hornblende C) groundmass altered to prehnite, albite, epidote (Green) and possibly pumpellynite. Photomicrographs are from Teagle et al., (2006)

Teagle et al., (2006) report much more diverse alteration below 1244 msb within the dyke screen and basaltic rocks. Alteration is much more intense, with near total replacement of the primary groundmass in the dyke screen between gabbro 1 and gabbro 2 (1244.9-1257.1 msb). Alteration includes partially recrystallised sub rounded Titanomagnetite, replacement of clinopyroxene by dusty secondary clinopyroxene + actinolitic hornblende + magnetite, and replacement of orthopyroxene by actinolitic hornblende and chlorite. Teagle et al., (2006) observed a smectite rich phyllosilicate (unconfirmed) within the basalt immediately overlying the top of Gabbro 2 (Sample

312-1256D-230R-1, 49-54 cm) the same authors suggest that the phyllosilitates may be remnants from when the plutonic section may have been altered at low temperatures (<200^{o}C).

Teagle et al., (2006) note extensive alteration within a dike complex that consists of basaltic dikes that are, in turn, indruded by thin mafic and felsic dykes, and trondhjemite and quartz-rich oxide diorite dykelets. The dyke complex between the gabbros and dikelets within gabbros are altered to secondary plagioclase, actinolitic hornblende, chlorite, titanite, epidote, prehnite, sulfides and minor calcite (Teagle et al., 2006).

The timing of secondary mineral paragenisis of the plutonic section at ODP/IODP Site 1256 is not clear and will require a much more detailed analysis in the future. However several generations of veins that have been identified by cross cutting relationships led Teagle, (2006) to suggest the following order: 1) thin wispy actinolitic-hornblende veins with 1-2mm halos, 2) well defined actinolitic-hornblende veins with halos, and 3) Chlorite-actinolite, quartz-chlorite, and 0.5-2mm braided quartz veins with 1-2mm chlorite margins.

4.3. Alteration Geochemistry

In order to fully characterize low temperature hydrothermal alteration at Site 1256, a large selection of altered basement whole rock samples, breccias, matrixes and secondary minerals in veins were analyzed for their major, trace, and rare-earth element concentrations, strontium isotopic ratios, and where possible, sulfur, oxygen and carbon isotopic ratios (See Chapter 2 'methods' for analytical details). Insights into the fluid evolution during hydrothermal circulation from the chemistry of anhydrite are discussed separately in Chapter 8. This together with measurements carried out on leached samples, 'fresh' samples, and sample pairs allow for a comprehensive characterization of low temperature hydrothermal alteration at Site 1256. In this section, the chemistry is cross referenced with the petrographic observations described earlier. The chemistry and petrography is used to give a quantitative estimate of the chemical change that has occurred at Site 1256 as a result of low temperature hydrothermal alteration.

4.3.1 Whole Rock Geochemistry

A total of 253 whole rock samples were analyzed, where possible, for major elements (XRF), trace elements (XRF, ICP-MS and ICP-AES), REE (ICP-MS), and Sr isotopic ratios (TIMS). Table 4.1 shows representative analyses from Site 1256 lavas. The full data table is located in Section C, 2 of the Appendix. Sample sets include background basalts and alteration halos, fresh glass analyses, and whole rock leaches. This sample set extends through the ponded lava flow, inflated flow, sheet and massive flows, and into the lithological transition zone towards the dykes.

Major element oxide, trace and REE concentrations for whole rock samples are plotted vs. depth in Figure 4.30 a and b. Analyses are grouped according to their alteration style, so that they can be compared directly with the least altered background rocks. In addition, Site 1256 stratigraphy and minerals vs. depth are shown for comparison. For the most part, however, alteration remains slight (See section 4.2, alteration). The ponded lava flow exhibits higher TiO_2, Fe_2O_3, Na_2O, P_2O_5, S, and Y, and lower SiO_2, Al_2O_3, MgO, and Sc than the rest of the extrusive rocks at Site 1256.

Leg	206	206	206	206	206	309	309	309
Hole	1256D	1256D	1256D	1256D	1256D	1256D	1256D	1256D
Core	6R-7	12R-8	22R-2	41R-2	60R-2	117R-1	122R-2	126R-1
Interval	117-124	71-79	120-127	26-33	29-34	97-107	28-33	39-47
Depth (mbsf)	304	351	408	526	670	1004	1028	1047
Depth (msb)	54	101	158	276	420	754	778	797
unit	1c	1d	4d	15	24e	40	42a	43
rock type	massive flows	massive flows	massive flows	massive flows	Sheet flows	cataclastic massive	min volc br	sheet flow
Lithological subdevision	Lava pond	Lava pond	Inflated Flows	Inflated Flows	sheet and massive flows	sheet and massive flows	transition zone	transition zone
Alteration type	grey bkd + dis pyrite	dark grey bkd	dark grey bkd + mot patches	grey bkd+ sap patch	grey bkd and 'black' patches	fg cataclastic basalt, unit 40	hyalocl + dk gr gls+sulf cemnt	ux basalt w/ dis pyrite
$^{87}Sr/^{86}Sr_{(m)}$	0.703003	0.703030	0.703150	0.703002	0.702965	0.703221	0.705208	0.703027
2SE	13	14	13	11	10	13	13	13
$\delta^{18}O_{(VSMOW)}$	6.3	5.9	6.5	5.6	6.4	6.3	7.5	5.6
SiO_2	50	51	50	50	50	51	53	50
TiO_2	1.77	1.52	1.21	1.41	1.25	1.10	1.18	1.43
Al_2O_3	13.5	14.2	13.7	13.6	13.9	13.8	9.4	13.5
Fe_2O_3	13.3	12.4	12.4	13.7	12.5	11.8	14.9	12.8
MnO	0.21	0.19	0.22	0.20	0.18	0.15	0.16	0.21
MgO	6.9	6.8	7.8	7.1	7.7	8.4	6.3	7.5
CaO	10.9	10.4	11.3	11.0	11.3	10.3	4.9	11.4
Na_2O	3.0	2.9	2.6	2.6	2.4	1.5	2.5	1.9
K_2O	0.12	0.11	0.08	0.05	0.09	0.03	0.04	0.02
P_2O_5	0.14	0.11	0.09	0.11	0.10	0.07	0.06	0.09
Total	100.0	99.8	99.9	100.1	100.0	99.9	99.6	99.9
C (%)	0.02	0.02	0.03	0.01	0.02	-	-	-
S (%)	0.12	0.02	0.05	0.15	0.16	-	-	-
LOI	0.51	0.63	0.39	0.12	0.53	2.27	7.22	1.05
Mg #	53	55	58	53	58	61	48	57
Sc	43	54	44	45	43	46	43	45
V	339	346	267	315	271	350	330	364
Cr	88	22	44	29	150	259	105	57
Co	41	46	43	48	40	-	-	-
Ni	55	45	51	43	67	100	32	52
Cu	39	82	73	78	63	100	66	77
Zn	76	102	81	90	75	114	-	106
Rb	0.57	0.72	0.85	0.63	1.52	0.46	0.45	0.40
Sr	69	75	80	92	74	64	54	80
Y	38	36	25	30	28	28	29	35
Zr	89	76	64	78	62	61	68	84
Nb	3.56	3.33	1.82	3.20	2.57	3.41	2.71	3.01
Cs	0.01	0.01	0.02	0.01	0.03	0.01	0.00	-
Ba	11.3	12.0	5.6	10.1	11.8	8.4	13.4	8.8
La	2.78	2.54	2.16	2.78	2.31	2.22	2.10	2.89
Ce	9.4	8.4	6.6	8.7	6.8	6.3	6.0	8.6
Pr	1.78	1.54	1.23	1.52	1.19	1.09	1.08	1.55
Nd	10.0	9.0	7.4	9.1	7.0	6.3	6.4	8.6
Sm	3.68	3.42	2.59	3.37	2.51	2.35	2.39	3.14
Eu	1.26	1.24	0.96	1.19	0.90	0.92	0.90	1.22
Gd	5.00	4.70	3.67	4.66	3.60	3.08	3.31	4.11
Tb	0.96	0.89	0.69	0.91	0.67	0.62	0.66	0.81
Dy	6.59	6.23	4.70	6.27	4.50	4.24	4.34	5.38
Ho	1.46	1.37	1.14	1.37	1.10	0.91	0.96	1.18
Er	4.14	4.12	3.32	4.09	3.15	2.70	2.82	3.55
Tm	0.75	0.65	0.43	0.56	0.42	0.42	0.43	0.54
Yb	4.03	4.10	3.16	4.28	3.04	2.67	2.80	3.49
Lu	0.71	0.68	0.45	0.64	0.47	0.43	0.44	0.55
Hf	2.52	2.52	1.75	2.25	1.67	1.72	1.84	2.30
Ta	0.26	0.22	0.17	0.23	0.17	0.19	0.15	0.22
Pb	0.24	0.38	0.37	0.43	0.75	0.30	8.00	-
Th	0.18	0.24	0.17	0.19	0.19	0.22	0.16	0.21
U	0.06	-	0.09	0.34	0.05	0.06	2.60	0.06

Table 4.1. Representative analyses for Site 1256 whole rock basalts from each lithological group. Bkd = background, diss = disseminated, sap = saponite, fg = fine grained, dk = dark, gr = grey, gls = glass, sulf = sulfide, ux = microcrystalline, hayloclastite.

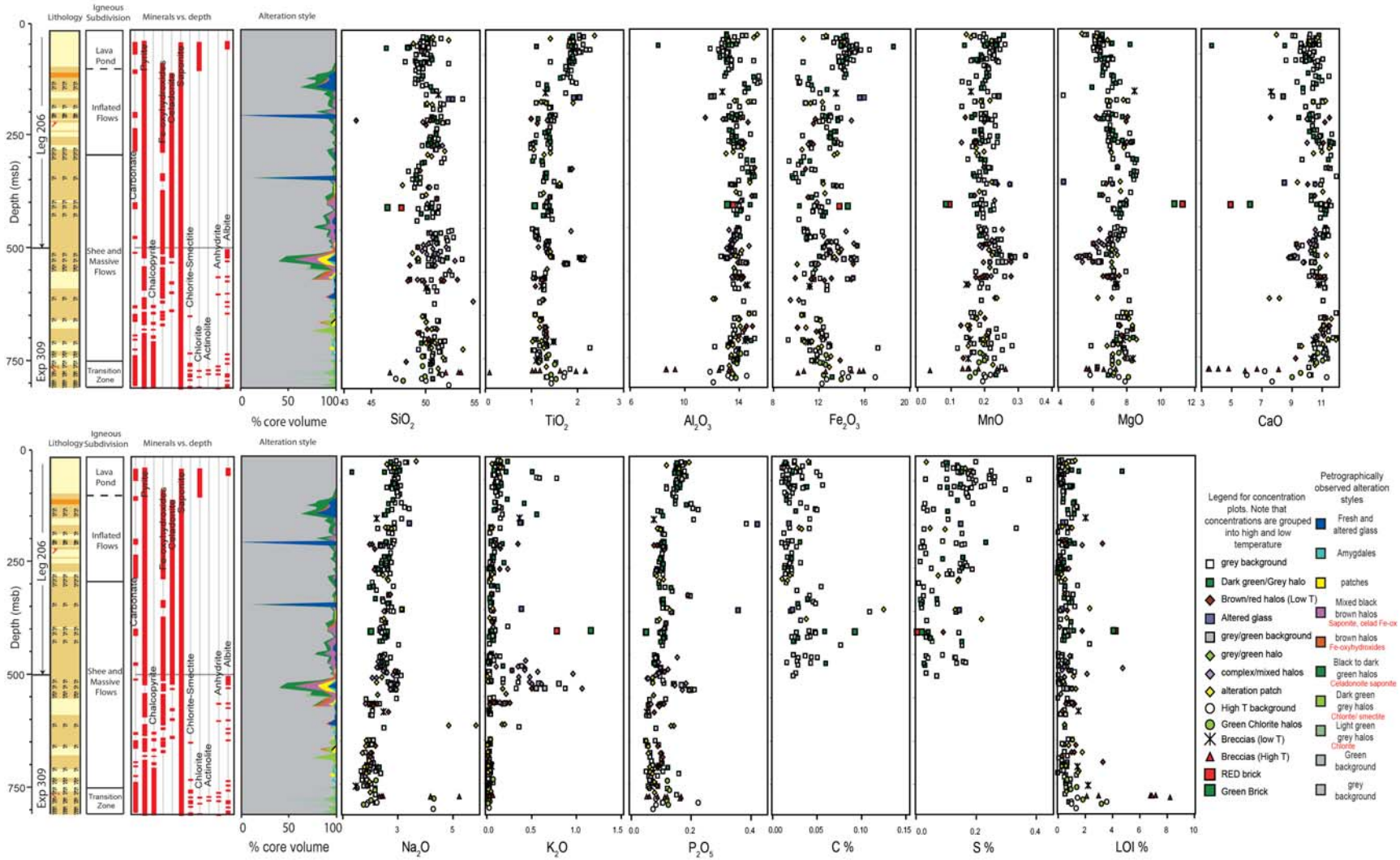

Figure 4.30a Selected major element, trace element and REE concentrations in Site 1256 whole rock samples vs. depth. Data points highlight alteration styles, in addition Site 1256 stratigraphy, minerals vs. depth and halo percentage vs. depth is included for reference. Stratigraphy, minerals vs. depth and halo abundance data are sourced from Wilson et al., (2003) and Teagle et al., (2006).

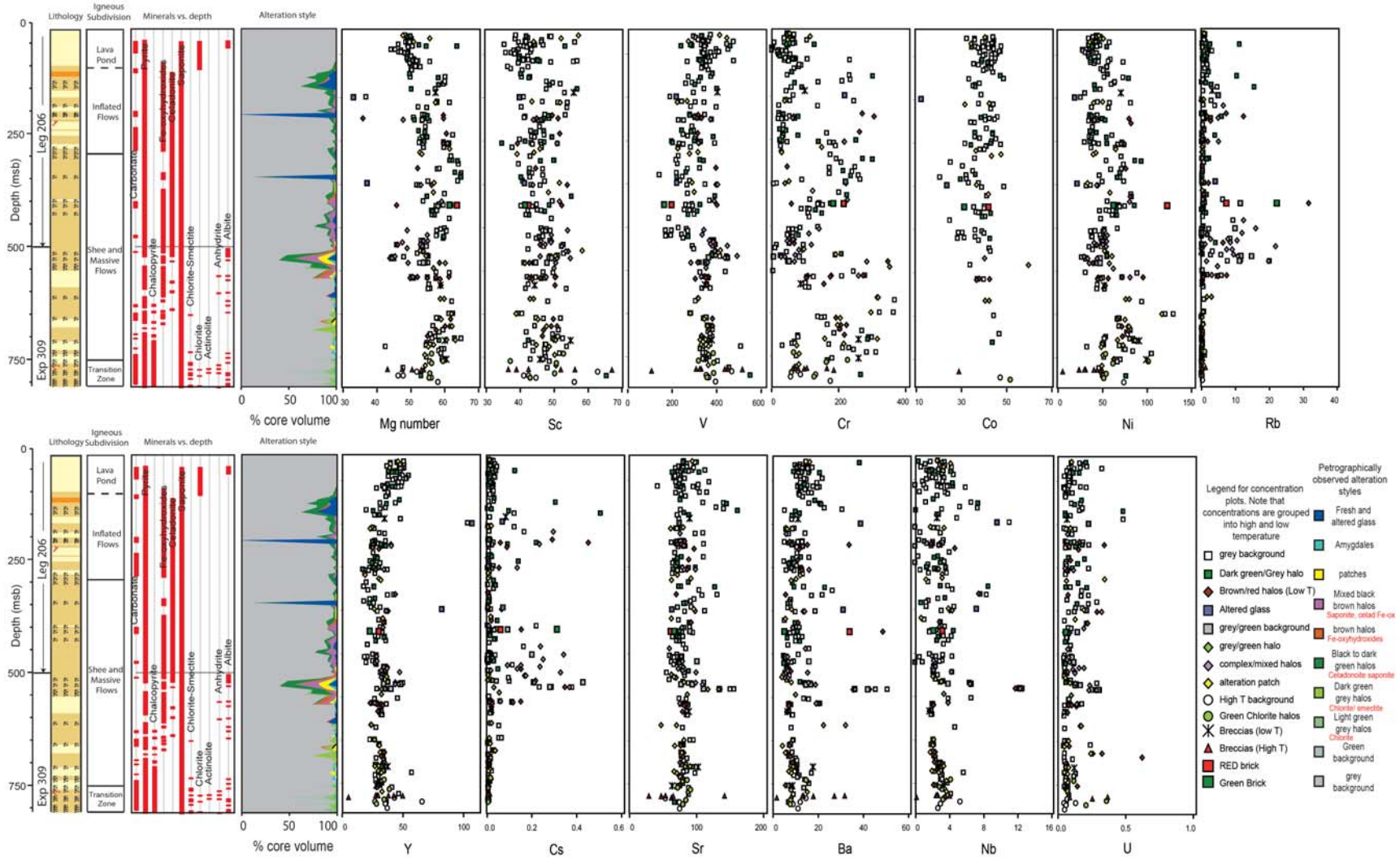

Figure 4.30b. Selected trace element and REE concentrations in Site 1256 whole rock samples vs. depth. Data points highlight alteration styles, in addition Site 1256 stratigraphy, minerals vs. depth and halo percentage vs. depth is included for reference. Stratigraphy, minerals vs. depth and halo abundance data are sourced from Wilson et al., (2003) and Teagle et al., (2006)

These differences are thought to reflect variations in source magma for the ponded flow (Wilson et al., 2003). Loss on ignition (LOI) at Site 1256 ranges from <0.1 wt% to 12%, indicating that Site 1256 basalts are significantly hydrated compared to N-MORB (0.1 – 0.2 wt%; Michael, 1988, Dixon et al., 1988). However, most whole rock LOI is within the range of 0 to 2 wt% and it is only breccias and a few highly altered samples that exhibit LOI above this range. Broad increases in Fe_2O_3 occur between 0 and 150 msb (Ponded lava flow), 450 and 550 msb and in the lithological transition zone (750 to 812 msb).

At these intervals high levels of oxidative secondary phases (iron-oxyhydroxides) were observed in the whole rock samples (See Section 4.2 'Alteration' and Wilson et al., 2003 and Teagle et al., 2006). Similar, though less intense increases in Fe_2O_3 are observed in the series of complex halos, brown halos, and green halos between 200 and 300 msb. This coincides with a zone of relatively high fracturing with a high abundance of vein minerals, breccias and iron-oxyhydroxide halos (Section 4.2, 'Alteration and Wilson et al, 2003 and Teagle et al., 2006). Increased Fe_2O_3 at the transition zone at Site 1256 coincides with the increase in vein abundance and overall alteration intensity. However, in this interval, brown oxidation halos are absent, which suggests that the additional Fe_2O_3 may be due to primary magmatic variation. Section 206-1256D-57R-2, 117-127 cm and 57R-3, 13-18 cm (green/red brick) is intensely altered and has very high Fe_2O_3 concentration together with increased MgO, LOI, K_2O, Rb decreases in MnO, and CaO compared to the surrounding material (Figure 4.30a). This reflects the intensity of oxidation and the emplacement of secondary minerals at this interval. Loss of silica and calcium at the green/red brick interval is most likely the result extensive replacement of primary igneous phases, including plagioclase, olivine, and clinopyroxene, which, despite the presence of calcium and silica bearing secondary mineral phases, results in an overall decrease in the volume percentage of these elements. K_2O follows a similar trend to $Fe_2O_3^T$ in the lava pond, red/green brick, and interval 450-550 msb, reflecting the incorporation of low temperature phyllosilicates (e.g. celadonite) into the host rock. The transition zone, is noticeably low in K_2O with concentrations ranging from 0 to 0.08 wt%. This coincides with the absence of celadonite past 650 msb (Figure 4.30a). Large and variable apparent losses of SiO_2, Al_2O_3, MnO, MgO, CaO, V, Sc, Sr, and Ni are reported within the high temperature breccias. These breccias also have high (up to 12 wt%) LOI and Na_2O, and highly variable concentrations in the other major, traces and REE reported

in Figure 4.30b. The high variability reflects the variable content of these breccias, high fluid flow, and the loss of large portions of the original igneous assemblage. A selection of major, trace and REE are plotted vs. LOI for pairs of halo and adjoining less altered rock in Figure 4.31. Almost all sample pairs show distinct variation with LOI. Dark green/grey halos and brown halos almost all have lower SiO_2, MgO, MnO, Na_2O, CaO, Ni, and Zr concentrations compared to their less altered counterparts. $Fe_2O_3{}^T$, K_2O, Rb, Sr, and Cs concentrations are all elevated in these alteration halos. Less intense green/grey halos broadly mirror the trends of the dark green and brown halos however they are more variable. Change in MgO, MnO, Al_2O_3, and Sr with LOI are not regular, with variable increases and decreases within all alteration styles. Complex halos variably exhibit the most change including increased concentrations of K_2O, Rb, and Cs, and decreases in SiO_2, MgO, CaO, Sr, and Zr.

Three subsamples taken from Intervals 206-1256D, 80-R-2, 60-66 cm and 309-1256D, 28R-1, 0-8 cm which contained enough sample to recover a portion of background, green halo, brown halo or complex halo are plotted in Figure 4.31. Progressively increased chemical changes, and further disparity between altered sample and grey background are observed on moving from the grey background into the halos towards the vein/fracture.

Overall, the intensity of alteration within each style is variable; however, most changes appear to be linked with LOI. It is likely that these changes reflect the successive emplacement of secondary minerals (Figures 4.32 to 4.34). Although it is possible some secondary phases contain elements originally sourced from the basalt. If this is the case, one would expect to see minimal change in elemental concentrations. The changes shown in Figure 4.32 to 4.34 imply that, in the case of these samples, the complex halo and the brown/red halo (iron-oxyhydroxides/saponite) replace the green/grey celadonitic halo. We would expect the concentration of K_2O to be at its lowest in the grey background of Sample 309-1256D, 80R-2, 60-66 cm (Figure 4.32), however in a plot of K_2O vs. LOI (Figure 4.34) K_2O is high in the background and it successively decreases in concentration in the green and complex halos. Given that K_2O in fresh basalt is ~0.17 wt% (McKenzie and O'Nions.,1991) and that K_2O is low in the majority of least altered rocks at Site 1256 (Figure 4.31), the grey 'background' in Sample 309-1256D, 80R-2, 60-66 cm is altered and that the reduction of K_2O in the green and complex halos represent replacement by Fe-oxides (Figure 4.33) of the original alteration phase.

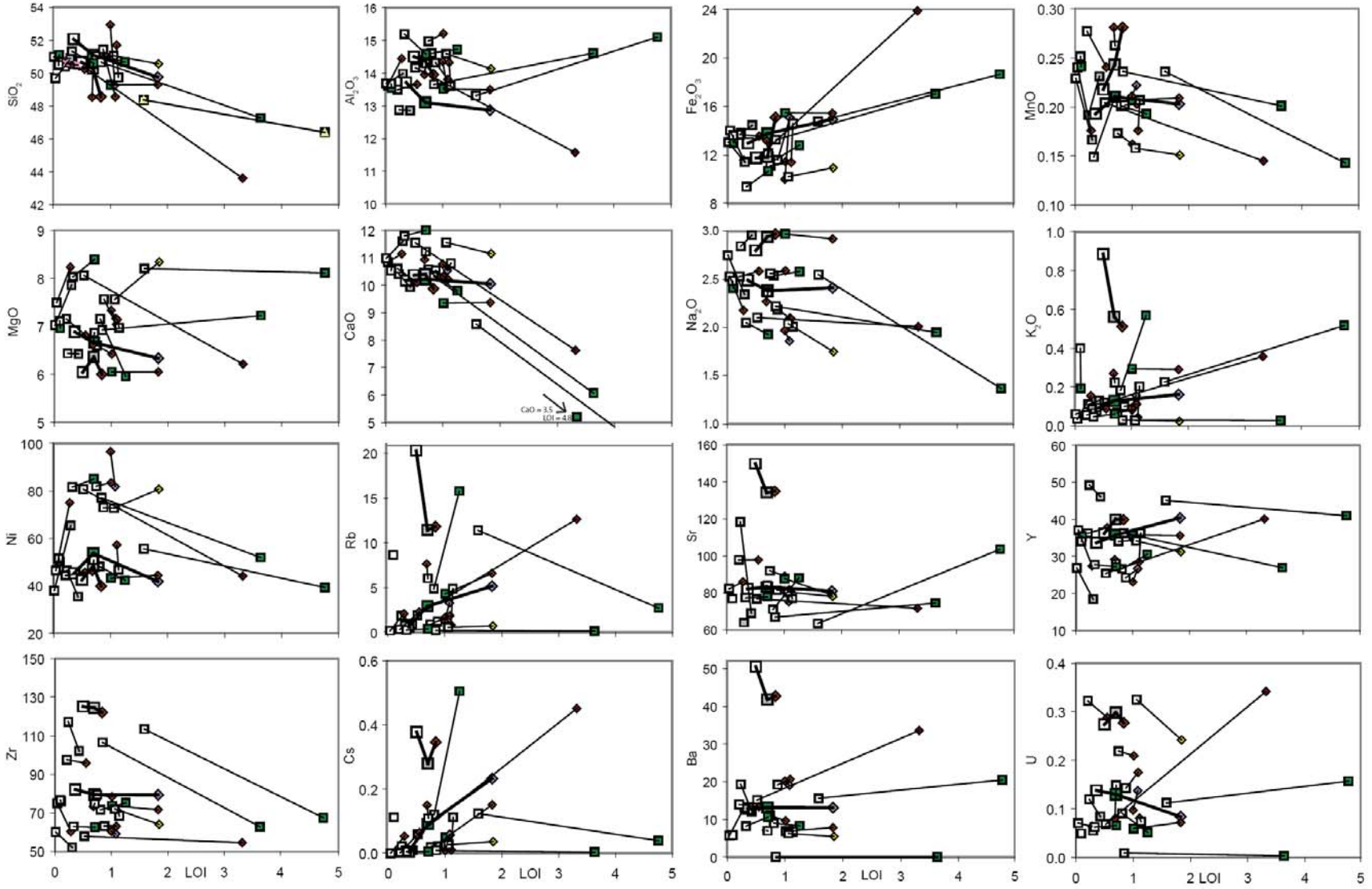

Figure 4.31. Selection of major (wt %), trace (ppm) and RRE (ppm) plots vs. LOI (w t%)of 1256 sample pairs, in which halos directly adjoin relatively fresh basalt. Square fills: White = grey background, grey = grey/green background, green = dark green/black halo. Diamond fills: Brown = brown halos, purple = complex halos, yellow = alteration patch.

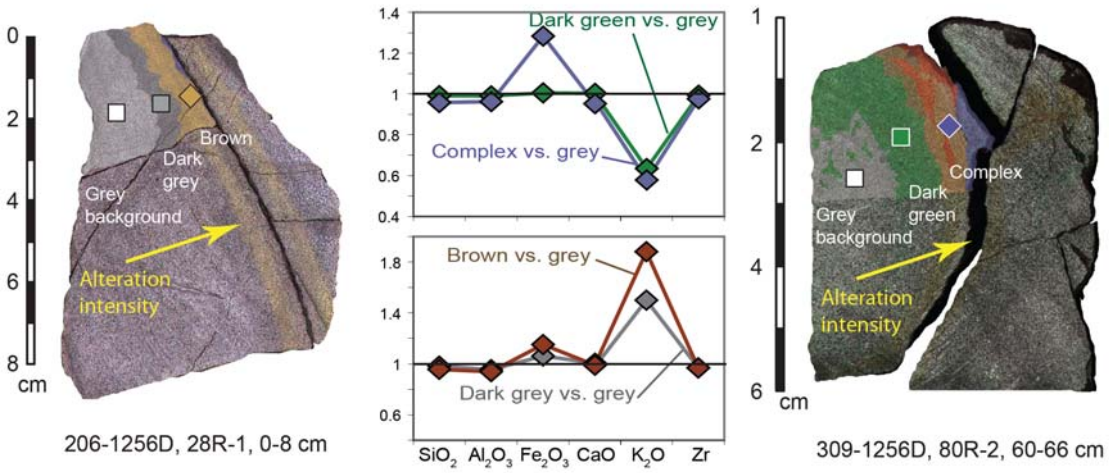

Figure 4.32 Plots of Fe_2O_3, SiO_2 Zr, Al_2O_3, CaO, and K_2O normalized to the least altered background for two samples with a three way split. Sample 206-1256D, 28R-1, 0-8 cm includes: brown halo (Brown diamond), dark grey halo (Grey square), and grey background (White square) subsamples. Sample 309-1256D, 80R-2, 60-66 cm includes: complex halo (Purple diamond), dark green (Green square), and grey background (White square) subsamples.

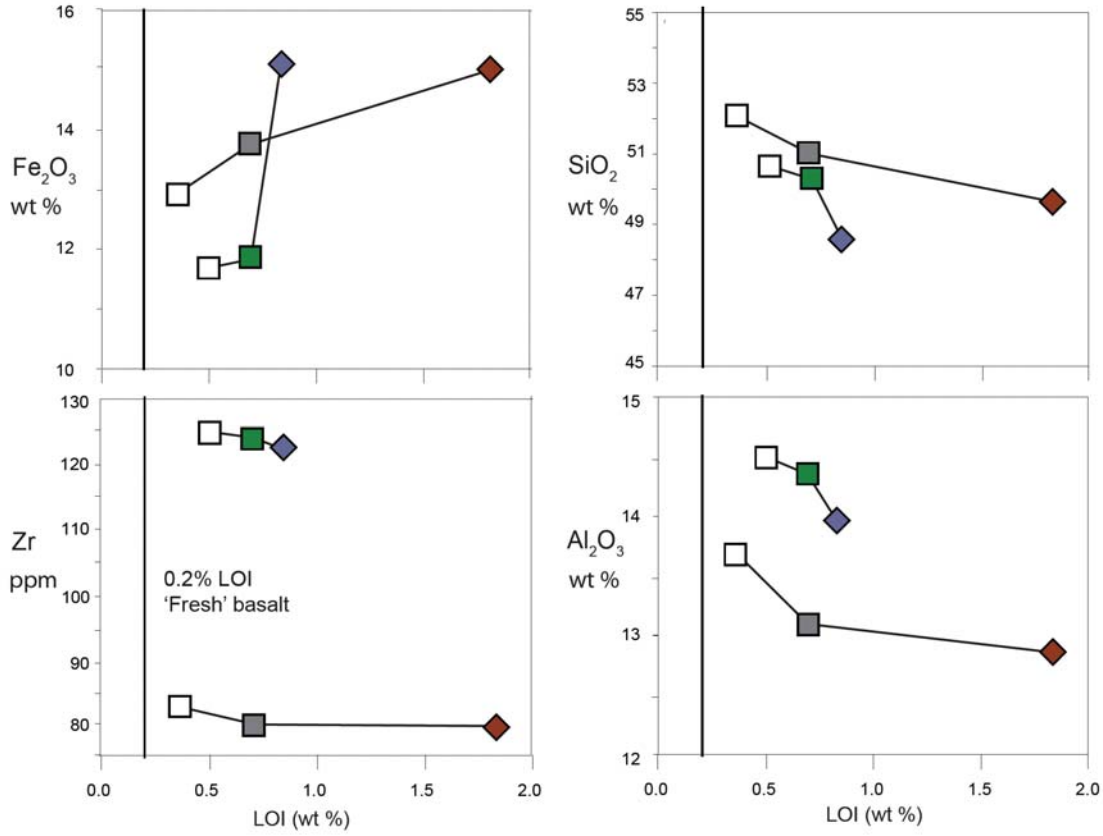

Figure 4.33 Plots of Fe_2O_3, SiO_2 Zr, Al_2O_3, vs LOI for samples outlined in Figure 4.32 ample 206-1256D, 28R-1, 0-8 cm includes: brown halo (Brown diamond), dark grey halo (Grey square), and grey background (White square) subsamples. Sample 309-1256D, 80R-2, 60-66 cm includes: complex halo (Purple diamond), dark green (Green square), and grey background (White square) subsamples.

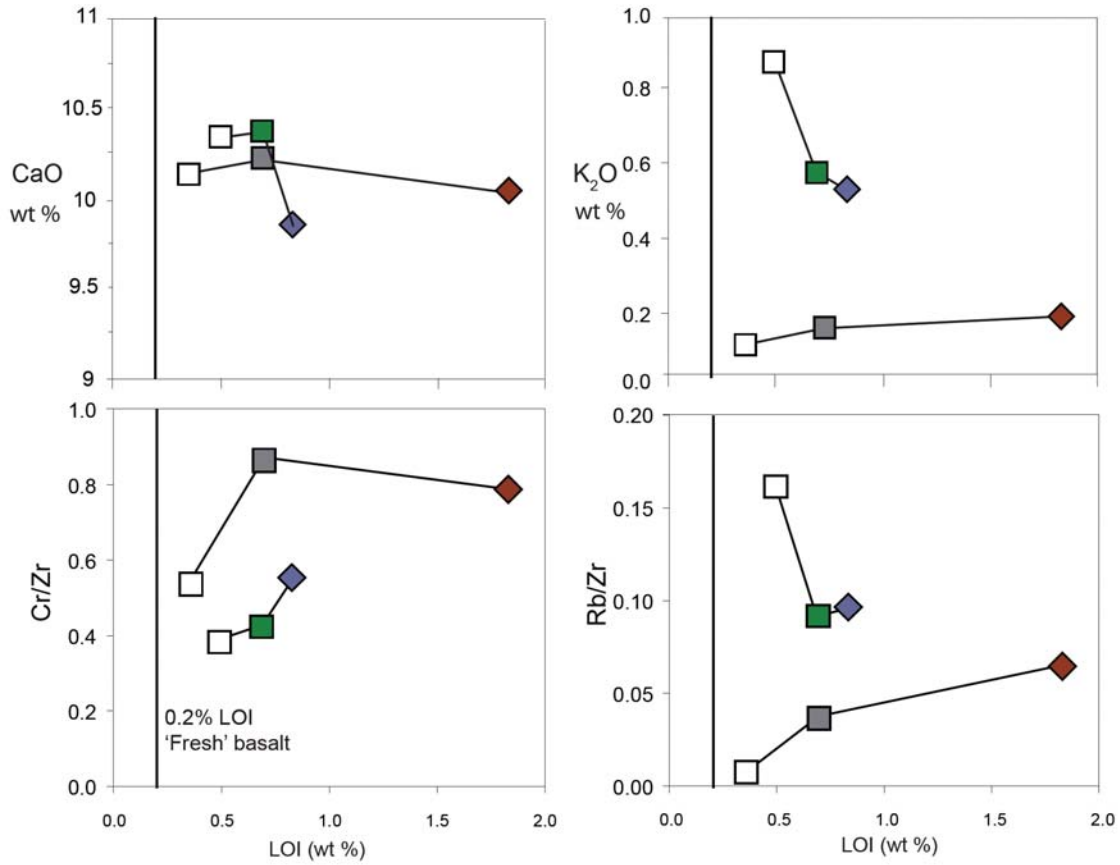

Figure 4.34 Plots of CaO, K_2O, Cr/Zr, Rb/Zr, vs LOI for samples outlined in Figure 4.32 ample 206-1256D, 28R-1, 0-8 cm includes: brown halo (Brown diamond), dark grey halo (Grey square), and grey background (White square) subsamples. Sample 309-1256D, 80R-2, 60-66 cm includes: complex halo (Purple diamond), dark green (Green square), and grey background (White square) subsamples.

4.3.2 Chemical changes

Chemical changes were calculated for all samples based on a sample by sample protolith approach that utilizes the immobility of TiO_2 as a monitor of igneous fractionation. The presence of Ti hydrogarnets at 411.7-499.3 msb and 502-669.1 msb suggest that there is limited mobility of Ti at Site 1256 (Laverne, 2006). However these garnets are rare within these intervals therefore Ti is not considered mobile. Potentially, a more detailed study, utilizing other 'immobile' elements may be carried out to assess chemical change.

As with the other sites in this study, the least altered samples used for detecting igneous fractionation trends were sampled on the basis of low LOI (<1.10) and low K_2O (<0.2). This is done in an attempt to determine, the true extent of alteration rather

than estimates from pairing 'least altered' whole rocks with halos. See Chapter 3 for a full discussion of chemical change methodology. Within the extrusives at Site 1256 a range of rock types were encountered, including a ponded lava flow, inflated flows, sheet and massive flows, and a transition zone consisting of intrusive dykes, lavas, breccias and sheeted dykes. The likely igneous source for these groups is briefly discussed in Section 4.1. A more detailed report of the petrography at Site 1256 can be found in Wilson et al, 2003 and Teagle et al., 2006. Because, differing igneous sources are likely to produce magmas of different chemical composition with variable fractionation trends, Site 1256 samples are grouped according to their igneous sub divisions. As with the Site 1179 samples in chapter 3 the protolith composition are derived from either: 1) best fit linear regression lines of the element in question vs. TiO_2, or, when no fractionation trend is observed, 2) average compositions of the least altered samples. LOI for fresh basalt is assumed to be 0.20% based on work by Alt et al., (1989) and Danyushevsky (2001).

All TiO_2 regression plots and the selected 'least altered' samples are included in Section C, 2, (Appendix). The average chemical change for each alteration style is calculated and this is weighted according to the volume of core that each style accounts for, including additional material added from secondary minerals in veins and breccia matrices and cements. The weighted average chemical change for Site 1256 is then calculated. The chemical changes associated with high temperature alteration are also calculated for the transition zone and upper sheeted dykes. However, the calculation for total chemical change in the extrusives of Site 1256 only includes lower temperature assemblages because an appraisal of higher temperature alteration requires a similar study for the full depth of Site 1256 into the sheeted dykes and gabbros. Following the method from Chapter 3, the sensitivity of this calculation is governed by the range of immobility observed within immobile elements Ti, Y, Zr and Nb in grey background rocks and the assumption that no volume change has taken place. Errors associated with analytical precision are discussed in Chapter 2. At Site 1256 a change of less than 10% is considered to represent no significant change.

4.3.2.1 Results

Multi-element diagrams show the chemical changes for major, trace and REE associated with low temperature alteration in the volcanic section and the lithological transition zone.

Mineral	Site source	Reference
Saponite	504	Bach et al, (1996), Noack et al (1996)
	896	Laverne et al, (1996), Teagle et al, (1996)
	1224	Paul et al, (2006)
	843	Waggoner (1993), Alt (1993)
	1256	This Study
Celadonite	504	Bach et al, (1996), Noack et al (1996)
	896	Laverne et al, (1996), Teagle et al, (1996)
	843	Alt (1993)
	1256	This Study
Iron-oxyhydroxides	504	Noack (1993)
	843	Alt (1993)
Carbonate	504	Noack (1993)
	896	Teagle et al, (1996)
	843	Alt (1993)
Chlorite/smectite	504	Noack (1993)
	896	Teagle et al, (1996)
Chlorite	504	Bach et al, 1996)
	896	Laverne et al, (1996), Teagle et al, (1996)
Prehnite	504	Bach et al, (1996), Noack et al (1996)
Talc	504	Bach et al, (1996), Noack et al (1996)
actinolite	504	Bach et al, (1996), Noack et al (1996)
Zeolites	504	Bach et al, (1996), Noack et al (1996)

Table 4.2. Sources for secondary mineral data from other ODP sites. Secondary mineral compositions were calculated as an average of all available compositions from basement within the Pacific Ocean. Outliers and samples with multiple phases were excluded prior to calculation.

Because the transition zone encompasses phases associated with higher temperature greenschist facies metamorphism, these chemical changes are also plotted. Figure 4.35 and 4.36 depict chemical changes in g/100g and mg/100g for each alteration style observed for both high and low temperature at Site 1256. A comparison chart including all alteration styles and vein mineral incorporation is included in Figures 4.37 and 4.38. Chemical analysis of vein and breccia minerals at Site 1256 are given in Section D of the Appendix. Because there are only a few mineral analyses at Site 1256, the average composition for each secondary mineral was sourced from a combination of Site 1256

analyses and other basement sites (See Table 4.2). This makes the assumption that secondary minerals from other oceanic basement sites are similar to Site 1256.

4.3.2.2 Low temperature chemical changes

The chemical changes and percentage changes within each low temperature alteration style is shown in Figure 4.35 A and B, respectively. Low temperature alteration across all alteration styles at Site 1256 is varied, with most alteration styles displaying distinctive features, despite high errors present on the average chemical changes. Background rocks (Figure 4.36) show only slight chemical change. Minor increases in P_2O_5, Cr, and Nb are reported. Moderate to high C, Ni, Ta and K_2O, S, LOI, and Cs respectively are observed. Dark green/black alteration halos by contrast exhibit the greatest chemical change of all alteration styles, Major increases include MnO, MgO, CaO, K_2O, P_2O_5, C, LOI, most trace elements, and Ta, Pb, Th, and U. Other increases include LREE. Decreases observed include Na_2O, S, Cr, Y, Zr, and HREE. Such large changes, particularly K_2O, LOI, C, and MgO reflect the incorporation of clay minerals (celadonite, saponite). Changes in trace and REE might be explained by the partial replacement of primary igneous phases, for example feldspar, olivine and clinopyroxene and perhaps unaccounted for volume change within the dark green/black halos.

Brown and red halos exhibit the greatest increase in Fe_2O_3 and moderate to high increases in K_2O, C, LOI, Cr, Rb,Y, Zr, Cs, Ba, Ta, Pb, and U. Minor increases in LOI and decreases in CaO, S, and Th are observed. Increased Fe_2O_3, K_2O, C, and LOI reflect the presence of iron-oxyhydroxides, saponite, celadonite and carbonate. The green to pale green saponitic alteration halos, that predominantly appear in the lower lava portion of Site 1256 exhibit slight increases in C, Sr, Zr, and REE, moderate to high increases in Na_2O, K_2O, P_2O_5, LOI, Cr, Ni, Rb, Cs, Ba, Ta, Pb, Th, and U. Slight decreases in Fe_2O_3, S, Tm are also observed. With the exception of dark green/black halos, complex halos exhibit some of the greatest chemical change including increased Fe_2O_3, MgO, K_2O, P_2O_5, C, LOI, V, Rb, Nb, Cs, Ce, Ta, U, and decreased Na_2O, S, Cr, Zr, and La. A higher degree of uncertainty is associated with this halo type as shown by the range of compositional change in Figure 4.35. This may be attributed to either high variability in secondary mineral content of the halos, caused by complex

fluid histories, and/or complex overprinting. The latter is likely in a few cases because variations in texture and the mineral appearances can be very subtle that are hard to distinguish by petrographic observations alone.

Patches with identical mineral assemblages to that of other halo styles were grouped with their respective alteration styles, all other less distinct patches are grouped into a separate patch category (Figure 4.35 A and B). Patches represent minor alteration, not too dissimilar from background alteration with minor increases in MgO, Ni, Rb, Nb, Ta, Th, and U. Moderate and high increases include Cr, Cs and C, LOI respectively. The change in chemistry as a result of vein minerals is very low. Only major elements, Rb, Zr, and Cs show discernable increases. Relatively high ranges and the high levels of exchange exhibited in Figure 4.35 with signatures that are similar to all the dominant low temperature alteration styles imply multiple phases of alteration, with overprinting and variation of fluid chemistry through time. This supports earlier Petrographic observations of multiple overprinting of mineral phases within these halos (See Section 4.2 ‘Alteration’ and Wilson et al., 2003 and Teagle et al., 2006).

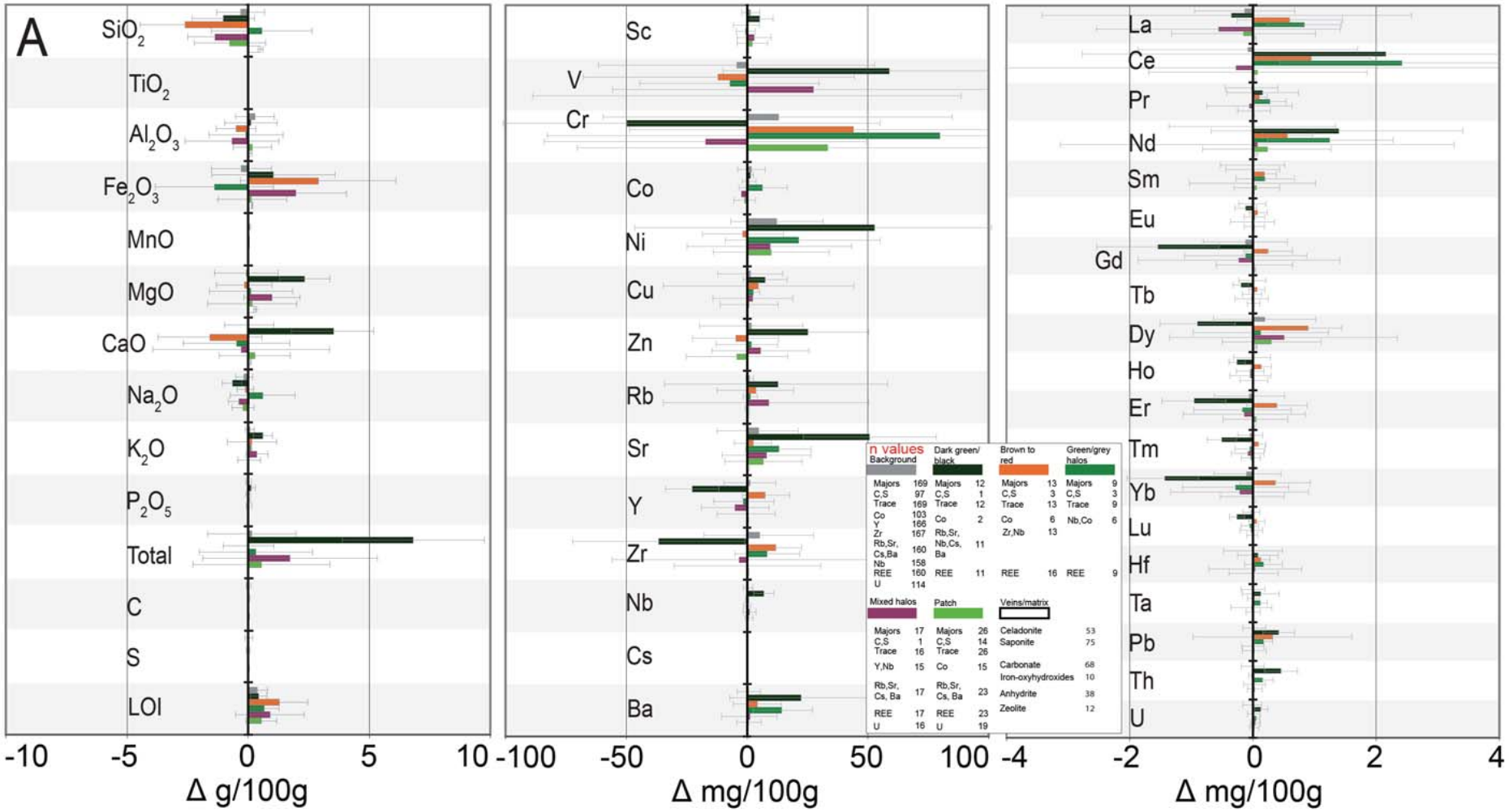

Figure 4.35. Multi-element diagrams showing the average chemical changes in mass (A) and % changes (B, overleaf) for major element oxides, trace elements and REE with regards to low temperature seawater alteration at Site 1256. Bars indicate propagated error.

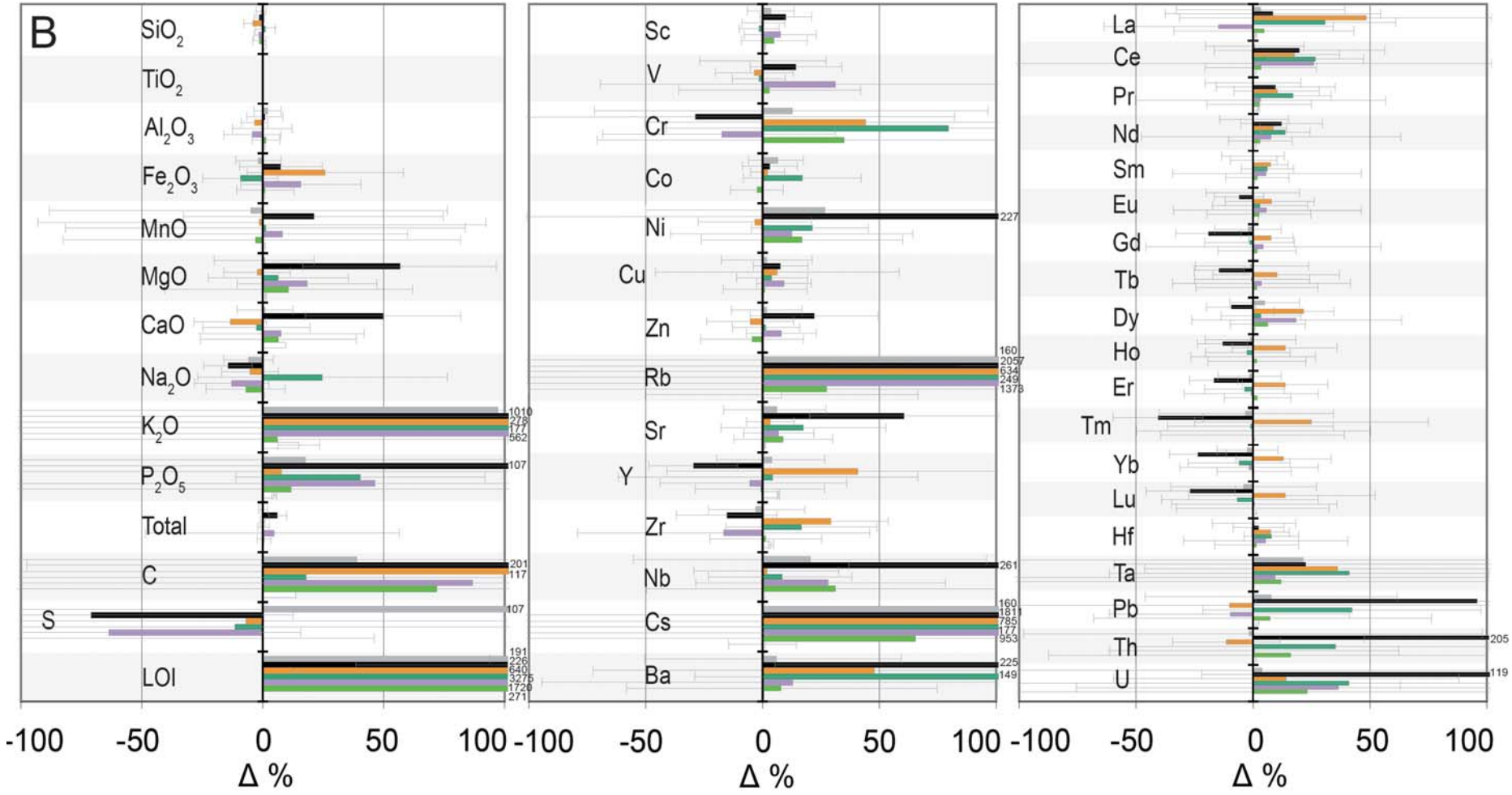
B
SiO2
TiO2
Al2O3
Fe2O3
MnO
MgO
CaO
Na2O
K2O
P2O5
Total
C
S
LOI
Sc
V
Cr
Co
Ni
Cu
Zn
Rb
Sr
Y
Zr
Nb
Cs
Ba
La
Ce
Pr
Nd
Sm
Eu
Gd
Tb
Dy
Ho
Er
Tm
Yb
Lu
Hf
Ta
Pb
Th
U
-100
-50
0
50
100
Δ %

Element	Background	Dark green/Black	Red/Brown	Green/Grey	Complex	Patch	Veins
SiO_2	(-)	(-)	(-)	(-)	(-)	(-)	(+)
TiO_2							
Al_2O_3							
Fe_2O_3			+	-	+		
MnO		+					
MgO		++			+	+	
CaO		+	-				(+)
Na_2O		-		+	-		
K_2O	++	++++	+++	+++	+++		+
P_2O_5	+	+++		+	+	+	(+)
C	+	+++	+++	+	++	++	
S	+++	--		-	--		+
LOI	+++	+++	+++	+++	++++	+++	
Sc							
V		+			+		
Cr	+	-	+		-	+	
Co				+			
Ni	+	+++		++	+	+	
Cu							
Zn		+					
Rb	+++	++++	+++	+++	++++	+	+
Sr		++		+			
Y		-	+				
Zr		-	+	+	-		(+)
Nb	+	+++			+	+	
Cs	+++	++++	+++	+++	+++	++	(+)
Ba		+++	++	+++	+		
La			+	+	-		
Ce		+	+	+	+		
Pr			+	+			
Nd		+		+			
Sm							
Eu							
Gd		-					
Tb		-	+				
Dy			+		+		
Ho		-	+				
Ef		-	+				
Tm		-	+	-			
Yb		-	+				
Lu		-	+				
Hf							
Ta	+	+	+	++	++	+	
Pb		+++	++	++			
Th		+++	-	++		+	
U		+++	+	++	+	+	

Table 4.3. Summary of low temperature chemical changes of alteration styles at Site 1256. (+) = change in silica and change as a result of vein minerals (minimum = + 5% in veins). ++ = 50 to 99 % increase, +++ = 100 to 999 % increase, ++++ = >1000 % increase, vice versa for negative signs.

Only one sample (206-1256D, 20R-1, 42-47 cm) of low temperature breccia was analyzed as a whole rock (including clasts and matrix), therefore it may not be representative of all low temperature breccias at Site 1256. Nevertheless, chemical

changes include increased Fe_2O_3, MgO, K_2O, LOI, V, Ni, Cu, Zn, Sr, Ba and decreased Al_2O_3 CaO, Na_2O, and Cr (Figure 4.35 and 4.36). The increases reflect secondary mineral emplacement of saponite, quartz, and iron-oxyhydroxides, whereas depletions, such as CaO perhaps reflect the loss of primary mineralogy due to replacement of groundmass by secondary minerals within the clasts and loss of volume due to fracturing and infill. For the purposes of calculating the total weighted chemical change, as discussed earlier in the section, breccia matrix and cement compositions are grouped with 'veins'. In addition, Low temperature breccia clast alteration mirrors that of alteration observed in vein related halos and patches. Therefore, altered clasts that have been analyzed separately from their cement are placed in the appropriate alteration style.

4.3.2.3 High temperature chemical changes

High temperature alteration within the transition zone at Site 1256 is represented by grey background, dark green to dark grey halos, and patches (See Section 4.2'Alteration' for petrographic details and mineral assemblages). Overall chemical change is relatively minor compared to low temperature alteration. High propagated error (Especially the range of changes for each sample) in many elements, especially Mn, K, P, Cr, Ni, Cu, Zr, Rb, Cs, and most REE (shown as error bars in Figure 4.36 A and B) precludes precise appraisal of the change associated between each alteration style. The high degree or range of changes reflects overprinting and highly variable alteration intensities within each alteration style.

All alteration types exhibit a reduction in SiO_2, and increases in LOI, Th and U (Figure 4.37 and 4.38). These reflect partial loss of primary igneous phases during secondary mineral replacement, and/or volume loss, and the incorporation of secondary mineral phases, perhaps most notably chlorite. Excluding breccias (discussed later), alteration patches represent the most highly altered whole rock samples with increased Na_2O, K_2O, LOI, Ni, Zn, Rb, Ba, Hf, Tm, and decreased SiO_2, Nb, Cs, La, Ta, Pb, Th and U. Veins, however, have minimal impact, with only very minor increases in major element oxides and Sr. The overall low chemical change reflects restricted fluid flow within the sheeted dykes of Site 1256 which is manifested in thin veins with narrow halos and patches.

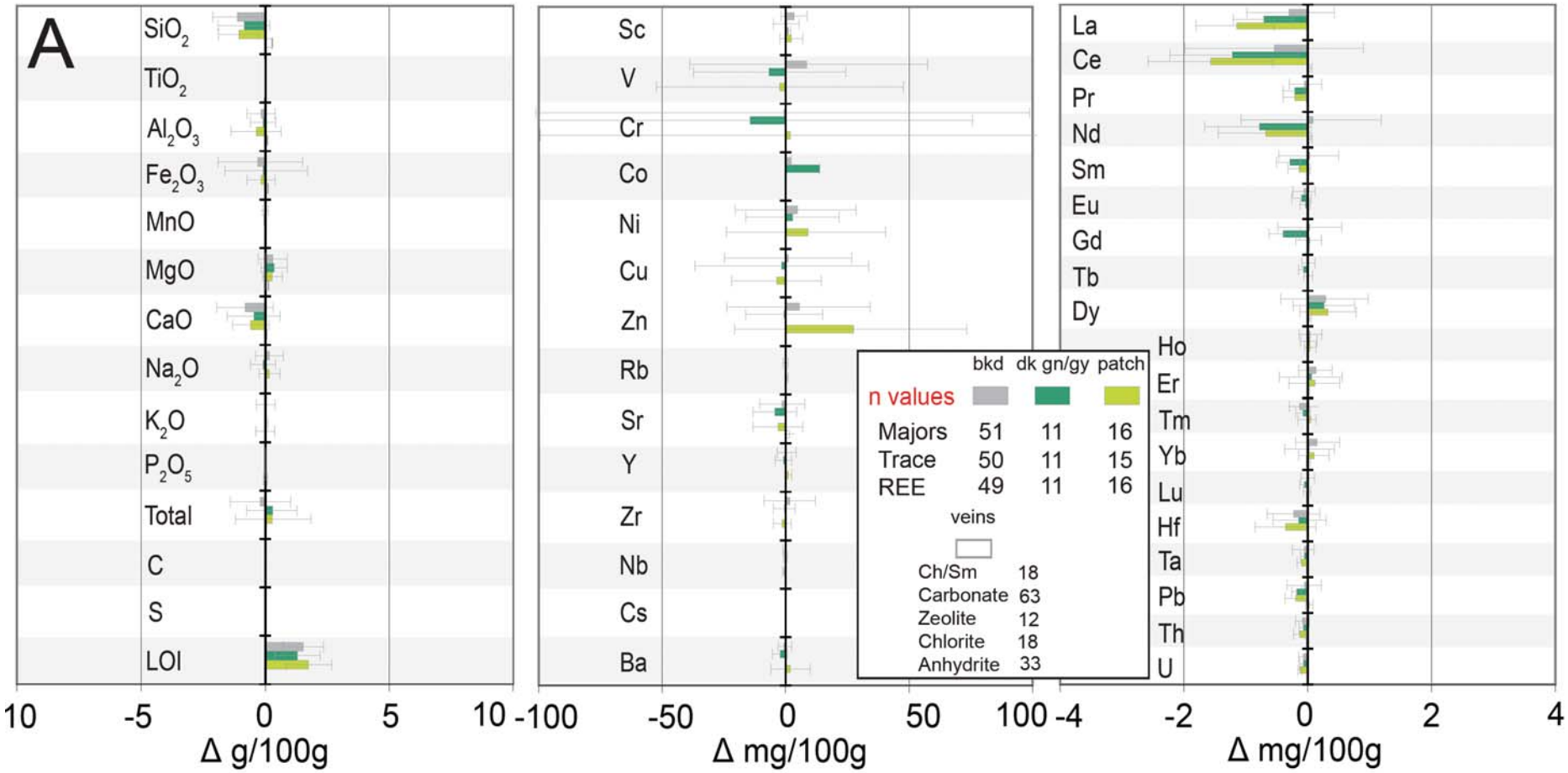

Figure 4.36. Multi-element diagrams showing the average chemical changes in mass (A) and % (B, overleaf) for major element oxides, trace elements and REE with regards to high temperature seawater alteration at Site 1256. Bars indicate propagated error.

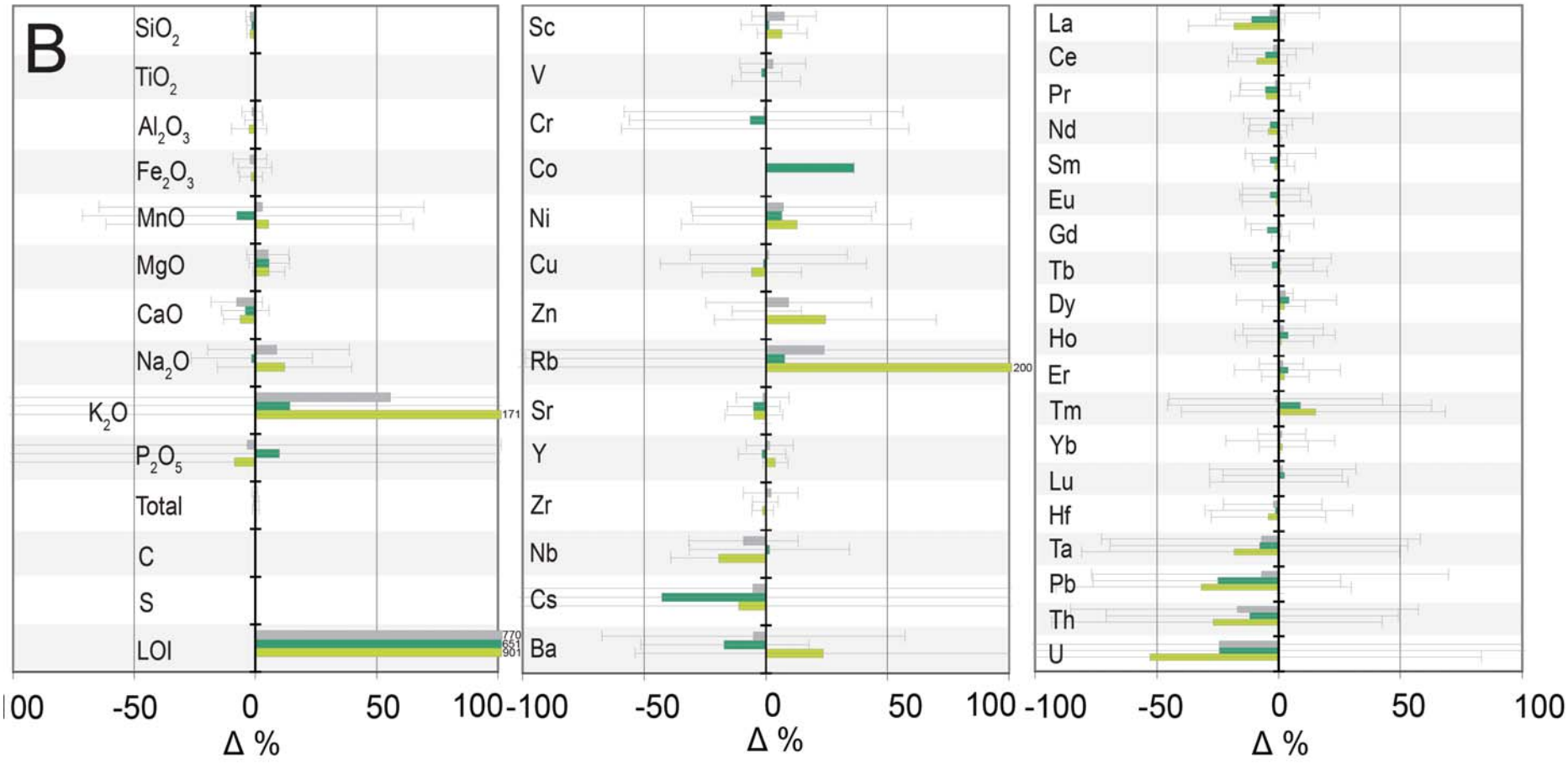
B
SiO2
TiO2
Al2O3
Fe2O3
MnO
MgO
CaO
Na2O
K2O
P2O5
Total
C
S
LOI
171
779
651
901
Sc
V
Cr
Co
Ni
Cu
Zn
Rb
Sr
Y
Zr
Nb
Cs
Ba
200
La
Ce
Pr
Nd
Sm
Eu
Gd
Tb
Dy
Ho
Er
Tm
Yb
Lu
Hf
Ta
Pb
Th
U
-100
-50
0
50
100
Δ %

Element	Background	Green/grey	Patch	Veins	Element	Background	Green/grey	Patch	Veins
SiO_2	(-)	(-)	(-)	(+)	Zr				
TiO_2					Nb			-	
Al_2O_3					Cs		-	-	
Fe_2O_3					Ba		-	+	
MnO					La		-	-	
MgO					Ce			-	
CaO					Pr				
Na_2O			+		Nd				
K_2O	++	+	+++		Sm				
P_2O_5					Eu				
C					Gd				
S					Tb				
LOI	+++	+++	+++		Dy				
Sc					Ho				
V					Ef			+	
Cr					Tm		(+)	+	
Co		+			Yb				
Ni			+		Lu				
Cu					Hf				
Zn			+		Ta		-	-	
Rb	+		+++		Pb	(-)	-	-	
Sr				(+)	Th	-	-	-	
Y					U	-	-	--	

Table 4.4. Summary of high temperature chemical changes of alteration styles at Site 1256. (+) = change in silica and change as a result of vein minerals (minimum = + 1% in veins). ++ = 50 to 99 % increase, +++ = 100 to 999 % increase, ++++ = >1000 % increase, vice versa for negative signs.

4.3.2.4 Chemical changes associated with lithology

Chemical changes associated with lithology (sheet flows, massive flows, pillow lavas, and breccias) are shown in Figure 4.37 A and B. The change in breccias is based on whole rock compositions (clasts and matrix). Sheet and massive flows exhibit similar changes with increases in K_2O, LOI, Rb, and minor increases in C, Ni, Sr, Ba, Ta, Pb, Th and U. Pillow lavas appear to be more altered with a greater range of elements exhibiting changes, including increased K_2O, P_2O_5, C, LOI, V, most trace elements, La, Dy, Er, Tm, Hf, Ta, Pb, Th, and U. Pillow lavas exhibits loss in MnO and CaO. These changes likely reflect emplacement of secondary minerals within the numerous cooling fractures and chilled margins of the lavas. A reduction of Ca suggests replacement of primary igneous phases, such as plagioclase. Volume change may have resulted in the apparent change observed in some REE. The greatest change observed between lithologies is within the breccias. Concentrations of most elements have

undergone changes. These include, increased Fe_2O_3, Na_2O, K_2O, P_2O_5, C, S, LOI, Rb, Nb, Cs, Ba, Eu, Er, Tm, Hf, Pb, Th, U and decreased Al_2O_3, MnO, MgO, CaO, Sc, Cr, Ni, Cu, and Sr. Changes reflect the intensive replacement of primary phases at high water-rock ratios with secondary phases, including saponite, iron-oxyhydroxides, chlorite/smectite, anhydrite, and secondary sulfides observed.

Despite high ranges observed in Figure 4.37, A and B, the variation of chemical change in the different litholgies is significant. Pillow lavas appear more altered than sheet and massive flows, and breccias are even more altered. These changes imply that lithological variation at Site 1256 may play a significant role in the extent of alteration at this site.

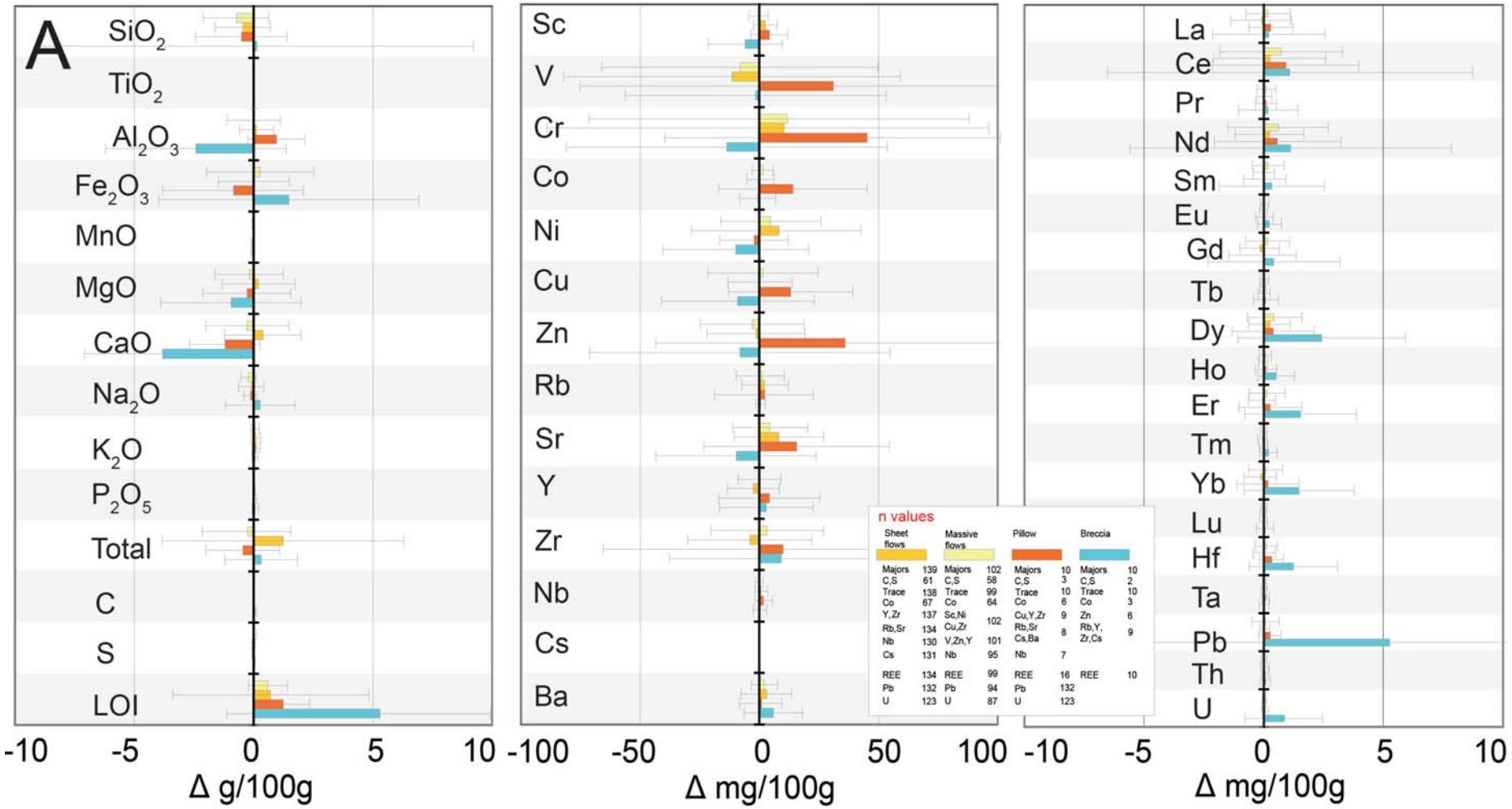

Figure 4.37. Multi-element diagrams showing the average chemical changes in mass (A) and % (B, overleaf) for major element oxides, trace elements and REE with regards to lithology at Site 1256. Bars indicate propagated error.

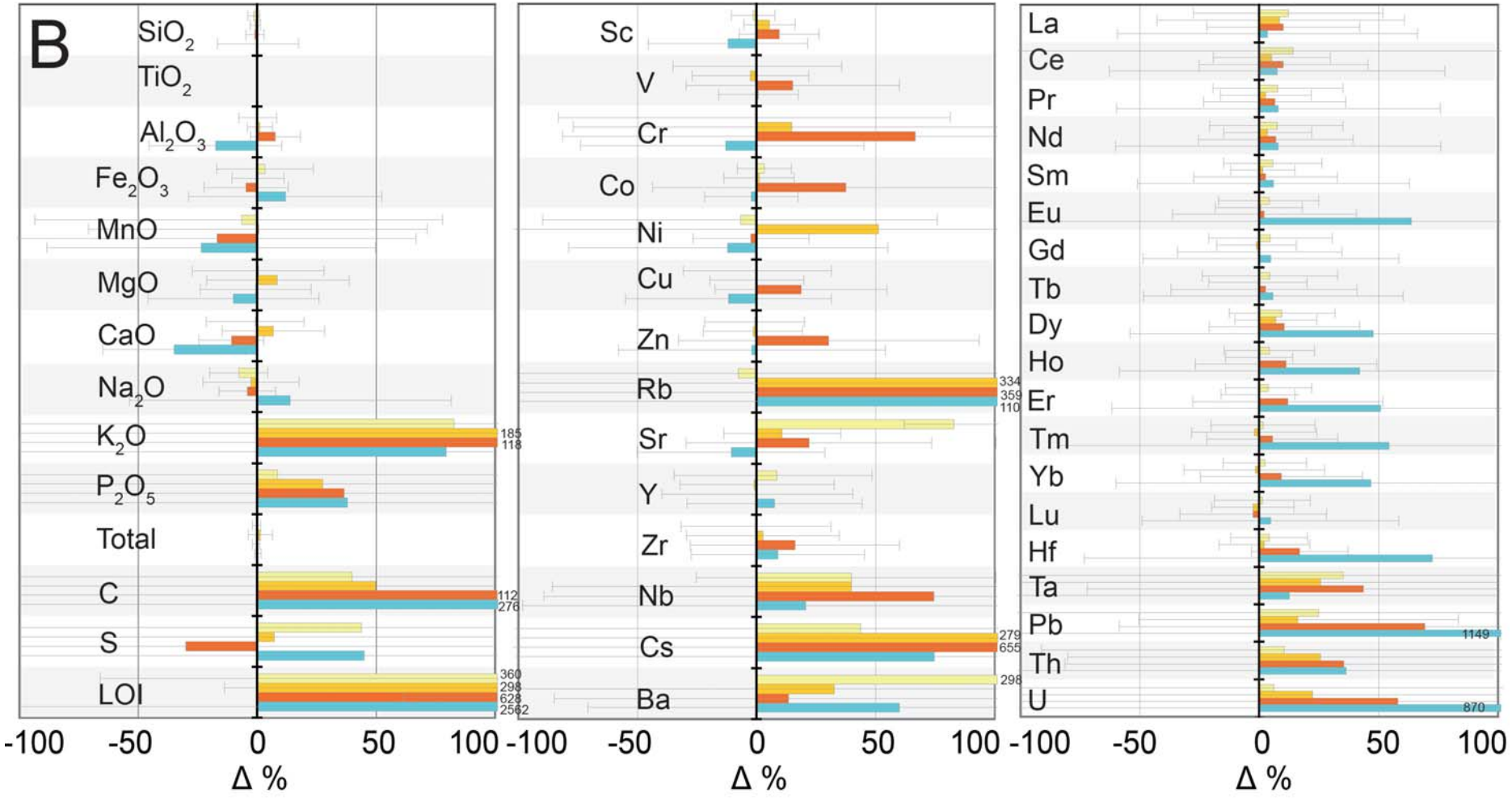
B
SiO2
TiO2
Al2O3
Fe2O3
MnO
MgO
CaO
Na2O
K2O
P2O5
Total
C
S
LOI
185
118
112
276
360
298
628
2562
Sc
V
Cr
Co
Ni
Cu
Zn
Rb
Sr
Y
Zr
Nb
Cs
Ba
334
359
110
279
655
298
La
Ce
Pr
Nd
Sm
Eu
Gd
Tb
Dy
Ho
Er
Tm
Yb
Lu
Hf
Ta
Pb
Th
U
1149
870
-100
-50
0
50
100
Δ %

Element	Sheet	Massive	Pillow	Breccia	Element	Sheet	Massive	Pillow	Breccia
SiO_2	(+)	(+)	(+)	(+)	Zr			+	
TiO_2					Nb	+		++	+
Al_2O_3				-	Cs	+++	+++	+++	++
Fe_2O_3				+	Ba	+	+	+	++
MnO			-	-	La		+	+	
MgO				-	Ce		+	+	
CaO			-	-	Pr				
Na_2O				+	Nd				
K_2O	+++	++	+++	++	Sm				
P_2O_5	+		+	+	Eu				++
C	+	+	+++	+++	Gd				
S		+	-	+	Tb				
LOI	+++	+++	+++	++++	Dy			+	+
Sc				-	Ho			+	+
V			+		Ef			+	++
Cr	+		++	-	Tm				++
Co			+		Yb				+
Ni	++	+		-	Lu				
Cu			+	-	Hf			+	++
Zn			+		Ta	+	+	+	
Rb	+++	+++	+++	+++	Pb	+	+	++	++++
Sr	+		+	-	Th	+	+	+	+
Y					U	+		++	+++

Table 4.5. Summary of chemical changes associated with lithology. (+) = change in silica + = 10 to 49 % increase. ++ = 50 to 99 % increase, +++ = 100 to 999 % increase, ++++ = >1000 % increase, vice versa for negative signs. Breccia compositional change includes clasts and matrix.

4.3.2.5 Summary

At Site 1256 the variation in major elements, trace elements and REE and their changes associated with alteration reflect the petrographic observations of alteration mineral assemblages and their intensity. Sample pairs, and 'triples' show relatively consistent trends with LOI, which is consistent with petrographic observations of secondary minerals within the groundmass. The overall increasing K_2O reflects the emplacement of celadonite and later iron-oxyhydroxide phases, these phases are commonly associated with oxidizing conditions in which open seawater circulation takes place (e.g., Alt, 1993; Alt and Honnorez, 1984).

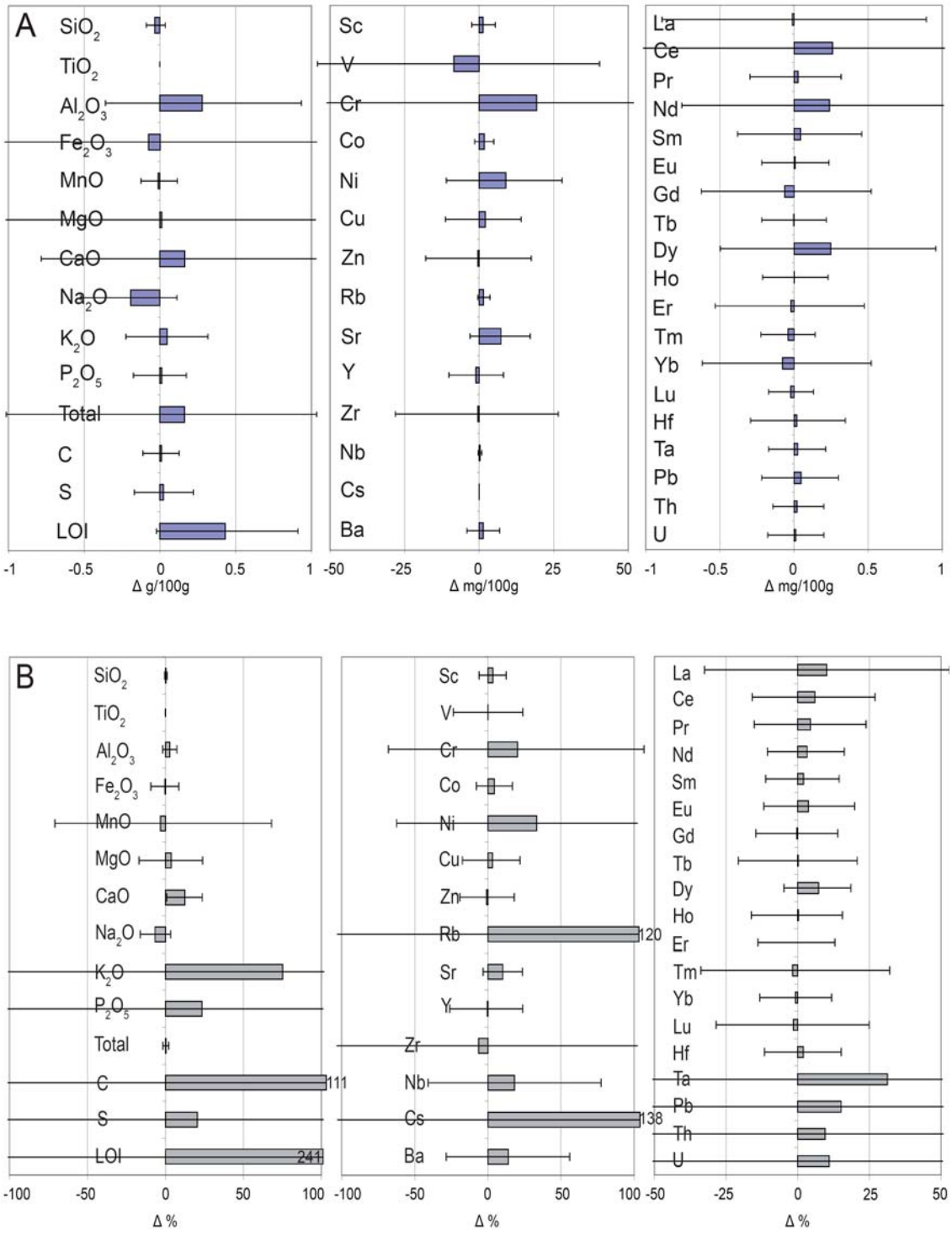

Figure 4.38. Summary of the weighted average chemical changes (A; g/100g and mg/100g B; % changes) for the volcanic section of Site 1256 (Low temperature alteration).bars indicate propagated error

The chemical variation and changes associated with higher temperature alteration assemblage within the lowermost lavas and transition zone at Site 1256 indicate much more restricted fluid flow, with no oxidation and limited replacement. This is supported by the petrographic observations that show much narrower halos, less replacement of primary phases and fewer veins.

Figure 4.38 indicates the weighted average chemical changes as a result of low temperature alteration for the whole of Site 1256. Changes are summarized in Table 4.6. As discussed earlier in this chapter, the calculated chemical changes for each style were weighted according to the proportion of core they occupy. The weighted averages plus the weighted average secondary mineral compositions residing in veins, vein nets and breccias are combined to give a grand total chemical change for Site 1256. Overall chemical change at Site 1256 is small, with gains in K_2O, C, LOI, Rb, Cs and minor gains in CaO, S, Cr, Ni, Sr, Nb, Ba, Ta, Pb, and U. A slight loss of Na_2O and MnO is reported. Given the very high propagated error relating to the range of changes in Rb, Zr, Cs, and REE (Notably Ta, Pb, Th and U), the change calculated is not meaningful. In the case of Ta, Pb, Th and U no trend was detected between these elements and the chosen immobile element TiO_2 and the chosen precursor composition (based on the least altered samples) has a very high error due to the range within the least altered samples. The high errors exhibited in elements Mn, K, P_2O_5, C, S, LOI, Cr, Ni, and Rb reflect the range of changes observed rather than imprecise precursors, therefore overall change in these elements are better constrained, despite the ranges.

The incorporation of large amounts of K_2O, and LOI reflect formation of clay minerals. Low change in Fe_2O_3 reflects only minor iron-oxyhydroxide emplacement. Leaching of elements from the host rock and their replacement as vein minerals potentially reflects the apparent lack of change within Site 1256. This would also help to explain the high LOI. In addition, clay minerals in veins and halos may explain the increased abundance of Rb, and Cs because these elements are relatively mobile and will partition into the interlayer sites within clay mineral structures. The slight reduction in MnO, and Na_2O reflects the partial replacement of some primary igneous phases, such as clinopyroxene and plagioclase at Site 1256. Significant replacement of primary igneous phases only occurs within the alteration halos and patches (See earlier); therefore the majority of Site 1256 low temperature alteration is associated with minor replacement and filling of interstices and partial replacement of olivine.

Despite the changes associated with the incorporation of clay minerals and the presence of moderate to highly altered intervals, overall alteration within the lavas at Site 1256 remains slight, which supports the petrographic evidence in Section 4.2.

Element	Change %	Element	Change %	Element	Change %	Element	Change %
SiO2	(+)	Sc		Ba	+	Yb	
TiO2		V		La		Lu	
Al2O3		Cr	+	Ce		Hf	
Fe2O3		Co		Pr		Ta	+
MnO		Ni	+	Nd		Pb	+
MgO	(+)	Cu		Sm		Th	
CaO	+	Zn	+	Eu		U	+
Na2O	(-)	Rb	+++	Gd			
K2O	+ +	Sr		Tb			
P2O5	+	Y		Dy			
C	+ + +	Zr		Ho			
S	+	Nb	+	Ef			
LOI	+ + +	Cs	+ + +	Tm			

Table 4.6. Summary of the average chemical changes for low temperature alteration at Site 1256. Only change that is greater than ~10% is highlighted. 10-50 % gain = +, 50-100 % gain = + +, and >100 % = + + +. Losses are recorded as – (10 – 50 % loss). (-) and (+) refers to minor variations <10% in SiO_2, Na_2O, and MgO.

High temperature alteration within the sheeted dykes is summarized in Figure 4.39 and Table 4.7. The total chemical change within the hydrothermally altered rocks in the transition zone was calculated based on the weighted averages for each alteration style (See section C, 2 in Appendix). Both actual changes and percentage changes within the high temperature portion of the transition zone and upper sheeted dykes are minimal, which implies that majority of rocks recovered in this section are relatively fresh. Changes include slight reductions in SiO_2 and CaO and increases in MgO, Na_2O, K_2O, LOI, Rb. These changes reflect minor emplacement of secondary minerals e.g. chlorite and actinolite. Reduction in CaO and SiO_2 reflects minor replacement of the groundmass.

At Site 1256 changes associated with lithological variation may be important in controlling the style and intensity of alteration. Large changes in the pillow lavas and breccias highlight the need for an accurate appraisal of Site 1256 stratigraphy. Determination of igneous stratigraphy at Site 1256 from core-log integration indicate that 18 % of Site 1256 may be composed of breccias (Tominaga et al., 2009). Given

current estimates of breccia and the other litholgies at Site 1256 that are based on core recovery and the high degree of alteration within breccias, it is likely that the estimate of chemical change in this study is an underestimate and therefore must be treated as a minimum value for change.

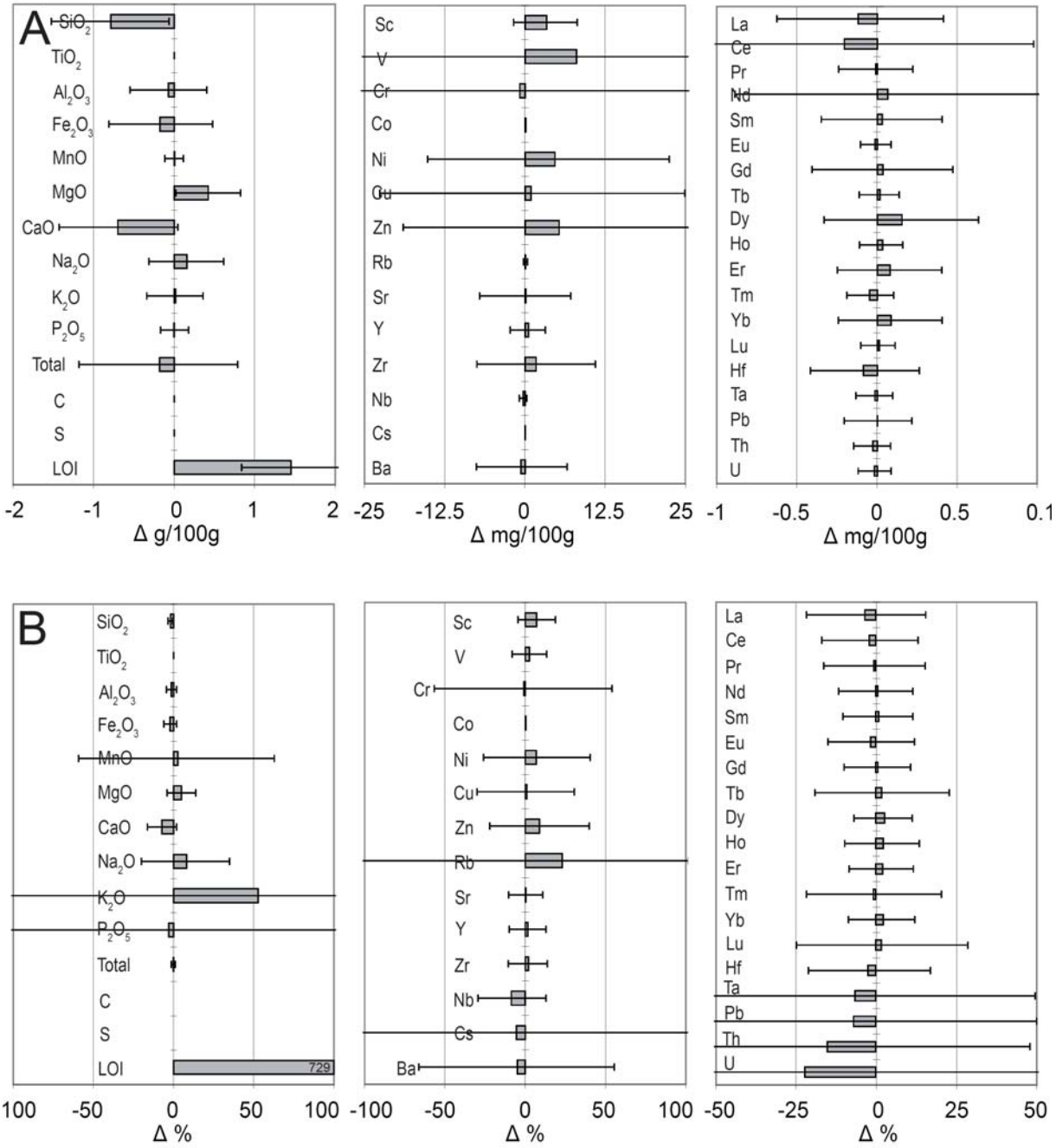

Figure 4.39. Percentage chemical change for transition zone and upper sheeted dyke rocks at Site 1256 that have been subjected to high temperature alteration. Bars indicate the propagated error, including the range of chemical changes for Site 1256.

Element	Change %	Element	Change %	Element	Change %	Element	Change %
SiO2	(-)	Sc		Ba	+	Yb	
TiO2		V		La		Lu	
Al2O3		Cr		Ce		Hf	
Fe2O3		Co		Pr		Ta	
MnO		Ni		Nd		Pb	
MgO	(+)	Cu		Sm		Th	+
CaO	(-)	Zn		Eu		U	+
Na2O	(+)	Rb	+	Gd			
K2O	+ +	Sr		Tb			
P2O5		Y		Dy			
C	No data	Zr		Ho			
S	No data	Nb		Ef			
LOI	+ + +	Cs		Tm			

Table 4.7. Summary of the average chemical changes for high temperature alteration at Site 1256. Only change that is greater than ~10% is highlighted. 10-50 % gain = +, 50-100 % gain = + +, and >100 % = + + +. Losses are recorded as – (10 – 50 % loss). (-) and (+) refers to minor variations <10% in SiO_2, MgO, CaO, and Na_2O.

In addition to the analysis and observations relating to alteration in this study and work carried out by Wilson et al., (2003) and Teagle et al., (2006), more work needs to be done to constrain the chemistry of secondary minerals at Site 1256 and their variation/transition with depth. Despite a number of secondary mineral analyses for Site 1256 in this study (saponite, carbonates, anhydrite, and chlorite). Further sampling and analysis of secondary minerals, particularly iron-oxyhydroxides, more chlorite, zeolite, and secondary sulfides is necessary to properly constrain Site 1256 secondary mineralogy compositions. Errors associated with the selection of protoliths, particularly within REE need to be addressed.

4.3.3 Whole rock and clay isotopic results

A total of 228 whole rock samples were measured for $^{87}Sr/^{86}Sr$ at Site 1256 (See Chapter 2 for methodology). Of which 156 were sampled from the lavas and transition zone (~0 to 815 ms). Data is shown in Section B, 2 and D, 2 of the appendix initial (Age corrected to 15 Ma) and measured $^{87}Sr/^{86}Sr$ are shown . The young age of the samples and the low concentrations of Rb has meant that the age corrected $^{87}Sr/^{86}Sr$ is not significantly different to the measured values, because the difference is within the size of the data points when plotted. A number of samples at Site 1256 were leached of secondary minerals utilizing an aggressive multi-step acid attack (HCl) procedure Mahoney, (1987) and Mahoney et al., (1983). Section 2.5 in Chapter 2 details the leaching procedure and the results of whole rock leaching. Six leached sample residues were analyzed by TIMS for their Sr-isotopic composition and they yield a range of 0.702828 to 0.702901 with an average of 0.702868. These values are near the expected range for fresh MORB (0.7024-0.7027, Saunders, et al., 1988) and therefore can be regarded as the primary Sr isotopic composition for Site 1256. Figure 4.40 is a plot of $^{87}Sr/^{86}Sr$ vs. depth for Site 1256 with respect to their different alteration types, including leached samples with stratigraphy and alteration style. All samples (except for the leached whole rock samples) are elevated above primary Sr at Site 1256 yet, for the most part they remain significantly below 15 Ma and modern seawater of 0.70878 and 0.70917 respectively, (McArthur et al., 2001). Radiogenic Sr decreases very slightly with depth from the lava pond to the sheet and massive flows. The low $^{87}Sr/^{86}Sr$ in the massive units is consistent with restricted fluid flow in more competent rocks with fewer fractures, which implies minimal Sr-isotopic interaction with the host rock. The Sr-isotopic composition within the transition zone is slightly elevated compared to the rest of the lavas. A number of breccias recovered in this zone with high $^{87}Sr/^{86}Sr$ (0.7051-0.7061) indicate high Sr-isotopic exchange and a high water rock ratio. The paucity of samples between 575 and 650 msb is due to limited sampling.

Many of the least altered ‘fresh’ grey background samples deviate only slightly from MORB, and variation of $^{87}Sr/^{86}Sr$ between the different alteration styles is minimal, However, the more altered samples exhibit slightly higher values than the background samples. A number of samples, most of which are highly altered, are strongly elevated in $^{87}Sr/^{86}Sr$. These include breccias, both at high and low temperature alteration, and samples with intense replacement of primary phases by secondary

minerals. For example the 'red brick' section (Figure 4.40) where $^{87}Sr/^{86}Sr$ are strongly elevated compared to the surrounding rocks. No obvious trend occurs between the extent of alteration (measured as volume % alteration style vs. depth) and the $^{87}Sr/^{86}Sr$ for the whole rock samples (Figure 4.40).

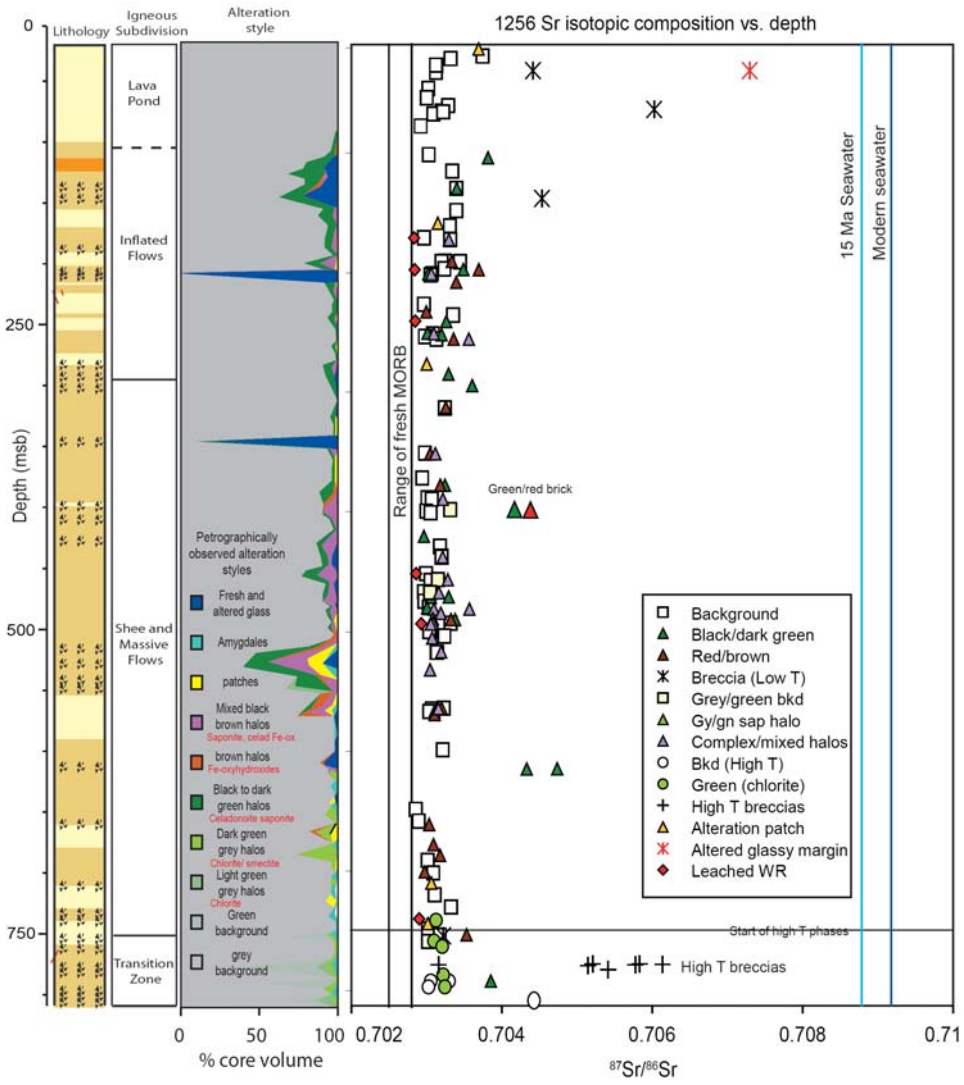

Figure 4.40. Whole-rock strontium ($^{87}Sr/^{86}Sr$) vs. depth for Site 1256 extrusives. Included are leached whole rock samples. Samples are shown in accordance to their alteration styles. (seawater composition after McArthur et al., 2001) stratigraphy modified from Wilson et al., (2003) and Teagle et al., (2006).

Histograms of Sr-isotopic compositions for low temperature alteration styles (Figure 4.41) indicate the variability within each alteration style. Background rocks exhibit the most MORB-like $^{87}Sr/^{86}Sr$ values, whereas breccias are variably least MORB-like. All alteration styles are variably elevated above the leached samples and background with complex halos and dark green/black exhibiting the greatest deviation.

Assuming exchange of Sr with seawater at 15 Ma and that the leached samples of 'fresh' basalts represent the primary Sr isotopic composition, the proportion of Sr in each sample that is sourced from seawater can be estimated. The proportion of seawater Sr in whole rocks $^{F}Sr^{SW}$ is calculated from the simple expression below (Bach and Humphries, 1999):

$$^{F}Sr^{SW} = (R_{sample} - R_{fresh\ basalt})/(R_{seawater} - R_{fresh\ basalt})$$

Where $R_{fresh\ basalt}$ is initial $^{87}Sr/^{86}Sr$, $R_{seawater}$ is seawater $^{87}Sr/^{86}Sr$. An $^{F}Sr^{SW}$ values of 0 and 1 = none and total exchange respectively. Figure 4.41 is a histogram illustrating the distribution of $^{F}Sr^{SW}$ with respect to alteration styles, all samples and the weighted average $^{F}Sr^{SW}$ for Site 1256 lavas and transition zone. All basalts at Site 1256 appear to have undergone at least minor exchange with seawater Sr. All major alteration styles (grey background, brown halos, black/green and complex halos) have a distribution centered on 0.075. $^{F}Sr^{SW}$ in alteration halos are slightly elevated compared to background. Even the majority of complex halos, where we would expect greater seawater exchange exhibit low $^{F}Sr^{SW}$. Breccias range from ~0.075 to ~0.575 the majority of which range between 0.4and 0.575. These ranges perhaps reflect the higher fluid fluxes that occurred at these intervals imparting a greater seawater component to the host rock. The weighted average $^{F}Sr^{SW}$ was calculated by taking the average Sr isotopic ratio for each sample and weighting these averages according to the volume % that each alteration style occupies at Site 1256. The sum total of these weightings gives a weighted Sr isotopic value of 0.703482, to which we derive $^{F}Sr^{SW}$. The weighted average $^{F}Sr^{SW}$ for Site 1256 is 0.107, which implies that ~10% of Sr is derived from seawater.

Because LOI and exchange of seawater Sr are often used as a proxy for alteration intensity, Sr isotopic data is compared to LOI in Figure 4.43. Correlations between the extent of hydrothermal alteration and $^{87}Sr/^{86}Sr$ are weak and variable. In general background rocks have lower LOI vs. $^{87}Sr/^{86}Sr$ than the altered rocks. Highly altered samples, however, have high LOI compared with $^{87}Sr/^{86}Sr$.

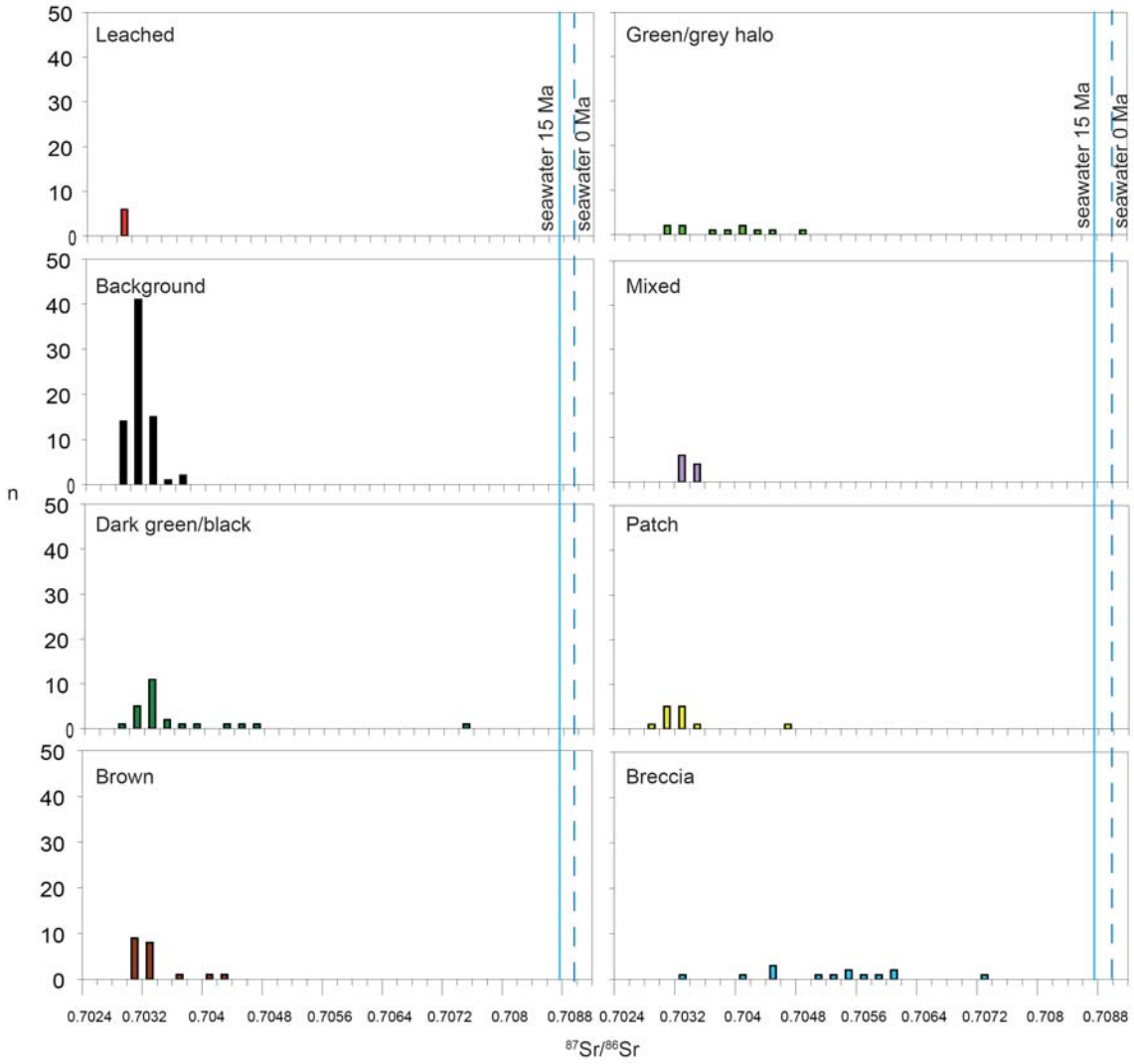

Figure 4.41. Histogram of whole rock Sr-isotopic compositions for different low temperature alteration types observed at Site 1256. Leeched samples, modern seawater and 15 Ma seawater are included for reference (seawater composition after McArthur et al., 2001)

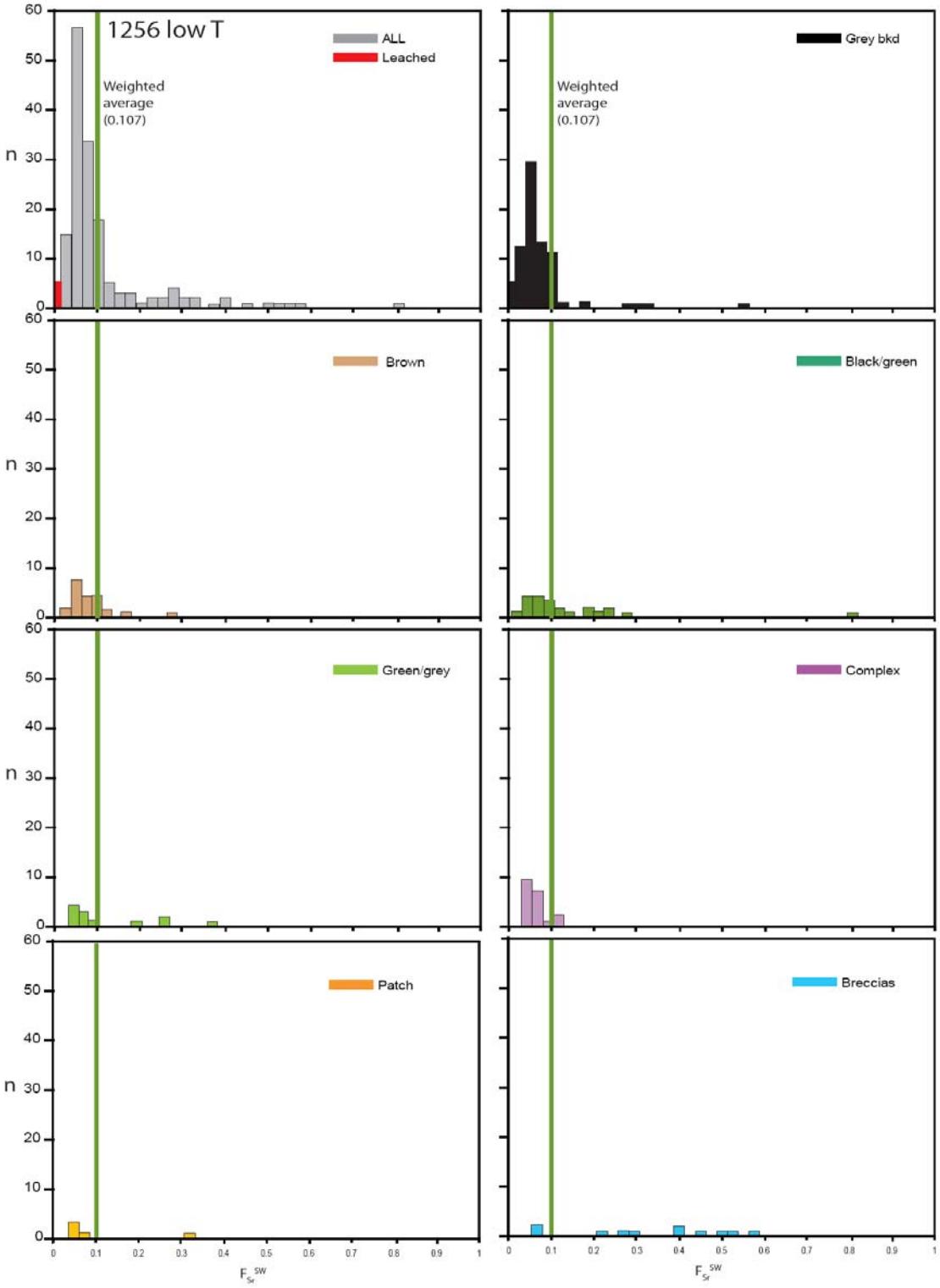

Figure 4.42. Distribution of $^{F}Sr^{SW}$ (Based on Bach and Humphris, (1999) calculation of proportion of seawater) in whole rock basalts in the lavas and transition zone at Site 1256 with respect to alteration styles. Included is the distribution of all samples and the average $^{F}Sr^{SW}$ weighted according to alteration style volume %.

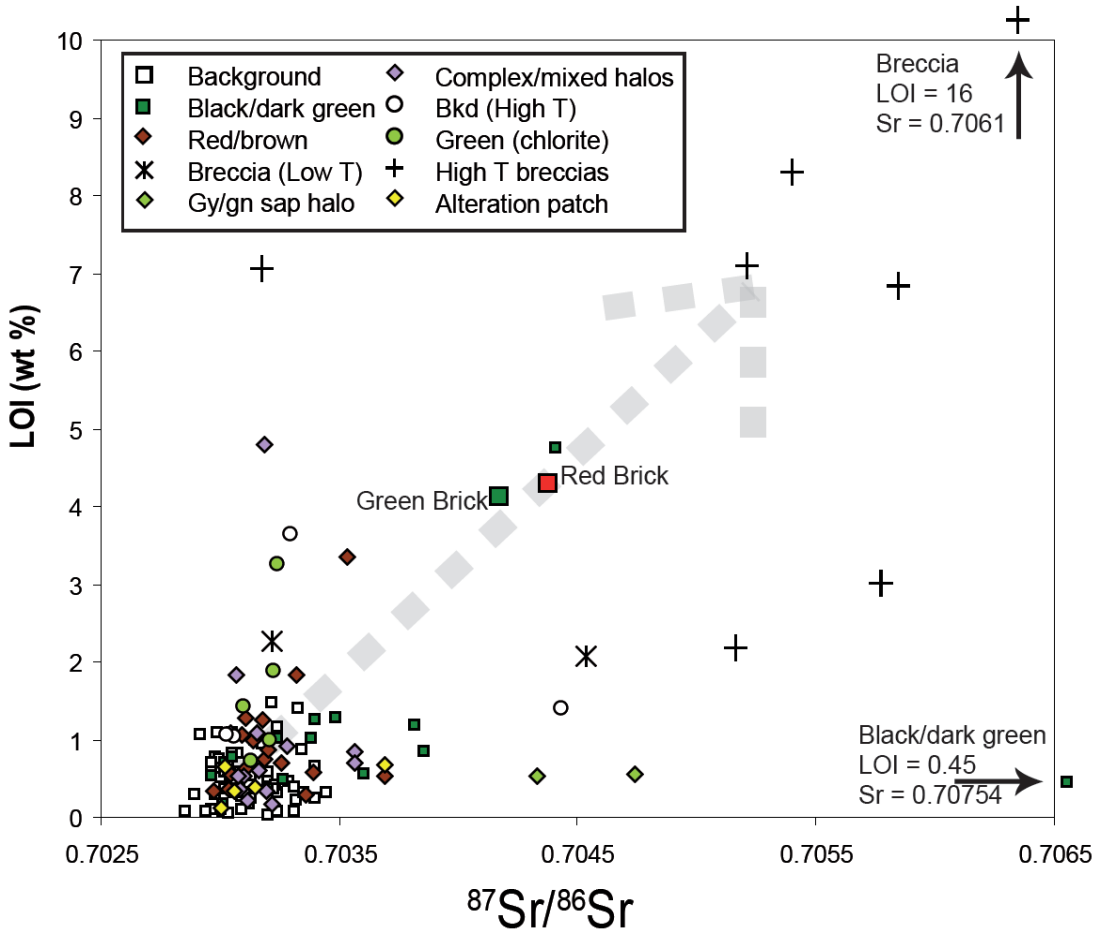

Figure 4.43. $^{87}Sr/^{86}Sr$ vs. LOI for the extrusives and transition zone at Site 1256. Alteration styles are indicated using the same symbols as Figure 4.3.10. The grey arrow indicates expected trend with LOI, which is most apparent in the highly altered breccias and the 'brick' samples.

The lack of a trend suggests either that, at low temperature Sr the relationship between LOI and seawater Sr exchange is not linear, or that there is insufficient resolution in the isotope data to compare results with alteration styles. Because alteration at Site 1256 is only slight, and that even within halos, alteration is not high, it is more likely that the Sr has undergone only minor exchange with basement rocks at Site 1256 rather than poor sampling.

Leaching of pure hand picked clay mineral separates was carried out for saponite and chlorite samples using a multi-stage leaching process in which 1N NH_4Cl solution was applied in an attempt to remove Sr, trace elements and REE interlayer cations from the crystal structure, so that only trace, REE and Sr bound to the crystal structure were measured (See chapter 2, Methods). The Sr-isotopic composition of leached saponite ranges from 0.70416 to 0.70761. Only one leached chlorite mineral with an $^{87}Sr/^{86}Sr$ of 0.70587 was analyzed. When plotted vs. depth (Figure 4.44)

leached samples indicate that most samples formed from fluids with a mixture of seawater Sr and MORB derived Sr, almost all leached samples exhibit a decrease in Sr after leaching. $^{87}Sr/^{86}Sr$ decreases slightly with depth, indicating greater interaction with the wall rock as temperatures increase. The Sr-isotopic composition of unleached clay minerals exhibit a more pronounced decrease with depth than the leached samples. Two possibilities may account for the trends observed in Figure 4.44. 1) later fluids circulating in the ocean crust are undergoing further interaction with basalts at depth before depositing interlayer cations into the clay minerals. 2) that, with depth, less fluid penetrates the crust during off axis circulation resulting in less interlayer cations and, therefore less radiogenic Sr to remove during leaching.

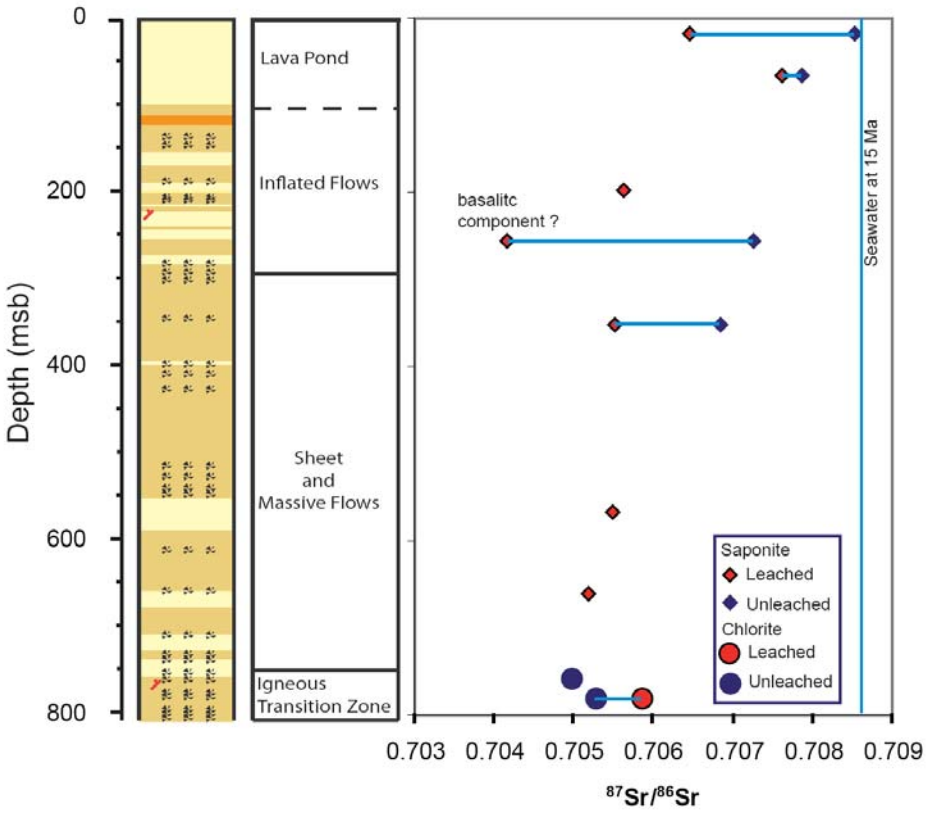

Figure 4.44. Sr-isotopic composition of Saponite and Chlorite unleached and leached clay mineral separates vs. depth at Site 1256. Seawater Sr-isotopic composition after McArthur et al, (2001) and Stratigraphy modified from Wilson et al., (2003) and Teagle et al., (2006).

4.3.4 Carbonate veins at Site 1256 and their constraints on low temperature hydrothermal fluid evolution

Throughout the volcanic section of Site 1256 carbonate vein minerals were recovered by hand picking, and then analyzed for major elements, C, S, $^{87}Sr/^{86}Sr$, and $\delta^{18}O$ (Coggon, 2006). Much work has been carried out regarding carbonate veins at Site 1256 by Coggon (2006) and therefore only a summary is outlined here.

Carbonate by volume makes up approximately 0.018% of the core and it is typically a minor phase in multiminerallic veins that are composed of saponite ± pyrite, iron-oxyhydroxides, celadonite, and silicates (see Section 4.3 'Alteration'). Rare carbonate only veins occurs in cross-cutting all other phases. The relationship of Mg/Ca, Fe/Ca and Mn/Ca with Sr/Ca, provide a means of differentiating between calcite, aragonite, or mixtures of the two (Coggon et al., 2006). Incorporation of small cations (Mg) will preferentially incorporate themselves into the crystal structure of calcite, which has a relatively small site (6 fold coordination). Large cations, in this case Sr, will preferentially substitute into aragonite, because it has a large site (9 fold coordination), (Deer et al., 1992).

Carbonate $\delta^{13}C$ compositions at Site 1256 range from -3 and 4 $‰_{VPDB}$ and there is an observed decrease in the carbon isotopic composition with depth (Figure 4.45). Oxygen isotopes range from 20-32 $‰_{VSMOW}$ with little relationship with depth of Site 1256 and a strong relationship with depth between ~190 and 400 msb (Figure 4.45) (Coggon, 2006). Formation temperatures following Friedman and O'Neil (1977), assuming precipitation from fluids with $\delta^{18}O_{water}$ = 0 ‰ range from ~10 to 75 ^{o}C. The range of temperatures and their relationship with depth shown in Figure 4.45 was interpreted to represent cold (10-35 ^{o}C) seawater dominated precipitation for the ponded lava flow, which formed ~5km off axis (Wilson et al., 2003) and warmer (60-75 ^{o}C) more restricted fluid flow and precipitation in the sheet and massive flows that underlie the massive flow unit. The deeper carbonate veins represent an increase in fluid temperature of ~0.075 ^{o}C/m (Coggon, 2006). Coggon, 2006 further suggests that the decreasing carbon isotopic composition at Site 1256 reflects the increased incorporation of magmatic carbon to the veins.

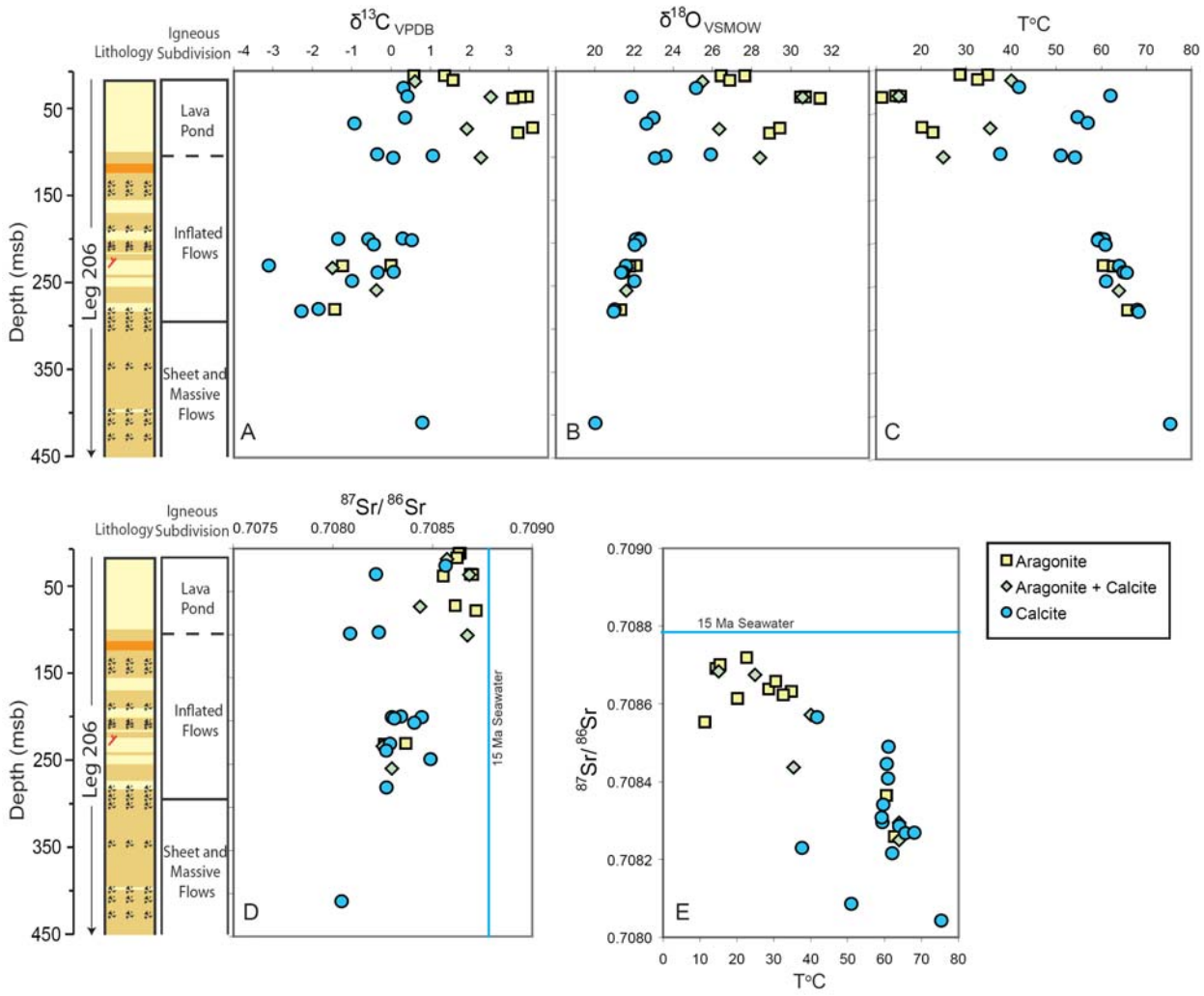

Figure 4.45. Site 1256 carbonate plots. A and B: Stable isotopic (C and O) compositions of carbonate veins with depth. Errors are less than width of the data points. C: Calculated formation temperatures for carbonates vs. depth following Friedman and O'Neil (1977), assuming precipitation from fluid with $\delta^{18}O$ = O ‰. D: Sr isotopic composition of carbonates vs. depth with seawater at 15 Ma shown for comparison. E: $^{87}Sr/^{86}Sr$ vs. calculated temperature of carbonates. For all vs. depth plots Site 1256 stratigraphy is shown for comparison. Figures are redrawn from Coggon (2006). Stratigraphy modified from Wilson et al., (2003) and Teagle et al., (2006). and seawater Sr-isotopic composition from McArthur et al, (2001).

Strontium isotopic compositions for carbonates at Site 1256 range from ~0.7080 to ~0.70872 with $^{87}Sr/^{86}Sr$ trending away from seawater compositions at ~15 Ma (~0.70875) with depth (Figure 4.45). In addition, the warmer carbonates tend to exhibit less seawater like $^{87}Sr/^{86}Sr$ (Figure 4.45), which suggests that with depth fluids become more evolved in which seawater Sr is undergoes greater exchange with basaltic Sr (Coggon, 2006). The proportion of basaltic Sr incorporated into carbonates at Site 1256 Sr ranges from ~1 to 18 % following the Bach and Humphries (1999) method.

4.3.5 Anhydrite at Site 1256

Because the observed anhydrite straddles the boundary between low and high temperature alteration, and anhydrite exhibits retrograde solubility, anhydrite is a useful tool for recording the evolution of seawater derived fluids during mid-ocean ridge circulation. A comprehensive review of anhydrite and the constraints on fluid evolution at Site 1256 are discussed in Chapter 8. However, because data, particularly $^{87}Sr/^{86}Sr$, $\delta^{18}O$, have a bearing on the conditions to which low temperature alteration at Site 1256 formed, a summary is provided here.

Anhydrite is observed at ~530 to ~1000 msb within the lowermost lavas, the lava dyke transition zone and the sheeted dykes (Figure 4.46). Anhydrite makes up 0.0062 % of the total volume of Site 1256 and it typically occurs within multi-minerallic veins, or on its own as thin late-stage veins that cross cut most other phases, anhydrite is rarely present within the groundmass. Anhydrite was sampled by hand picking of veins and analyzed for their majors, trace elements, REE, Sr-isotope ratios, S-isotope ratios, and oxygen isotopes (Table D, 1. Appendix). Formation temperatures were calculated following Chiba et al., (1981) range from ~45 to 400^{o}C however most anhydrite temperatures range from ~100 to 225^{o}C. Anhydrite formation temperatures within the extrusives and transition zone at Site 1256 ranges from ~50 to 400^{o}C. Although only 3 samples of anhydrite were recovered in the sheet and massive flows, they exhibit relatively low temperatures (~105-140^{o}C) compared to the variably higher temperatures in the transition zone (~50 – 400^{o}C) (Figure 4.46). These temperatures highlight the change from low temperature seawater dominated alteration to high temperature alteration. The Sr isotopic ratios of anhydrite range from 0.7046 to 0.7085 and, when plotted vs. depth in Figure 4.46, cluster into there are two distinct groups One dominated by hydrothermal fluids and another controlled by seawater derived fluids, these trends are discussed in Chapter 8.

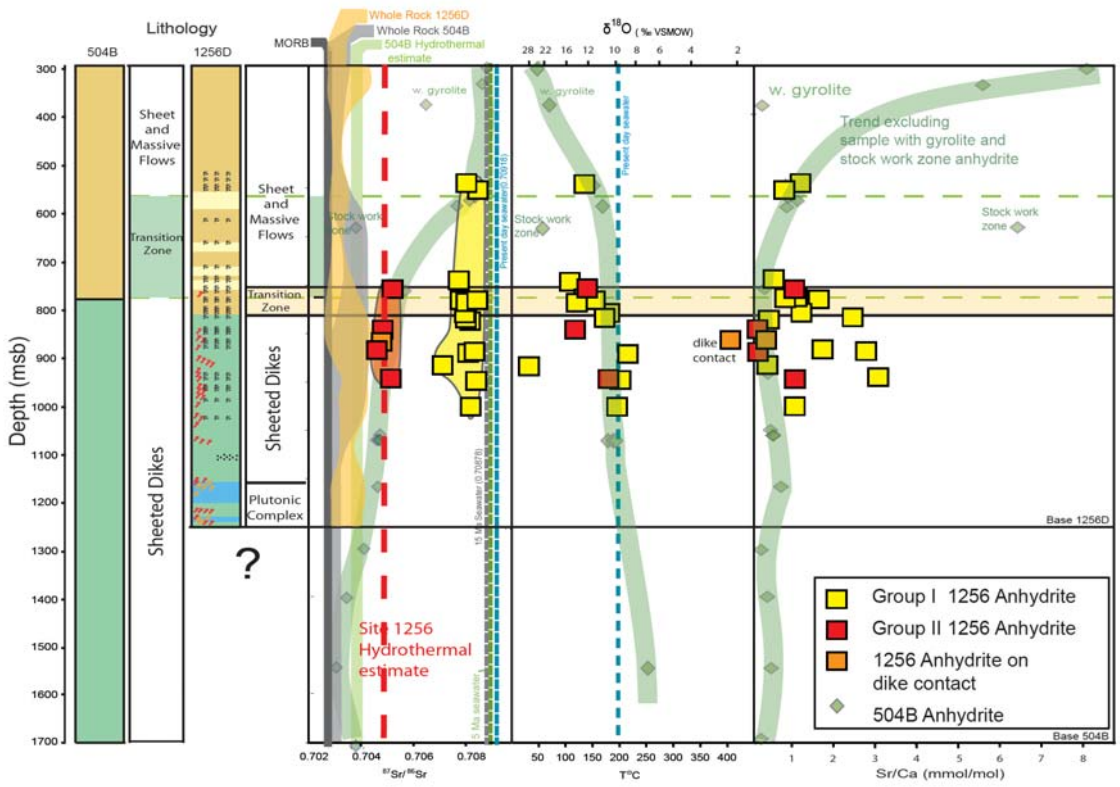

Figure 4.46. Site 1256 Anhydrite $^{87}Sr/^{86}Sr$, $\delta^{18}O$ $_{(\%\ SMOW)}$, calculated temperature and Sr/Ca vs. depth. Site 1256 stratigraphy, $^{87}Sr/^{86}Sr$ of whole rock samples, MORB and seawater at 0 Ma and 15 Ma are included. Red squares highlight anhydrite with significant basaltic Sr. Seawater Sr-isotopic composition after McArthur et al, (2001). Stratigraphy modified from Wilson et al., (2003) and Teagle et al., (2006).

Chapter 5

Site 1149

5.1. Introduction

5.1.1 Site 1149

Site 1149 (143^0 22.5′ E, 31^0 20.0′ N) is located on the northwest Pacific plate within the Nedezhda Basin approximately 700 km Southeast of Japan. Site 1149 lies on marine magnetic anomaly M11 of the NE trending M-Series magnetic lineations as charted by Nakanishi et al, 1992 (Figure 5.1). Correlations between the magnetic lineations and the Channel et al, (1995) timescale (based on biostratigrapic and radiometric dating techniques) indicates that basement at Site 1149 formed during late Valanginian or ~132 Ma at a spreading rate of 102 mm/yr (Full). The timing of Site 1149 formation coincides with a period of super-plume activity which included the formation of Shatsky Rise, Ontong Java Plateau and the East Pacific Rise, which is still active (Larson, 1991). Palaeomagnetic data indicates that plate motion was non-uniform and that Site 1149 moved from ~10^0 to 15^0 South of the equator during the Early Cretaceous to its present location (Plank et al., 2000). Site 1149 currently resides on a bathymetric high approximately 100 km east of the Izu-Bonin trench. The bathymetric high is caused by lithospheric flexure that occurs prior to subduction of the oceanic plate.

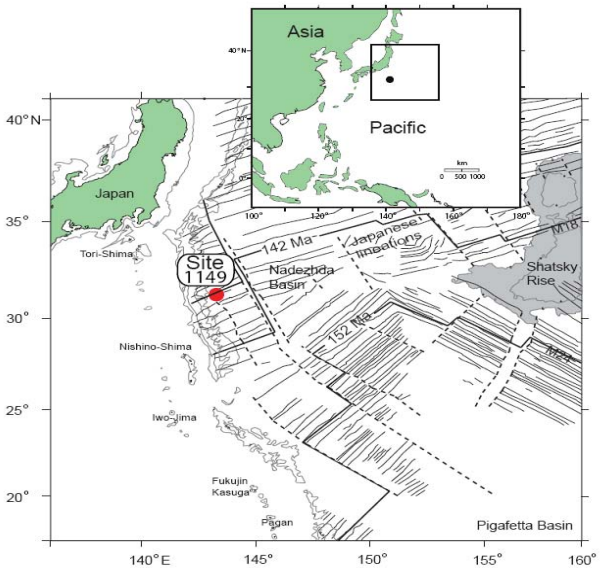

Figure 5.1. Location of Site 1149. Magnetic lineations from, Nakanishi et al, (1992)

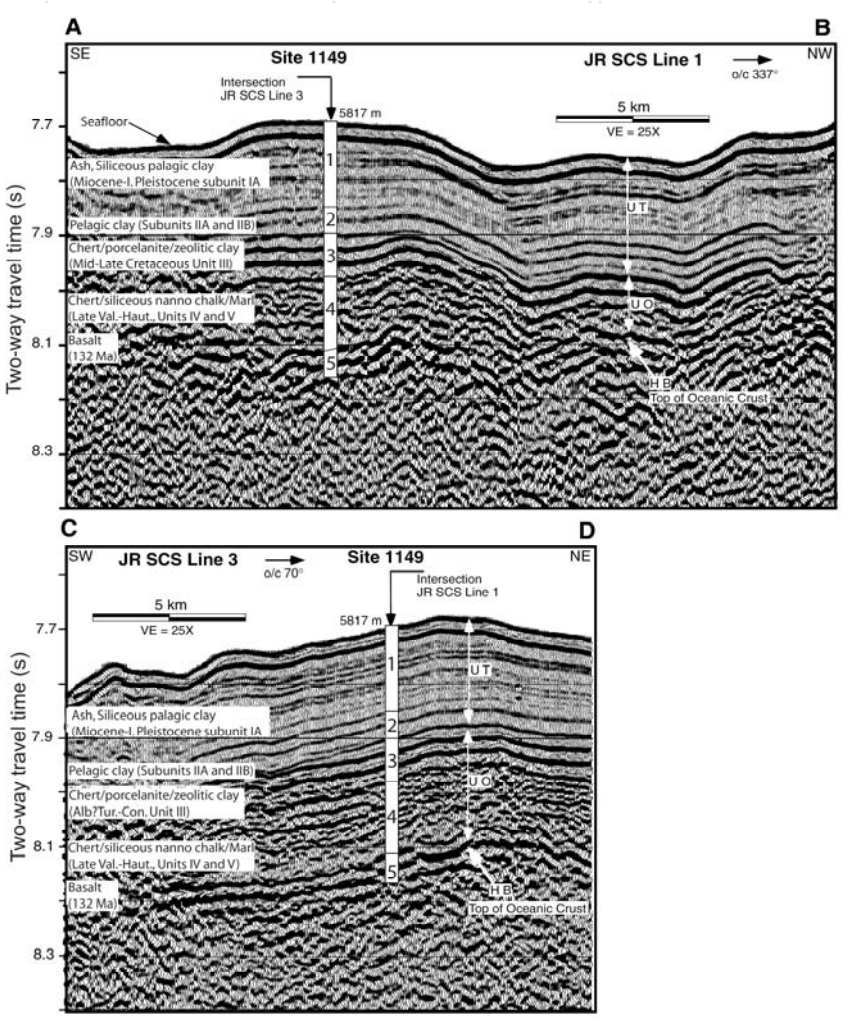

Figure 5.2. Seismic profile of Site 1149 including correlated stratigraphy of Hole 1149 D. The thick reflector at about 8.15 seconds (twt) marks the contact between seafloor sediment and oceanic basement. Scaling of the lithostratigraphic column was carried out using the velocity-depth relationship of Carlson et al. (1986) to calculate the two-way traveltime of unit boundaries derived from core observations (Plank et al., 2000)

The interpretations of the seismic stratigraphy at Site 1149 by Plank et al., (2000) is largely consistent with the original work by Ewing et al, (1968), which defined the acoustic stratigraphy of large sections of the western Pacific. Figure 5.2. shows the correlation between lithologic units and the seismic profile. Horizon B begins at 8.1 s two-way traveltime (s twt) or 0.28 sbsf. This is interpreted as the contact between nannofosil chalk/marl and fractured basalt at 410 mbsf (Plank et al., 2000). Directly above Horizon B is the upper opaque layer, which is interpreted to represent a stratified pelagic drape at 0.20 to 0.28 sbsf (7.891-7.971 s twt). At 0.16-0.2 sbsf the reflection is

interpreted to represent chert/porcelanite with clay interbeds at ~180 mbsf (for Holes 1149A, B and C) and 155 mbsf (Hole 1149 D). Unit IV (0.28 sbsf is interpreted to be high carbonate sediment interbedded with chert. The upper transparent layer (~0.16-0.2 sbsf) is largely reflection free in the upper section whilst the lower section is characterised by low amplitude partially continuous reflections. The transparent layer has been correlated to the unlithified siliceous ash bearing clay of litholigical unit IA.

5.1.2 Sedimentry stratigraphy

The sedimentary succession at Site 1149 consists of a 408 m thick succession of carbonate-free clays with variable mixtures of volcanic ash, siliceous microfossils, cherts, porcelanites, and calcareous nannofossil chalks or marls. Figure 5.1.3 shows the sedimentary stratigraphy for Site 1149 including lithological units, recovery, cores and depth as classified by Plank et al., (2000).

Unit I is a 118 m-thick carbonate-free clay with common ash particles and siliceous microfossils that is dated as late Miocene to late Pleistocene. Unit II comprises a 62 m thick dark brown pelagic clay of unkown age with several discrete ash layers. Siliceous or calcareous nannofossils are absent in this unit, however, ichthyoliths are present. Unit III is a 104 m-thick sequence of radiolarian chert with porcelanite and siliceous clay of around the mid-Cretaceous age (A. Bartolini, unpub data., 2001). Unit IV is defined by a 125 m thick series of intercalated radiolarian chert, porcelanite and siliceous chalks or marls. These have been dated as upper Valanginian to upper Hauterivian. Unit V is only present in the upper 2 metres of basement within fractures.

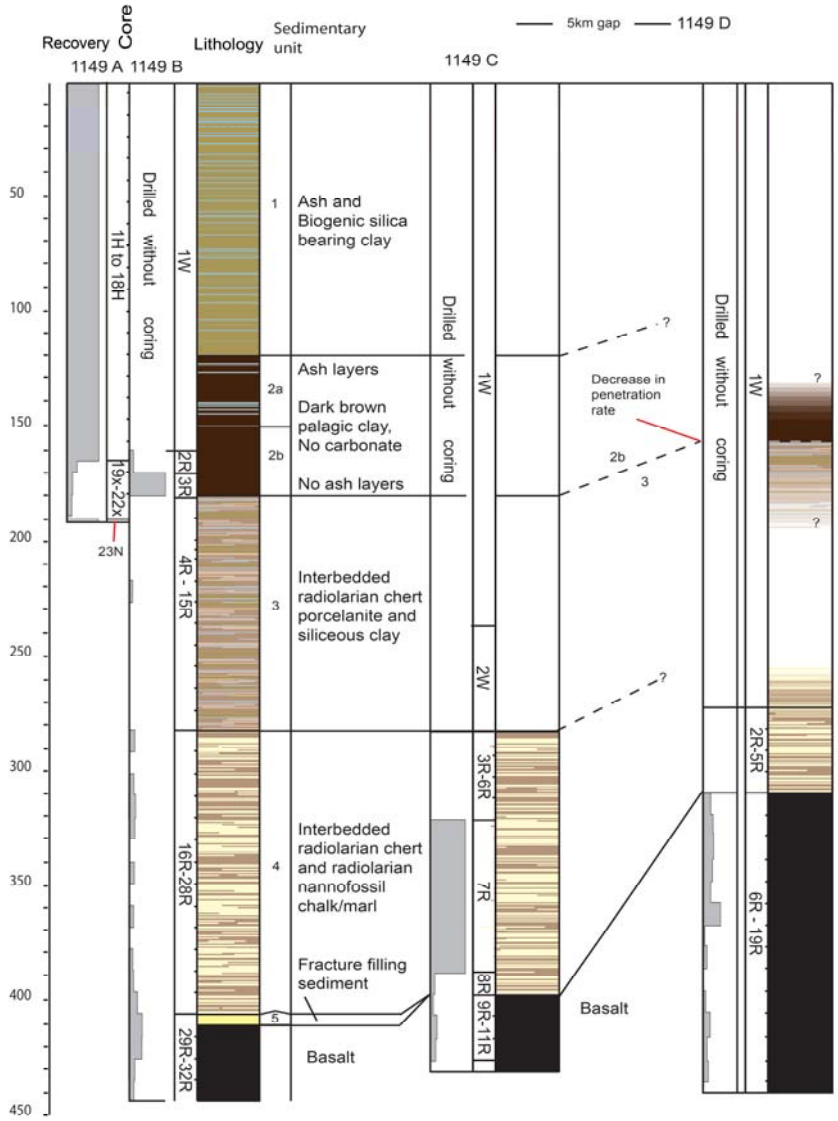

Figure 5.3. Site 1149 stratigraphy including core recovery, lithology and lithostratigraphic unit columns. Interpretation of stratigraphy is sourced from recovered material from Holes 1149 A to D. (After Plank et al., 2000).

Unit V formed from recrystallized calcareous marlstone and is dated to Upper Valaginian. The evolution of sedimentation with time is indicated in Figure 5.4. A lack of age control for a large portion of the sedimentary column has left a gap of over 120 Myr in the record (7 Myr to 125 Ma). Therefore, rates for this time period are not known. Early and late sedimentation history suggests high rates of sedimentation ~20-34 m/m.y., with a large period where the average sedimentation were very low at around 1-2 m/m.y.

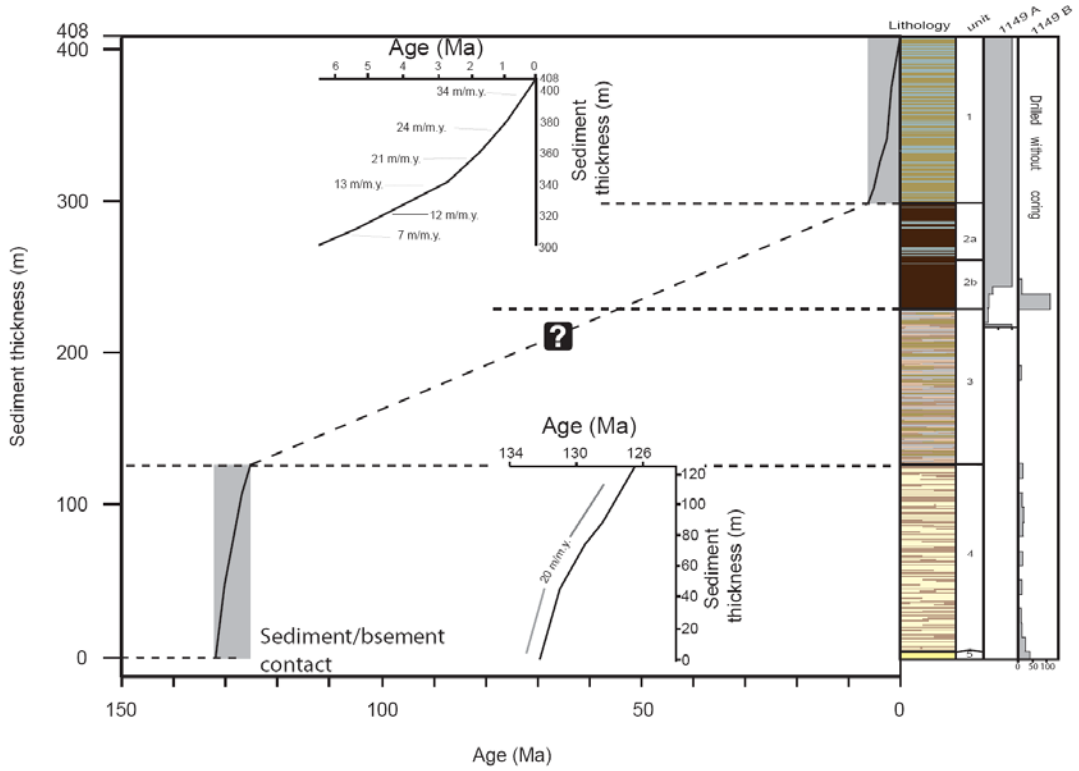

Figure 5.4. Rates of sedimentation through time at Site 1149. Rates are derived from palaeomagnetic and biostratigraphic data from Holes 1149 A and 1149 B. The dashed interval indicates a region where a lack of fossil evidence and/or low recovery has left a gap in the record (from 125 Ma to 8 Ma). Plot is modified from Plank et al., (2000).

5.1.3 Basement stratigraphy

Basement was encountered in Holes 1149B (407.77 mbsf), 1149C (398.41 mbsf) and 1149D (300.46 mbsf). Hole 1149B recovered 37.43 m (185-1149B-29R to 32R) with recovery of ~23 %. Hole 1149C recovered 28.29 m of basement from Cores 185-1149C-9R to 11R at ~14% recovery and Hole 1149D recovered 130.24 m of core (185-1149 D-5R to 19R) at a recovery rate of 20% (Figure 5.5). Overall recovery is lower than that of nearby Site 801. This may be due to the low competency of thin fractures flows, pillow basalts and breccia.

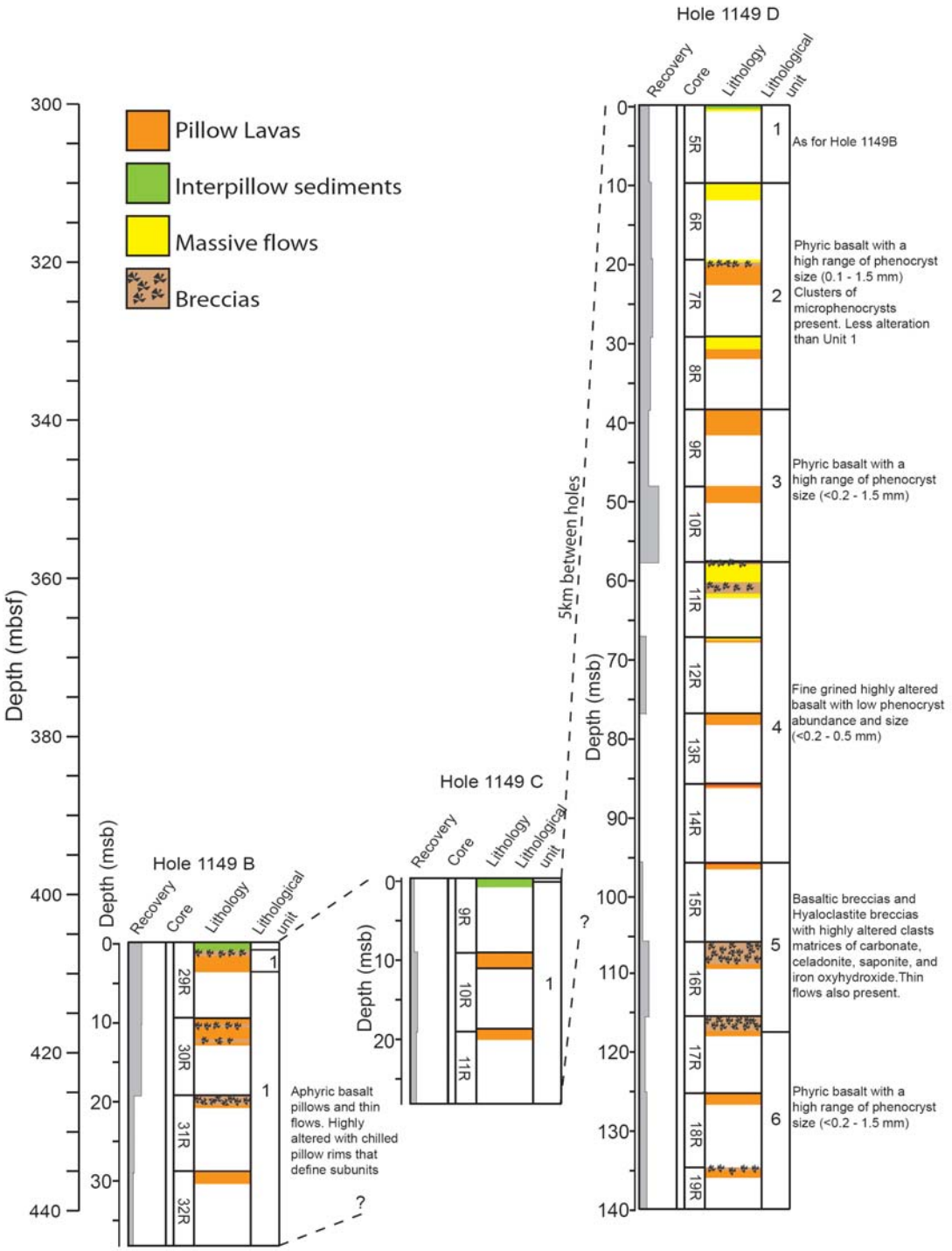

Figure 5.5. Basement stratigraphy at Site 1149, including core recovery, lithology and lithological units. Modifed from Plank et al., (2000).

Basement rocks are all aphyric basalts with only minor amounts of plagioclase and olivine observed as phenocrysts phases. The basalts include a mixture of thin (<50cm) pillows and some intermediate thickness (50cm -1m) cooling units that may represent either pillows or flows. A few cooling units up to 2.88m thick were present in

hole 1149 D, however, these are fractured and not massive. Additional intervals of breccia and interpillow sediment were also recovered.

Igneous Units at Site 1149 are based on petrographic observations of recovered samples, including flow margins, mineral content, and textural relationships. Holes 1149 B and C contain only 1 Unit, of which Hole 1149 B has 15 subunits that are defined by individual cooling units and breccia intervals. Hole 1149 C has 6 subunits also defined by breccias and individual cooling units and these are described in detail in Plank et al., (2000). The differences between each unit at Site 1149 are outlined in Figure 5.5.

Most basalts recovered are aphyric with <1% phenocrysts. Pillow rims are glassy to cryptocrystalline, where pillow interiors are microcrystalline. The groundmass typically consists of skeletal subhedral laths of plagioclase with anhedral pyroxenes. Euhedral plagioclase crystals forms the majority of phenocrysts with some rare olivine phenocrysts. Pyroxene phenocrysts are only present in 1149 B-29R-2 (Piece 13). These occur as glomerocrysts with plagioclase and olivine, have euhedral crystal shapes, and range from 0.2 to 0.4mm. Piece 5 from 185-1149D-5R-1 (0.5 msb) has its own unit designation. This piece has ~2% olivine glomerocrysts and lacks alteration halos. Olivine phenocryst abundance increases toward the bottom, exceeding 1% at last 30m.

5.1.4 Bulk geochemistry

Analysis of whole rock basement samples includes shipboard XRF and shore based ICP-AES and ICP-MS analysis. Of the analyzed samples, two are from Hole 1149B, and 15 samples from Holes 1149B, 1149C and 1149D. Additional analyses includes major and trace element concentrations from 31 whole rock and glass samples by Kelley et al., (2003), and 62 whole rock samples from this study.

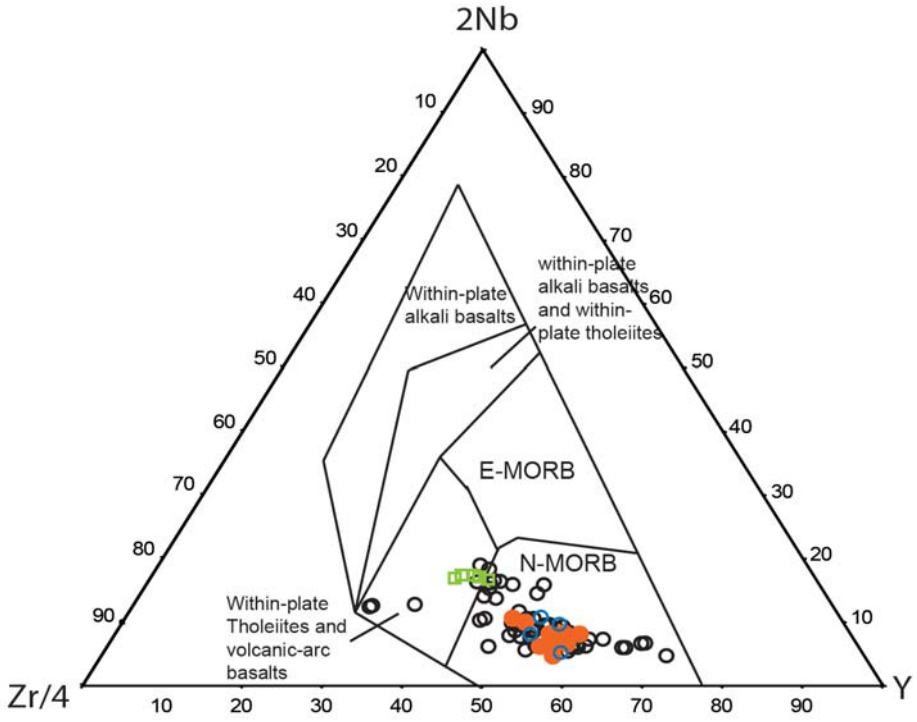

Figure 5.6. Nb-Zr-Y ternary diagram showing the fields for different basalt types. Samples taken from Site 1149 mostly all lie in the N-MORB field. Squares = Hole 1149 D (Unit 6), Open circles = Hole 1149 C, Closed circles = Hole 1149 B (Shipbaord data after Plank et al., 2000). Black Circles are a combination of whole rock and glass data from this study and Kelley et al., (2003).

First order interpretations of these samples indicate that Site 1149 basalts are MORB (Plank et al., 2000). When plotted on the Zr,Y,Nb ternary discrimination diagram (Meschede, 1986) most samples plot on the N-MORB field, although some samples from Hole 1149D plot on the 'within plate tholeiite' field due to their relatively enriched Nb and Zr concentrations (Figure 5.6). Samples from Hole 1149D-Unit 6 plot on the 'within-plate' tholeiite field. Chondrite normalised REE patterns for all whole rock basalt samples at Site 1149 (Figure 5.7) broadly trend with the average values for MORB. The average value for Site 1149 plots within the average MORB field. Samples 185-1149B-31R-1, 93-94 cm, 185-1149D-11R-1, 30-37 cm, both breccias, are depleted in REE. Direct comparisons with Hole 801C indicate that Site 1149 is more primitive than Site 801. The main line of evidence for this comes from lower Fe_2O_3 at Site 1149. However, Plank et al., (2000) point out that Mg and Fe concentrations are likely to have been effected by alteration. For example, Sample 185-1149 B-30R-1, 19-94 cm has the highest MgO concentrations and lowest Fe_2O_3 concentrations. In addition, it contains 100 ppm Ba which is very high for MORB and it is likely to be the result of alteration.

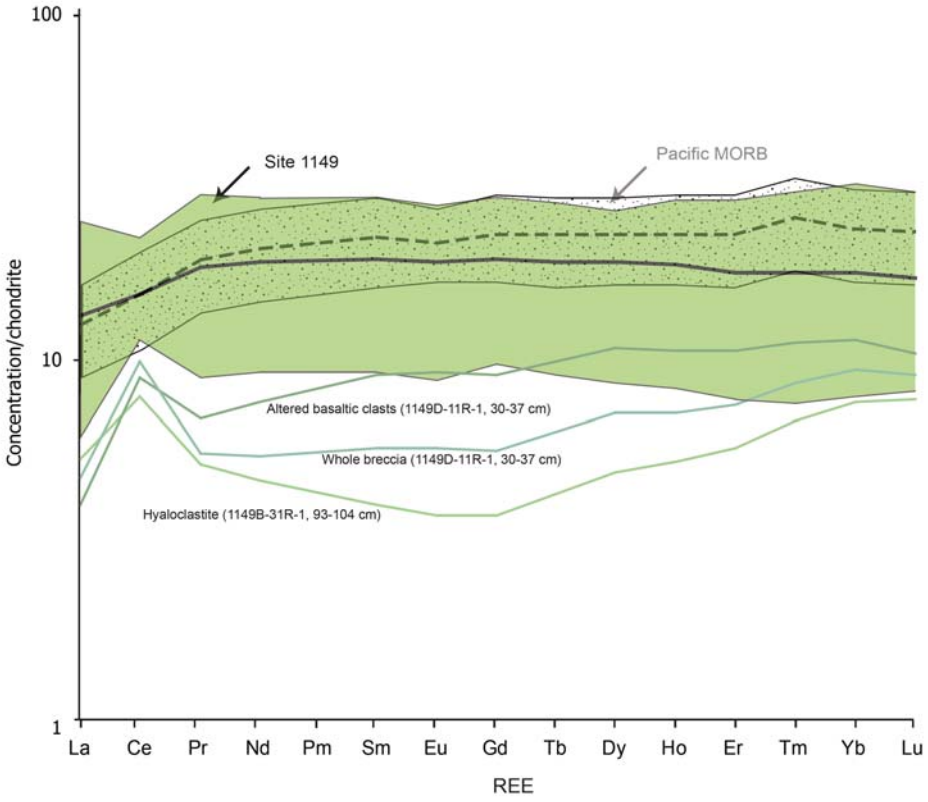

Figure 5.7. Chondrite normalised REE patterns for all whole rock and glass samples at Site 1149. Pacific MORB is included for comparison. Chondrite-normalization factors from Taylor & Gorton (1977). Site 1149 data is a compilation of Kelley et al, (2003) and this study. Pacific MORB data from Jenney and Castillo, (1997). Black line indicates average REE pattern for Site 1149. Green lines indicate breccia samples and Pm is not analysed.

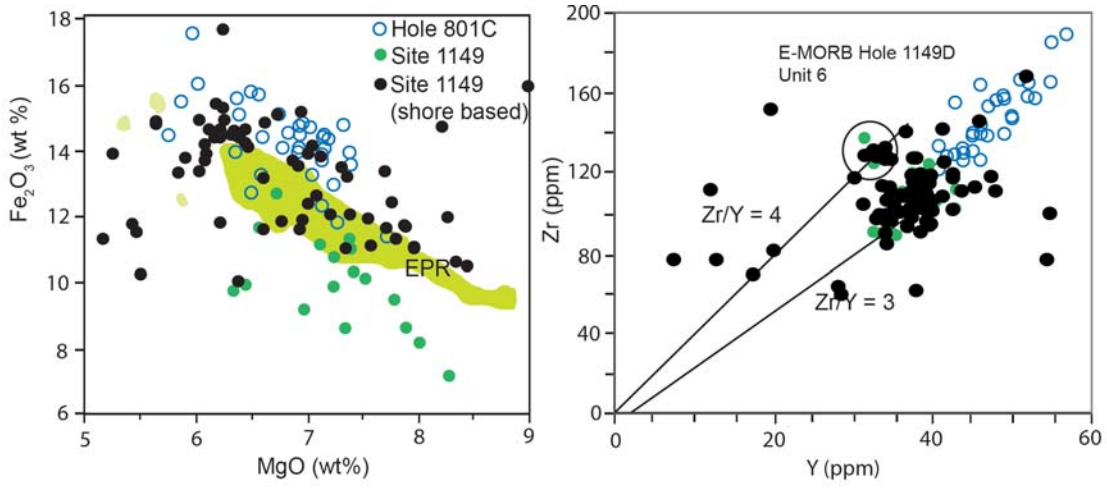

Figure 5.8. A. MgO vs. Fe2O3, and B. Zr vs. Y for Site 1149 and Site 801 tholeiitic lavas. Solid (black) circles = Site 1149 basalts; open (blue) circles = Hole 801C tholeiites; and crosses = data from modern East Pacific Rise (Langmuir, et al., 1986). After, Plank et al., (2000). Black circles are a combination of Site 1149 whole rock analyses from this study and Kelley et al., (2003).

Therefore, alteration is the most likely reason for scatter in the MgO vs. Fe_2O_3 plot (Figure 5.8) for Site 1149 basement. Two populations of MgO vs. Fe_2O_3 emerge in Figure 5.8 in which shipboard samples have distinctively lower Fe. The most likely cause is sampling, since the shipboard samples represent the least altered samples (Plank et al., 2000). The shore based samples, including those from this study, are variably altered, with saponite, celadonite and iron-oxyhydroxides, all of which may serve to increase Fe in the whole rocks.

With the exception of basalts from base of Unit 6, the immobile trace elements in basalts from Site 1149 are similar to N-MORB and those from Site 801. The basalts from Hole 1149D-Unit 6 point to E-MORB with high Zr/Y and Nb which compare well to E-MORBS from EPR (Figure 5.6). Work by Talbi and Honnorez, (2003), Kelley et al, (2003), indicate emplacement of secondary minerals and chemical exchange with the basement at Site 1149. Such observations preclude the use of mobile elements to assess the primary chemistry of Site 1149 basement. Variation in Sr-Nd-Pb systematics at Site 1149 (Hauff et al., 2003) indicate that extensive isotopic exchange has taken place at Site 1149. Some very high $^{206}Pb/^{204}Pb$ (23.70-26.86) and $^{207}Pb/^{204}Pb$ (15.73-15.83) is reflect increases in $^{238}U/^{204}Pb$ ratios, that indicate input of seawater derived U (Hauff et al., 2003). In addition, the same authors indicated that alteration of the ocean crust may affect mixing within the Mariana arc. Hydrothermal alteration clearly plays a critical role in the evolution of basement at Site 1149, therefore, based on work from previous studies and observations made this study, the petrographic, geochemical, and isotopic trends with alteration are discussed in this section.

5.2. Basement Alteration

Shipboard and shore based studies and additional material from this study is used to characterize alteration at Site 1149. Hand specimen descriptions, petrography, alteration logs and vein logs are used to assess the extent and distribution of secondary mineralogy, the relationships and distribution of alteration halos, and the characteristics of veins and breccia. Ultimately, as with Site 1179, these observations will form the foundations for insights from geochemical data, because chemical changes as a result of seawater alteration are fundamentally tied to the nature and characteristics of the secondary mineralogy.

The upper basement of Site 1149 is made up of pillow lavas, pillow lavas breccias, hyaloclastites and thin flows that are slightly to intensely altered. Plank et al., (2000) identified the visible manifestations of alteration at Site 1149 as the replacement of groundmass minerals and phenocrysts, the filling of vesicles and interstices, and formation and filling of veins and miarolitic zones by secondary minerals. Secondary minerals observed at Site 1149 include celadonite, Mg-saponite (Talbi and Honnorez, 2003), iron-oxyhydroxide and calcite.

Bright green/blue celadonite occurs throughout the basement at Site 1149, replacing mesostasis and rare plagioclase phenocrysts, filling vugs, vesicles and fractures. It is typically overprinted by late stage iron-oxyhydroxides and saponite, hence its identification in hand specimen and thin section is difficult.

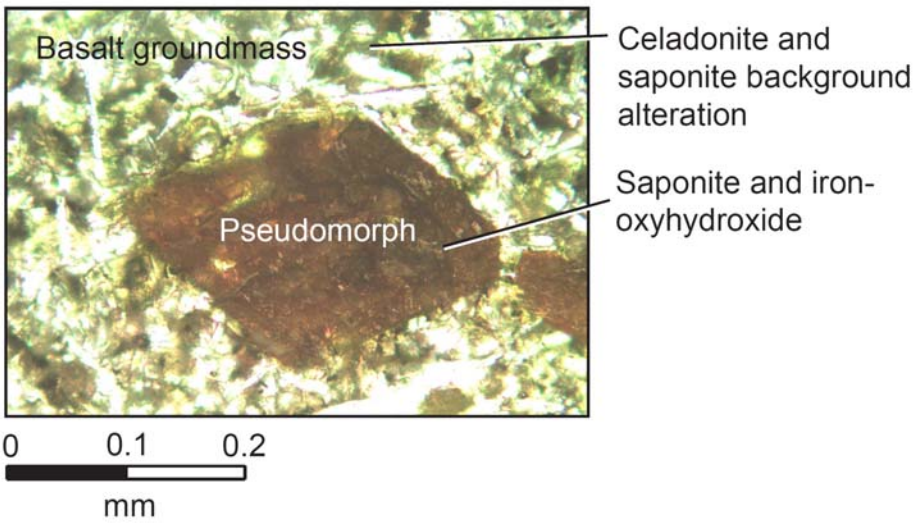

Figure 5.9. Sample 185-1149D-18R-1, 75-18cm. Olivine phenocryst replaced by saponite and iron-oxyhydroxide to form a pseudomorph. Plane Polarized light 200x magnification.

Saponite occurs throughout Site 1149 and it fills vugs, vesicles, interstices, and replaces glass, plagioclase and olivine. Saponite at ODP Site 1149 occurs as amorphous green to brown agglomerations and/or fine needle-like crystals in plane polarized light. Identified as Mg-Saponite by Talbi and Honnorez, (2003), Saponite may occur as a pseudomorph that results from the replacement of olivine, however more commonly such pseudomorphs occur as saponite and iron-oxyhydroxide (185-1149B-29R-2, 27-32 cm, Figure 5.9). Saponite at Site 1149 commonly occurs with celadonite and iron-oxyhydroxides and although these associations are largely the result of overprinting, saponite may have a varying amount of iron oxhydroxide present within clay lattice (possibly the result of mixed interlayers during crystallization of the clays).

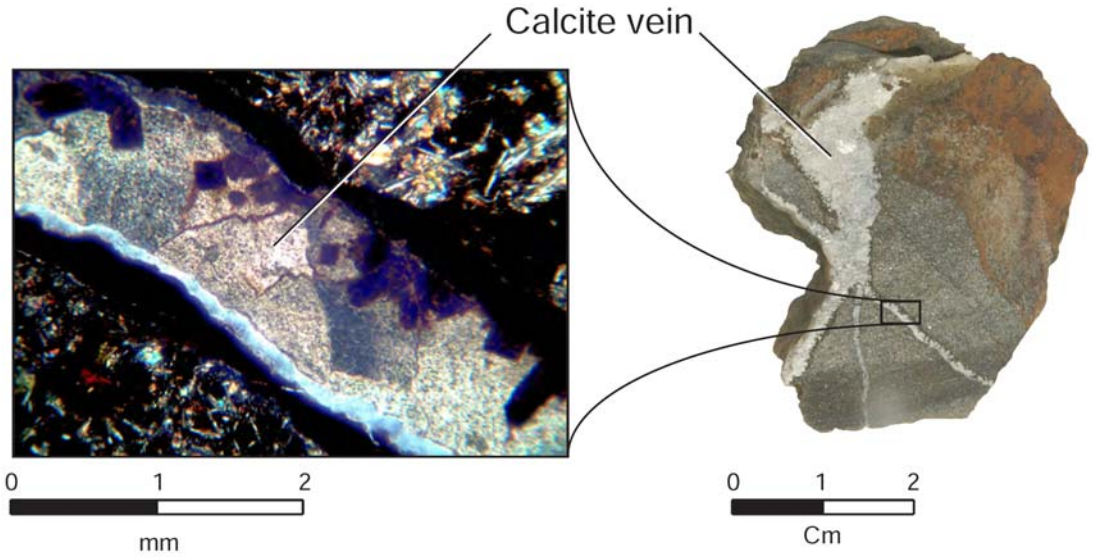

Figure 5.10. Example of carbonate vein in hand specimen and thin section (Sample 185-1149D-19R-1, 18-14 cm). Photomicrograph is taken in cross polarized light at 50x magnification.

Iron-oxyhydroxide is characterised by dark red or brown patches replacing plagioclase, clinopyroxene, mesostasis and olivine. Typically, iron-oxyhydroxide overprints saponite and celadonite but it may also intermix (see earlier) giving rise to translucent brown to yellow brown patches. A detailed study of the compositional variation of clay minerals by Talbi and Honnorez (2003) established that iron-oxyhydroxides formed from a K and Fe rich oxidative solution and that the colour change reflects the varying content of celadonite, iron-oxyhydroxide and saponite.

Finally, carbonate is bright white in thin section (Figure 5.10) and hand specimen and forms veins and fills vugs, vesicles and, rarely replaces interstitial areas

within the groundmass carbonate crystals tend to be fine to medium grained and anhedral. In vugs and large veins euherdal ‘dog tooth’ calcite may form.

Rare phillipsite was identified as open space fillings in hyaloclastites (Talbi and Honnorez, 2003).

5.2.1 Veins

Throughout Site 1149, veins filled with secondary minerals saponite, celadonite, iron-oxyhydroxide and calcite occur in varying proportions (Plank et al., 2000). The abundance of veins at Site 1149 is high at 34 veins per metre (Plank et al., 2000), similar to Sites 504 (31 veins per metre), Site 1256 (27 veins per metre), and Site 801 (24 veins per metre). Core 185-1149C-7R exhibits an extremely high vein density of 50 veins per metre. However, the volume percentage of veins at Site 1149 is relatively low (2.3%), This partially relates to shipboard logging because the majority of secondary minerals at Site 1149 are contained within the breccias (discussed later in this section) and vein nets. Some of these sections are composed of as much as 7% by volume of vein nets.

Vein thickness varies from <0.1 to 20 mm, with a number of large spectacular veins of carbonate with subordinate saponite and iron-oxyhydroxides. These veins can be vuggy, for example Samples 185-1149B-30R-2, 130-134 cm and 185-1149B, 30R-1 93-95 cm (Figure 5.2.3).

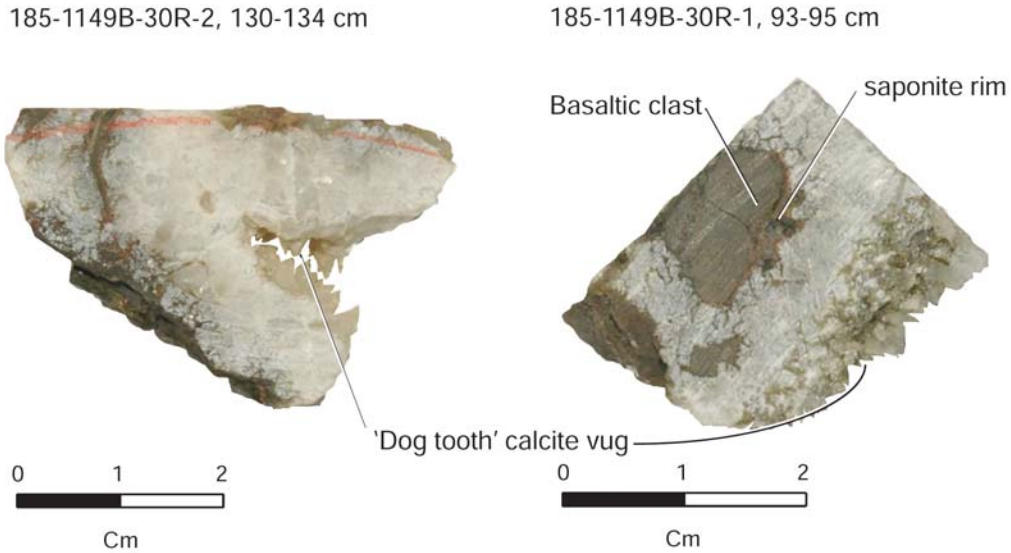

Figure 5.11. Examples of calcite vugs at ODP Site 1149.

Celadonite occurs in veins as a rare and minor phase in multi-minerallic veins or as thin hairline (<0.1mm) veins; for example, Sections 185-1149B-32R-1, 107-111 cm and 25-28 cm (Figure 5.12). Celadonite is commonly replaced and/or overprinted by iron-oxyhydroxide, saponite, and carbonate. Although no direct evidence is available, it is likely that remnant celadonite halos are associated with the celadonite veins. Overprinting has nearly obscured all of this mineral phase with <0.5 % by volume of veins remaining as celadonite.

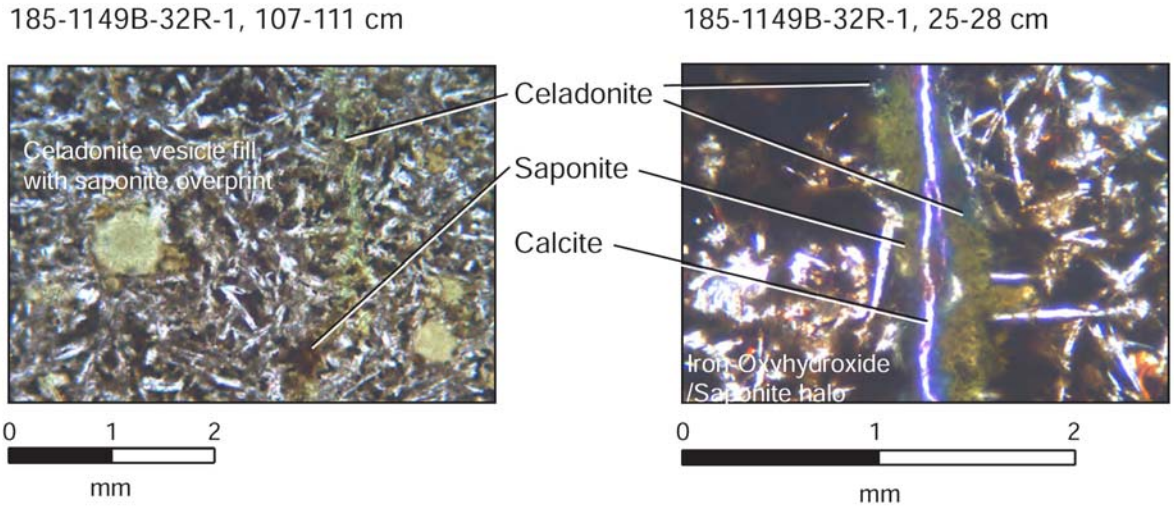

Figure 5.12, Examples of celadonite veins at ODP-Site 1149. A vesicle with discrete celadonite and saponite is shown. The vein in Sample 185-1149B-32R-1, 25-28 cm shows discrete celadonite that is overprinted by saponite, followed by iron-oxyhydroxide and finally, carbonate. Photomicrographs are taken in cross polarised light at 50x and 100x magnification respectively.

Saponite veins comprise 32 vol % of veins and range in thickness from <0.1 mm to 2.5 mm. Most saponite rich veins are <1 mm. Saponite is present as a minor phase in larger carbonate or iron-oxyhydroxide veins and it can either cross cut previous celadonite zones, or form as a late fill of celadonite veins; for example, in Sample 185-1149B-32R-1, 25-28 cm (Figure 5.13) and 85-1149B-32R-1, 25-28 cm. Multiple stages of vein opening and mineral precipitation are indicated by multiple overprinting and veins where saponite overprints iron-oxyhydroxide or saponite can be overprinted by celadonite. This supports interpretations by Talbi and Honnorez, (2003) who imply that alteration occurs as a series of 'waves' during which alteration conditions, such as solution chemistry, water/rock ratio, and f_{O2} change.

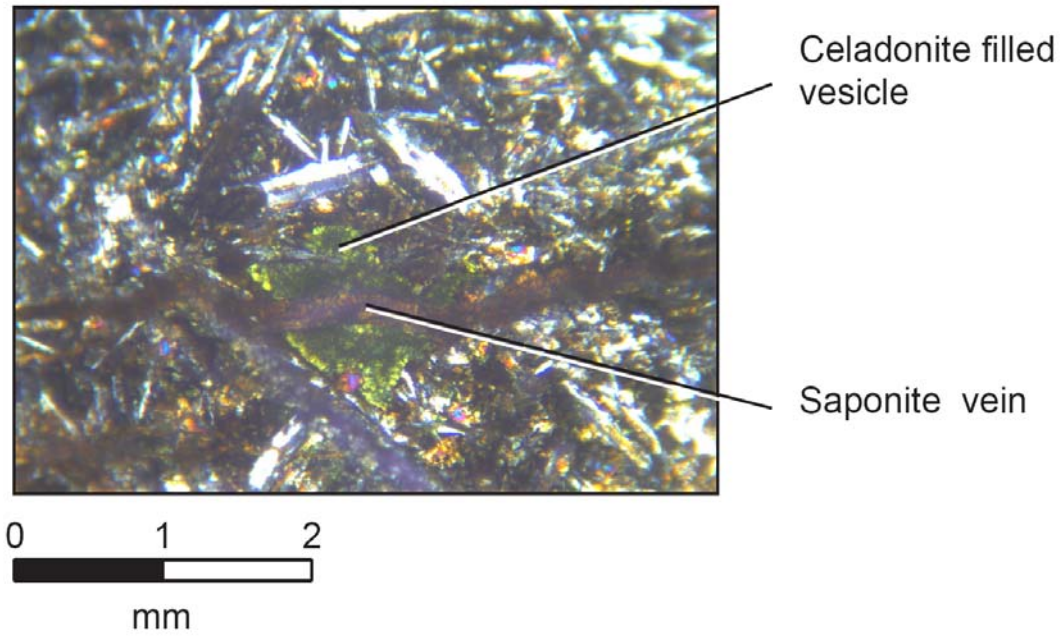

Figure 5.13. Example of Saponite vein cross cutting a celadonite filled vesicle. Sample 185-1149D-17R-2, 29-32 cm. Photomicrograph is in cross polarised light and taken at 50x magnification.

Iron-oxyhydroxide veins are present throughout Site 1149 range in thickness from 0.1 mm to 5 mm thick, and it is typically a major component of multi-minerallic veins forming ~4.6 vol % of veins. Formation of iron oxyhydroxide veins may be the result of oxidation of early secondary Fe sulphides or alteration of igneous Fe oxides (Plank et al, 2000). Figure 5.14 A shows an example of a small iron-oxyhydroxide vein with an associated halo and examples in which iron-oxyhydroxide occurs prior to saponite (B and C).

Carbonate veins cross cut all other secondary mineral phases (Figures 5.11 and 5.15) and often fill re-opened veins. A number of carbonate veins exhibit multiple fill stages where crystal growth into a void is followed by a later growth of anhedral calcite (Figure 5.15). Carbonate veins make up 61 % of all vein material recovered. Rare quartz and pyrite were observed in veins in Hole 1149B. Pervasively

The distribution of veins at ODP Site 1149 is shown in Figure 5.16. With the exception of quartz and pyrite, all other vein minerals appear throughout ODP Site 1149. The volume of veins remains fairly consistent with depth. Depths of 70 msb and 100 msb have the lowest volume of veins.

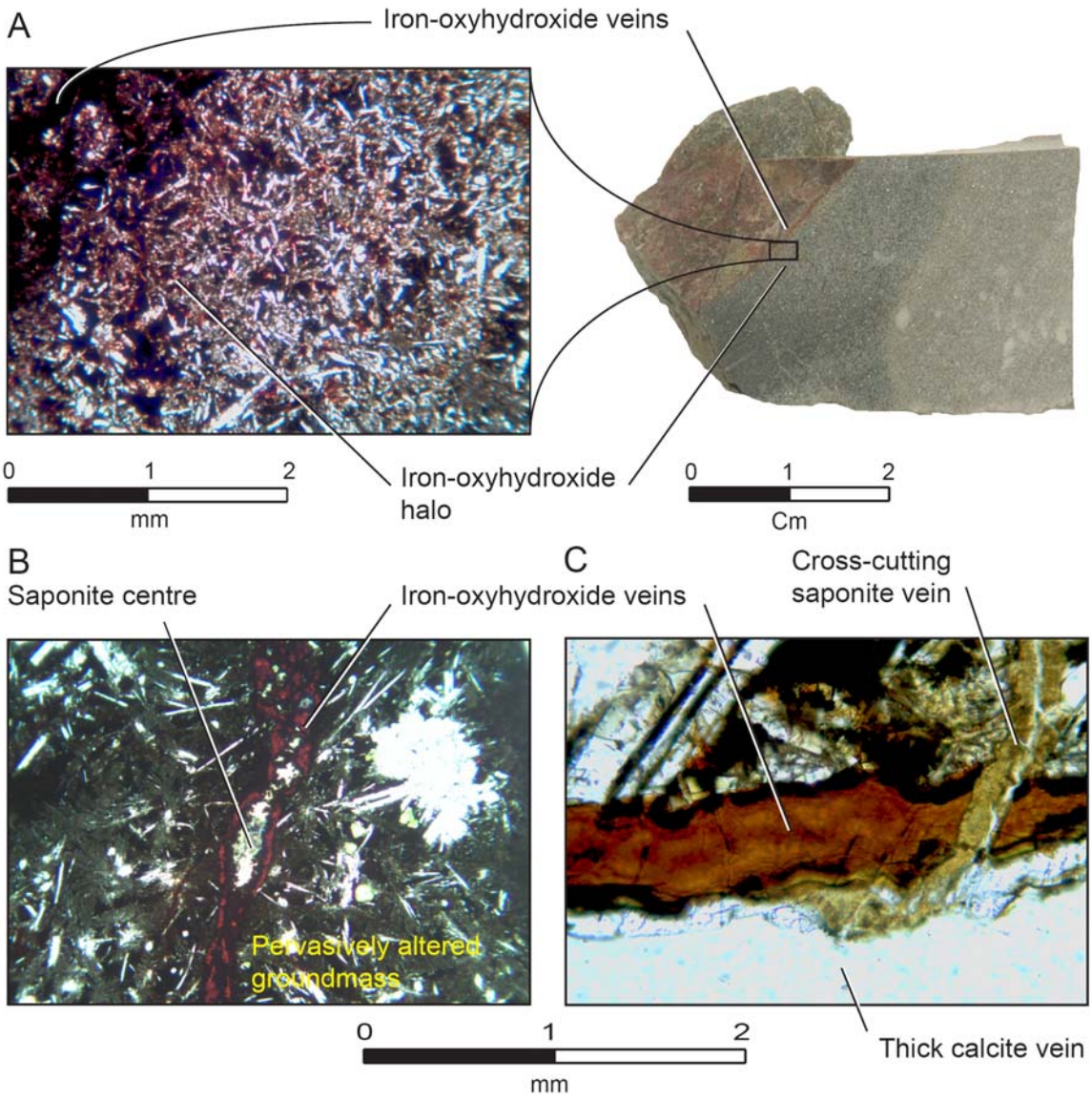

Figure 5.14. A. Iron oxyhydroxide veins and halo within Sample 185-1149D-10R-1, 92-96 cm. Photomicrograph is taken in plane polarised light (PPL) at 50x magnification. B. Iron oxyhydroxide vein with saponite centre in Sample 185-149D-8R-1, 108-110 cm (100x magnification in crossed polarised light). C. Example of Iron oxyhydroxide vein cross-cut by saponite vein in Sample 185-1149D-9R-2, 24-28 cm (100x magification in PPL).

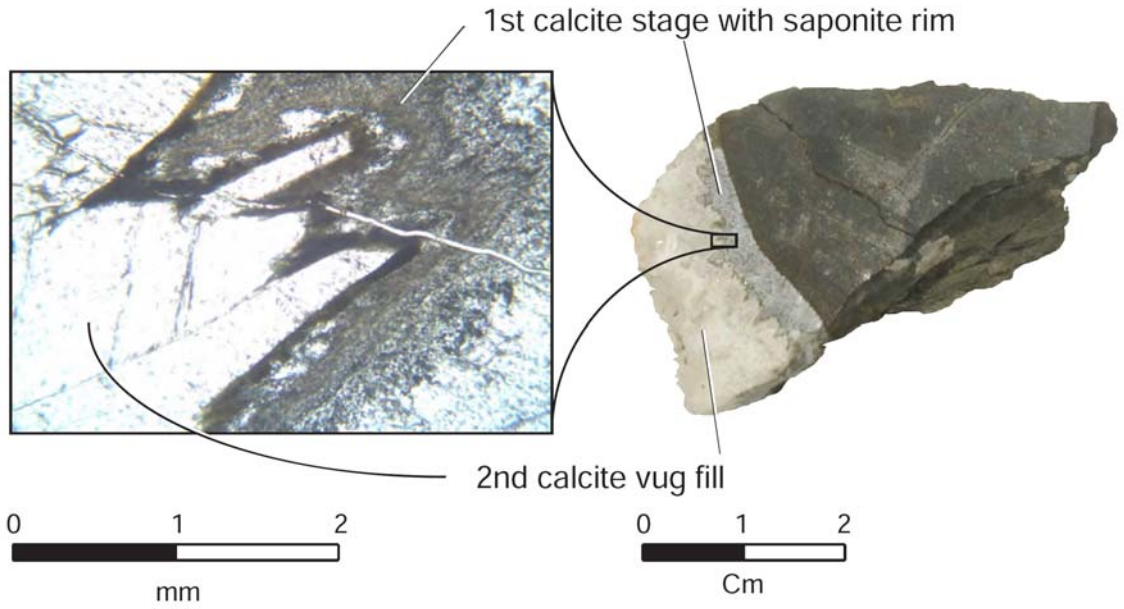

Figure 5.15. Example of secondary calcite fill within a vug. Sample 185-1149D, 11R-2, 78-80 cm. Photomicrograph is taken in plane polarised light at 50x magnification.

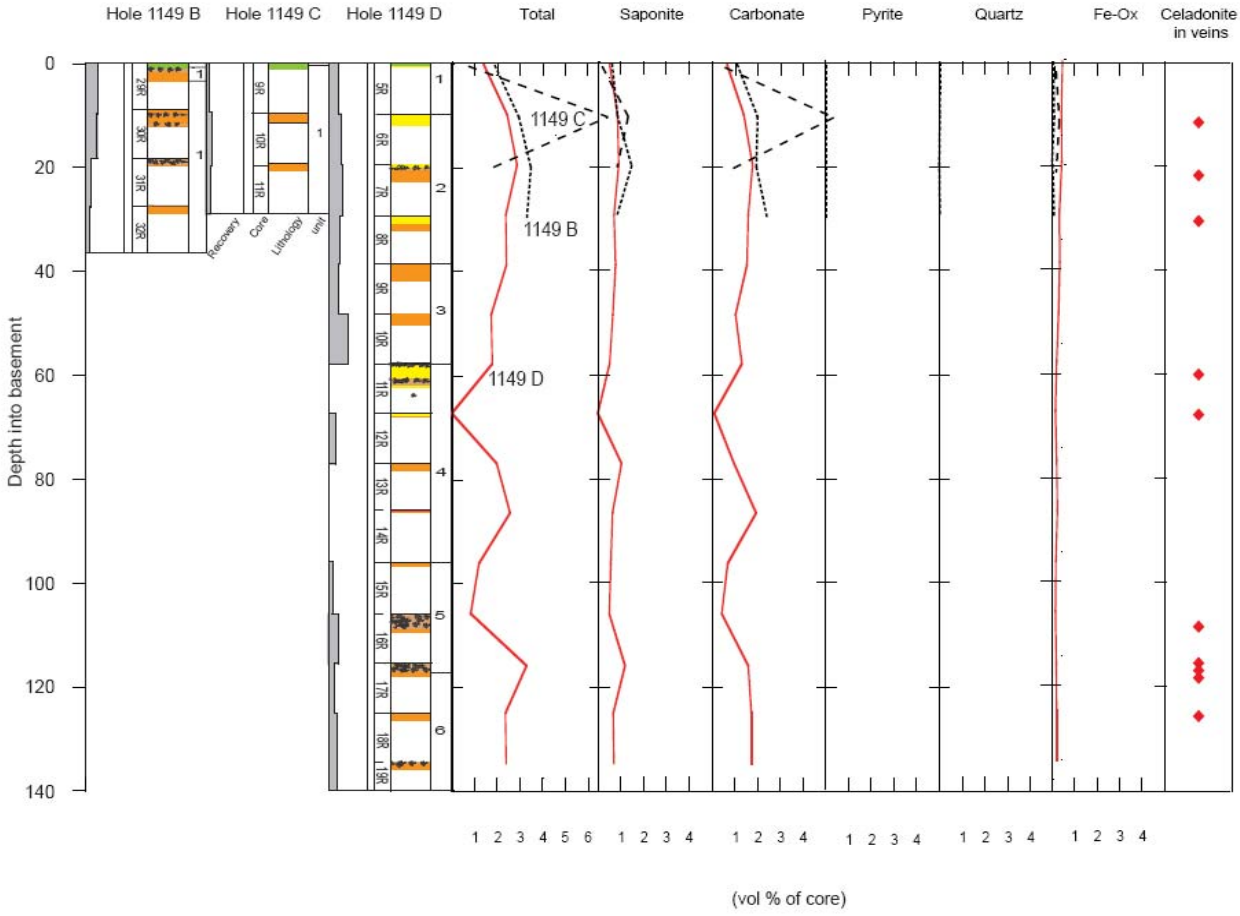

Figure 5.16. Volume percentage of veins at ODP Site 1149. Volumes are calculated on a core by core basis and they are normalised to account for recovery. The presence of celadonite within veins in thin section is also recorded.

5.2.2 Halos

The occurrence of alteration halos is strongly related to zones of fracturing and surfaces that are exposed to circulating fluids. These include veins, brecciated zones, cooling fractures and pillow boundaries. The variation in halos observed by Plank et al., (2000) and Talbi and Honnorez, (2003) mirror observations made in this study. Complex halos vary in colour from brown on the exposed surface, followed by a dark green halo that forms the bulk of the halo (cm scale). The dark green halo is commonly fronted by a narrow discontinuous red band (~1-2 mm thick) which forms a boundary between the host rock and the halo (Figure 5.17 E). Classification of halos are based on relatively distinct secondary mineral assemblages, which relate to colour variation including; dark green to dark grey, buff to brown / patchy buff to brown, red to dusky red and complex mixed halos.

Dark green to dark grey halos are characterised by the presence of celadonite replacing mesostasis, and vesicles although celadonite is typically overprinted by later saponite and iron oxyhydroxide. The extent of dark green to dark grey halos is clearly defined due to the relatively sharp halo front (Figure 5.17 C). Beyond this front only saponite (brown/pale yellow green/buff coloured) and iron oxyhydroxide (dusky red/brown) are identified. Dark green to dark grey halos occur in similar abundances throughout Site 1149.

Buff to brown coloured halos are ubiquitous throughout Site 1149 and nearly always overprint and extend over dark green halos (See Figure 5.2.9A and E). These halos are characterised by replacement of mesostasis, olivine, and occasionally plagioclase and clinopyroxene by saponite. Vesicles and amygdales are also filled with saponite. Buff to brown halos commonly form a mottled/patchy halo front (Figure 5.17 D and E) that ranges from complete to slightly patchy. Plank et al., (2000) suggest that the mottling are zones that are lacking in primary Ti magnetite and they may have formed by dissolution of iron oxide. What is also apparent, is that mottling only occurs where the brown outer halos are directly associated with the veins, this suggests that the mottling is the result of fluid flow. Brown halos cover ~20% of basalts recovered at Site 1149, however, the true figure is around 40 to 50% when the effects of overprinting are taken into account.

Dusky red to red/brown halos are predominantly composed of iron-oxyhydroxide and mixtures (possibly interlayered) iron-oxyhydroxide and saponite.

The halo may be narrow (~1-5mm) or large enough to encompass the whole sample. Red/brown halos are typically associated with iron-oxyhydroxide veins. Interstitial zones and primary mineral phases, including plagioclase, olivine, and clinopyroxene are partially to entirely replaced by saponite and iron-oxyhydroxide. Iron-oxyhydroxide halos at Site 1149 produce well defined halo fronts, some of which are lined by discontinuous irregular patches of iron-oxyhydroxide where near or total replacement has taken place, e.g., Figure 5.2.9D.

Other styles of halos present include complex overprinting in which the original sequence is obscured by further stages of secondary mineral emplacement or where there is local variation in halo coverage across all stages, (e.g. Sample 185-1149D-16R-2, 77-81 cm, Figure 5.17 A). Incomplete halo assemblages, where one or more mineral phase is missing, occur throughout ODP Site 1149 and potentially reflect local variation in fluid composition.

Halos cover approximately 34% by volume of basalt of which 14% is dark green and 20% is brown (Plank et al., 2000). All other halo types, including the red alteration front represent <1% of total volume. Figure 5.18 shows the variation in alteration halo styles vs. depth, The top three fifths of Site 1149 (0-55 msb) is dominated by dark green/dark grey halos, whilst the lower two fifths of the hole (55 to 140 msb) is composed of saponite and iron-oxyhydroxide dominated halos. Overprinting by iron-oxyhydroxide halos has obscured the original extent of the dark green halos. These halos would have been present at similar volumes throughout ODP Hole 1149.

Based on the relationships observed between secondary mineral phases within the veins and groundmass the relative timing of secondary mineral paragenisis is outlined in Figure 5.19. Multiple stages of overprinting, and locally variable alteration conditions make timing hard to assess, particularly between saponite and iron-oxyhydroxides. Based on element distribution patterns and variations in the octahedral atoms in clay minerals at Hole 1149D and 801C, Talbi and Honnorez (2003) indicate that celadonite, saponite and iron-oxyhydroxides are evolutionary stages in which mixed layered clays form from a phyllosilicate precursor.

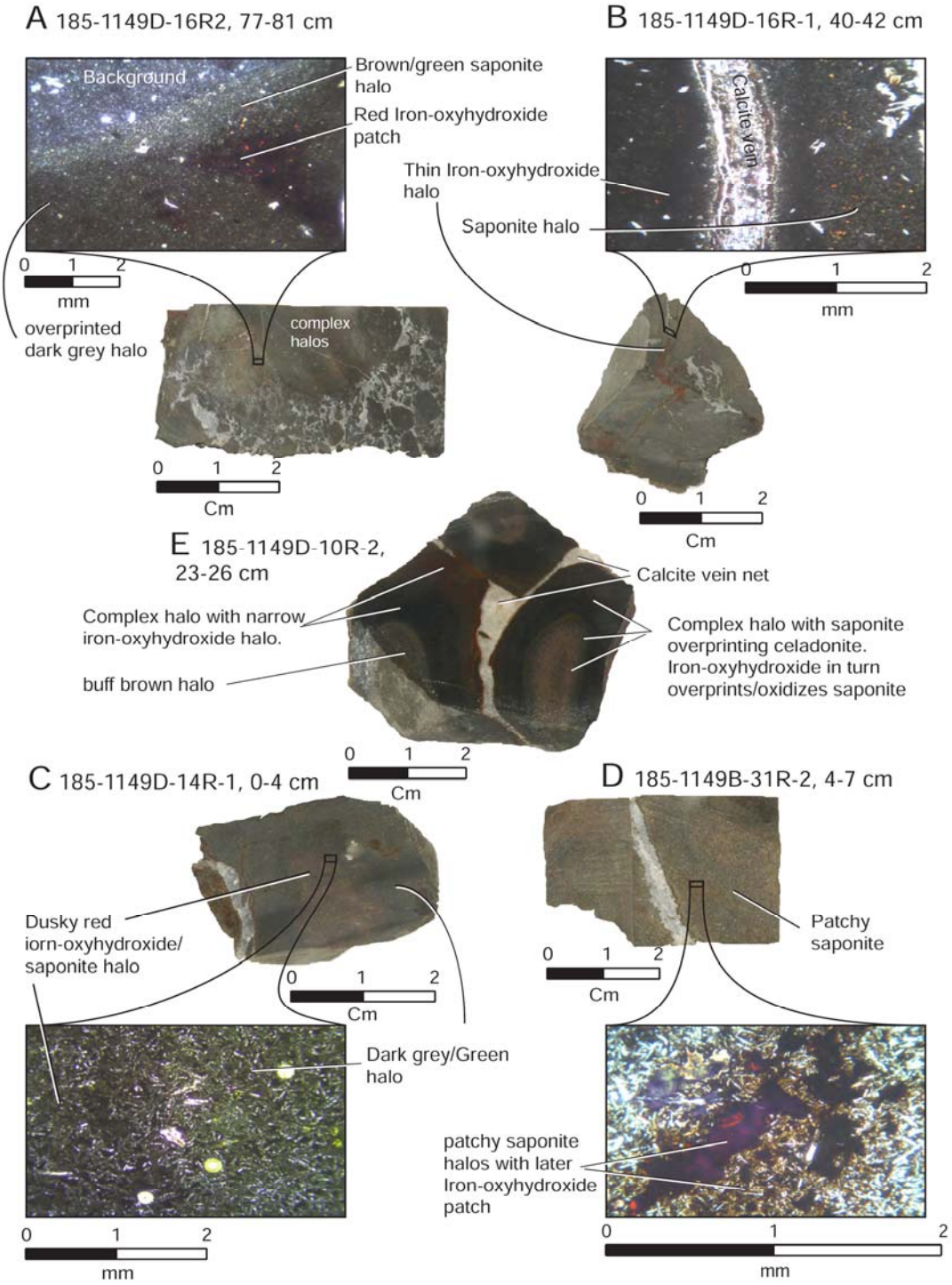

Figure 5.17. Variation in alteration halos at ODP Site 1149. A: Alteration front of saponite which overprints celadonite halo giving distinctive dark colour and late Iron-oxyhydroxide patches. The sample has extreme local variation B: Narrow Iron oxyhydroxide halo around carbonate vein overprinting earlier saponite halo. C: Dark grey/green halo (Celadonite) halo and saponite/ iron-oxyhydroxide halo. D: Iron oxyhydroxide patch overprinting saponite patch. Patchy texture of saponite in thin section gives rise to mottled effect in hand specimen. E: Complex halos demonstrating the main alteration phases. Photomicrographs A, B, C, and D are at 25x, 50x, 50x, and 100x magnification and they are (except 'C' which is in cross polarised light) in plane polarised light.

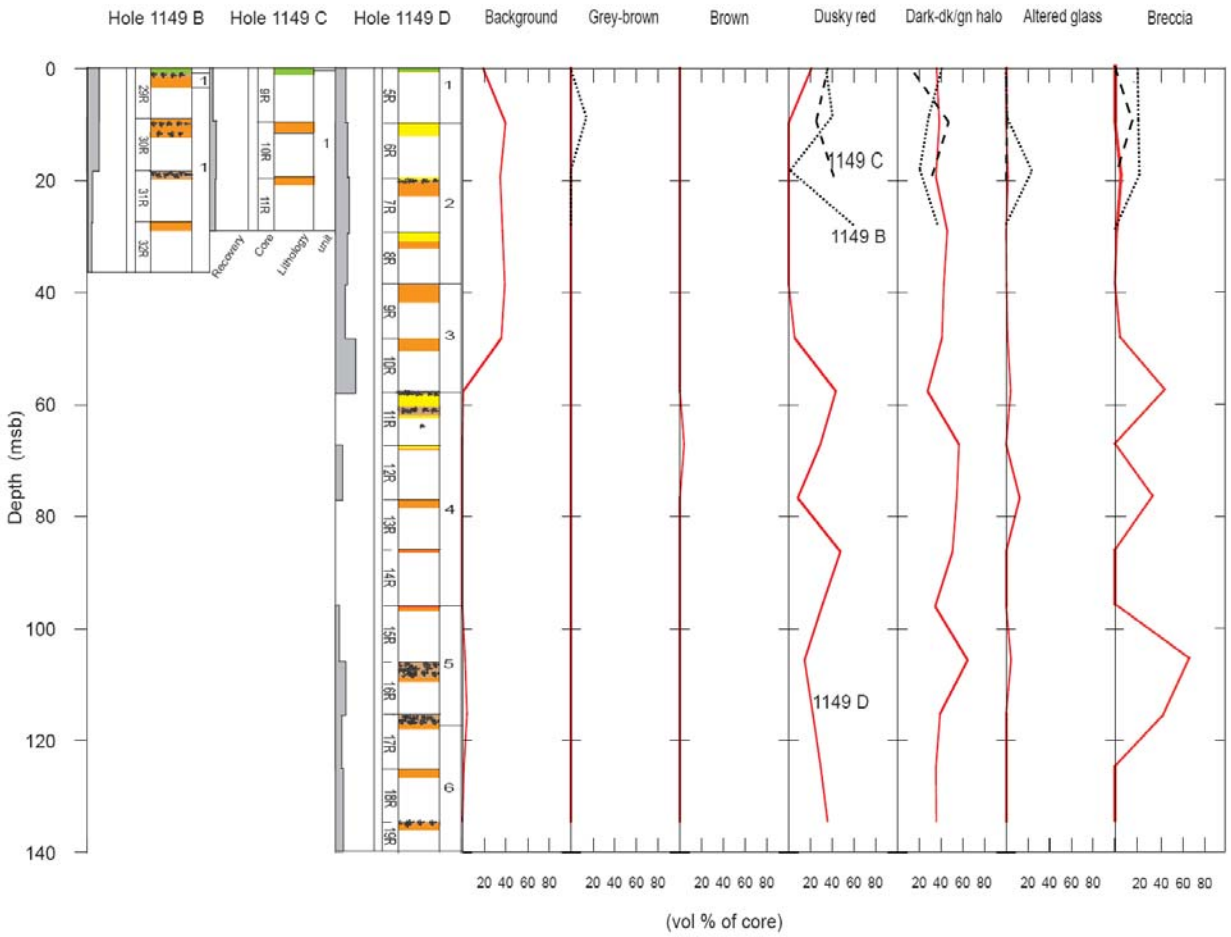

Figure 5.18. Extent and distribution of alteration styles and breccias vs. depth (msb) at ODP Site 1149. Volumes are normalised to account for recovery.

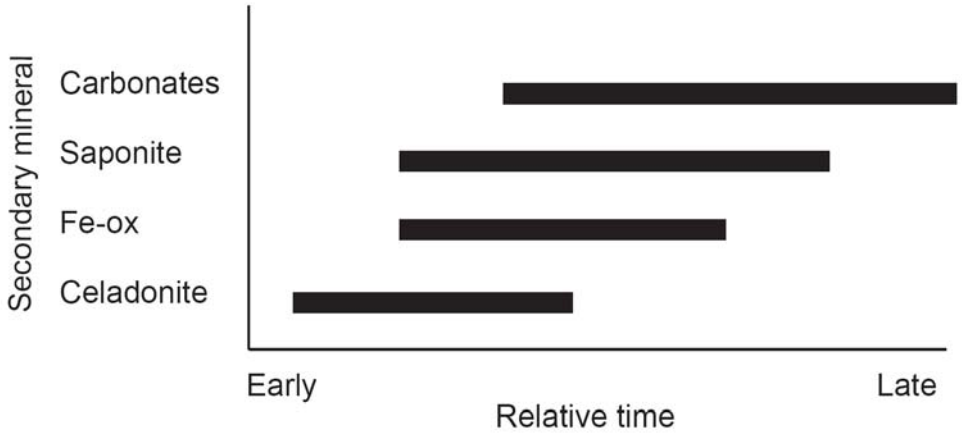

Figure 5.19. Relative timing of secondary mineral paragenisis at Site 1149.

5.2.3 Breccias

Breccias are present in ODP Hole 1149B (4 subunits), Hole 1149C (1 subunit) and Hole 1149D in sections 185-1149D-11R-1 to 11R-2, 13R-1 and 16R-1 to 16R-2. The distribution and extent of breccias are recorded in Figure 5.2.10. They consist of basaltic breccias, hayaloclastite breccias and pillow-rim breccias, and make up 13.5% of the recovered basement. The sections in ODP Hole 1149D that contain hyaloclastite and pillow-rim breccias are the most intensely altered portions of recovered ODP Site 1149 basement (Plank et al., 2000).

Basaltic breccias (Figure 5.20 B) form the majority of Section 185-1149D-11R-3. Basalt clasts are subangular to angular and vary in size from 5-20 cm and they exhibit alteration similar to that of Sections 185-1149D-11R-1 to 11R-2, 13R-1 and 16R-1 to 16R-2. The cement is largely composed of calcite with minor saponite and rarely, iron-oxyhydroxide on the margins of the clasts. Sample 185-1149D-11R-1, 78-80 cm exhibits a boundary of euhedral 'dog tooth' calcite crystals within the matrix, indicating at least two stages of calcite fill (Figure 5.15). Other basalt breccias, including sample 185-1149D-16R-2, 77-81 cm (Figure 5.20 C), contain tiny <0.5mm basalt fragments within the matrix. A lack of any well rounded clasts and the lack of any sorting suggest the basaltic breccias formed in-situ.

Hyaloclastite breccias are composed of highly altered, zoned, angular glass shards that range in size from <1 mm to 10 mm in a cement of saponite, celadonite and minor calcite (Figure 5.20A). Hyaloclastite breccias commonly occur on the boundaries of pillow basalts and where this is clearly evident, these are termed pillow-rim breccias. Some units (e.g., ODP Hole 1149B, Subnunits 1-12 and 1149D subunits 4-5) contain highly altered rounded glassy clasts. Rare bands of interpillow sediment occur at ODP Site 1149 (e.g., Section 1149B-29R-1, 134-140 cm, Figure 5.21).

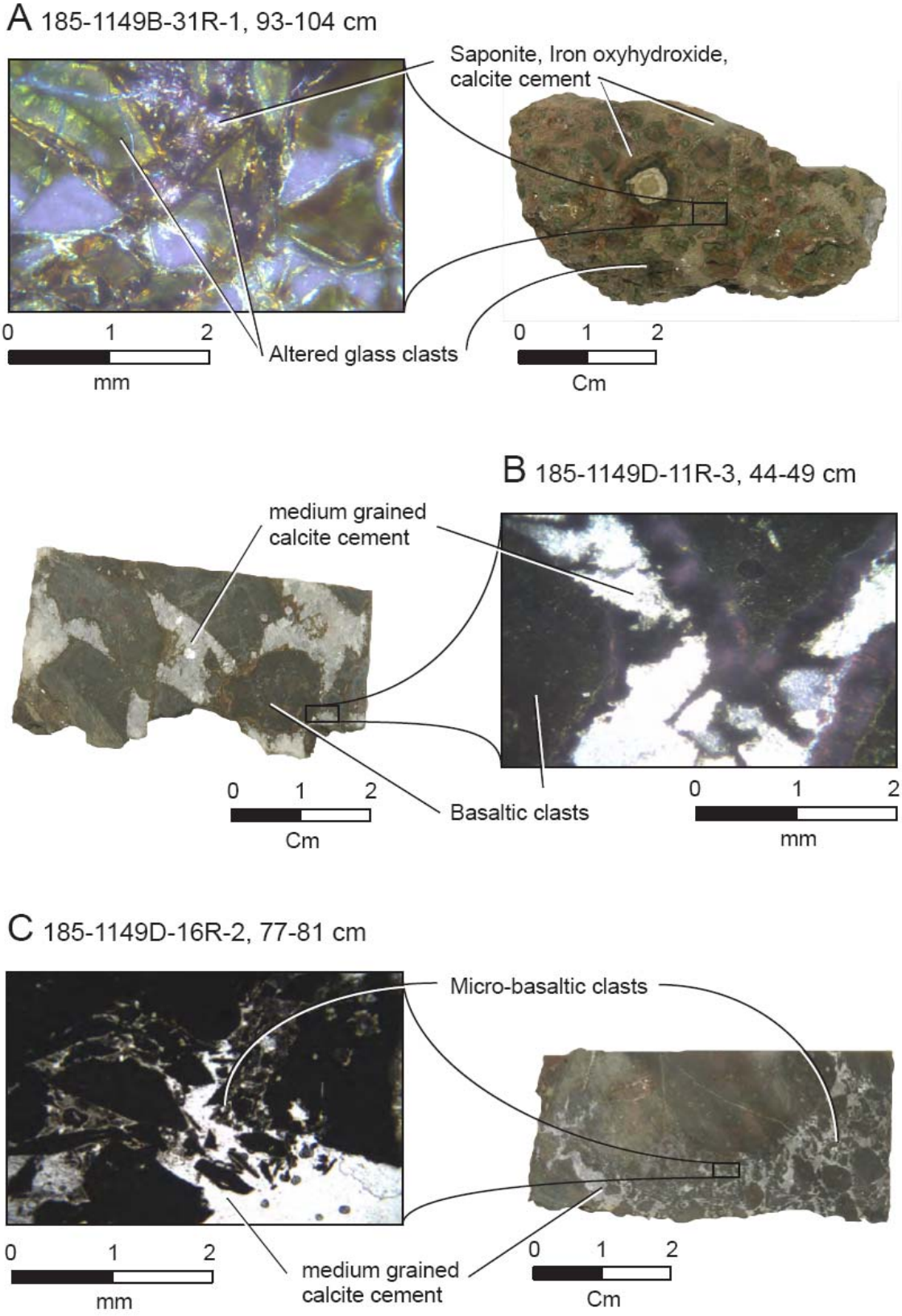

Figure 5.20. Examples of breccias at ODP Site 1149. A, Hyaloclastite breccia B, Basaltic breccia C, Microbreccia. Photomicrographs are in plane polarised light at 25x magnification.

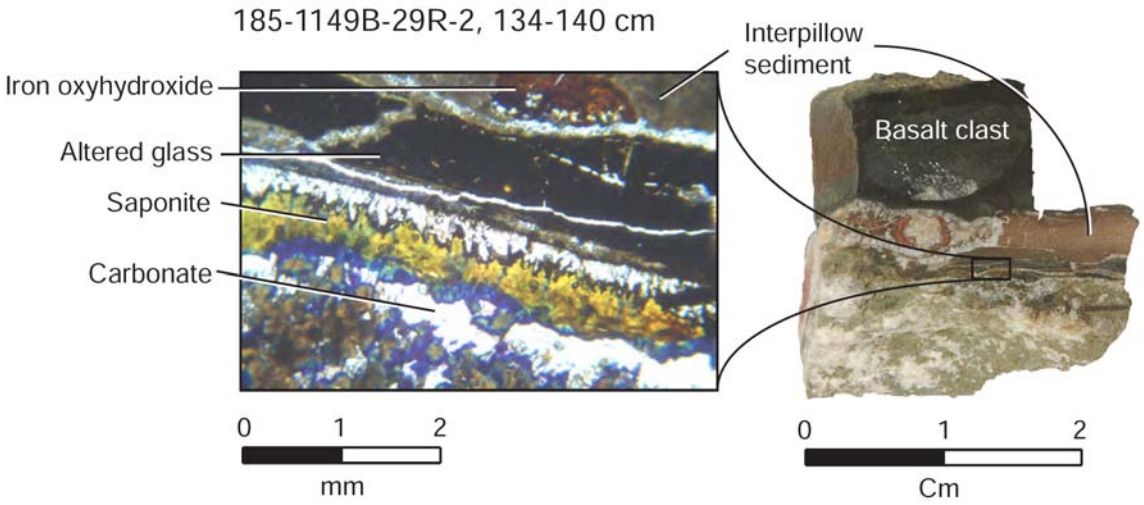

Figure 5.2.13, Matrix composed of interpillow sediment, elongate heavily altered glass shards, saponite, iron-oxyhydroxide and calcite. Photomicrograph taken in plane polarised light at 25x magnification.

5.2.4 Summary

The petrographic observations made in this study, Plank et al., (2000), and Talbi and Honnorez (2003) provide insights into the timing of secondary mineral formation at ODP Site 1149. Sections 185-1149D-11R-1 to 11R-2, 13R-1 and 16R-1 to 16R-2 are the most altered samples at ODP Site 1149. They are intensely altered to a dark brown to orange tan colour with no distinct halo present. This is thought to be caused by the high degree of fracturing in these sections coupled with a fine grained texture (see 'Breccias') (Plank et al., 2000). Low temperature (< Sub 100^0C) alteration at ODP Site 1149 consists of at least four alteration stages, all of which are sourced from open fissures and exposed surfaces.

- Stage One (Celadonite) is marked by formation of thick dark green/grey celadonite alteration halos that propagate from celadonitic veins, filling vesicles, interstitial areas and replacing some olivine and mesostasis.
- Stage Two is defined by overprinting of the dark green/grey halos by saponite with variable iron content and a distinctive mottled alteration front. Celadonite veins are completely or partially replaced by saponite.
- Locally variable brown to dusky red iron-oxyhydroxide halos and oxidation and/or overprinting of the saponite/celadonite veins marks Stage Three. Stage Two and Three are likely to be transitional given the gradation present in some

alteration halos and the variable iron content of saponite (as suggested by colour variation) in addition, saponite can cross-cut iron veins.

- Finally, precipitation of multiple late stage carbonate veins fill reopened veins, form new veins or can replace the pre-existing vein minerals. Figure 5.22 summarises the timing of secondary mineral emplacement and alteration at ODP Site 1149.

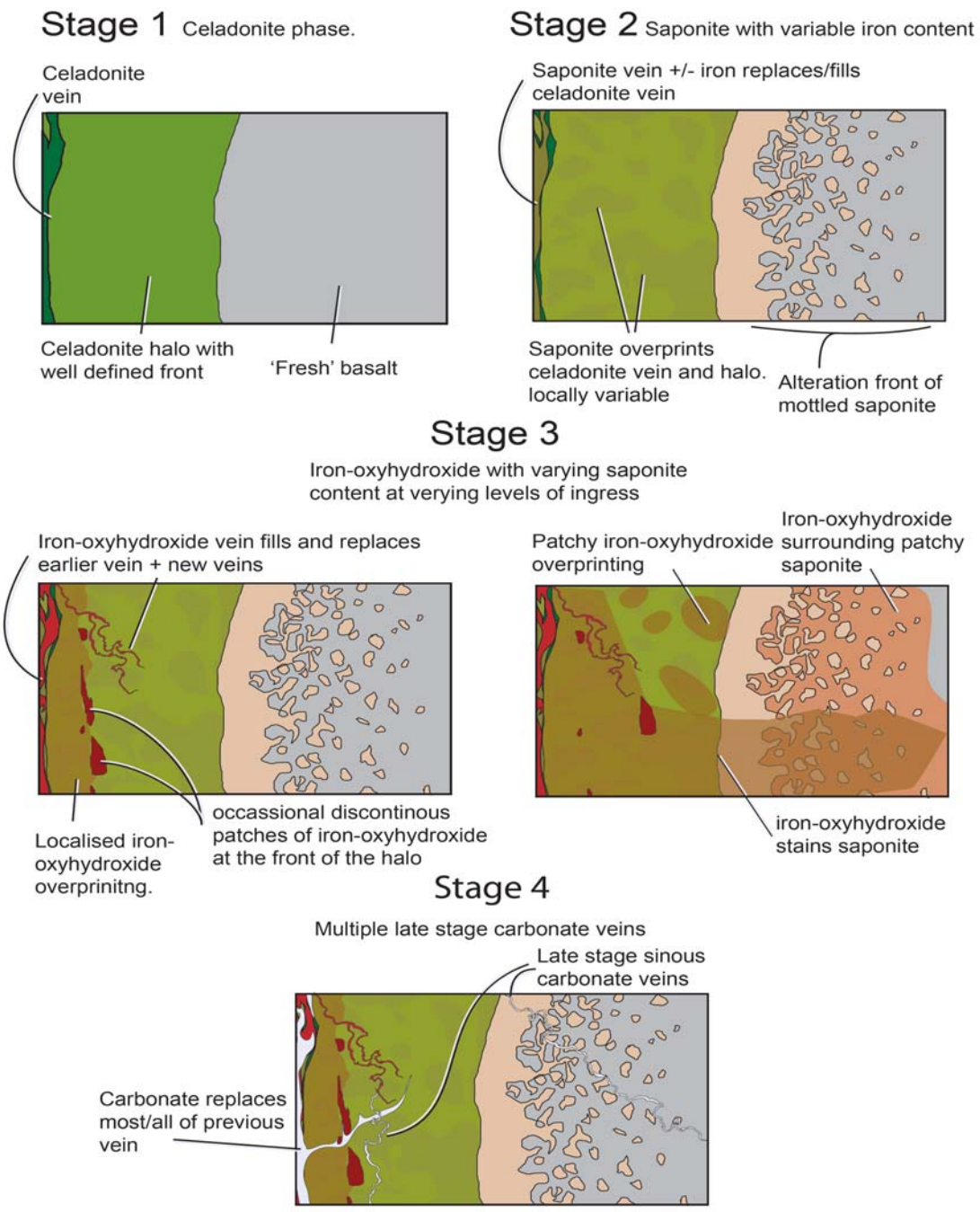

Figure 5.22. Relative timing of secondary mineral paragenisis and alteration assemblages at ODP Site 1149.

The change from celadonite to saponite and iron-oxyhydroxide probably reflects the transition from an open, oxidizing system, where the relatively young crust has little or no sediment cover, to a more restricted regime, where reducing conditions are set up. Such a change may occur as secondary mineral precipitation fills up all available fissures and pore space. Increased sediment cover over time may also contribute to restrictive conditions and a slight rise in temperature at Site 1149. Further study is required to determine the thermal regime for each alteration stage. Late stage carbonate veins may reflect late reopening, possibly due to earthquakes and/or flexure of the ocean crust due to its position near the Izu-Bonin trench (Plank et al., 2000). Flexure of the ocean crust may explain overprinting of alteration sequences with earlier phases, forming complex halos (Figure 5.17 A).

5.3. Alteration Geochemistry

Following similar methods and analysis carried out for Sites 1256 and 1179, Whole rock samples, secondary minerals in veins and breccias have been analysed for their concentrations of major elements, trace elements, REE, Sr-isotopic ratios and where possible, oxygen, carbon isotopic ratios (See chapter 2 'methods' for analytical details). Separation of alteration assemblages, least altered whole rocks, and leachates augment the petrographic observations to help characterise low temperature alteration at Site 1256. Comparisons with the petrographic observations described earlier and sample by sample calculation of the protolith composition help to establish a quantitative estimate of chemical change that has occurred at Site 1149 because its formation. Vein minerals and Sr-isotopic ratios of secondary carbonate and whole rocks help define the conditions in which secondary minerals precipitated and the evolution of fluid during low temperature hydrothermal alteration.

5.3.1 Whole Rock Geochemistry

In order to constrain the isotopic and chemical variation as a result of alteration, analysis of 95 whole rock samples and 24 Carbonate vein minerals separates were carried out for Site 1149. Analyses include $^{87}Sr/^{86}Sr$, $\delta^{18}O$, $\delta^{13}C$, Major elements, trace elements and REE. These include pairs of alteration halo/background and leaches (See appendix B, 3 for whole rock, D, 3 for carbonate, and Chapter 2 for leachate data tables). Samples were selected based on alteration assemblage and their distribution down hole at Site 1149. At 65 to 84 msb and 85 to 105 msb low recovery has led to a lack of available samples within these intervals, therefore unless further samples can be acquired these gaps in sample distribution will remain.

Selected major element and trace element profiles are plotted vs. depth in Figures 5.23 and 5.24 with regard to their alteration styles and basement stratigraphy.

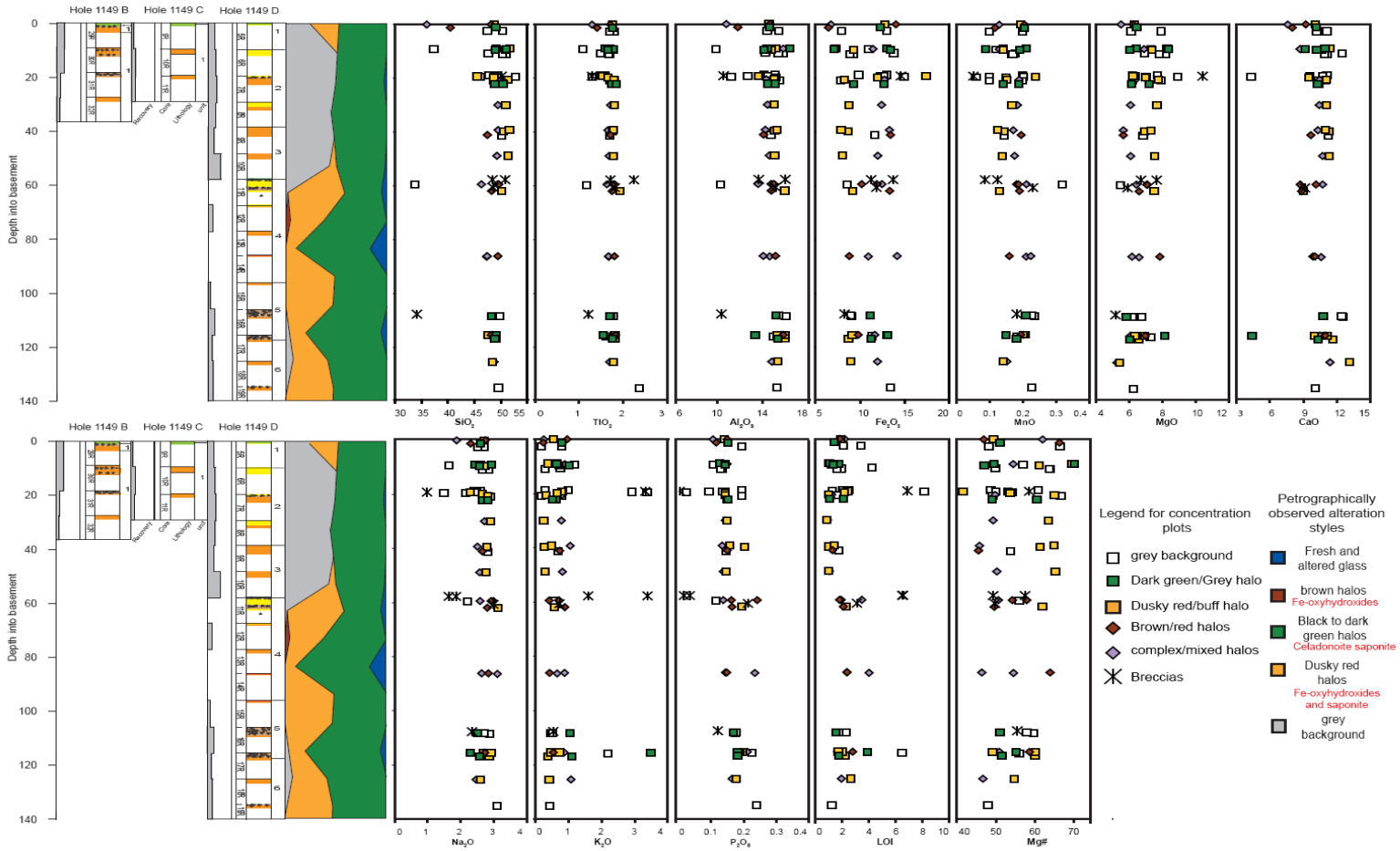

Figure 5.23. Selected major and trace concentrations in Site 1149 whole rock samples vs. depth. Alteration styles are highlighted within the data points. Site 1149 stratigraphy, recovery and the cumulative total of each alteration style at Site 1149 vs. depth is included for reference. White squares = data from Hauf et al, (2003); Kelley et al, (2003); and Rouxel, (2003). Stratigraphy is redrawn from Plank et al., (2000)

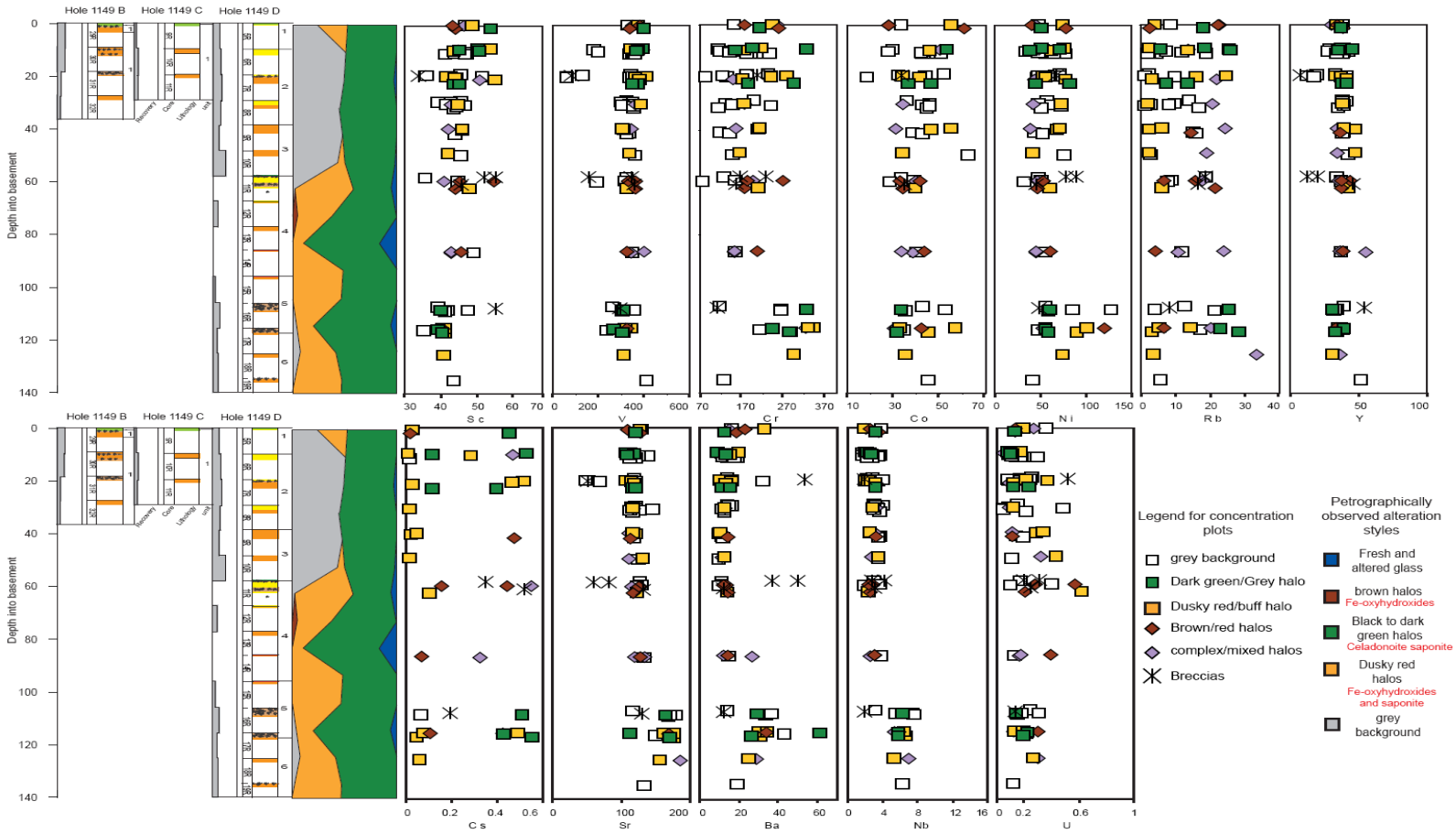

Figure 5.24. Selected trace and REE concentrations in Site 1149 whole rock samples vs. depth. Alteration styles are highlighted within the data points. Site 1149 stratigraphy, recovery and the cumulative total of each alteration style at Site 1149 vs. depth is included for reference. White squares = data from Hauf et al, (2003); Kelley et al, (2003); and Rouxel, (2003). Stratigraphy is redrawn from Plank et al., (2000)

Variation between major/trace/REE, alteration style, and depth are indistinct. The greatest range in alteration styles and intensities occurs within the mixed halos and brecciated regions. Buff/grey background exhibits low K_2O, Fe_2O_3, MnO, LOI, Rb, Cs, and the highest Mg# compared to the other assemblages. These observations are consistent with the relatively minor emplacement of secondary minerals observed petrographically in buff/grey background rocks. In contrast, Dark green to dark grey halos have high K_2O, Fe_2O_3, MnO, LOI, Rb, Cs, low Mg# and slightly reduced CaO compared to buff/grey background . Incorporation of celadonite, iron-oxyhydroxides and saponite and the partial replacement of plagioclase witnessed in these halos (See section 5.2 'alteration') is the most likely explanation for these changes. Similarly red/brown halos (High Fe_2O_3, Rb, Cs and low CaO, Mg#) and mixed halos (Elevated Fe_2O_3, K_2O, Rb, Cs, LOI and low CaO, Al_2O_3, MgO, Mg#) reflect the incorporation of secondary phases into the host rock and the replacement of primary phases. Breccias at Site 1149 exhibit the greatest chemical variation with notable increases in Fe_2O_3, K_2O, and LOI, and apparent reductions in CaO, Na_2O, MgO and Mg#. One sample has greatly reduced SiO_2 this probably reflects the large proportion of secondary minerals within the matrix and clasts resulting in a volumetrically lower proportion of primary silica bearing phases. Low CaO and Mg reflects the partial replacement of plagioclase and olivine respectively. K and Fe most likely reflect celadonite and iron-oxyhydroxide emplacement whereas elevated mobile trace elements such as Sr, Rb and Cs reflect their incorporation into clay minerals such as saponite and celadonite. Determination of the Fe-oxidation ratio is required to determine the oxidised proportion of Fe hence we can make better estimations of the oxidation levels at Site 1149 (e.g. Alt et al., 1993).

Selected major trace and REE vs. LOI for a range of sample pairs are shown in Figure 5.25. Despite some clear changes in the concentrations of SiO_2, Fe_2O_3, K_2O, MgO, Rb, and Cs, trends between sample pairs and LOI are highly variable and indistinct. However the concentrations of the same selected major, trace and REE vs. $^{87}Sr/^{86}Sr$ (Figure 5.26) and Fe_2O_3 (Figure 5.27) for Site 1149 sample pairs exhibit clear trends between altered 'halo' portions and least altered 'background' alteration. Reductions in SiO_2, Al_2O_3, MgO, Na_2O, Ni, Y, U and Increases in Fe_2O_3, MnO, K_2O, Rb, and Cs within the altered 'halo' samples supports the petrographic observations that a greater proportion secondary minerals replaces groundmass/phenocrysts and fills vesicles within the halos. Variations between the chemical change for different

alteration styles within these plots remains indistinct. Mixed and brown halos appear to show the most variability which reflects the varying degrees of alteration intensity and overprinting these samples have been subjected to. Samples 149-1149D-16R-2, 143-146 cm; 17R-1, 39-42 cm; 17R-2, 29-32 cm; and 18R-1, 75-80 cm all have elevated Sr, Cs, Ba and La/Sm values compared to the other sample pairs. In addition there is little change in the concentration of Sr, Cs, and Ba between the background and halo subsamples despite comparisons with LOI, $^{87}Sr/^{86}Sr$, and Fe_2O_3. The differences in these samples strongly imply primary magmatic variation, and that the interval from which these samples were taken (108.35 to 125.39 msb) represents a slightly different source to the rest of the basement at Site 1149, This is consistent with the E-MORB affinity that has been ascribed to this interval (Plank et al., 2000).

5.3.2 Chemical changes

Utilising the same methods employed at Sites 1179 and 1256 (See Chapters 3 and 4 respectively), chemical change at Site 1149 has been calculated. For consistency and so that direct comparisons can be made with the other sites (See later in Chapter 7) in this study the immobile element Ti is used as the monitor of fractionation and a protolith is calculated for each sample in an attempt to remove as much of the alteration effects from the basaltic samples, this includes 'background' alteration associated with the least altered grey and buff coloured background rocks (full methodology is discussed in Chapter 3). As with Sites 1179 and 1256, the protolith composition for each sample is derived from, 1) best fit linear regression lines of the element in question vs. TiO_2, 2).

Element	Concentration	Unit	Reference
SiO_2	49.93	wt%	Mckenzie and O'Nions (1991)
Al_2O_3	15.90	wt%	Mckenzie and O'Nions (1991)
CaO	11.62	wt%	Mckenzie and O'Nions (1991)
MnO	0.171	wt%	Mckenzie and O'Nions (1991)
LOI	0.20	wt%	Alt et al, (1989); Danyushevsky (2001)

Table 5.1. List of protolith element concentrations derived from sources other than Site 1256 whole rock samples.

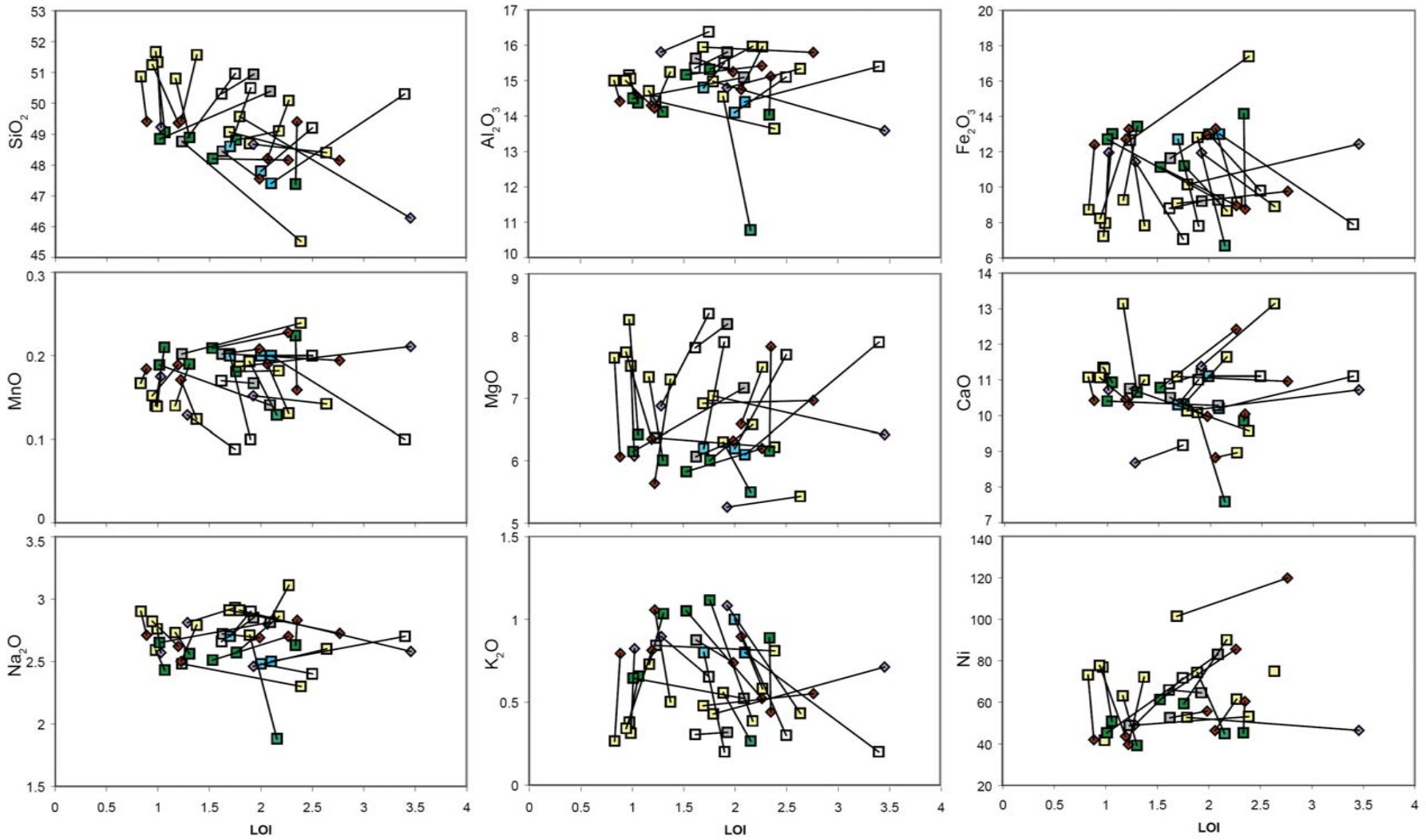

Figure 5.25 A. Selection of major (wt %), trace (ppm) and REE (ppm) plots vs. LOI (wt %) for Site 1149 Sample pairs in which halos directly adjoin relatively fresh background. Data point legend shown in Figure 5.24 Grey squares = grey background. White squares = data from Hauf et al, (2003); Kelley et al, (2003); and Rouxel, (2003).

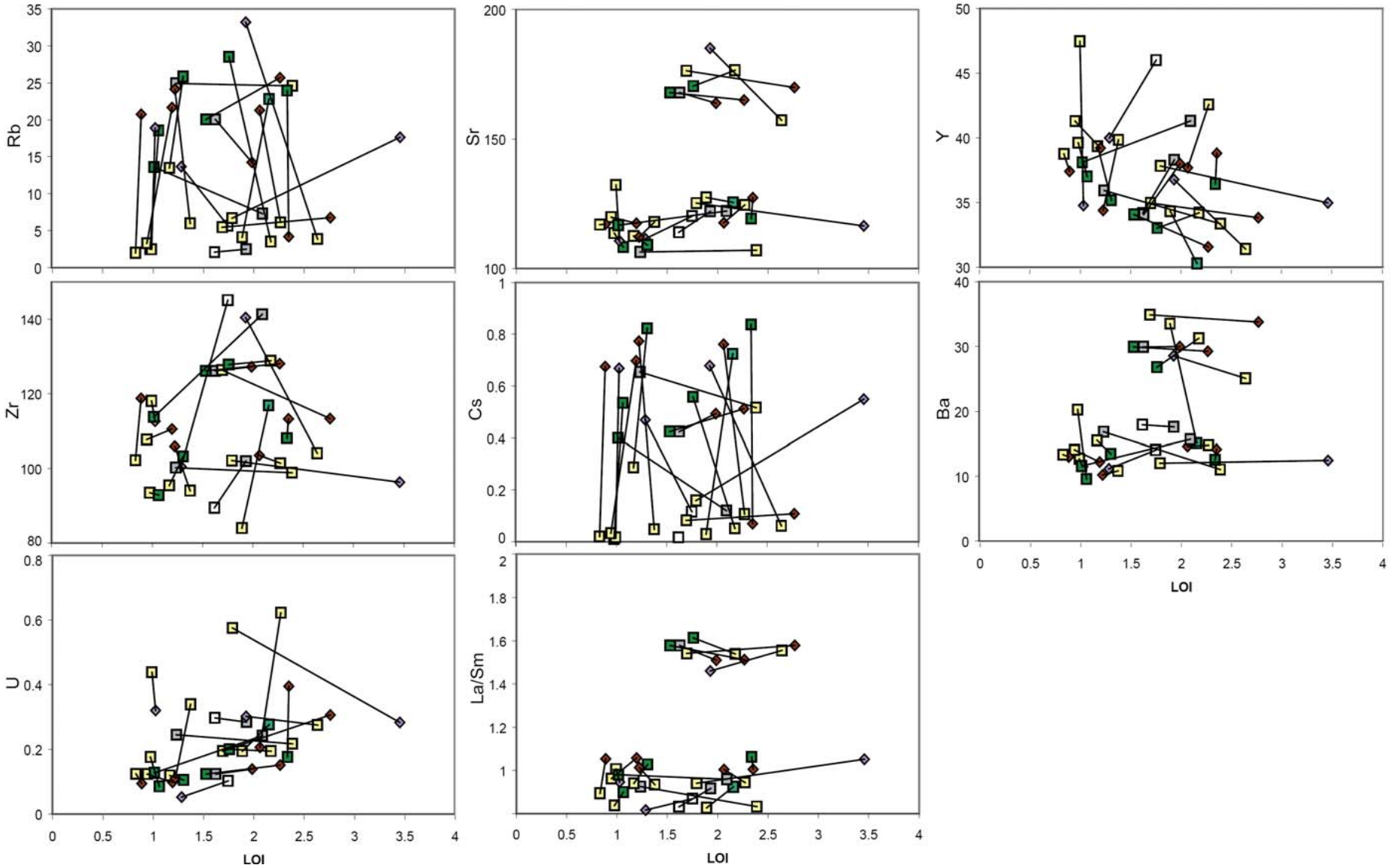

Figure 5.25 A, continued.

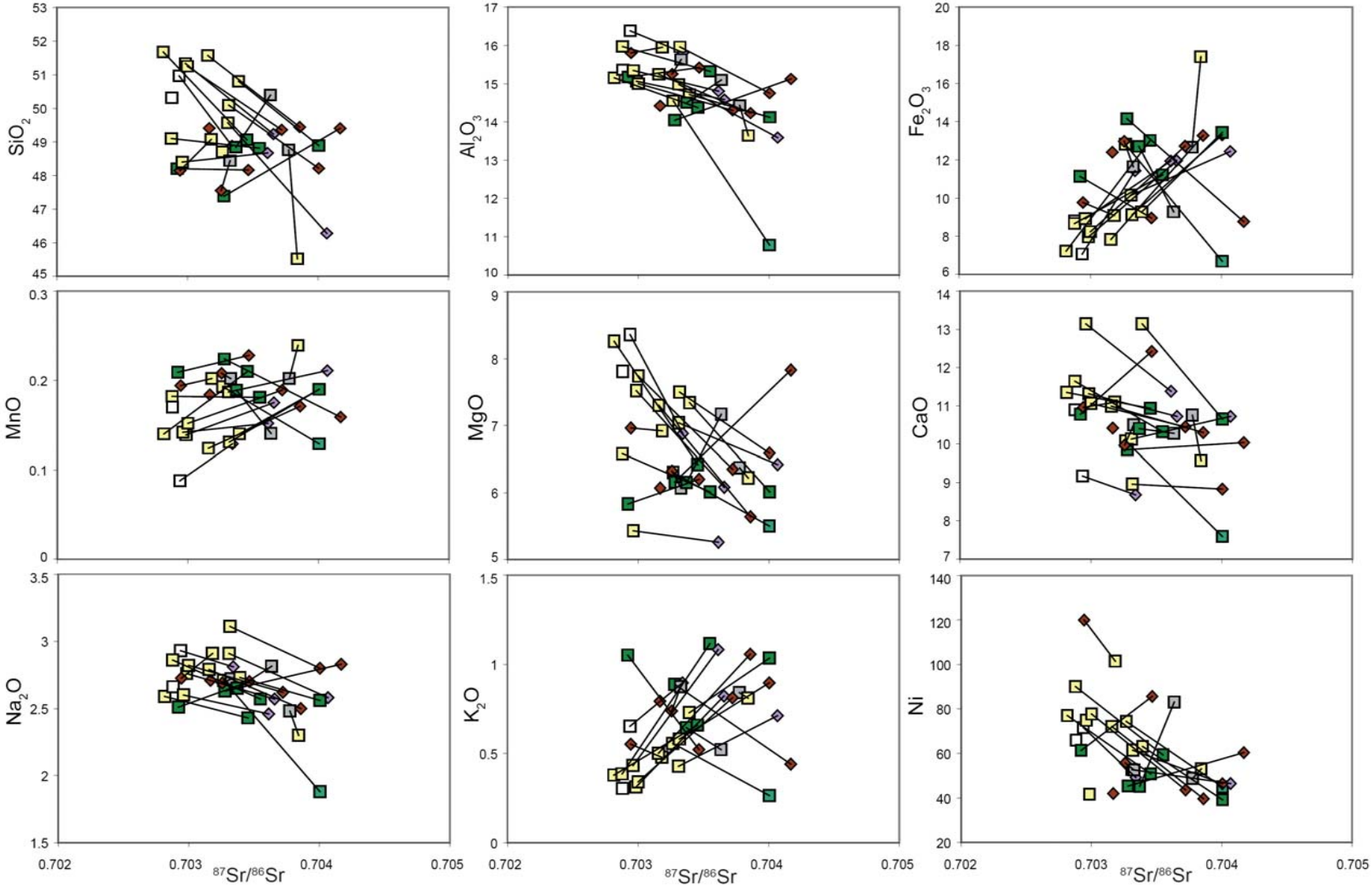

Figure 5.25 B, Selection of major (wt %), trace (ppm) and REE (ppm) plots vs. $^{87}Sr/^{86}Sr$ for Site 1149 Sample pairs.

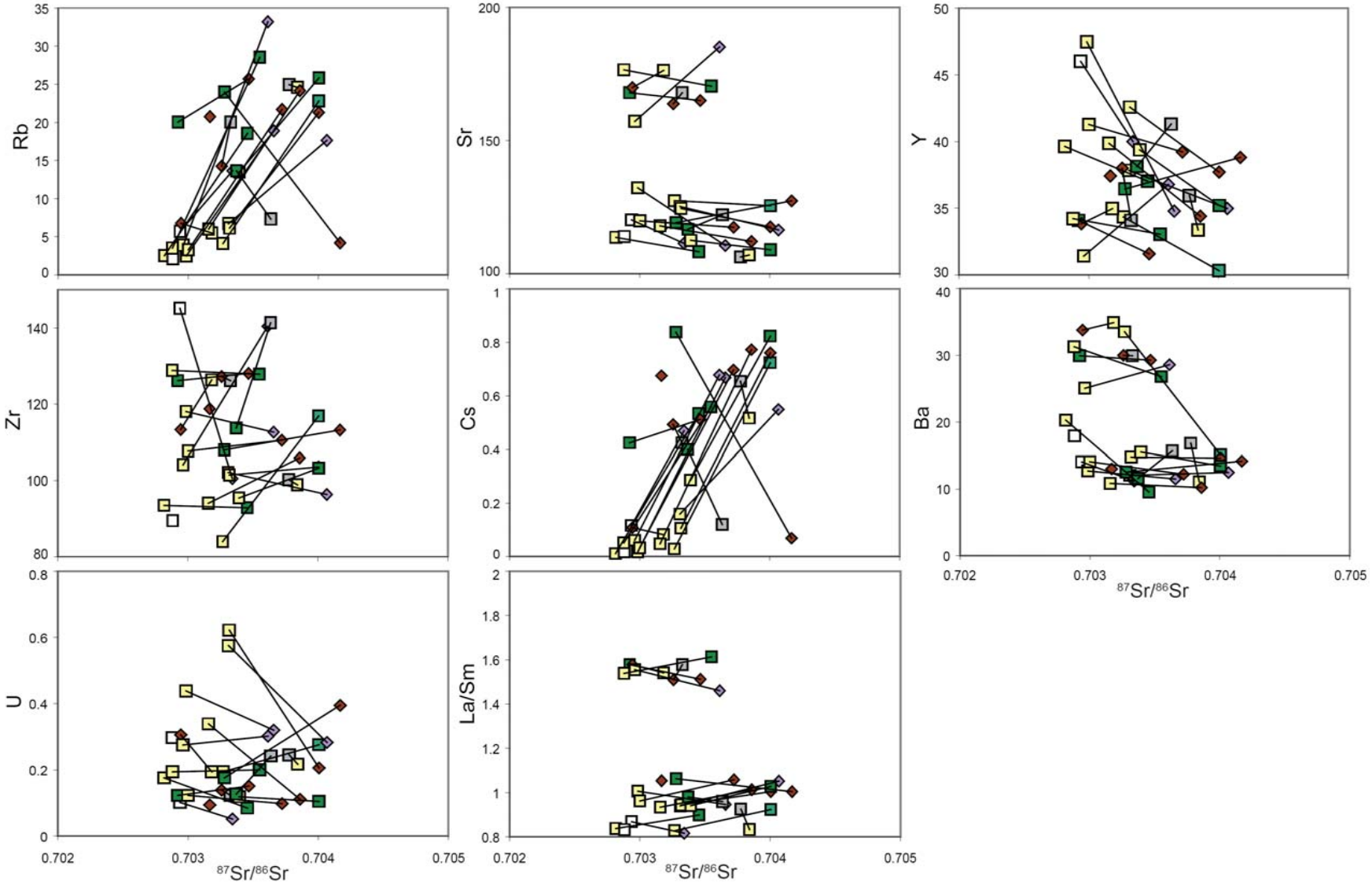

Figure 5.25 B, continued.

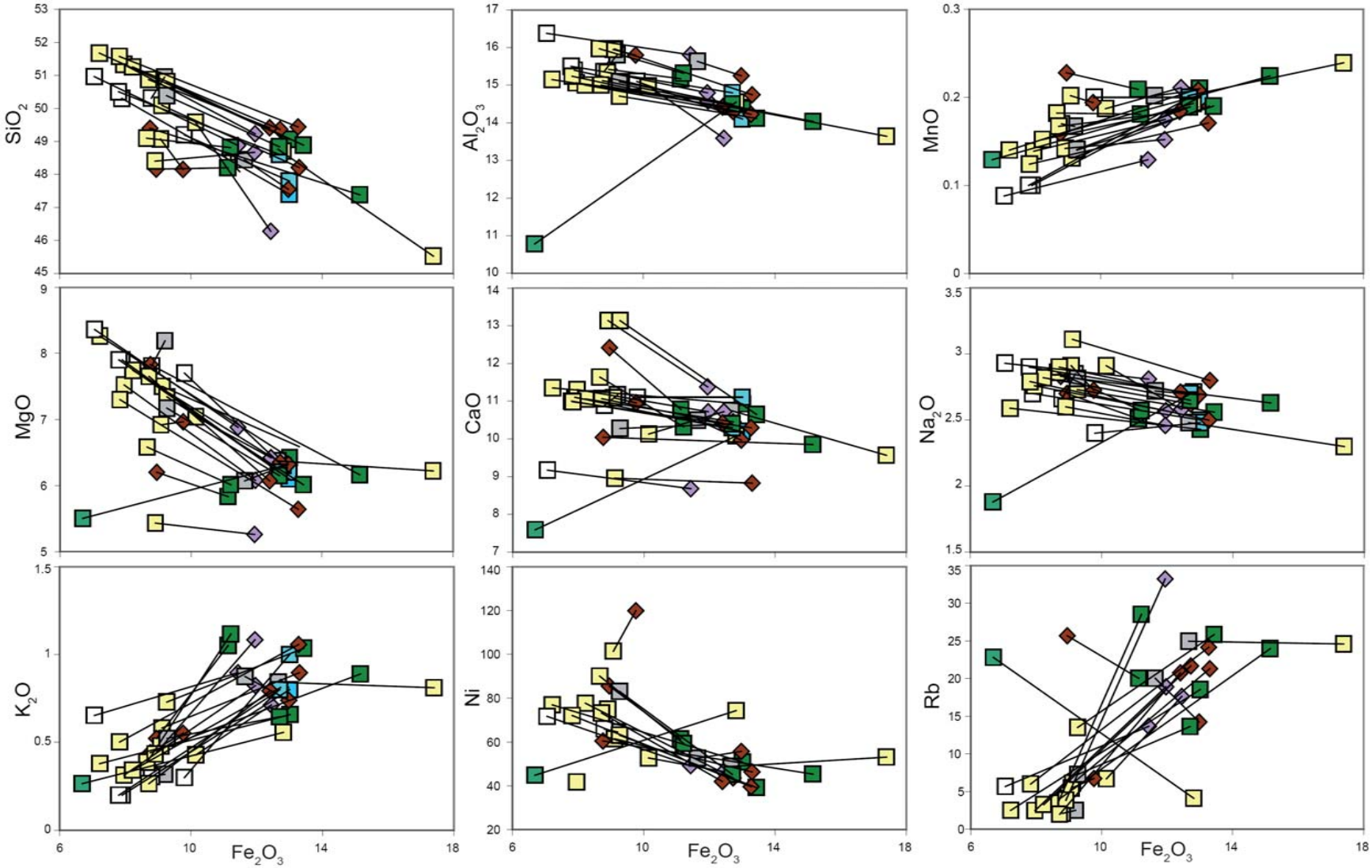

Figure 5.25 C, Selection of major (wt %), trace (ppm) and REE (ppm) plots vs.Fe_2O_3 (wt %) for Site 1149 Sample pairs.

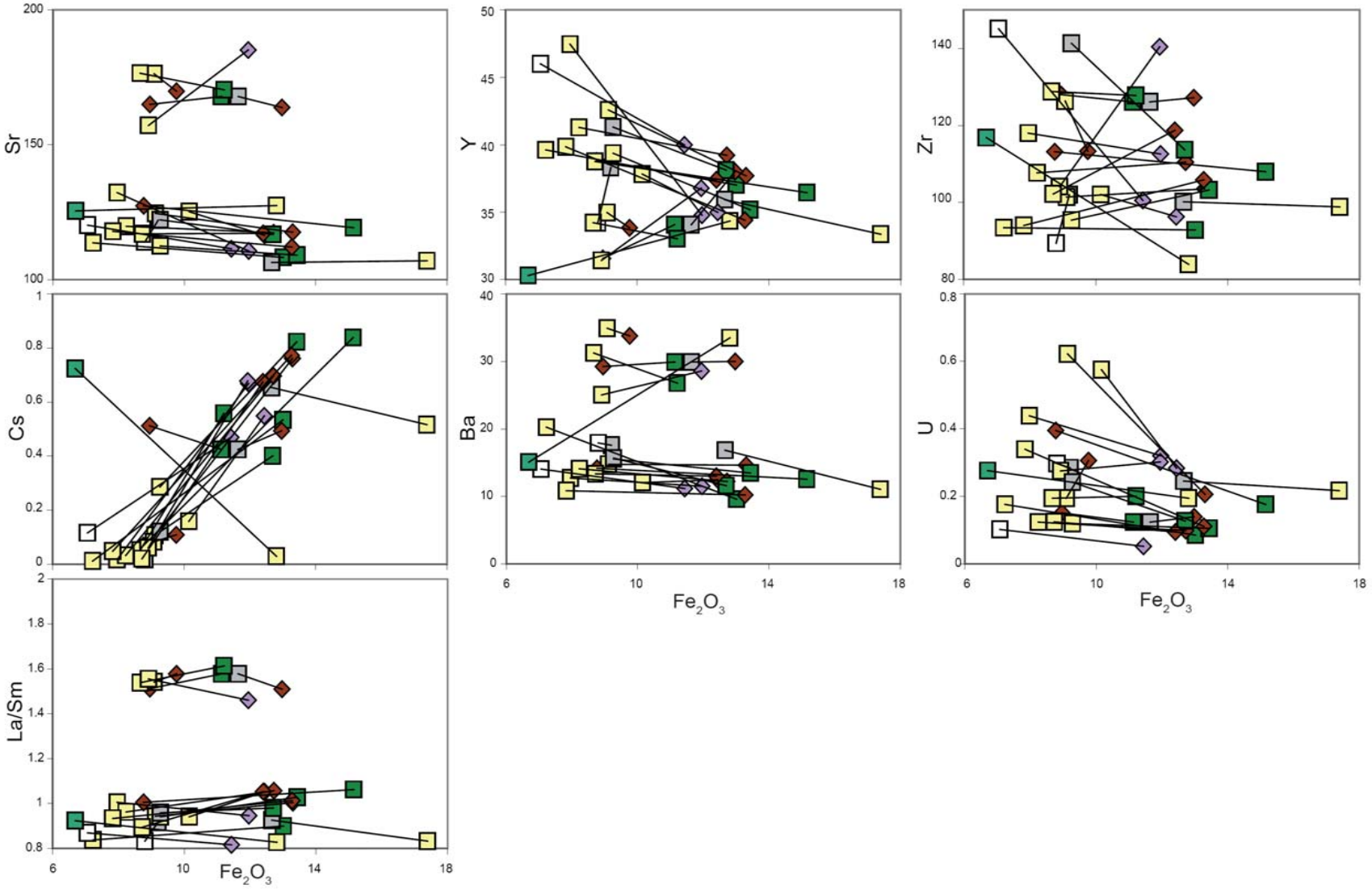

Figure 5.25 C. Continued.

Where best fit linear regression is not possible by the average compositions of the least altered samples, or 3) average N-MORB or EPR-MORB from the literature. The process from which these changes are calculated is outlined in Figure 3.24., in addition the values for N-MORB and EPR-MORB used for calculations at this site are outlined in Table 5.1.

Regression plots for all elements vs. TiO_2 and the selected least altered samples at Site 1149 are included in the Appendix (Section C, 3). Chemical change for each alteration style is calculated and then weighted according to the volume of core that each alteration style occupies. The compositions and abundances of vein and breccia matrixes are factored to produce an overall weighted average chemical change for Site 1149. The petrography and chemical changes observed within sample of brown altered breccia clasts 185-1149D-11R-3, 44-49 cm, is comparable to that seen in whole rocks that exhibit the equivalent alteration style (Table 5.2).

Expedition, hole, core, interval (cm)	185 1149B 31R-1 93-104	185 1149D 11R-1 30-37	185 1149D 16R-2 77-81	**185 1149D 11R-3 44-49**	**185 1149D 11R-1 30-37**	185 1149D 11R-2 65-68	185 1149D 11R-4 24-27	185 1149D 11R-2 78-80	185 1149D 11R-2 65-68	185 1149D 9R-2 24-28	185 1149D 17R-1 39-42	185 1149D 14R-1 0-4	185 1149D 17R-1 39-42
Depth (mbsf)	426.9	358.2	408.2	**361.11**	**358.2**	359.9	362.4	425.9	359.9	340.2	415.9	386.6	415.9
Rock type	Hyalo	pillow breccia	pillow lava	**basaltic breccia**	**Breccia clasts**	Massive flow	Massive flow	Massive flow	Massive flow	Pillow lava	pillow lava	pillow lava	pillow lava
Notes	whole breccia	whole breccia	whole breccia	**brn clasts**	**red clasts/matrix**	brn/gy/rd mix	Brn/red mixed	brn/red mixed halo	red/bn mixed halo	brn	brn	red	red halo
SiO_2 (wt %)	50.12	48.36	34.16	**48.53**	**50.76**	46.28	48.21	49.37	49.57	50.51	47.55	49.40	48.15
Al_2O_3 (wt %)	10.53	15.99	10.35	**15.13**	**13.65**	13.59	14.75	14.74	14.98	15.06	15.25	15.12	15.80
Fe_2O_3 (wt %)	14.57	11.22	8.22	**11.81**	**13.69**	12.44	13.30	11.86	10.15	8.62	12.97	8.76	9.76
MgO (wt %)	10.39	7.64	5.17	**5.89**	**6.70**	6.42	6.59	7.08	7.04	6.90	6.32	7.83	6.96
CaO (wt %)	1.66	2.32	22.08	**9.13**	**1.26**	10.72	8.83	8.71	10.13	11.26	9.97	10.04	10.95
Na_2O (wt %)	0.99	1.86	2.34	**2.98**	**1.64**	2.58	2.80	2.98	2.91	2.79	2.69	2.83	2.73
K_2O (wt %)	3.31	1.60	0.55	**0.74**	**3.37**	0.71	0.90	0.72	0.43	0.29	0.74	0.44	0.55
TiO_2 (wt %)	1.30	2.25	1.22	**1.81**	**1.71**	1.64	1.75	1.78	1.81	1.77	1.80	1.81	1.83
MnO (wt %)	0.05	0.12	0.18	**0.23**	**0.09**	0.21	0.19	0.18	0.19	0.14	0.21	0.16	0.19
P_2O_5 (wt %)	0.01	0.04	0.13	**0.22**	**0.02**	0.14	0.17	0.25	0.17	0.21	0.20	0.15	0.20
LOI	6.87	6.54	15.24	**3.09**	**6.49**	3.46	2.06	1.91	1.79	0.96	1.99	2.35	2.77
Total	99.80	97.94	99.64	**99.56**	**99.38**	98.19	99.55	99.58	99.17	98.51	99.68	98.89	99.89
FeO* (wt %)	13.11	10.10	7.40	**10.63**	**12.32**	11.19	11.97	10.67	9.13	7.76	11.67	7.88	8.78
Co (ppm)	33.6	80.8		**34.5**		39.9	34.3	32.9	41.3	46.6	33.1	43.6	42.4
Cr (ppm)	205.9	227.6	110.3	**157.5**	**167.5**	198.0	175.1	269.3	184.0	211.9	344.0	208.5	487.4
Cu (ppm)	41.1	91.1	41.1	**46.4**	**107.7**	77.4	43.8	68.8	94.9	37.1	38.4	66.7	52.1
Ni (ppm)	67.4	77.6	47.7	**44.6**	**89.5**	46.5	46.4	53.3	52.7	69.5	55.7	60.4	119.9
Sc (ppm)	34.3	56.5	56.2	**46.4**	**53.2**	41.5	44.9	55.8	46.3	46.9	41.2	46.6	41.2
V (ppm)	80.6	342.2	294.7	**355.2**	**153.5**	353.9	364.4	363.4	332.7	311.3	341.9	326.4	327.5
Zn (ppm)	72.2	85.0	92.5	**126.2**	**110.5**	124.5	129.6	114.7	109.2	85.7	110.4	111.3	94.8
Rb (ppm)	65.2	18.5	8.4	**16.4**	**53.5**	17.6	21.3	15.8	6.7	2.5	14.2	4.2	6.7
Sr (ppm)	52.2	82.9	130.5	**132.9**	**60.6**	116.4	117.6	128.4	125.2	121.5	163.8	127.3	169.9
Y (ppm)	7.5	19.8	54.5	**45.4**	**12.1**	35.0	37.7	43.8	37.8	48.0	38.0	38.8	33.8
Zr (ppm)	76.2	151.4	76.1	**112.6**	**111.1**	96.3	103.5	110.6	102.1	110.2	127.2	113.2	113.3
Nb (ppm)	1.96	4.19	1.92	**3.14**	**2.84**	2.59	2.64	2.98	2.47	2.56	6.57	3.13	5.88
Cs (ppm)	0.70	0.35	0.20	**0.52**	**1.05**	0.55	0.76	0.44	0.16	0.02	0.49	0.07	0.11
Ba (ppm)	53.60	36.52	11.96	**11.92**	**50.09**	12.46	14.62	13.38	12.03	9.76	29.99	14.16	33.78

Table 5.2 Breccia samples and selected samples of red/brown halos (**bold**). A representative suite of major and trace element data is included for illustration. For comparison, whole breccia analyses is included. Halo = Hyaloclastite, brn = brown, gy = grey. Samples in bold are clasts sub-sampled from breccia. The complete dataset for Site 1149 can be found in Appendix section B, 3.

As such the analysis of this clast has been included with the other brown halos. Sample 185-1149D-11R-1, 30-37 cm (clasts) is extensively altered when compared to other 'red halo' samples, with very high LOI, K_2O, Fe_2O_3, Sr, Ba and low CaO, Na_2O. As such this sample represents very high fluid fluxes with intensive replacement of the groundmass that is not characteristic of other red/brown halos at Site 1149. In addition these clasts are riddled with numerous fractures and veins, therefore the 'clasts' analysed actually contained a large proportion of matrix material. As such it is not classified as a halo, rather a mix of clast and matrix.

5.3.2.1 *Results*

Multi-element diagrams show the chemical changes for major, trace elements and REE for Site 1149. Chemical changes (g/100g and mg/100g) are plotted with regards to alteration style in Figure 5.26 charts the chemical changes across all alteration styles and associated vein and breccia matrixes. Calculations from which these results are derived are provided in Section D (Appendix). To compensate for the lack of in-situ analyses of secondary minerals at Site 1149, secondary mineral compositions are sourced from a range of basement sites (See Table 5.3).

Mineral	Site source	Reference
Saponite	504	Bach et al, (1996), Noack et al (1996)
	896	Laverne et al, (1996), Teagle et al, (1996)
	1224	Paul et al, (2006)
	843	Waggoner (1993), Alt (1993)
Celadonite	504	Bach et al, (1996), Noack et al (1996)
	896	Laverne et al, (1996), Teagle et al, (1996)
	843	Alt (1993)
Iron-oxyhyroxides	504	Noack (1993)
	843	Alt (1993)
Carbonate	504	Noack (1993)
	896	Teagle et al, (1996)
	843	Alt (1993)
Zeolites	504	Bach et al, (1996), Noack et al (1996)

Table 5.3. Sources of secondary mineral composition data from oceanic basments Sites other than that of Site 1149 or those analysed in this study. Secondary mineral compositions were calculated as an average of all available compositions from basement within the Pacific Ocean. Outliers and samples with multiple mineral phases were excluded prior to calculation.

By utilizing data for secondary minerals from a variety of sites, potentially a more accurate appraisal of the true chemical change can be obtained because this will provide compositions for mineral phases where no analysis has been made. The assumption however, is that the composition of secondary minerals from these basement sites is the same as those of Site 1149, and different hydrothermal regimes may have led to very different chemical compositions. In order to minimise potential variation, secondary mineral compositions are only sourced from in-situ basement sites within Pacific ocean crust. Only secondary minerals from low temperature fluids <100^{o}C are used to construct secondary mineral compositions for Site 1149. Chemical analyses of vein minerals at Site 1149 and other sources is located in Section D (Appendix)

The chemical changes exhibited within the various alteration styles reflect the varying levels of alteration intensity and overprinting at Site 1149. 'Background' whole rocks, defined as 'grey' in the centre of rocks, and buff coloured background (Also in the centres of rocks), exhibit similar chemical changes, albeit with some minor but significant differences. Grey background rocks exhibit increased Fe_2O_3, K_2O, LOI, Cr, Sr, Ba, Dy and decreased SiO_2, Al_2O_3, MgO, CaO, Total and Cs. Buff coloured background rocks have increased concentrations of MgO, K_2O, LOI, Total, Rb, Sr, Ba and decreased Si, Al, Fe, Ca, V, Zr and Cs. These changes reflect minor incorporation of clay minerals (saponite and celadonite) into the background, paticulary the buff coloured rocks and minor replacement of interstitial material and groundmass minerals. Buff halos have a marked decrease in Fe_2O_3 compared to the grey background rocks. 'Background' differs slightly in that it has, in addition to the changes observed in the buff whole rock samples, increased Fe_2O_3, Nd, Gd, Dy, and Hf. The relatively elevated Sr, Y, and REE and within these background samples compared to other alteration styles (See Figure 5.26) implies that greater interaction between host rock and hydrothermal fluids occurred in these rocks, perhaps during initial cooling near the ridge axis. Dark green/grey halos exhibit large increases in Fe_2O_3, K_2O, LOI, Rb, Ce, Nd and minor increases in Sr, Ba, Dy. Decreases in the concentrations of SiO_2, Al_2O_3, CaO, Total, Cs, and Cr are also observed. High Fe and K in these halos reflect the incorporation of celadonite and iron-oxyhydroxides. Partial replacement of primary phases for example, plagioclase, olivine and clinopyroxene may explain the decrease in Al, Ca, and Cr. Brown and red halos similarly record incorporation of iron-oxyhydroxides and replacement of primary phases. Changes within these halos include the highest increases in Fe_2O_3 and LOI, increases in K_2O, Rb, Sr, Ba, Ce, Nd, and Dy,

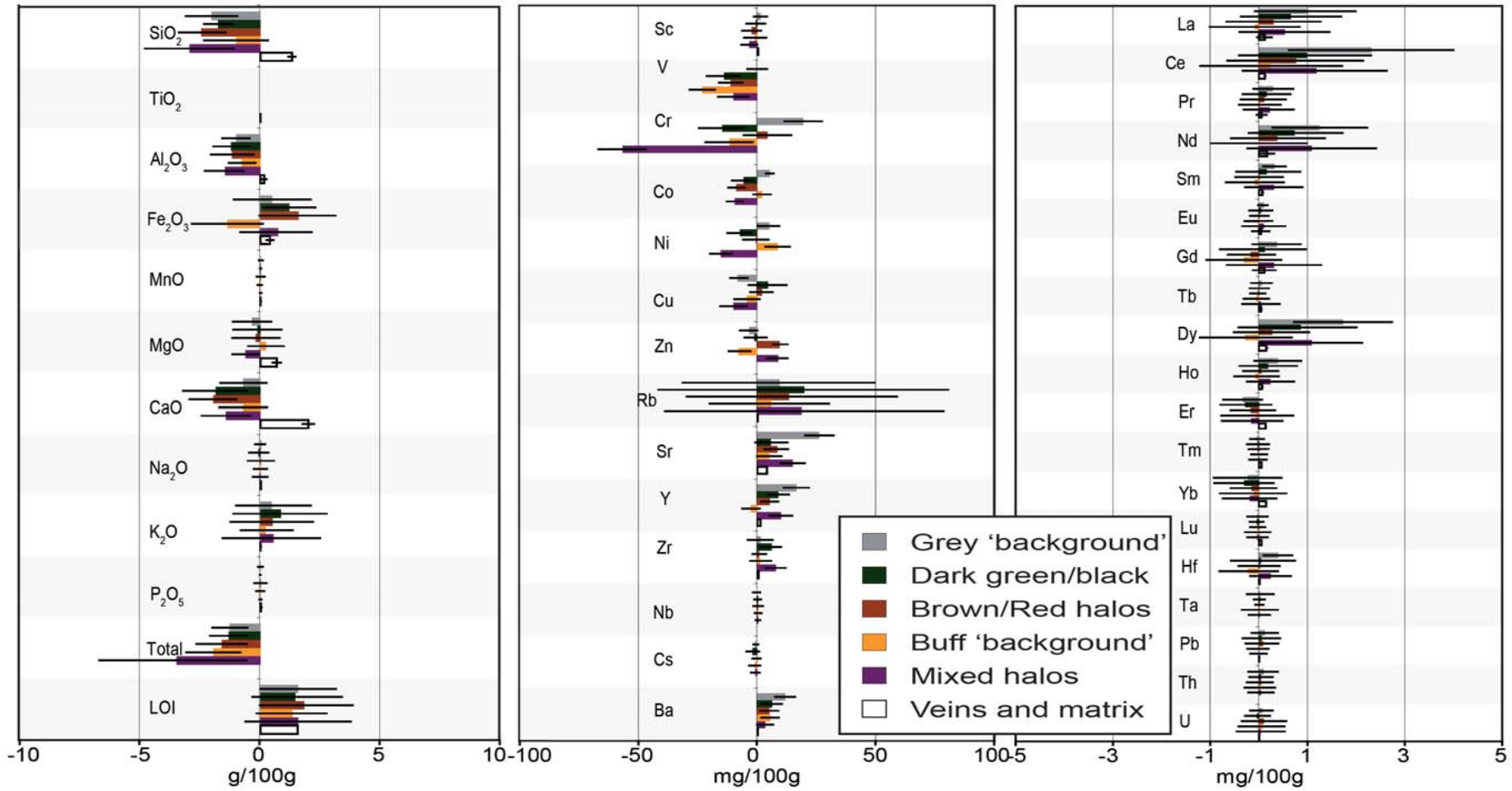

Figure 5.26. Chemical changes across all alteration styles and vein minerals for low temperature alteration within the basement section of 1149. The addition of elements from vein minerals and breccias is a weighted average abundance based on the volume of core occupied by veins and breccia. Bars indicate propagated error.

and decreases in SiO_2, Al_2O_3, CaO, and Total. The relatively high levels of LOI and Fe reflect high fluid flux of cold oxidizing seawater. Decreases in SiO_2, Al_2O_3, CaO reflect the partial replacement of groundmass, including plagioclase, olivine, and clinopyroxene. Mixed halos at Site 1149 represent perhaps the most variable levels of chemical change because they have the highest degree of error associated with the changes. Mixed halos record increases in Fe_2O_3, K_2O, LOI, Rb, Sr, Y, Ba, and REE (La, Ce, Nd, Gd, Sm, Dy and Hf). In addition, decreases in SiO_2, Al_2O_3, MgO, CaO, K_2O, Total,Cr, Ni and Cu are reported. These changes reflect chemical changes in the buff halos, grey halos and brown halos. As such these halos probably represent a complex history of multiple alteration stages with extensive overprinting.

5.3.2.2 Summary of Site 1149 chemical change

The chemical changes at Site 1149 reflect the petrographic observation of secondary mineral assemblages, the replacement of primary phases and its intensity. Although trends with LOI were highly variable, sample pairs showed consistent trends when compared to the other proxies of alteration (Fe and Sr-isotope ratios). These trends reflect the emplacement if iron-oxyhydroxides, celadonite, saponite and carbonate and the replacement of primary phases by these secondary minerals. The style of alteration is similar to that of the upper volcanic section of Site 1256, 1179, and 504 in which open seawater circulation has led to pervasive oxidation (e.g., Alt, 1993, Alt and Honnorez, 1984). Figure 5.27 and 5.28 charts the overall weighted average chemical change in absolute values (g/100g and mg/100g) and percentage change respectively for Site 1149 (Based on volume % of core each alteration style and vein mineral occupies). Overall changes at Site 1149 include increased in Fe_2O_3, MgO, CaO, K_2O, C, LOI, Rb, Sr, Y, Zr, Ba, and LREE and decreased SiO_2, Al_2O_3, Na_2O, Total, V, Cr, Co, Zn, Cs, Er and Yb. The percentage changes shown in Figure 5.28 indicate the relative change in concentration compared to the precursor. The greatest changes observed include large increases in Fe_2O_3, MnO, K_2O, P_2O_5, LOI, Rb, Y, Nb, Ba, and LREE and decreases in Al_2O_3, Cs, Hf and Tb. These changes reflect the presence of Celadonite and Iron-oxyhydroxide within veins, and replacing groundmass minerals. The high Rb (>1600%) and LOI (>600%) reflects the large volumes of seawater circulation at Site 1149 and the mobility of Rb.

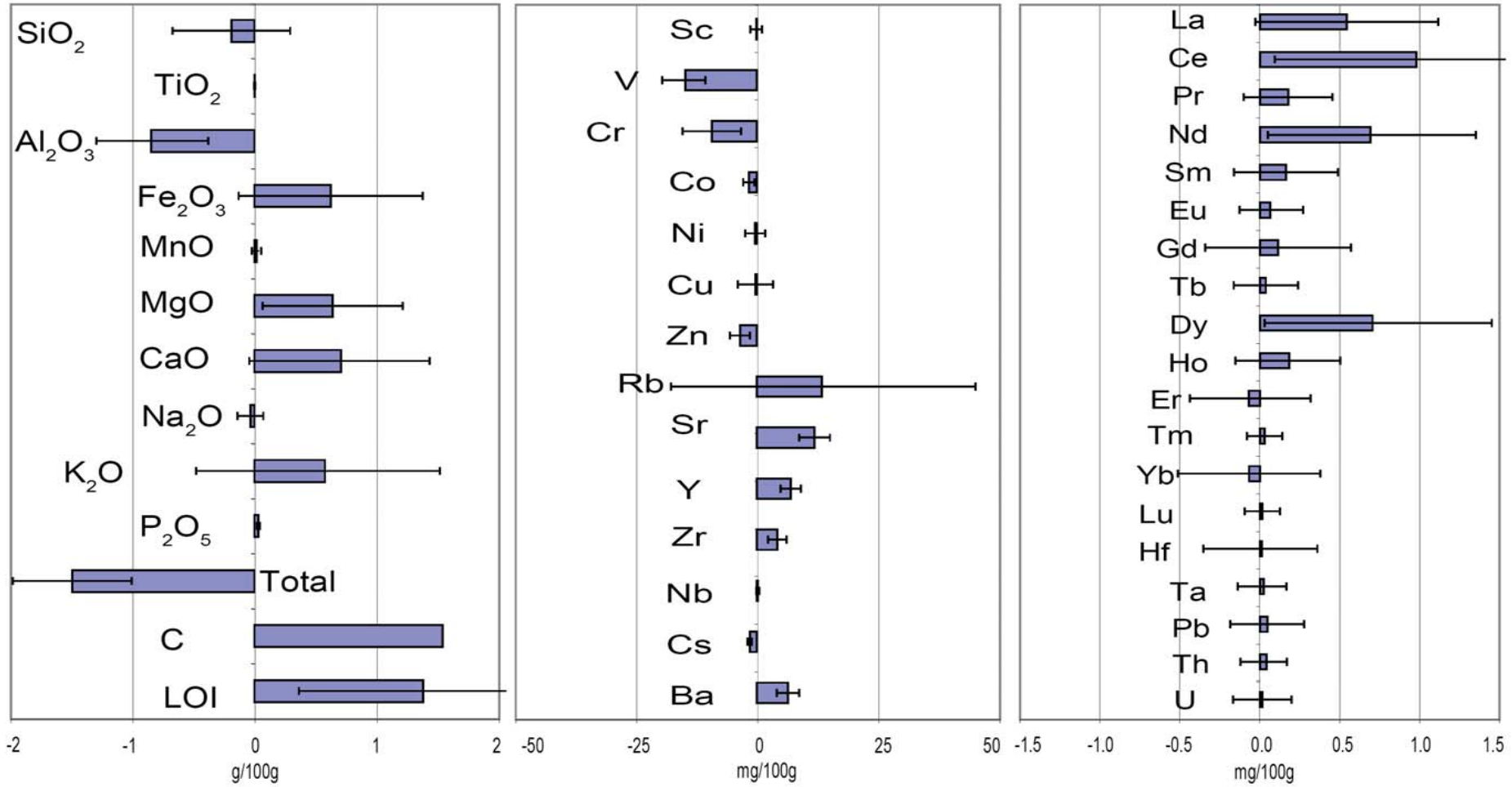

Figure 4.27. Summary of the weighted average chemical changes for Site 1149 volcanics. Changes are expressed as mass gains or losses per 100g of precursor (Major elements = g/100g, Trace and REE = mg/100g). Bars indicate the propagated error.

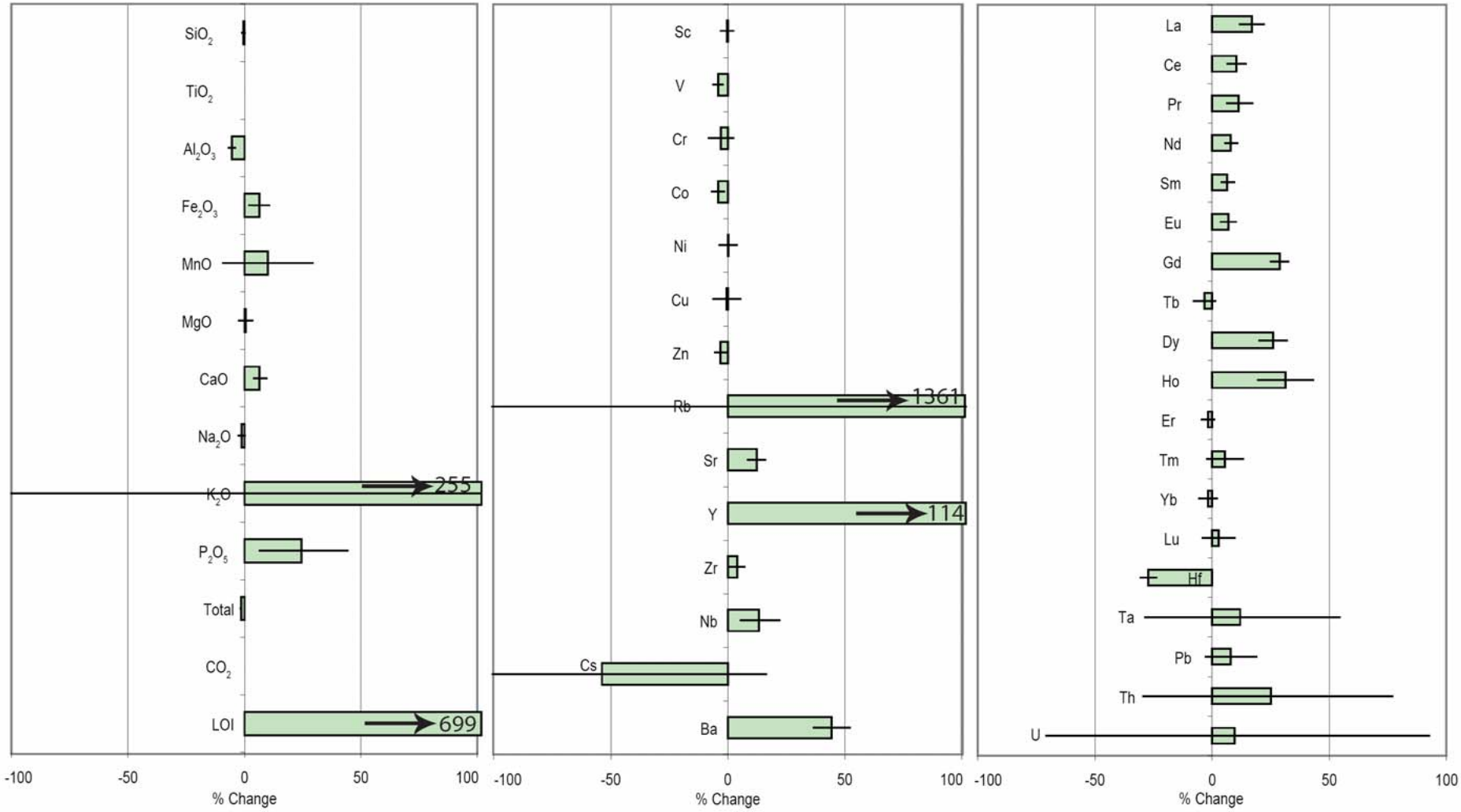

Figure 5.28. Summary of the percentage chemical change for Site 1149. Bars indicate propagated error.

Element	Change %	Element	Change %	Element	Change %	Element	Change %
SiO2		Sc		Nb	+	Dy	+
TiO2		V	(-)	Cs	+ + +	Ho	+
Al2O3	(-)	Cr	(+)	Ba	+ +	Er	
Fe2O3	(+)	Co	(-)	La	+	Tm	(+)
MnO	+	Ni		Ce	+	Yb	
MgO		Cu		Pr	(+)	Lu	
CaO	(+)	Zn	(-)	Nd	++	Hf	-
Na2O	(-)	Rb	+ + +	Sm	(+)	Ta	+
K2O	+ + +	Sr	+	Eu	+ +	Pb	(+)
P2O5	+	Y	+ + +	Gd	+	Th	+
LOI	+ + +	Zr	(+)	Tb	(-)	U	+

Table 5.4. Summary of percentage chemical changes at Site 1149. + indicates increases where + = 10-49 %; + + = 50 – 99 %; + + + = over 100 %. – indicates decreases where - = 10-49 % decrease (+) or (-) indicates significant elements that have undergone less than 10% change.

Within the whole rocks there is a drop of Silica (~3%) however the addition of silicates (quartz and chalcedony) as vein minerals and some breccia matrixes effectively reduces the deficit of Si to -0.38 %. This implies that most of the silica leached from primary phases is re-precipitated as secondary phases.

5.3.3 Whole rock isotopic results

A total of 50 whole rock samples were measured for their Sr-isotopic compositions by TIMS (See Chapter 2 for methodology). An additional 3 samples were leached to determine the primary Sr isotopic composition of Site 1149 basement (Discussed in Chapter 2 ‘methods’). In addition Sr and Rb concentrations measured by ICP-MS have been used to correct the Sr-isotopic data for Rb-decay. A list of all Sr-isotopic results can be found in Table B 3 of Appendix for whole rocks and Chapter 2 for leachate). Figure 5.29 is a plot of whole rock Sr-isotopic composition vs. depth at Site 1149 with respect to the differing alteration styles. The $^{87}Sr/^{86}Sr$ of seawater (0 and 132 ma) and MORB, basement stratigraphy, and abundance of alteration style is included.

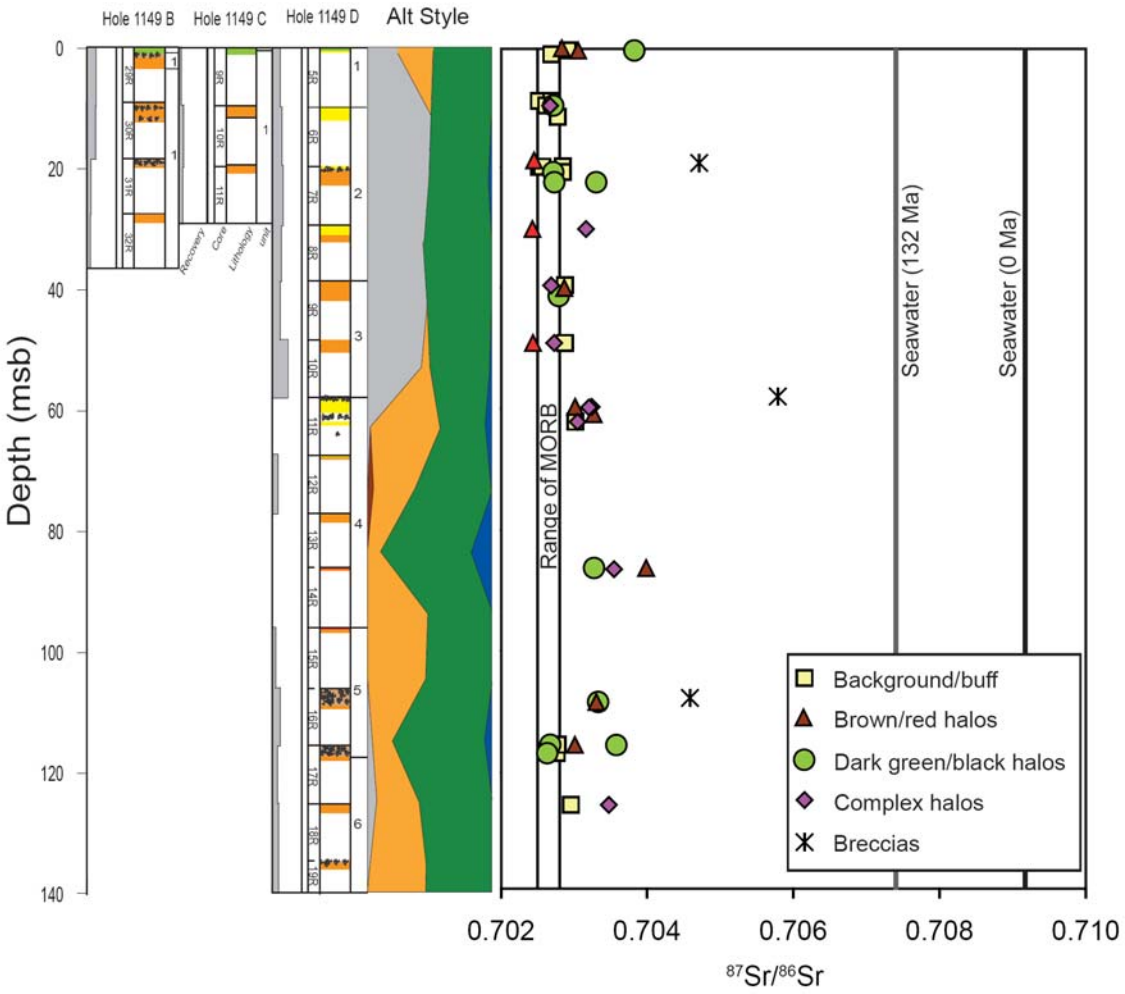

Figure 5.29. Whole-rock strontium ($^{87}Sr/^{86}Sr$) vs. depth for Site 1149 basement. Leached whole rock samples are included (Red triangles). Seawater at 0 and 132 Ma (McArthur, 2001) and Site 1149 stratigraphy (Plank, Ludden, Escutia, et al., 2000) and alteration styles are included.

For the most part, samples are elevated with respect to the average MORB value (0.7024-0.7027) and they are all elevated compared to the leached samples (red triangles). The incorporation of seawater Sr varies slightly with slightly more elevated compositions between 60 and 110 msb. This broadly reflects the variation in alteration styles with depth. Because at 60 to 110 mbsf the volume percentage of grey 'background' is at its lowest.

Variation between alteration styles is minimal however the least radiogenic samples tend to be the grey/buff background. Dark green/black halos are slightly more radiogenic albeit variable, many of these samples are only slightly radiogenic and they appear to contain less seawater Sr than their buff coloured counterparts. Brown/red halos and mixed halos are also highly variable, although, overall they have higher

$^{87}Sr/^{86}Sr$ than green/black or background halos. Whole breccia samples exhibit the greatest incorporation of seawater Sr (0.7045-0.7057). All leached samples have Sr-isotopic compositions comparable to fresh MORB values, as such they represent the best estimate for the primary composition for Site 1149 which is 0.70244 ± 1.03 x 10^{-5} (See Chapter 2, 'methods' for details).

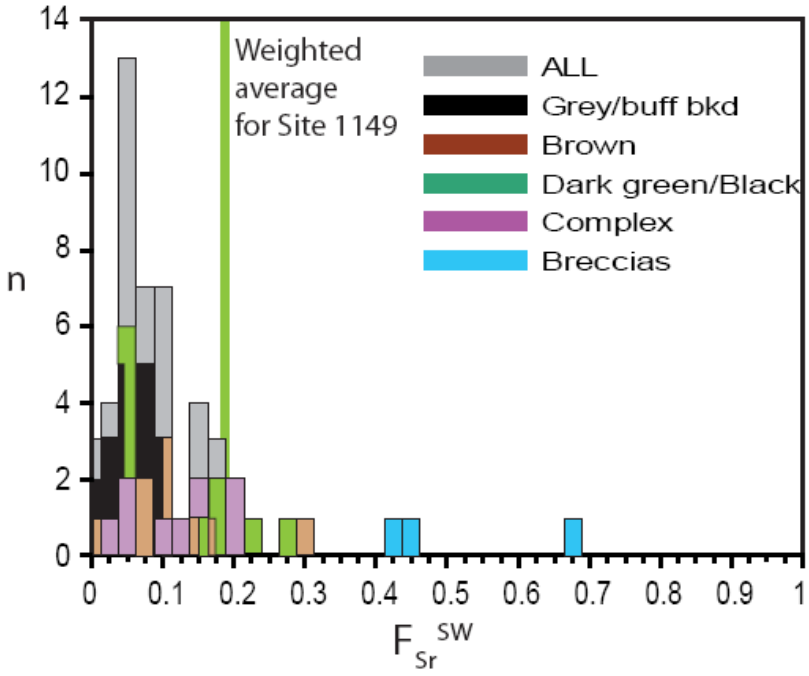

Figure 5.30. Distribution of $^{F}Sr^{SW}$ (following Bach and Humphris, (1999) calculations) in whole rock basalts basalts in the lavas and transition zone at Site 1149 with respect to alteration styles. Included is the distribution of all samples and the average $^{F}Sr^{SW}$ weighted according to the proportion of each alteration style present.

Based on value of fresh MORB from leaching experiments and the value of seawater Sr at 132 Ma, the proportion of seawater Sr $^{F}Sr^{SW}$ has been calculated following Bach and Humphris, (1999) (See chapter 4 'Site 1256' for details).

Figure 5.30. is a histogram illustrating the distribution of $^{F}Sr^{SW}$ with respect to alteration styles, all samples, and the weighted average $^{F}Sr^{SW}$ for Site 1149. The distribution of $^{F}Sr^{SW}$ is centred around ~0.075. $^{F}Sr^{SW}$ in alteration halos are slightly elevated compared to background, although the majority of the dark green/black halos share peak distribution with the grey/buff background (~0.05). Complex halos are variable (0.025 to 0.2), reflecting the variable alteration styles present within these halos. Breccias have $^{F}Sr^{SW}$ between 0.425 – 0.675, which is significantly higher than that of the other whole rock values. The distribution of $^{F}Sr^{SW}$ implies that all samples have undergone some exchange with seawater Sr. The incorporation of secondary

minerals derived from intense circulation cold seawater sourced fluid perhaps best explains such elevated $^{F}Sr^{SW}$ in the breccias. Following the method discussed in chapter 4, (Site 1256), the weighted average $^{F}Sr^{SW}$ for Site 1149 is calculated by weighting the Sr-isotopic values according to the volume % of alteration styles. The weighted Sr-isotopic value and $^{F}Sr^{SW}$ for Site 1149 is 0.7033 and 0.179 respectively. These imply that ~18 % of Sr at Site 1149 is derived from seawater.

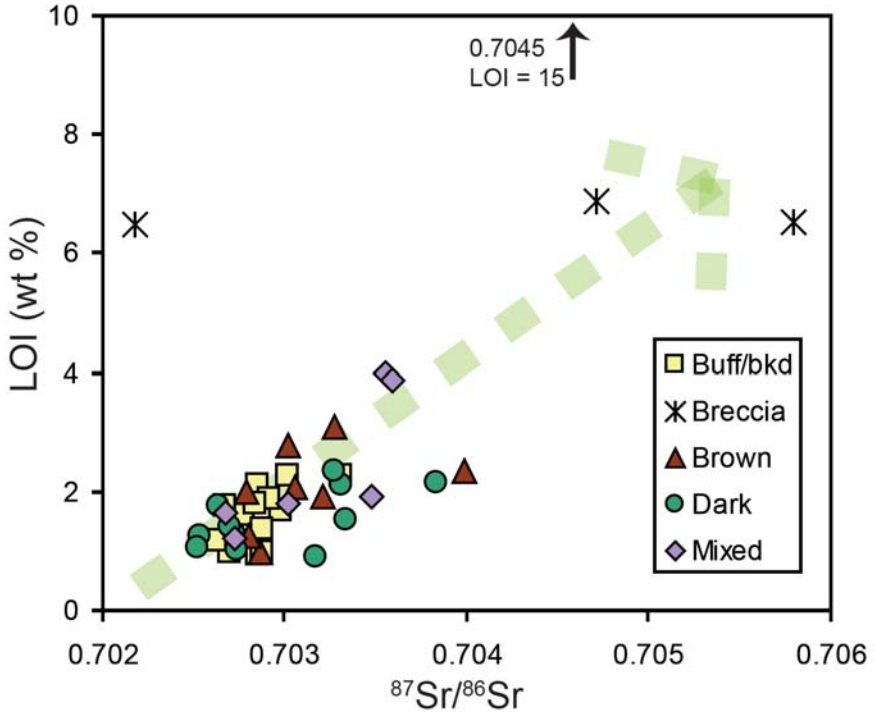

Figure 5.31. $^{87}Sr/^{86}Sr$ vs. LOI for Site 1149 basement. Arrow indicates trend.

Sr-isotopic data is compared to LOI in Figure 5.31. Because LOI and $^{87}Sr/^{86}Sr$ may be used to gauge the intensity of alteration then we would expect a reasonable trend when the two are compared. In the case of Site 1149, a slight trend is reported. Despite significant overlap, a weak trend between alteration styles is also present, grey background/buff show the least alteration, which is closely followed by green, brown then mixed halos. Breccias demonstrate the highest LOI and most radiogenic Sr which is expected due to the high proportions of secondary minerals observed (See section 5.2 'alteration'). One breccia, with an unusually low primary $^{87}Sr/^{86}Sr$ of 0.7024, has a very high Rb concentration (53.49 ppm), which has greatly affected the Rb-decay correction. Because Rb appears to be highly mobile and given its high overall increase (+ 1361 %), emplacement of Rb may be the result of secondary minerals emplacement from a fluid containing ubundant Rb, most likely seawater. The other possibility is that the fluid

from which secondary minerals precipitated contained significant basaltic Sr, however given the lack of evidence to support this, it seems unlikely that the latter is true. Overall, Site 1149 has undergone slight to moderate interaction with cold seawater derived fluids. Despite significant overlap trends between alteration styles are visible with buff/grey background exhibiting the least chemical change and breccias demonstrating the greatest degree of change.

5.3.4 Carbonate veins at Site 1149 and their constraints on low temperature hydrothermal fluid evolution.

Carbonate vein mineral separates were sampled throughout Site 1149 and these were analysed for Major elements, REE, C, $^{87}Sr/^{86}Sr$, and $\delta^{18}O$. Carbonate veins make up approximately 7.9 % by volume of the core, it is present in high quantities in breccia matrices and often makes up the major component in thick, multi-minerallic veins (see Section 5.2 'Alteration'). Following Coggon et al., 2006, the relationship between Mg/Ca, Fe/Ca and Mn/Ca with Sr/Ca provides a means of differentiating between calcite, aragonite or mixtures of the two. Preferential incorporation of small cations (Mg) into the calcite crystal structure (Deer et al., 1992) help identify Site 1149 carbonates sampled as Calcite. Sr concentration ranges from 36 to 247 ppm (average = 101 ppm) whereas Mg concentration ranges from 737 to 6845 ppm (average = 3740 ppm).

Carbon isotopic compositions for calcite at Site 1149 range from -4.3 to 2.5 $‰_{VPDB}$ with most samples within the range of 1-3 ‰. No systematic variation is observed with depth and only a few samples in the mid to upper portion of the hole have $\delta^{13}C$ values less than 1 (Figure 5.32 A). Oxygen isotope values range from 26 to 31 $‰_{VSMOW}$ and they exhibit similarly little relationship with depth as does the $\delta^{13}C$ (Figure 5.32 B). Formation temperatures following Friedman and O'Neil (1977), assuming precipitation from fluids with $\delta^{18}O_{water}$ = 0 ‰ range from 11 to 39 ^{o}C. Once again no relationship with depth is observed in Figure 5.32 C. The highest temperature ($39^{o}C$) observed at Site 1149 co-insides with the lowest $\delta^{13}C$ value. This implies perhaps a minor basaltic input in these samples from slightly more evolved fluids. The nature and distribution of Sr-isotopes at Site 1149 is illustrated in a plot of $^{87}Sr/^{86}Sr$ vs.

depth in Figure 5.32 D. Strontium isotopic compositions for carbonates at Site 1149 range from 0.70711 to 0.70752.

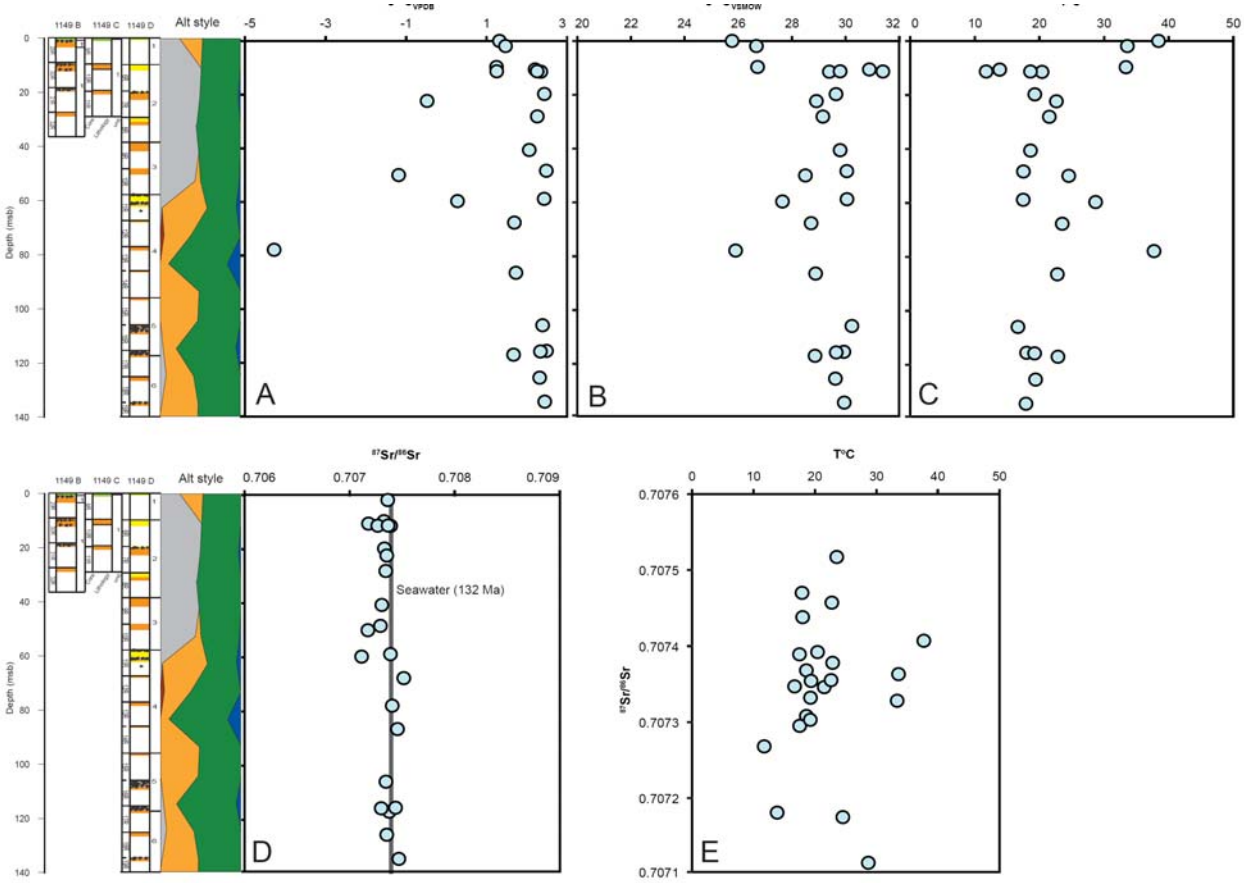

Figure 5.32. Site 1149 carbonate plots. A: $\delta^{13}C_{VPDB}$ vs. depth, B: $\delta^{18}O_{VSMOW}$ vs. depth, C: T°C vs. depth calculated from oxygen isotopic values in B following Freidman and O'Neil, (1977) assuming precipitation from fluid with $\delta^{18}O$ = 0 ‰. D: Sr isotpioc composition vs.depth including seawater at 132 Ma for comparison (seawater value after McArthur, 2001. E: Sr-isotopic composition vs. calculated temperature. Site 1149 Stratigraphy (Plank et al., 2000) and alteration styles are also shown.

These isotopic values are highly radiogenic with values close to and even exceeding that of seawater at 132 Ma. No systematic variation with depth or temperature of formation (Figure 5.32 E) is observed. Given the similarity between the $^{87}Sr/^{86}Sr$ of seawater and carbonates and the temperatures of 11-39°C, this strongly suggests that calcite at Site 1149 precipitated from cold fluids near or at Seawater compositions. Following Bach and Humphris (1999) method for calculating the proportion of basaltic Sr in the final precipitate (See whole rock equation earlier) the basaltic component ranges from 0.2 to 4.6 %, assuming no formation in these samples took place after 132 Ma. However because some samples demonstrate $^{87}Sr/^{86}Sr$ above seawater, seawater ingress and precipitation of secondary calcite must have continued for several million

years after Site 1149 formation. Figure 5.33 plots the high $^{87}Sr/^{86}Sr$ values on the seawater Sr curve (As compiled by McArthur et al., 2001). These points mark the possible maximum age at which the sample could have formed, assuming no interaction with basement rock took place, One sample suggests that precipitation took place after at least 50 m.yr after the formation of Site 1149. If partitioning between basaltic Sr and seawater Sr took place then it is possible that this and all the other carbonate veins at Site 1149 are much younger. In this respect these samples are similar to those of Site 1179, which is similar in age (129 Ma).

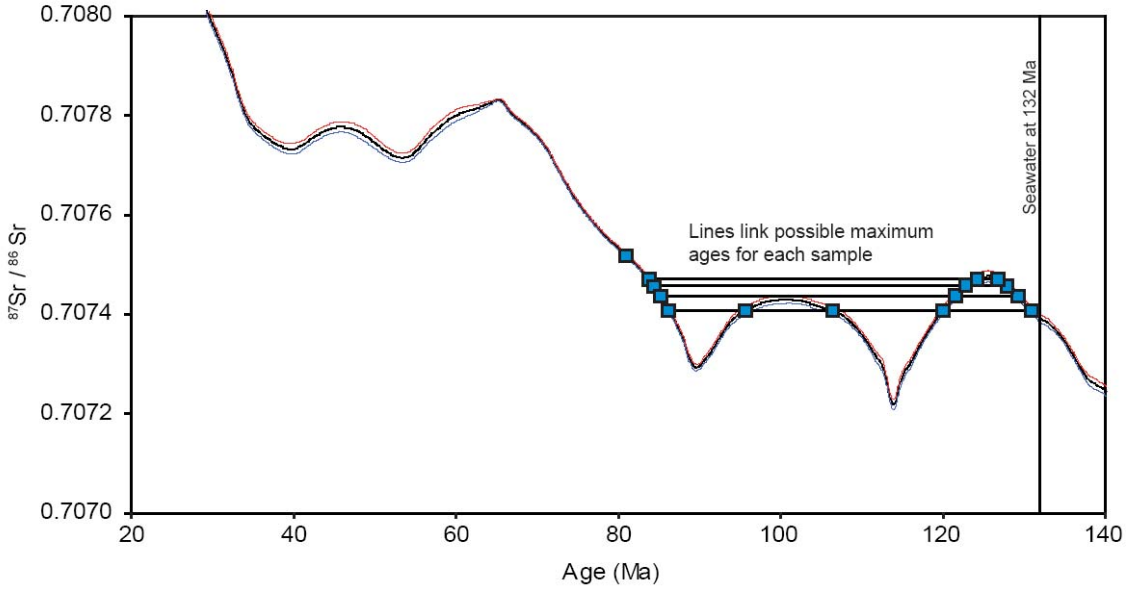

Figure 5.33. Seawater Sr Curve for the period 20 to 140 Ma. Vertical line indicates the time of Site 1149 formation. Blue squares indicate carbonate samples with $^{87}Sr/^{86}Sr$ values greater than 132 Ma seawater and their minimum age of formations. Seawater Sr cure after McArthur et al, (2001)

Chapter 6

Sites 504, 896, 1224, 1243, and 843.

6.1. Site 504

DSDP/ODP Site 504 is located at 1°13.6'N, 83°44.0'W in 6.9 m.y. old crust of the southern flank of the Costa Rica Rift (Figure 6.1). Site 504 is positioned in the middle of an east-west spreading segment bound by the Panama Fracture Zone and the Ecuador Fracture Zone. Geophysical data indicates that it is within an area of relatively pronounced ridge trough topography with ~100-200 m relief (Cann et al., 1983). The rate of crustal accretion is moderate at approximately 65 mm/yr (full rate, Hey et al., 1977). DSDP/ODP Hole 504B penetrates over 274.5 m of sediment and over 1800 m into basement through the entire volcanic sequence, two fault zones (525.5 msb and 1836.5 msb), and the majority of the sheeted dike complex (Alt et al., 1993). This makes it one of only two holes to have successfully recovered a complete lava sequence and a near complete dike sequence in modern in-situ ocean crust. DSDP/ODP Site 504B has thus formed the reference section for modern oceanic in an attempt to characterise the alteration characteristics of ocean crust (e.g. Alt et al 1996a, 1996b; Alt, 1989; Laverne et al, 1983; Chan et al., 2002) and model hydrothermal circulation (e.g., Teagle et al, 1998; Sleep, 1991; Bach et al., 2003). Even though Site 504 formed at intermediate, and not, fast spreading rates its inclusion is necessary because it allows comparisons to be drawn with Site 1256, the only other hole to penetrate into the dikes, and augments study of any relationship between alteration and spreading rate.

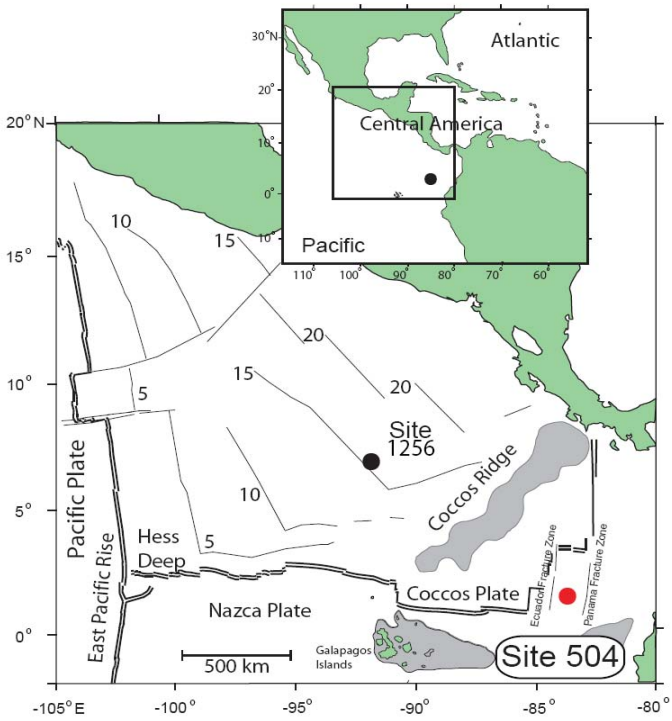

Figure 6.1. Location of Site 504B.

6.1.1. Sea floor sediment, stratigraphy and sedimentation rates

A summary of the sedimentary and igneous stratigraphy for Site 504 is illustrated in Figure 6.2. Sediment at Site 504 is comprises a 274.5 m thick sequence of siliceous oozes, chert limestone and chalk. At 274.5 m thick, the sediment thickness for such young crust is unusual, generally this level of sedimentation is observed at older crustal sites (Stein and Stein. 1994) where sediment rates are much lower. The high sediment thickness and the low relief of Site 504 effectively seals Site 504 basement from direct contact with seawater, thus this may have implications for the fluid flux and its geothermal gradient (Alt et al. 1996). Three main sedimentary units are defined by Cann et al., (1983). Unit I (0-143.4 mbsf) is composed of siliceous-nannofossil and nannofossil-radiolarian oozes that have variable proportions of clay. Unit II (143.5-227.3 mbsf) is a siliceous nannofossil chalk; and Unit III (227.2-274.5 mbsf) is comprised of interbedded nannofossil chalk, limestone and chert.

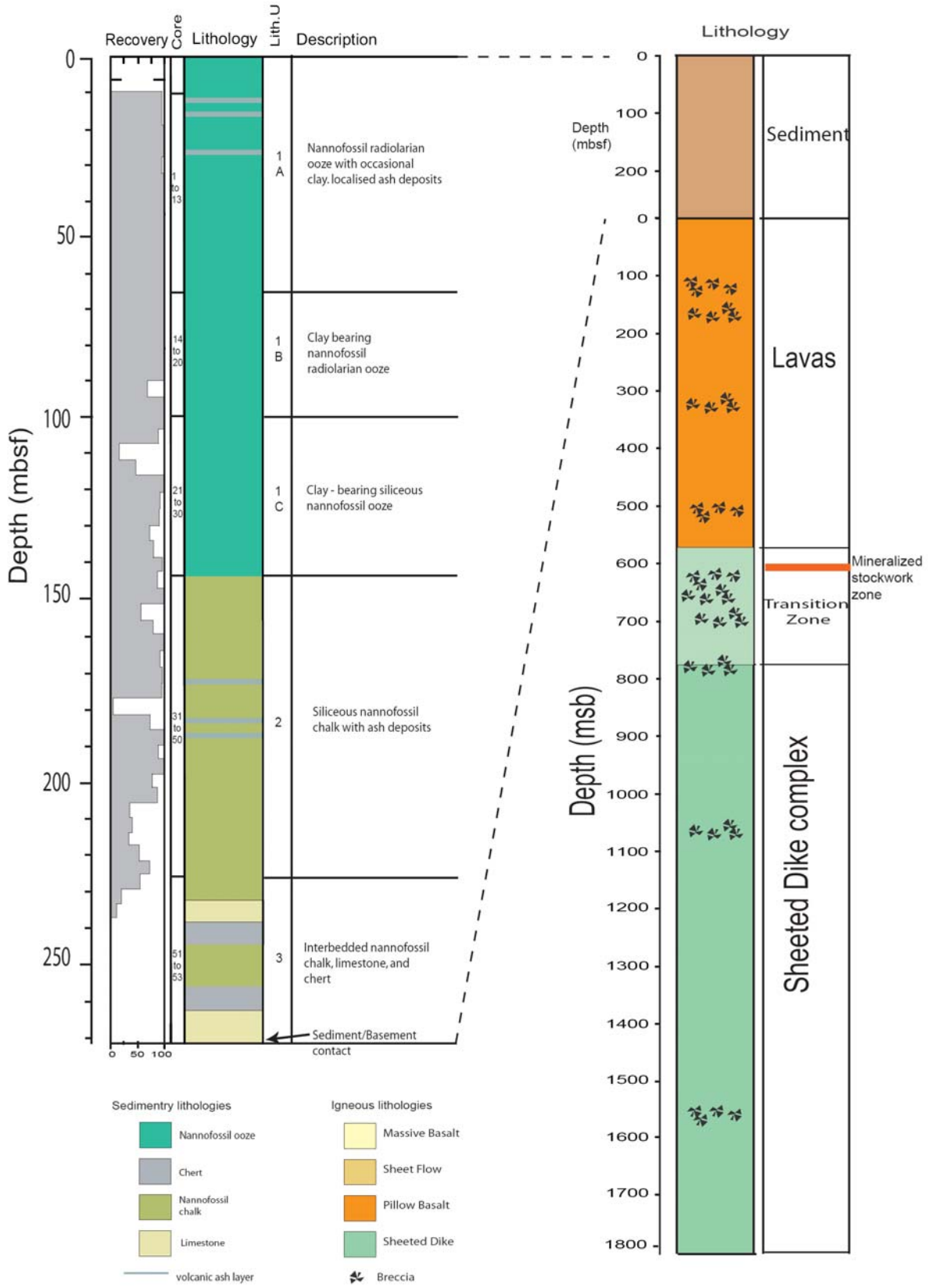

Figure 6.2. DSDP/ODP Hole 504B stratigraphy modified from Alt et al., (1993).

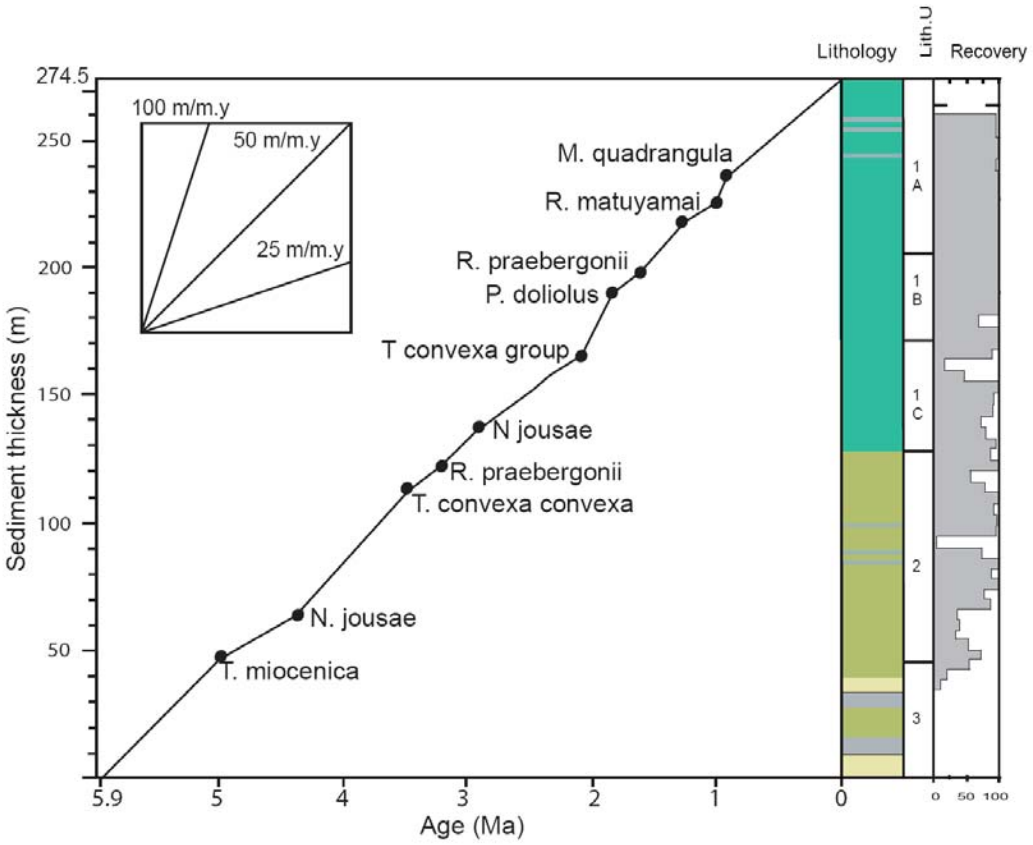

Figure 6.3. DSDP/ODP Hole 504B sediment accumulation rate with time. Rates are established from biostratigraphic and palaeomagnetic constraints. (Redrawn from Sancetta et al., 1985). Average accumulation rate is 50 m/m.y.

Sedimentary accumulation rates were derived from palaeomagnetic studies and stratigraphic correlation of nannofossils (Sancetta et al., 1985; Figure 6.3). Sediment has accumulated at Site 504 at a rate of ~50 m/m.y with no significant change in rate since its formation. Of all the basement Sites in this study, this represents the fastest sediment accumulation rate.

6.1.2. Basement at Site 504, Petrography and Igneous geochemistry

Over 1800 m of basement was penetrated at Site 504, spanning the lavas, transition zone and the majority of the sheeted dikes. Recovery of basement material is variable (29 % for the volcanic section, 25.3 % in the transition section and 13.7 % in the sheeted dikes), however, core was recovered from the majority of Hole 504B. The rocks recovered range from aphyric to highly phyric tholeiitic basalts and four major

groups of basalt are observed throughout Site 504 including: aphyric basalt (most abundant), olivine-plagioclase-clinopyroxene phyric basalts, olivine-plagioclase phyric basalts, and olivine-plagioclase-clinopyroxene-spinel bearing basalts. Olivine-plagioclase-clinopyroxene phyric basalts and olivine-plagioclase phyric basalts occur deeper in the hole. Within the dikes aphyric rocks, which are present throughout Site 504, become more common with depth in the dike section. The volcanic section occurs from 0 to 571.5 msb and is composed of pillow basalts (57 %), massive flows, (22 %) thin flows (17.5 %) and minor dikes (3 %).

A Transition Zone occurs from 571.5 to 780.5 msb. Rocks in the transition zone consist of a mixture of highly fractured, altered and brecciated pillows and dikes. Strong to total recrystallisation prevails in this zone; in some cases almost completely obscuring primary mineralogy and textures. The dike section (780.5 msb to ~1807 msb) is composed of sheeted dikes which have undergone varying degrees of crystallization.

The rocks at Hole 504B are chemically very similar throughout the extrusive and intrusive section. Fifty chemical units were defined, each of which is thought to represent subtle variations in the source magma chamber composition. Natland et al, (1983) propose that these variations may be the result of periodic injections of new magma into a differentiating magma chamber. However, despite these subtle variations the relative uniformity of Site 504 implies that the magma chamber beneath the rift axis was operating at close to steady state. Mg numbers for Site 504 basement range from 0.63-0.74 (Autio and Rhodes, 1983) and Site 504 is depleted in incompatible elements such as TiO_2 (0.7 – 1.2 %), Nb (<0.5 -1.2 ppm) and Zr (34 – 60 ppm). Figure 6.4 (redrawn from Kempton et al., 1985) indicates MgO, CaO, Al_2O_3, and FeO^*/MgO vs. Zr for ODP Hole 504B. The depletion of Zr compared to MORB is clearly evident across most samples, whilst major element oxides fall within the expected rang for MORB. In addition, Site 504 has high CaO/Na_2O ratios, which implies equilibrium with very calcic plagioclase (Alt et al., 1996).

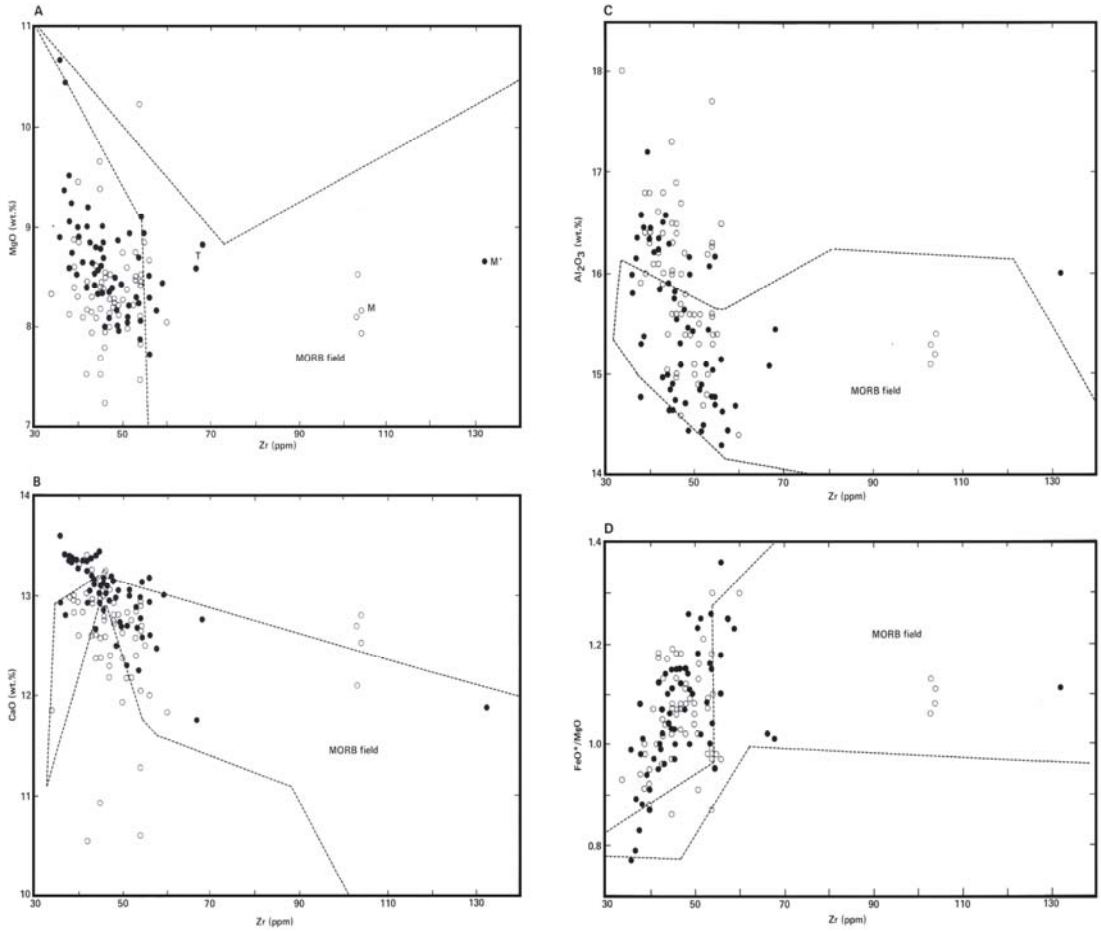

Figure 6.4. MgO, CaO, Al_2O_3, and FeO^*/MgO vs. Zr. Circles are data from Legs 69-70 and Filled circles are data from Leg 83. Basalts from Site 504 are depleted in Zr relative to MORB. CaO and Al_2O_3 are elevated. MgO and FeO^*/MgO are typical of MORB (Figure after Kempton et al., 1985).

Low incompatible elements and the potential for equilibrium with very calcic plagioclase imply that the rock is derived from magmas generated by partially melting the source rock (I- type MORB, Bryan et al., 1976). This supports the original hypothesis of differentiation within the magma chamber. The chondrite normalised REE patterns for Site 504 (Figure 6.5) indicate strong depletion of LREE (La/Sm enrichment factor of 0.4). Units 5 and 36 represent near chondritic or LREE enriched basalts that might suggest that these units were derived from plume melts (Kempton, et al., 1985). The majority of Site 504 basalts, however, are thought to be either highly primitive (Emmermann, 1985) or sourced from multi-stage melts of N-MORB basalts with additional fractional crystallization (Emmermann et al., 1985).

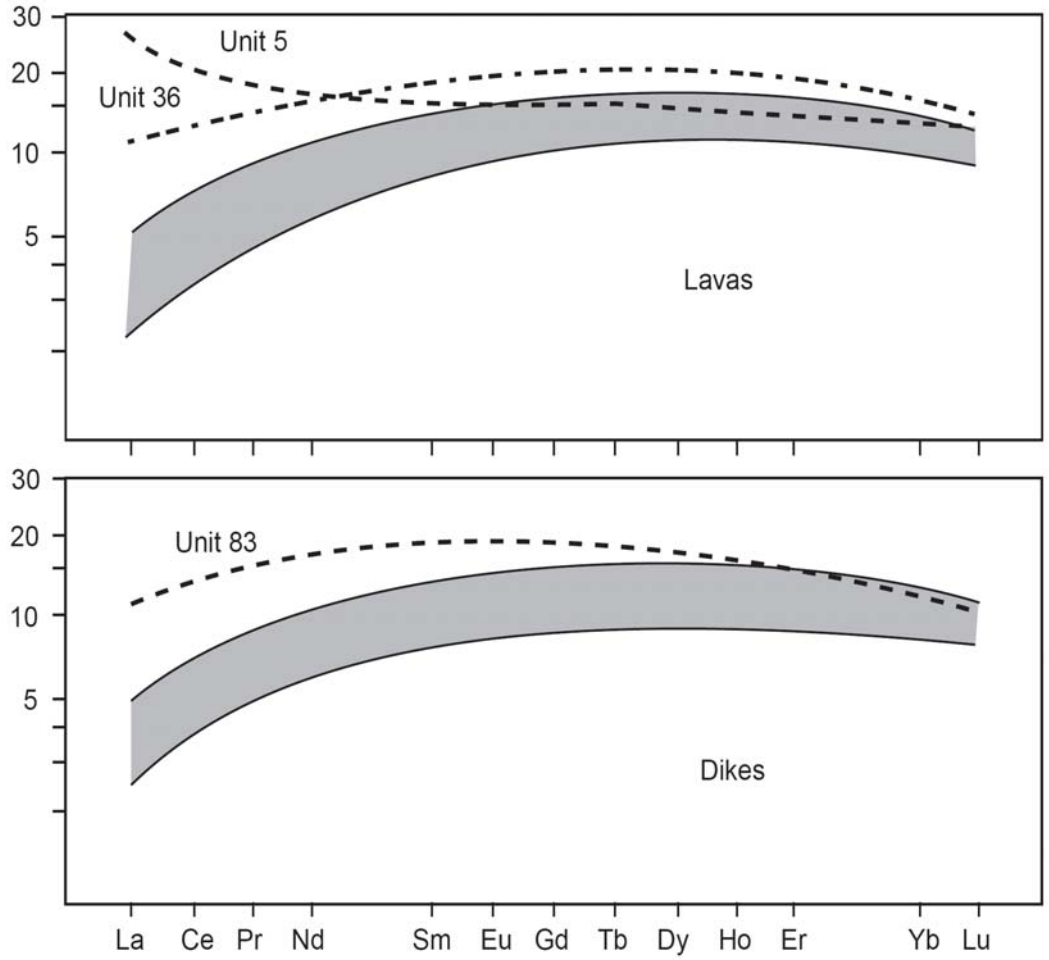

Figure 6.5. Chondrite normalised REE patterns for DSDP/ODP Hole 504B whole rocks in the lava and dike section (After Emmerman et al., 1985). Note the similarity between the lavas and the dikes.

6.1.3. Basement alteration

Alteration at Site 504 is discussed in much greater detail in Noack et al, (1983), Honnorez et al, (1983), Alt (1984), Alt et al, (1986a, 1986b) and Laverne (1987) and a detailed synthesis of hydrothermal alteration at Site 504 is given by Alt et al., 1996. A brief summary of the major alteration features is outlined here for direct comparison to other basement sites in this study.

Overall, alteration at DSDP/ODP Site 504 is slight to moderate, and it is interspersed with intervals of high to intense alteration and brecciation, most notably the lava/dike transition zone. At Site 504 low temperature and high temperature alteration is reported. These features are best demonstrated by the distribution of

secondary minerals vs. depth (Figure 6.6), where observations change from low temperature secondary minerals for example celadonite, iron oxyhydroxides, and saponite, to high temperature phases, including chlorite, prehnite and actinolite.

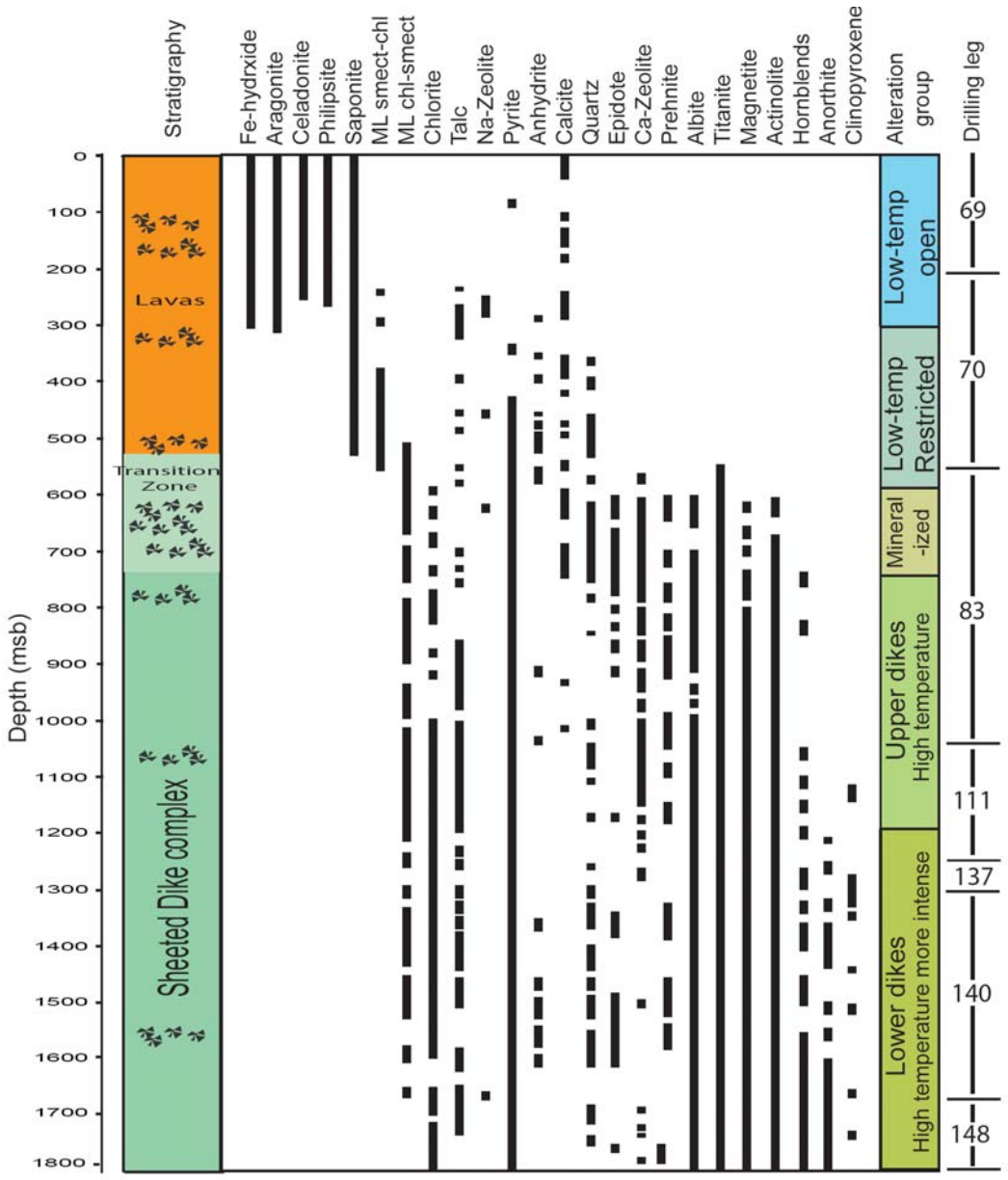

Figure 6.6. Distribution of secondary minerals in DSDP/ODP Hole 504B.The alteration regime, lithostratigraphy and penetration for each depth is also indicated in this figure. ML = mixed layer, chl = chlorite, smect =smectite. (Modified from Alt et al., 1996).

In this study we focus on low temperature, seawater dominated alteration, but both alteration types are summarised here. The volcanic section is divided into an upper and lower alteration zones based on the extent and variability of halo types. Alteration in the volcanic section is slight (5 - 15 %) and it is characterised by secondary

minerals filling fractures, vesicles and interstitial areas, and partially replacing primary igneous phases to form alteration halos. Alteration in the volcanic section is expressed in terms of halos and breccias and these are illustrated in Figure 6.7. Halos consiste of ; 1) Dark grey (saponite-rich) rocks that occur throughout the volcanic section, 2) red, iron oxyhydroxide rich alteration halos, and 3) black celadonite/saponite rich alteration halos.

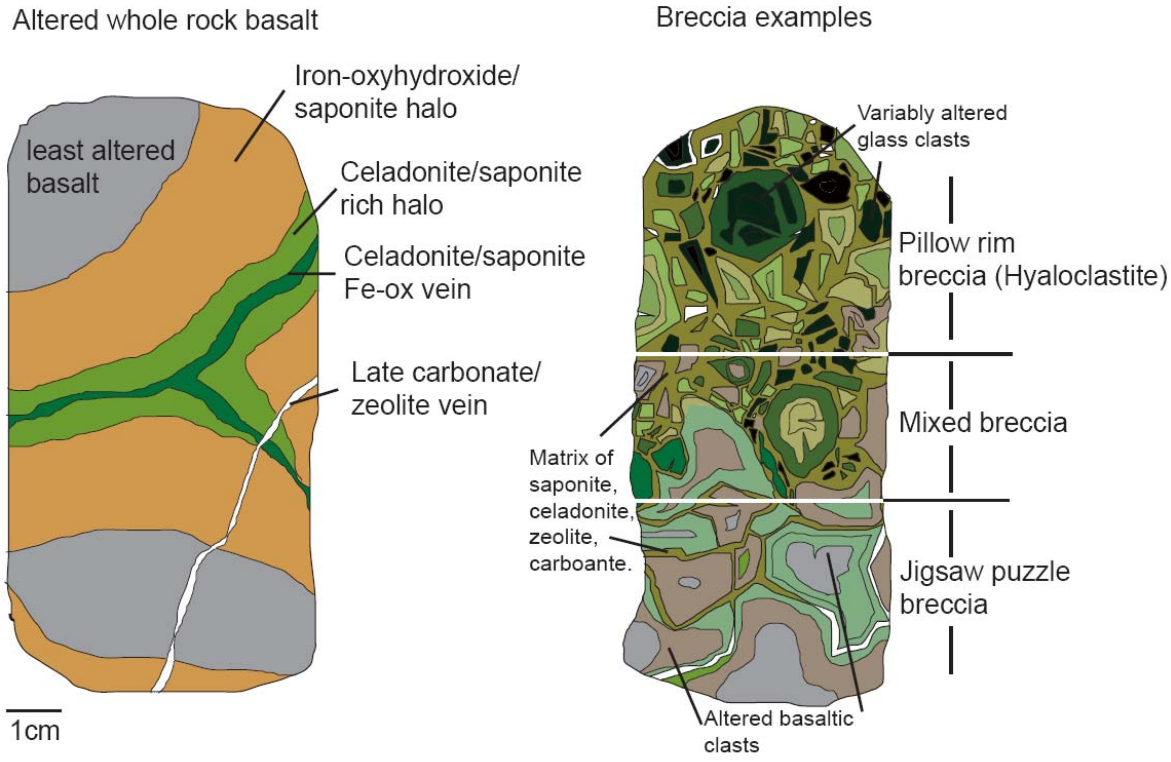

Figure 6.7. Sketch illustrating the main alteration features within the volcanic section at Site 504. Breccias types do not necessarily occur together and are shown together for illustrative purposes only. In addition, the matrix lists only the major secondary minerals. In the lower volcanic zone only dark grey halos are present. A lack of available close up photos for the volcanic section precludes demonstration with real samples.

The red and black alteration halos are most abundant in the upper portion of the volcanic sequence. The dark grey rocks are characterised by saponite which partially replaces olivine, fills pores and fractures, cements breccias, and partially replaces plagioclase and glass. This alteration assemblage forms the majority of the lower volcanics in Hole 504B. Accessory minerals include talc, carbonates, pyrite, and rare secondary K- feldspar and albite. Red alteration halos are controlled by veins, and contain (in addition to the alteration assemblages reported in the dark grey rocks)

iron-oxyhydroxides replacing olivine and staining saponite. The upper volcanic section comprises 27% red halos; however, there are no red halos in the lower volcanic zones (Alt, 1995). Black alteration halos occur together with red halos, usually as thin (5mm) bands around the edge or within the halo. These halos are characterised by celadonite that replaces olivine and fills pore spaces and they are not present in the lower volcanics. The lack of red and black halos, lower intensity of alteration and the absence of iron-oxyhydroxide and celadonite reflect a shift from oxidizing seawater dominated alteration to more restrictive alteration, with reducing rather than oxidizing conditions (Laverne et al., 1996).

Veins within the upper volcanics are multi-minerallic, and they are most commonly filled with saponite ± carbonate, phillipsite, and rare celadonite. Anhydrite, quartz, pyrite and chalcopyrite are rare but present, and these minerals are more common in the lower volcanics.

In areas of very high fluid flow brecciation has taken place of pillow rims and highly fractured basalts. Brecciation comprises (9.2 % of the recovered core at Hole 504B). The upper volcanics (0-320 msb) contains 6 % breccia whereas the lower section is composed of 19 % breccia (Alt et al., 1996). Breccias were divided into three types (Alt et al., 1993) and they are described below 1) pillow rim hyaloclastite breccias with glass shards and pillow fragments cemented saponite, carbonate and minor zeolites, 2) 'jigsaw- puzzle' breccias in which the basaltic clasts are angular and in-situ with a saponite and carbonate matrix, and 3) mixed, matrix supported breccias with a variety of clasts that exhibit variable alteration. At interval 253.5 to 288.5 msb, a zeolite-rich zone that is characterised by abundant thick (~20 mm) veins of zeolites, zeolite-cemented breccias and 10 mm wide zeolite rich alteration halos are reported (Figure 6.8). This zone also includes the alteration assemblage typical of the dark grey rocks described above, which is overprinted by the zeolite phase thus is thought that this zone represents late, focussed fluid flow of cold seawater-like fluids (Honnorez et al., 1983; Alt et al., 1986a).

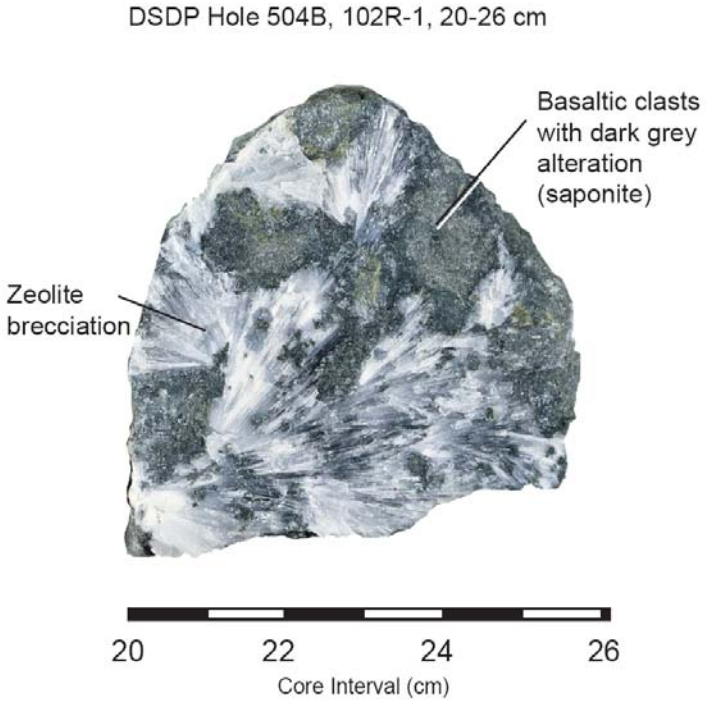

Figure 6.8. Example of zeolite rich zone, basalt clastic breccia with matrix almost entirely composed of zeolite (Photo taken from the Janus database).

As summarised by Alt et al., (1996), chemical variation in the upper volcanic section as a result of alteration includes increased K, Rb, B, CO_2 and H_2O contents and elevated $\delta^{18}O$, δD, $\delta^{11}B$, $^{87}Sr/^{86}Sr$, and lower S and $\delta^{34}S$ compared to the least altered rocks and glass. The increase in K, Rb and CO_2 is likely to be the result of celadonite saponite and carbonate emplacement. Water, fixed by clay minerals that fill pore space and replace primary phases may explain the increase in H_2O. The elevated O, D, B, and Sr-isotopic compositions also reflect the ingress of seawater into the basement. A reduction of S, and $\delta^{34}S$ may be due to the leaching of sulfides from the volcanic rocks. The greatest change was observed in the black and red halos (Alt et al., 1996).

Alteration in the transition zone is characterised by highly-fractured, hydrothermally-altered, brecciated pillows and dikes, together with intense mineralization and mineral stockwork (Figure 6.8). Alteration is very similar to the lower volcanic section, with the notable exception that intensity is much greater and chlorite/smectite, titanite, laumontite and more abundant anhydrite is present. There is an abrupt change in alteration style at 623.5 msb, where hydrothermally altered rocks

are reported for the first time. These consist of dark grey to green-grey rocks with minor and extensive recrystallization, respectively. Plagioclase (usually cores) is recrystallised to albite-oligoclase and other minor phases including chlorite. Olivine is replaced by chlorite and quartz or mixed layer smectite/chlorite, whereas pyroxene may be partially replaced by actinolite, magnetite, titanomagnetite, and titanite.

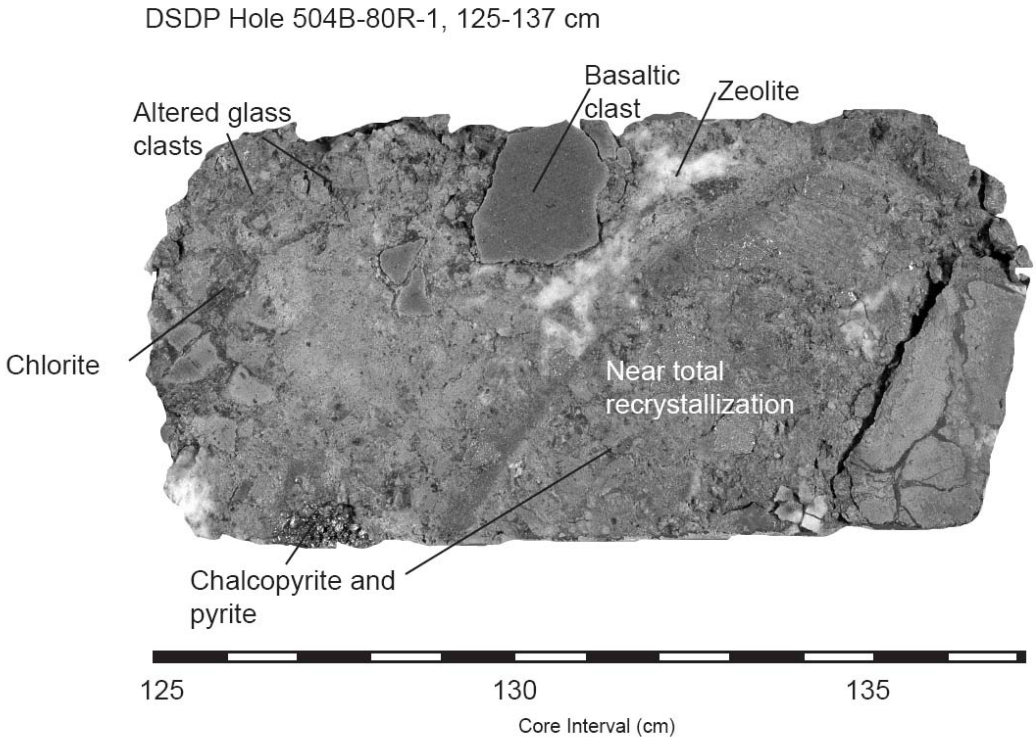

Figure 6.9. Example of the mineralized stockwork zone. (Photo taken from the Janus database)

Glass is typically replaced by chlorite. Veins and breccia matrices are composed of chlorite, actinolite, quartz, epidote, laumontite, heulandite (minor), albite, calcite, analcite (trace) and pyrite. Veins are typically multiminerallic in which all or some of the above minerals are present. 635.5 to 653.5 msb is a mineralised stock work zone with quartz and sulfide minerals in highly fractured/brecciated pillow units (Figure 6.9). Such mineral assemblages are indicative of high temperature (~350^{o}C) alteration (Alt et al., 1996).

The upper sheeted dikes (780.5 to 1225.5 msb) have light to dark grey halos, and recrystallization and assemblages that are very similar to the high temperature alteration observed in the transition zone. Figure 6.10 illustrates the main alteration

features of the upper dikes. Calcite is not present, heulandite is less common and scolecite and prehnite become more common. Localised replacement of olivine by talc and magnetite is observed and titanomagnetites are partly altered to titanite. A number of alteration patches (30-100% recrystallization) containing chlorite, actinolite, and zeolite are reported. These patches represent zones in which the primary porosity was higher, allowing greater fluid flow and higher extent of alteration. ~17% of the upper dikes are composed of halos and patches. Veins consist of the same mineralogy as those in the transition zone, except that they contain no calcite and they are less common. The following sequence of veins is reported by Alt et al, (1996): Chlorite ± actinolite ± titanite veins cross cut by quartz ± epidote ± sulfide veins that are, in turn reopened by zeolite (laumontite and scolecite), prehnite and calcite (stockwork zone). Anhydrite occurs in the reopened veins, in one sample anhydrite is cross cut by a prehnite vein.

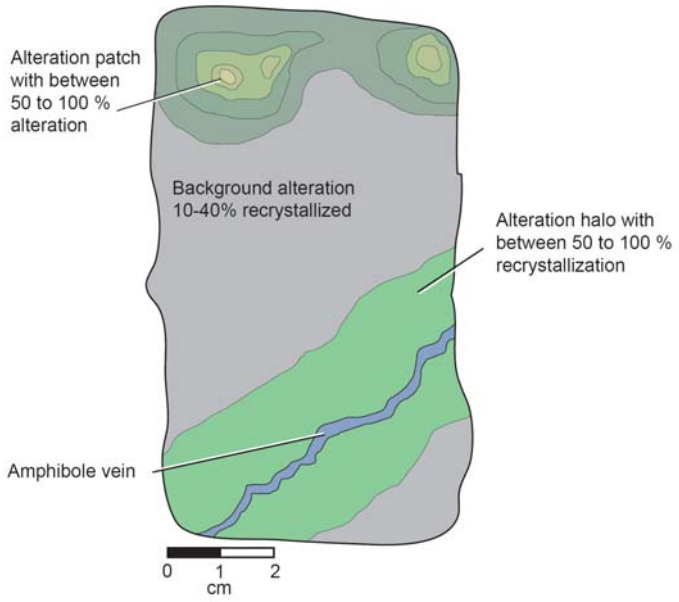

Figure 6.10. Illustration of alteration styles within the upper sheeted dikes. (Redrawn from Alt et al, (1996). Similar alteration characteristics are observed in the lower sheeted dikes. However, when petrographically observed recrystallization is more intense and secondary phases differ.

The chemical changes, based on comparisons between altered and least altered, rocks for the transition zone and upper dikes are described together, due to their similarity. They are summarised in detail by Alt et al (1996). Change in chemistry within the transition zone and the upper dikes ranges from moderate to intense. High chemical changes are thought to reflect the high temperatures and the

subsurface mixing zone environment, and the greatest changes are reported within alteration halos and patches. Increases in Cu, Zn, Mn, and S, particularly within mineralised rocks at 635.5 msb, reflect the increased abundance of metal sulfides, Mn bearing chlorite, and the reduction of seawater (by oxidation of ferrous iron at shallower levels). Increased H_2O and $^{87}Sr/^{86}Sr$ reflect higher levels of alteration and the increased interaction between the hydrothermal fluid and host rock. The reduction of K_2O, Fe^{2+}/Fe^{T} and TiO_2 is the result of K leaching from rocks and the mobilization of Ti to form titanite within the dikes. The variable formation of secondary calc-plagioclase and albitization may explain the variable CaO and Na_2O, and the disappearance of the negative Eu anomaly with depth. Low $\delta^{18}O$ in halos may be explained by the observed higher intensities of alteration (Alt et al 1996). Alt et al, (1996) note an unusual lack of change in MgO. Locally intensive interaction with seawater in narrow chlorite rich zones along veins indicate that all the available Mg from seawater was taken up. However, these zones are small and most of the rock interacted with low volumes of seawater, indicating that reactions within the majority of the basement were limited by the amount of seawater flow. Alt et al., (1996) note that there may still be a net uptake of Mg via chlorite filling fractures and cementing dike margin breccias. The timing of secondary mineral paragenisis at Site 504 is summarised as follows: 1) early chlorite, actinolite, albite-oligoclase, and titanite, 2) quartz, epidote, and sulfides, 3) anhydrite, and 4) zeolites and local calcite. Alteration temperature estimates range from 350°C to 380°C.

The lower sheeted dikes (1225.5 to 1836.5 msb) exhibit alteration that is similar to the upper sheeted dikes, albeit with some significant changes. These include, increased abundance of secondary calcic-plagioclase, amphibole, ilmenite exsolution, and the first appearance of secondary clinopyroxene, magnesiohornblende, and anhydrite within the groundmass rather than veins. In addition, losses in sulfur/metals and higher levels of recrystallisation are reported within the lower sheeted dikes. Variable Mg number, Cr, Ni, Sr, TiO_2, SiO_2, Y and Zr are thought to represent primary igneous variation. Losses of Cu, Zn, and S reflect the breakdown of sulfide minerals and titanomagnetite at high temperatures, where the solubility of metals and sulfide in hydrothermal fluids increase significantly (Alt et al., 1996). Alt et al., (1996) and Vanko et al., (1996) suggest that these effects may be evidence that the lower sheeted dikes are part of a subsurface reaction zone that

supplies metals and sulfur to hydrothermal fluids that ultimately vent as black smokers on the sea floor. In addition, slightly elevated $\delta^{34}S$ + local S enrichment reflect anhydrite formation within the rocks (Alt et al., 1995). Other chemical changes within the lower sheeted dikes are relatively minor. Once again alteration halos and patches exhibit greater chemical change than their less altered counterparts (Alt et al., 1996). Detailed reports and comprehensive summaries of the lower sheeted dikes are described and discussed elsewhere (e.g. Alt et al., 1993; Alt et al., 1995; Laverne et al., 1995; Vanko et al., 1996: Alt et al., 1996).

6.2. Site 896

ODP Site 896 is located at 1°13.006'N, 83°43.392'W ~1 km southeast of Hole 504B. Like Site 504, Site 896 is situated on 6.9 Ma-old crust at the eastern equatorial Pacific that spread at approximately 68 mm/yr full-rate from the Costa Rica Rift (Figure 6.11). However, in contrast to Site 504, Site 896 is located on a bathymetric high that coincides with the topographic high point of a tilted basement fault block (Langseth et al., 1988). Site 896 penetrates through 179 m of sediment and 290 m of basement that is composed of pillow lavas, massive flows, breccias, and two subvertical dikes. Site 896 is located at a local heat flow maximum, which is consistent with the correlation between areas of high heat flow and both elevated topography and basement topography with basement troughs being zones of lower heat flow (Alt et al., 1993; Teagle et al., 1996). Modelling of the heat flow by Fisher et al., 1990, 1994) imply significant hydrothermal convection within the area and that convection is controlled by basement topography and sediment thickness. In contrast, Hole 504B is in an area, of ambient heat flow (Alt et al., 1996), therefore it is potentially useful to compare the alteration characteristics for each of these sites. The petrography and geochemistry at Site 896 has been extensively characterised, for example by Teagle et al, (1996) and Alt, et al., (1996). This section presents a short summary of the geological characteristics of Site 896 including sedimentation, igneous petrology, and alteration.

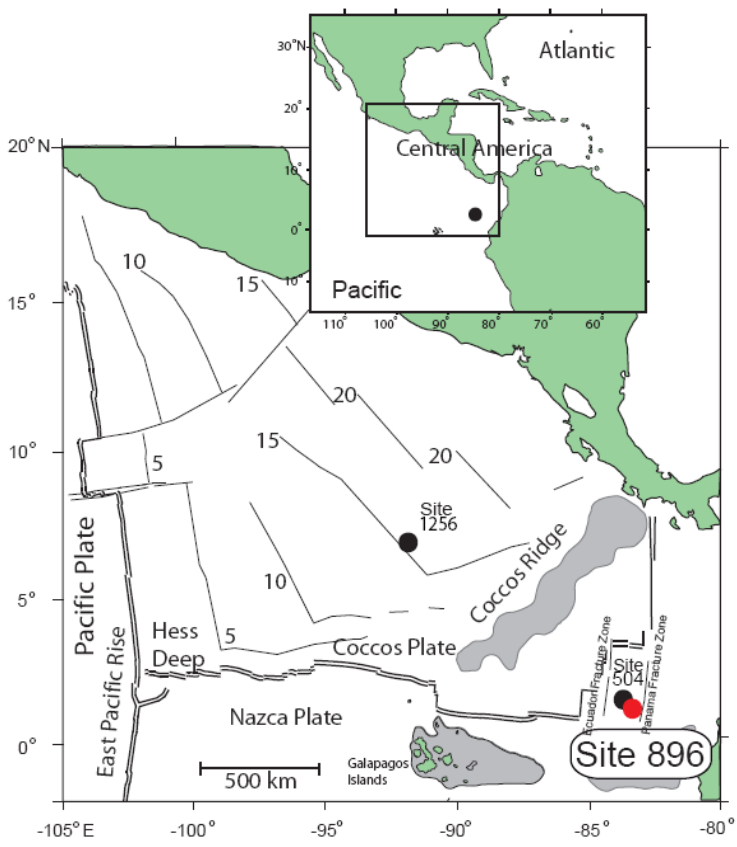

Figure 6.11. Location of Site 896. Sites 1256 and 504 are included for comparison.

6.2.1 Sea floor sediment, stratigraphy and sedimentation rates

The lithostratigraphy for Site 896 is illustrated in Figure 6.12. ODP Hole 896A represents a reoccupation of an earlier Site (ODP Site 678), as such the sedimentary stratigraphy is based on sampled recovered from Site 678 during Leg 111 (Becker et al., 1988). Spot coring was carried out during Leg 111 to recover a representative section of the ~170.8 m thick sediment pile. Four sediment Units were recovered and these consist of the following: 1) Radiolarian and diatom ooze (0-100 mbsf), 2) Clay-like diatom-nannofossil chalk (100 – 169.8 mbsf), 3) Muddy limestone (169.8- 170 mbsf), and 4) metal rich muds intercalated with basaltic pebbles, conglomerates, and white calcic material (170 – 170.8 mbsf). The sediment basement interface was not recovered; however the presence of basaltic pebbles in Unit 4 suggests that this unit may represent the deepest sediment at Site 896. Sedimentation at Site 896 is characterised by a period of rapid sedimentation (~20 m/m.y) for the first 4 Ma

followed by 2 Ma of very fast sedimentation (~40 m/m.y). This transition from fast to very fast is marked by a change in lithology, in which the content of nannofossils increases. These changes mark increased productivity in the region at ~1.9 Ma (Figure 6.13).

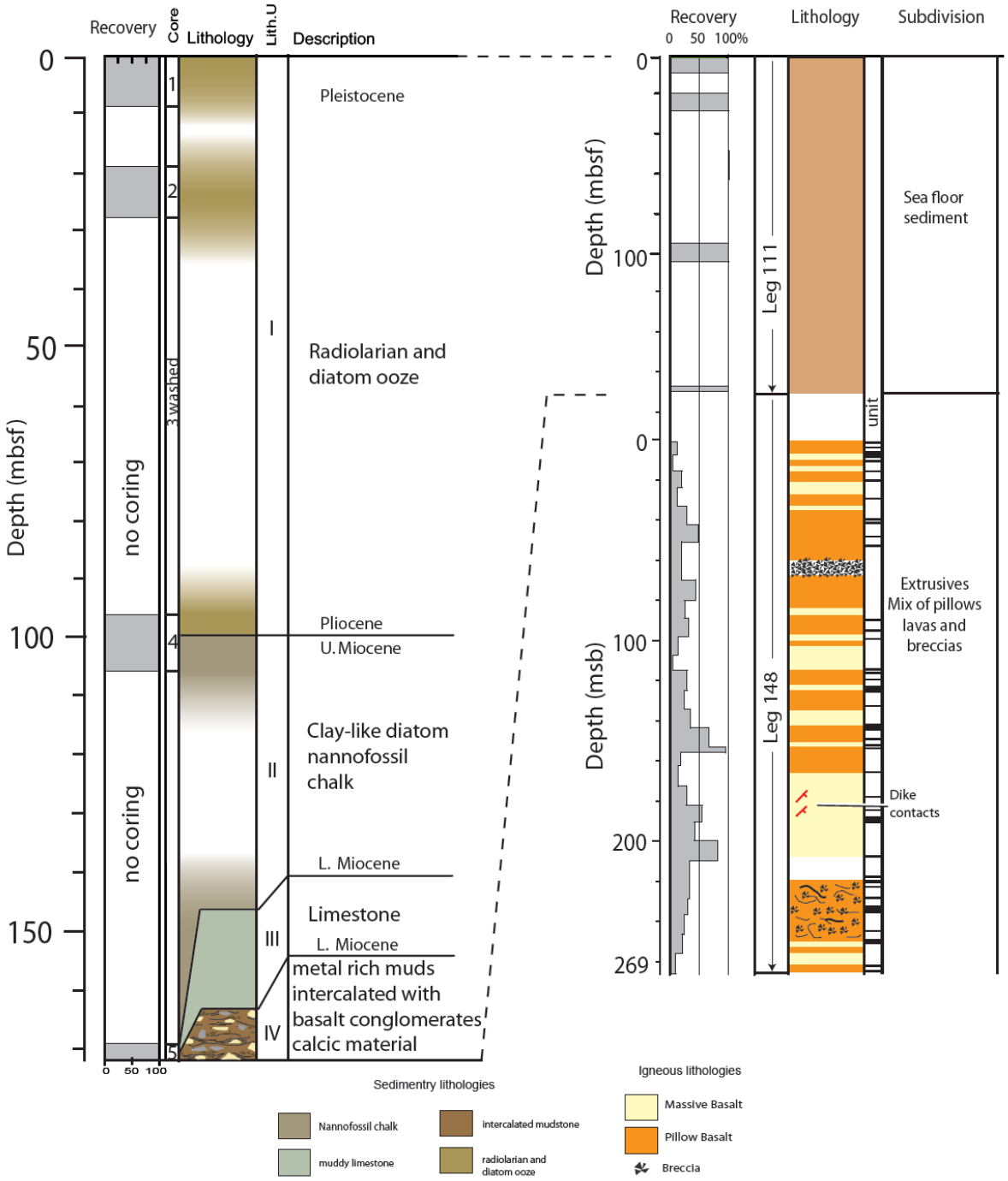

Figure 6.12. Site 896 Stratigraphy including recovery, lithological unit subdivisions and igneous lithology. Sedimentary stratigraphic data sourced from Becker et al., (1988); Igneous stratigraphic data after Alt et al, (1993). Cores of the sedimentary coverare from DSDP Hole 678B (Leg 111). Site 896 represents reoccupation of this site. Hole has been renamed 896A.

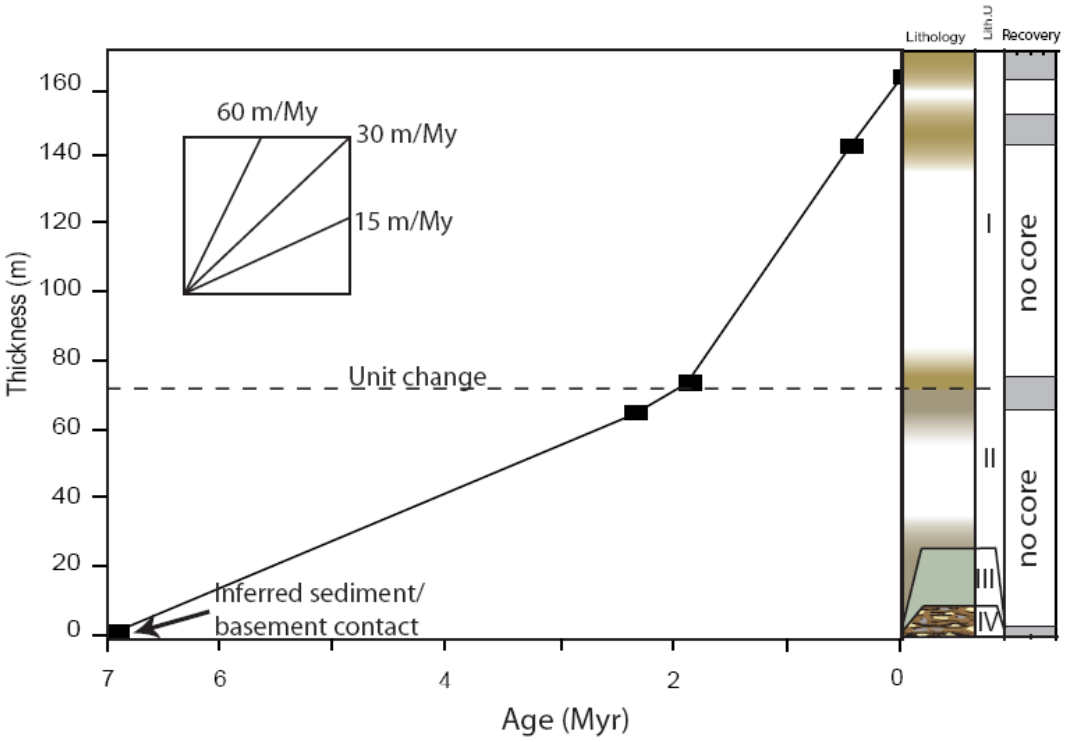

Figure 6.13. Sediment accumulation rate with time for Site 896 (Becker, Sakai, et al., 1988).

6.2.2 Basement at Site 896, Petrography and Igneous geochemistry

Hole 896A penetrates 290 m into basement recovering lavas, massive flows, and breccias that make up the uppermost extrusive section at Site 896 (Figure 6.12), with 27.7% recovery. Based on cores recovered from the upper volcanic section at Site 896, basement comprises Pillow lavas (57%), massive flows (38%), breccias (5%) and two subvertical dikes (Alt et al.,1993). The basalts are cryptocrystalline to fine-grained, sparsely to highly phyric plagioclase-olivine tholeiitic basalts. Below 194 msb olivine becomes the dominant phenocryst phase and massive flows are more common. 51 Units were defined based on variation of mineral abundance and mineral type and these are described in detail in Alt et al., (1993). Massive units were defined based on the lack of pillow lava textures and the presence of glassy margins and curved margins. Most of these massive flows were classified as thin flows; however some discontinuous sections may be interiors of large pillows. Two dike contacts at Intervals 148-896A-21R-2, pc 9B to C (202.71 msb) and 148-896A-22R-4, pc 3-5 (216.44 to 216.63 msb) in which coarse grained material forms a steep (78^{o}) contact with no glass or variolitic textures.

Primary igneous variation and magmatic features are discussed in detail by Brewer et al, (1996) and Alt et al., (1993). Assessment of the primary igneous chemistry at Site 896 is also based on a detailed study of pristine glass by Fisk et al, (1996). Major, trace and REE concentrations indicate that Site 896 is strongly depleted, moderately evolved MORB (MgO: 6.69-9.74 wt%, Fe_2O_3: 8.10-10.32 wt %, $Mg^{\#}$: 0.609-0.698, Ni: 82-198 ppm, Cr 293-407 ppm, Zr: 32-53 ppm, Nb <3ppm) (Brewer et al., 1996; Alt et al., 1993). The chondrite normalised REE pattern for (Site 896) attests to the depleted nature of Site 896.

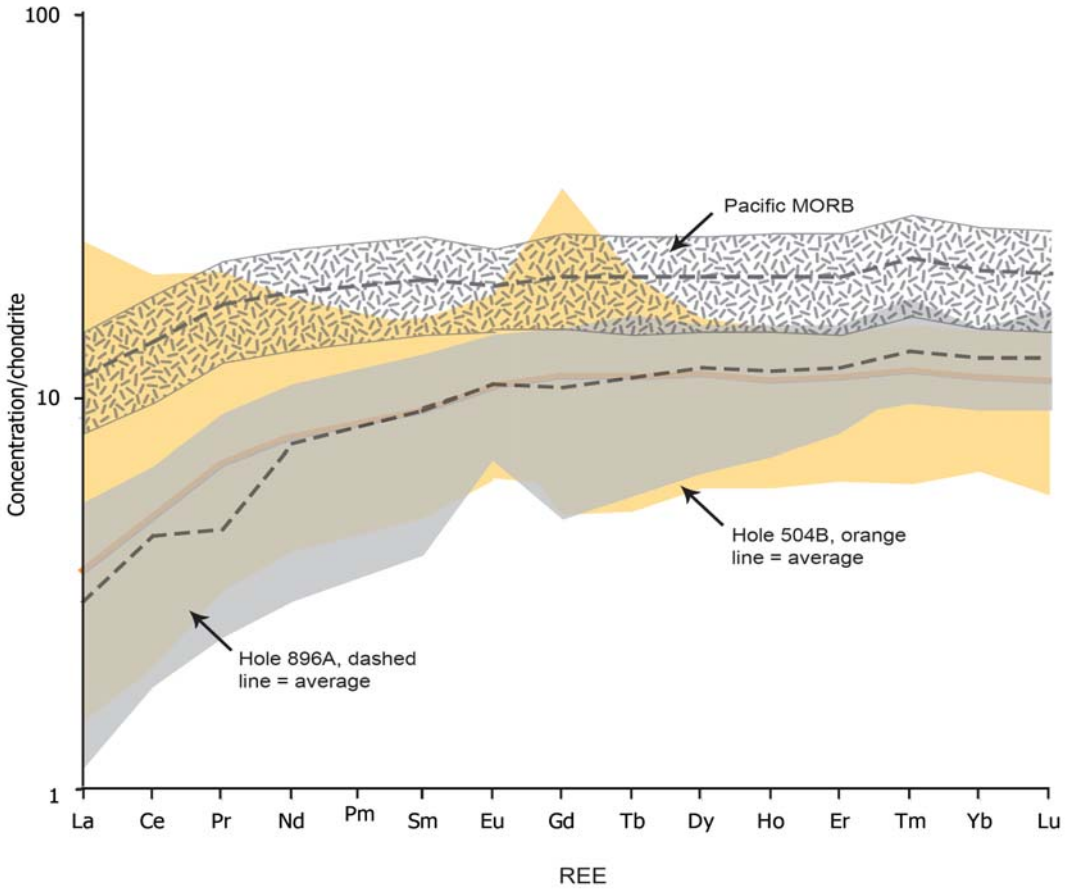

Figure 6.14. Chondrite normalised REE patterns for all samples at Site 896. Pacific MORB and Site 504 are included for comparison. Chondrite-normalization factors from Taylor & Gorton (1977). Hole 504B data is a compilation of Legs 69, 70 (Cann, et al., 1983); 83 (Anderson et al., 1985), 111 (Becker, Sakai et al., 1989), and 140 (Erzinger et al., 1995) Pacific MORB data from Jenney and Castillo, (1997). Pm is not analysed.

In the upper 150 of Site 896 basalts are higher in SiO_2, Al_2O_3, and CaO and lower in $Fe_2O_3^*$, TiO_2, V, Cr, Y, Zr and Zn than those at Site 504. Variability between Sites 896 and 504 are minimal and indistinct (Alt et al., 1993) and Brewer et

al, (1996) suggest that the slight chemical and plagioclase/olivine phenocryst variation between igneous units represents magmatic cyclicity with depth, which is the result of crystallisation of magma chambers at varying depths.

6.2.3 Basement alteration

Characterisation of the secondary mineralogy and geochemistry at Site 896 is discussed in detail by Alt et al., (1993), Teagle et al, (1996) and Alt et al, (1996). However, to facilitate discussion and comparisons later in this study a summary of the key points is provided here.

With the exception of rare fresh vitreous glass fragments all rocks recovered at Site 896 have been subjected to slight to moderate alteration. Alteration may include the replacement of groundmass minerals by secondary phases, the filling of primary vugs and interstices by secondary minerals and the presence of veins and breccias. Alteration within the groundmass may manifest itself in terms of alteration halos associated with fractures or 'background' in which alteration is less intense. Based on petrographic observations, four major alteration assemblages are defined for Site 896 (Alt et al., 1996) and these are summarised in order of their abundance. 1) Saponite 'background' alteration occurs throughout the core. Olivine is partly to totally replaced by saponite (Figure 6.15 A) and carbonate, whereas plagioclase may be part replaced by saponite and minor albite. Alteration within 'background' is slight and the rock is grey to dark grey in colour. 2) Saponite + iron-oxyhydroxides is the second most abundant assemblage and these manifest themselves as red/yellow/brown alteration halos (Figure 6.15 E) that form along veins and fractures. Small pillow fragments, olivine and pore spaces may be altered to saponite and iron-oxyhydroxides. Alteration of olivine to saponite and iron-oxyhydroxides is often referred to as iddingsite (Figure 6.15 A). 3) Celadonite + saponite + iron-oxyhydroxides is essentially the same as '2', but with celadonite. Celadonite may be intergrown with iron-oxyhydroxide or it may occur alone. Halos are typically black to red. 4) Celadonite + saponite is the least common assemblage, these tend to form mm to cm sized dark grey patches or bands in pillows (Figure 6.15 E). Celadonite may line veins and vesicles (Alt et al., 1993).

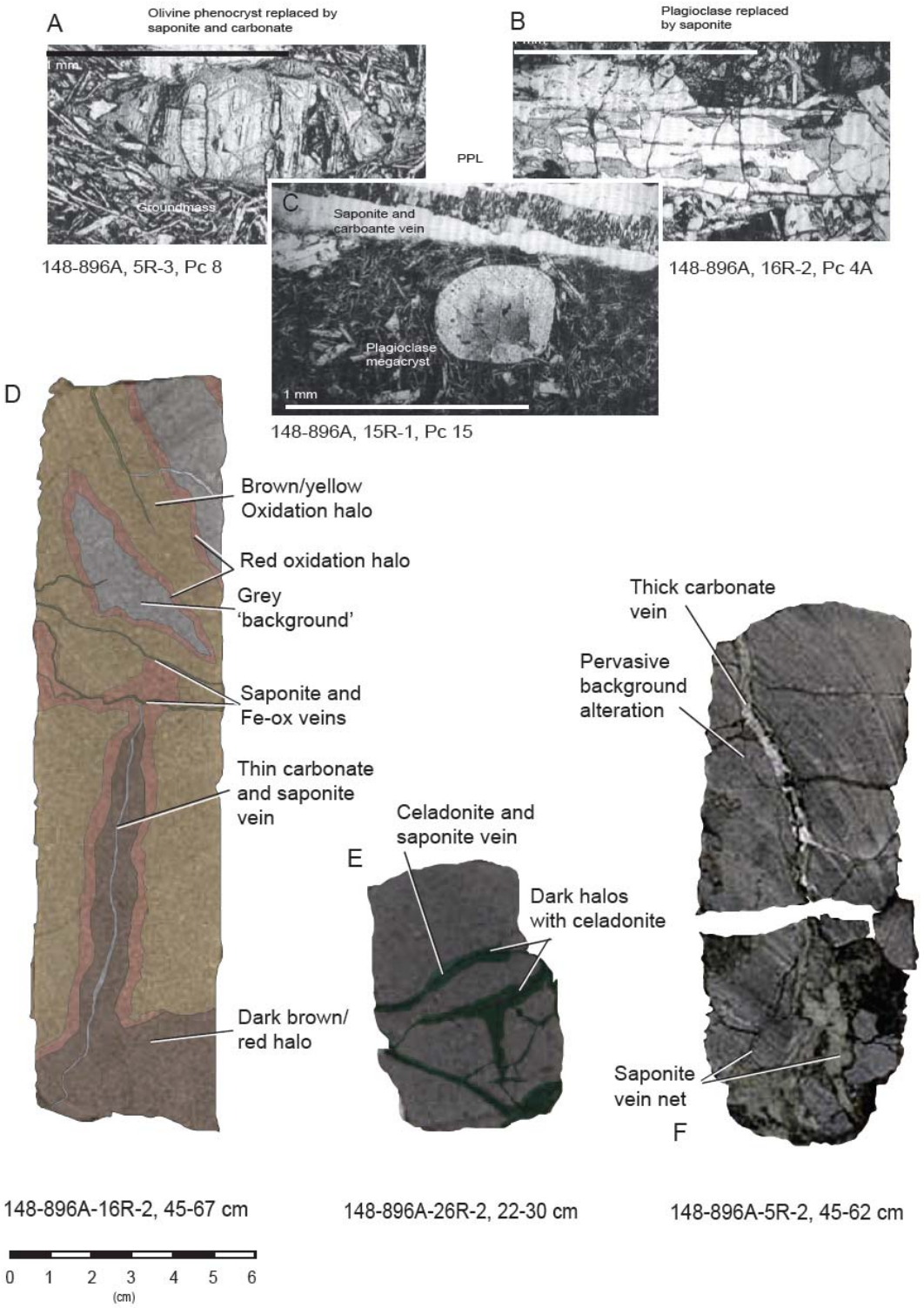

Figure 6.15. Examples of alteration styles at Site 896. A) Photomicrograph of olivine phenocrysts replaced with saponite and minor carbonate. B) Photomicrograph of plagioclase partially replaced by saponite. C) Photomicrograph of a plagioclase megacryst and saponite + carbonate vein. D) Enhanced core photo displaying various oxidation halos, saponite, carbonate and iron-oxyhydroxide veins. E) Enhanced core photo of celadonite + saponite assemblage. F) Thick carbonate and saponite vein surrounded by pervasive background alteration. A, B, C are after Alt et al., (1993). In addition, rare (<0.1 mm) celadonite veins occur that may pre-or-post date saponite.

Veins at Site 896 are common and abundant (2018 veins at 27 vn/m) and they comprise saponite, saponite + carbonate, saponite + iron-oxyhydroxide, saponite + iron-oxyhydroxide + carbonate, carbonate, and fine (<0.5 mm) phillipsite veins. Saponite is commonly stained with iron-oxyhydroxide which imparts a yellow-brown appearance to many saponite + iron-oxyhydroxide veins. Saponite is by far the most common vein mineral, it occurs in 93% of all veins and makes up 1.7% by volume of the core. In contrast, Hole 504B has 0.8% saponite. Saponite veins are evenly distributed throughout Hole 896A. Carbonates are more common at 0-104 and 195 – 220 msb and their abundance decreases with depth.

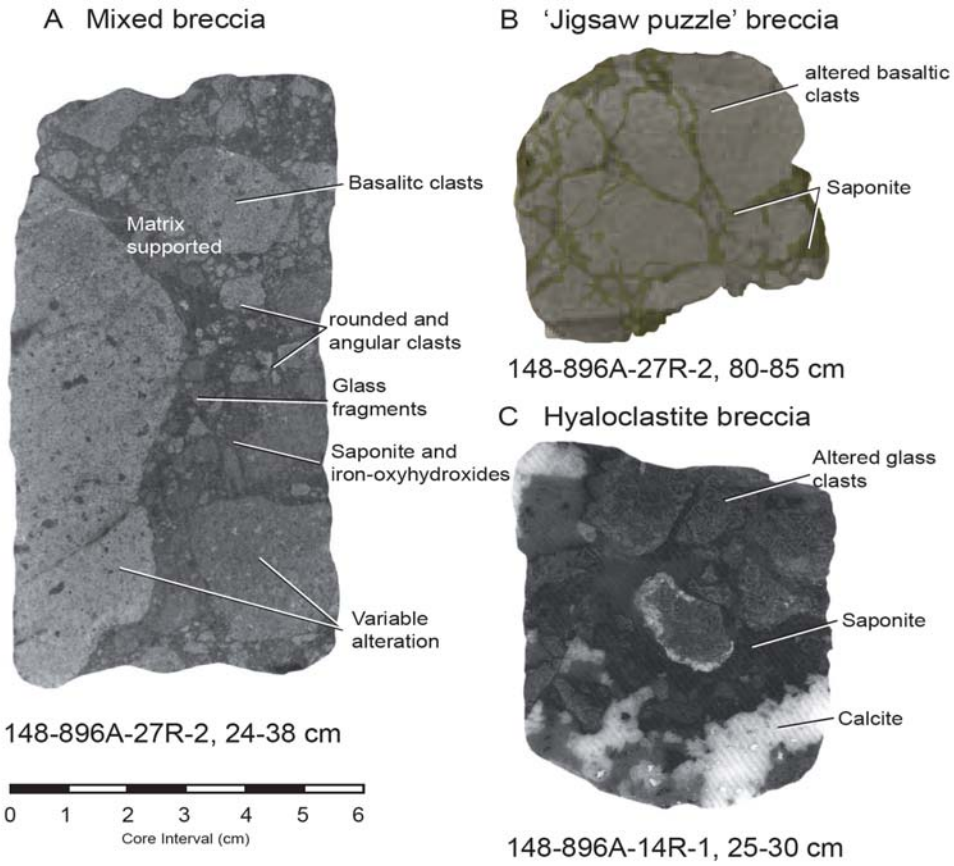

Figure 6.16. Examples of breccia types reported at Site 896. A) Mixed breccia. B) Jigsaw puzzle breccia C) Hyaloclastite breccia.

They may consist of calcite or aragonite, typically they are late stage and they can form part of multi-minerallic veins ranging from 0.1 mm to 4 mm thick. Carbonate veins make up 0.4% of the recovered core, which is an order of magnitude greater than that of Site 504 (0.04%). Overall vein abundance at Site 896 is comparable to Site 504 (31.6 vn/m), however, Site 896 contains a higher proportion of thick ~2-10

mm veins thus by volume Site 896 contains more vein minerals (~2.1%) compared to Site 504 (1.2%) based on saponite and carbonate.

Approximately 5% of the recovered core at Site 896 is breccia, however, studies by Brewer et al (1994) from core-log integration suggest breccia content may be as high as 47 %. Three types of breccia were encountered at Site 896, these include: 1) pillow rim or hyaloclastite breccia, which consists of altered glassy shards and pillow fragments in a saponite + carbonate + zeolite matrix, 2) Jigsaw puzzle breccia, which consists of in-situ angular basaltic clasts cemented by saponite + minor carbonate, and 3) mixed breccias, that contain a mixture of basaltic and glassy clasts that have been subjected to a range of alteration assemblages and they are supported by a cement of saponite and minor carbonate. These breccias are very similar to those encountered at Site 504 (Figure 6.16). Estimates for the percentage of matrix are sourced from Hole 504 which is around 10% of which 94.5 % is saponite 5.2 % is zeolite and 0.3 % is carbonate (Alt et al., 1993). Rare pillow and hyaloclastite breccias may contain carbonate rich matrixes at Site 896 (Alt et al., 1993).

Geochemical analyses for whole rocks and secondary minerals carried out by Alt et al., (1996), Alt et al., (1993), Teagle et al., (1996) are used to define the secondary mineralogy and to qualitatively define chemical changes associated with alteration at Site 896. Analysis of secondary minerals by XRD indicate that saponite at Site 896 are Mg-Smectites with Fe/(Fe + Mg) of 0.13-0.24 (Teagle et al., 1996). Celadonite ranges from high K and low Al tetrahedral to glauconite. In addition, celadonite exhibits divalent rends to high Mg contents that suggests mixing with saponite. XRD analyses also confirm the presence of chlorite in coarse grained portions basalt. Chlorite replaces interstitial material and fills primary pore-space and it may have formed during initial cooling of the massive flows soon after eruption. Sr-isotopic analyses of carbonate veins at Site 896 range from 0.7079 to 0.7087 with two distinct groups that imply an open, cool phase of seawater circulation followed by a more restricted warmer period with greater interaction between the fluid and host rock. This hypothesis is supported by the $\delta^{18}O$ of carbonates which record two temperature ranges (26-35^{o}C and 47-67^{o}C) that coincide with Sr and-isotope ranges (0.7087 and 0.7079-0.7084) and the concentrations of Mg, Fe, and Mn (Alt et al., 1996). Most saponite records a $^{87}Sr/^{86}Sr$ close to seawater ~0.7084 to 0.7092, however, one sample with an Sr- isotopic ratio of 0.7044 implies a great deal of basaltic interaction, perhaps from

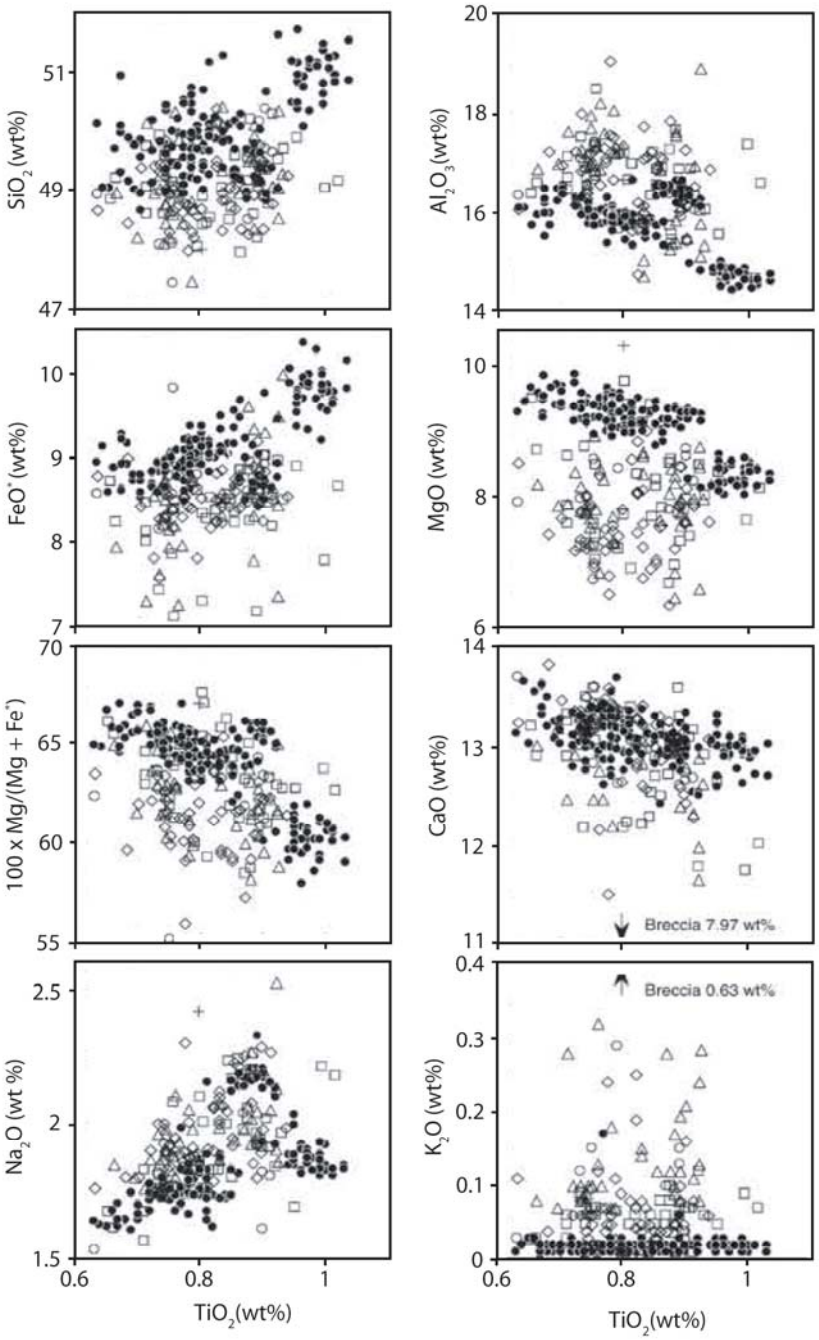

Figure 6.17 Whole rock major element concentrations compared with TiO_2. Dots = fresh glass compositions. Squares = Saponite, Diamonds = Saponite + Iron oxyhydroxides, Triangles = Celadonite + saponite + Iron oxyhydroxides, Circles = Celadonite + saponite (After Teagle et al., 1996).

upwelling fluid in a zone where cold seawater circulation was restricted (Teagle et al., 1996).

Whole rock major trace and REE, when compared to analyses of fresh glass, largely reflect primary igneous variation (see earlier in section and Alt et al., 1996;

Alt et al., 1993). However, as illustrated in plots of various elements vs. TiO_2 for glass and whole rock samples (Teagle et al., 1996), there are a number of chemical changes reported that appear to reflect alteration of the host rock. Whole rocks at Site 896 exhibit increased H_2O, CO_2 Fe^{3+}/Fe^{T}, K, Rb, Cs, U, P, $\delta^{18}O$, and $^{87}Sr/^{86}Sr$ which reflect the incorporation of secondary minerals into the host rock and ingress of cold seawater throughout Site 896. Variable loss and gains of S and Ti are reported, reflecting perhaps a change in volume as primary phases are replaced. Gains in Mg within whole rock are minimal; however the crust appears to have undergone a net increase in Mg due to the abundance of saponite veins (Alt et al., 1996). All whole rocks have elevated $^{87}Sr/^{86}Sr$ compared to MORB (Figure 6.18).

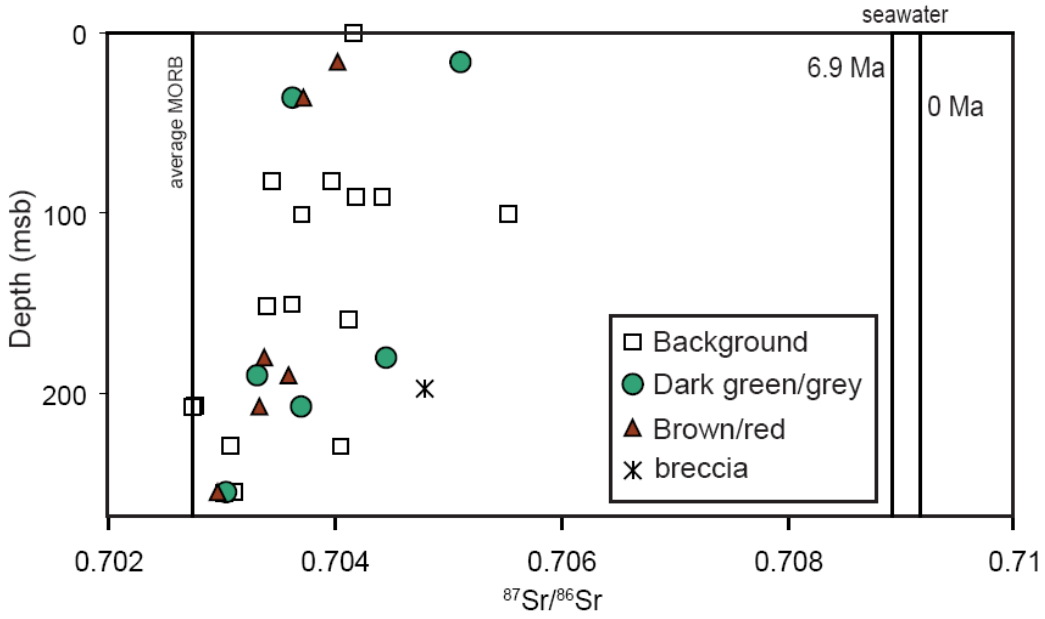

Figure 6.18. Sr-isotopic profile vs depth for Site 896. Redrawn based on data from Teagle et al, (1996). The average composition of MORB and Seawater at 0 Ma and 6.9 Ma is illustrated for comparison (McArthur et al., 2001).

$^{87}Sr/^{86}Sr$ decreases with depth. This implies reduced fluid flow, and therefore less incorporation of seawater Sr into the basalts. $\delta^{18}O$ exhibits trends with Fe^{3+}/Fe^{T} and LOI (Teagle et al., 1996). The greatest geochemical changes are observed in breccias, where extreme enrichments of Mg, alkalis and CO_2 are reported. The Sr-isotopic composition for Sample 148-896A-23R-1, 24-28 (Breccia) is highly elevated (0.7048) relative to MORB. A large proportion of this breccia is composed of secondary mineral phases saponite and carbonate, therefore an elevated Sr-isotopic composition is expected (Teagle et al., 1996).

Alteration at Site 896 has been summarised based on detailed work by Teagle et al., (1996); Alt et al., (1996), and Alt et al., (1996). Overall the alteration at Site 896 reflects cold (<100^{o}C) oxidising seawater ingress to the ocean crust that is very similar to that encountered in the upper portions of Site 504. The only significant difference between the two sites is the higher proportion of carbonate forming thick veins, and breccias at Site 896. Core log integration by Brewer et al., (1994) imply that the estimate for lithostratigraphic estimate from recovered core is highly biased towards more competent rocks. Formation Micro Scanner (FMS) and Gamma Logging Tool (GLT) log data calibrated to recovered core strongly suggest a much greater proportion of breccias than were recorded based on core descriptions alone. At Site 896, lithologic variation appears to exert a strong control on oxidation. Figure 6.19 illustrates the relationship between recovered massive units and oxidation.

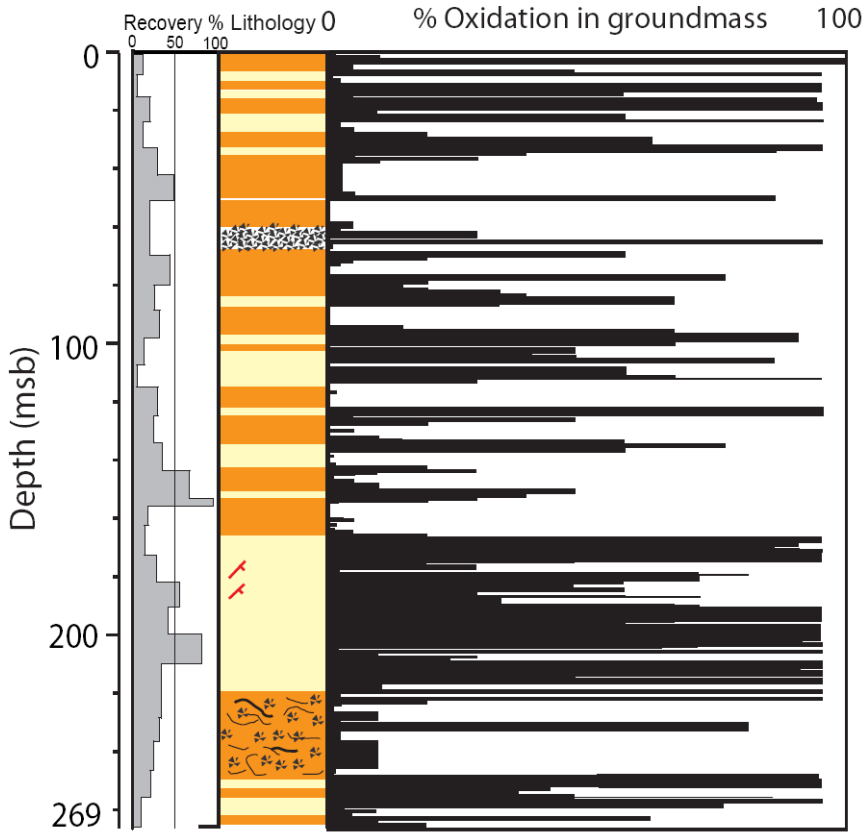

Figure 6.19. Percentage of oxidation vs. depth for each piece at Site 896 together with stratigraphy and recovery Shard pattern = breccia, Pale yellow = sheet and massive flows, orange = pillow lavas (Modified from Alt et al., 1993).

On the basis of core-log integration by Brewer et al., (1994), a new stratigraphy consisting of 47% breccias, 33% pillows and 34% flows has been recommended. Samples at Site 896 ultimately record the integrated affects of six alteration phases. These phases are summarised below:

1). Initial precipitation of chlorite within coarse grained massive units during initial cooling and penetration of cold seawater into the rocks

2). Emplacement of celadonite and iron-oxyhydroxides early (<1 m.y. after crust formation) to form thin band-like alteration halos. During this phase deep solutions may have supplied the necessary Fe and Si for alkalis and celadonite formation. This phase may have contributed to increased H_2O, K, Fe^{3+}/Fe^{T}, $\delta^{18}O$, $^{87}Sr/^{86}Sr$.

3). Iron-oxyhydroxides that form red halos appear to form after celadonite during open circulation of seawater in a young crust. This phase records increases in H_2O, alkalis, U, P, $\delta^{18}O$, $^{87}Sr/^{86}Sr$ and local losses in S, Ti, Ca, and Mg.

4). Emplacement of saponite partially replaces olivine/plagioclase phenocrysts, fills fractures and cements breccias. Chemical changes include increased Mg, H_2O, $\delta^{18}O$, and slight alkali, S, and Ti increases. In addition, the majority of saponite has $^{87}Sr/^{86}Sr$ ratios of 0.70842 to 0.70875 and implies slightly evolved seawater during precipitation. Saponite is thought to occur in slightly older crust than '3', reflecting restricted circulation at temperatures above 40^{o}C (Teagle et al., 1996).

5). Late stage carbonate veins that are either formed together with, or post-date saponite appear to represent two generations of emplacement. Evidence from $^{87}Sr/^{86}Sr$ and $\delta^{18}O$ imply a cold (26-35^{o}C) open seawater emplacement followed by a warmer (47-67^{o}C) period with more restricted fluid flow that has undergone greater interaction with the host rock.

6). The final phase consists of zeolites which, by observations of cross-cutting relationships, formed during and after carbonate precipitation. Sr-isotopic compositions (0.7074-0.7091) reflect variability between localised open and restricted zones.

6.3. Site 1224

Site 1224 is located seawater depth of 4967 m in the north Pacific Ocean between Hawaii and San Diego (27°53.37'N, 141°58.75'W) south of the Moonless Mountains seamounts (Figure 6.20). Site 1224 was formed ~46 Ma (Eocene) between the Farallon and Pacific plates at spreading rate of 142 mm/yr full rate (Stephen et al., 2003), in a similar mid-ocean ridge setting to the present day EPR (Stephen et al., 2003). ODP Leg 200 penetrated 28 m of seafloor sediment and 146.8 m of basement at a. The primary objective of Leg 200 was to prepare a borehole in basaltic crust for the installation of a broadband borehole seismometer. A secondary objective was to use this drilling opportunity to recover and describe basement material at the Site. Site 1224 is useful in this study because it represents a relatively deep penetration of basalt formed at fast spreading rates at an age of formation that is not covered by any other site in this study. Its position, relatively far from any plume activity, faults and/or other unusual geological features makes it a good candidate for assessing hydrothermal alteration in the context of fast spreading rates.

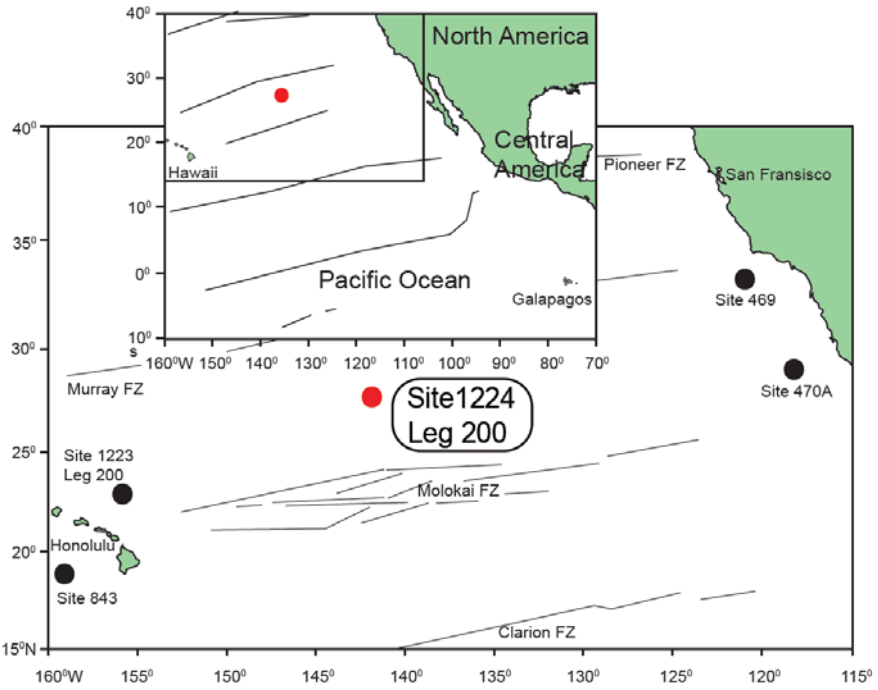

Figure 6.20. Location of Site 1224.

6.3.1 Sea floor sediment, stratigraphy and sedimentation rates

Sediments at ODP Site 1224 were recovered in Holes 1224 A, C, D and E. Most of the sedimentary section is represented with recovery ranging from 5% to 100%. The sediments are largely composed of pelagic clay of eolian origin with rare coarser horizons that contain radiolarians, sponge spicules, coccoliths and discoasters. A summary of ODP Site 1224 Stratigraphy is outlined in Figure 6.21 .Hole 1224A recovered a few pebbles, granules and a small amount of clay which contains radiolarians and very rare sponge spicules. Hole 1224B recovered 20cm of clay with

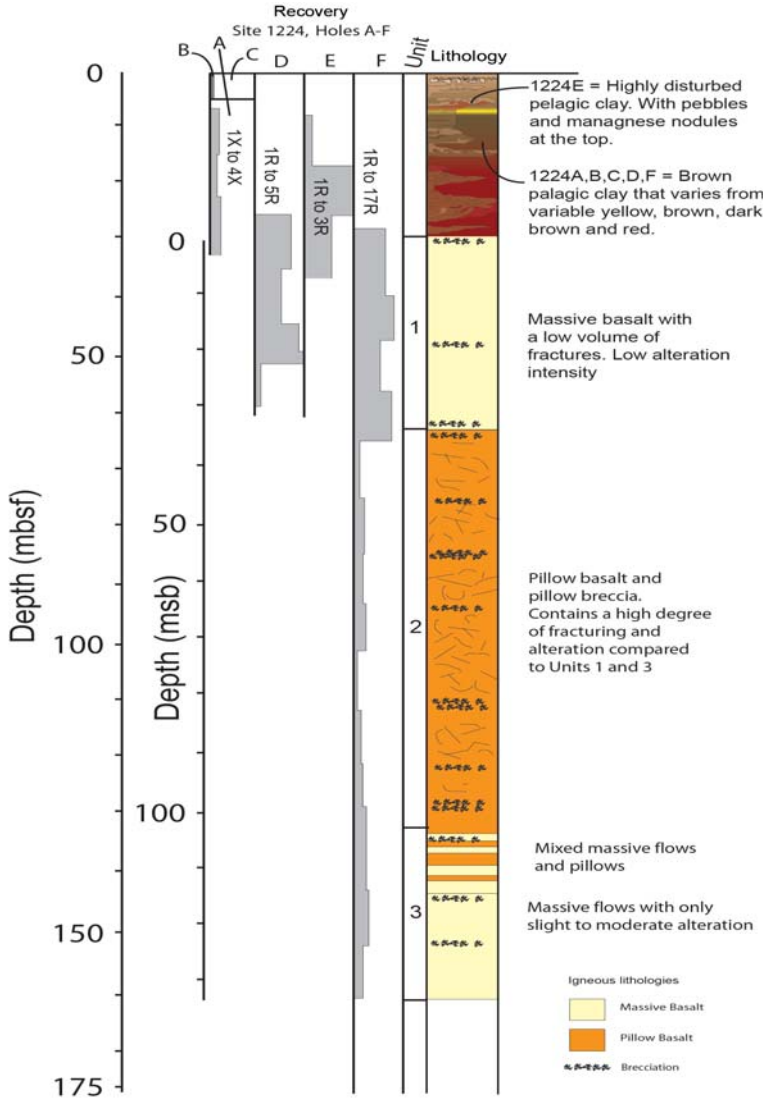

Figure 6.21. Composite lithostratigraphy for Site 1224. Based on stratigraphic observations by Stephen et al., (2003).

few radiolarians. Hole 1224C recovered 6.53 m of massive pelagic clay which darkens from light brown to very dark brown to the base of the hole.

The dark portion contains common radiolarians and sponge spicules. ODP Hole 1224E recovered 10.52 m of sediment in a 27.1 thick sediment pile. The sediment consists of pelagic clay of varying shades of brown and they include intervals with infilled burrows and manganese nodules. Radiolarians were recovered at the top of the hole whereas coccoliths and discoasters occur below 17.5 mbsf (Stephen et al., 2003). The majority of sediment at ODP Site 1224 is of mid to late Eocene between 44 and 46 Ma (Firth, 2003) suggesting rapid sedimentation (4.5 m/Myr) followed by ~36 ma of very low or no sedimentation (<1 m/Myr) (Figure 6.22). A lack of microfossil and palaeomagnetic data precludes a greater resolution in the rate of burial at Site 1224.

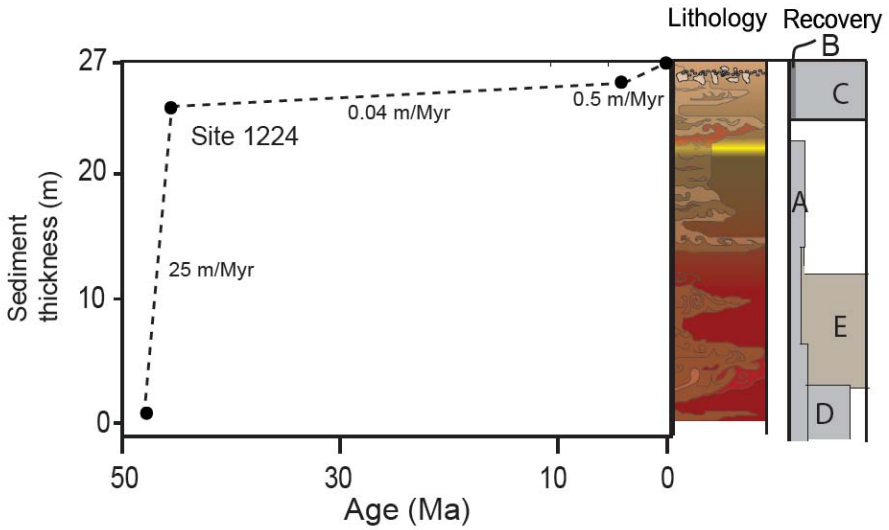

Figure 6.22. Sediment burial rates at Site 1224.

6.3.2 Basement at Site 1224, Petrography and Igneous geochemistry.

Basement petrography and geochemistry for ODP Site 1224 is discussed in greater detail by Stephen et al., (2003), Haraguchi and Ishii (2006), Lustrino (2006), and Paul et al., (2006). ODP Leg 200 recovered basalt in Holes 1224A, D, E and F with ~58.14 cm of core recovered from ~191 m of penetration. Hole 1224F penetrated 146.5 m into basement (Figure 6.21). Basement at Site 1224 comprises ~ 54 % pillow lavas and ~ 42 % massive flows. The remaining lithologies consist of breccias, associated with the alteration of glassy pillow margins and fracture zones. Basement is

composed of aphyric, holocrystalline to hypocrystalline basalt with rare olivine that is pseudomorphically replaced by a combination of saponite and iron-oxyhydroxide. Site 1224 basement is subdivided into 3 Igneous Units based on geophysical trends (including porosity, density), petrographic variation and geochemical trends. Unit 1 (0-35 msb) consists of two massive basalt flows with rare vesicles. Chill margins and degassing structures at the top of the lower flow, relatively high alteration compared to the other Units, and the change in density and porosity all define Unit 1. Unit 2 (35-106 msb) is composed of thin flows and pillow fragments. The abundance of fractures, breccias, and pillow lavas are reflected by the low recovery (~15%) of this Unit. Lithological Unit 3 (106-135 msb) consists of thick flows with alternating thin flows and pillow lavas with slightly higher recovery (~21%) than Unit 2. Alteration halos and fractures are present in all units however; the less altered Units 1 and 3 have a higher recovery rate.

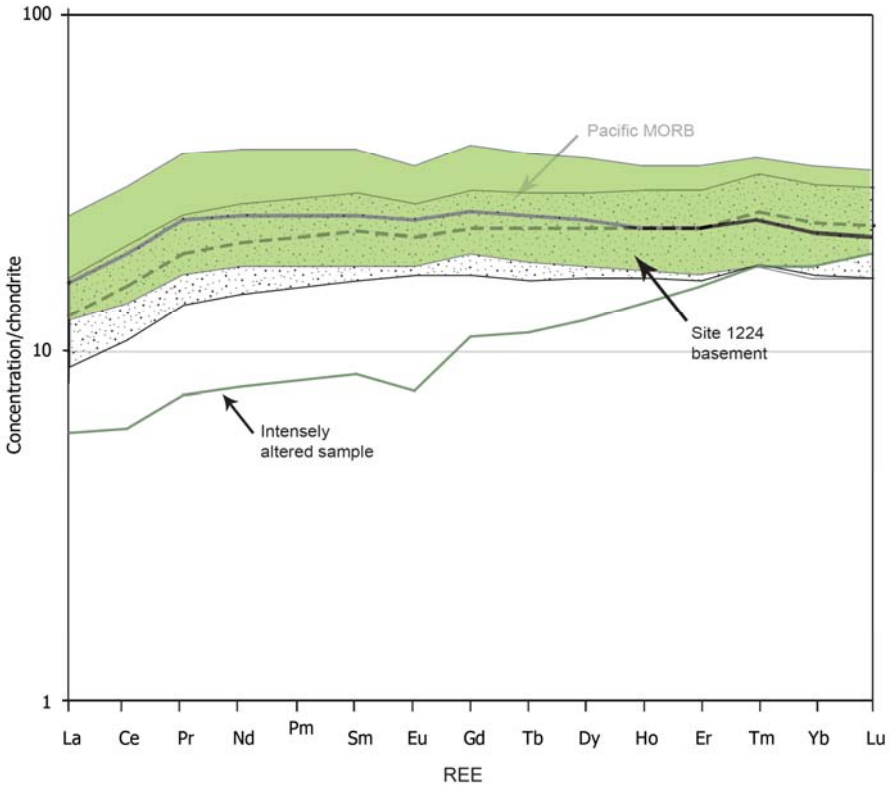

Figure 6.23. Chondrite normalised REE patterns for Site 1224 basement. Average composition is shown with bold black line. The composition of an altered sample 200-1224F-2R-2, 82-92 cm is shown with a green line. Chondrite-normalization factors from Taylor and Gorton (1977). Pacific MORB after Janney and Castillo, (1997). Pm is not analysed.

Geochemical studies of Site 1224 Basement carried out by Lustrino (2006) and Haraguchi and Ishii (2006) are based on microprobe analyses of primary mineral

phases and XRF analyses on a suite of the least altered whole rock samples. Samples were selected on the basis of low LOI and petrographic observation. Within these samples, SiO_2 ranges from 48-52 wt % and MgO varies from 5-7 wt %, both of which are typical N-MORB compositions (Stephen et al., 2003). A plot of chondrite normalised REE for Site 1224 basement (Figure 6.23) mirrors that of Pacific MORB, albeit slightly LREE elevated compared to average Pacific MORB. One extensively altered sample (200-1224F-2R-2, 82-92 cm) is strongly depleted in LREE implying extensive replacement of primary phases by low temperature secondary minerals, for example saponite and celadonite. A plot of immobile elements Zr, Nb, and Y on a Zr-Nb-Y ternary discrimination diagram (Figure 6.24) place Site 1224 basement compositions within the N-MORB field.

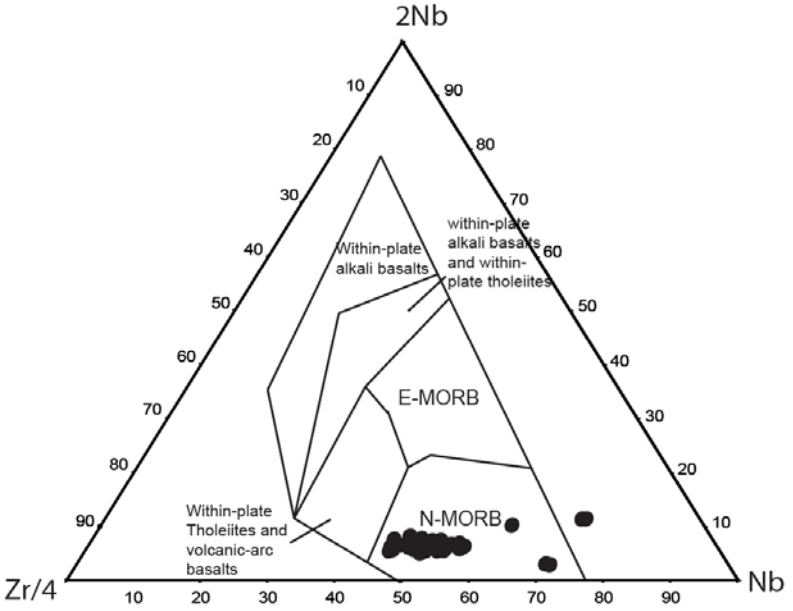

Figure 6.24. Zr-Nb-Y discrimination diagram for basalts at Site 1224. Whole rock data sourced from Stephen et al., (2003), Haraguchi and Ishii (2006), Lustrino (2006). Field data are after Meschede (1986).

Plots of Zr vs Ti Al_2O_3 vs. Fe_2O_3, and Fe_2O_3 vs. Mg# (Figure 6.25) indicate that significant fractionation has occurred at Site 1224, because Zr and Ti are elevated above the field for typical MORB. Evidence for fractionation is supported by elevated Ti and Zr when compared to Site 896, which is typical of a depleted MORB at the Costa Rica Ridge and all igneous groups, especially Group 3 are elevated. Although major element plots in figure 6.25 supports evidence for fractionation, the extent of low temperature alteration means that the interpretation of primary igneous origins of site 1224 basalts from major elements are used with caution.

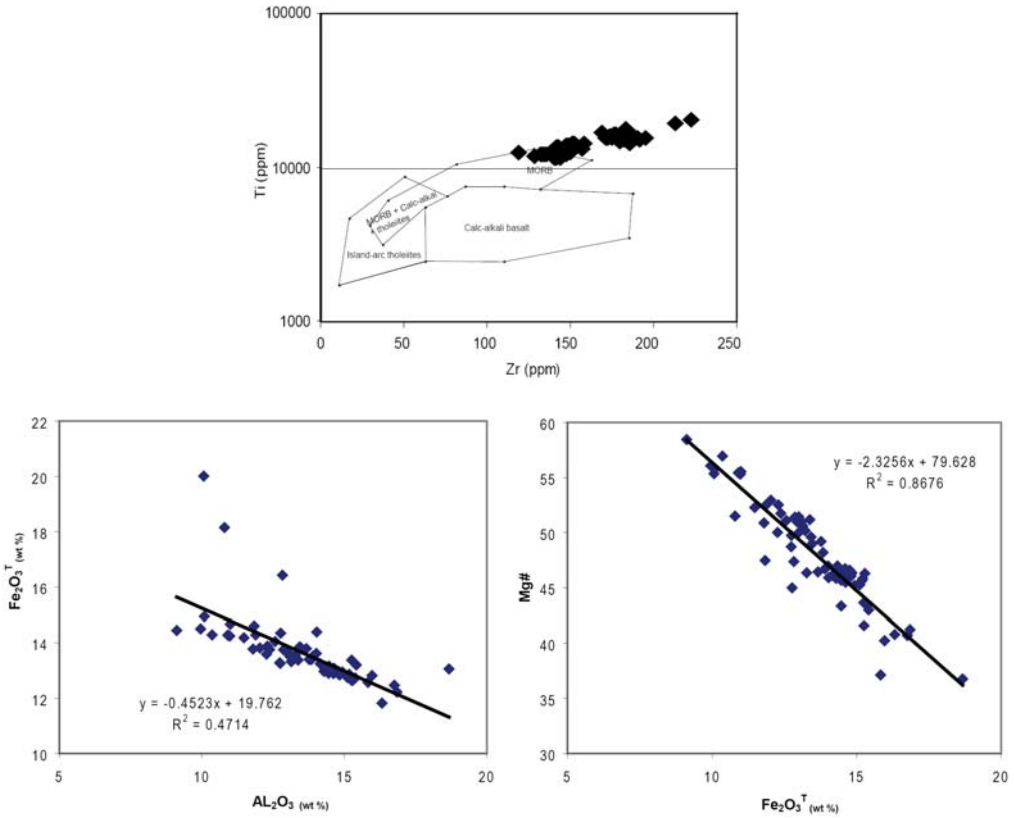

Figure 6.25. Zr vs. Ti, Al_2O_3 vs. Fe_2O_3, and Fe_2O_3 vs. Mg# for Site 1224 basalt. Zr vs. Ti plot outside the expected range for basalts. Extensive fractionation within Site 1224 basalts has resulted in elevated Zr and Ti. Whole rock data sourced from Stephen et al., (2003), Haraguchi and Ishii (2006), Lustrino (2006), and Paul et al., (2006). Field data after Pearce and Cann, (1973); Pearce (1982)

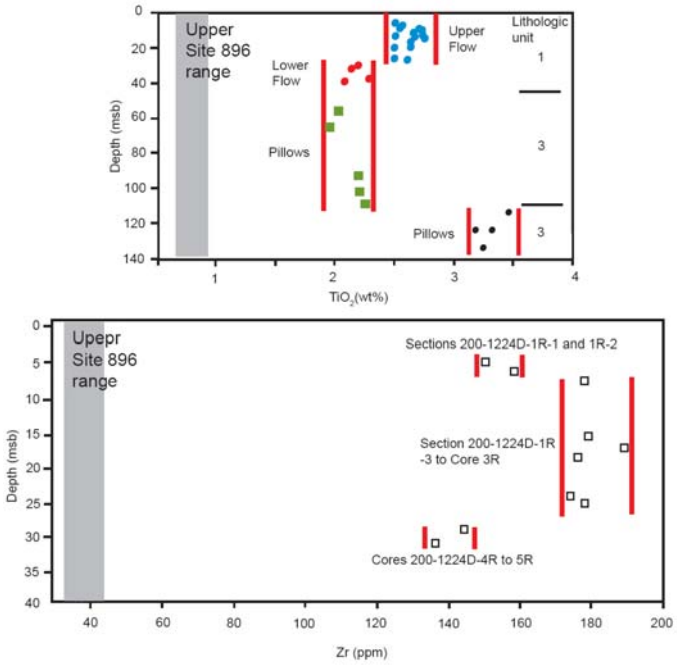

Figure 6.26. TiO_2 and Zr vs. Depth for Site 1224 basalts shown with Site 896. 1224 data after Stephen et al., (2003), 896 Data after Cann et al., (1983); Aderson et al., (1985).

6.3.3 Alteration

The characteristic alteration features for ODP Site 1224 are described in detail by Stephen et al., (2003) and Paul et al. (2006). The basement at Site 1224 is slight to moderately altered with a secondary mineral assemblage of celadonite, saponite, Fe-oxyhydroxides, carbonate, secondary sulphides, quartz and phillipsite. These secondary minerals occur throughout Site 1224 and they are concentrated in veins and alteration halos. In the groundmass, plagioclase and clinopyroxene are partially altered (<1%) to iron-oxyhydroxides, saponite and calcite. Fe-Ti oxides show signs of minor oxidation. Olvine is almost always replaced by saponite. Celadonite predominantly occurs in the uppermost 15 m of the core filling vesicles, veins and interstitial areas within the groundmass. Below 15 m, Celadonite occurs as a mixture (overprinted?) with other phases, such as iron-oxyhydroxide and saponite forming similar alteration features. Figure 6.27 shows the typical range of alteration styles present at Site 1224. Figure 6.27 A is an example where alteration has not been extensive, with only the early celadonite/saponite halo present. Figure 6.27 B is an example of more pervasive alteration under oxidizing conditions, with the intense red/orange halo overprinting an earlier saponite/celadonite halo.

Halos cover ~10% of the recovered core and they range in colour from dark grey/green (90% of halos) to brown (10% of halos). In dark grey halos, interstitial material is replaced by saponite, celadonite and rare Fe-oxyhydroxides to a low level (~5%). Brown halos are more pervasively altered (10-20%) to Fe-oxyhydroxides, celadonite and saponite. Most halos at Site 1224 are typically associated with multiminerallic veins of saponite, celadonite, calcite, Fe-oxyhydroxides, minor secondary sulphides and rare phillipsite. All vein minerals and vein abundances are relatively evenly distributed within Units 1 and 3 except for celadonite, saponite, and pyrite which decrease in abundance down-hole. Unit 2 has a greater abundance of vein material, much of which is bordering on incipient brecciation. Veins make up ~0.73% by volume of the core and there are approximately 18 veins per metre of recovered core. Saponite and celadonite by volume make up the majority of vein minerals, each contributing 32% of the total vein material. Iron-oxyhydroxides and sulfides contribute 16 % and 15 %, respectively, and carbonate makes up 5% of the total vein material.

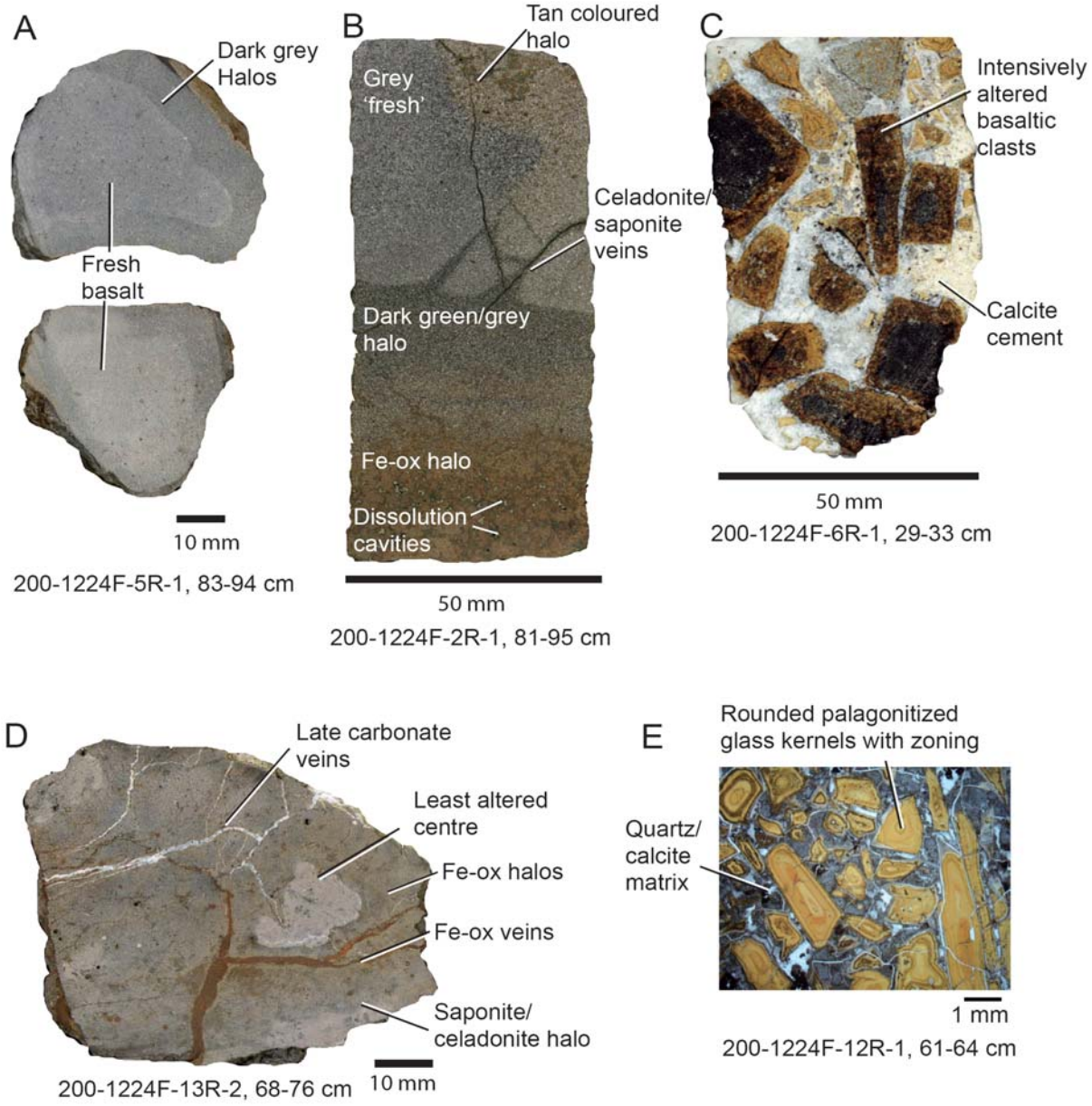

Figure 6.27. Range of alteration styles encountered at Site 1224. A) Relatively grey fresh basalt cores with a dark grey/green alteration halo. B) Complex alteration assemblage with an intense dark orange/red halo close to the vein (bevelled off during coring) with an overprinted dark grey/green halo that extends along celadonite/saponite filled veins. Lastly there is a tan-coloured halo, possibly saponite/iron-oxyhydroxide. The intensely altered zone appears to have dissolution cavities. C) Basalt clastic breccia with highly altered basaltic clasts cemented by calcite. D) Fine grained basalt with two generations of fracturing that overprint. Complex halos are bound by the earlier iron-oxyhydroxide veins. E) Example of a hyaloclastite with zoned, rounded palagonitized glass fragments. Modified from Paul et al. (2006) and Stephen et al., (2003). Fe-ox = iron-oxyhydroxides

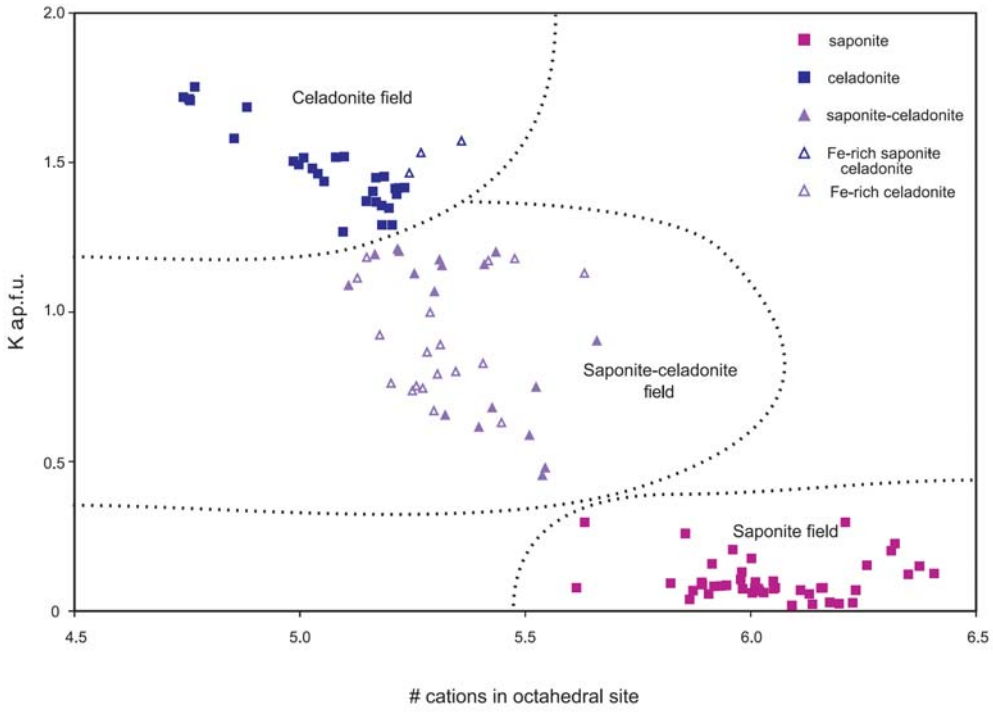

Figure 6.28, Octahedral site occupancy (Fe + Mg + Mn + Ti + Al^{vi}) versus K atoms per formula unit (a.p.f.u) content for saponite, celadonite, and saponite-celadonite mixtures ± Fe-oxyhydroxides. This plot is used to discriminate between saponite, celadonite, and saponite-celadonite data from a range of DSDP and ODP drill sites and ophiolite studies. Figure sourced from Paul et al., (2006).

The presence of celadonite, saponite-celadonite and saponite was confirmed by comparing the octahedral site occupancy (Fe + Mg + Mn + Ti + Al^{vi}) with K atoms per formula unit (Figure 6.28). Samples of clay minerals from Site 1224 plot on the saponite, celadonite-saponite, and celadonite fields (Paul et al., 2006). Vesicles are typically filled with saponite, celadonite, calcite and Fe-oxyhydroxides they make up <1% of the core (Paul et al 2006). Breccias predominantly consist of hyaloclastites and pillow margin fracture breccias. They occur throughout Site 1224 but they are most ubundant in Unit 3. The hyaloclastites are composed of numerous sub angular to sub rounded glassy shards that vary in size from 0.5 mm to ~3cm (Figure 6.26 E). The glass is strongly altered to palagonite with substantial zoning (Figure 6.26 E). Fragments of highly altered basaltic groundmass and chilled margins may be present. The cement is predominantly made up of calcite ± quartz.

6.3.4 Chemical changes and summary

The chemical changes associated with cold seawater hydrothermal alteration have been calculated by Paul et al. (2006) using a selection of sample pairs. Their study indicates that rocks with halos show enrichments of K_2O, FeO^T, MnO, CO_2, and Rb and minor enrichments of SiO_2, MgO, CaO and Na_2O relative to the non haloed sample pair (Figure 6.29).

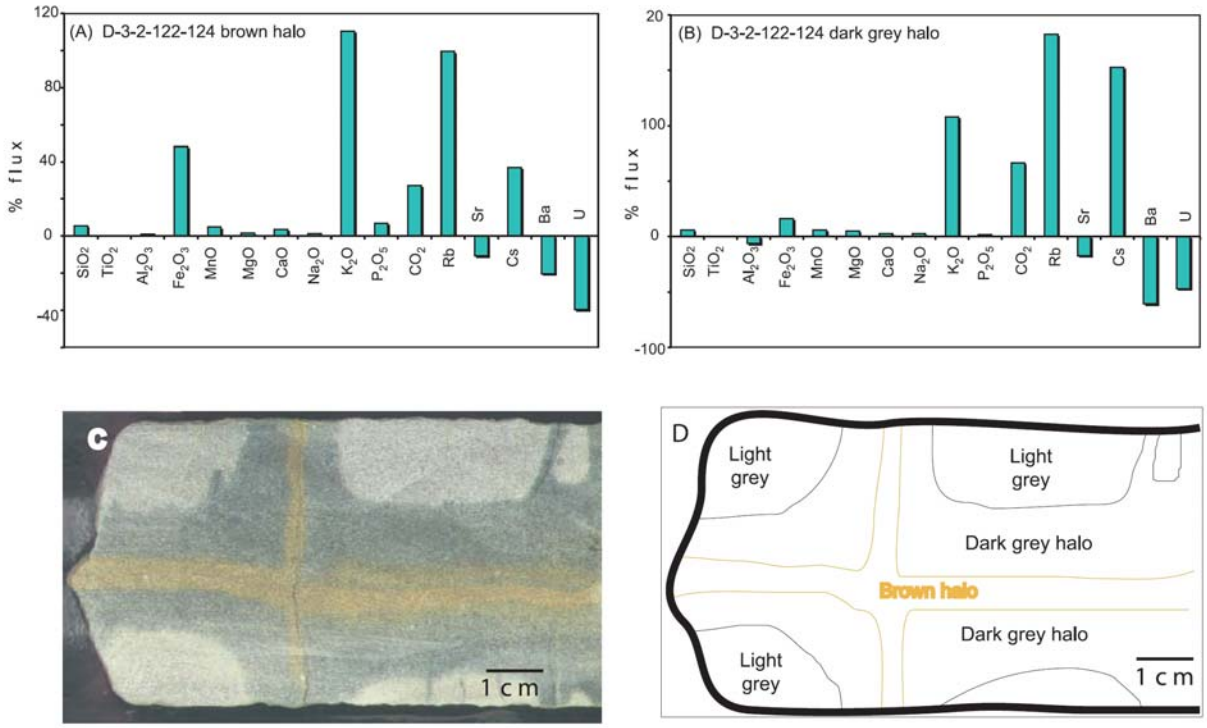

Figure 6.29. Percent flux of major element oxides, CO_2, Rb, Sr, Cs, Ba, and U for (a) brown and (b) dark gray haloes illustrated in (c) close up photo of sample 200-1224D-3R-2-122-124 cm. d) halo zones which calculated changes are based on (labelled 'brown 'and 'dark gray' in Figure 8d and non-haloed 'light grey' areas). After Paul et al. (2006).

Brown halos exhibit the greatest increases in K_2O and FeO^T. These increases broadly reflect the incorporation of secondary minerals; celadonite, Fe-oxyhydroxides, saponite, and carbonate into the host rock. Paul et al. (2006) consider REE and High field strength (HFS) elements to be immobile, suggesting that variation in Cu and Ni reflect the distribution of primary sulfide phases. Because these calculations are based on a non-haloed counterpart, it is likely that their results represent minimum values due to the fact that the non-haloed 'fresh' rock have undergone minor levels of alteration. Overall, Paul et al. (2006) conclude that the chemical changes reflect the formation of celadonite, iron-oxyhydroxide, saponite and

carbonate and many elements with low net gains and losses were simply remobilized. Gains in K and Fe indicate supply by seawater and other basalts respectively.

The relative timing of secondary mineral paragenisis proposed by Paul et al. (2006) is based on detailed petrographic studies of mineral assemblages, and cross cutting relationships between vein minerals, and halos. The nature and extent of low temperature seawater alteration at Site 1224 is very typical of upper ocean crust and it is similar to the alteration of other sites in this study. Initial emplacement of Fe-oxyhydroxides and celadonite formed veins and dark grey halos under oxidizing conditions at low temperatures. This is succeeded by a decrease in the oxidation potential of seawater where the system is more rock dominated and reducing. (Andrews, 1977 and Seyfried et al., 1978). Here, saponite which cross cuts veins, and overprints the earlier assemblages. Uncommonly, saponite can be contemporaneous or rarely earlier than the celadonite and iron-oxyhydroxides, suggesting complex fluid chemistry, perhaps as the result of reopening stages with increased fluid flow. Carbonate forms late stage veins which cross cut earlier veins. In addition earlier veins may be re-opened and filled with carbonate and secondary sulphides forming multi-minerallic, zoned veins. Paul et al. (2006) point out that the massive flow (Unit 1) that caps the basement at Site 1224 may have inhibited the ingress of seawater into underlying crust, thus inhibiting hydrothermal alteration. A similar lithostratigraphy is reported at Site 1256, which shows similarly low extents of alteration.

6.4. Site 1243

Site 1243 is located in the eastern equatorial Pacific, west of the East Pacific Rise at 5°18.0541'N, 110°4.5798'W for Hole 1243 A and 5°18.0543'N, 110°4.2544'W for Hole 1243 B (Figure 6.30). Site surveys indicate that Site 1243 is on a plateau in close proximity to a 100 m deep trough (Figure 6.31). At a water depth of 3882 m, Site 1243 penetrates 117 m of sediment and 87.1 m of basement (Hole 1243 B).
An estimated age of 10-12 Ma for Site 1243 formation is based on spreading rate of 141 mm/yr and an East Pacific Rise subsidence curve (Orcutt et al., 2003). This age is consistent with palaeomagnetic studies and microfossil evidence from the near basement section of nearby Hole 851, drilled by ODP Leg 138 (Psias et al., 1995; Shackleton et al., 1995).

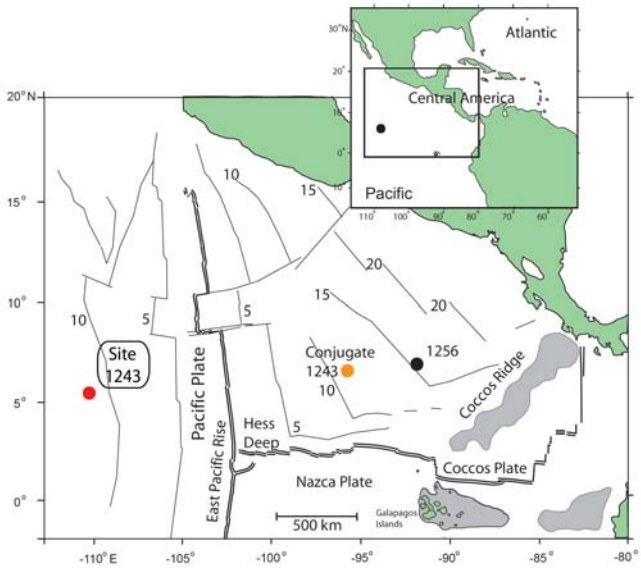

Figure 6.30. Location of Site 1243, including its estimated counterpart location and Site 1256.

Important differences between these sites need to be considered before any parallels can be drawn, Site 1243 differs from Site 1256 in that it has thinner sediment cover, and lacks the ponded lava flow and inflated flows of Site 1256.

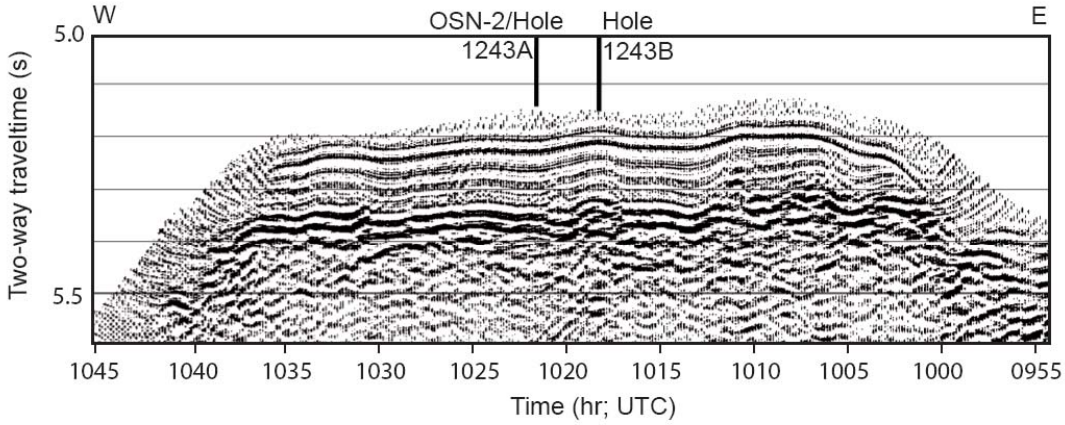

Figure 6.31. Seismic profile for Site 1243. Data is migrated and includes the locations of Holes 1243A and 1243B. OSN-2 = Ocean Seismic Network-2. UTC = Universal Time Coordinated. Modified from Orcutt et al., (2003).

However, despite these differences its provenance makes this site an important addition to the suite of fast spread sites used in this study to characterise hydrothermal alteration formed at fast spreading rates. As with Sites 1224 and 843, a representative suite of samples were analysed and described in terms of hydrothermal alteration, therefore a brief summary based on previous work by Orcutt, Schultz., Davies., et al, (2003) and Moberly, (2003) is provided here.

6.4.1 Sea floor sediment, stratigraphy and sedimentation rates

Approximately 117m of sediment was cored with less than 1 % total recovery. The only successfully recovered portion of the sedimentary overburden was Core 203-1243B-1R. This consists of mud slurry and nannofossil ooze, containing coccoliths and a low percentage of planktonic foramanifers, discoasters, radiolarians, iron oxide and glass fragments. Sediment recovered from interval 203-1243B-2R-1, 46-49 cm include an oblate shaped white limestone with brown clay mineral veins. At interval 203-1243B-10R-2, 66-71 cm, thin vestiges of a pink to grey limestone containing palagonite grains, black specks, relict foramanifers and glassy rinds were observed. Units of basalt above and below the Section 203-1243B-2R-1 limestone and the presence of glassy rinds in the limestone imply that the limestone is an interpillow sediment (Orcutt et al., 2003). The limestone unit at section 203-1243B-2R-1 contains abundant prismatic shaped pore spaces and Orcutt et al., (2003) suggest that these represent dissolved anhydrite crystals which must have formed in warmer

environments during digenesis. Shipboard petrographic analyses suggest that up to 6% of the limestone fragment may have been composed of anhydrite. However, no anhydrite was identified in thin section or by XRD. In addition, no record is made of the presence of anhydrite, past or present in the basaltic units.

Sedimentary stratigraphy for Site 1243 is almost non existent (Figure 6.32), with only the lowermost portion of material recovered. This portion does, however, provide the sediment/basement contact, and, using preserved microfossils, provides the age at which sedimentation began (10-12 Ma) (Orcutt et al., 2003).

The rate of sedimentation is inferred from the age of initial sedimentation, and thickness. The average burial rate is 10.6 m/m.y, however a lack of recovery for a large portion of sediment, precludes any detailed investigation of sedimentary rates.

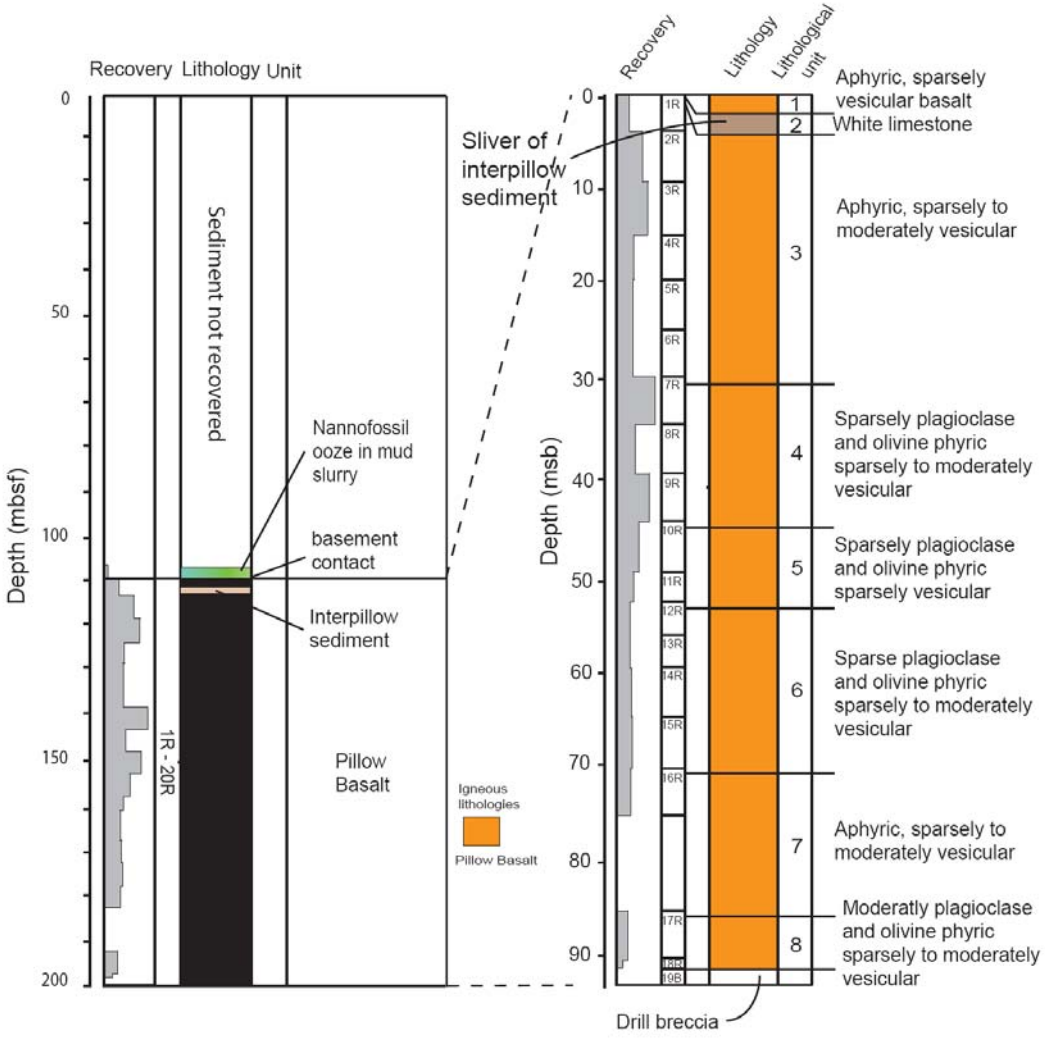

Figure 6.32. Lithostratigraphy of Site 1243.

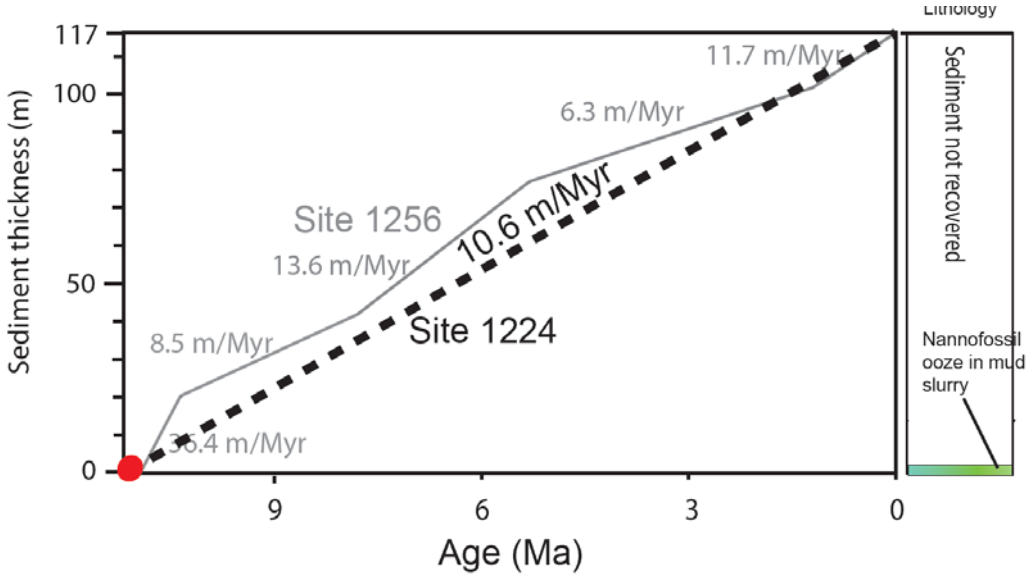

Figure 6.33. Sedimentary burial rate at Site 1243. Burial rate is inferred from a biostratigraphic date from sediment/basement contact (Orcutt et al., 2003). Site 1256 burial rates up to the age of Site 1243 is shown for comparison.

However, when the inferred burial rate at Site 1243 is compared to the burial rate at Site 1256 (Figure 6.33), sedimentary rates are broadly comparable. This implies that Site 1224 has undergone a similar burial history to Site 1256.

6.4.2 Basement at Site 1243, Petrography and Igneous geochemistry.

The sediment/basement interface was recovered in Core 203-1243B-2R at 108.6 mbsf. Sediment and basalt continued to be recovered to a depth of 117 mbsf, below which basalt with only minor inter-pillow sediment was recovered. Drilling continued to a total depth of 195.3 mbsf or 77.8 msb. Recovery ranged from 1% to 63% (Figure 6.31). The basement section consists entirely of pillow lavas that are divided into 8 units based on petrographic description and shipboard geochemistry. Units 1, 3, 4, 5, 6, 7, and 8 are basaltic whereas Unit 2 is an interpillow sediment (see limestone, Section 203-1243B-2R-1, discussed earlier). Units at Site 1243 are broadly similar, only slight textural changes and variability in olivine content distinguishes them. See Orcutt, et al., (2003) for detailed descriptions of Site 1243 igneous units.

Shipboard geochemical analyses (ICP-AES) were carried out for 9 samples of pillow interior In addition, shore based analyses of whole rock basalts were carried out to obtain major, trace, REE, and Sr-isotopic compositions (Orcutt et al., 2003).

Figure 6.33 indicates the chondrite normalised REE pattern for Site 1243 basalts. One group exhibits slight REE depletion compared to MORB and a second group, is LREE enriched. A discrimination plot that compares immobile elements Ti and Zr (Figure 6.35) and a ternary Zn-Nb-Y plot (Figure 6.36) indicate that Site 1243 basalts can be split into two groups: one alkalic and the other tholeiitic.

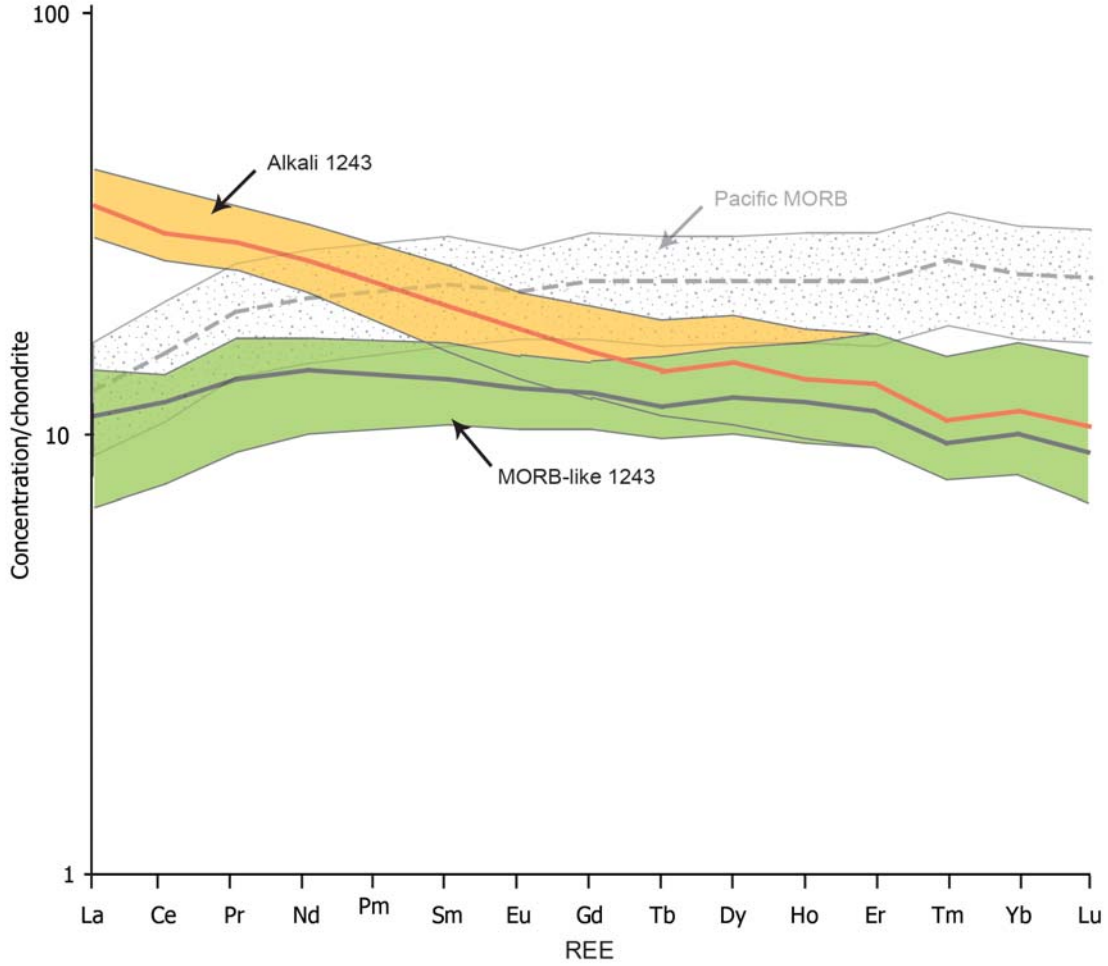

Figure 6.34. Chondrite normalized REE patterns for Site 1243 basalts. Bold lines indicate average REE patterns for the two geochemically distinct groups. Data sourced from Orcutt et al, (2003). Pacific MORB data sourced from Janney and Castillo, (1997). Pm is not analysed.

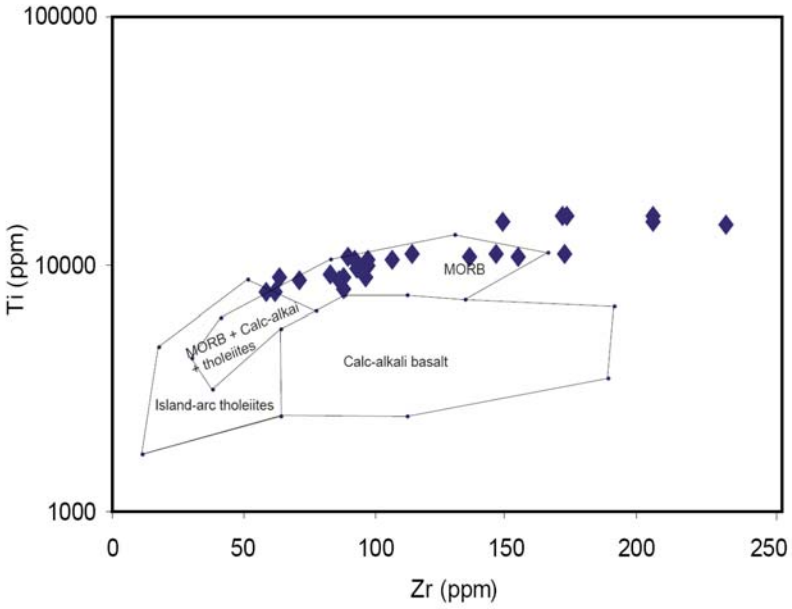

Figure 6.35. Plot of Zr vs. Ti. Site 1243 basement, with most samples plotting within the expected range for MORB (field after Pearce and Cann, 1973 data from Pearce, 1982). Site 1243 data sourced from Orcutt et al., (2003).

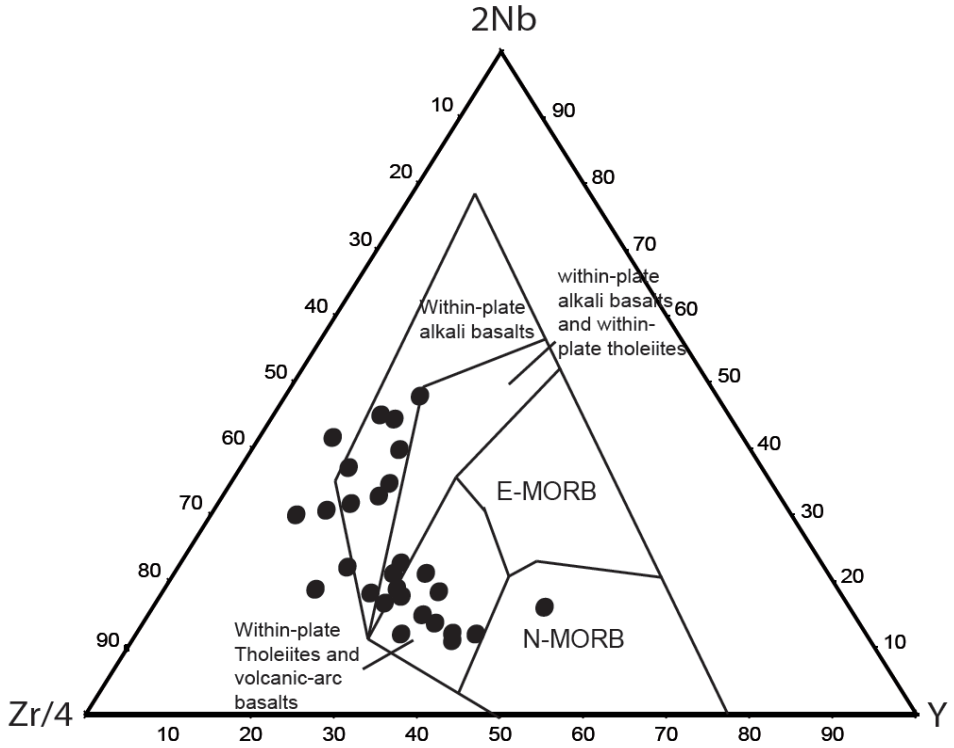

Figure 6.36. Zr-Nb-Y discrimination diagram for basalts at Site 1243. Site 1243 data sourced from Orcutt et al., (2003). Field data are after Meschede (1986).

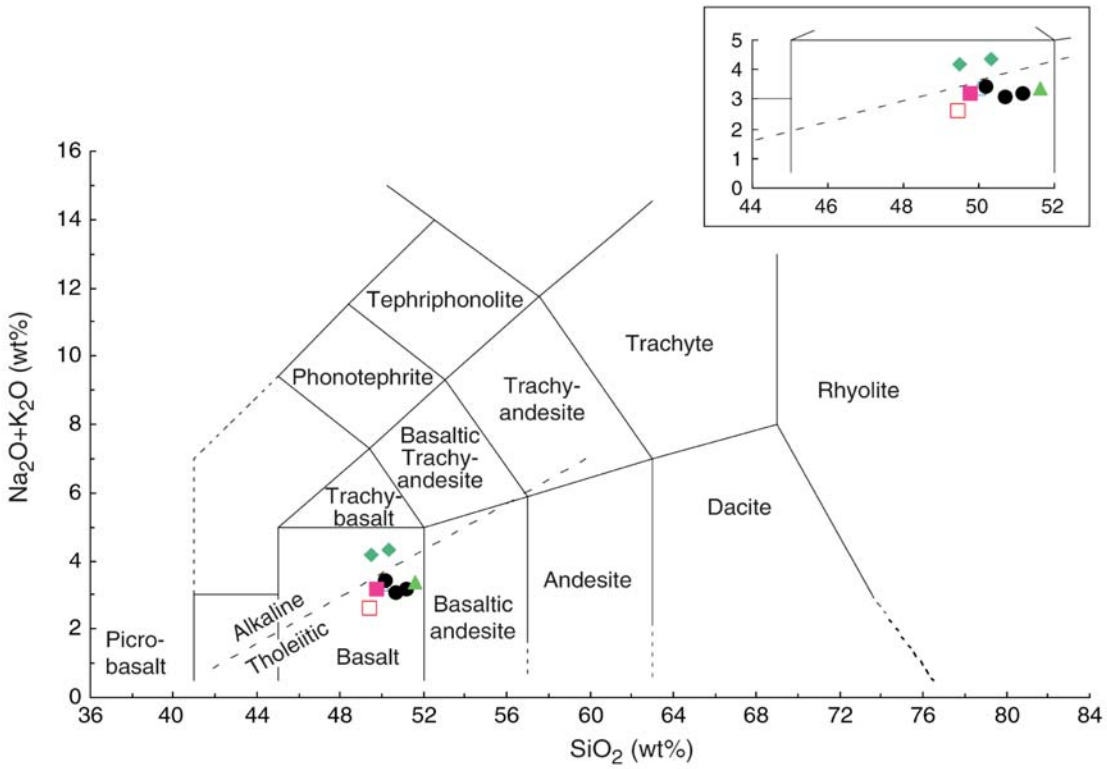

Figure 6.37. Hole 1243B igneous rock composition on the Na2O + K2O vs. SiO2 (in weight percent) classification diagram (Le Bas et al., 1986). Alkalic and tholeiitic basalt fields are separated by the Macdonald and Katsura (1964) line. Blue triangle = Unit 1, black circle = Unit 3, green diamond = Unit 4, green triangle = Unit 5, purple square = Unit 7 red square = Unit 8.

On a discrimination plot of SiO_2 vs $Na_2O + K_2O$ (Figure 6.37), Units 1,3,5,7, and 8 are tholeiitic whereas Unit 4 is alkali. The variable chemistry of Unit 4 is further supported by high TiO_2, Ba, Zr and Nb. With the exception of Unit 4, Al_2O_3, Ti/Zr, and Ba/Sr do not vary with depth and fractionation trends are minor for Site 1243. Units 1,3, and 5 are homogenous whereas Units 7 and 8 are more differentiated (Figure 6.23). A high degree of fractionation occurs in Unit 7 as indicated in the Ti/Zr vs. Zr/Y and Ba/Sr and Al_2O_3 vs. Mg# plots (Figure 6.38). Orcutt, Schultz, Davies et al, (2003) suggest that alteration at Site 1243 is sufficiently low (See *Alteration*) that the normally mobile elements such as Ba and Sr can be considered in terms of their primary igneous compositions, and therefore the high TiO_2, Ba, Zr and Nb represent the original magmatic features of Unit 4 basalts.

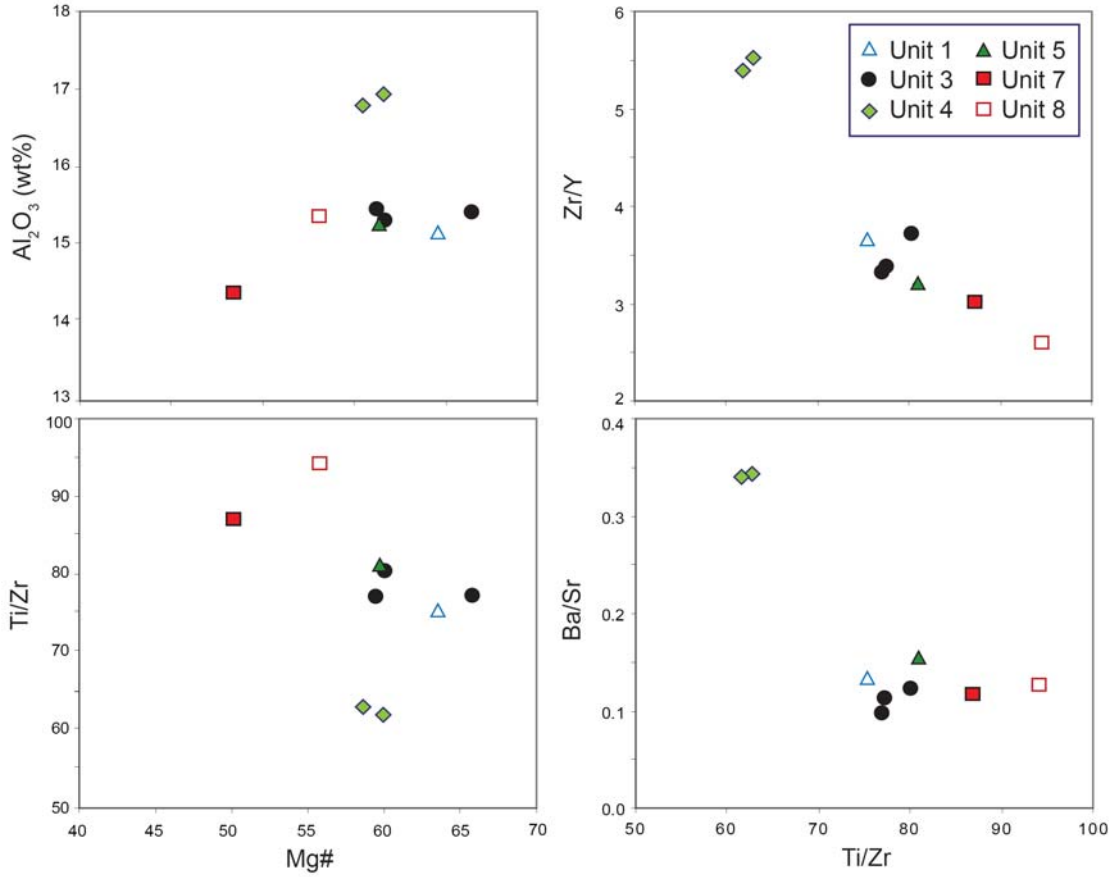

Figure 6.38. Al_2O_3 and Ti/Zr ratios vs. Mg#. These indicate that tholeiitic basalt of Units 1, 3, 5, 7, and 8 are probably derived from a similar mantle source, whereas alkalic basalt of Unit 4 are derived from an enriched mantle source. In addition Abundance ratios of Zr/Y and Ba/Sr vs. Ti/Zr are used to distinguish between tholeiitic and alkalic basalt. These ratios are sensitive to the presence of a metasomatic component in the basaltic mantle source however Ba and Sr may have been affected by hydrothermal alteration. After Orcutt et al., (2003)

Shore-based microprobe analyses of relatively fresh glass chippings by Moberly et al, (2003) distinguish 5 groups of glass, all of which are tholeittic N-MORB to enriched T-MORB. The glass chippings were recovered from a drill breccia at the base of the hole, and the chemistry suggests that the chippings are from the lower units of Site 1243.

From the shipboard geochemistry, Orcutt et al., (2003) conclude that Units 1,3,5,7, and 8 are sourced from un-evolved magmas and that the thoeiities came from a single mantle source. The alkali basalt in Unit 4 suggests that either, 1) that a small degree of partial melting occurred from the same depleted mantle source as the other units or 2), that Unit 4 represents a partial melt from a distinct enriched mantle source, such as a metasomatized mantle.

Moberly et al, (2003) comes to similar conclusions as Orcutt et al., (2003), in that the basalts may have come from two separate parental magmas, one of which may be the Galapagos plume.

6.4.3 Alteration

Typical alteration a Site 1243 is shown in Figure 6.39. Alteration at Site 1243 varies from very slight to moderate. The overall alteration at Site 1243 is slight. Alteration intensity is concentrated along pillow margins, vesicles and brecciated regions and colours vary from light grey to grey in the least altered portions to pale brown, yellow/orange /red brown halos in the fine grained pillow lobe margins, veins and vesicles. In a few sections, green/black iron-oxyhydroxide halos are common. Halos occur throughout the core with little variation with depth. Approximately 48 % by volume of the core is made up of the relatively fresh 'grey' background, whereas black/mixed and brown/red/yellow halos make up 35 % and 17 % by volume of the core respectively. Within the groundmass, alteration consists of nontronite and iron-oxyhydroxide and vesicles are filled with celadonite, saponite, iron-oxyhydroxides, zeolites and carbonates. On average there are 11 veins per metre which form 0.74% by volume of the core. Veins are filled with nontronite, saponite, iron-oxyhydroxides, zeolites and carbonates and they range from <0.1 mm to 2 mm wide.

Alteration in Unit 1 is slight with <10% secondary minerals, Alteration in Units 3 and 7 are very slightly altered with less than 10% alteration. Units 4, 5 and 6 are slight to moderately altered with ~10% to 15% alteration. In Section 203-1243B-7R-2, olivine microphenocrysts are partially replaced by brown iron-oxyhydroxide and rarely, plagioclase is partially altered to sericite. The groundmass is slightly altered to nontronite and iron-oxyhydroxide and glass is partly replaced by palagonite (Orcutt et al., 2003). Unit 8 is similarly altered, but alteration halos are yellow-orange in colour, reflecting variation in the Iron-oxyhydroxide content in the secondary mineral assemblages.

Brecciation is limited to in-situ fracturing of glassy margins for 0.13 % of the recovered core. Because recovery of the core is only ~25% of the total penetration, recovery may be bias towards more competent material, therefore a proportion of the breccias at Site 1243 may be unaccounted for. In comparison Site 1256 recovered

13.5% breccias. However overall recovery is better at Site 1256 suggesting that a greater proportion of the breccias were recovered. Relatively comprehensive wire-line logs using Triple-combo and formation-micro-scanner tools obtained high quality log data (Orcutt et al., 2003), therefore Core log integration may allow a more quantitative assessment of downhole lithology.

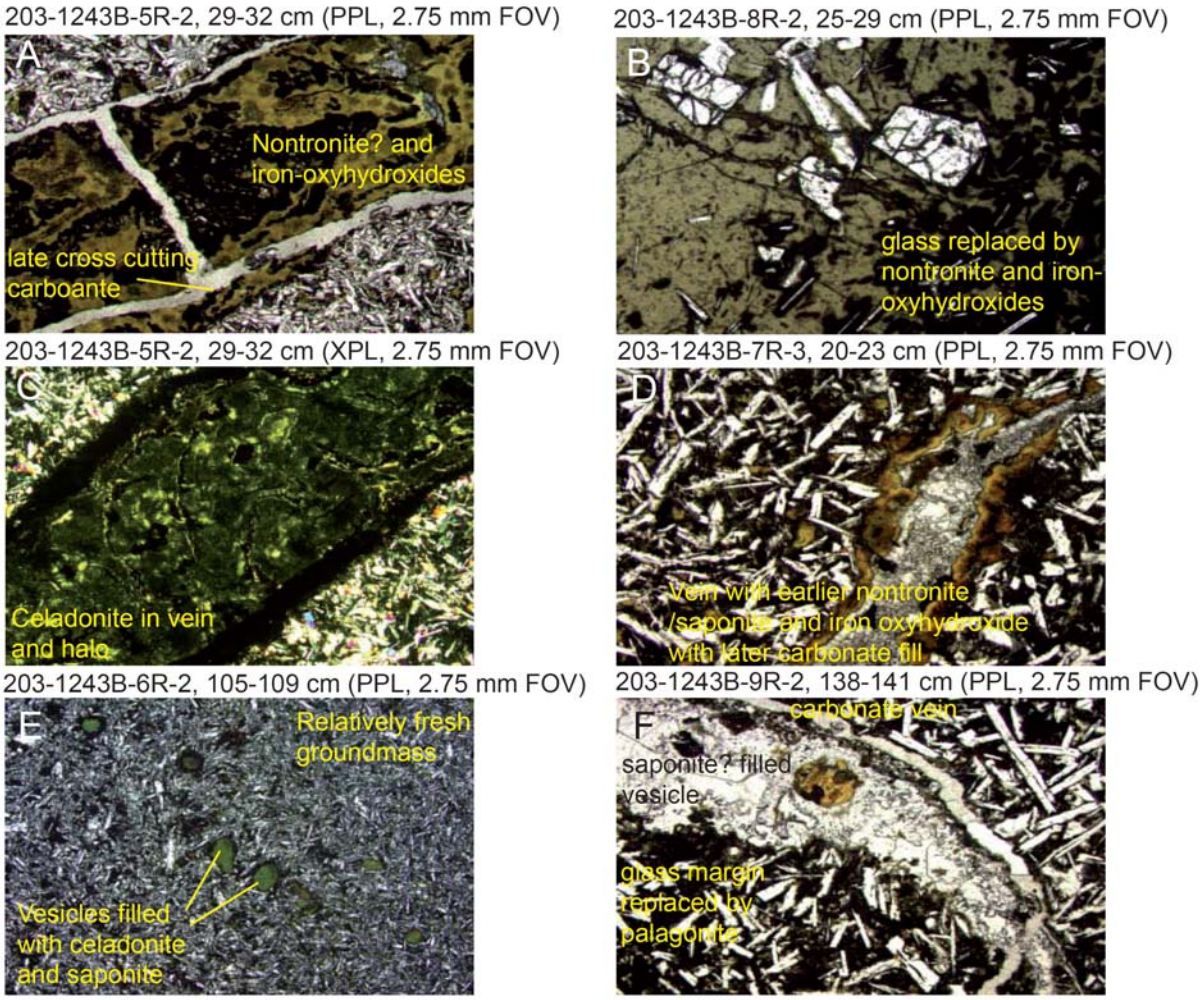

Figure 6.39. Alteration styles at Site 1243. Photomicrographs after Orcutt et al., (2003).

Loss on Ignition (LOI) at Site 1243 is typically less than 0.9 wt% but it ranges from 0.1 to 2.7 wt% which, as suggested earlier, represents slight to moderate alteration. Orcutt et al., (2003) conclude that secondary mineral paragenisis is dominated by iron-oxyhydroxide, various brown clay minerals, and late carbonates and zeolites. This assemblage is typical for low temperature seawater alteration at less than < 150^{o}C, including alteration at Site 1256.

6.5. Site 843

Site 896 was originally drilled to place a seismic observatory, part of the Ocean Seismograph Network, on the Hawaiian arch southwest of Hawaii. Site 843 would then form part of the OSN, which is used to study the earth's structure, upper mantle dynamics, ocean crust structure and seismic noise. A secondary goal at this Site was to determine the physical and chemical composition of basement at this site and its relationship with Hawaiian lavas (Wilkens et al., 1993). ODP Site 843 is located on the Hawaiian Arch, 225 km southwest of Oahu at 19°20.54'N, 159°5.68'W (Figure 6.40). At a water depth of 4407.1 m, Site 843 sits directly on top of a NW-SE trending abyssal hill and penetrates 313.4 mbsf, of which 242.5 m is sediment and 70.9m is basement.

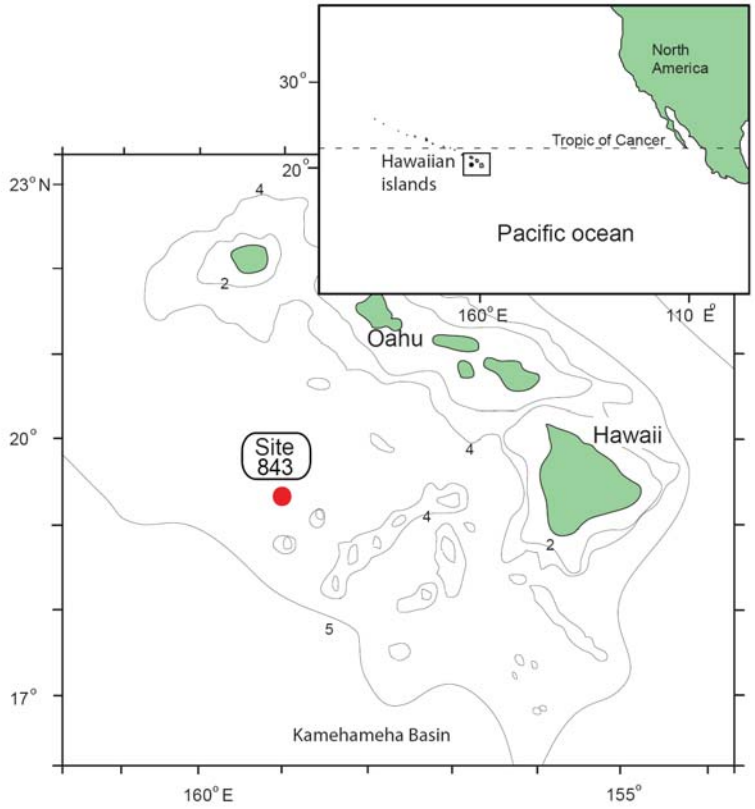

Figure 6.40. Location of Site 843.

A basement age of 94-100 Ma (Late Albian to early Cenomanian) was determined by dating nannofossils within the sedimentary succession (Wilkins et al., 1993). Palaeomagnetic studies of the basement rocks and the Hawaiian hot spot trace of

Pacific plate motion suggest a palaeolatitude of 10^{o}S for Site 843 along the Pacific/Fallaron plate boundary (Wilkins et al.,1993). Studies of the magnetic reversal patterns indicate that Site 843 formed at a fast spreading rate of ~100 mm/yr (full). Site 843 represents fast spread crust at an age that helps to fill a large gap in the sample of old oceanic crust used in this study.

6.5.1 Sea floor sediment, stratigraphy and sedimentation rates

Much of Site 843 basement was drilled without coring and only spot cores were taken at selected intervals. Intermittent sampling and a lack of seismic data preclude a detailed lithostratigraphy for Site 843. However, a summary of Site 843 stratigraphy is illustrated in Figure 6.41 using all available sample data from Wilkens et al., (1993). Sediment was recovered intermittently with no contacts (except for the sediment/basement contact), therefore no units are defined. Zeolitic and brown clays and rare ash/chert nodules were recovered from a depth of 0-121.8 mbsf. The interval from 121.8 to 228 mbsf consists of occasional red/brown chert and chalk fragments that overlie a brown nannofossil limestone.

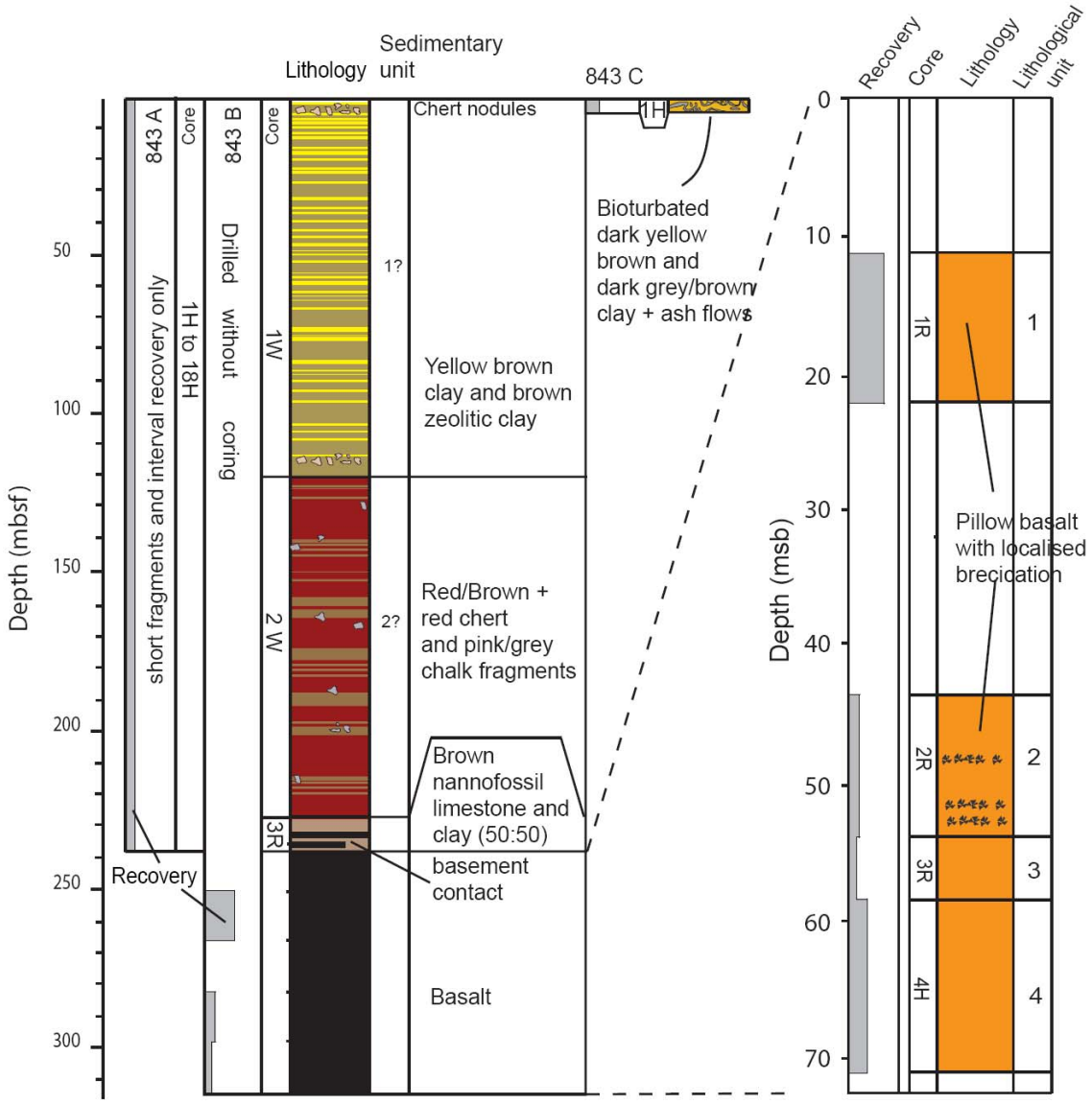

Figure 6.41. Composite stratigraphy of Site 843 showing the sedimentary overburden and basaltic basement rocks cored from Hole 843A, 843B and 843C. Data sourced from Wilkins et al., (1993).

This limestone forms the sediment/basement interface for ODP Hole 843A. A similar sediment/basement interface was recovered in Hole 843B at 242.5 mbsf. Tentative identification and stratigraphic correlation of radiolaria, ichthyolith, and palaeomagnetic data from the uppermost 40 m and the lowermost 5 m at Sites 843 and 842 were used to infer a formation age of 94-100 and a mean average sedimentation rate of ~3 m/My. A more detailed burial history is inferred in Figure 6.42 which shows sediment accumulation rates at Sites 842, 843, and nearby DSDP Site 164. Sedimentation at Sites 843 and 842 indicate initial fast rate of deposition (~10 m/My) to ~83 Ma followed by a period of slow sedimentation (~0.7 m/My)

between 83 and 68 Ma. The next 40 Ma is not dated, however sedimentation averages at ~2 m/m.y. An apparent slow period of sedimentation for 20 Ma leads to a short and rapid accumulation towards present day. This rapid accumulation coincides with the formation of the Hawaiian Arch at 4 Ma. (Clague and Dalrymple, 1987).

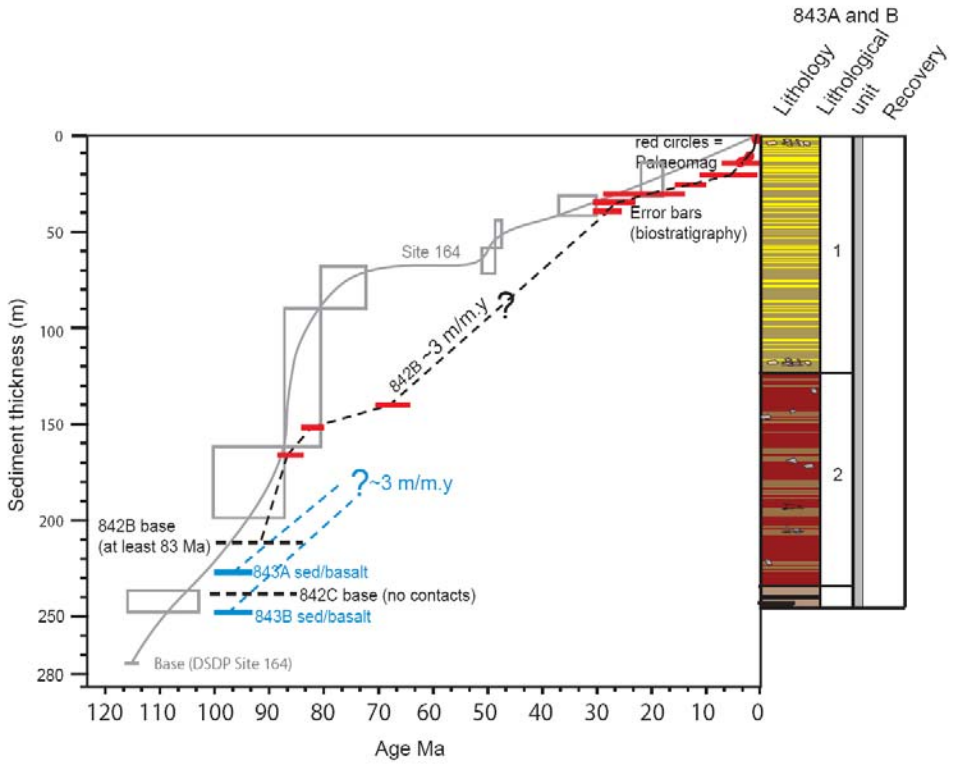

Figure 6.43. Sediment accumulation rates for Site 843. A more detailed sedimentary history is inferred from nearby Site 842 because it retains more comprehensive biostratigraphic dates. Data sourced from Winterer, Firth, Bender et al. (1993) and Edward, Ewing, Douglas et al. (1973).

6.5.2 Basement at Site 843, Petrography and Igneous geochemistry.

A more exhaustive description of the petrography and primary geochemical trends at Site 843 is discussed in Dziewonski et al., (1992) and King, et al, (1993), respectively This section serves as a summary of work relevant to this study. In addition, conclusions based on samples recovered at Site 843 are limited because Site 843 was spot cored.

Basement recovered at Holes 843A (3 m) and 843B (70m) is highly fractured and it had been subjected to slight to moderate alteration. All recovered basalts are almost aphyric (<0.1% phenocrysts) with only few vesicles that are largely contained

within the pillow margins. The groundmass ranges from microcrystalline to cryptocrystalline and it is composed of plagioclase, clinopyroxene, accessory iron oxides and rare olivine. Only four igneous units at Site 843 were recovered principally due to limited coring and these are defined by textural differences and margins. Unit 1 is holocrystalline and dark grey whereas Unit 2 is slightly darker grey and finer grained. The occurrence of gabbroic xenoliths distinguishes Unit 3 from Unit 2. Unit 4 also contains xenoliths but it is separated and distinguished from Unit 3 by a glassy margin (Dziewonski et al., 1992).

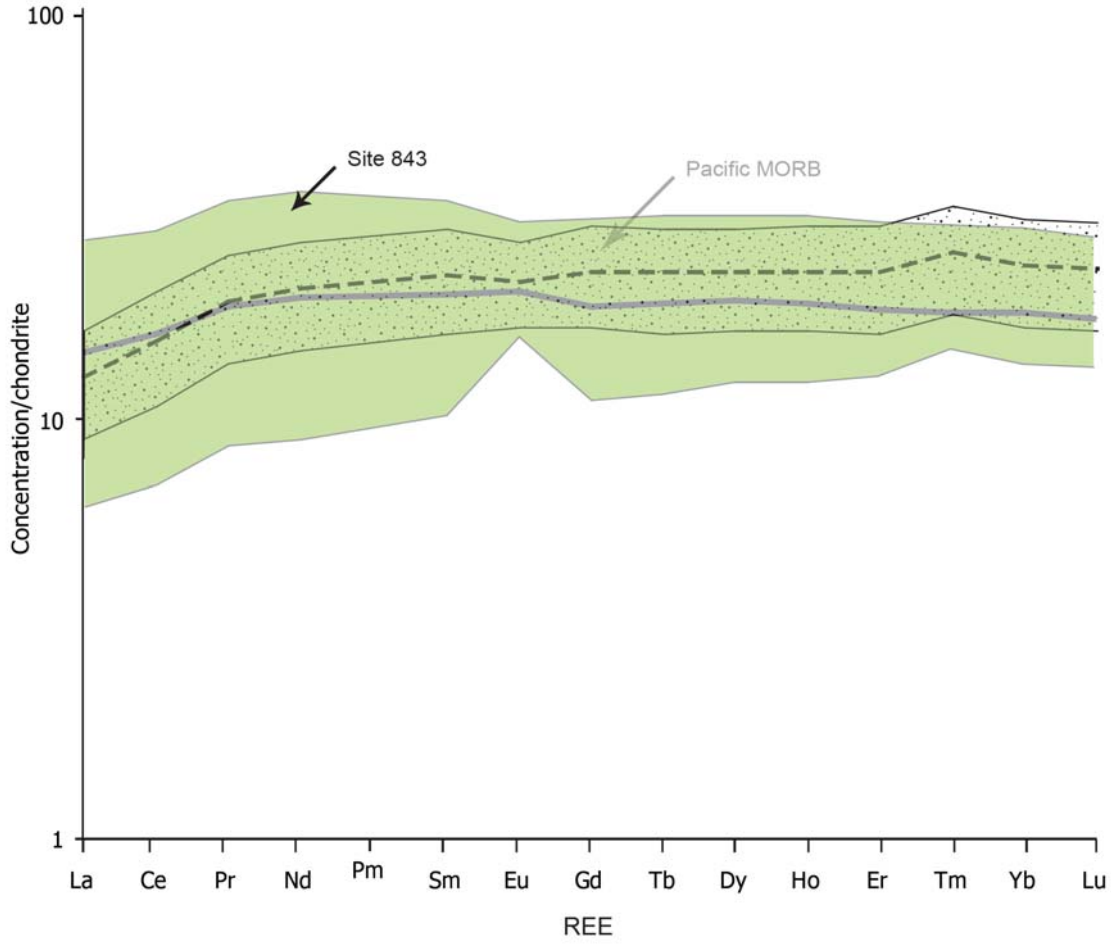

Figure 6.43. Chondrite normalized REE patterns for Site 843 basement rocks. Data sourced from this study Dziewonski et al., (1992) and King, et al, (1993). Chondrite-normalization factors from Taylor & Gorton (1977).

A range of shipboard and shore-based analyses were carried out on a selection of the most visibly fresh samples for geochemical classification (Dziewonski et al., 1992; King, et al. 1992). The least altered samples were selected based on macroscopic observation of light grey massive basalt sections (Alt, 1992) and they were analysed by XRF on board *JOIDES Resolution* for major elements, XRF at the

University of Hawaii for trace elements, and ICP-MS at Washington State University for trace and REE. Sr, Nd and Pb isotopic ratios and abundances were determined at the University of Hawaii and whole rock $\delta^{18}O$ were measured at the University of Michigan. Chondrite normalised REE patterns for Site 843 broadly overlap with the MORB field, with greater variation in LREE (Figure 6.43).

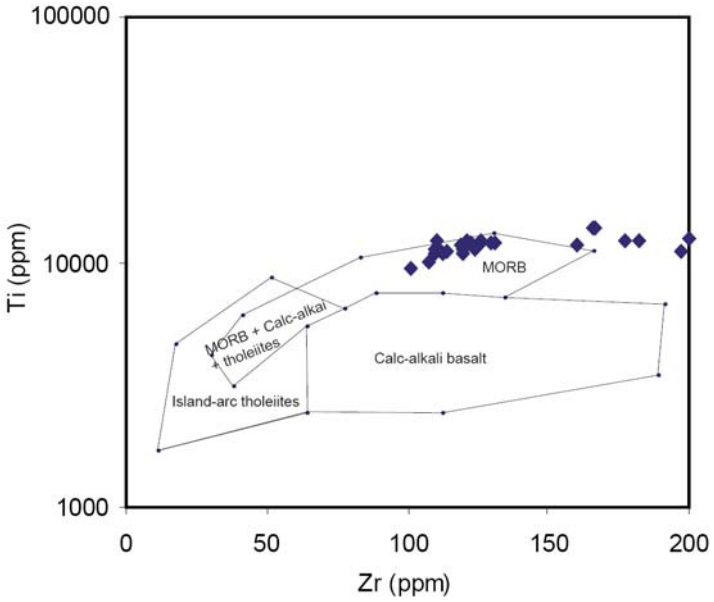

Figure 6.44. Plot of Zr vs. Ti discrimination diagram. Site 843 basalt plot within the expected range for basalts a number of basalts have elevated Zr, possibly the result of fractionation. Site 843 Data from this study Dziewonski et al., (1992) and King, et al, (1993). Field data after Pearce and Cann, (1973); Pearce (1982).

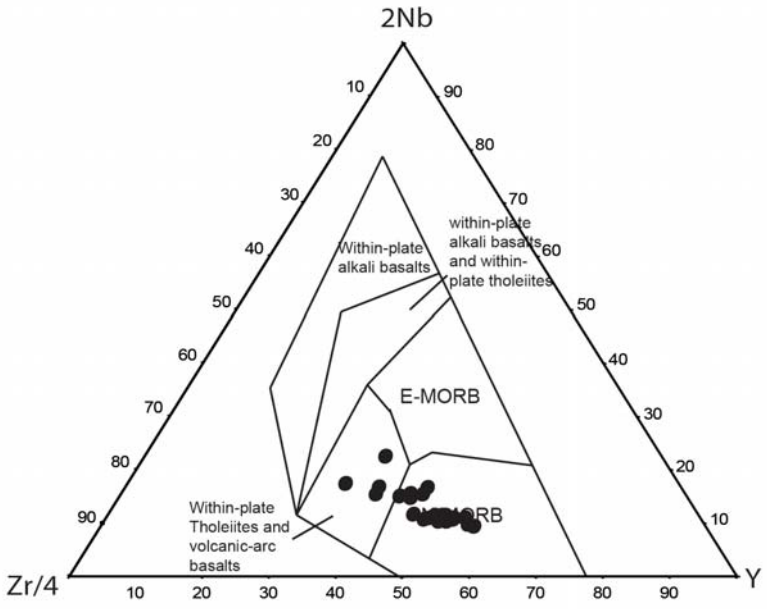

Figure 6.45 Zr-Nb-Y discrimination diagram for basalts at Site 843. Data from this study Dziewonski et al., (1992) and King, et al, (1993). Field data are after Meschede (1986).

Because Zr, Nb and Y are relatively immobile and incompatible they can be used on a variety of discrimination plots to characterise Site 843 basalts. On a plot of Zr vs. Ti (Figure 6.44) Site 843 basalts cluster into two groups one within the N-MORB field and another with elevated Zr. The samples with elevated Zr are also distinctive on a Zr-Nb-Y ternary plot (Figure 6.45), which indicates a number of basalts are evolved. A plot of Zr/Nb vs.Y/Nb (Figure 6.46) indicates that ODP Hole 843 basement represents both transitional (T)-MORB and N-MORB (King et al, 1992).

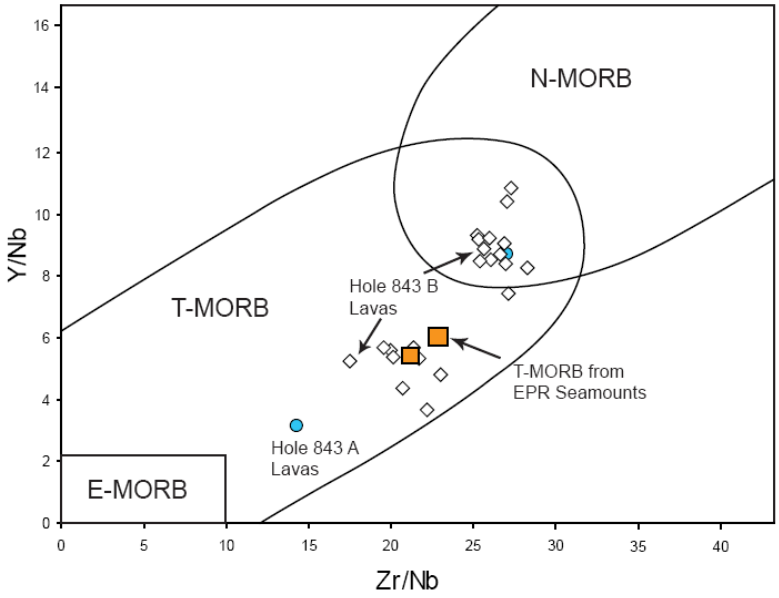

Figure 6.46. Discrimination plot of Zr/Nb vs Y/Nb with fields for E-MORb, T-MORB and N-MORB. After King et al., (1992).

However on a plot of MgO and LOI vs. K_2O (Figure 6.5.8) ODP Hole 843B basalts have greatly elevated K_2O and LOI concentrations compared to concentrations compared to N-MORB basalts (King et al, 1992). Two possible explanations for high K_2O concentration include: 1) Precipitation of clay minerals that are rich in K (e.g. celadonite) during low temperature seawater alteration, or 2) The basalts truly represent Transitional (T) –MORB (Bass, 1972). Given that the relatively immobile and incompatible elements Y/Nb vs Zr/Nb (Figure 6.47) in these samples plot in the same field as T-MORB it seems likely that a component the elevated K_2O concentration within these basalts reflects T-MORB compositions (King et al., 1992).

However, the presence of clay minerals at Site 843 (Alt et al, 1993) imply that at least some of the K_2O must be the result of low temperature seawater alteration.

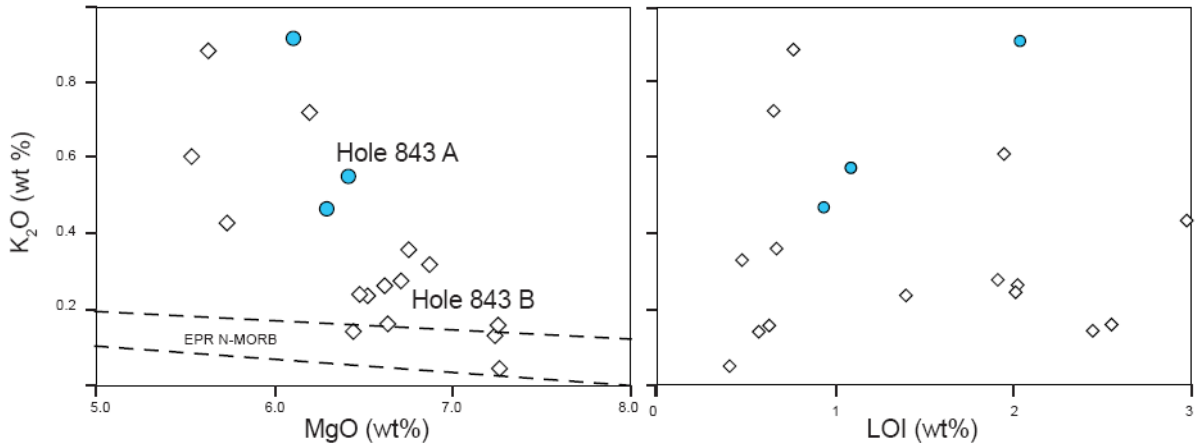

Figure 6.47. Plot of MgO and LOI vs. K_2O with the field for N-MORB shown. After King, et al. (1992).

Basalts recovered at ODP Hole 843A are slightly more enriched in Ti, K, P, Cr, Sr, Y, Zr, Nb, Ba, Ta, and light and mid REE compared to ODP Hole 843B. However, Zr/Nb, Hf/Ta, La/Sm and trace elements indicate that both lavas from Holes 843A and B come from a similar source. Chondrite normalised REE patterns for Site 843 reported by King, et al. (1992) are slightly elevated compared to N-MORB but not enough to be E-MORB. In addition, King, et al. (1992) argue, from a study of plagioclase phenocrysts, that a strong positive Eu anomaly associated with high concentrations of Nd and Zr suggests that the Eu comes from an enriched mantle source. Lack of corrosion on plagioclase phenocrysts implies that the high Nd and Zr concentrations are not the result of alteration (King et al, 1992). A detailed report of the isotopic systematics at Site 843 by King et al. (1993) also imply that the source melt for Site 843 basement is evolved.

Strontium isotopic composition of leached and unleached splits range from and 0.7027-0.7028 and 0.7037-7034 respectively (King et al., 1992). These results reflect the removal of secondary phases by leaching revealing primary Sr values. These values are similar to the leached values in this study and EPR MORB.

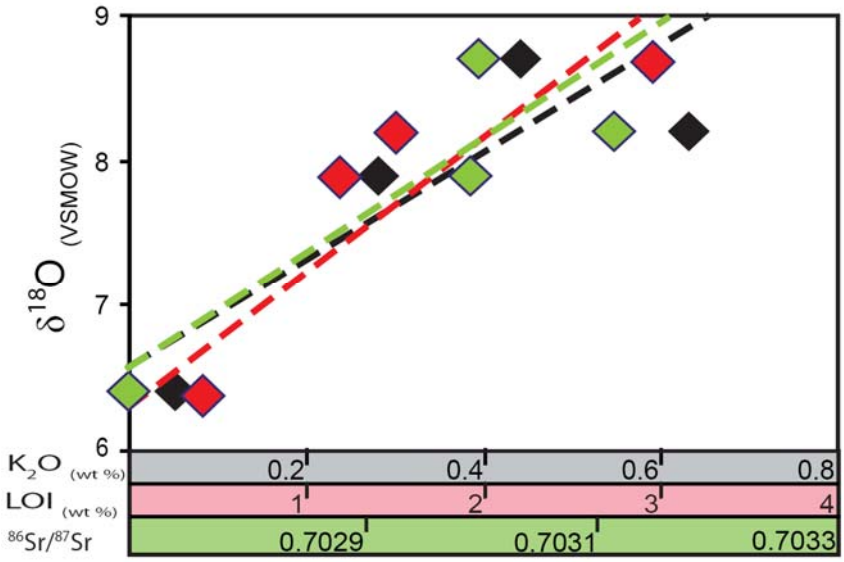

Figure 6.48. Combined plot of LOI, K_2O, and $^{87}Sr/^{86}Sr$, vs. $\delta^{18}O$ compiled from King et al. (1992). All three chemical parameters, traditionally used as a proxy for alteration intensity, increase with $\delta^{18}O$. Red diamonds = LOI, black diamonds = K_2O, and green diamonds = $^{87}Sr/^{86}Sr$.

Oxygen isotope ratios range from + 6.4 ‰ to 8.7 ‰. Considering that this value is higher than fresh EPR N-MORB $\delta^{18}O$ is + 5.6± 0.1 ‰ (Ito et al., 1987), and that there is a trend between $\delta^{18}O$ with increased LOI, K_2O, and $^{87}Sr/^{86}Sr$, (Figure 6.48) King et al. (1992) deduce that $\delta^{18}O$ is greatly affected by alteration and that Site 896 has been subjected to seafloor weathering. High K_2O appears to be the result of low temperature alteration and therefore it is not a reliable means to assess the primary composition of Site 843 basalts.

6.5.3 Alteration

Alteration at ODP Site 843B is discussed in detail by Alt, (1993) and Waggoner (1993) and a brief summary is made here. The low temperature alteration assemblage of ODP Site 843B is dominated by dark green/grey and brown/red halos and patches around fractures and veins, and grey host rocks with slight to moderate background alteration. Examples of the alteration of basement rocks at Site 843 are summarised in Figure 6.46. The majority of the core contains 1 mm to 3 mm wide dark green/grey alteration halos that are associated with veins of celadonite and iron-oxyhydroxides. Alteration intensity within these halos is typically 5-15% with pore spaces and vesicles filled and olivine replaced by celadonite ± iron-oxyhydroxides respectively.

Halos make up 8.5% by volume of which 27% are grey, 11% are brown/red and 62% are dark grey/green. Vesicle fill may be zoned, commonly with the following sequence: 1) celadonite, 2) iron-oxyhydroxide, 3) saponite. Rarely vesicles may be lined with green celadonite, and then in-filled with by blue-green celadonite and calcite. Sections 136-843B-1R-3 and 1R-4 are dominated by brown halos and uncommon red patches that overprint the dark green/grey alteration halos. These zones are also characterised by an increase in vein abundance. Red/brown zones are 10-15% altered with iron-oxyhydroxide filling pore space and replacing olivine. Microprobe analyses carried out by Alt (1993) on these zones indicate high K_2O and SiO_2 which suggests that celadonite is also present.

This supports the macroscopic evidence that brown halos have overprinted the earlier celadonite rich halos. In the grey background, pore spaces are filled with saponite + calcite and plagioclase and clinopyroxene is rarely replaced by saponite + calcite. The dark grey background is typically ~15 % altered.

Veins consists of celadonite, saponite, iron-oxyhydroxides, and calcite and they typically make up 1-3% of the core. However, veins and breccias combined make up ~9 % of the core, which is significantly more than Sites 1224, 1243, and1256. Sections 136-843B-1R-3 and 1R-4 are composed of 2-5% veins and Core 136-843B-2R is composed of 10% veins. Petrographic analyses of vein minerals and cross cutting relationships carried out by Alt (1993) and Dziewonski et al, (1992) suggest the following vein filling sequence; 1) green celadonite ± iron-oxyhydroxides forming <0.1 to 0.2mm veins, 2) iron-oxyhydroxide and iron-hydroxide overprint and/or form new veins of similar thickness, 3) blue-green celadonite + saponite ± pyrite, and 4) late calcite + pyrite veins cross cutting all earlier veins. All vein mineral assemblages occur throughout the ODP Hole 843 with no distinct variation with depth, with the exception of pyrite, which is most abundant near the top of the basement. Iron-oxyhydroxide is most abundant in sections 136-843B-1R-3 and 1R-4, which coincides with an increase in vein frequency and abundance of brown halos. Sections 136-843B-1R-1 and 2R-1 have abundant blue/green celadonite and calcite. Brecciation in Core 136-843B-2R consists of moderately altered, angular to sub-angular basaltic clasts in a calcite ± saponite and iron-oxyhydroxide cement.

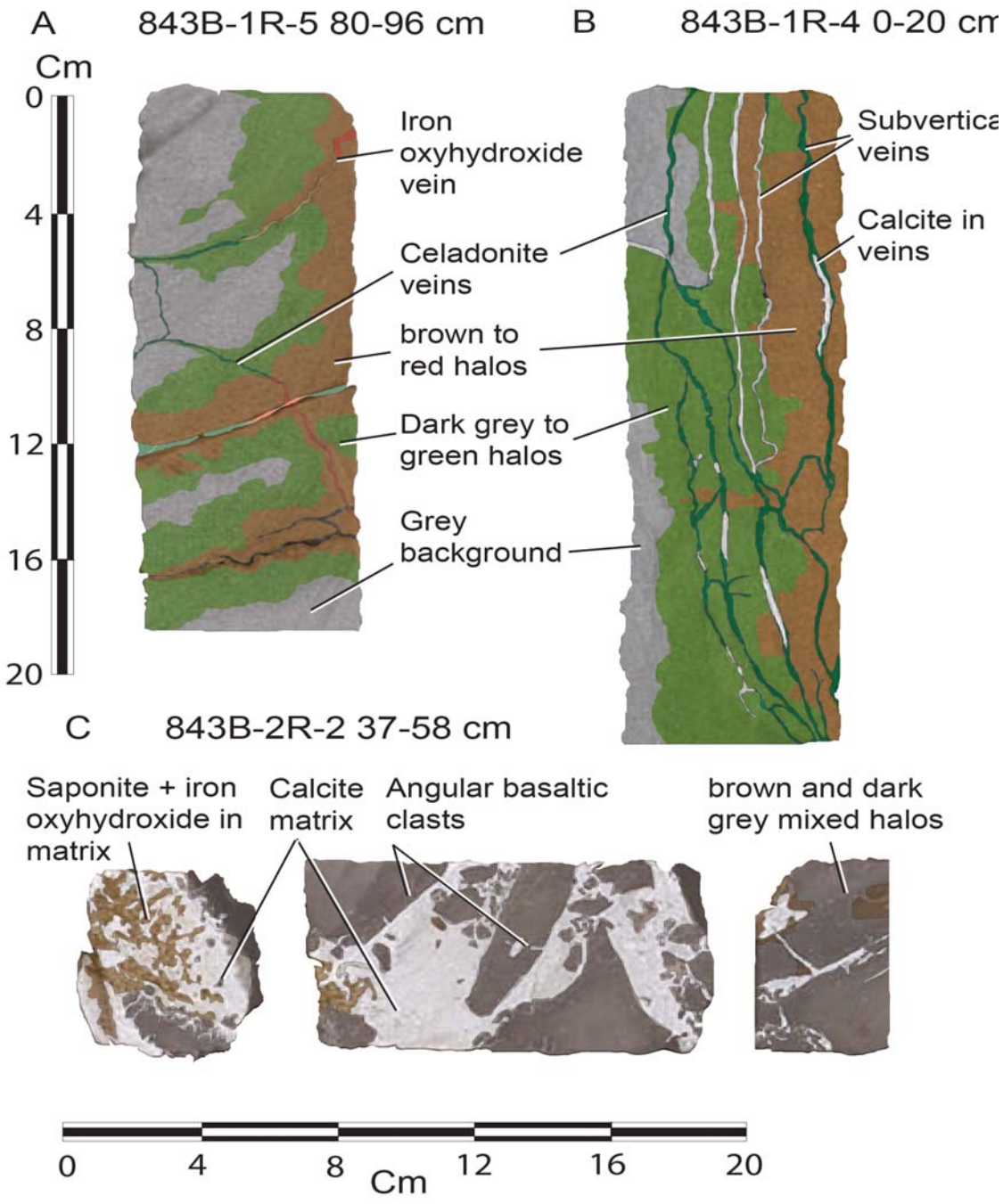

Figure 6.49. Examples of the style and intensity of alteration exhibited at Site 843. A) Early celadonite veins and halos are overprinted by saponite/Iron-oxyhydroxide halos. B) Same arrangement of halos as A, however vertical veins indicate vertical fluid flow, in addition late calcite overprints all earlier phases. C) Basalt clastic breccia comprising moderate to highly altered subangular basaltic clasts in a matrix composed of calcite and iron-oxyhydroxides.

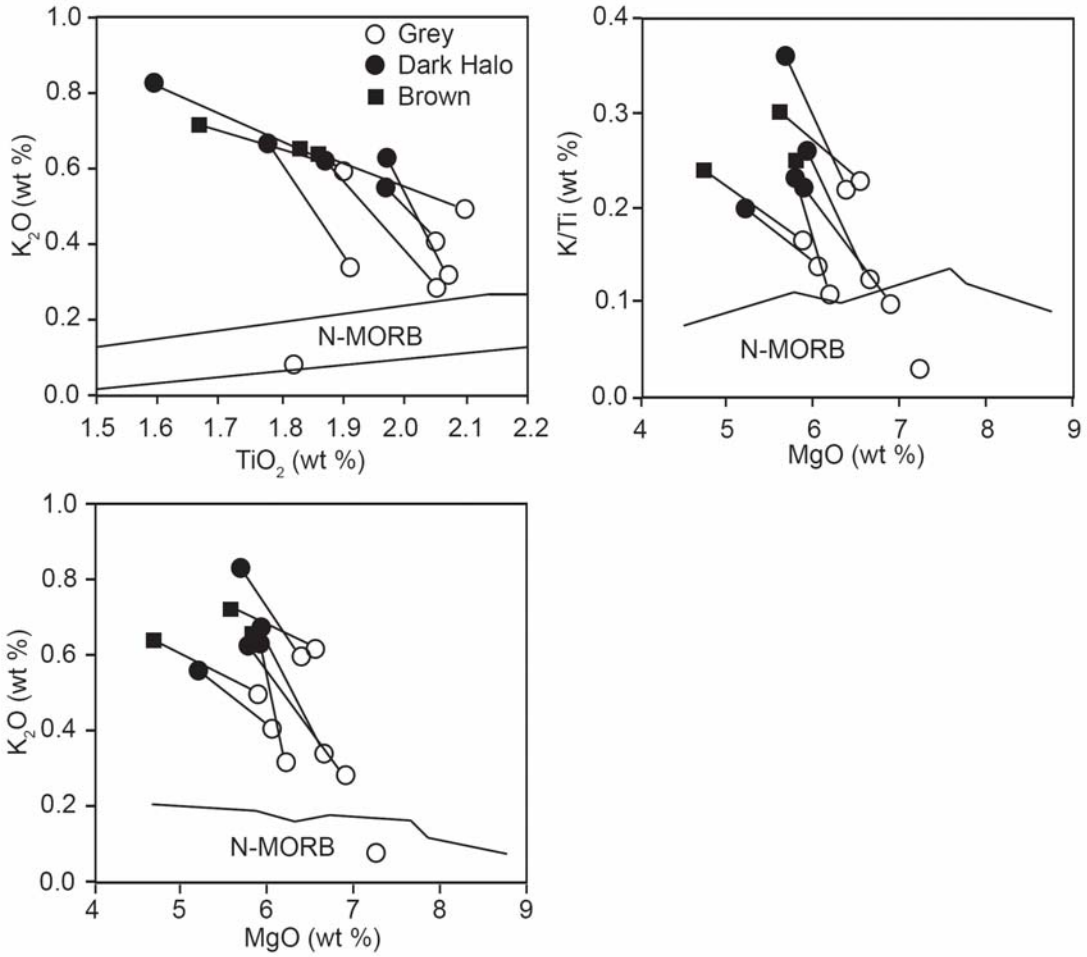

Figure 6.50. Alteration trends of basalts from Site 843B compared to N-MORB. After Alt, (1993) Fields for N-MORB taken from Natland and Melson (1980) and Sinton et al. (1991).

Chemical analyses carried out by Alt (1993) reveal that the dark halos are enriched in H_2O, CO_2, $Fe_2O_3{}^T$, K_2O, MnO, and Fe^{3+}/Fe^T and depleted in SiO_2, Al_2O_3, MgO and TiO_2 relative to the grey host rocks. Figure 6.50 demonstrates this enrichment in a selection of elements relative to MORB. Brown halos are enriched in $Fe_2O_3{}^T$ and Fe^{3+}/Fe^T whereas the grey background has elevated H_2O, CO_2 and K_2O relative to EPR N-MORB. However, it remains important that the high K_2O in the altered rocks is not confused with the high K_2O in the least altered rocks that is indicative of T-MORB primary compositions, where chemical changes for Site 843 are measured (see later chapter) the T-MORB basalts are treated separately so as not to distort the overall chemical change values for Site 843. Stable isotopic compositions ($\delta^{18}O$) of carbonates analysed by Alt (1993) suggest that alteration at

Site 843 took place under cold seawater conditions ranging from 5^{o}- 40^{o}C, which is similar to the alteration encountered in the other sites in this study.

Alt (1993) outlined the sequence of secondary mineral formation based on the cross cutting relationship of veins, vesicle fillings and alteration halos. 1) Celadonite and iron-oxyhydroxides form in oxidising conditions at low temperatures, possibly within 1Ma of crustal formation. 2) Saponite formed later under more reducing conditions, perhaps with a lower seawater/rock ratio. 3) Calcite and pyrite appear to form last in veins and vesicles at temperatures of 5^{o}- 40^{o}C. Site 843 exhibits a secondary phase of celadonite, formed at the time of calcite that is compositionally different from the early celadonite. This may be related to renewed fracturing leading to the introduction of less evolved seawater. Overall this sequence is very similar to the low temperature assemblages encountered in the other fast spread sites in this study.

Chapter 7

Variability of alteration in fast spread sites: Synthesis of results.

7.1. Introduction

One of the major mechanisms for chemical exchange between the lithosphere and hydrosphere is the heat driven circulation of seawater through the ocean crust. This mechanism has profound influence on the chemistry of the atmosphere, oceans, and through subduction and recycling of the ocean crust, the mantle and volcanic arcs (Thompson, 1973; Honnorez, 1981; Staudigel et al., 1981). However, the factors that influence the geometry and extent of hydrothermal systems, such as fluid and heat fluxes, the evolving chemical compositions of fluids as they circulate through the systems and, the architecture of the flow system remain poorly understood.

Models of heat flow by Stein and Stein, (1994) suggest that seawater circulates for up to 65 Myr. More recent calculations of heat flow surveys (Von Herzen, 2005) imply that ongoing hydrothermal circulation is common, even in >95 Ma crust and that off axis circulation accounts for the majority of heat output (Stein et al., 1995; Mottl, 2003) and fluid output (Hutnak et al., 2008). Studies that compare geophysical parameters that are sensitive to alteration, such as density, porosity, and hydration with age indicate that the extent of alteration in ocean crust is dependent on age (e.g., Jarrard et al, 2003). There is also evidence that hydration, a measure of the extent of alteration (Alt et al., 1992), increases with increasing age (Hart, 1970, 1973; Donnelly et al., 1979; Muehlenbachs, 1979). In addition analyses of CO_2 from basement penetrations spanning ~170 Myr indicate that the amount of carbon fixed into the ocean crust increases with age (Alt and Teagle, 1999). A recent review of fluxes of water, CO_2, Cl, and K by Jarrard et al., (2003) indicate that lithological variation within the extrusives and time have the greatest impact on low temperature alteration. In the same review, seafloor topography, sedimentary cover and lithologic permeability are also thought to control the extent of hydrothermal alteration.

Modelling of heat flow based on basement relief, distribution of sediment cover, conductive heat transfer through sediments and thermal and geochemical constraints by Fisher et al., (1990, 1994) imply that off axis circulation is induced by topographic variations. Studies by Wheat and Mottl, (2000), Fisher et al, (2003a 2003b), Wheat et al, (2004) and Hutnak et al., (2008) suggest that selective extraction and fluid flow may be facilitated by conduits at basement outcrops for example seamounts.

Work to characterise hydrothermal alteration and chemical change by petrographic observations and geochemical observations and comparisons to other drilled sites have also been used to suggest that lithology and sedimentation on site has a crucial role (Paul et al., 2006). In addition Paul et al, (2006) use Sr-isotopic ratios and trace element ratios (Mg/Ca) for carbonates from a variety of Sites (504, 896, 417 and 418) to suggest Ca-carbonate formed within 20 Ma of crustal formation. These observations are in close agreement based on age dating of secondary minerals in the ocean crust (Staudigel et al., 1981) and celadonite in the Troodos ophiolite (Booij et al., 1995). Seismic surveys (Grevemeyer et al., 1999) also imply that the majority of alteration ceases early at around <10-15 Ma of crustal formation.

Haymon et al, (1991) demonstrated that hydrothermal features such as vent sites are commonplace on fast-spreading mid-ocean ridge axes. In addition a study of Sr and O isotopes from a range of end-member hydrothermal fluids at differing sites by Bach and Humphris, (1999) imply that the greater exchange between upper ocean crust and fluid occurs at slow spread crust due to increased fluid-flow paths and greater depths of fluid penetration at slow spreading ridges. Alt and Teagle, (2003) note that alteration at fast spread sites is similar with relatively low alteration intensity. However these authors suggest that a low abundance of brown alteration halos at Site 801 is the result of smooth basement topography and high sedimentation rate that restricted the flow of oxygenated seawater.

Clearly there remains a problem elucidating which are the most important factors in controlling the style and intensity of hydrothermal alteration in upper ocean crust. As discussed earlier, factors including basement topography, sedimentation rate, lithology, age, spreading rate, and the structure of oceanic basement may all have a significant role. An understanding of which parameters has the greatest control over the nature of hydrothermal alteration in ocean crust may have implications on the geochemical and thermal budgets associated with seafloor hydrothermal circulation. To address this, a range of sites, where oceanic crust formed at intermediate and fast spreading rates has been recovered, have been characterised in terms of their hydrothermal alteration. Sites 504, 896, 1243, 1256, 1224, 843, 1179, and 1149 (Figure 1.5)span ~133 Myr in age and they represent crust of variable lithological compositions, differing tectonic histories, topographic variation and spreading rate (Table 7.1). In addition these sites have been subjected to a variety of burial histories

(Table 7.1). Analysis of major, trace elements, REE, and isotopic analyses have been used in conjunction with petrographic observations from basement recovered at Sites 504, 896, 1243, 1256, 1224, 843, 1179, and 1149 to characterise hydrothermal alteration, and to obtain sample by sample precursor compositions and calculate the chemical changes associated with low temperature hydrothermal alteration for each site. In addition, the contribution to the total chemical change by vein minerals and breccia matrixes is included to estimate the total chemical change at each of these sites (See Chapter 3 'Site 1179' for method). Comparisons based on the alteration characteristics of Sites 504, 896, 1243, 1256, 1224, 843, 1179, and 1149 made in this thesis and in other sources are used to assess which factors, including spreading rate, age, burial, basement topography, and lithology, have the greatest effect on chemical and isotopic exchange. In addition observations of carbonate veins across these sites are used to infer the duration of alteration within modern ocean basins.

	504B	896A	1243B	1256C	1256D	597C	1224F	595B	843B	1179D	1149D	801C
Age (Ma)	6.9	6.9	11	15	15	30	46	80	95	129	133	170
Sediment thickness (m)	275	179	110	251	251	53	28	70	243	377	416	462
Basement cored (m)	1837	290	87	90	1257	91	147	55	71	98	133	474
Spreading rate	I	I	F	F	F	F	F	F	F	F	I	F
Lava morphology*	76 P 20 M 1 Bx 3 D	57 P 38 M 5 Bx 1 D	100 P	40 M 60 F	64 F 3 P 14 H 20 M	100 M	50 M 50 P	100 P	100 F	10 Bx 40 P 50 M	20 M 50 P 30 Bx	60 M 38 P 2 Ht
Basement topography (m)	>100	>100	<100	<10	<10	<40	<40	low		<50	<100	<100
Initial Sedimentation (m/Myr)	30	20	11	36	36	3	25	2	3	1.3	25	2.5
Time to accumulate 50m sediment (Myr)	~1.3	<2	~6	~1.8	~1.8	~15	2	~25	17	38	~2.5	~20

Table 7.1. Regional data for intermediate and fast spread sites from this study and sites with potential for future analysis (grey). P= pillow lavas, M = massive flows, Bx = breccias, F = flows, D = dikes. Data represents the range of variables that can be tested.

This study also highlights the limitations associated with attempts to characterise hydrothermal alteration of ocean crust on a large scale. Variations in results may reflect site specific variations that part-obscure major trends.

Alternatively, poor recovery, a lack of good estimates of igneous stratigraphy and potentially inappropriate precursor compositions, caused by sample bias or unaccounted for mobility of TiO_2 give rise to errors that serve to obscure real trends.

7.2. Variation in sedimentary rates and basement topography

7.2.1 Sedimentary rates

A potentially important control on the style and intensity of low temperature hydrothermal alteration of the ocean crust is the extent and duration of sediment deposition onto basement. Models of heat and chemical fluxes at mid-ocean ridge flanks indicate that sediment thickness, along with permeability, crustal age, and basement topography determines the change in the composition of seawater in the basement (Mottl and Wheat, 1994). Thin sediment cover near the ridge axes gives rise to relatively open circulation of seawater in the volcanic section at low temperatures (<25^{0}C) (Mottl and Wheat, 1994; Wheat and Mottl, 1994; Alt, 1995). Thicker sediment cover at the ridge flanks, where basement outcrops are less common, restricts seawater penetration, thus resulting in less oxidizing conditions and warmer temperatures in the basement (Mottl and Wheat, 1994; Wheat and Mottl, 1994; Alt et al., 1986; Alt 1995).

Analysis of the chemistry of pore fluids across the Juan de Fuca Ridge indicate a distinct relationship between the chemistry of pore fluids and sedimentation, Observations include increased temperatures caused by the burial of basement by a semi-permeable sediment blanket and subsequent decrease in the Sr-isotopic composition of the fluids, perhaps a result of increased interaction with basement rocks (Coggon, 2004). Sedimentation at Sites 504, 896, 1243, 1256, 1224, 843, 1179 and 1149 are highly variable (Figure 7.1). Thicknesses vary from ~30 to over 400m and accumulation rates range from <1 m/m.y to upwards of 50 m/Myr.

The range of sedimentary conditions at these sites reflects a number of variables that influence sedimentation, including, age, proximity to plate margins, biological productivity, and local basement topography. High burial rates in the last ~10 -15 Ma at Sites 504, 896, 1256, and 1243 are the result of high biological productivity zones, such as the equatorial Pacific zone (Farrel et al., 1995). Proximity to plate margins also influences sedimentary conditions. Seismic profiles of the Juan de Fuca Ridge (Davis et al., 1997) indicate increasing burial as the crust moves away from the ridge axis (Figure 7.2). Young basement near the ridge axes has minimal sediment, which progressively increases with age and distance from the axes as basement subsides sedimentation in the ‘rough basement’ area marked in Figure 7.2 is due to erosion of the North American continental plate. Rapid sedimentation may also occur on near continental margins, for

example glacial turbidite sediments from the proximal North American continental margin (Elderfield et al., 1999; Fisher and Davis, 2000).

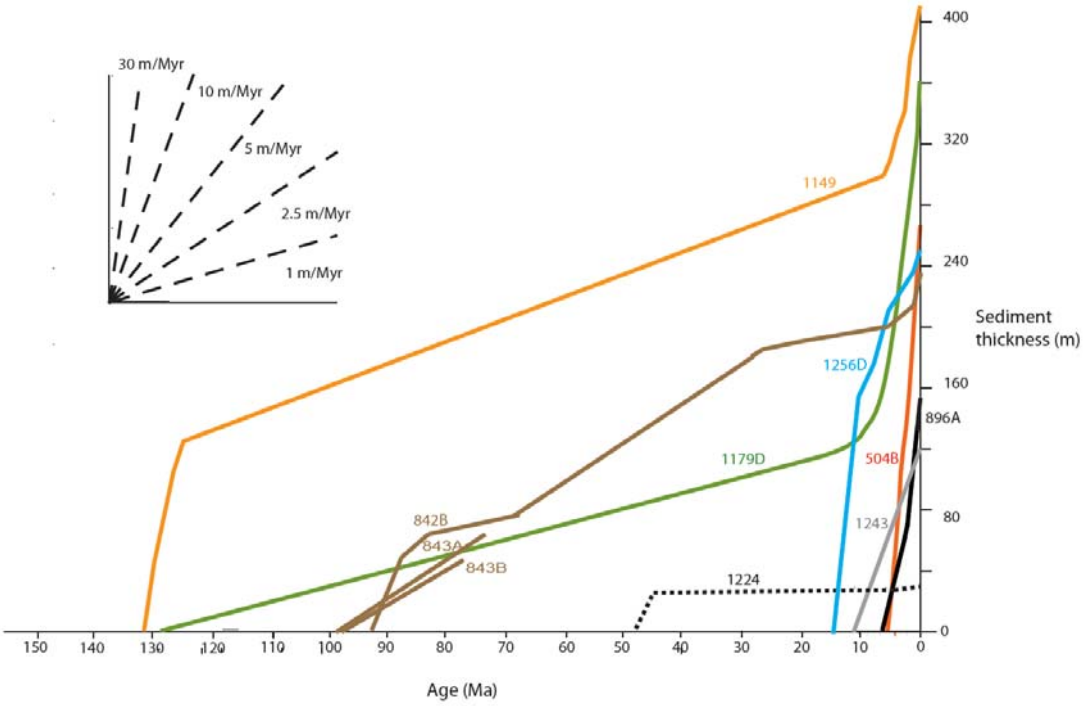

Figure 7.1. Sedimentation rates for Sites 896, 504, 1243, 1256, 1224, 843, 1179, and 1149. With the exception of Site 1224, sedimentation between 0 and ~15 Ma is rapid for all sites.

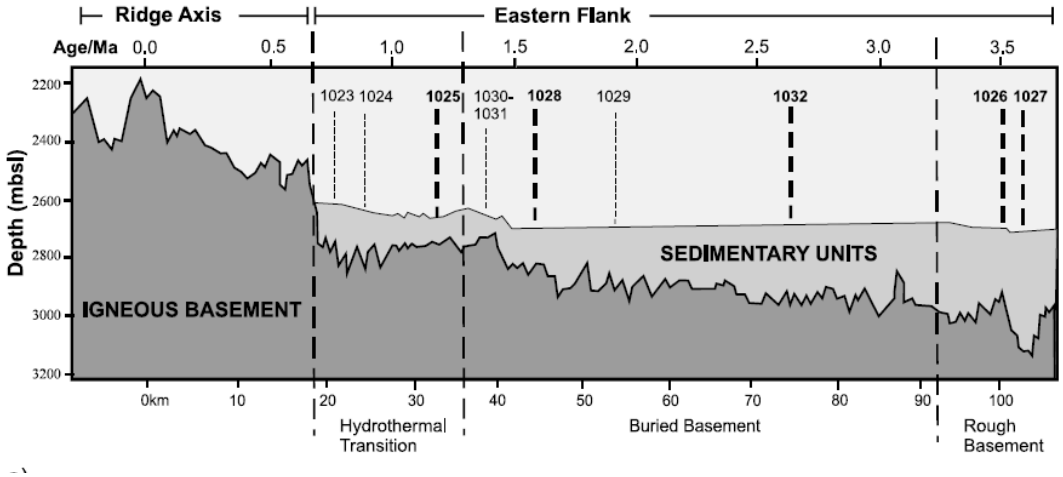

Figure 7.2. Schematic cross section of the eastern flank of the Juan de Fuca Ridge showing drill sites of Leg 168, basement age sedimentary cover and distance from the ridge axes, hydrothermal transition, buried basement (from proximal continental shelf margins), and rough basement topography with variable sediment cover are also indicated. After Coggon et al., (2004).

7.2.2 Basement topography

Variation in basement topography can lead to sinks for sedimentary deposition, where turbidity flows and other sediment will naturally accumulate, whereas topographic highs tend to accumulate less sediment. One of the best examples of topographic variation is Site 504 and 896 which are located within a trough and on a topographic high respectively, see section 7.6.1 for details.

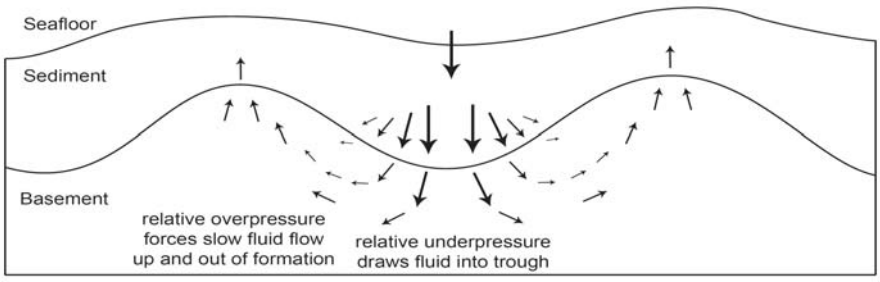

Figure 7.3. Illustration indicating topographic- induced fluid flow caused by the relative differences in pressures in crests and troughs. Cartoon is based on model by Fisher et al, (1994).

Modelling of off axis circulation at Site 504 suggests that sites with highly variable basement topography may result in increased hydrothermal circulation due to changes in isobaric pressure and focussing of fluid flow in areas with low sedimentation (Fisher et al., 1994). Conversely, areas with even sedimentation would have less vigorous hydrothermal circulation (Fisher et al., 1994), which is consistent with work by Mottl and Wheat (1994), Wheat and Mottl (1994), Alt et al, (1986), and Alt (1995). Like Site 896, Site 1243 is located on a topographic high in close proximity to a ~100 m trough. Site 1256 has a basement relief of <10 m (Wilson et al., 2003), however, at least 100m of topography is required for the lava pond. Given that the axial lava pond formed within ~50 ka (~5 km off axis), (Wilson et al., 2003) any effect on alteration that may have been associated with basement relief is probably negligible compared to the axial fluid fluxes at the time. Site 1256 basement topography, it therefore considered smooth. With the exception of Sites 896, 504 and 1243, all other sites in this study have a relatively smooth basement topography (where known) <150 m over a 10 km square and they are all thought to be well below the Carbonate Compensation Depth (CCD).

7.3. Alteration trends

Sites 504, 896, 1243, 1256, 1224, 843, 1179, and 1149 have all been subjected to low temperature oxidative alteration that is typical in modern ocean crust (This study, Andrews, 1977; Staudigel et al., 1981b; Alt and Honnorez, 1984; Alt et al., 1996; Laverne et al., 1996; Paul et al., 2006; Teagle et al., 2006; Alt, 2006). Overall alteration at these sites ranges from slight to moderate and it is pervasive throughout all penetrations with alteration concentrated within halos that surround veins, fractures and pillow rims. Low temperature secondary minerals present at all Sites include iron-oxyhydroxides, saponite, celadonite, carbonates (calcite and aragonite), and zeolites. The timing of secondary mineral paragenisis is broadly similar across all sites, and it is broadly similar to the timing outlined by Alt, (2006) and in this study. It can be summarized as follows: 1) Emplacement of celadonite as veins and forming dark green/black halos, 2) emplacement of iron-oxyhydroxide, forms veins and halos and it typically replaces/overprints earlier celadonite halos, 3) Saponite occurs usually as a later transition from iron-oxyhydroxide, however saponite veins and halos commonly cross-cut and overprint iron-oxyhydroxide veins and halos respectively, and finally 4) late stage carbonates and zeolites forming veins and filling fractures and vesicles. These may occur in multiple phases, in which reopening may occur (such as Sites 1256, 1149, 1179, and 843).

Despite clear similarities between the alteration styles for each site there exists significant variation in alteration intensity and distribution between the intermediate and fast spread sites. Variation of alteration styles across all sites, including the weighted average volume of volcanic section for each alteration style, is illustrated in Figure 7.4. Stratigraphy of the recovered core is included for comparison, and, for Site 1256 the predicted axial lava zone is shown (Tominaga et al., 2009). Halo coverage for most sites is slight (2-10%) to moderate (10-50%) with the majority of alteration consisting of brown halos that overprint green/black halos. Halo coverage between the different sites is highly variable, older sites tend to show a greater degree of alteration and a higher proportion of green/black celadonitic halos and red/brown iron-oxyhydroxide halos.

7.3.1 Trends with volcanic morphology

Lithological composition for each site is outlined in Table 7.1 and illustrated in Figure 7.4. All lithological compositions are based on recovered core . A lack of wire-line logging data for the majority of Sites precludes core-log integration, thus comparisons between Sites that are 'corrected' by such methods to those that are not, would be unrealistic. The issue of core recovery is discussed later in this chapter.
Across Sites 504, 896, 1243, 1256, 1224, 843, 1179, and 1149 a number of trends are evident between the style and intensity of alteration and lithology.

In almost all Sites in this study, abundant alteration halos are associated with breccias. At Site 896 the abundance of alteration halos trends with areas that are composed of ubundant sheet flows (Alt et al., 1993). The trend between sheet flows and halos at Site 896 was first observed by Alt et al, (1993).

Recent core-log integration at Site 1256 by Tominaga et al, (2009) indicates that the relatively high alteration intensity between 750 and 800 msb may relate to an isolated pillow lava zone. These pillow lavas thought to represent lavas on the axial slope (Tominaga et al, 2009) thus the relatively high alteration in this interval may represent relatively open hydrothermal circulation. Sites 1256 and 1224, the least altered in the suite of sites in this study, have a massive flow unit at the top of the basement section (Figure 7.4). Paul et al., (2006) point out that ingress of seawater into the ocean crust may have inhibited by the relatively impermeable massive flow, thus reducing alteration. Site 1256 also exhibits similarly low alteration intensity, which may also be the result of early emplacement of the ponded lava flow. Despite being younger, Sites 504 (6.9 Ma), 896 (6.9 Ma), and 1243 (10-12 Ma) exhibit higher alteration intensities than Site 1256 and 1224. Unlike Site 1256, Site 1243, which also formed on the East Pacific rise, does not have massive lava flow units at the top of its basement section (Figure 7.4). Without an effective cap rock, fluid flow is likely to be less restricted. In addition the basement section at Site 1243 is composed of a much higher volume of pillow lavas (~50%) compared to Site 1256 (~3%), which may have permitted open seawater circulation for longer at Site 1243. Sites 504 and 896 share similar lithological features to 1243 in that there is 1) no massive lava flow unit at the top of their basements, 2) a greater proportion of pillow lavas than at Site 1256, and 3) they are younger than Site 1256. At Site 896 a relationship between the recovered

massive units and percentage of oxidation (Figures 6.19 and 7.4) indicates that lithology had a strong influence on the style and intensity of alteration at that Site.

The relationship between the style and intensity of alteration and lithology implies that local litholgical variations may strongly influence the style and intensity of alteration in ocean crust. If this is the case then accurate appraisals of the volcanostratigraphy of basement sections are critical to determine the true extent of alteration within the crust. Table 7.2 outlines the variations between lithological estimates based on core recovery alone compared with estimates using core-log integration techniques.

	Site 896				Site 1256	
Interpretation	Core descriptions	Core-log integration	Core-log integration		Core descriptions	Core-Log integration
Reference	Alt et al, (1993)	Brewer et al, (1994)	Haggas et all, (2002)		Wilson et al, (2003)	Tominaga et al, (2009)
Breccias	5 %	47 %	16 %	Massive	41.2 %	18.8 %
Pillows	57 %	33 %	35 %	fractured massive	-	16.6 %
Flows	38 %	34 %	49 %	Fragmented flows	-	32.1 %
				Thin flows/thick pillows	-	4.8 %
				Massive sheet	2.3 %	-
				Sheet	50.9 %	-
				Pillow	2.7 %	1.9 %
				Breccias	2.5 %	18.6 %
				Dike contacts	2.3 %	16.6 %

Table 7.2. Composition of volcanostratigraphy at Sites 896 and 1256. Comparison between interpretations based on recovered core and core-log integration highlights large differences.

At Site 896 and 1256, profound differences between core-log integration and recovery based interpretations of volcanostratigraphy, particularly within breccias, pillows and fragmented flows suggest that shipboard core descriptions of recovered core is not an adequate means of estimating the lithological composition at basement sites. In addition, at both Sites, estimates of lithology based the recovered core alone grossly underestimate less competent rocks such as breccias and fragmented flows. The trends between lithology and alteration discussed earlier imply that rocks such as breccias and fragmented rocks exhibit high alteration intensities. Therefore, because core recovery is biased towards more competent lithologies the estimates of alteration in Figure 7.4 must be treated as a minimum

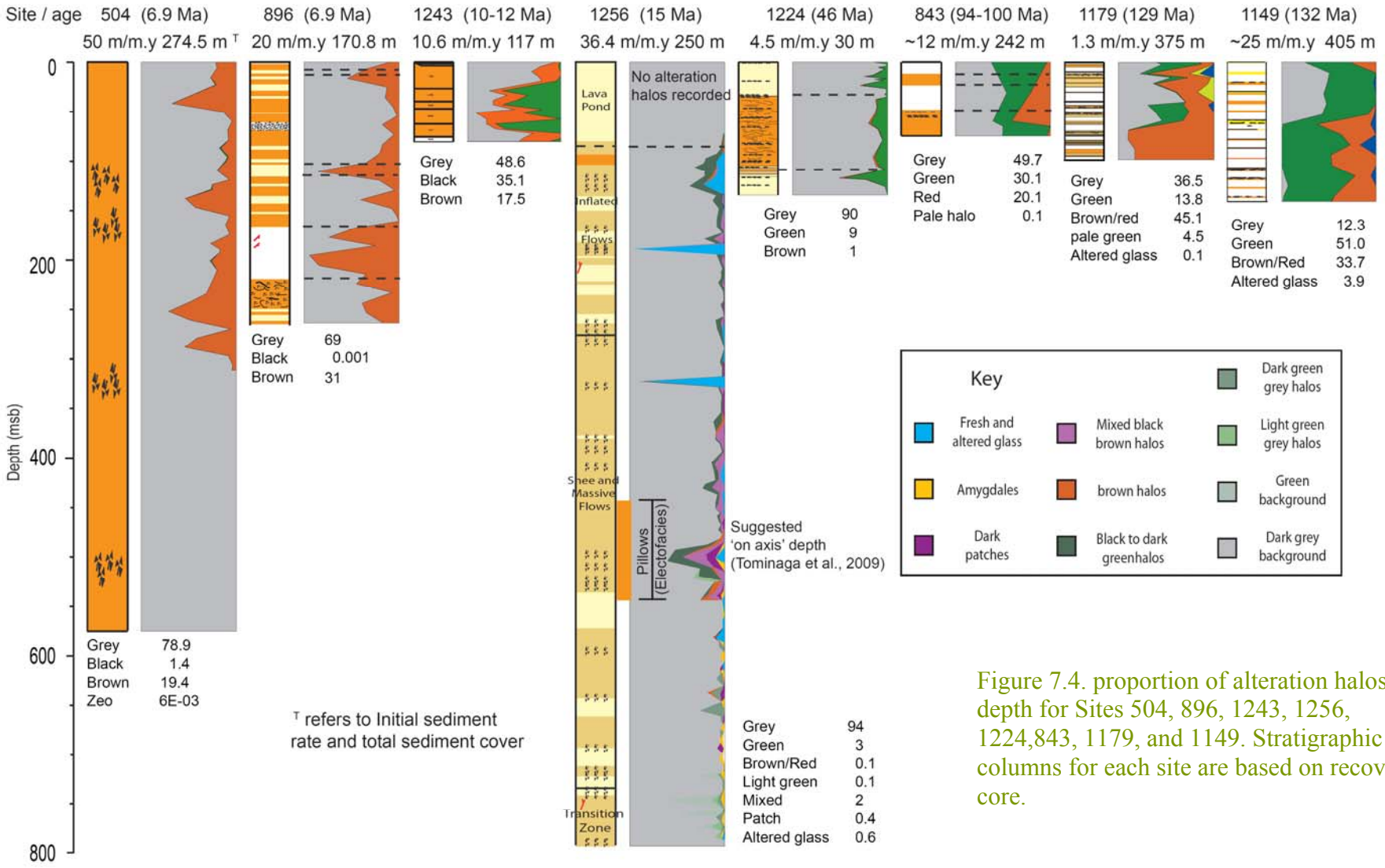

Figure 7.4. proportion of alteration halos vs. depth for Sites 504, 896, 1243, 1256, 1224,843, 1179, and 1149. Stratigraphic columns for each site are based on recovered core.

7.3.3. Correlations with alteration trends

In this study a range of variables with a wide variety of parameters need to be tested, therefore the Spearman's rank coefficient of correlation is used. Spearmans rank of correlation allows us to assess the strength of correlations for a range of variables, including outliers variables that are not normally distributed. Spearmans rank is calculated using the following equation:

$$r_s = 1 - \left[\frac{6\sum D^2}{n\left(n^2 - 1\right)} \right]$$

D is the difference in ranking between values for *x* and *y*, and *n* is the number of pairs. In this calculation it is assumed that *x* and *y* are continuous random variables which are ranked and are independent paired observations. Rank orders that are the same (D = 0) then r_s = +1 i.e a perfect positive correlation. Reverse order = -1. The significance of these correlations can be assessed following Sachs (1984). An r_s of 0 indicates no relationship between each sample set. The degree of confidence that the correlation holds true for the entire population may be taken at varying levels of significance. In this study confidence limits are assessed at the 5 % (0.05) and 1 % (0.01) level (95 % and 99 % respectively) using tables from Sachs (1984) that are outlined in each correlation matrix. Both the 1 sided ($\rho > 0$ or $\rho < 0$) and 2 sided ($\rho \neq 0$) tests are used in this study to define the strength of correlation. Because *r* is an estimate of the population coefficient (ρ), i.e. the correlation that exists in the total population of which only a sample has been measured, the ρ notation used to determine significance of correlations is interchangeable.

The petrographic observations that are used to assess alteration in these matrixes include volume of halo cover, weighted average volume of each halo type, weighted average of veins and each vein type, and veins per metre. These are compared to spreading rate, age, initial sedimentation rate, sediment cover, and the weighted percentage of each lithology (defined as pillows, breccia, massive flows and sheet flows), based on recovery (Figure 7.5). Correlation coefficients in Figure 7.5 are relatively weak. Most are only just above rejection of the null hypothesis in the two sided test at 95% confidence (Sachs, 1984).

Despite weak correlations, examples of the strongest trends are plotted in Figure 7.6. The trend between sheet flows and spreading rate, however, may not be real because no distinction between massive flows and sheet flows was made at sites other than 1256 and 1149, therefore it is not plotted. Trends between vein and halo abundance, and spreading rate, age and lithology (Figure 7.6) indicate that age, initial sedimentation and spreading rate all appear to exert an influence on alteration style and intensity. The relationship with age is consistent with progressive alteration as a result of continued hydrothermal interactions during passive off axis circulation whilst the crust is still warm (e.g., Bass, 1976; Andrews, 1977; Bohlke et al., 1980; Alt and Honnorez, 1984; Gillis et al., 1992; Alt, 1993; Alt et al., 1986a, 1996a,b; Teagle et al., 1996; Hunter et al., 1998; Alt and Teagle, 2003). Negative correlations between initial sedimentation and vein/halo abundance imply that sediment burial of the ocean crust may influence the nature of fluid flow. In Figure 7.5 and 7.6 trends with sediment cover indicate that increased sediment cover may inhibit open seawater circulation. Such a trend would be consistent with the observation that most alteration takes place within 5-10 m.y. of crustal formation (Hart and Staudigel, 1978; Richardson et al., 1980; Staudigel et al., 1981; Grevemeyer et al., 1999; Teagle et al., 1996; Alt, 2004).

perameter	Spreading rate	Age	Initial sed rate	sediment cover	Pillows	Breccia	Massive Flows	Sheet flows	Veins/m	Vol% veins	Saponite	Celad-onite	Carbo-nate	Fe-ox	Grey Bkd	Tot % halo cover	Green/ black	Brown/ Red
Spreading rate	1.000																	
Age	-0.180	1.000																
Initial sed rate	0.099	-0.535	1.000															
sediment cover	-0.237	0.669	-0.050	1.000														
Pillows	-0.718	-0.003	-0.064	-0.062	1.000													
Breccia	0.116	0.169	0.517	0.698	-0.133	1.000												
Massive Flows	0.139	0.223	-0.358	-0.084	-0.631	-0.481	1.000											
Sheet flows	0.836	-0.274	0.369	0.056	-0.683	0.518	-0.124	1.000										
Veins/m	-0.528	0.258	0.366	0.593	0.506	0.685	-0.666	-0.119	1.000									
Vol% veins	-0.321	0.657	-0.687	0.505	0.083	-0.113	0.172	-0.263	0.171	1.000								
Saponite (vol % vn)	-0.465	0.323	-0.304	0.496	-0.165	0.037	0.379	-0.188	0.203	0.691	1.000							
Celadonite (vol % vn)	-0.103	0.256	-0.460	0.024	0.469	-0.205	-0.406	-0.150	0.184	0.629	-0.016	1.000						
Carbonate (vol % vn)	-0.264	0.754	-0.738	0.524	0.095	-0.116	0.176	-0.283	0.134	0.980	0.568	0.650	1.000					
Iron-oxyhydroxide	0.127	0.468	-0.760	0.020	0.187	-0.403	0.033	-0.195	-0.277	0.582	-0.136	0.773	0.692	1.000				
Grey Background	0.422	-0.760	0.522	-0.651	-0.293	-0.152	-0.050	0.486	-0.244	-0.438	-0.218	-0.085	-0.542	-0.382	1.000			
Total % halo cover	-0.430	0.747	-0.528	0.639	0.316	0.140	0.032	-0.496	0.243	0.438	0.207	0.103	0.541	0.395	-0.999	1.000		
Green/black	-0.081	0.592	-0.403	0.352	0.383	0.118	-0.225	-0.304	0.129	0.140	-0.361	0.264	0.311	0.579	-0.811	0.818	1.000	
Brown/Red	-0.694	0.546	-0.416	0.643	0.183	0.081	0.256	-0.550	0.290	0.545	0.732	-0.119	0.524	-0.007	-0.769	0.764	0.259	1.000

Degree of significance of the values from the Correlation coefficient. Confidence limits of 99% and 95% are shown. Table of values from Sachs (1984)

	One sided		Two sided	
DF	95%	99%	95%	99%
1	0.997	0.999	0.988	0.999
2	0.950	0.990	0.900	0.980
3	0.878	0.959	0.805	0.934
4	0.811	0.917	0.729	0.882
5	0.754	0.875	0.669	0.833
6	0.707	0.834	0.621	0.789

Figure 7.5. Correlation coefficient matrix for petrographic observations of alteration vs. parameters that potentially affect alteration style and intensity. Sites 896, 504, 1243, 1256, 1224, 843, 1179, and 1149 are included. Vol = Volume, Bkd = background, Tot = total, Fe-ox = iron oxyhydroxides, sed = sedimentation.

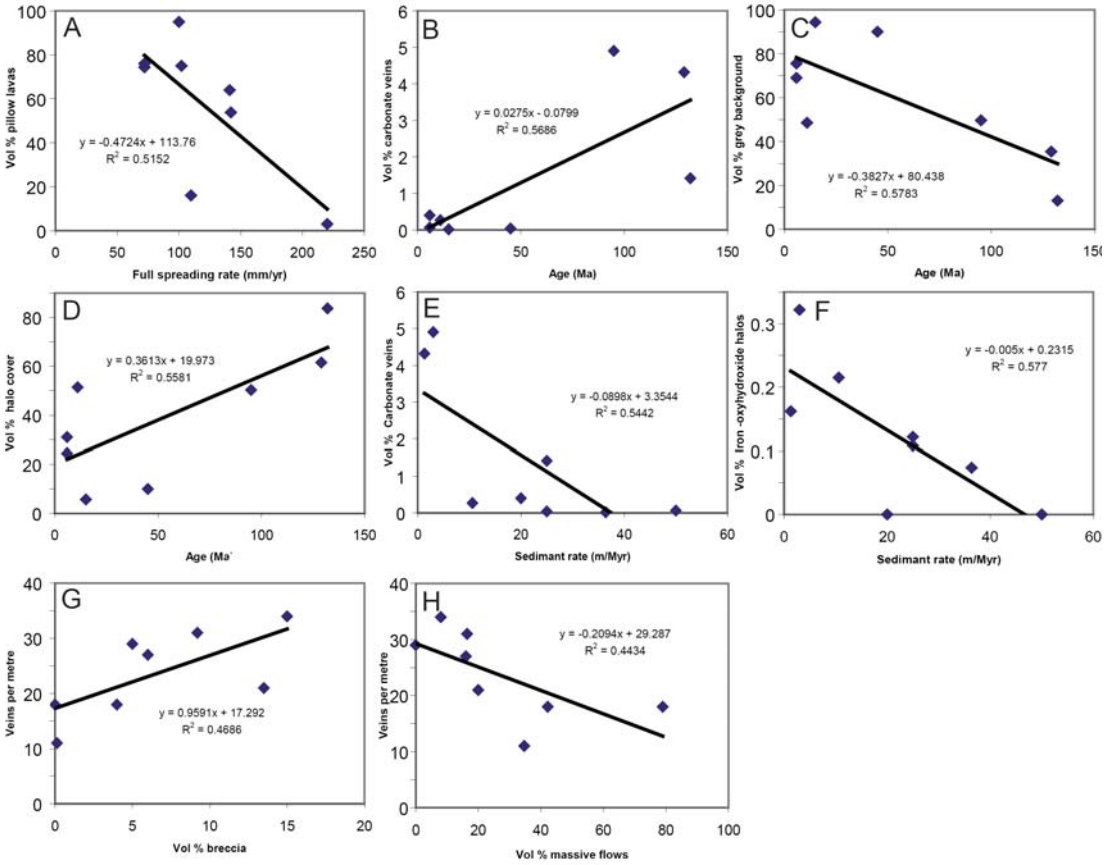

Figure 7.6. Plots indicating the strongest trends between petrological observations of alteration and factors that may control observation. Plots are selected based on the strength of correlation in Figure 7.5.

There are a few trends with spreading rates with only weak trends between brown/red halos and the proportion of sheet flows occur. This trend may imply that crust which moves off the axis at a faster rate may spend less time in the zone of axial hydrothermal alteration and as it rapidly moves off the ridge axes, open seawater circulation may be inhibited by sedimentation. However, this trend is weak, and no other petrological observation shows correlation with spreading rate, therefore such interpretations remain speculative. Data regarding basement topography and heatflow is currently not available for Sites 1224, 1243, 843 and 1149. As discussed in section 7.3, these parameters may be important in terms of hydrothermal alteration thus further work is required.

7.4. Isotopic and geochemical variation

All sites in this study have been measured for their Sr-isotopic compositions and their major, trace and REE concentrations. The proportion of seawater Sr in whole rocks $^{F}Sr^{SW}$ is calculated from the simple expression (Bach and Humphris, 1999):

$$^{F}Sr^{SW} = (R_{sample} - R_{fresh\ basalt})/(R_{seawater} - R_{fresh\ basalt})$$

Where $R_{fresh\ basalt}$ is initial $^{87}Sr/^{86}Sr$, $R_{seawater}$ is seawater $^{87}Sr/^{86}Sr$ at the time of crustal formation. Values for $^{F}Sr^{SW}$ lie between 0-1, where 0 and 1 represents no (0 %) exchange and total (100 %) exchange respectively. Figure 7.7 shows the distribution of $^{F}Sr^{SW}$ for alteration styles, all rocks, and the weighted average $^{F}Sr^{SW}$ for each site whereas Figure 7.8 indicates the distribution of $^{F}Sr^{SW}$ for each Site in terms of lithology.

All sites in this study have a low seawater Sr component, with grey background rocks exhibiting the least exchange (Figure 7.7). A large degree of overlap of $F_{Sr}{}^{SW}$ occurs between each alteration type for all Sites within this study. Such overlapping reflects the overprinting of halos that occur at each Site and it is consistent with petrographic observation of alteration at in-situ ocean crust (e.g., Bass, 1976; Andrews, 1977; Bohlke et al., 1980; Alt and Honnorez, 1984; Gillis et al., 1992; Alt, 1993; Alt et al., 1986a, 1996a,b; Teagle et al., 1996; Alt and Teagle, 2003; Alt, 2004). Beccias and complex halos, in which more than one alteration style has been distinguished, exhibit the greatest variation in $F_{Sr}{}^{SW}$. Brown halos are typically more seawater Sr-enriched than green/black rocks, which have very similar distributions to grey background. Breccias at all sites are the most seawater Sr-enriched, with $F_{Sr}{}^{SW}$ approaching total replacement of primary Sr (0.9) at Site 504. Typically $F_{Sr}{}^{SW}$ for breccias ranges from 0.3 to 0.6., these values reflect high seawater/rock ratios and therefore high fluxes needed to induce widespread replacement of primary mineral phases with secondary minerals and to precipitate matrixes to form breccias. The weighted averages for each site, calculated from the proportion of core that each alteration style occupies, provide the best estimate of the total seawater Sr component for each site. $F_{Sr}{}^{SW}$ for all sites ranges from 0.07 to 0.18 (7% to 18% seawater Sr). Most Sites have weighted average $F_{Sr}{}^{SW}$ that are higher than the distributions of analysed samples would indicate. The weighted averages take into account the proportion of halo coverage, thus reducing any

sample bias, for example, at Site 1149 most samples measured for $^{87}Sr/^{86}Sr$ are grey background rocks despite ~51 % and ~ 32 % green and brown halo coverage respectively. The slightly higher overall F_{Sr}^{SW} in Sites 1179 and 1149 (Weighted average F_{Sr}^{SW} in Figure 7.7) imply late emplacement of secondary minerals in the crust by cold seawater circulation formation, which supports the hypothesis that alteration can occur for 10's of millions of years after crustal formation (e.g., Bass, 1976; Andrews, 1977; Bohlke et al., 1980; Alt and Honnorez, 1984; Gillis et al., 1992; Alt, 1993; Alt et al., 1986a, 1996a,b; Teagle et al., 1996; Hunter et al., 1998; Alt and Teagle, 2003; Alt, 2004). Site 896 has a very strong seawater component (F_{Sr}^{SW} 0.16 or 16%) for its age (6.9 Ma), which contrasts with Hole 504 (0.1 or 10%). The high F_{Sr}^{SW} at Site 896 may reflect increased fluid flow associated with the relatively thin layer of sediment cover (Alt et al., 1996; Chan et al., 2002).

The variation of F_{Sr}^{SW} between each lithology across all sites in this study (Figure 7.8) broadly reflects the petrographic relationships with lithology observed in Section 7.3. F_{Sr}^{SW} of pillows and massive flows, across all sites, ranges from <0.025 to ~0.1. Breccias, although not sampled well enough to produce a distribution curve, typically exhibit a much greater proportion of seawater Sr (F_{Sr}^{SW} = 0.25 to 0.9). The differences indicate that massive flows have undergone the least exchange of Sr with seawater. At Site 1256, the distribution of F_{Sr}^{SW} between sheet and massive flows are very similar, indicating similar seawater Sr exchange. Alt et al, (1993) demonstrated a relationship between massive flows and level of oxidation at Site 896 (See Chapter 5), however the distribution of F_{Sr}^{SW} between these lithologies is less distinct (Figure 7.8). However, the distribution of F_{Sr}^{SW} between Sites 504 and 896 indicates overall greater alteration at Site 896, since a greater proportion of seawater Sr is present in the whole rocks (Figure 7.8) which supports earlier petrographic and geochemical observations in this study and (Alt et al., 1996; Chan et al., 2002).

The chemical change as a result of hydrothermal alteration has been deduced from calculated sample by sample precursor compositions based on the method described in Chapter 3 (Site 1179) for major trace and REE concentrations. Figure 7.9 charts the chemical change at Sites 504, 896, 1243, 1256, 1224, 843, 1179, and 1149 for a selection of major, and trace elements that are sensitive to hydrothermal alteration.

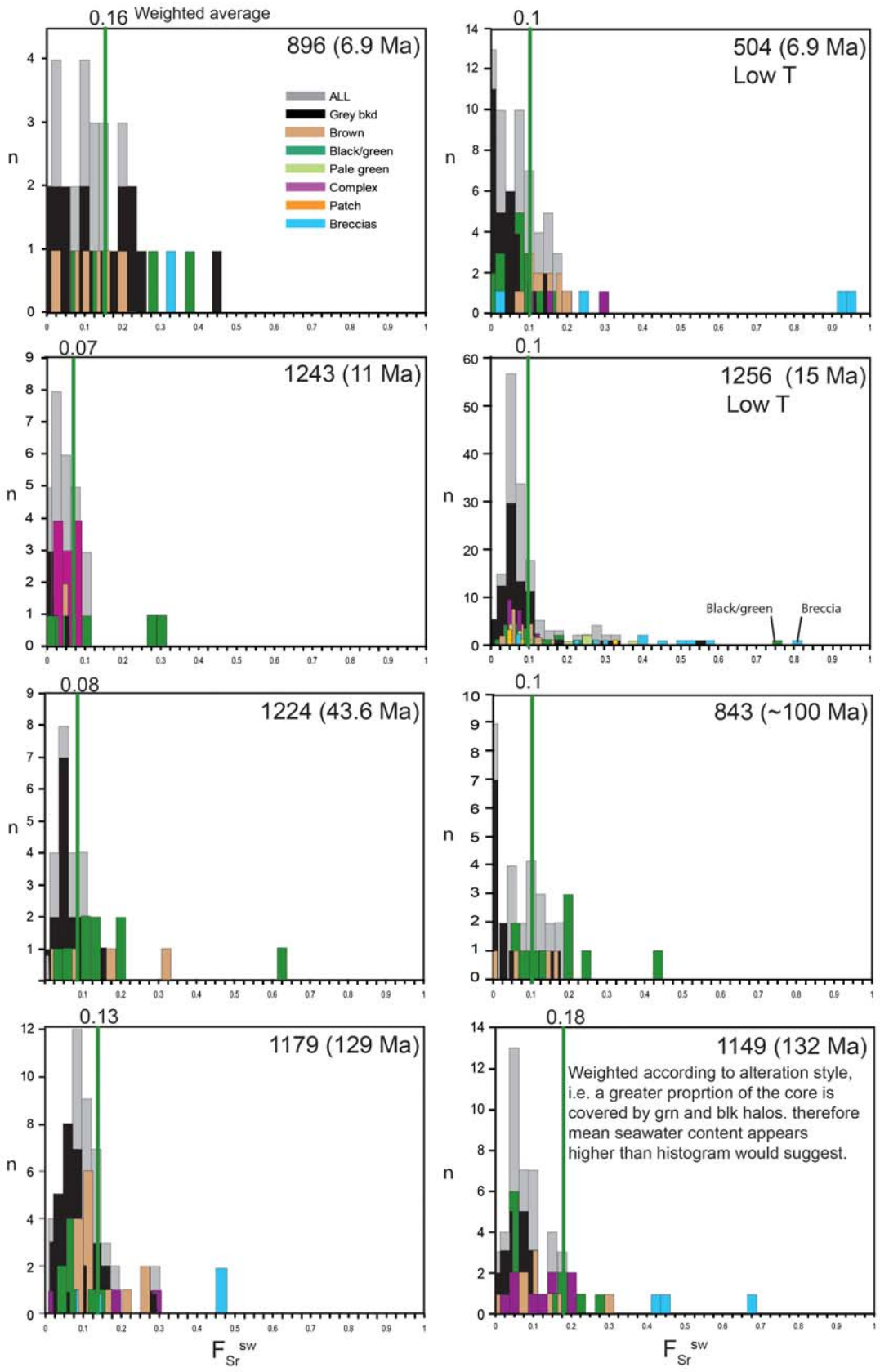

Figure 7.7. Histograms indicating the distribution of the proportion of seawater Sr in basaltic samples for each alteration type, including the weighted average proportion of seawater Sr for the entire hole. F_{Sr}^{SW} is calculated based on Humphris and Bach, (1999).

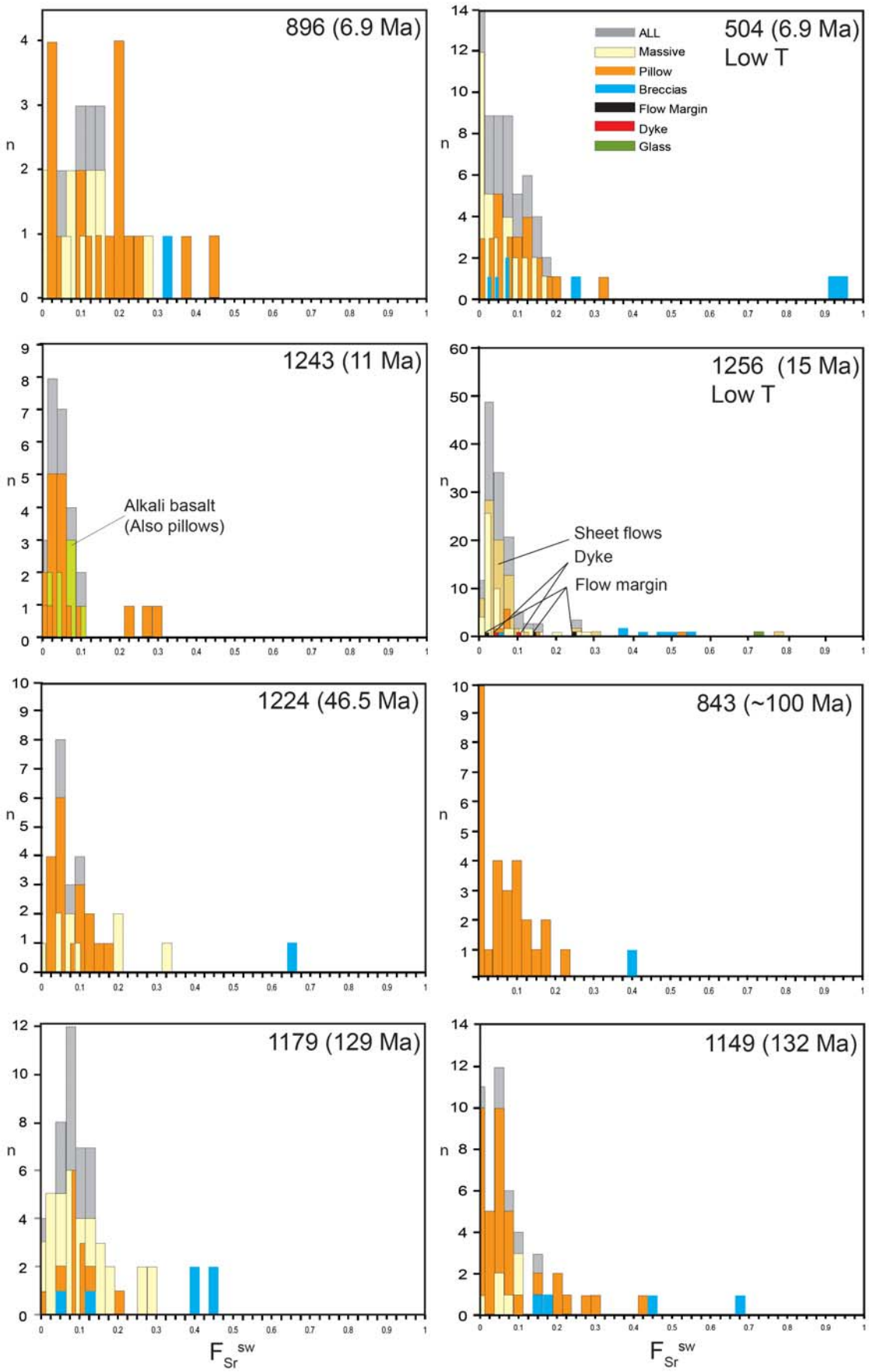

Figure 7.8. Histograms indicating the distribution of seawater Sr in basaltic samples based on lithological groups. F_{Sr}^{SW} (is calculated based on Humphris and Bach, (1999).

Changes at these sites reflect the replacement of primary igneous mineral phases with secondary precipitates from seawater dominated hydrothermal fluids. Chemical change across all sites is variable, and the high error bars reflect the great range of chemical changes observed at each Site. Although, in the petrographic observations (Figures 7.4-7.6) younger sites (504 volcanics, 1243, 1256, and 1224) have undergone less change compared to older sites (843, 1179, and 1149), there is very little linear correlation between chemical change and Age. Sites 843, 1179 and 1149 however, exhibit increases in Fe_2O_3, CaO, K_2O, LOI and decreased SiO_2 respectively. The best trend (excluding Sites 896 and 1243) exists between LOI and Age (Figure 7.10), which exhibits a markedly steady increase with age. If Site 896 is excluded, the decrease in SiO_2 (Figure 7.10) may reflect progressive replacement of primary phases over time. Changes in Site 896 may reflect focussed fluid flow as a result of topographic variation (Fisher et al, 1990, 1994; Alt et al., 1996; Chan et al., 2002). Seismic profiling of Site 1243 (Orcutt et al., 2003) show that it is situated on a plateau at close proximity to a ~100 m deep trough (Section 6.4). This topographic morphology is similar to that of Site 504 and 896, thus, Site 1243 may be undergoing focussed fluid flow. Detailed heat flow surveys will be required to investigate any potential anomalies. Another possible cause for the relatively high alteration at Site 1243 may be the lack of a thick massive flow at the top of the basement to seal the basement section from open circulation.

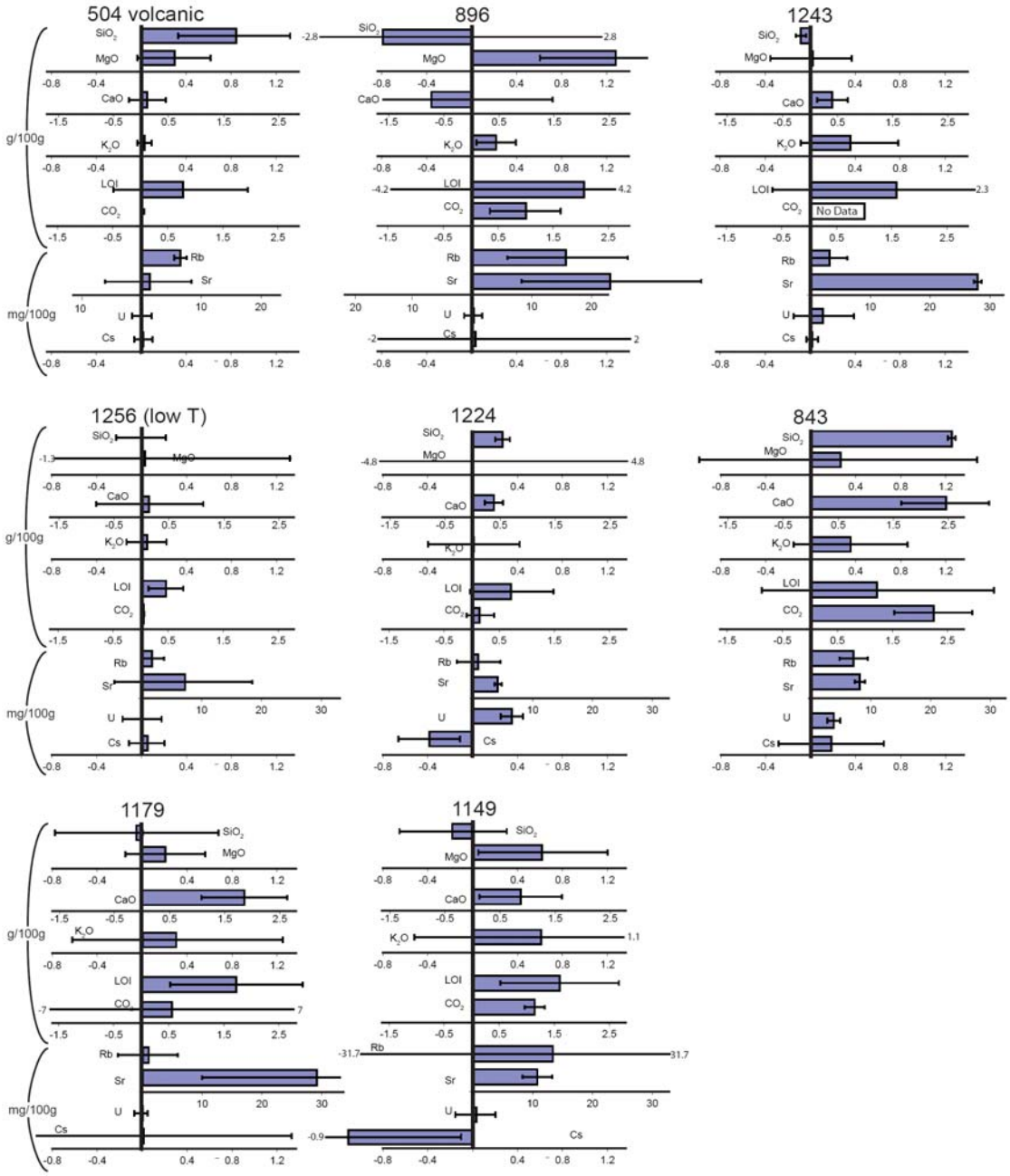

Figure 7.9. Chemical change for selected elements at Sites 504, 896, 1243, 1256, 1224, 843, 1179, and 1149. Volcanic zone of 504 is defined by (Alt et al., 1996). Bars indicate propagated error, including the error associated with the range of changes at each Site.

The loss of silica in whole rocks and the concordant increase in silica in vein minerals suggests that secondary silicates source silica from primary phases within the volcanics. The incorporation of SiO_2 in vein minerals is largely responsible for these variations, and this indicates that chemical changes within whole rocks only record a bulk loss of Silica (Figure 7.11).

Chemical changes exhibited shown in Figure 7.9 indicate that Sites 504, 1243, 1256, and 1224 exhibit variably lower increases in MgO, CaO, K_2O, LOI, CO_2, Rb, Sr, and U than Sites 896, 843, 1179, and 1149. Cs indicates little or no change for most sites, with the exception of 1149 and 1224 which exhibit depletions, whereas Rb and Sr are depleted at Site 504. Site 1243 (11 Ma) appears to have undergone a greater degree of chemical change than Site 1256 (15 Ma) or Site 1224 (43.7 Ma), in addition chemical change at Site 1179 (129 Ma) is greater than Site 1149 (132 Ma).

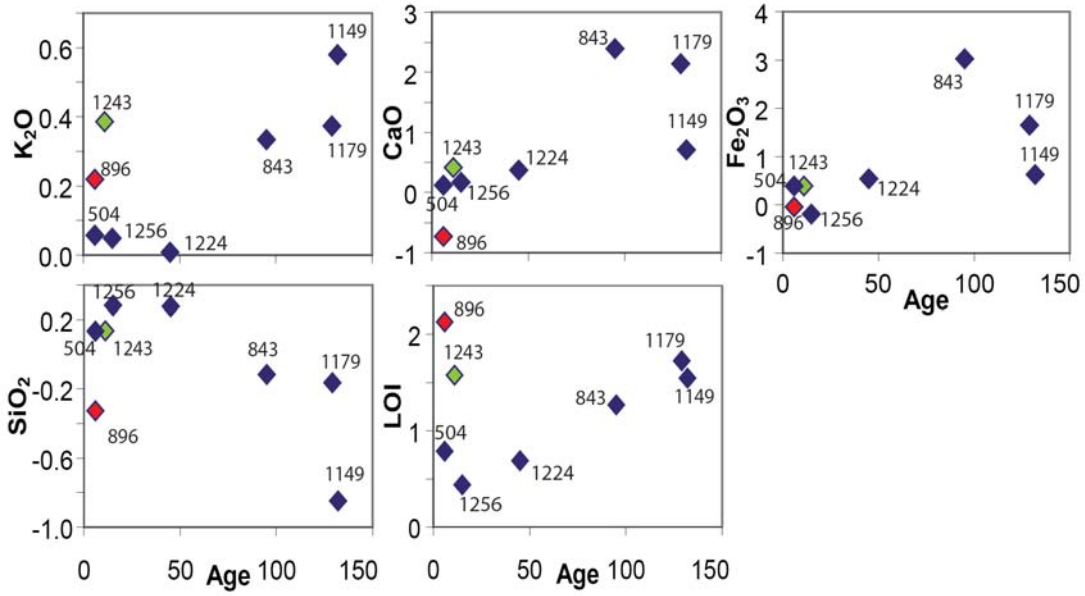

Figure 7.10. Plots indicating chemical change (g/100g) with age (Myr). Apart from Sites 896 and 1243, Greater chemical change occurs in older sites.

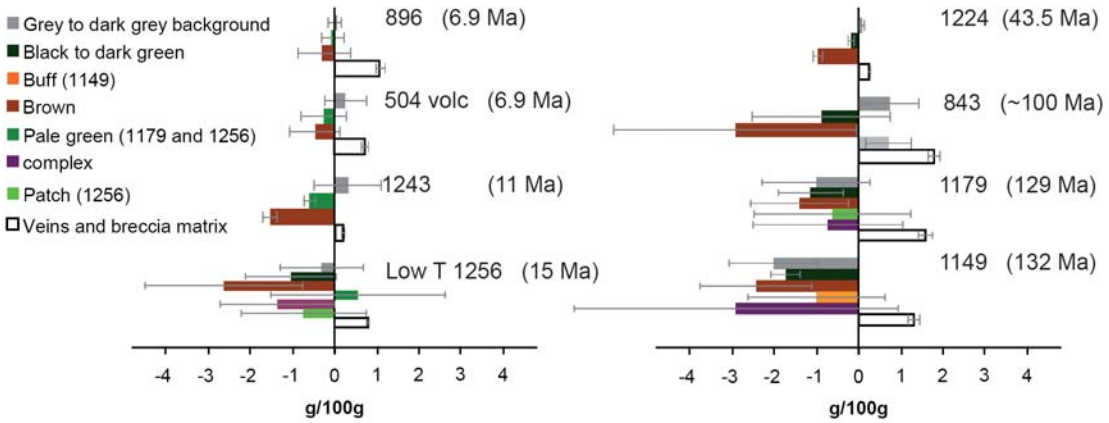

Figure 7.11. Change in SiO_2 (g/100g) within each identified alteration style at Sites 896, 504, 1243, 1256, 1224, 843, 1179, and 1149. Low T = Low temperature alteration. Grey bars highlight uncertainty. Progressively more intense changes occur in older sites, in addition, the loss of silica within alteration styles is buffered by a net gain in silica by vein mineral precipitate, which suggests that Silica in the fluids is sourced locally from the host rock. Variation in alteration types at each site is the result of differing levels of identification.

Site 896 is variably enriched in MgO, K_2O, LOI, CO_2, Rb, and Sr and depleted in SiO_2, CaO (Figure 7.9). These changes are pronounced compared to the other young sites of similar age, most notably Site 504 and they reflect the relatively high F_{Sr}^{SW} compared with Site 504 discussed earlier. Increased chemical change at Site 896 and high seawater-Sr component is consistent with focussed fluid flow at Site 896 (Teagle et al., 1996; Alt et al, 1996; Chan et al., 2002), which is in line with petrographic observations discussed earlier in this chapter.

7.5. Trends with potential controlling factors

7.5.1 General trends

In order to assess the large amount of data for all these sites the variables that may affect alteration, including age, spreading rate, lithological variation, sediment cover, and initial sediment rates, are directly compared to mineral and carbonate vein abundance, halo abundance, F_{Sr}^{SW}, and changes in SiO_2, MgO, CaO, K_2O, LOI, CO_2, Rb, Sr, U and Cs by using Spearmans correlation matrix, as outlined in Section 7.3 of this chapter. Both correlation coefficient matrixes (Figures 7.12 and 7.13) exhibit similar trends, albeit weak, especially in terms of percentage chemical change. Strong trends occur between halo/vein coverage and chemical/isotopic (F_{Sr}^{SW}) change. Positive trends occur between F_{Sr}^{SW} and changes in Al_2O_3, MgO, Rb, and C (Figure 7.14). Halo coverage also exhibits trends with the percentage of carbonate in veins and breccia, Al_2O_3, K_2O and LOI. The trend with K_2O is particularly strong ($r^2 = 0.95$). Compared with spreading rate, MgO, Na_2O and Rb indicate negative trends, both matrixes demonstrate strong trends between carbonate veins and halo cover. In terms of factors that may control hydrothermal alteration, weak trends occur between Age and volume percentages of halos (Figure 7.6). Slightly better trends occur between Age and CaO, Fe_2O_3, SiO_2 and LOI (Figure 7.14). A strong trend ($R^2 = 0.94$) occurs between K_2O and halo coverage (Figure 7.14) highlights the enrichment of K into basement. In addition the older Sites (1149, 1179, and 1243) exhibit greater enrichment of K than the younger Sites (1256, 1224, and 504) Site 896, which is located in an upwelling hydrothermal zone (Alt et al, 1996) is more enriched in K compared to 504. Relatively weak trends with spreading rate include

volume percentage of halos (Figure 7.6) and MgO, Na_2O and Rb (Figure 7.14). Although the trends observed for spreading rate are weak, correlations are better than those concerning other potential factors that may influence alteration. Minor trends with lithological variation include; MnO, Rb, U (Figure 7.12) and % change in MnO, CaO and C (Figure 7.13). Minor trends between sediment cover and sediment rate include Al_2O_3, Fe_2O_3, CaO, K_2O, LOI, Sr and U (Figure 7.12) and breccia abundance, percentage halo cover and percentage of red/brown halos.

Perameter	Spread rate	Age	Init sed rate	Sed cover	Pillows	Breccia	Msve Flows	Sheet flows	Fsr sw	total % halo cover	vol % carb in veins + breccia	SiO_2	Al_2O_3	Fe_2O_3	MnO	MgO	CaO	Na_2O	K_2O	C	LOI	Rb	Sr	Cs	U
Spreading rate	1.000																								
Age	-0.180	1.000																							
Initial sed rate	0.099	-0.535	1.000																						
sediment cover	-0.237	0.669	-0.050	1.000																					
Pillows	-0.718	-0.003	-0.064	-0.062	1.000																				
Breccia	0.116	0.169	0.517	0.698	-0.133	1.000																			
Massive Flows	0.139	0.223	-0.358	-0.084	-0.631	-0.481	1.000																		
Sheet flows	0.836	-0.274	0.369	0.056	-0.683	0.518	-0.124	1.000																	
Fsr sw	-0.478	0.428	0.015	0.616	0.216	0.587	-0.240	-0.172	1.000																
total % halo cover	-0.430	0.747	-0.528	0.639	0.316	0.140	-0.032	-0.496	0.527	1.000															
vol % carb in vn+br	-0.285	0.922	-0.423	0.767	0.232	0.378	-0.114	-0.271	0.601	0.857	1.000														
Δ SiO_2 (g/100g)	-0.300	0.173	0.004	0.074	0.471	-0.176	0.246	-0.338	-0.384	-0.015	-0.154	1.000													
Δ Al_2O_3 (g/100g)	0.510	-0.630	0.237	-0.654	-0.377	-0.451	0.244	0.359	-0.910	-0.808	-0.819	0.215	1.000												
Δ Fe_2O_3 (g/100g)	-0.291	0.636	-0.657	0.323	0.320	-0.248	0.004	-0.383	-0.091	0.429	0.563	-0.691	-0.158	1.000											
Δ MnO (g/100g)	-0.388	0.224	-0.121	0.173	0.841	0.159	-0.802	0.322	0.216	0.356	0.478	-0.542	-0.419	0.507	1.000										
Δ MgO (g/100g)	-0.629	-0.018	0.022	0.217	0.412	0.271	-0.329	0.287	-0.823	0.223	0.177	-0.388	-0.657	-0.184	0.223	1.000									
Δ CaO (g/100g)	-0.053	0.760	-0.657	0.448	-0.017	-0.161	0.256	-0.204	-0.138	0.484	0.616	-0.553	-0.118	-0.918	0.239	-0.397	1.000								
Δ Na_2O (g/100g)	-0.786	0.220	-0.227	0.101	0.585	-0.157	0.187	-0.596	0.423	0.123	0.235	0.320	-0.363	0.464	0.427	0.632	0.169	1.000							
Δ K_2O (g/100g)	-0.303	0.680	-0.581	0.570	0.281	0.147	-0.026	-0.384	0.514	0.974	0.818	-0.116	-0.799	0.366	0.364	0.238	0.419	0.035	1.000						
Δ C (g/100g)	-0.436	0.558	-0.511	0.420	0.599	0.148	-0.489	-0.325	0.479	0.552	0.714	0.303	-0.644	0.699	0.804	0.427	0.492	0.628	0.570	1.000					
Δ LOI (g/100g)	-0.595	0.274	-0.605	0.206	0.332	-0.198	0.132	-0.573	0.559	0.651	0.361	0.365	-0.650	0.154	0.104	0.671	0.057	0.428	0.682	0.445	1.000				
Δ Rb (mg/100g)	-0.657	0.074	0.074	0.313	0.655	0.394	-0.602	-0.347	0.825	0.399	0.371	0.175	-0.778	-0.075	0.551	0.908	0.316	0.561	0.413	0.587	0.587	1.000			
Δ Sr (mg/100g)	-0.130	0.137	-0.665	0.044	-0.166	-0.369	0.529	-0.267	0.142	0.472	0.091	-0.530	-0.243	0.012	0.356	0.220	0.102	0.067	0.540	0.006	0.800	0.047	1.000		
Δ Cs (mg/100g)	0.064	-0.485	-0.165	-0.346	-0.162	-0.479	0.204	-0.121	-0.592	-0.503	-0.609	0.205	0.684	0.190	-0.256	-0.185	0.107	-0.114	-0.490	-0.180	-0.066	-0.399	-0.174	1.000	
Δ U (mg/100g)	0.138	-0.043	-0.241	-0.704	0.268	-0.670	0.019	-0.277	-0.549	-0.278	-0.185	0.395	0.397	0.280	0.248	-0.417	-0.154	-0.115	-0.270	-0.052	-0.286	-0.344	-0.286	-0.053	1.000

Degree of significance of the values from the Correlation coefficient. Confidence limits of 99% and 95% are shown. Table of values from Sachs (1984)

	One sided		Two sided	
DF	95%	99%	95%	99%
1	0.997	0.999	0.988	0.999
2	0.950	0.990	0.900	0.980
3	0.878	0.959	0.805	0.934
4	0.811	0.917	0.729	0.882
5	0.754	0.875	0.669	0.833
6	0.707	0.834	0.621	0.789
7	0.666	0.798	0.582	0.750

Figure 7.12. Correlation coefficient matrix for comparison of alteration style and intensity as measured by chemical changes for selected Major and trace elements. Sites 896, 504, 1243, 1256, 843, 1179, and 1149 are included. Highlighted values indicate the degree of confidence above the null hypothesis based on Sachs (1984) definitions. Units are the same for both sides of the matrix.

Perameter	Spread rate	Age	Init sed rate	Sed cover	Pillows	Breccia	Msve Flows	Sheet flows	Fsr sw	total % halo cover	vol % carb in veins + breccia	Δ SiO_2	Δ Al_2O_3	Δ Fe_2O_3	Δ MnO	Δ MgO	Δ CaO	Δ Na_2O	Δ K_2O	Δ C	Δ LOI	Δ Rb	Δ Sr	Δ Cs	U
Spreading rate	1.000																								
Age	-0.180	1.000																							
Initial sed rate	0.099	-0.535	1.000																						
sediment cover	-0.237	0.669	-0.050	1.000																					
Pillows	-0.718	-0.003	-0.064	-0.062	1.000																				
Breccia	0.116	0.169	0.517	-0.698	-0.133	1.000																			
Massive Flows	0.139	0.223	-0.358	-0.084	-0.631	-0.481	1.000																		
Sheet flows	0.836	-0.274	0.369	0.056	-0.683	0.518	-0.124	1.000																	
Fsr sw	-0.478	0.428	0.015	0.616	0.216	0.587	-0.240	-0.172	1.000																
total % halo cover	-0.430	0.747	-0.528	-0.639	0.316	0.140	0.032	-0.496	0.527	1.000															
vol % carb in vn+br	-0.285	0.922	-0.423	-0.767	0.232	0.378	-0.114	-0.271	0.601	-0.857	1.000														
Δ SiO_2 (%)	0.188	-0.170	0.465	-0.385	-0.082	-0.225	0.145	0.010	-0.582	-0.501	-0.348	1.000													
Δ Al_2O_3 (%)	0.514	-0.588	0.284	-0.670	-0.349	-0.413	0.187	0.369	-0.870	-0.862	-0.786	0.681	1.000												
Δ Fe_2O_3 (%)	-0.254	0.585	-0.592	0.357	0.317	-0.140	-0.113	-0.270	0.059	0.359	0.544	-0.090	-0.124	1.000											
Δ MnO (%)	-0.294	0.198	-0.358	0.097	0.775	-0.045	-0.663	0.330	0.018	0.421	0.424	-0.241	-0.297	0.631	1.000										
Δ MgO (%)	-0.326	-0.445	0.123	-0.137	0.051	0.050	-0.087	0.000	0.442	-0.257	-0.361	0.515	-0.160	-0.369	-0.276	1.000									
Δ CaO (%)	0.555	0.424	-0.198	0.375	-0.818	0.130	0.664	0.405	-0.171	0.192	0.215	-0.044	0.053	-0.004	-0.470	-0.466	1.000								
Δ Na_2O (%)	-0.455	-0.327	-0.083	-0.198	0.307	-0.087	-0.198	-0.212	0.477	-0.105	-0.212	-0.576	-0.274	-0.190	-0.003	-0.939	-0.637	1.000							
Δ K_2O (%)	-0.720	-0.114	-0.250	-0.402	0.461	-0.147	-0.202	-0.448	-0.690	-0.562	-0.326	-0.794	-0.766	-0.076	-0.272	-0.599	-0.366	-0.677	1.000						
Δ C (%)	-0.206	-0.596	-0.486	-0.502	-0.427	-0.021	-0.712	-0.182	-0.414	-0.460	-0.409	-0.394	-0.433	-0.147	-0.430	-0.173	-0.554	-0.106	-0.353	1.000					
Δ LOI (%)	-0.618	-0.162	-0.434	-0.176	-0.297	-0.086	-0.058	-0.473	-0.679	-0.454	-0.252	-0.776	-0.682	-0.005	-0.069	-0.706	-0.317	-0.811	-0.886	-0.520	1.000				
Δ Rb (%)	-0.091	-0.337	-0.051	-0.338	-0.261	-0.438	-0.291	-0.143	-0.569	-0.650	-0.562	-0.295	-0.728	-0.280	-0.233	-0.177	-0.011	-0.084	-0.294	-0.031	-0.200	1.000			
Δ Sr (%)	-0.385	-0.382	-0.425	-0.375	-0.225	-0.116	-0.201	-0.114	-0.459	-0.172	-0.401	-0.496	-0.339	-0.657	-0.311	-0.389	-0.263	-0.500	-0.463	-0.348	-0.522	-0.286	1.000		
Δ Cs (%)	-0.100	-0.177	-0.046	-0.137	-0.225	-0.068	-0.418	-0.160	-0.302	-0.261	-0.114	-0.034	-0.317	-0.610	-0.435	-0.020	-0.246	-0.026	-0.010	-0.302	-0.238	-0.608	-0.460	1.000	
Δ U (%)	-0.022	-0.039	-0.333	-0.531	-0.429	-0.570	-0.184	-0.293	-0.423	-0.223	-0.049	-0.379	-0.382	-0.514	-0.499	-0.280	-0.426	-0.034	-0.375	-0.419	-0.215	-0.330	-0.232	-0.269	1.000

Degree of significance of the values from the Correlation coefficient. Confidence limits of 99% and 95% are shown. Table of values from Sachs (1984)

	One sided		Two sided	
DF	95%	99%	95%	99%
1	0.997	0.999	0.988	0.999
2	0.950	0.990	0.900	0.980
3	0.878	0.959	0.805	0.934
4	0.811	0.917	0.729	0.882
5	0.754	0.875	0.669	0.833
6	0.707	0.834	0.621	0.789
7	0.666	0.798	0.582	0.750

Figure 7.13. Correlation coefficient matrix for comparison of alteration style and intensity as measured by % chemical changes for selected Major and trace elements. Sites 896, 504, 1243, 1256, 843, 1179, and 1149 are included. Highlighted values indicate the degree of confidence above the null hypothesis based on Sachs (1984) definitions. Units are the same for both sides of the matrix.

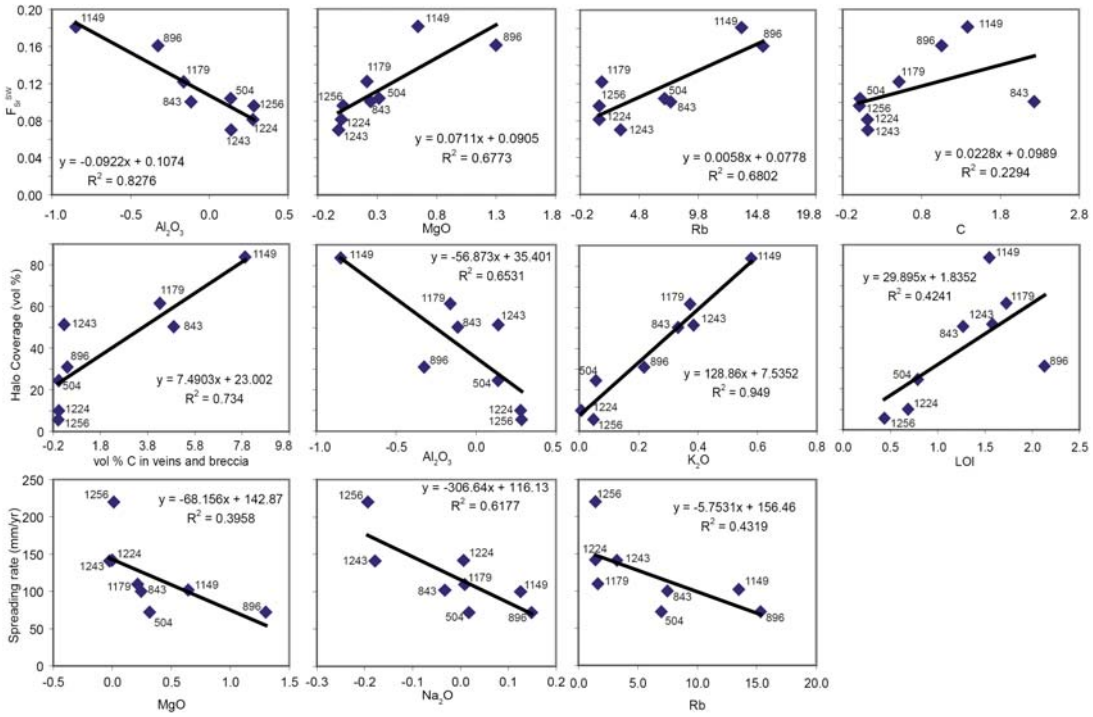

Figure 7.14. Trends observed between F_{Sr}^{SW}, halo coverage and spreading rate and chemical change, expressed as Δ g/100g for major elements and Δ mg/100g for Rb. Volume of C in veins and breccia is also included for comparison.

7.5.2 Petrographic trends

Trends between the abundance of halos and chemical and isotopic exchange are consistent with the petrographic observations of secondary minerals and the replacement of primary phases within the halos (This study and Alt et al., 1996a and b., Alt and Teagle, 2003). The trend between vein abundance and halo coverage reflects progressively higher water rock ratios at the more intensively altered Sites. The progression of alteration intensity in this sample of IODP sites is demonstrated by the relatively strong trends between crustal age and total halo cover and carbonate vein abundance (Figure 7.6)

7.5.3 Trends with Age

The trends observed in Section 7.3, the trends following chemical indicators of alteration imply that off axis circulation of cold seawater into the crust continues for

10's of millions of years after crustal formation. This remains consistent with observations throughout this study and numerous previous studies (e.g., Bass, 1976; Andrews, 1977; Bohlke et al., 1980; Alt and Honnorez, 1984; Gillis et al., 1992; Alt, 1993; Alt et al., 1986a, 1996a,b; Teagle et al., 1996; Hunter et al., 1998; Alt and Teagle, 2003; Alt, 2004). The same trend occurs with carbonate vein abundance, implying similar continued circulation. Sr-isotope analysis of carbonates at Sites in this study and secondary minerals at other site (Alt and Teagle, 1999; Coggon, 2004; Alt and Honnorez, 1984; Burns et al., 1992; Alt, 1993; Teagle et al., 1996) also indicate prolonged off axis circulation for 10's of millions of years. Sr – isotope values for carbonates are all elevated above MORB, and, despite the likelihood of basaltic Sr present in fluids from which the carbonates precipitated, samples from Sites in this study are elevated above seawater at the time of crustal formation. Intersects between the seawater Sr-isotopic curve and elevated carbonate samples provide a minimum estimate for the duration of alteration at each site (Figure 7.15).

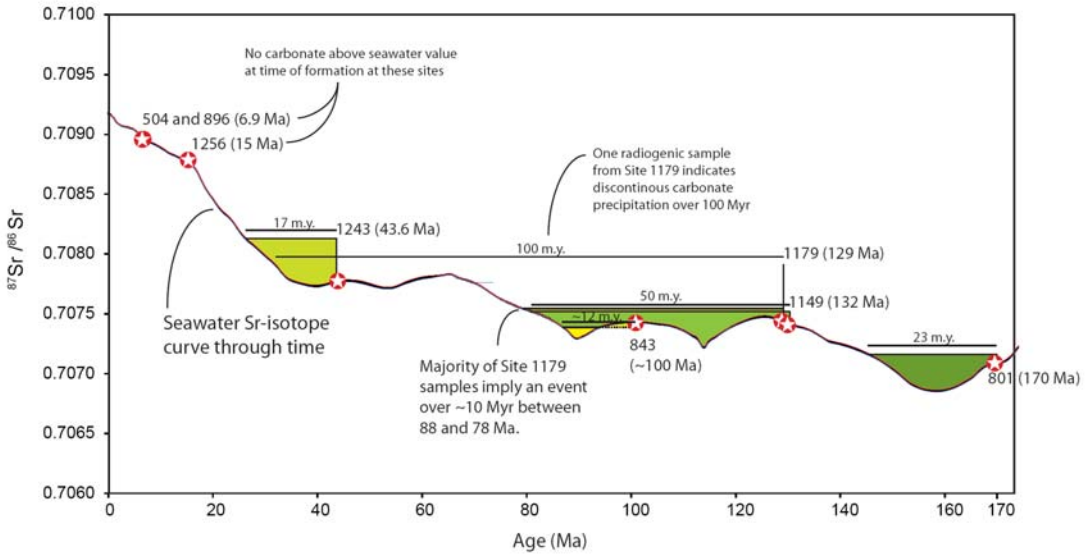

Figure 7.15. Seawater Sr-isotopic composition through time (McArthur, 2001) including seawater composition at the time of formation for Sites 504, 896, 1243, 843, 1179, 1149, and 801 (Stars). The minimum duration for carbonate precipitation is indicated by the intersect from the most radiogenic carbonate sample. Shaded boxes indicate the range of Sr-isotopic ratios for carbonates at each site.

Based on the trends in Figures 7.12 and 7.13 and the elevated Sr-isotopic compositions of carbonates, age appears to play a critical role in the development of low temperature alteration in ocean crust. Investigations into the rates at which crust is altered as it spreads away from the ridge axes are hampered by a lack of sampling. Carlson et al., (1986) suggests that a layer of high permeability may be persistent in the ocean crust

due to localised crustal heterogeneities and/or new tectonic activity. It has been implied that late stage alteration at Site 1149 is a consequence of pre-subduction processes (Jarrard et al., 2003). In such circumstances crustal extension and normal faulting occurs at the lithosphere flexes, which may provide vertical permeability in addition to the already existing horizontal permeability (Fisher and Becker, 2000).

Based on numerical modelling and heat flow data, convection in the ocean crust on average continues to 65 Ma (Stein and Stein, 1994). In addition, heat flow evidence from Cretaceous crust by Noel and Hounslow, (1988) and Von Herzen, (2005) showed that localised convection in the ocean crust may continue at least to 100 Ma. Based on observations of carbonates in this study and analysis carbonate veins by Alt and Teagle (1999) imply that the vast majority of alteration is complete within 10 to 40 Ma and that carbonate and other secondary minerals may form as a result of minor secondary fractures from localised conditions upwards of 165 m.y.

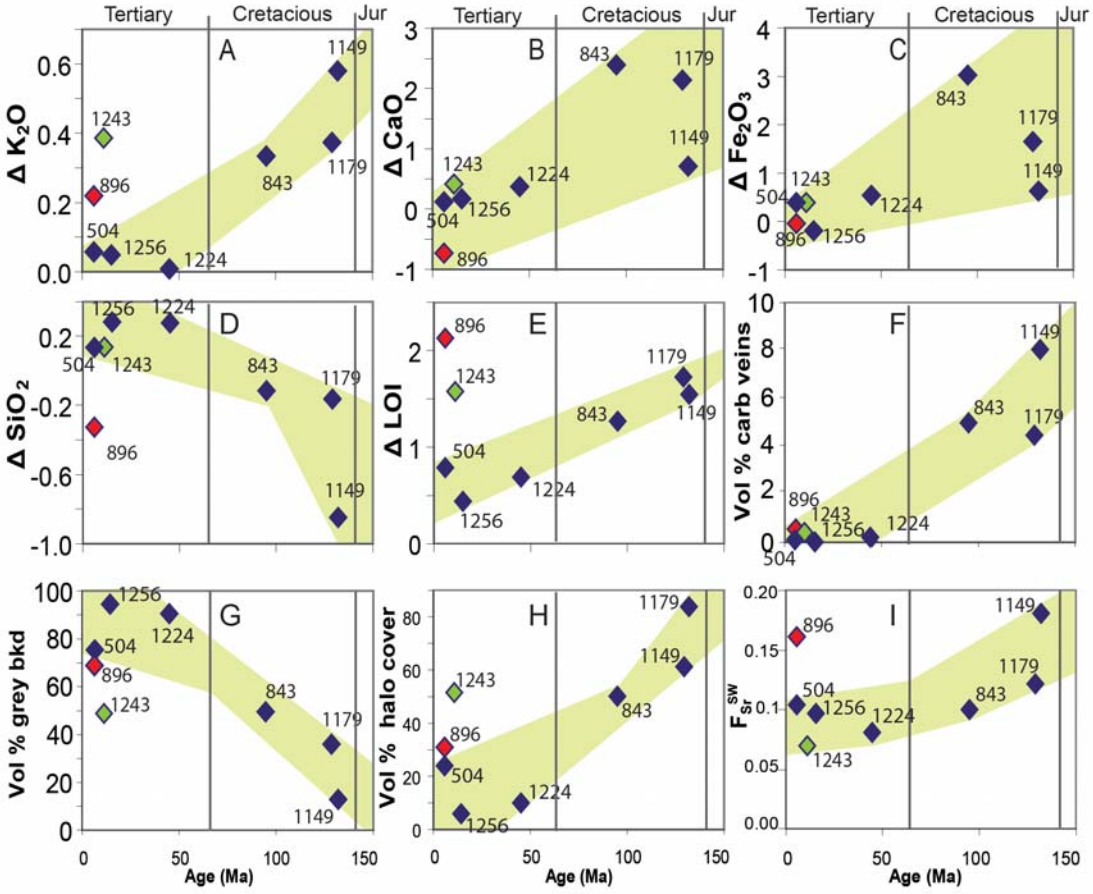

Figure 7.16.Chemical change (g/100g) and petrographic trends vs. age. Field indicates the potential changes that may occur. Site 896 represents zone of focussed fluid flow, and therefore has higher alteration compared to other basement Sites. Site 1243 may also represent a similar alteration regime to Site 896.

Plots of selected chemical changes, carbonate veins, halo cover, and F_{Sr}^{SW} vs. age for sites in this study (Figure 7.16) are used to imply a general progression of alteration with age. K_2O, CaO, Al_2O_3, LOI, Carbonate in veins, halo coverage and F_{Sr}^{SW} increase with age. Although the trend is less clear at Site 1224, Sites 896 and 1224 may be more influenced by local variations in topography, where focussing of fluid flow has led to increased alteration. Carbon in veins indicate uptake of carbon through time and that C uptake may continue for 10's of Myr after crustal formation (Alt and Teagle., 1999). Outliers such as Site 1243 and 896 indicate that variation is too great to simply imply that age alone controls the style and intensity of alteration in modern ocean crust.

7.5.4 Spreading rates

Fast spreading centres are subject to steady state volcanism, leading to higher frequency of hydrothermal vents, a simple crust with smooth basement topography and abundant sheet flows (Macdonald, 1998; Haymon et al., 1991; Karson, 2002; Carbotte and Scheirer 2004). White et al, (2002) suggested that spatial correlations of morphologic, structural, seismic and petrological data on the East Pacific Rise indicate that hydrothermal activity on fast spread ridges is relatively evenly distributed and that it will endure for as long as the ridge segment remains stable. Slow spread crust is formed from intermittent magmatism, large throw faults leading to a more complex crustal structure and more common pillow lavas (Huang and Solomon, 1988; Mevel and Cannet, 1991; Baker et al., 1996). Despite the problems associated with trying to estimate the lithological composition of in-situ penetrations of ocean crust (Discussed in parenthesis), a negative trend between percentage of pillow lavas and spreading rate together with a strong positive trend between sheet flows and spreading rate implies that lithological composition is affected by spreading rate. The relative weakness of the pillow lava correlation coefficient (-0.699, Figure 7.13) compared with that of sheeted flows (+0.857) may be related to preferential recovery of rheologically stronger sheet flows and limited effective core-log integration. As indicated in Figure 7.14 trends between chemical change and alteration styles with spreading rate are relatively weak. The negative trends in elements MgO, Na_2O, and Rb (Figure 7.14) may indicate that chemical change decreases with increased spreading rate, which is consistent with petrographic observations of slower spread crust.

7.5.5 Sedimentary burial

The variability of sedimentation rates across Sites 896, 504, 1243, 1224, 843, 1179, and 1149 discussed earlier in this chapter is great. Sites spanning ~150 m.y. have endured sedimentation that ranges from almost zero over millions of years to upwards of ~50 m/Myr. Since sedimentation may inhibit open circulation (Alt et al., 1996; Coggon et al., 2004), its effect on the style and intensity of alteration in the upper ocean crust might be considerable. Correlation coefficients between various petrographic alteration parameters and sedimentary rate and cover described in section 7.3 are weak. Positive trends between sediment cover and F_{Sr}^{SW}, carbonate in veins, Cs and U, and trends between sediment rate and CaO, C, and LOI indicate that sedimentary burial may have a minor effect on the overall alteration of the upper oceanic crust. In both correlation coefficient matrixes using chemical alteration indicators (Figures 7.5 and 7.12) sediment cover shows a weak trend with crustal age, consistent with progressive sediment burial of basement as the crust ages. Al_2O_3 decreases with decreasing sedimentation, hinting at less replacement of primary phases. Slight trends between sedimentation and the change in MgO, K_2O, halo coverage, % C in veins, F_{Sr}^{Sw} and Rb are outlined in Figure 7.17. These trends indicate that sedimentation may have a minor role in controlling the style and intensity of alteration in ocean crust. No clear trends are present between Sites 1224, 843, 1179, or 1149. The age, spreading rate, locations, and tectonic histories of Sites 1224, 843, 1179, and 1149 are highly variable. Such disparity across these Sites may be sufficient to obscure the detection of chemical changes that may be caused by sedimentation.

The location of Site 896, is thought to give rise to the relatively high levels of alteration at 896 compared to Site 504 (This study and Teagle et al., 1996; Alt et al., 1996; Chan et al., 2002). Site 1243 (11 Ma), which is at an almost contemporaneous position to Site 1256 (15 Ma) was formed at fast spreading rates (142 mm/m.y) and endured ~117 m of sediment burial (Orcutt et al., 2003). In contrast Site 1256 (15 Ma, 220 mm/m.y full spreading rate) endured ~250 m of sedimentation (Wilson et al., 2003). Comparisons between the sedimentation and alteration intensity, including tie lines, which highlight the difference between Sites 896 and 504, and 1243 and 1256 in Figure 7.17 indicate that lower sedimentation increases open circulation, hydrothermal activity and chemical change. Sites 1243 and 896 exhibit increased halo coverage, C in veins, K_2O, and Rb when compared to the more deeply buried Site 1256 and 504

respectively. A decrease in Al_2O_3 within Sites 896 and 1243 indicate increased replacement of primary phases compared to Sites 504 and 1256 respectively. In addition to sedimentation at Site 1256 the presence of a ~100 m thick lava pond may contribute to the lack of alteration relative to Site 1243 since it forms a relatively thick 'cap' above the volcanics that erupted at the ridge axes (Wilson, et al., 2003).

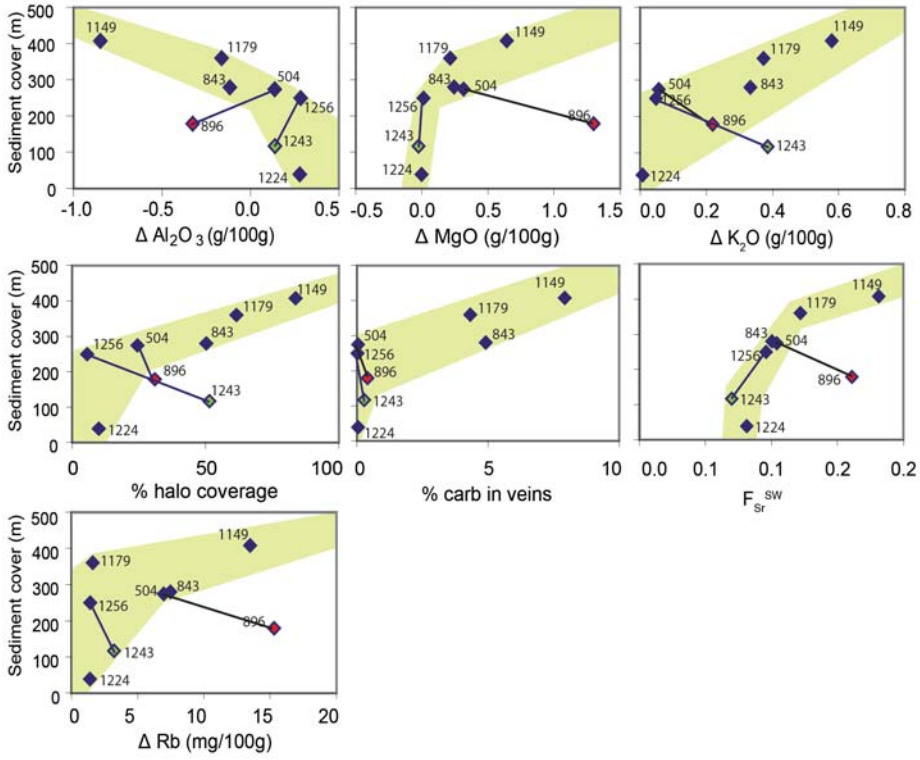

Figure 7.17. Halo coverage and selected elements indicative of low temperature hydrothermal alteration vs. sediment cover. Sites 504, 896, 1243 and 1256 are highlighted with tie lines to indicate the potential link between hydrothermal activity and sediment cover.

Stronger correlations coefficients between Age and spreading rate indicate that their influence on low temperature hydrothermal alteration is much greater than sedimentary rates. Potentially, sampling of basement rock at sites along transects, for example the eastern flank of the Juan de Fuca Ridge, in crust that have formed under similar spreading rates with similar crustal morphology may help resolve the potential influence on sedimentation, and provide a reference transect for the different stages of alteration that occur during low temperature ridge flank and off axis hydrothermal circulation. Because Site 1243 may represent a similar alteration setting to that of Site 504, heat flow surveys of the area may be a useful test to determine if Site 1243 is being altered under upwelling conditions, and if so, how common topographically controlled focussing of fluid flow is in the ocean crust.

7.6. Trends between Holes 504B, 896A and 1256D

7.6.1 Holes 504B and 896A

Basement recovered at Sites 504 and 896 are the same age (6.9 Ma), same spreading rate, 65 mm/yr full (full rate, Hey et al., 1977) and both are thought to have been formed under similar tectonic conditions along the Costa Rica rift (See Sections 6.1 and 6.2 and references therein respectively). Sites 504 and 896 are in an area of pronounced topographic variation (Cann et al., 1983). Site 504 was sampled in a topographic low, with a 274.5 m thick sediment pile, whereas and Site 896 is situated on a Site 896 is located near the crest of an abyssal hill near the centre of a 4 km wide trough where sedimentation totals 179 m. The majority of indicators used in this study point towards greater alteration at Site 896 than at Site 504. These include; 1) Increased abundance of halos at Site 896 than Site 504 (Figure 7.4) with ~31 % brown halos compared to 19 % brown halos respectively. Alt et al., (1993) also observed a higher abundance of breccias and carbonates at Site 896 compared to 504B. 2) A greater proportion of seawater Sr incorporated into whole rock basalts (Figure 7.7 and 7.8), $F_{Sr}^{SW} = 0.16$ for Hole 896A compared to 0.1 for Hole 504B, 3) a greater degree of chemical change at Hole 896A, with greater changes observed in SiO_2, MgO, CaO, K_2O, LOI, CO_2 Rb, Sr, U and Cs than 504B (Figure 7.9).

Given that Site 896 resides on basement formed at the same time and spreading rate at Site 504 the variation in alteration between these sites cannot be a function of age or spreading rate, thus it plots as an outlier when all the Sites in this study are compared against age and spreading rate (Figures 7.10, and 7.16)

The age of sediments is comparable at both Site 896 and 504 (Becker et al., 1988), however, sediment on the basement high is thin (~171-179 m) at Site 896 when compared to sedimentation in the surrounding basin within Site 504 (274.5 m) and Site 677 (306 m). Figure 7.18 indicates basement topography and heat flow in a cross section and heat flow contour map.

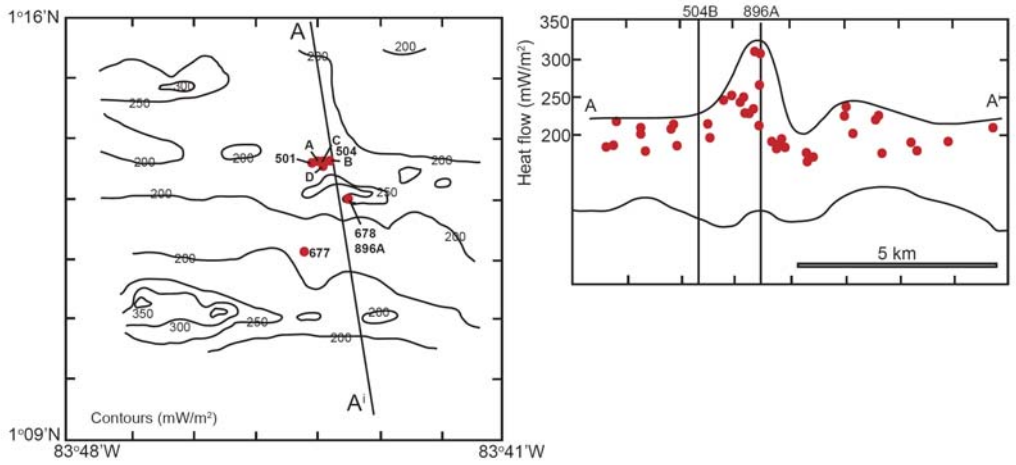

Figure 7.18. Heat flow contour map and cross section (Line A and A^{i}) for Site surrounding Hoe 896A and Hole 504B. Relative basement topography is indicated on the cross section. Redrawn from Teagle et al, (1996).

Heat flow anomalies at Site 896 and 504 (Langseth et al., 1988) that run sub-parrallel to the Costa Rica Rift are strongly correlated with highs in basement topography. Modelling of basement topography and heat flow by Fisher et al., (1990, 1994) indicate that fluid flow and convection takes place as a result of the variable hydrostatic pressures the change in topography provides (see earlier). This supports earlier work by Mottl, (1989) who observed bottom seawater being drawn into the crust in areas of low heat flow. The observed increase in alteration with decreased sediment cover at Site 896 (Figure 7.17) implies that topographic variation at Site 896 and 504 has a greater control on the style and intensity of alteration than sedimentation.

7.6.2 Sites 504/896 and 1256.

DSDP/ODP Hole 504B and ODP/IODP Hole 1256D represent the most complete sections of ocean crust recovered to date. Hole 504B penetrates the volcanic sequence and vast majority of the sheeted dike complex, whereas Hole 1256D penetrates the volcanic sequence, sheeted dikes and into gabbroic bodies. Although comparable in terms of their penetration and sedimentation rate, Site 1256 formed earlier (~15 Ma) from crust at a much faster spreading rate (220 mm/yr, full rate), with smooth basement topography. In addition there are distinct lithological differences between Site 1256 and Site 504/896. The volcanic section at Site 504 is composed of 57 % pillow basalt, 22 % massive flows, 17.5 % thin flows, and 3 % minor dikes (Alt et al. 1996), whereas Site

1256 volcanics are predominantly composed of 51 % sheet flows, 41 % massive flows, and 2.7 % pillow lavas (Wilson et al., 2003). Site 1256 is also capped by a ~100 m thick ponded lava flow (Wilson et al., 2003). Site 896 is composed of 57 % Pillow lavas, 38 % massive flows, and 5 % breccias (Alt et al., 1993). These petrographic variations between Site 504, 896 and 1256 are directly compared (including alteration styles) in Figure 7.19.

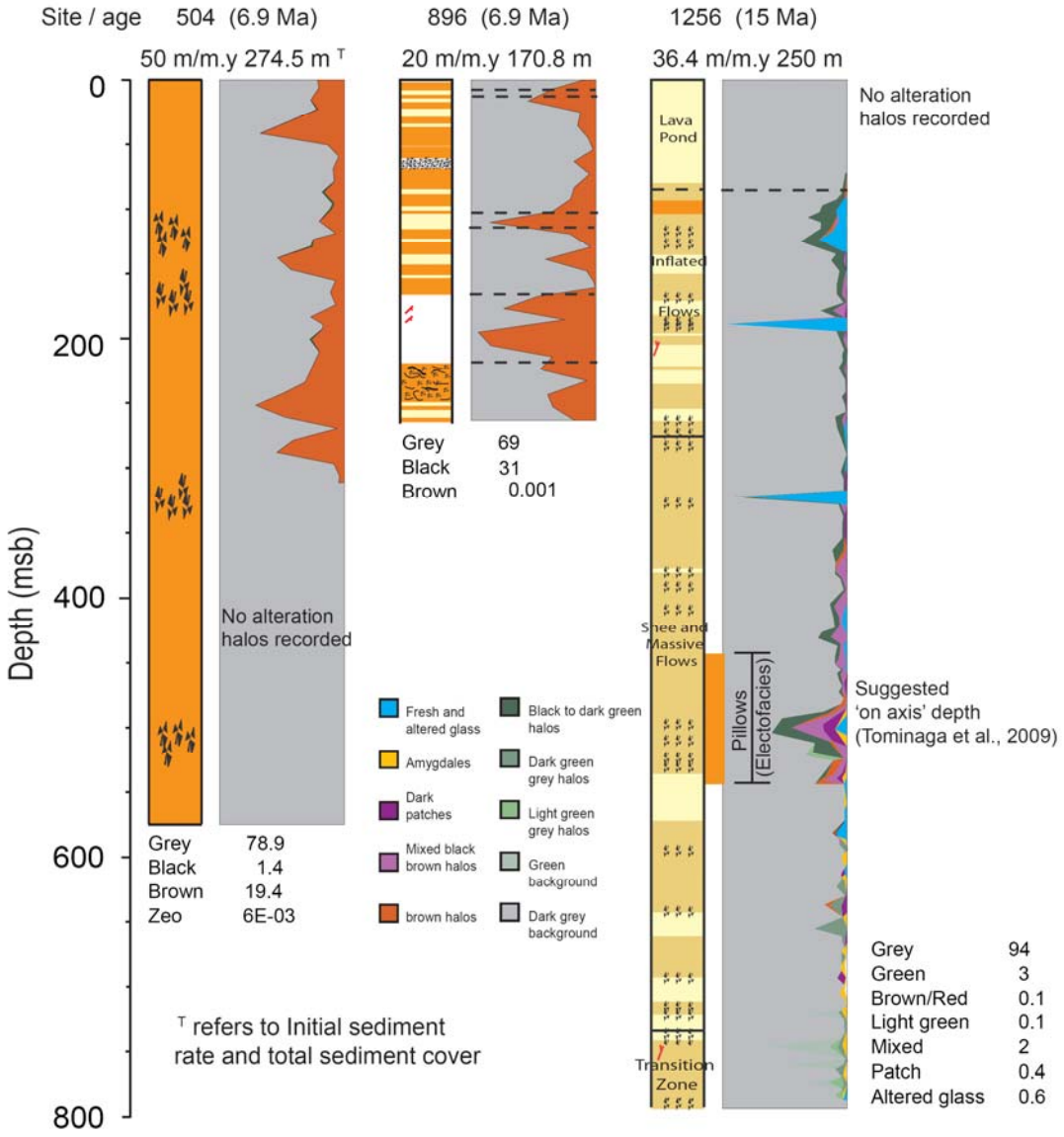

Figure 7.19. Summary of stratigraphy (Based on shipboard observations) and alteration style at Sites 504/896 and 1256, including the suggested 'on axis' depth inferred from core log integration studies (Tominaga et al., 2009).

The percentage of alteration halos at Site 504 and 896 is greater than that of Site 1256. Brown iron-oxyhydroxide/saponite halos comprise 19.4 % and 31 % of the core at Sites 504 and 896 respectively. Whereas Site 1256, which is an older site, only contains 3 %

green celadonitic halos and 0.1 % brown halos. The most intensively altered sections of Site 1256 correspond to zones of brecciation and pillow lavas. Lava flows, and the lava pond, exhibit the least alteration (Figure 7.19). At Site 896 The most intensively altered sections correspond to sheet flows (Alt et al., 1993).

Histograms of whole rock F_{Sr}^{SW} that have been subdivided into lithology (Figure 7.8) indicate that breccias have the greatest proportion of seawater Sr (up to 80 %), followed by pillow lavas (0 to 45 %) and lastly, sheet and massive flows (0 to ~20 %). At Site 1256 F_{Sr}^{SW} for the majority of whole rock samples range from 0 to 10 %. This is in contrast to Site 896, in which whole rock samples contain between 2.5 and 45 % seawater Sr. Site 504 contains 0 to ~20 % seawater Sr in whole rocks. These observations are consistent with restricted seawater circulation and low halo content at Site 1256 and focused fluid flow at Site 896 as predicted by Fisher et al., (1990, 1994) and Teagle et al, (1996). In addition, within Sites 896 and 1256 lithological variation appears to exert some control over the style and intensity of alteration, correlations between lithology and alteration in Figures 7.5, 7.12 and 7.13 are very weak when all sites are compared, however, as discussed earlier trends between massive flows and pillow lavas and alteration styles are evident when directly compared to downhole stratigraphy (Figure 7.19). The major controlling feature of alteration at Site 1256 may be that the ponded lava flow is acting as a cap rock inhibiting fluid flow. As discussed in section 7.3.1, Site 1224 also exhibits low alteration (Figure 7.4) and it has a thick massive lava flow unit at the top of the basement.

Chemical changes at Sites 1256, 896 and 504 are summarised in Figure 7.9. Site 896 exhibits the greatest changes with increases in MgO, K_2O, LOI, CO_2, Rb, Sr, U and Cs, and decreases in SiO_2 and CaO. Chemical change at Site 504 and 1256 are similar albeit with a slight decrease in SiO_2 and MgO at Site 1256. Trends between the proportion of alteration halos that make up the volume of recovered core and chemical changes in Figure 7.14 demonstrate increased chemical change with increased alteration halos. However, despite the large difference between halo coverage at Site 504 and Site 1256 (Figure 7.4), chemical change at Site 504 is only slightly greater than Site 1256. This may be because cold seawater circulation at Site 504 caused little chemical exchange with basaltic rock or that the error associated with calculating precursor composition is too great.

7.7. Summary

Cross comparisons between petrological and geochemical observations for multiple penetrations into upper oceanic crust imply that the style and intensity of alteration in fast and intermediate spread crust is governed by several factors. Despite the limitations associated with this kind of study, which are discussed in parentheses; age, spreading rate, initial sedimentation, total sediment cover, and lithological variation all appear to exert influences on alteration. Local variations at each site appear to set precedence over which factor the greatest influence on alteration. For example, Site 896 is considerably more altered than 504B, despite being of very similar age and stratigraphy. Since Site 896 is located on an abyssal hill the difference in basement topography compared to Site 504 has led to focused fluid flow and increased circulation of cold seawater derived fluids (Alt et al; 1996; Chan et al., 2002). As discussed earlier, a similar scenario may occur at Site 1243.

The greater abundance of significant trends associated with age and spreading rate imply that these may be the overriding factors that control the style and intensity of alteration, however, the importance of sedimentation may be obscured by our sample of oceanic crust which attempts to characterise alteration from samples over great age ranges (0-132 Ma), spreading rates (65-220 mm/yr Full rate), lithological variety, and topography. Trends between Site 1243 and 1256, and 504 and 896 indicate that sedimentation inhibits alteration.

Analysis of carbonate veins and the observed increase in alteration intensity with age right up to 132 Ma crust, implies that off axis circulation may continue in excess of 100 m.y. after formation, albeit at slower rates. Re-opening of fractures and the creation of new fractures (interconnected porosity) by localised tectonic events and/or lithospheric flexure prior to subduction may be responsible for minor renewed circulation.

7.6.1 Limitations

A number of limitations arise from attempting to characterise hydrothermal alteration in modern oceanic crust, and until such limitations can be addressed, they will continue to

hamper any attempt at understanding hydrothermal systems on a regional and global level.

1) There still exists a profound lack of penetrations of modern in-situ oceanic crust greater than 50 metres sub basement. Oceanic crust can form at a wide range of spreading rates in a variety of tectonic settings. In addition crust may endure variable levels of sedimentation, off axis volcanism, and variable, often localised structural changes (formation of graben etc).

2) Local variations at Sites within this study may set precedence over regional trends in controlling the style and intensity of alteration, thus hampering attempts to quantify and understand which factors control hydrothermal alteration.

3) Detailed study of local topographic variations and heat flow data is incomplete. Both heat flow and basement relief are potential factors that may affect hydrothermal alteration. Since basement topography is linked to spreading rate (Carbotte and Scheirer, 2004; Karson, 2002: Haymon et al., 1991; Macdonald, 1998) and heat flow forms the basis for many of our models of crustal cooling and hydrothermal fluid and chemical flux (e.g. Sclater and Francheteau, 1970; Sclater et al., 1971; Richter, 1973; Richter and Parsons, 1975; Stein et al., 1994; Stein and Stein, 1992; Mottl., 2003; Fisher et al, 1990; 1994) acquiring complete heat flow and basement topographic data set for all sites may prove critical if we are to understand what controls hydrothermal alteration.

4) Sites 896, 504, 1243, 1256, 1224, 843, 1179, and 1149 all suffer from incomplete recovery due to the obliteration of variably weak horizons during drilling operations. Apart from the obvious reduction in sample, incomplete recovery is likely to assert a strong bias towards more competent lithologies e.g. massive flows, whereas less competent (and more altered rocks), such as pillow lavas and breccias remain unaccounted for. Recent comprehensive core-log integration suggest profound differences between observations of recovered material and electrofacies compositions, clearly illustrate the problem with recovery. Since more altered rocks are less likely to be recovered, estimations of chemical change and alteration intensity remain a minimum. The best expression of this is at Site 1256. If chemical change, and alteration intensity is calculated on the basis of the recent electrofacies interpretations by Tominaga et al., (2009) the proportion of Site 1256 that is composed of breccias and fractured lithologies is much greater.

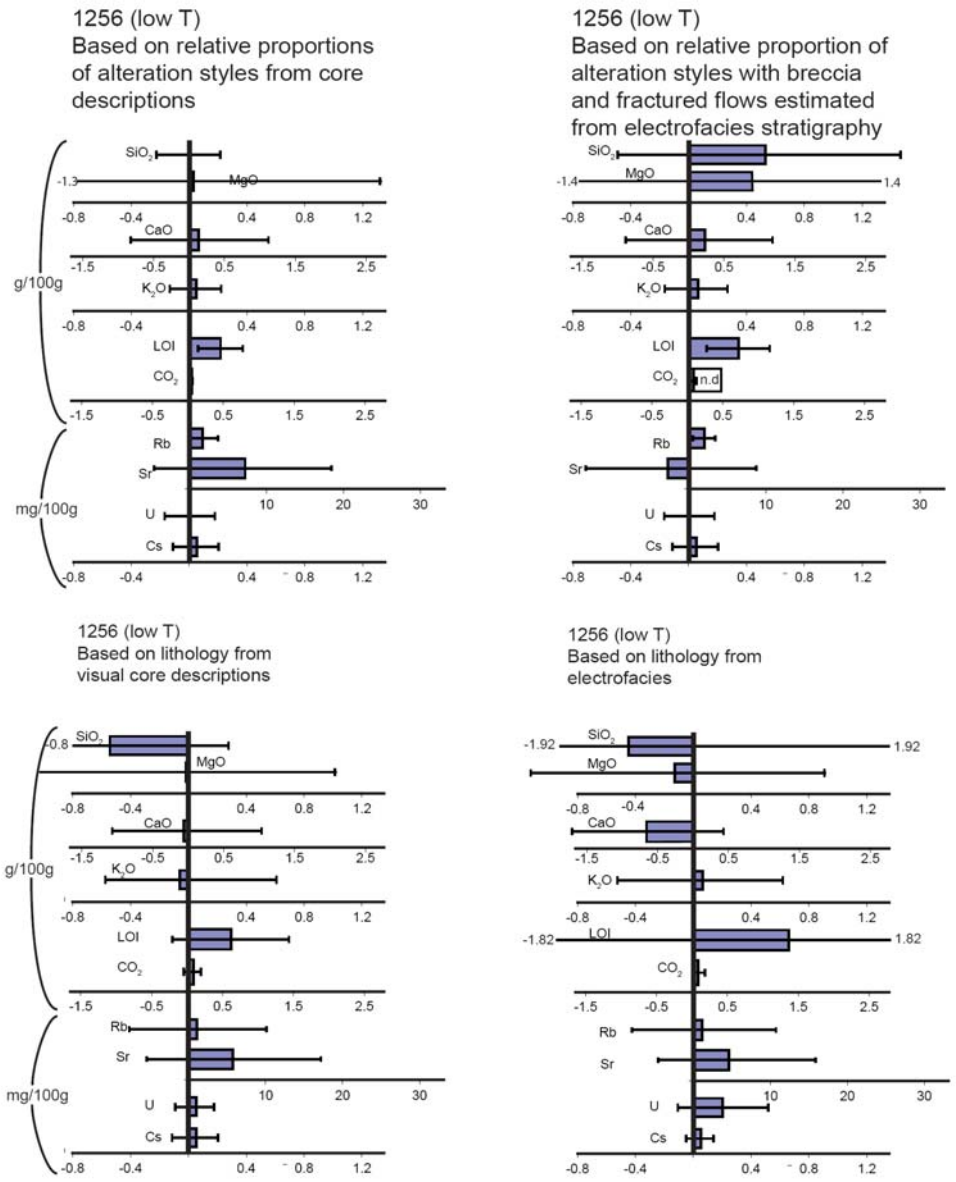

Figure 7.20. Comparison between the calculated chemical changes at Site 1256 for selected elements based on shipboard observations alone and electrofacies observations.

So that direct comparisons can be made between the changes measured based on shipboard observations of stratigraphy and electrofacies reconstrauctions, the fractured flows and fragmented flows described in Tominaga et al., (2008) are grouped as breccias in the same way such lithologies were grouped during shipboard analysis (See appendices C, 2) vii). The overall chemical changes are recalculated with the higher proportion of breccia factored in. Where changes associated with lithology are considered, the electrofacies are factored in. Overall chemical change within the volcanic section at Site 1256 is much higher when compared to overall change calculated based on the stratigraphy from visual core descriptions alone (Figure 7.20).

Despite the large difference in alteration observed in Figure 7.20, these changes must represent a conservative estimate, since electrofacies cannot make up for any potentially unaccounted for alteration in terms of halos and veins. Such large difference in chemical changes measured at Site 1256 must bring into question the validity of any chemical changes of basement made using recovered core observations alone.

5) One factor that is not well represented well in this study is the 3D architecture of the ocean crust and the role that faulting might have in channelizing hydrothermal fluids through the crust. Better recovery, core log integration (point 4) and detailed seismic surveys are required if any relationship between fluid flow and faulting are to be found and what the overall impact faulting has on hydrothermal alteration of the oceanic crust.

Chapter 8

Constraints on fluid evolution during mid-ocean ridge hydrothermal circulation from anhydrite sampled by ODP Hole 1256D.

8. Constraints on the Fluid Evolution during Mid-Ocean Ridge Hydrothermal circulation From Anhydrite Sampled by ODP Hole 1256D.

8.1. Abstract

Key words: Anhydrite, Fluid Evolution, Site 1256

Understanding the evolution of the seawater-derived fluids in active mid-ocean ridge hydrothermal systems (which act as the major heat and chemical transport device) is critical to gaining insights into many aspects of hydrothermal systems in the ocean crust. These include the geometry of recharge and discharge pathways, the relative importance of ridge axis and ridge flank circulation, and the nature of chemical and thermal fluxes. Anhydrite ($CaSO_4$) is a potentially useful mineral for recording the evolution of seawater-derived fluids during mid-ocean ridge hydrothermal circulation because it exhibits retrograde solubility and precipitates from seawater at temperatures greater than >120^oC Anhydrite can precipitate due to the simple heating of seawater, and reaction with basalt, or through mixing of seawater-derived recharge fluids with upwelling, hot black smoker fluids.

New insights into the chemical and thermal evolution of seawater during hydrothermal circulation through analyses of anhydrite recovered from ODP Hole 1256D are based on measurements of $^{87}Sr/^{86}Sr$, major element ratios, REE and $\delta^{18}O$. These data suggest that the vast majority of sulfate is returned to the oceans as warm (as yet undetected) diffuse fluids near the axis. The presence of two chemically and petrographically distinct anhydrite groups, and anhydrite forming at temperatures in excess of 400^oC suggest rapid mixing of low Sr, SO_4-bearing, seawater with high Sr, no SO_4, hydrothermal fluid.

8.2. Introduction

Hydrothermal circulation of seawater through the oceanic crust profoundly influences the composition of the oceans, oceanic crust, and, through subdution of altered crust, the mantle and island arcs. In addition it provides an effective method of heat transfer from the Earth's interior to the oceans (Edmond, et al, 1979; Palmer and Edmond, 1989; Stein and Stein, 1994;). Since confirmation of deep sea vents at the Galapagos in the late 70's (Corliss et al., 1979), our understanding of deep sea hydrothermal systems and their abundance has greatly advanced with the discovery and sampling of many more vent sites. Much work has also been carried out to constrain the physical and thermal structure of ocean crust and its implications on the geometry of fluid flow in the ocean crust (e.g. Morton et al., 1987; Rohr et al., 1988; Sleep, 1991; Teagle, et al., 1998a; 1998b).

However, there remains many fundamental aspects of hydrothermal circulation that are not well understood, including the geometry of recharge and discharge pathways, the relative importance of ridge axis and ridge flank circulation, and the nature of chemical and thermal fluxes (Teagle, et al., 1998). Pivotal to gaining insights into these aspects of hydrothermal circulation is the chemical evolution of seawater-derived fluids that are the principal agents of heat and mass transfer. One of the major steps towards constraining the geometry of hydrothermal fluid flow is to understand sulfur cycling at mid-ocean ridges and in particular to reconcile the large disparity between the sulfate content observed in seawater with that observed at mid-ocean ridge vent sites. Cold seawater that enters the ocean crust is abundant in sulfate (~ 27.9 mmol/kg) yet at black smoker sites HS^- ranges from 0.25-1 mmol SO_4^{2-} (Seyfried and Ding, 1995).

To account for the loss of sulfur observed at vent sites, the sulfate must either precipitate as secondary mineral phases, such as anhydrite or other sulfides or be reduced to sulphide and exit at black smokers. Estimates of high temperature fluid flux (e.g. 5-9 $x10^6$ kg m^2; Sleep, 1991) that are based on heat flow models, indicate that hydrothermal circulation has the capacity to deliver a much greater amount of sulfur to axial discharge zones than observed in the ocean crust (Sleep et al 1991). Anhydrite ($CaSO_4$) precipitates when seawater reaches temperatures in excess of ~120^{o}C (Bischoff and Seyfried, 1978). This retrograde solubility of anhydrite coupled with the fact that a large proportion of ocean crust resides at temperatures over ~120^{o}C

implicates anhydrite as the main sulfur precipitate. In addition, since there is insufficient Ca within seawater to precipitate all the available sulfate as anhydrite, formation of anhydrite in any significant volume relies on either the leaching of Ca from the basalts, for example Ca-rich phases such as plagioclase or volcanic glass (Mottl, 1983), or by mixing with Ca- rich upwelling hydrothermal fluids similar to that of black smokers (Alt et al., 1985).

Anhydrite is a useful mineral because Sr readily partitions with Ca. Measurement of Sr concentration and $^{87}Sr/^{86}Sr$ from anhydrite allow insights into the compostion of hydrothermal fluids and their evolution with depth in the ocean crust (e.g., Teagle et al., 1998a, 1998b; Teagle, 2003). In addition S and O isotope ratios from anhydrite can be similarly used to assess how hydrothermal fluid has interacted with the host rock and the thermal regime at the time of anhydrite precipitation (e.g., Chibu et al., 1981; Teagle et al., 1998; Alt et al., 1996).

Other possible secondary minerals with significant S include pyrite, chalcopyrite and magnesium hydroxysulfate hydrate (MHSH) (Mottl, 1983). Secondary pyrite and chalcopyrite have been documented at most basement sites with significant penetration, for example, Hole 504B (Alt et al., 1986; Vanko, et al., 1996; Alt et al., 1996) Hole 1256 (This study and Teagle et al., 2006). However, the quantities of these minerals remain accessory (Teagle et al., 1998) and MHSH has only been documented as discrete intergrowths with anhydrite at hydrothermal vent sites (Mottl, 1983). In this Chapter, petrographic observations and chemical analysis of anhydrite recovered at Site 1256 and Site 504 will be used to: 1) Assess the chemical and isotopic evolution of seawater-derived fluids during hydrothermal recharge; 2) infer the architecture of fluid flow including timing and fluid mixing; and 3) discuss how the distribution and abundance of anhydrite at Sites 1256 and 504 tie in with current geochemical and theoretical models of hydrothermal interaction and fluid flow.

8.3. Geological Setting of Sites 1256 and 504.

ODP/IODP Site 1256 is located within the Guatemala Basin on the Cocos plate which resides on the eastern flank of the East Pacific Rise (EPR). The crust fromed at a super fast spreading rate (220 mm/yr full rate) ~15 M.yr ago on a 400 km-long ridge segment, ~100 km north of the ridge triple junction between the Cocos, Pacific and Nazca plate. Site 1256 is currently the second deepest hole drilled into intact ocean crust and it penetrates sediments, extrusives, dykes, and for the first time gabbros to a depth 1507.1 mbsf. Previous to the drilling of Hole 1256D, Hole 504B was the only site to sample anhydrite in-situ (Teagle et al., 1998). Figure 8.1 illustrates the stratigraphy of Hole 1256D and Hole 504B together with the distribution of anhydrite at these holes. Hole1256D comprises 250 m of sediment, 54 m of ponded lava flow, 176 m of inflated flow, and 474 m of sheet and massive flows down to 756 msb (meters sub basement) that has been slightly (<10 %) altered to low temperature (<100^{o}C) mineral assemblages with few brecciated intervals. A transition zone of extrusives and intrusives is reported between 756 and 813 msb. This coincides with the occurrence of mineralised breccia zones that mark the start of high temperature alteration at Site 1256. This transition zone is followed by 345 m of sheeted dykes to 1156 msb, that exhibit doleritic textures and massive basalts cross-cut by subvertical dyke margins that commonly have highly brecciated and mineralized chill margins. Between 1098 to 1156 mbsf the basalts in the lower sheeted dyke complex are partly to completely recrystallized to granoblastic textures. Below this a ~100 m dyke-plutonic transition zone of gabbros intruded into contact metamorphosed dykes was recovered to a total depth of 1257 msb (Teagle et al., 2006).

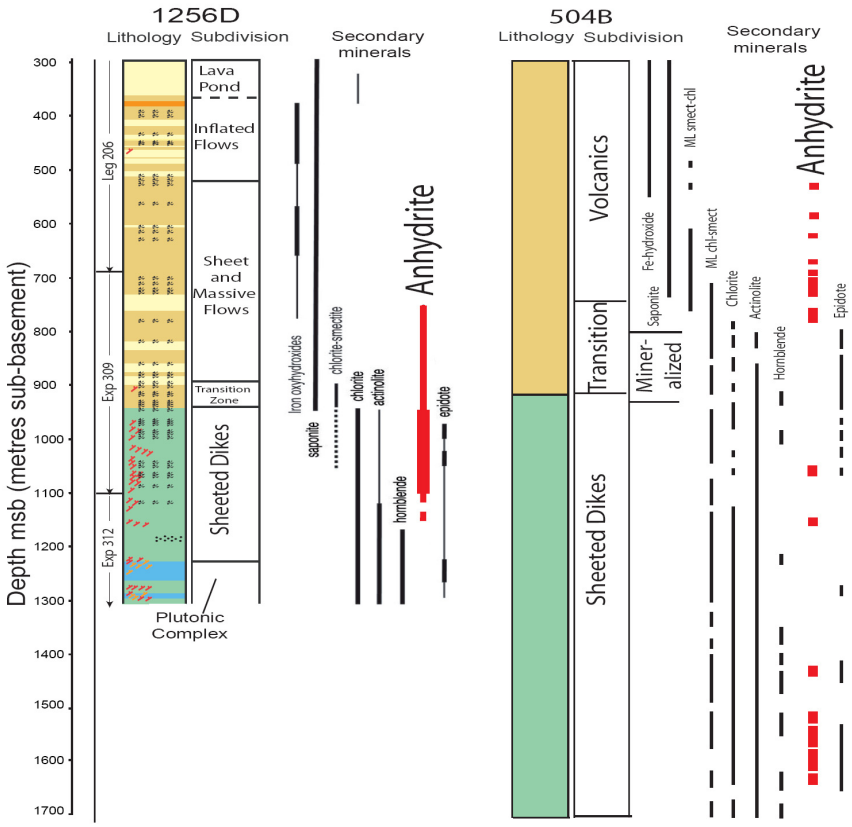

Figure 8.1. Selected secondary mineral occurrence at Sites 1256 and 504. Anhydrite is highlighted in red. Thick lines at Site 1256 depict relative abundance (Data sourced from Teagle et al., (2006) and Alt et al., (1996))

DSDP/ODP Hole 504B is located ~259 km south of the intermediate spreading rate Costa Rica Rift in the eastern equatorial Pacific. Basement at IODP/ODP Hole 504B is 6.9 Ma and it remains the deepest penetration of upper oceanic crust to date (over 1800 m of basement), with recovery of rocks from the entire volcanic sequence and most of the sheeted dyke complex. Despite the recent success of Site 1256, Site 504B remains the reference section of ocean crust to which all other sites are compared to and it has contributed much to our understanding of hydrothermal systems (Alt et al., 1986; Alt et al, 1996). Hole 504B penetrates 274.5 m of sediments, 571.5 m of volcanics, 209 m of a dyke and lava screen transition zone, and 1056 m of sheeted dykes.

Like Site 1256 alteration at Site 504 can be divided into upper and lower alteration zones that exhibit only slight (5-15 % secondary minerals) alteration. A number of highly altered, strongly recrystallised sections are reported, such as breccias and, in the case of site 504B, a mineralised stock work zone at 635.5-653.5 msb

The volcanic section was subjected to low temperature alteration with secondary phases, including saponite, celadonite, iron-oxyhydroxides. Oxidizing conditions in the upper lavas give way to more restricted fluid flow and reducing conditions at the base of the lavas. Within the lithological transition zone, alteration shifts from low temperature (<100^{o}C) to high temperature sub-greenschist facies assemblages (250-350^{o}C) that include actinolite, prehnite, and chlorite. Alt et al, (1996) and Vanko et al, (1996) note that depletions in Cu, Zn and sulfur contents in halos and secondary minerals assemblages, and the abundance of metal sulfides and Mn bearing chlorite in the transition zone in Hole 504B may relate to the 'reaction zone' in which hydrothermal fluids acquire their black-smoker compositions.

8.4. Distribution of anhydrite at Sites 1256 and 504.

Logging of veins and alteration phases were carried out for the entire sections of ODP/IODP Holes 1256D and DSDP/ODP 504B (Alt et al, 1996; Teagle et al., 1998; Teagle., 2006). To calculate the abundance of sulfate in the ocean crust as shown in Figure 8.2, volume percentages of SO_4 in veins and breccia in the recovered core are recorded. At Site 504 whole rock SO_4 is also included in Figure 8.2. Anhydrite at Site 1256 occurs from a depth of ~530 to ~1000 msb, and it is concentrated in the lava-dyke transition zone and uppermost sheeted dykes (754 to 811 msb). Anhydrite most commonly occurs as a minor, late stage component in multi-minerallic veins, or it may be present within breccia matrixes and vesicles. In only rare cases anhydrite is present in the groundmass, filling interstitial areas and replacing plagioclase (Teagle et al., 2006). In the low temperature assemblages anhydrite is rare and when present it cross-cuts iron-oxyhydroxide, saponite, and celadonite. Cross cutting relationships between anhydrite and late-stage carbonates and zeolite are not observed.

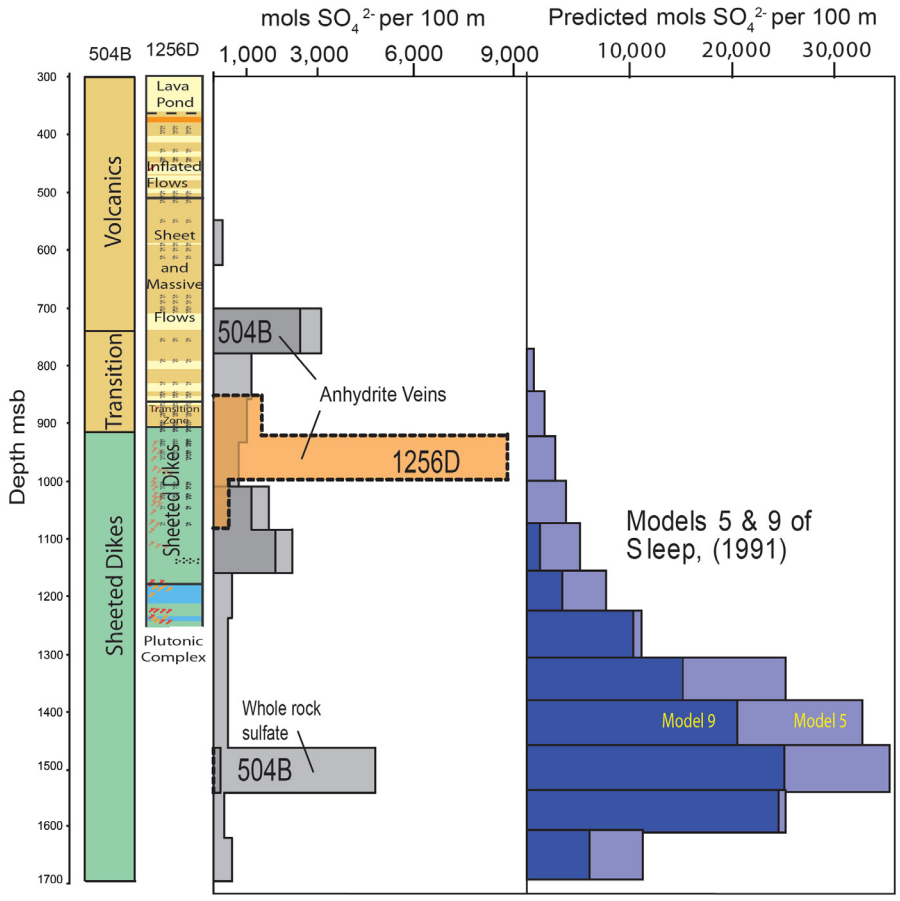

Figure 8.2. Distribution and abundance of sulfate as anhydrite filling veins and porespaces and SO_4^{2-} concentration in whole rock powders for Site 504 (Teagle et al., 1998) and Site 1256 at 100m depth incraments per m^2, Note there is no whole rock SO_4 data present and the different scales of SO_4^{2-}. This data is compared to the amount of anhydrite required to reconcile the fluid flux models of Sleep (1991), Teagle, pers comm.

In the lowermost lavas and lithological transition zone, anhydrite is more common. Despite the relatively low temperatures of the lava section at Site 1256, no evidence of dissolution or pseudomorphing is present. Anhydrite in the mid to upper section of the sheeted dykes typically postdates the the greenschist facies minerals chlorite, epidote, prehnite and laumontite. Within the mid to lower sheeted dykes the abundance of anhydrite drops markedly, with only discrete anhydrite crystals within the groundmass remaining. Again, there is no evidence of subsequent dissolution which may have otherwise explained the lack of anhydrite at this depth.

The distribution of anhydrite at Site 504 is more widespread. It has been reported from 300 msb to the base of DSDP/ODP Hole 504B (~1700 msb). Anhydrite straddles both temperature regimes, with similar mineralogical associations as those observed for Site 1256. However, the greatest abundance of anhydrite, like Site 1256, is

in the lowermost lavas, the transition zone and the uppermost dykes. Alt et al, (1985) report rare minor replacement of anhydrite by prehnite in the shallower portions of the dykes, but evidence for widespread dissolution is lacking. Anhydrite observed in the lower dyke portion is minor and present within the groundmass rather than as veins. Measurements of the whole rock sulfate contents at Site 504 by Alt, (1995) indicate that most rocks have <100 ppm sulfate. Some have elevated concentrations of between 200-1000 ppm, and rarely up to 4860 ppm in samples that have visible anhydrite. Whole rock sulfate at Site 1256 typically ranges from 63 ppm to 2000 ppm, and rarely upto 6090 ppm.

Estimates on the total amount of sulfate present are in the order of 17 x 10^3 mol per square metre of ocean floor for Hole 504B. Most sulfate observed at Site 504 is within the whole rock, while the rest (1/3) is present at veins, cavity fillings and breccia matrixes. Since no whole rock sulfate measurements have been made for Site 1256, we can only assume that the amount of SO_4 reported from veins and breccia matrixes at Site 1256 is a minimum, and that the real value is likely to be higher thus approaching a similar SO_4 composition to Hole 504B

8.5. Results

8.5.1 Petrographic observations

Twelve samples of Site 1256 anhydrite that were hand separated from veins and breccia matrixes, were sectioned for petrographic analysis. Due to the use of cold water during the cutting and polishing process, some samples of anhydrite underwent dissolution leaving behind skeletal remnants or gaps in the section. Where possible, interpretations are made where anhydrite is clearly preserved.

All anhydrite sampled here is sourced from vein material and breccia matrixes. Anhydrite has a moderate relief, which is higher than most surrounding minerals, for example, calcite and quartz. On good crystal surfaces cleavage at {010} (perfect), {100} and {001} (good) is visible. In addition birefringence is high with third order colours and extinction is straight on all cleavages. These features, coupled with partial dissolution during the sectioning process, are diagnostic of anhydrite (Gribble and Hall,

1992). Crystal structure variation includes large to small patches of anhydrite that range from euhedral prismatic, to numerous, fine needle-like crystals.

Anhydrite occurs as a late-stage assemblage, replacing/overprinting all previous mineral assemblages including quartz, saponite, celadonite, chlorite, and iron oxyhydroxides. Cross cutting relationships between anhydrite and carbonate and zeolite are not defined, however it is suspected that these late stage minerals precipitated within a similar time frame. Unlike the majority of anhydrite samples at Site 1256 Samples 309-1256D-118R-1, 11-13 cm; 135R-1, 104-106 cm; 144R-1, 111-114; and 156R-2, 86-91 cm (Figure 8.3) appear to predate quartz, and uncommonly chlorite or chlorite/smectite. Notably these samples occur in the transition zone and the upper dykes (Figure 8.3). One sample of anhydrite (Sample 309-1256D-140R-1, 29-33 cm) occurs within an intrusive margin breccia that consists of a chlorite, quartz, pyrite and chalcopyrite cement with host rock and intrusive clasts (Figure 8.4). The breccia represents a complex interplay between host rock, intrusives and hydrothermal fluid that appears to have come in direct contact with the intrusive body. Anhydrite in this sample is anhedral and surrounds euhedral quartz crystals.

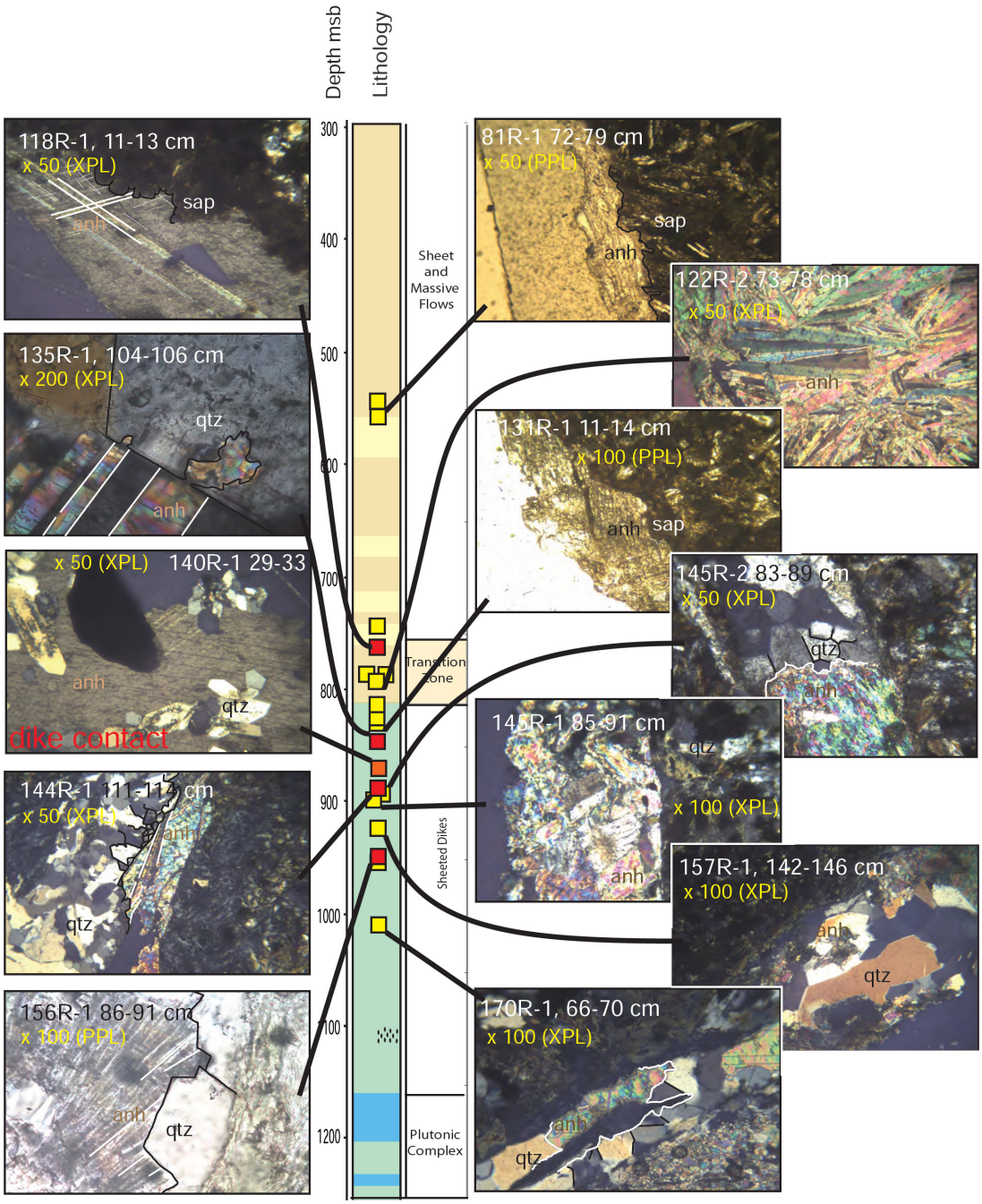

Figure 8.3. Locations of samples analysed and their petrographic distinctions. Group I anhydrites are highlighted in yellow (overprints Quartz and Saponite). Group II anhydrites are overprinted by quartz and saponite. The orange square is a superheated dyke contact breccia. In this sample anhydrite is late stage and it surrounds euhedral quartz crystals.

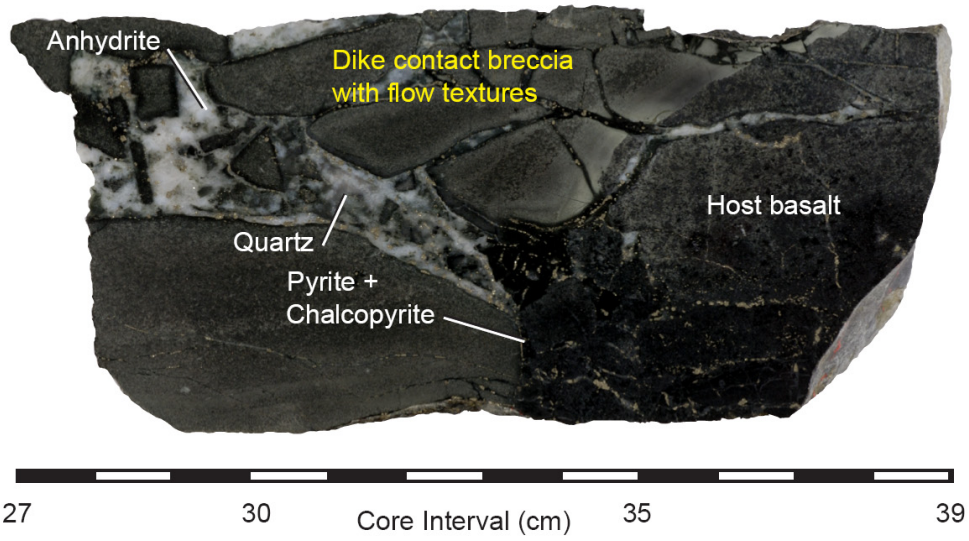

Figure 8.4. Sample 309-1256D-140R-1, 27-39 cm. Dyke contact breccia, clasts consist of an intrusive body, containing flow textures and chill margins, matrix is composed of anhydrite, quartz, pyrite and chalcopyrite. Interval 34 to 39 cm is the host basalt, probably an earlier dyke (Image sourced from the Janus database).

8.5.2. Sr isotopic composition of anhydrite

The Sr-composition of 19 pure hand picked anhydrite samples for Hole 1256D was measured by TIMS (Table 8.1) following the methodology outlined in Chapter 2. Whole rock $^{87}Sr/^{86}Sr$ of the lavas trends from elevated compositions (0.7040) towards primary MORB compositions mid way through the volcanic section. In the lower volcanics to upper dyke section at Site 1256 $^{87}Sr/^{86}Sr$ is once again elevated above MORB, these enriched compositions remain throughout the dykes and into the gabbros. Moderate to highly elevated Sr-isotopic ratios in whole rock samples generally reflect the intensity of alteration, with the most intense alteration (and highest $^{87}Sr/^{86}Sr$) present in breccias. The lithological transition zones represent the most intense alteration, at both Sites this zone marks the transition between low and high temperature alteration. Detailed descriptions of the whole rock Sr isotopic profile and alteration assemblages for Sites 1256 and 504 are reported in Chapter 4 of this thesis (Site 1256); Teagle et al, (2006).

Overleaf: Table 8.1. Sr-isotope, $\delta^{18}O$, major trace and REE concentrations of Site 1256 anhydrite.

Expedition, hole, core, interval (cm)		309 1256D 81R-1, 58-60	309 1256D 84R-1, 72-79	309 1256D 114R-1, 113-116	309 1256D 118R-1, 11-13	309 1256D 122R-2, 71-73	309 1256D 122R-2, 73-78	309 1256D 123R-1, 31-34	309 1256D 128R-1, 47-51	309 1256D 130R-1, 85-89	309 1256D 131R-1, 11-14	309 1256D 135R-1, 104-108	309 1256D 140R-1, 29-33	309 1256D 144R-1, 111-114	309 1256D 145R-1, 85-91	309 1256D 145R-2, 83-89	309 1256D 151R-1, 111-114	309 1256D 156R-2, 86-91	309 1256D 157R-1, 142-146	309 1256D 170R-1, 66-70
Depth	(mbsf)	789.4	802.5	989.9	1008.1	1029.5	1029.5	1032.4	1056.6	1066.6	1070.6	1090.7	1114.0	1133.6	1137.9	1139.8	1166.4	1191.7	1195.6	1252.5
	Host	Haloclastite	massive basalt	massive basalt	massive alt basalt	volcanic breccia	volcanic breccia	Flow basalt	Haloclastite	massive basalt	massive basalt	volcanic breccia	intrusive margin breccia	flow basalt	massive slight alt basalt	massive slight alt basalt	dyklet	massive basalt (intrusive)	massive basalt (intrusive)	massive basalt (intrusive)
	Occurrence	matrix	pure vein + rim of sap	anh+zeo vn	alt patches	anh+glass + zeo+sulph matrix	anh+glass+ zeo+sulph matrix	pure vein	sap, zeo, sulph matrix	anh+sap +silica vein	anh+sap+silica vein	single anh vug+gls+sil+sulph	anh+chalpy+clh/sm matrix	anh (young)+ py+ chl/sm vein	anh(young) +chl/sm+ py	anh(young) +chl/sm+ py	anh+chl +py vein	anh(young)+chl +silica+py vein	pure anhydrite vein	anh(young)+qtz + chl vein
	Group	I	I	I	II	I	I	I	I	I	I	II	II	II	I	I	I	II	I	I
	87Sr/86Sr	0.708027	0.708513	0.707739	0.705229	0.708486	0.708159	0.707908	0.707960	0.708091	0.708201	0.704843	0.704750	0.704621	0.708113	0.708394	0.707079	0.705153	0.708436	0.708181
Error	2σ	13	14	10	17	11	11	10	14	11	11	14	17	17	14	11	13	13	13	10
[x] MORB	Present	17.3	10.0	21.6	59.1	10.4	15.3	19.0	18.3	16.3	14.7	64.9	66.3	68.2	16.0	11.8	31.5	60.3	11.1	15.0
	15 Ma	12.1	4.4	16.7	56.6	4.8	10.0	14.0	13.2	11.1	9.3	62.7	64.2	66.3	10.7	6.3	27.2	57.8	5.6	9.7
$\delta^{18}O$	(‰ vs. SMOW)	14.5	n.d	17.7	14.1	14.9	14.5	13.1	10.9	11.3	n.d	16.3	2.2	n.d	n.d	9.0	29.0	11.0	9.7	9.8
T^c	(°C)	135.9	n.d	105.4	140.3	131.5	136.0	151.4	180.4	174.2	n.d	117.3	408.2	n.d	n.d	211.4	35.5	178.9	198.8	196.8
Sr/Ca	(mmol/mol)	1.36	1.21	0.82	0.56	1.10	1.08	0.84	1.68	1.27	2.53	0.42	0.09	0.35	1.78	2.88	0.04	0.43	3.15	1.10
Mg	(ppm)	107	221	211	167	194	267	166	124	213	309	262	n.d	n.d	344	475	n.d	n.d	n.d	670
Mn	(ppm)	1.8	0.0	3.3	6.6	4.0	12.7	46.8	3.6	4.9	7.4	12.7	n.d	n.d	5.6	5.8	n.d	n.d	n.d	14.7
Fe	(ppm)	242	712	496	348	298	236	430	226	531	735	629	n.d	n.d	323	731	n.d	n.d	n.d	1104
Rb	(ppm)	1.46	1.11	0.78	0.03	0.93	0.73	1.14	1.65	1.08	1.92	1.90	0.00	0.02	1.20	0.53	0.03	0.03	0.01	1.62
Sr	(ppm)	876	776	528	363	711	697	541	1079	815	1627	273	56	223	1145	1851	24	274	2025	705
Y	(ppm)	0.47	0.73	0.38	0.39	0.77	0.61	2.45	0.78	0.34	2.17	0.05	9.64	0.03	0.79	1.03	0.12	0.11	1.14	1.03
Zr	(ppm)	0.05	0.05	-0.01	0.08	0.06	0.05	0.03	0.05	0.02	0.11	0.03	0.03	0.03	0.02	0.03	0.01	0.03	0.04	0.03
Nb	(ppm)	0.003	0.009	0.007	0.010	0.005	0.002	0.005	0.005	0.004	0.025	0.007	0.006	0.003	0.006	0.006	0.005	0.001	0.002	0.006
Cs	(ppm)	0.008	0.001	0.002	0.001	0.000	0.001	0.002	0.002	0.001	0.004	0.069	0.000	0.001	0.001	0.000	0.002	0.001	0.000	0.001
Ba	(ppm)	4.10	2.81	5.37	0.87	4.05	4.63	2.54	8.80	7.14	40.72	5.42	0.66	2.85	7.21	4.18	1.95	1.47	5.49	14.16
La	(ppm)	0.24	0.07	0.04	0.08	0.15	0.13	0.51	0.14	0.05	0.21	0.01	1.21	0.01	0.18	0.21	0.10	0.02	0.17	0.39
Ce	(ppm)	0.42	0.12	0.10	0.13	0.38	0.36	1.16	0.45	0.09	0.56	0.02	2.32	0.02	0.32	0.36	0.09	0.03	0.39	0.88
Pr	(ppm)	0.05	0.02	0.02	0.02	0.06	0.06	0.22	0.09	0.02	0.14	0.00	0.35	0.00	0.06	0.07	0.01	0.00	0.06	0.17
Nd	(ppm)	0.26	0.13	0.14	0.09	0.36	0.35	1.22	0.58	0.11	0.95	0.01	1.99	0.01	0.32	0.42	0.04	0.02	0.33	0.91
Sm	(ppm)	0.07	0.04	0.05	0.03	0.11	0.10	0.33	0.17	0.05	0.39	0.01	0.58	0.003	0.10	0.15	0.01	0.01	0.11	0.24
Eu	(ppm)	0.02	0.01	0.02	0.01	0.02	0.02	0.12	0.05	0.03	0.20	0.01	0.47	0.001	0.05	0.06	0.01	0.01	0.05	0.30
Gd	(ppm)	0.08	0.07	0.06	0.04	0.15	0.14	0.44	0.20	0.07	0.48	0.02	0.93	0.005	0.15	0.23	0.01	0.01	0.14	0.28
Tb	(ppm)	0.01	0.01	0.01	0.01	0.02	0.02	0.06	0.02	0.01	0.07	0.00	0.15	0.001	0.02	0.03	0.00	0.00	0.02	0.04
Dy	(ppm)	0.07	0.09	0.06	0.04	0.11	0.09	0.35	0.11	0.05	0.36	0.02	0.95	0.003	0.11	0.17	0.01	0.01	0.14	0.19
Ho	(ppm)	0.01	0.02	0.01	0.01	0.02	0.02	0.07	0.02	0.01	0.06	0.00	0.21	0.001	0.02	0.03	0.00	0.00	0.03	0.04
Er	(ppm)	0.04	0.05	0.02	0.03	0.04	0.03	0.16	0.04	0.02	0.14	0.01	0.52	0.003	0.05	0.07	0.01	0.01	0.07	0.08
Tm	(ppm)	0.004	0.006	0.002	0.003	0.003	0.003	0.017	0.005	0.007	0.016	0.002	0.071	0.001	0.005	0.007	0.001	0.001	0.009	0.010
Yb	(ppm)	0.015	0.026	0.009	0.066	0.014	0.011	0.098	0.022	0.010	0.071	0.008	0.471	0.004	0.023	0.037	0.006	0.008	0.049	0.049
Lu	(ppm)	0.0024	0.0033	0.0013	0.0027	0.0019	0.0011	0.0154	0.0028	0.0017	0.0090	0.0014	0.0638	0.0003	0.0036	0.0048	0.0019	0.0010	0.0082	0.0074
Hf	(ppm)	0.0045	0.0036	0.0025	0.0020	0.0009	0.0019	0.0076	0.0051	0.0023	0.0077	0.0016	0.0053	0.0001	0.0020	0.0010	n.d	0.0006	0.0009	0.0031
Ta	(ppm)	0.0402	0.0022	0.0016	0.0106	0.0021	0.0059	0.0103	0.4242	0.0030	0.0031	0.0013	0.0009	n.d	0.0015	0.0011	0.0005	n.d	n.d	0.0017
Pb	(ppm)	0.15	1.63	0.41	0.12	0.23	0.10	0.16	0.05	0.16	0.14	0.61	0.18	0.22	0.08	0.09	0.09	0.21	0.06	0.05
Th	(ppb)	1.64	1.38	1.81	0.43	0.36	0.19	2.07	1.01	3.99	2.50	2.56	-0.13	0.40	0.45	0.33	0.21	0.52	1.45	0.47
U	(ppb)	1.94	3.20	2.98	0.19	0.60	1.25	2.34	5.66	1.65	3.85	2.71	-0.07	-0.05	0.95	0.85	-0.23	3.91	-0.08	1.22

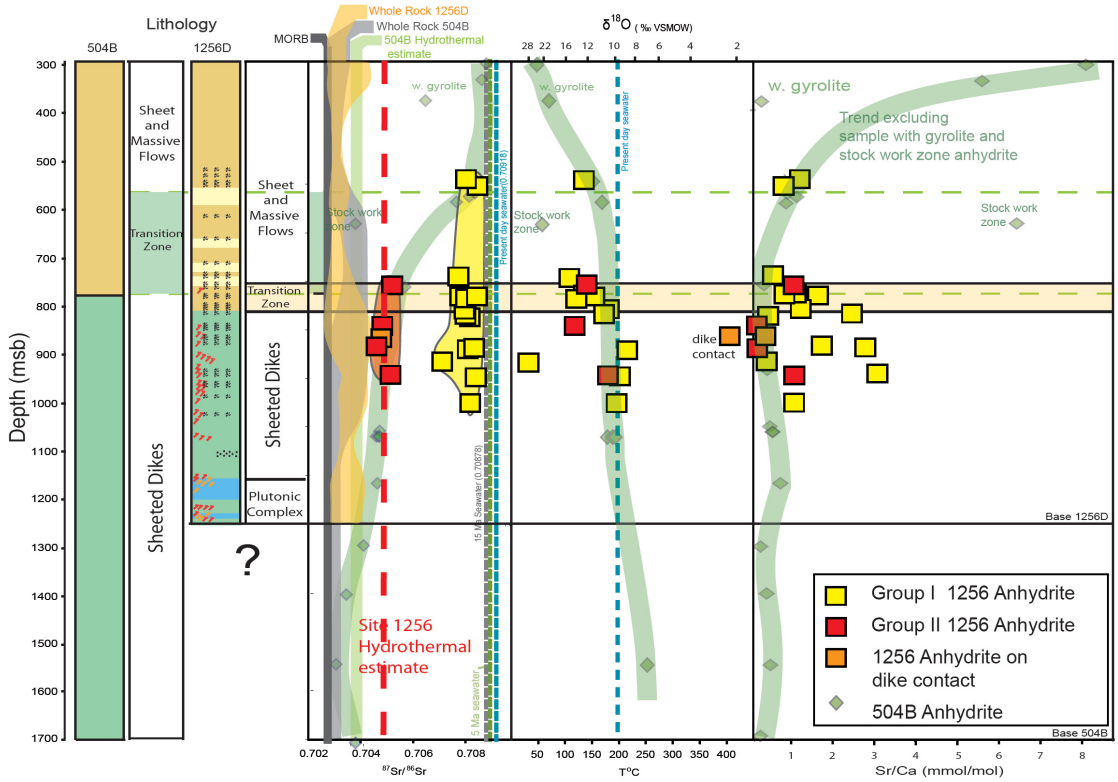

Figure 8.5. Distribution of Sr-isotopic ratio for anhydrite vs depth for Sites 1256 and 504B.$\delta^{18}O$ and Sr/Ca vs. depth are also displayed. For reference average EPR MORB (Saunders et al., 1988), whole rock $^{87}Sr/^{86}Sr$ for Sites 504 (Erzinger et al., 1995; Teagle et al., 2006) and 1256 (This study, Harris, Cooper, Unpub. data) The hydrothermal estimate for Site 1256 (Harris et al., 2008), and seawater $^{87}Sr/^{86}Sr$ for modern oceans and oceans at the time of formation for Sites 1256 and 504 (McArthur et al., 2001) are included. Site 504 anhydrite measurements are from Teagle et al., (1998).

Hole 1256D Epidote have measured $^{87}Sr/^{86}Sr$ of ~0.705 (Harris et al., 2008), these estimates may reflect the composition of ancient 'black smoker' type fluids for Site 1256 following Teagle et al., (1998).

The Sr-isotopic composition of anhydrite at Site 1256 ranges from 0.70462 to 0.70851 (Table 8.1 and Figure 8.5) and they broadly fall into two groups that exhibit $^{87}Sr/^{86}Sr$ that ranges from 70708 to 0.70851 (Group I) and 0.70462 to 0.70523 (Group II). Group II anhydrites exhibit Sr-isotopic compositions that are close to that of Epidote (~0.705). The anhydrites with 'hydrothermal' Sr-isotopic compositions only occur in the transition zone and sheeted dykes, the region in which high temperature alteration is recorded (Chapter 4, and Teagle et al., 2006) whereas Group I anhydrites extend into the higher temperature sheeted dykes (Figure 8.5). Anhydrite recovered from Sample 309-1256D-140R-1, 29-33 cm is sourced from a dyke contact and it exhibits hydrothermal $^{87}Sr/^{86}Sr$ (0.70475).

Observations of Site 1256 are in stark contrast to Site 504, in which anhydrite records, with increasing wall rock exchange, a gradual shift from a cold, (>150^{o}C) seawater-dominated fluid (0.70883-0.7084) to an intermediate source (0.70766-0.70561), towards hydrothermal compositions (0.70497-0.70292) (Teagle et al., 1998). One sample, with a $^{87}Sr/^{86}Sr$ of 0.7038 within the mineralized stockwork zone at Site 504 mirrors that of coexisting epidote (0.7038) and like Site 1256 may represent the composition of upwelling black smoker type hydrothermal fluids (Teagel et al., 1998). A sample from 381 msb with intermediate $^{87}Sr/^{86}Sr$ (~0.7065) contains intergrowths of gyrolite (Figure 8.5), therefore represents a complex hydrothermal history, in addition this sample has an unusual $\delta^{34}S$ (+36‰) which is well above $\delta^{34}S$ observed from the other anhydrites at Site 504 (~21‰) (Teagle et al., 1998).

8.5.3. Sr/Ca ratios

The Sr/Ca ratio of anhydrite at Site 1256 and Site 504 provide insights into the Sr/Ca ratio of the fluid from which anhydrite precipitated. A range of experimental Sr partition coefficients have been determined from the following expression (Shikazono and Holland, 1983) which are similar to the empirically derived partition coefficient for TAG anhydrite (Teagle et al., 1999).

$$K_d^{Sr} = \left(\frac{{}^{a}SrSO_4}{{}^{a}CaSO_4} \right) \Big/ \left(\frac{{}^{a}Sr^{2+}}{{}^{a}Ca^{2+}} \right)$$

Calculations for Site 1256 are carried out following Teagle et al, (1998) so that they may be directly compared to Site 504. Following from Teagle et al, (1998), a plot of $^{87}Sr/^{86}Sr$ vs. Sr/Ca, for Site 1256 and 504 is shown (Figure 8.6). Anhydrite from Hole 504B shows major decreases in Sr/Ca with only minor change in $^{87}Sr/^{86}Sr$, which is followed by a reduction in $^{87}Sr/^{86}Sr$ with no real change in Sr/Ca.

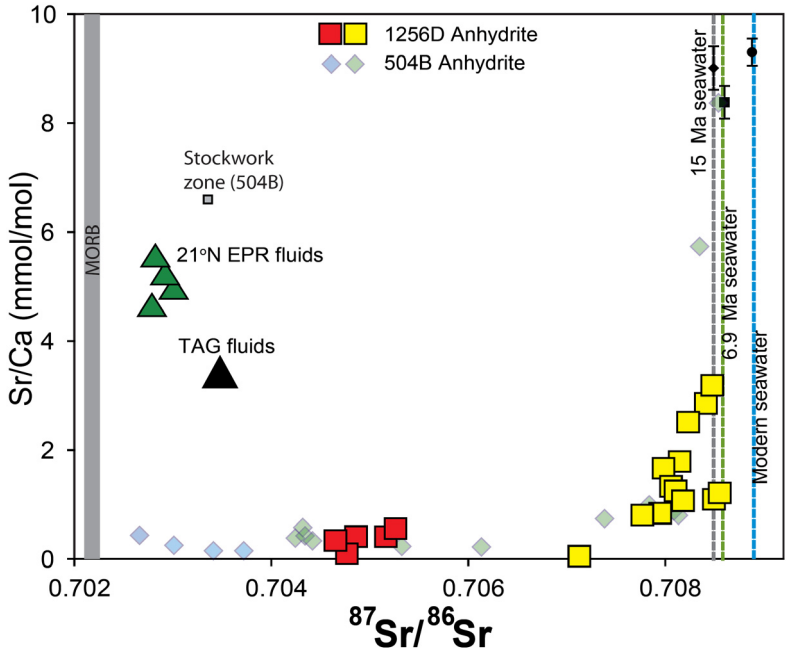

Figure 8.6. Sr-isotopic ratio vs. Measured Sr/Ca ratios for Sites 1256 and 504B anhydrites. Group I anhydrites (yellow) Group II anhydrites (red). Hole 504B anhydrites are grey diamonds. Blue diamonds represent leached samples. TAG and 21°N EPR are included for reference. Figure is updated from Teagle et al, (1998).

Two samples from Site 504 have high Sr/Ca implying precipitation from seawater or seawater derived fluid (Teagle et al., 1998). These high Sr/Ca values may indicate the lack of Ca available for anhydrite due to precipitation of carbonates. One 504B sample within the stock work zone exhibits high Sr/Ca (Figure 8.5) as well as low $^{87}Sr/^{86}Sr$ (Discussed earlier). Teagle et al, (1998) suggest that this anhydrite represents mixing between black smoker fluids and sulphate bearing hydrothermal fluids. Other samples have very low Sr/Ca ratios which are lower than fluids predicted for black smoker fluids. Site 1256 Sr/Ca ratios vs. $^{87}Sr/^{86}Sr$ exhibit a similar pattern as Hole 504B, however, Site 1256 has no intermediate Sr isotopic compositions which once again highlights the distinction between Group I and II anhydrites. (Figure 8.5)

8.5.4 $\delta^{18}O$ of anhydrite

The $\delta^{18}O$ for 15 anhydrite samples from Site 1256D were measured and results, normalised to VSMOW are shown in Table D, 1 (Appendices). Low sample volume precluded O-isotope measurement in Samples 309-1256D-84R-1, 72-79 cm, 131R-1,

11-14 cm, 144R-1, 111-114 cm and 145R-1, 85-91 cm. Sample 309-1256D-151R-1, 111-114 cm returned an anomalously high $\delta^{18}O$ value (+29.0 $‰_{(VSMOW)}$) even after two repeat runs. $\delta^{18}O$ measurements for anhydrite at Site 1256 range from +29 ‰ to +2.2‰, Most samples, however, range from +8 ‰ to +16 ‰. $\delta^{18}O$ values are both higher and lower than seawater sulfate ($\delta^{18}O$ ~ + 9.6 ‰) implying that isotopic exchange has taken place. $\delta^{18}O$ decreases with depth, although the shallowest recorded anhydrite is not the highest value (Figure 8.6). Anhydrite recovered between the transition zone and the upper sheeted dykes variably exhibit a greater decrease that ranges from + 16 ‰ to 10 ‰ for the deepest sample.

The $\delta^{18}O$ of anhydrite has been used to determine the temperature of the fluid during precipitation, following a temperature-dependant oxygen isotope fractionation factor which has been determined for temperatures between 100^o and 550^{o}C (Chibu et al., 1981):

$$10^3 \, In\alpha_{anhydrite-water} = 3.21 \times \left(10^3 / T\right)^2 - 4.72$$

Calculated temperatures all make the assumption that the anhydrite was in equilibrium with heated seawater that had a $\delta^{18}O$ of 0 ‰ during precipitation. In Hole1256D calculated formation temperatures range from 35^{o}C to 407^{o}C, although most calculated temperatures range from 100-220^{o}C. With the exception of Sample 309-1256D-151R-1, 111-114 cm, anhydrites at Site 1256 record an increase in formation temperature with depth (Figure 8.5). Anhydrites from both Group I and Group II are not distinct in terms of $\delta^{18}O$ (Figure 8.6). Sample 309-1256D-151R-1, 111-114 cm, with a $\delta^{18}O$ of + 30 ‰ (35^{o}C) indicates great exchange and very low temperatures at depth. Sample 309-1256D-140R-1, 29-33 cm, which formed as part of a dyke contact breccia has an ultra-low $\delta^{18}O$ of + 2.2 ‰ which indicates a temperature of ~407^{o}C. In this sample, such a high temperature supports the hypothesis that the fluid came in direct contact with the intrusive body. In addition, despite the absence of anhydrite in the lower sheeted dykes and the gabbro section, Sample 309-1256D-140R-1, 29-33 cm clearly demonstrates that anhydrite can precipitate at very high temperatures at depth.

By contrast, Site 504B exhibits a relatively monotonous decrease in $\delta^{18}O$ from +28 ‰ in the lavas to +7 ‰ in the lowermost sheeted dykes. This represents an increase in temperature from $50^{o}C$ to $250^{0}C$.

8.5.5 REE of Site 1256 Anhydrites.

The Rare Earth Element (REE) concentrations of Site 1256 anhydrite were measured by ICP-MS (See Chapter 2 'Methods'). Table D,1 (Appendix) displays the results of REE analysis for anhydrite and REE patterns are shown in Figure 8.7 All anhydrite samples at Site 1256 have low concentrations of REE compared to the average Site 1256 whole rock values and MORB. All anhydrites are, however, enriched compared to seawater and hydrothermal fluid. Concentrations vary by up to three orders of magnitude. In most anhydrite samples HREE are slightly depleted compared to LREE. Group II anhydrite REE patterns exhibit overall lower concentrations than Group I anhydrites, in addition the Group II patterns are more variable. Eu anomalies (Eu*), defined as the relative difference in concentrations between chondrite normalised neighbouring elements (Sm_N) and (Gd_N) where: $Eu^* = Eu \Big/ \sqrt{Sm_N \times Gd_N}$, range from 0.59 to 3.59. Comparatively high Thulium in Sample 309-130R-1, 85-89 cm and high ytterbium in Sample 309-118R-1, 1-13 cm are also observed in Figure 8.7.

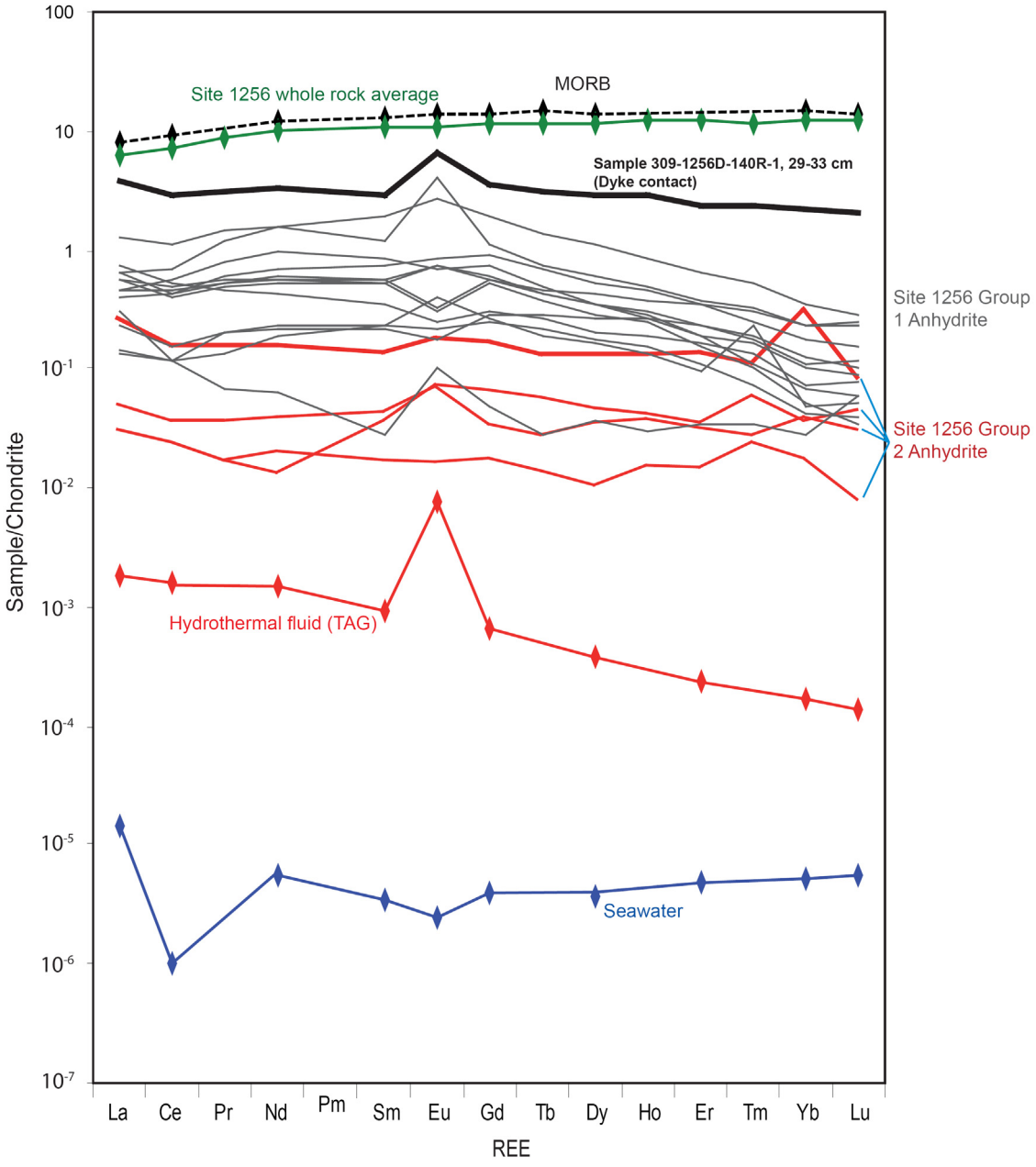

Figure 8.7. Chondrite normalised REE patterns for Site 1256 anhydrite, hydrothermal fluid (TAG) and average seawater (Seawater and TAG from Mitra et al., 1994). The Average Site 1256 whole rock pattern and average MORB (Bevins et al., 1984; Sun and McDonough, 1989) are shown.

8.6. Discussion

The trends between Group I and Group II anhydrites reflect the incorporation of basaltic Sr into the fluid (Figure 8.6). Basalt-fluid Sr exchange, temperature, and fluid fluxes have profound effects on the Sr-isotopic composition of the secondary minerals which can precipitate from a hydrothermal fluid. Group I anhydrites reflect precipitation from a fluid with near seawater Sr-isotopic compositions that has endured only limited wall rock reaction. In contrast, Group II anhydrites are indicative of anhydrite that formed in hydrothermal fluids that have undergone much greater interaction with the wall rock, probably at high temperatures. The overprinting of Group II anhydrite by quartz and other secondary phases compared with the late Group I anhydrite, which overprints quartz and saponite (Figure 8.3), suggests that Group II anhydrites formed early in Site 1256 basement. Intriguingly Group I anhydrites extend well into the sheeted dykes, overlapping Group II anhydrites (Figure 8.3). These observations imply two separate fluid histories for Site 1256.

Neither Site 504 nor 1256 have Sr/Ca vs. $^{87}Sr/^{86}Sr$ that come close to the composition of venting 'black smoker' fluids. In addition, no black smoker fluid to date has a low enough Sr/Ca to suggest that the fluids deep in Sites 504 and 1256 represent black smoker fluids. The evolution of fluid for both Sites 504 and 1256 in this study and Teagle et al, (1998) suggest that: 1) Precipitation of carbonates leads to evolved Sr/Ca ratios in the fluids since carbonates, being Sr-poor compared to seawater, take Ca out of the fluid. Most carbonate. 2) That the low Sr/Ca ratios at the lower portion of Site 504 and Group II anhydrites at Site 1256 represent the reduction of Sr rather than concomitant increase in Ca strongly affects the Sr/Ca ratio of a fluid (Seyfried and Mottl, 1982). The petrographic evidence for the timing of carbonate precipitation at Site 1256 and 504 (This study; Teagle et al., 2006; Alt et al., 1993) appears to be late stage therefore a reduction of Sr/Ca in the fluid via carbonate precipitation would have to take place off axis.

One possible mechanism, outlined by Teagle et al, (1998), to reduce the Sr concentration is to form albite. Both Sites 504 and 1256 contain secondary albite to which Sr is more strongly partitioned into than Ca. This partitioning would further lower the Sr/Ca ratio by releasing Ca into the fluid as it partitions with Sr (Teagle et al., 1998). Klinkhammer et al., (1994) suggest that the formation of secondary calcic plagioclase (adsorbing the Ca in the fluid) could raise the Sr/Ca ratio to black smoker

fluid compositions. Group II anhydrite at Site 1256 may have been formed by mixing of sulfate bearing recharge fluids with upwelling black smoker fluids. This mixing with recharge fluids may provide the necessary Sr to increase Sr/Ca to hydrothermal fluid compositions. Teagle et al, (1998) also suggest that mixing can explain the high Sr/Ca and low $^{87}Sr/^{86}Sr$ anhydrite sample within the mineralized stockwork zone at Site 504B.

An adapted figure from Berndt et al., (1988) based on experimental and theoretical constraints of Ca and Sr exchange reactions indicates a series of hypothetical fluid pathways that could result in black smoker-type fluids seen at EPR 21°N or TAG, together with data from 1256 and 504 anhydrite (Figure 8.8) A: dissolution of Sr from basalts (Thereby increasing the Sr concentration in the fluid towards MORB like compositions) followed by removal of Sr by later reaction and precipitation (bringing Sr concentration back towards vent fluid compositions). B: Initial precipitation of seawater Sr in mineral phases followed by reaction with the host rocks the black smoker fluids. C: Dissolution and precipitation occur simultaneously. D: where precipitation of secondary phases with little wall rock reaction takes place followed by a second phase of greater fluid rock interaction in which basaltic Sr is taken up by the recharge fluid. Mixing lines are calculated assuming a closed system with the following expressions:

$$[Sr]_{Mix} = \left(X_{SW} \times [Sr]_{SW}\right) + \left([Sr]_{MORB} \times \left(1 - X_{SW}\right)\right)$$

$$^{87}Sr/^{86}Sr_{MIX} = \frac{\left(^{87}Sr/^{86}Sr_{SW} \times [Sr]_{SW} \times X_{SW}\right) + \left(^{87}Sr/^{86}Sr_{MORB} \times [Sr]_{MORB} \times \left(1 - X_{SW}\right)\right)}{[Sr]_{MIX}}$$

Where $^{87}Sr/^{86}Sr_{SW}$ and $^{87}Sr/^{86}Sr_{MORB}$ = seawater and MORB Sr-isotopic composition end members respectively, *[Sr]* is concentration X_{SW} is the proportion of seawater in the mixture $^{87}Sr/^{86}Sr_{MIX}$ and $[Sr]_{MIX}$ is the Sr-isotopic composition and Sr concentration of the mixtures respectively. The model, as discussed in Teagle et al., (1998) is summarised as follows: 1) lower Sr/Ca caused by the precipitation of carbonates and anhydrite with minimal interaction with basaltic Sr, 2) Fluid rock interaction increases resulting in an increased basaltic Sr component (lower $^{87}Sr/^{86}Sr$) and very low Sr/Ca ratios in anhydrite in addition increased wall rock interaction lowers fluid $^{87}Sr/^{86}Sr$ to near MORB compositions, however, no net gain in Sr means Sr/Ca remains low, and

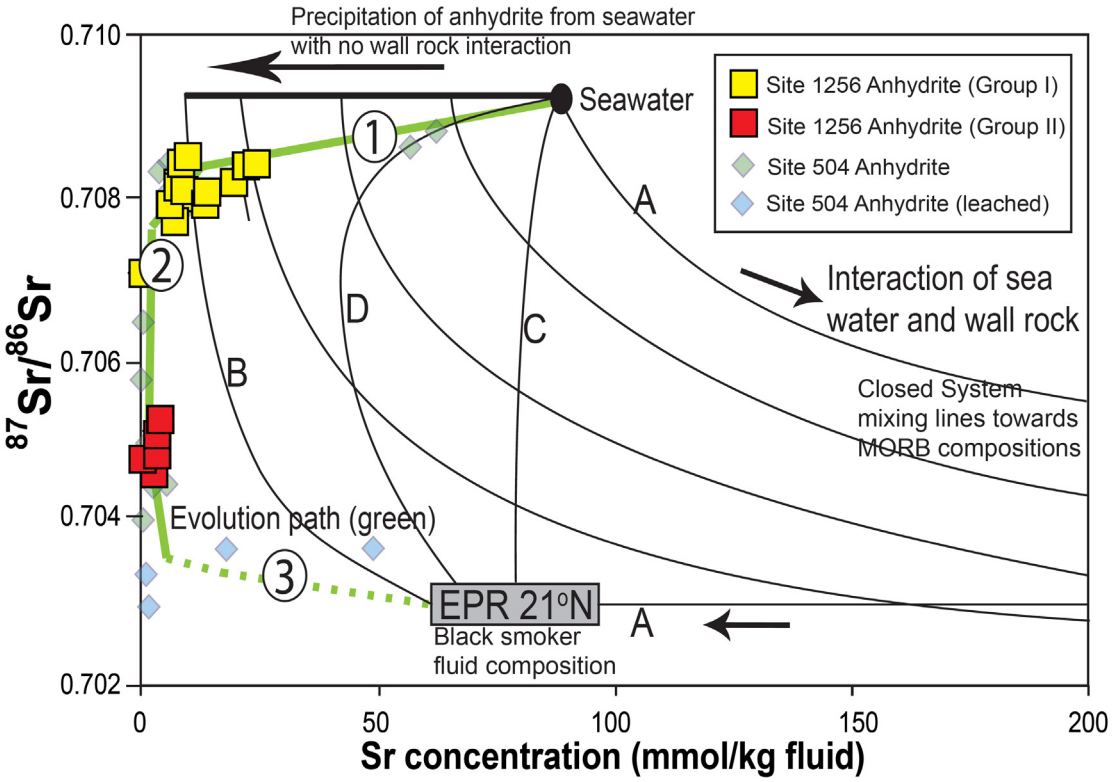

Figure 8.8 Hypothetical fluid pathways for Sr concentration and $^{87}Sr/^{86}Sr$ for fluid evolution to black smoker-like compositions. Redrawn and updated from Berndt et al, (1988) with Sites 504 and 1256 data included.

3) potentially, the formation of secondary calcic plagioclase can take up Ca raising the Sr/Ca ratios to hydrothermal compositions before discharge takes place (Klinkhammer et al., 1994; Blundy and Wood, 1991). The anhydrites recovered from Site 1256 favour an extreme version of Path B, which is similar to Teagle et al, (1998) estimate from Site 504 anhydrite. The only other possibilities are that black smoker fluids at Site 504 had a lower $^{87}Sr/^{86}Sr$ than modern fluids, Or that fluids at Site 504 and 1256 do not contribute to black smoker type venting (Teagle et al., 1998).

The Sr-isotopic composition of the hydrothermal epidote (~0.705, Harris et al, 2008) indicate that hydrothermal fluids that existed at the time Site 1256 formed are comparable to modern fluids, therefore, is seems highly unlikely that the Sr-isotopic composition of black smoker fluid changed significantly with time. Unlike Site 504, no Site 1256 anhydrite was recovered with MORB $^{87}Sr/^{86}Sr$ compositions. This may imply that; 1) that the fluids that produced the hydrothermal Sr isotope values represent upwelling fluids that have yet to gain Sr or loose calcium (Would require sulfate within the hydrothermal fluid), 2) that anhydrite with MORB $^{87}Sr/^{86}Sr$ compositions was not available in great enough quantities to sample, or that it is deeper in the crust where

sampling has yet to take place, or 3) that SO_4^{2-} bearing fluid with very low Sr mixes with high temperature hydrothermal fluid that has high Sr and low SO_4^{2-}.

Since we know that the wall rock Sr can exchange with Sr from hydrothermal fluids, we might expect a similar leaching of REE from whole rock basalts into hydrothermal fluid, and ultimately into secondary minerals that precipitate from the fluid, including anhydrite. However, the chemical change calculated for Hole 1256D whole rock samples (Chapter 4) indicates slight depletion of HREE and a slight gain in LREE thus this cannot fully explain the REE patterns observed in the anhydrites. A weak trend between Sr/Ca ratio and ∑REE concentration is present (Figure 8.9), which implies that a proportion of the REE present in Site 1256 anhydrites must be sourced from basement rocks or that the partitioning of REE from basalt into fluids is not related to Sr exchange.

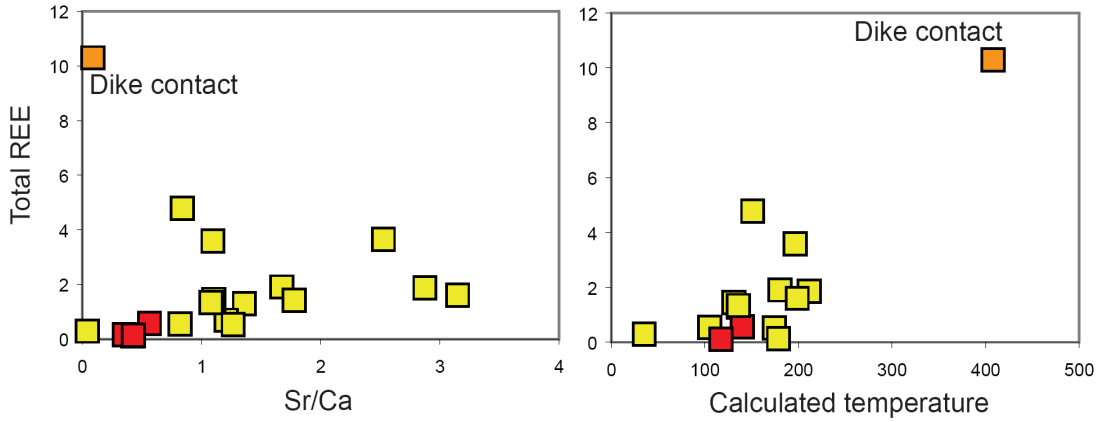

Figure 8.9. Sr/Ca ratio and calculated temperature vs. sum of REE for Site 1256 anhydrites.

The anhydrite sampled from contact breccia 309-1256D-140R-1, 29-33 cm has the highest concentration of REE, close to MORB amounts and the highest calculated temperature (Figure 8.5). In addition this sample has low $^{87}Sr/^{86}Sr$, this demonstrates that it might be possible to impart a significant proportion of MORB REE at high temperatures. Given that the anhydrites at Site 1256 have generally low REE concentrations (much lower than MORB), any transfer of REE from the host rock is likely to impart a strong influence on the REE pattern in the fluid. The lower total concentration of REE in Group II anhydrites (Figure 8.9) and the variable chondrite normalised REE patterns in Figure 8.7 imply a complex fluid history. Since seawater has a low REE concentration, the lower REE concentrations suggest that the fluids that

the Group II anhydrites precipitated from may have mixed with cool, seawater derived fluids. The high thulium and ytterbium in some samples (Figure 8.7) cannot be simply explained by fluid mixing alone, implying complex fluid histories.

A plot of Total REE vs. calculated temperature in Figure 8.9 tentatively suggests a trend of increasing Total REE with temperature, although only the high temperature dyke contact has a convincing MORB-like signature. A rank depth plot of REE patterns for Group I anhydrites indicates a weak trend towards hydrothermal fluid compositions (Figure 8.10). Group II anhydrites do not show any trend with depth, however their fluid history is likely to be separate from Group I. For Group I anhydrites, Eu anomalies are more positive with depth and HREE becomes more depleted relative to LREE with depth. The deepest sample (309-1256D-170R-1, 66-70 cm exhibits an REE pattern very similar to black smoker fluids that have been observed at the TAG hydrothermal mound (Humphris, 1998), yet this sample exhibits an Sr-isotopic composition similar to that of seawater (0.70818). The superheated dyke contact (Sample 309-1256D-140R-1, 29-33 cm) exhibits an REE pattern close to that of TAG, and a hydrothermal $^{87}Sr/^{86}Sr$ of 0.70475, which is similar to the hydrothermal estimate of ~0.705 (Harris et al., 2008). Caution must be used when basing any interpretation of the trends shown in Figures 8.9 and 8.10.

Although there are indications that REE may indicate fluid evolution, the anhydrite to fluid distribution coefficients for REE are not known for the fluid compositions, redox conditions, pressures, and temperatures that are relevant when dealing with warm to hot hydrothermal activity deep in the oceanic crust (Bach et al., 2003). REE partitioning between anhydrite and solutions of $CaSO_4$ have been determined for temperatures up to 70^{o}C (Kagi et al. 1993), however, as Bach et al, (2003) demonstrate that the apparent distribution coefficients of anhydrite recovered from Pacmanus (determined by using the seawater:hydrothermal fluid mixing proportions from Sr-isotopes to calculate hypothetical REE contents of fluids from which anhydrite precipitated, and dividing measured REE by these values) are in orders of magnitude higher than the ones reported by Kagi et al., (1993).

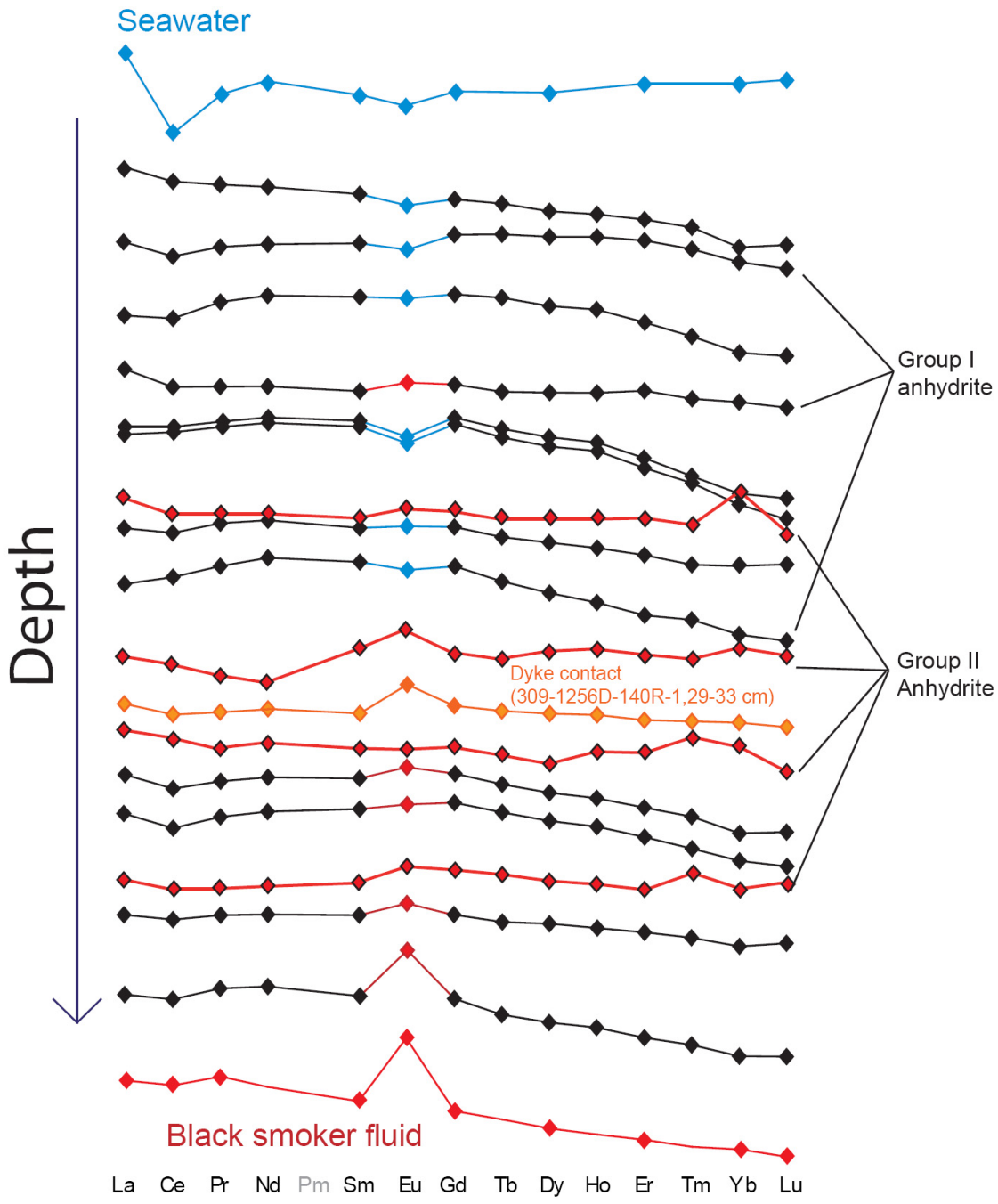

Figure 8.10. Rank order plot of Site 1256 anhydrite REE pattern with regards to depth. Eu-anomalies are highlighted. Patterns variably trend towards patterns that mimic black smoker fluid compositions. The absolute concentrations are not depicted in this figure, black smoker fluid and seawater REE compositions have much lower concentrations. In addition REE are for anhydrites and not fluid. Black smoker fluid and seawater REE sourced from Humphris, (1998).

8.7. The anhydrite conundrum

The magnitude of hydrothermal fluid flux and the path that fluids take to achieve hydrothermal circulation remain poorly understood, and there are many discrepancies that occur between the theoretical models of fluid/chemical flux and the observed chemical/fluid flux. The current model of hydrothermal fluid flow implies that cold seawater percolates through the upper ocean crust which causes interactions with the host rock leading to changes in the chemistry of the water (which evolves to become a hydrothermal fluid) and alteration of the host rock (Figure 8.11). Ultimately, due to continued heating from a number of sources (cooling of the ocean crust, mid-ocean ridge magma chamber) the hydrothermal fluid rises and vents into the oceans, thus completing the convection cell and transferring a multiplicity of elements and compounds sourced from the basement rocks and the mantle to the oceans. Alt et al., (1995) defined three zones that might make up a hydrothermal system. These are the recharge zone, the reaction zone and finally the discharge zone, which are outlined in Figure 8.11.

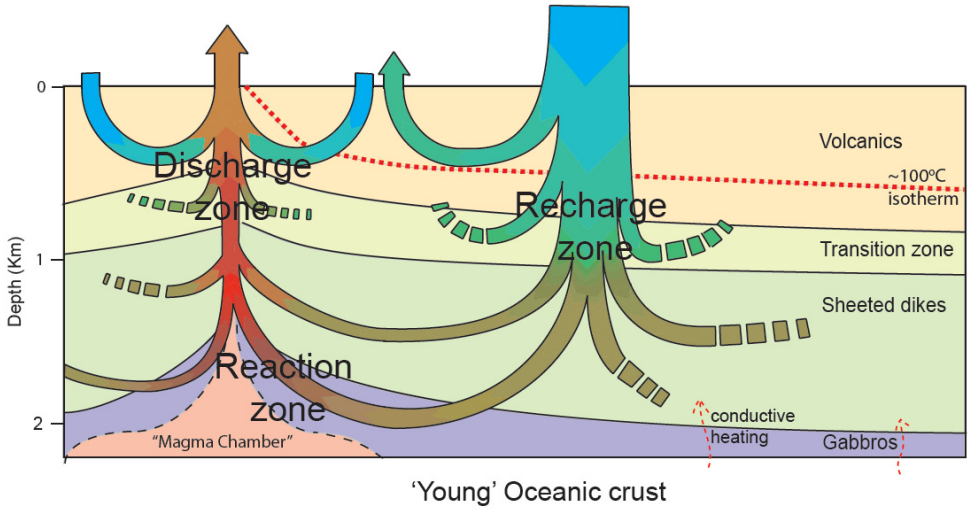

Figure 8.11. Stylised model of a hydrothermal system outlining possible directions of fluid flow and their evolution within oceanic basement. The Recharge zone outlines the area at which seawater percolates into the ocean crust, slowly heating up (~0 to ~150°C) with only minor interaction with the ocean crust. The Reaction zone is the hypothetical area where on or near a large heat source e.g. the mid-ocean ridge magma chamber, the fluid intensively reacts with the host rock to form hot (~450°C) hydrothermal fluids. After reaction, the hot buoyant fluid rises and cools slightly to (~350°C) and discharges out at vent sites. Based on Alt et al. (1995).

Modelling of the hydrothermal system imply that the entire system is operational within only 1-3 km of the spreading centre (Brikowski and Norton, 1989; Sleep, 1991;).The major problem is that modelled hydrothermal fluxes are far removed from estimates based on global geochemical budgets. Despite these differences all models predict that large volumes of seawater should heat to temperatures (>150^{o}C) that induce precipitation of anhydrite (Sleep, 1991; Mottl and Wheat, 1994).

To balance the predicted heat flow with the observed heat flow with age, it is now widely recognised that off axis hydrothermal fluid flow must transfer approximately 80% of the advective heat loss from the crust (Stein and Stein, 1994; Mottl and Wheat, 1994; Mottl., 2003). Teagle et al., (1998) compared the axial high temperature fluid flux by Mottl and Wheat (1994), with fluid flux models by Sleep, (1991), and Morton and Sleep, (1985) (5.5 to 9.0 x 10^6 kg/m^2) with their own estimate (1.36 x 10^6 kg/m^2). Because very little to no sulfate has been detected at mid-ocean ridge vent sites, the vast majority of sulfate in seawater must either precipitate as anhydrite or be reduced to sulfide. Alt et al., (1989) and Alt, (1995) calculated a global axial fluid flux of 4.7 x 10^{12} kg/yr based the minimum volume of seawater entering the crust based on the amount of anhydrite in veins and pore filling and the amount of seawater sulfate reduced to sulphide (from S concentrations and S-isotopic compositions). This implies that axial hydrothermal fluid flux is between 4 and 25 times lower than estimates based on chemical budgets or heat flow models (Teagle et al., 1998). Sleep, (1991) suggested that very large volumes of anhydrite may be precipitated deep in the sheeted dykes. Figure 8.2 indicates the volume of sulfate observed in the ocean crust for both Site 1256 and Site 504 next to the volume of sulfate required down hole to balance the models of Sleep, (1991). The time-integrated fluid flux, based on the Sr-isotopic composition of anhydrite and whole rocks at ODP Hole 504B, of 1.7 ± 0.2 x 10^6 kg m^{-2} is in close agreement with the fluid flux (1.4 x 10^6 kg m^{-2}, Teagle et al., 1998) estimated from the mass of water sulfur in Hole 504B (Teagle et al., 2003). The fluid flux calculated by Teagle et al., (2003) is much lower than that of Morton and Sleep, (1985) (5.5 to 9.0 x 10^6 kg/m^2), which is based on thermal models that assume all magma is intruded into a high level magma chamber at the base of the sheeted dykes (Teagle et al., 2003). If the thermal models are correct then much more fluid flow is required to cool the magma chambers, therefore much more anhydrite should be preserved. Clearly there is a very large deficit.

Similar to the hypothesis of Teagle et al., (1998), three possible escapes from the deficit of sulfide observed compared to the large amounts predicted are presented. 1) That the recovered core at Sites 504 and 1256 do not reflect the true composition of the ocean crust or that anhydrite may exist deeper within the crust, 2) That subsequent dissolution of anhydrite at shallow levels in the crust took place allowing the sulfate to return to seawater, or 3) that a large proportion of seawater sulfate does not precipitate as anhydrite during hydrothermal circulation and that large volumes of sulfate bearing fluids return to the oceans as warm, but diffuse fluids.

8.7.1 Does anhydrite recovered in the ocean crust represent the true extent of sulfate in the basement?

Both Sites 504 and 1256 experienced very low recovery, as such they are susceptible to recovery bearing an influence on the composition on the crust within these areas. Recent electrofacies interpretations at Site 1256 point to a larger percentage of breccias and pillow flows than estimated based on recovered cores alone ~13.5% rather than 7 % (Tominaga et al., 2009), however in breccias recovered, only a minor fraction of the matrix was composed of anhydrite, therefore the relative increase in the amount of anhydrite at Site 1256 as a result of this interpretation still falls far short of the amount of sulfate required. In Hole 504B no significant sulfur anomaly in the wire line logs were detected and it is presumed that areas with high volumes of anhydrite should still show up in cores containing increased abundances of anhydrite veins, such as those found at TAG (Humpris et al., 1996). Site 1256 and 504 may contain large volumes of anhydrite deeper in the ocean crust, however this would be deeper than numerical models suggest (Teagle et al., 1998).

8.7.2 Early dissolution of anhydrite at shallow depths?

If one concentrates cold seawater recharge to within 500m of the axis and in the extrusive section, it can be modelled that anhydrite will precipitate in this warm region by mixing with upwelling fluids where it can later be leached back into the oceans (Sleep, 1991). This potentially resolves the problem of missing anhydrite within the

crust and it allows for a sufficient quantity of water to balance fluid flow models. However there are two major drawbacks to this model, 1) There are now two examples DSDP/ODP Hole 504B and ODP/IODP Hole 1256 in which such potential mixing zones are recovered and neither preserve sufficient quantities of anhydrite, in addition there is no evidence that these portions of crust have ever been cooler. Although the volcanic section have been in direct contact with cold seawater during eruption, subsequent burial and heating will reheat the volcanics to ~100 -150^{o}C to within 5000 years (Sleep, 1991). Only in the uppermost 200 to 300 meters of volcanics could such precipitation and dissolution take place. Site 1243B recovered a white interpillow limestone with pseudomorphs that indicate up to 6% of the rock speculated to be composed of anhydrite (Orcutt et al., 2003), however no evidence of anhydrite or pseudomorphs of anhydrite were recovered in either the basalts above or below the sediment which suggests that that sample represents unique conditions of formation and that it is not representative of past anhydrite content for Site 1243 basement.

8.7.3 Is sulfate returned to the oceans as warm diffuse fluids?

Since it seems unlikely that Sites 504 and 1256 drastically underestimate the amount of sulfate present in oceanic basement and that dissolution at shallow depths remains equally unlikely we are left with the proposition that sulfate may return to the oceans without ever having precipitated as anhydrite. There are several key features of the anhydrite sampled at Sites 504 and 1256 that suggest that seawater sulfate returns to the oceans as warm diffuse fluid:

1) Sulfate is present throughout the volcanics with very little change in the Sr or S-isotopic compositions in the downwelling fluid whereas below the volcanics fluids undergo greater reaction with the wall rock. This implies that sulfate bearing recharge fluids do penetrate most of the sheeted dykes. This allows the fluid to heat to moderate temperatures ~100 to 250^{o}C.

2) Anhydrite can form at temperatures in excess of 400^{o}C and sulfate can remain in solution even at ‘reaction’ zone temperatures. The high temperature of formation implies rapid heating. Hence we expect to see some limited precipitation of anhydrite and potentially sulfate in black smoker fluids. This is supported by the

observation of small amounts of sulfate (0.25-1 mmol SO_4^{2-}) in black smoker fluids (Seyfried et al., 1995) that are too low to account for the sulfate deficit within the crust 3) The low flux derived from the amount of seawater sulfur (Teagle et al 1998), is comparable to the observed thermal structure as recorded by secondary minerals at Site 504. This suggests that either high temperature fluid fluxes are much smaller than previously predicted or that most seawater sulfate does not precipitate out and remains in solution.

4) Site 1256 exhibits similar, low volumes of sulfate to that of Site 504, this draws parallels with Teagle et al., (1998) prediction that the majority of off axis recharge fluids are only heated to 200-250^{o}C before escaping as diffuse flows.

5) Heating the majority of hydrothermal fluids to only moderate temperatures and allowing diffuse flow would balance the models of hydrothermal fluxes based on heat flow and global geochemical budgets (Teagle et al., 1998).

Although there are some models that take into account circulation of large volumes of seawater at 200-250^{o}C at diffuse vent sites (Brikowski and Norton, 1989; Rosenburg et al., 1993), the majority of research into fluid modelling and indeed sampling has been carried out with regard only to high temperature mid-ocean ridge vent sites. Diffuse venting at ridge flanks may be difficult to detect (Hess et al., 1991) since the fluid is likely to be much more dilute than that of black smoker fluids. Teagle et al, (1998) suggest that because diffuse fluids would have a chemical composition in between seawater and hydrothermal fluids, they might be distinguishable from hydrothermal fluids by their elevated sulfate contents and low Mg concentrations. One might begin to look for sites in which diffuse flow may be focussed, such as upthrown fault blocks, seamounts, or areas with thin sedimentation rates near, but not on, the ridge axes.

8.8. Conclusions

The distribution and abundance of anhydrite at Sites 504 and 1256, together with the $^{87}Sr/^{86}Sr$, Sr/Ca, and $\delta^{18}O$ imply that seawater sulfate enters the crust and circulates deep within the lavas and the majority of the sheeted dykes. Site 1256 anhydrite supports the hypothesis by Teagle et al., (1998) that given the lack of sulfate within vent fluids, and the amount of flux required to cool the ocean crust, it seems likely that the vast majority of sulfate must remain in solution and return to the ocean at warm temperatures by diffuse venting off axis (Figure 8.12).

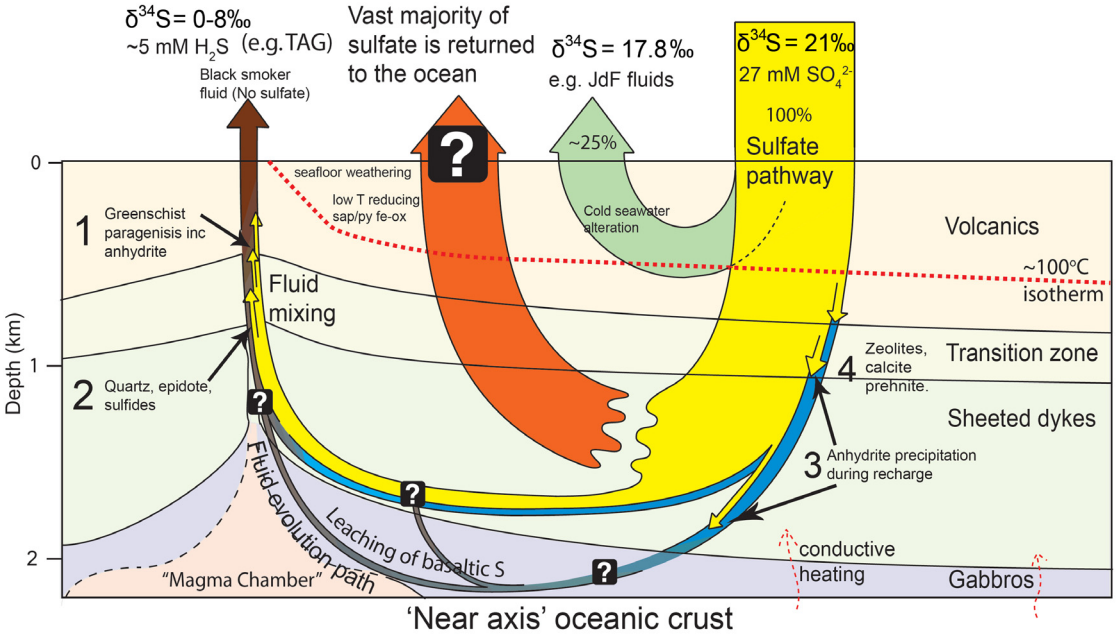

Figure 8.12. Hypothesised hydrothermal flow model for axial and off axial hydrothermal fluid flow depicting fluid evolution and the fate of seawater sulfate.

The petrographic and Sr isotopic distinctions between Group I and group II anhydrites at Site 1256 point towards two phases of anhydrite precipitation, one with early mixing of recharge fluids with upwelling hydrothermal fluids followed by later seawater dominated anhydrite precipitation during recharge. The $^{87}Sr/^{86}Sr$ ratios of the anhydrites formed though mixing of recharge fluids with hydrothermal fluids suggests that evolved recharge fluids have very low Sr concentrations.

The Sr/Ca and $^{87}Sr/^{86}Sr$ of Site 1256 anhydrites point to a similar fluid evolution pathway to that of Site 504 (Teagle et al., 1998). This suggests that Sr/Ca ratios reduced

during recharge before significant Sr exchange with the host basalts and that mixing of seawater, which has low Sr and high SO_4 with hydrothermal fluid, which has high Sr concentrations and only very low SO_4 took place.

The presence of anhydrite with a ~400^{o}C formation temperature at a dyke contact breccia implies that sulfate can still precipitate at extremely high temperatures within the ocean crust. In addition, the MORB-like REE pattern and low Sr-isotopic composition suggest at very high temperatures the host rock readily exchanges Sr and will transfer REE, to the fluid.